

# Gaseous Hydrocarbon Synfuels from H<sub>2</sub>/CO<sub>2</sub> based on Renewable Electricity

## Kinetics, Selectivity and Fundamentals of Fixed-Bed Reactor Design for Flexible Operation

zur Erlangung des akademischen Grades eines  
DOKTORS DER INGENIEURWISSENSCHAFTEN (Dr.-Ing.)

der Fakultät für Chemieingenieurwesen und Verfahrenstechnik des  
Karlsruher Institut für Technologie (KIT)

genehmigte  
DISSERTATION

von  
María Iglesias González  
aus León (Spanien)

Referent: Prof. Dr.-Ing. Georg Schaub

Korreferentin: Prof. Dr.-Ing. Bettina Kraushaar-Czarnetzki

Tag der mündlichen Prüfung: 21. Dezember 2015



*para mis padres*



# Contents

<b>1</b>	<b>Introduction</b>	<b>1</b>
1.1	Transformation of energy production systems: the role of renewable energy in the electrical supply system . . . . .	1
1.2	Storage of renewable electricity in form of chemical energy carriers: electricity-to-fuel . . . . .	6
1.3	CO <sub>2</sub> as C-source for chemical fuels . . . . .	10
1.3.1	Overview of potential CO <sub>2</sub> conversion routes . . . . .	10
1.3.2	CO <sub>2</sub> sources and availability . . . . .	11
<b>2</b>	<b>Objectives and approach</b>	<b>15</b>
<b>3</b>	<b>Literature review</b>	<b>19</b>
3.1	CO <sub>2</sub> hydrogenation to gaseous hydrocarbons . . . . .	19
3.1.1	Iron catalyst . . . . .	20
3.1.2	Reaction mechanism and organic product . . . . .	23
3.1.3	Thermodynamics . . . . .	26
3.1.4	Kinetics . . . . .	28
3.1.5	Iron catalyst deactivation . . . . .	29
3.2	Flexible operation of catalytic reactors . . . . .	32
3.2.1	Catalyst behaviour . . . . .	32
3.2.2	Industrial reactors . . . . .	35
<b>4</b>	<b>Preliminary studies</b>	<b>41</b>
4.1	Substitute Natural Gas (SNG) heating value adjustment using Fischer-Tropsch Synthesis . . . . .	41
4.1.1	Specifications for calculations . . . . .	42
4.1.2	Stand-alone plant . . . . .	43
4.1.3	Combination with methane synthesis . . . . .	46
4.1.4	Conclusion: heating value adjustment using Fischer-Tropsch synthesis	48
4.2	Effects of part-load operation of synthesis reactor on size of H <sub>2</sub> storage and reactor . . . . .	49
4.2.1	Estimation procedure and assumptions . . . . .	49

4.2.2	Case study: electricity production from an example wind farm . . .	54
4.2.3	Conclusion and motivation for flexible operation of a synthesis reactor	57
<b>5</b>	<b>CO<sub>2</sub> hydrogenation with iron catalyst, effect of catalyst composition and reaction conditions: experimental study</b>	<b>61</b>
5.1	Iron-based catalyst promoted with potassium: selection and preparation . .	61
5.2	Experimental plan and reaction conditions . . . . .	62
5.3	Experimental setups, procedures and methods . . . . .	63
5.3.1	Experimental studies in lab-scale fixed-bed reactor . . . . .	63
5.3.1.1	Experimental setup . . . . .	63
5.3.1.2	Procedure and methods . . . . .	65
5.3.1.3	Analysis of products . . . . .	66
5.3.1.4	Data analysis and definitions . . . . .	66
5.3.2	Supporting in-situ magnetic measurements . . . . .	69
5.3.3	Supporting in-situ and ex-situ measurements with X-ray diffractometer . . . . .	70
5.4	Experimental results and discussion . . . . .	72
5.4.1	Catalyst activity and selectivity in lab-scale fixed-bed reactor . . .	72
5.4.1.1	Catalyst formation . . . . .	72
5.4.1.2	Catalyst stability at reference conditions . . . . .	74
5.4.1.3	Variation of modified residence time . . . . .	75
5.4.1.4	Variation of ratio $(H_2/CO_2)_{in}$ and pressure . . . . .	78
5.4.1.5	Variation of temperature . . . . .	80
5.4.1.6	Effect of ratio $(p_{H_2O}/p_{H_2})_{out}$ on 100 g Fe / 2 g K . . . . .	83
5.4.1.7	Modeling of hydrocarbon product distribution . . . . .	85
5.4.2	Supporting in-situ and ex-situ measurements (X-ray diffractometer and magnetometer) . . . . .	86
5.4.2.1	Catalyst reduction . . . . .	86
5.4.2.2	Catalyst formation . . . . .	88
5.4.2.3	Analysis of fresh and spent catalyst samples: ex-situ XRD	90
5.5	Conclusion: selection of catalyst and operating conditions for heating value adjustment . . . . .	91
<b>6</b>	<b>Determination of CO<sub>2</sub> hydrogenation kinetics under steady-state conditions: mathematical modelling studies</b>	<b>95</b>
6.1	Fixed-bed reactor mathematical model . . . . .	95
6.2	Procedure to determine set of kinetic parameters . . . . .	97
6.3	Set of kinetic parameter values for CO <sub>2</sub> hydrogenation: 100 g Fe / 2 g K .	98
6.4	Range of validity of the kinetic parameters . . . . .	101

<b>7</b>	<b>Iron catalyst behaviour under variable operating conditions: experimental and mathematical modelling studies</b>	<b>103</b>
7.1	General approach . . . . .	103
7.2	Step change experiments combined with mathematical modelling . . . . .	105
7.2.1	Experimental setup and procedure . . . . .	105
7.2.2	Development of a mathematical model for the lab-scale setup . . . . .	106
7.2.2.1	Model equations . . . . .	106
7.2.2.2	Solution procedure . . . . .	109
7.2.2.3	Validation . . . . .	109
7.2.3	Example results . . . . .	110
7.2.3.1	Step change in inlet concentration . . . . .	110
7.2.3.2	Step change in inlet volumetric flow . . . . .	114
7.2.3.3	Step change in reactor temperature . . . . .	116
7.3	Magnetometer and XRD: in-situ techniques . . . . .	117
7.3.1	Results and discussion . . . . .	117
7.3.1.1	Step change in inlet concentration . . . . .	118
7.3.1.2	Step change in temperature . . . . .	120
7.4	Periodic changes . . . . .	120
7.5	Conclusion: catalyst behaviour under variable operating conditions . . . . .	124
<b>8</b>	<b>Industrial fixed-bed reactor design for part-load and transient operation: conceptual studies</b>	<b>125</b>
8.1	Multitubular fixed-bed reactor with recycle for CO <sub>2</sub> hydrogenation to gaseous hydrocarbons . . . . .	125
8.2	Single tube reactor model and catalyst particle . . . . .	130
8.2.1	Tube model equations . . . . .	130
8.2.2	Radial heat transport . . . . .	133
8.2.3	Catalyst particle: eggshell . . . . .	134
8.3	Recycle system for part-load operation . . . . .	135
8.3.1	Design procedure for the given design restrictions of the catalytic CO <sub>2</sub> hydrogenation . . . . .	135
8.3.2	Example results . . . . .	138
8.3.2.1	Selection of values for operation and design variables . . . . .	138
8.3.2.2	Reference case: tube diameter 3 cm and load range 70 - 100 % . . . . .	140
8.3.3	Simulation of example load change in a recycle reactor 100 to 70 % with a rate of 5 %/ min . . . . .	142
8.3.4	Characteristic times of the processes involved in a fixed-bed catalytic reactor . . . . .	145

8.4	Effects of chemical reaction/catalyst characteristics on reactor design for part-load operation . . . . .	150
<b>9</b>	<b>Conclusion and outlook</b>	<b>155</b>
<b>10</b>	<b>Summary</b>	<b>161</b>
<b>11</b>	<b>Zusammenfassung</b>	<b>173</b>
	<b>References</b>	<b>187</b>
	<b>Notation</b>	<b>205</b>
	<b>Appendix</b>	<b>213</b>
A	Heating value adjustment using Fischer-Tropsch Synthesis: combination Fischer-Tropsch and methane synthesis, extra figures . . . . .	213
B	Effects of part-load operation of synthesis reactor on size of H <sub>2</sub> storage and reactor: electricity production according to a sinus wave function . . . . .	216
C	Experimental studies in lab-scale fixed-bed reactor: plan and conditions . . . . .	220
D	Analysis of products: supporting information . . . . .	221
D.1	Offline gas chromatograph . . . . .	221
D.2	Online Gas Chromatograph . . . . .	223
D.3	Micro-GC . . . . .	227
E	Supporting results: in-situ and ex-situ measurements . . . . .	227
E.1	Magnetometer setup . . . . .	227
E.2	X-ray diffractometer setup . . . . .	228
E.3	Diffraction pattern for phase determination . . . . .	229
E.4	Catalyst reduction: Magnetometer . . . . .	231
E.5	Catalyst reduction: Diffraction patterns, X-ray diffractometer . . . . .	232
E.6	Catalyst formation . . . . .	237
E.7	Supporting ex-situ measurements: fresh and spent catalyst samples . . . . .	238
F	Experimental studies in lab-scale fixed-bed reactor: extra figures . . . . .	241
G	Basic dimensionless numbers . . . . .	243
H	Calculation of physical properties for a gas mixture . . . . .	243
H.1	Gas density, $\rho_g$ . . . . .	243
H.2	Dynamic viscosity, $\eta_g$ . . . . .	243
H.3	Kinematic viscosity, $\nu_g$ . . . . .	244
H.4	Binary molecular diffusion coefficient, $D_{12}$ . . . . .	244
H.5	Specific heat capacity, $c_{p,g}$ . . . . .	244
H.6	Thermal conductivity, $\lambda_g$ . . . . .	245



I	Transport coefficients: gas - catalyst particle . . . . .	246
I.1	Mass transfer coefficient gas-catalyst particle, $\beta$ . . . . .	246
I.2	Heat transfer coefficient gas-catalyst particle, $\alpha_g$ . . . . .	246
I.3	Mass transfer in the catalyst particle- effective pore diffusion coefficient, $D_{\text{eff}}$ . . . . .	246
I.4	Transport coefficients in fixed-bed reactor . . . . .	247
I.5	Axial dispersion-Peclet Axial- Bodenstein Number . . . . .	247
I.6	Thermal conductivity of the catalyst bed $\lambda_{\text{bed}}$ . . . . .	247
I.7	Effective radial thermal conductivity of the catalyst bed, $\lambda_{\text{eff,r}}$ . . .	248
I.8	Heat transfer coefficient at the internal reactor wall, $\alpha_{\text{wall}}$ . . . . .	249
J	Lab-scale fixed-bed reactor: mathematical model . . . . .	249
K	Determination of CO <sub>2</sub> hydrogenation kinetics under steady-state conditions: extra figures . . . . .	251
L	Solution of ordinary and partial differential equations . . . . .	254
L.1	Method of lines (MOL) . . . . .	255
M	Iron catalyst behaviour under variable operating conditions: experiments in lab-scale setup . . . . .	257
M.1	Characterization of the lab-scale setup . . . . .	257
M.2	Validation of the lab-scale mathematical model . . . . .	259
M.3	Extra experimental results for step changes combined with mathematical model . . . . .	260
M.3.1	Step changes in inlet concentration . . . . .	260
M.3.2	Step change in inlet volumetric flow . . . . .	263
M.3.3	Step change in reactor temperature . . . . .	264
M.4	Periodic changes . . . . .	265
N	Industrial fixed bed reactor design for part-load and transient operation: extra figures . . . . .	267
N.1	Heat transport in fixed-bed reactor . . . . .	267
N.2	Evaluation of criteria to use a pseudo-homogeneous mathematical model to describe the fixed-bed reactor . . . . .	271
N.3	Reactor with recycle: recycle compressor and separation units . . .	272
N.3.1	Recycle compressor . . . . .	272
N.3.2	Separation units needed for the CO <sub>2</sub> hydrogenation to gaseous hydrocarbons . . . . .	273
N.4	Design procedure for a recycle system with only temperature limitations . . . . .	274
N.5	Reference case recycle system: extra figures . . . . .	275
N.5.1	Effect of design variables on recycle system design . . . . .	277
N.6	Simulation of transient operation: extra figures . . . . .	280

N.7	Simulation of example load change in a recycle reactor 100 to 70 % : step change in fresh feed flow . . . . .	281
N.8	Characteristic times . . . . .	284

# 1 Introduction

*The only way of combining economic growth and low energy-related emissions, with an expected population of 9 billion by 2050, is through a transformation of the energy production system: from fossil to renewable resources, presumably those of wind and solar power (IEA 2015; Jess et al. 2011). The transition to a renewable energy system constitutes a major challenge for today's society. This chapter discusses the role of renewable energy in the electrical supply system and focuses on the necessity of long-term storage technologies. The conversion of electrical energy into chemical energy is presented together with the possibility to use CO<sub>2</sub> as carbon source.*

## 1.1 Transformation of energy production systems: the role of renewable energy in the electrical supply system

Present primary energy production in Germany is 80 % based on chemical energy carriers: organic raw materials from fossil sources such as petroleum, natural gas and coal together with biomass from renewable sources (i.e. bio-oils and biogas). The remaining 20 % corresponds to nuclear and renewable energies (i.e. solar, wind, water) (Table 1.1, year 2014). A transformation of the energy system is required to decrease fossil CO<sub>2</sub> emissions. Renewable energies need to substitute fossil resources for the production of electricity and heat (Table 1.2). Primary energy production in the future will be mainly based on electricity with a small contribution of chemical energy carriers, only in those sectors where advantages are present (e.g. transportation sector: liquid fuels, due to its high energy density). These chemical energy carriers should be produced based on non-fossil resources (e.g. biomass, CO<sub>2</sub>) and electricity.

In the present energy system, energy production follows fluctuations in demand. Due to the increasing contribution of renewable energies (RE) from fluctuating sources (i.e. wind and solar power), the energy system needs to become more flexible and operate with fluctuations in production and in demand. The flexibility of the energy system can be increased by electrical grid reconstruction and expansion, flexible operation of

thermal power plants, and flexible demand (Brunner et al. 2013). The remaining imbalance between supply and demand must be covered by storage. Storage systems will play an important role in the future energy system and become an integral part of future renewable-based infrastructures.

Different scenarios have already been calculated based on various assumptions (e.g. scenario A, scenario B, scenario 100 % in BMU (2010), grid development plan A2024, B2024, B2034, C2024 in Netzentwicklungsplan Strom (2015) and UBA 2050, UBA (2014a)). The BMU 2010 scenario A (average) and the UBA 2050 are selected in the present study; the first one due to the high detail of information and the second one because it describes one of many possibilities of achieving a greenhouse-gas (GHG)-neutral Germany ( $< 1 \text{ t CO}_{2\text{eq}}/\text{person year}$ ) based on a renewable energy supply. According to both scenarios the total primary energy demand is expected to decrease by 30 to 50 % by 2050 (Table 1.1).

Table 1.1: Total primary energy consumption divided by primary energy carrier (%) and Green-house-gas (GHG) emissions in  $\text{Mt CO}_{2\text{eq}}/\text{year}$  in Germany. Data for 1990 and 2014: AG Energiebilanzen (2014), AG Energiebilanzen (2015), GHG emissions data from BMU (2012) and UBA (2015); Data for 2020 and 2050 (BMU): scenario A BMU (2010); Data for 2050 (UBA): UBA (2014b)

		1990	2014	2020	2050 (BMU)	2050 (UBA)
Total	PJ/year	14905	13077	11266	7534	10800
Coal	%	37	25	20	2	0
Natural Gas	%	16	21	25	19	0
Petroleum	%	35	35	34	23	0
Nuclear	%	11	8	3	0	0
Renewable Energies	%	1	11	19	55	100
GHG emissions	$\text{Mt CO}_{2\text{eq}}/\text{year}$	1214	912	710	233	60

## Secondary energy production

Secondary energy or end energy production is the result of the conversion of primary energy in an end use form of energy (e.g. coal/natural gas in electricity). The secondary energy flow is lower than primary energy due to conversion losses and export.

Electricity generation in 2014 accounted for approx. 21 % of the secondary energy. Table 1.3 shows the electricity production according to the primary energy. The use of natural gas for electricity generation has increased markedly since 1990. Natural gas can increasingly be used as balancing energy for electricity generation due to the increasing presence of fluctuating renewable energies. In the future, electricity generation will be based to a larger extent on wind and solar sources and could be considered a primary instead of a

Table 1.2: Summarized overview about today energy system and future trends based on Germany as example of an industrialized country, based on Schaub et al. (2014)

	Today (2015)	Future (2050)
<b>Primary energy supply</b>	based on chemical compounds: coal, petroleum, natural gas (fossil) biomass (renewable)	based on renewable electricity: wind and solar power biomass (chemical compound)
<b>Secondary energy supply</b>	based on chemical compounds	based on electricity and non-fossil chemical compounds
Transport	- gas turbine and combustion engine with petroleum products (liquids)	- gas turbine and combustion engine with chemical fuels from biomass and RE - electric car
Heat	- combustion of fossil chemical compounds in furnaces	- combustion of non-fossil chemical compounds in furnaces - heat production from RE - solar collectors - buildings: reduced heat losses, solar energy - heat pumps
Electricity	- solar (thermal, PV) - wind power - thermal power plants (coal, natural gas) - nuclear power plant - hydropower - storage: mechanic (pumped-hydropower, compressed air)	- solar (thermal, PV) - wind power - combined process heat-power (non fossil chemical compounds) - fuel cells (non-fossil chemical compounds) - hydropower, tidal power, wave power - storage: mechanic, chemical, electrochemical, thermal
fossil CO <sub>2</sub> emissions	high (due to combustion of fossil fuels)	low (only due to industrial processes)

secondary energy. A reliable and affordable energy storage system is a prerequisite for the efficient use of the renewable energies.

Table 1.3: Electricity production (%) in Germany without imports of renewable energy. References: data for 1990 and 2014, AG Energiebilanzen (2014) and AG Energiebilanzen (2015), except GHG emissions from BMU (2012); data for 2020 and 2050 (BMU): scenario A BMU (BMU 2010); data 2050 (UBA): (UBA 2014)

	1990	2014	2020	2050 (BMU)	2050 (UBA)
Coal	57.0	43.3	37.7	2.3	0.0
Natural Gas	6.5	9.5	17.6	10.2	0.0
Petroleum	2.0	1.0			0.0
Nuclear	28.0	15.8	5.0	0.0	0.0
Renewable Energy (RE)	3.2	26.2	40.0	87.2	100.0
RE fluctuating (windenergy / photovoltaic)	0.0	56.6	67.5	74.6	86.1
RE non-fluctuating (hydropower, biomass, geothermal)	100	43.4	32.5	25.4	13.9

Heat generation in 2014 accounted for 51 % of the secondary energy. Heat production has a high potential regarding efficiency and decarbonisation. Buildings consume more than two thirds of the thermal energy in Europe and in the present around 60 % is produced from natural gas. Process industry is the other big heat consumer (European Commission 2015). Nearly all industrial chemical processes are based on the use of heat (high and medium temperature process heat) as source of energy for the chemical reaction, apart from very few processes using electrical energy (e.g. chlorine and soda production). Only 20 % of the input energy is used as electrical energy in typical chemical processes (5 % in the case of petroleum refining sector). The integration of renewable energies in the chemical industry (e.g. methanol, ammonia), reducing heat demand and CO<sub>2</sub> emissions, can be done by the production of reactants from renewable sources (e.g. H<sub>2</sub> from electrolysis)(Centi et al. 2013).

The transportation sector in 2014 accounted for 28 % of end energy supply mostly based on petroleum products (from petroleum refining). Liquid hydrocarbons will likely be indispensable as fuels in air traffic due to its high volumetric and gravimetric density. Chemical fuels may be produced from renewable energy and a non-fossil C-source (e.g. CO<sub>2</sub> or biomass). The use of CO<sub>2</sub> as C-source for the production of chemical fuels is discussed in section 1.3.

According to the German Federal Environment Agency (UBA) it will be possible to reach a 100 % renewable energy scenario in 2050. The proposed distribution of end energy is: electric power (30 %), methane (36 %) via Power-to-Gas (PtG) and liquid fuels (34 %) via Power-to-Liquids (PtL). This scenario needs a major increase in electricity production.

### **Greenhouse gas (GHG) emissions**

GHG are a group of gases that can absorb and emit infrared radiation, the fundamental cause of the greenhouse effect. Greenhouse gases include CO<sub>2</sub>, CH<sub>4</sub>, N<sub>2</sub>O, fluorocarbons, H<sub>2</sub>O and O<sub>3</sub>. CO<sub>2</sub> is the most significant greenhouse-gas, accounting for around 88 % of all emissions. Most of the CO<sub>2</sub> is released due to combustion of fossil fuels. Emissions of CH<sub>4</sub> are caused predominantly by animal husbandry, fuel distribution and landfills.

The energy sector (mainly electricity and heat generation) accounts nowadays for more than 80 % of the total GHG emissions in Germany, mainly due to the lower efficiency of the processes used (thermal power plants) and the CO<sub>2</sub> emissions of the chemical fuels used. The specific CO<sub>2</sub> emissions of natural gas are considerably lower than that of coal (e.g. lignite 92.6 kg CO<sub>2</sub>/GJ, bituminous coal 88.3 kg CO<sub>2</sub>/GJ, natural gas 49.4 kg CO<sub>2</sub>/GJ, (Schaub et al. 2011)). Other sources of CO<sub>2</sub> emissions are industrial processes 8 %, agriculture 7 % and waste 3 %.

The expansion of renewable energies makes a major contribution in the reduction of CO<sub>2</sub> emissions in the electricity production sector. According to UBA, assuming an energy supply system based on renewable energies, GHG emissions from electricity can be reduced to virtually zero and emission of CO<sub>2eq</sub> will be mainly connected with industrial processes, solvents and other product applications (14 Mt CO<sub>2eq</sub>/year) and agriculture (35 Mt CO<sub>2eq</sub>/year).

This transformation of the energy system presents numerous challenges and requires the development of effective and economically attractive new technologies adapted to the new context. Within the scope of this work, two aspects are considered in detail:

- Long-term storage of renewable electricity: transformation of electrical energy in chemical energy (electricity-to-fuel process chain)
- Production of chemical energy carriers based on non-fossil resources: CO<sub>2</sub> is evaluated as C-source for the production of chemical fuels

## 1.2 Storage of renewable electricity in form of chemical energy carriers: electricity-to-fuel

Figure 1.1 shows the electricity demand in Germany together with the fluctuating electricity production from wind power and photovoltaic (PV) during two example weeks in April 2013. Weekends can be identified with a lower energy demand, whereas weekdays have a higher demand, showing a characteristic pattern. The generation patterns for wind and PV are strongly different. PV has a day-night rhythm that strongly correlates with the daily demand and a fluctuation in the average feed-in production between summer and winter. Wind power can also be distinguished in daily and seasonal feed-in patterns, however compared to PV the nature of wind profiles are noticeably more stochastic, with high rates of change and potentially longer periods of zero input (Brunner et al. 2013; Jarass et al. 2009). During the two weeks shown in Figure 1.1, the production of electricity from wind power and PV covers around 13 - 20 % of the electricity demand in 2013. It is planned that by 2050 in Germany, 80 % of the electricity demand is covered by electricity produced from renewable sources (German Federal Government 2014). The curve PV+Wind 2050 is the simulated contribution of renewable energies to electricity production by 2050, which covers 80 % of the electricity demand (assuming the same demand in 2050 as in 2013). The comparison of demand and generation in 2050 shows that electricity is not always produced when it is needed, with time periods of high demand and low generation (e.g. day 10 in Figure 1.1) and time periods with low demand and high generation (e.g. day 13 in Figure 1.1). In these periods of excess situations, that might range between days, weeks or even months, the electric energy should be converted into storable forms of energy.

Energy storage options have different performance characteristics with regard to their response time, maximum storage capacity, lifetime, etc. In general, intermittent renewable electricity can be stored in electrical/electrochemical form (e.g. batteries, super capacitors, electromagnetic), chemical form (e.g. H<sub>2</sub>, hydrocarbons), thermal form (e.g. heat pumps) and mechanical form (e.g. compressed air). Short-term storage (e.g. batteries) have a low energy density (max. 2 MJ/kg or 3 MJ/dm<sup>3</sup>) and, consequently, a low storage capacity to deal with intermittent energy sources like wind or solar during a transition period like shown in Figure 1.1. Batteries, however, are viable alternatives to fossil fuel tanks for vehicles (electric car).

There are several medium-term storage technologies (e.g. in the range of hours) already available with a higher capacity than batteries, some examples are: (i) compressed air storage, where electricity is used to compress air and power is regained by passing the compressed air through a turbine. Storage cycle efficiency ranges between 40 - 50 % and



energy density approx.  $15 \text{ MJ/m}^3$ . Usually the storage is charged at night and discharge occurs during peak load hours. Long storage times will lower the cycle efficiency due to large heat losses. (ii) Elevated water storages (pumped-hydropower), mainly limited by geography, and suitable large reservoirs. (iii) Scaling-up of battery technologies from the smaller-scale applications that are already in place. This is a quite new development but requires cost reductions to be efficient. (iv) Hydrogen storage is technologically ready, but still expensive, and awaiting confirmation of the demand of  $\text{H}_2$  as a chemical energy carrier in the future energy system (e.g. transportation sector or electricity production (fuel cell)).

Long-term storage (e.g. in the range of days, weeks or months) is required in connection with a high contribution of renewable energies to electricity production (Figure 1.1). The most reasonable possibility is the transformation of electrical energy into chemical energy (chemical energy carriers). Chemical fuels similar to those being used nowadays can be produced if a carbon source is available (Droste-Franke et al. 2012; Muradov et al. 2010; Schüth 2011). Chemical energy carriers have in general a high energy density (Table 1.4).

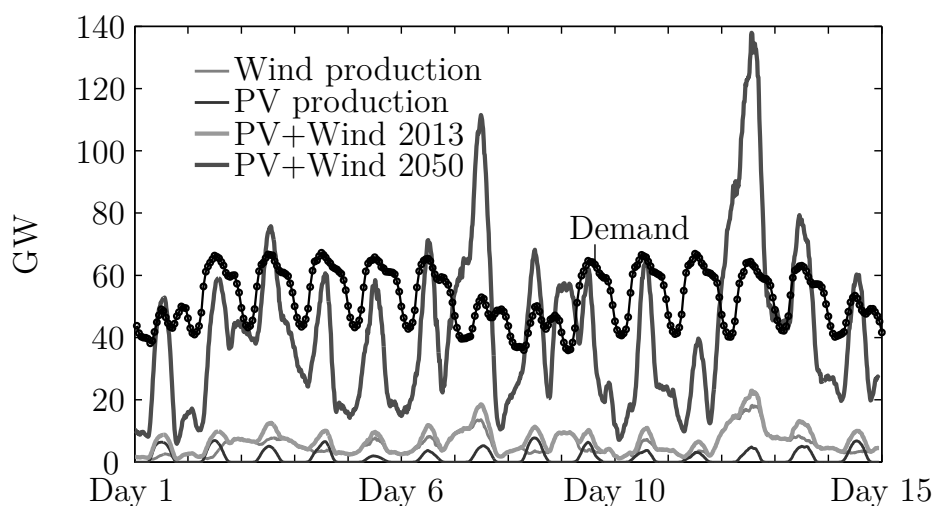


Figure 1.1: Hourly average demand, wind power and photovoltaic generation during two example weeks in Germany. PV+Wind 2050 assumed as factor 6 of the PV+Wind 2013, with factor 6 covering 80 % of electricity demand. Data source: demand (ENTSO-E 2014); wind power generation, (EEX 2014); photovoltaic generation, (TENNET 2014)

The selection of preferred energy carriers will be based on the following criteria: (i) fuel properties with respect to present infrastructures (e.g. energy density, combustion and handling properties); (ii) production cost, depending on availability and price of raw materials and the required process cost for transformation/conversion and (iii) environmental aspects (e.g. generation of pollutants and greenhouse gases during transformation

and combustion). It is presently an open question as to which kind of fuels may become most significant in the future (Schaub et al. 2013; Schüth 2011).

Table 1.4: Gravimetric and volumetric density of different chemical energy carriers.

Based on Schüth (2011) and Schaub et al. (2013)

Compound	Gravimetric density	Volumetric density
	MJ/kg	MJ/dm <sup>3</sup>
H <sub>2</sub>	120	5 (gas, 700 bar)
		8.5 (liq, 20.4 K)
CH <sub>4</sub>	50	9 (gas, 250 bar)
		21 (liq, 111 K)
LPG	46	26
Liquid hydrocarbons	43	35
DME	29	19.3
Ethanol	27	21
Methanol	20	16

### Electricity-to-fuel conversion

Figure 1.2 shows a general flow diagram for electricity-to-fuel conversion. This process chain offers the possibility to store electrical energy in the form of chemical energy carriers. The example here is gaseous hydrocarbons produced from H<sub>2</sub> and CO<sub>2</sub>. These hydrocarbons are fully compatible with today's natural gas grid, therefore transport and distribution grids can be used as storage, with additional underground storage capacities.

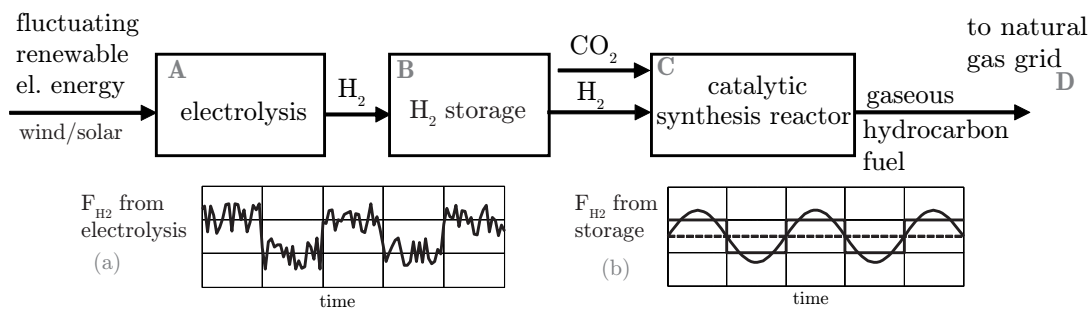


Figure 1.2: Flow diagram of an electricity-to-fuel process chain with H<sub>2</sub> as intermediate and gaseous hydrocarbons as product. (a) Example H<sub>2</sub> flow pattern produced via H<sub>2</sub>O electrolysis from fluctuating electricity, (b) example H<sub>2</sub> flow pattern at storage outlet for the production of hydrocarbon fuels using CO<sub>2</sub>; dashed line: large H<sub>2</sub> storage size, catalytic reactor operating at steady-state conditions; full lines: H<sub>2</sub> storage smaller with two different control strategies, catalytic reactor operating under transient conditions.

## A. Electrolysis

Electrolysis of  $\text{H}_2\text{O}$  is a proven electrochemical technology today for the production of hydrogen at small scale. There are different kinds of electrochemical cells, based on different kinds of electrolyte and electrodes (alkaline, polymer electrolyte membrane, solid oxide). They have different characteristics with respect to module capacity, efficiency, stability and dynamic operation. Today alkaline electrolysis is the cheapest and most reliable technology, however polymer electrolyte membrane (PEM) electrolyzers may be a better choice in the near future due to its fast-response capacities to changes in the electricity input. PEM electrolyser start up or shut down is possible within less than 15 minutes. The solid oxide electrolyser is in the development phase and shows a high potential for coupling with exothermic reactions. Although all of these presently have high specific investment figures (approx. 800 €/kW installed PEM electrolyser), there are positive expectations for investment reduction, high rates of load change, and operability (Smolinka et al. 2011).

## B. $\text{H}_2$ storage

Due to the fluctuating nature of electricity production,  $\text{H}_2$  flow fluctuates and therefore a  $\text{H}_2$  storage is needed to buffer these fluctuations. High pressures are usually needed to store significant amounts of  $\text{H}_2$  due to its low energy density. This causes problems with leaks and materials and requires the use of a compressor. Investment figures for  $\text{H}_2$  stores are, at present, relatively high. Several methods exist for  $\text{H}_2$  storage: compressed gas tanks, cryogenic compressed liquid hydrogen tanks, metal hydride storage, physical storage and underground storage (i.e. salt caverns). The best option for the temporary hydrogen storage are high pressure tanks (until 700 bar) (Götz et al. 2015)

## C. Catalytic reactor

The catalytic reactor commonly proposed for the production of gaseous hydrocarbons ( $\text{CH}_4$  and higher hydrocarbons) is a methanation reactor. Synthesis of methane from  $\text{H}_2/\text{CO}_2$  mixtures was recently proposed as a pathway to produce non-fossil methane, using  $\text{H}_2$  generated via electrolysis with renewable electricity (DENA Power to gas 2012). Hydrogen flows corresponding to typical  $\text{CO}_2$  flows of 500  $\text{m}^3/\text{h}$  (biogas plants), 10000  $\text{m}^3/\text{h}$  (industrial biomass combustion) will be around 2000  $\text{m}^3/\text{h}$  and 40000  $\text{m}^3/\text{h}$ , respectively (see section 1.3).

## D. Natural Gas Network

The gaseous hydrocarbons produced can be fed to the natural gas grid where they are transported and distributed, if they are fully compatible with today's natural gas components. The extensive German natural gas grid infrastructure is already available and offers efficient distribution and storage capacities. Limited amounts of  $\text{H}_2$  can also be fed into the natural gas grid.

The conversion process of electricity to gaseous hydrocarbon links two different energy sectors, electricity and gas. This connection is important because it adds flexibility and robustness to the entire energy system. Overall efficiencies for this process chain are envisaged to be around 60 % (as heating value of product gas per energy unit electricity). Losses could be decreased by using part of the thermal energy from the process in some suitable way (e.g. in combination with a high temperature electrolyser). The gaseous hydrocarbons could be reconverted to electricity (round-trip conversion efficiency approx. 36 %, assuming a power plant efficiency of 60 %) or used for other purposes (e.g. for transport, heat). There are several R&D projects ongoing in Germany, and the present time projection foresees commercial application from 2020 onward (DENA Power to gas 2012). Gahleitner (2013) gives an overview of electricity-to-fuels demonstration plants. The generation costs for SNG strongly depend on the annual operational time and the electricity price. Compared with natural gas (approximately 2-3 ct/kWh) the costs are higher (4 - 60 ct/kWh)(Götz et al. 2015).

### 1.3 CO<sub>2</sub> as C-source for chemical fuels

The production of CO<sub>2</sub>-based chemical fuels becomes reasonable only if direct use of renewable H<sub>2</sub> is not possible. The chemical conversion of H<sub>2</sub> in a further step always means a loss in energy efficiency, therefore the direct use of H<sub>2</sub> is always more efficient and should be favoured. As a carbon-containing raw material, CO<sub>2</sub> is relatively cheap and most abundant, with a low or even negative value. CO<sub>2</sub> is often considered as a waste, with a cost of disposal, instead of a resource. CO<sub>2</sub> is rather inert and its reactions are energetically highly unfavourable. In principal, the first issue can be solved with a good catalyst, however, the latter one is of thermodynamic origin and not solvable by catalysts. However, under certain operation conditions (temperature or pressure), a practical process might be feasible. The critical aspect is to provide the energy for the reaction, to overcome the thermodynamic barrier (Müller et al. 2014; Xiaoding et al. 1996).

#### 1.3.1 Overview of potential CO<sub>2</sub> conversion routes

The use of CO<sub>2</sub> worldwide can be divided in two different groups: (i) those using its physical properties (e.g. beverage industry, (0.75 MtCO<sub>2</sub>/year), enhanced oil recovery (6 - 7 MtCO<sub>2</sub>/year), dry ice used in refrigeration to replace CFCs (solid CO<sub>2</sub>, 1.5 MtCO<sub>2</sub>/year); (ii) those using its chemical properties (e.g. CO<sub>2</sub> as reactant) in the organic chemical industry: synthesis of urea (production of fertilizers and plastics), methanol, salicylic acid (pharmaceutical ingredient) or polycarbonates. The consumption of CO<sub>2</sub> in the produc-

tion of chemicals is in the order of 50 Mt CO<sub>2</sub>/year. The present uses of CO<sub>2</sub> account for 0.18 % of the global CO<sub>2</sub> emissions (32300 Mt CO<sub>2</sub> in 2014 (IEA 3.2015)).

In general there are four approaches to chemically transform CO<sub>2</sub>: (i) use a high energy starting material (e.g. H<sub>2</sub>, unsaturated compounds, small member ring compounds or organometallics); (ii) choose oxidized low-energy synthetic targets (e.g. organic carbonates); (iii) shift the equilibrium to the product side by removing a particular compound; (iv) supply physical energy such as light or electricity, this option becomes attractive in an electricity-based future energy system where the conversion of CO<sub>2</sub> may also be viewed as a way to store renewable energy (Centi et al. 2013).

The most intensively investigated route to transform CO<sub>2</sub> is the hydrogenation either to hydrocarbons (i.e. methane, short chain alkanes, short chain alkenes) or to oxygenates (i.e. alcohols and acids such as methanol, ethanol, dimethylether or formic acid). The reduction of CO<sub>2</sub> with hydrocarbons (commonly methane) to produce syngas (dry reforming of methane) is available in near industrial scale. In the long-term future, routes for CO<sub>2</sub> conversion could involve electrochemical, photo-electrochemical and photo-catalytic conversions (i.e. reduction of CO<sub>2</sub> using solar radiation). Biological conversion of CO<sub>2</sub> (e.g. production of chemical fuels by the use of micro-algae) are potential alternatives to the chemical processes.

### 1.3.2 CO<sub>2</sub> sources and availability

Most of the chemical processes necessary for the electricity-to-fuel process require a high concentrated CO<sub>2</sub> feedstock, free of impurities to avoid catalyst poisoning. In the short-medium term CO<sub>2</sub> conversion technologies will probably be a side process of carbon capture and storage. However, CO<sub>2</sub> capture from diluted flows requires energy. Jess et al. (2011) calculate the energy requirements of concentrating CO<sub>2</sub> from a gas mixture from flue gas (11 vol %) and from air (300 ppm) based on thermodynamic laws. An approximate energy demand of 1.2 MJ/kg CO<sub>2</sub> may be taken as first estimation of the energy required for CO<sub>2</sub> separation from flue-gases by chemical absorption and 3.6 MJ/kg CO<sub>2</sub> in the case of CO<sub>2</sub> from ambient air. Despite the high energy demand of CO<sub>2</sub> capture from ambient air (factor 3), this option is also considered in the literature (Jess et al. 2011; Weimer et al. 1996; Zeman 2007).

Table 1.5 shows present sources of CO<sub>2</sub> sorted by capacity under standard conditions, large (200000-25000 m<sup>3</sup> CO<sub>2</sub>/h), medium (25000-10000 m<sup>3</sup> CO<sub>2</sub>/h) and small sources (< 600 m<sup>3</sup> CO<sub>2</sub>/h).

Table 1.5: Stationary CO<sub>2</sub> emission sources, concentration and volumetric flow values.

References: Rebsdats et al. (2001), Metz (2005), Graf et al. (2014)

CO <sub>2</sub> emission source	concentration of CO <sub>2</sub> vol %	typical CO <sub>2</sub> flow/ plant m <sup>3</sup> /h (STP)	available in a future renewable energy system ?
Power station flue gas: coal <sup>1</sup>	12 - 15	200000	No
Iron and steel production (iron reduction in a blast furnace oven) <sup>1</sup>	20 - 30	200000	Yes <sup>2</sup>
Power station flue gas: NG <sup>1</sup>	7 - 10	60000	No
Cement industry (incl. calcination of limestone) <sup>3</sup>	14 - 33	60000	Yes <sup>2</sup>
Ammonia (H <sub>2</sub> production via steam reforming)	99.5	25000 <sup>4</sup>	No
Power station flue gas: biomass <sup>1</sup>	3 - 8	20000	Yes
Methanol (H <sub>2</sub> production via steam reforming)	high purity	15000 <sup>5</sup>	No
Ethylene oxide	5 - 10 <sup>6</sup>	12000	Yes
Biomass gasification <sup>7</sup>	10 - 25	10000	Yes
Glass production	60 <sup>7</sup>	600 <sup>7</sup>	Yes <sup>2</sup>
Fermentation: bio-methane <sup>7</sup>	50	500 - 100	Yes
Fermentation: bio-ethanol <sup>8</sup>	99	-	Yes

<sup>1</sup> Metz (2005)<sup>2</sup> UBA (2014b)<sup>3</sup> Size of the cement plant: 1 Mt cement/year, (Lasserre 2007); concentrations: (Ali et al. 2011)<sup>4</sup> Ammonia synthesis: assumed 1.15 tCO<sub>2</sub>/tNH<sub>3</sub> and 1000 tNH<sub>3</sub>/day (Zakkour et al. 2010)<sup>5</sup> Methanol synthesis: from natural gas, 0.25 Mt CO<sub>2</sub>/year/plant (Zakkour et al. 2010)<sup>6</sup> Typical plant: 0.2 Mt CO<sub>2</sub>/year/plant (Rebsdats et al. 2001; Zakkour et al. 2010).<sup>7</sup> Graf et al. (2014)<sup>8</sup> Schweitzer (2014)

Some of the present CO<sub>2</sub> emission sources will not be available in the future, for example flue gas from power stations, due to the production of electricity directly from wind

and solar power (Table 1.3), or CO<sub>2</sub> emissions from H<sub>2</sub> production via steam reforming for ammonia or methanol plants, that can be avoided by the use of H<sub>2</sub> produced via electrolysis. The CO<sub>2</sub> emissions in the cement and steel production might be lower in the future if the thermal energy and electricity demand are produced from renewable sources, however CO<sub>2</sub> emissions can not be completely avoided because CO<sub>2</sub> is a by-product in the calcination of CaCO<sub>3</sub> (approx. 0.5 t CO<sub>2</sub>/t cement) or in the reduction of iron ore to iron metal in the presence of coke.

The most attractive CO<sub>2</sub> sources for the future are biomass fermentation to ethanol, with almost a pure flow of CO<sub>2</sub>, or biomass fermentation to methane with a 50 % volume of CO<sub>2</sub>. However volumetric flows are low. Higher volumetric flows are available from biomass gasification and combustion, industrial processes like iron and steel production, or cement industry but require gas cleaning technologies to remove impurities from the CO<sub>2</sub> flow (e.g. NO<sub>x</sub>, SO<sub>2</sub>). If high CO<sub>2</sub> volumetric flows are required, then either gas cleaning of the CO<sub>2</sub> flow is required or the energy for the CO<sub>2</sub> captured from diluted flows (e.g. ambient air).





## 2 Objectives and approach

The present thesis addresses the following topics:

- The potential to produce gaseous hydrocarbon synfuels ( $C_2H_6$ ,  $C_3H_8$ ,  $C_4H_{10}$ ) from  $H_2$  and  $CO_2$  to adjust the heating value of methane (raw SNG). This topic should be approached based on experimental work considering different catalyst compositions. Evaluation of catalyst stability, activity and selectivity is required to select a promising catalyst to carry out the reaction. Formal kinetics should be determined based on experimental results for the selected catalyst.
- Flexibility of fixed-bed catalytic reactors as a future component of a renewable energy system (flexibility: operation at varying load with frequent changes between different load situations at different rates of load change). A methodology to study transient operation should be developed based on a combination of experimental work and conceptual studies using mathematical models. Catalyst behaviour under variable operating conditions, relevant for industrial operation, needs to be experimentally investigated in the lab-scale setup. Aspects of part-load operation regarding basic design of an industrial fixed-bed reactor and simulation of transient operation should be addressed using example calculations. Characteristics of the chemical reactions should be analysed to inspire similar usage in other fuel-related synthesis with potential to use  $H_2$ -electrolysis.

The approach and overall outline are shown in Figure 2.1. The production of hydrocarbons via Fischer-Tropsch synthesis using iron-based catalyst from  $H_2$  and  $CO_2$  is reviewed based on literature data. A preliminary study shows the potential of the Fischer-Tropsch synthesis to produce gas mixtures of gaseous hydrocarbons which can be used for heating value adjustment of raw substitute natural gas (mainly methane) according to specifications, (see Chapter 4). Chapter 5 summarizes the experimental work carried out in the lab-scale fixed-bed reactor using two different iron-based catalysts together with supporting results from in-situ and ex-situ catalyst characterization techniques. At the end of chapter 5 a catalyst is selected and operating conditions are recommended to produce gaseous hydrocarbons from  $H_2$  and  $CO_2$ . Chapter 6 deals with the mathematical model of the lab-scale reactor and the determination of the formal kinetics for the selected catalyst.

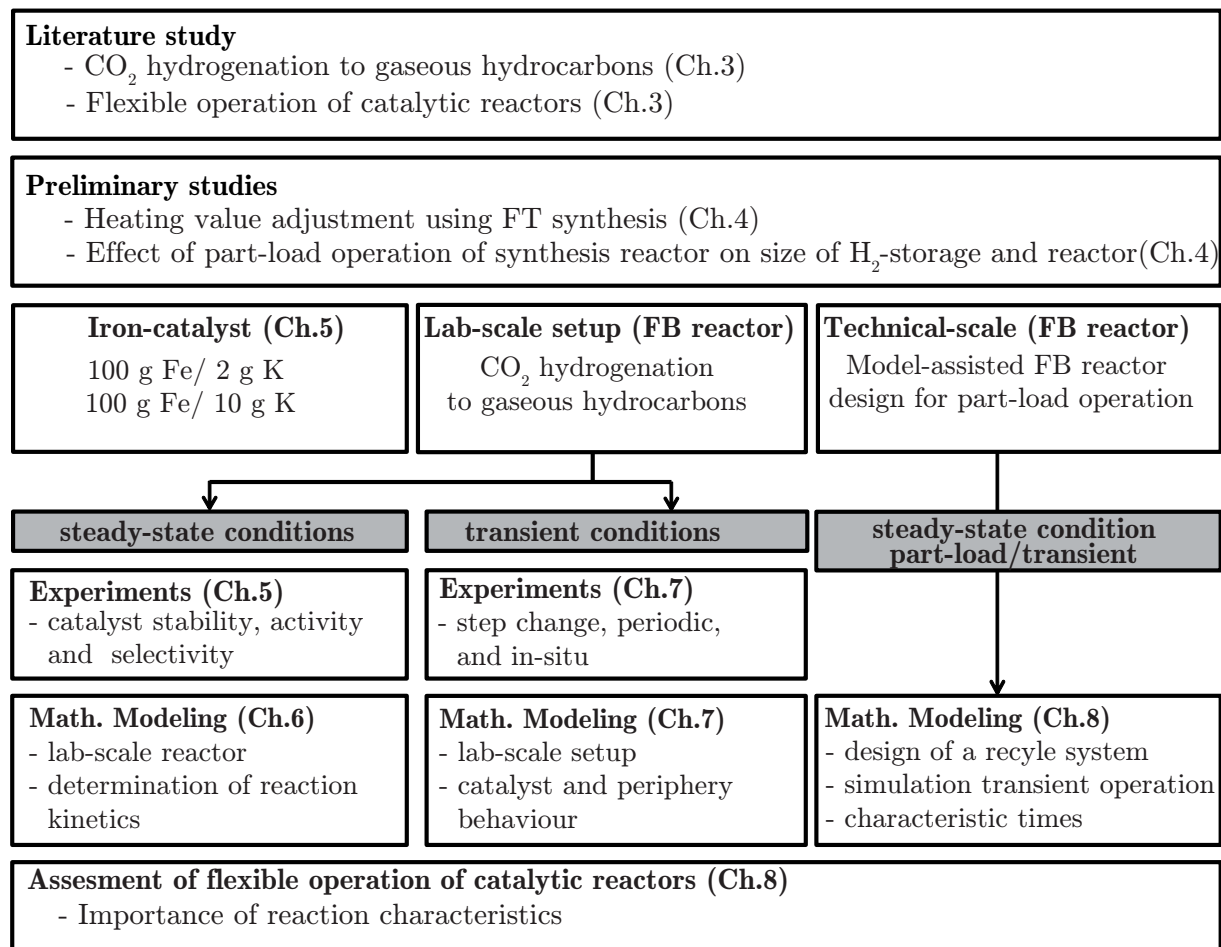


Figure 2.1: Scheme of the approach and outline of this thesis in chapters

Flexible operation of fixed-bed reactors is also investigated using the CO<sub>2</sub> hydrogenation to gaseous hydrocarbons as an example reaction. Research on the field of dynamic operation of catalytic reactors is summarized in chapter 3, with special focus on the removal of nitrogen oxides from flue gases, as it is a catalytic reaction operated under flexible conditions at industrial scale. The motivation and boundary conditions to operate a catalytic reactor under variable load are discussed in chapter 4 based on some example calculations. The behaviour of the catalyst selected in chapter 5 is evaluated under variable operating conditions, relevant for industrial operation. Step-change and periodic experiments are carried out in the lab-scale setup. The analysis of the experimental results is done using a mathematical model of the complete lab-scale setup including the lab-scale reactor. Complementary information about the dynamic behaviour of the catalyst is obtained using in-situ methods (see Chapter 7).

The thesis concludes with conceptual studies regarding part-load operation of industrial fixed-bed reactors for the CO<sub>2</sub> hydrogenation to gaseous hydrocarbons. The formal kinetics (chapter 6) and the information about the catalyst behaviour (chapter 7) are included in the mathematical model. A basic procedure for reactor design is discussed and tran-

sient operation of the recycle system is simulated using a non-steady state mathematical model. Characteristic times for the processes taking place in the catalyst particle and reactor are presented. The potential of other fuel-related chemical reactions to be operated under variable load conditions is qualitatively discussed based on the results obtained with the CO<sub>2</sub> hydrogenation to gaseous hydrocarbons.



## 3 Literature review

*This chapter gives an introduction to the CO<sub>2</sub> hydrogenation to gaseous hydrocarbons, and to the flexible operation of catalytic reactors. The main characteristics of the CO<sub>2</sub>-shift and Fischer-Tropsch reactions on iron-based catalysts are discussed, based on the limited amount of information available in literature. Next, activities involving variable operation of catalytic reactors are summarised, and special attention is given to the NO<sub>x</sub> reduction, as it is an important reaction nowadays which is operated under flexible operating conditions.*

### 3.1 CO<sub>2</sub> hydrogenation to gaseous hydrocarbons

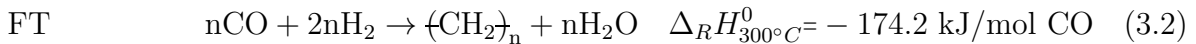
Methane is the most common gaseous hydrocarbon and the main component of substitute natural gas (SNG). Hydrogenation of CO<sub>2</sub> to methane has been widely studied in literature and high conversions and selectivity to methane are reported (e.g. Sabatier et al. (1902), Wang et al. (2011), Kopyscinski et al. (2010), Götz et al. (2015)).

Most of the research to obtain other hydrocarbons different from methane using H<sub>2</sub> and CO<sub>2</sub> has been focused on the production of short chain alkenes as bulk chemicals for the chemical industry (e.g. You et al. (2013), Kim et al. (1998)) or long chain hydrocarbons for transportation fuels (e.g. Riedel et al. (2001), Jess et al. (2011), Fiato et al. (1998)). Little information has been found in literature for the production of short chain alkanes (C<sub>2</sub>H<sub>6</sub>, C<sub>3</sub>H<sub>8</sub>, C<sub>4</sub>H<sub>10</sub>). These hydrocarbons can be used to increase the higher heating value (HHV) of raw SNG, mainly methane (HHV<sub>CH<sub>4</sub></sub> = 39.8 MJ/m<sup>3</sup>), before being fed into a high calorific value gas grid, H-gas (HHV<sub>H-gas</sub> = 40 - 47.2 MJ/m<sup>3</sup>), and replace the use of liquefied petroleum gas (LPG).

Both one or two stage approaches have been analysed for the production of short chain alkanes from H<sub>2</sub> and CO<sub>2</sub>. The two stage approach works either by a CO<sub>2</sub>-shift followed by Fischer-Tropsch (FT) or a stage of CO<sub>2</sub>-to-methanol followed by methanol to olefin, and a subsequent hydrogenation to convert the alkenes (Centi et al. 2009; Fujimoto et al. 1991). Examples of a working one stage approach are (i) use of promoted cobalt-based catalysts (Owen et al. 2013); (ii) use a combination of Fe-based catalysts and zeolites in

composite catalysts (Rongxian et al. 2004); (iii) combine a methanol catalyst (Cu-Zn) and a zeolite with a composite catalyst (Fujimoto et al. 1987).

The CO<sub>2</sub> hydrogenation to hydrocarbons is described in previous studies as a two-step catalytic reaction (Lee et al. 1992; Riedel et al. 2001). The CO<sub>2</sub>-shift reaction converts the CO<sub>2</sub> to the intermediate product CO (Equation 3.1). The CO reacts via the FT reaction to hydrocarbons (Equation 3.2). FT reaction enthalpy is calculated assuming that  $\langle\text{CH}_2\rangle$  is C<sub>3</sub>H<sub>8</sub>.



The direct hydrogenation (DH) is a parallel reaction for the direct conversion of CO<sub>2</sub> to hydrocarbons (Equation 3.3) (Fiato et al. 1998). According to Riedel (2002) the contribution of the DH to the conversion of CO<sub>2</sub> is low compared with the two step reaction path.



### 3.1.1 Iron catalyst

Iron-based catalysts show the most promising properties for the CO<sub>2</sub> hydrogenation to gaseous hydrocarbons, due to its activity for both CO<sub>2</sub>/CO shift and FT synthesis (Riedel et al. 1998) and additional advantage is that they are widely available and relatively cheap. Iron-based FT catalyst precursors consist of iron oxide Fe<sub>2</sub>O<sub>3</sub> crystallites, to which promoters are often added to improve the catalyst performance.

Potassium (K) is an essential promoter in iron catalysts for FT synthesis. The effect of other promoters and supports (e.g. copper to enhance catalyst reducibility, Al<sub>2</sub>O<sub>3</sub> or SiO<sub>2</sub> to improve the catalyst dispersion) is generally small in comparison to that of potassium. The effects of potassium on activity and selectivity were studied by different research groups using a H<sub>2</sub>/CO synthesis gas (e.g. Bukur et al. (1990), Raje et al. (1998)) and using H<sub>2</sub> and CO<sub>2</sub> mixtures (e.g. Choi et al. (1996), Cubeiro et al. (2000), Riedel et al. (2003), You et al. (2013), Martinelli et al. (2014)). Figure 3.1 shows that with increasing K content up to 5 wt %, the conversion of CO<sub>2</sub>, the hydrocarbon yield, and the selectivity to long chain hydrocarbons increases rapidly. The highest selectivity for C<sub>2-4</sub> is obtained for a catalyst with 2 wt% of K, with 40 % of the hydrocarbons being in the fraction alkenes. Further increase in the K content leads to a decrease in the CO<sub>2</sub> conversion and an increase in the alkene formation (catalyst with 32 wt% K, C<sub>2-4</sub> fraction contains 77 % alkenes).

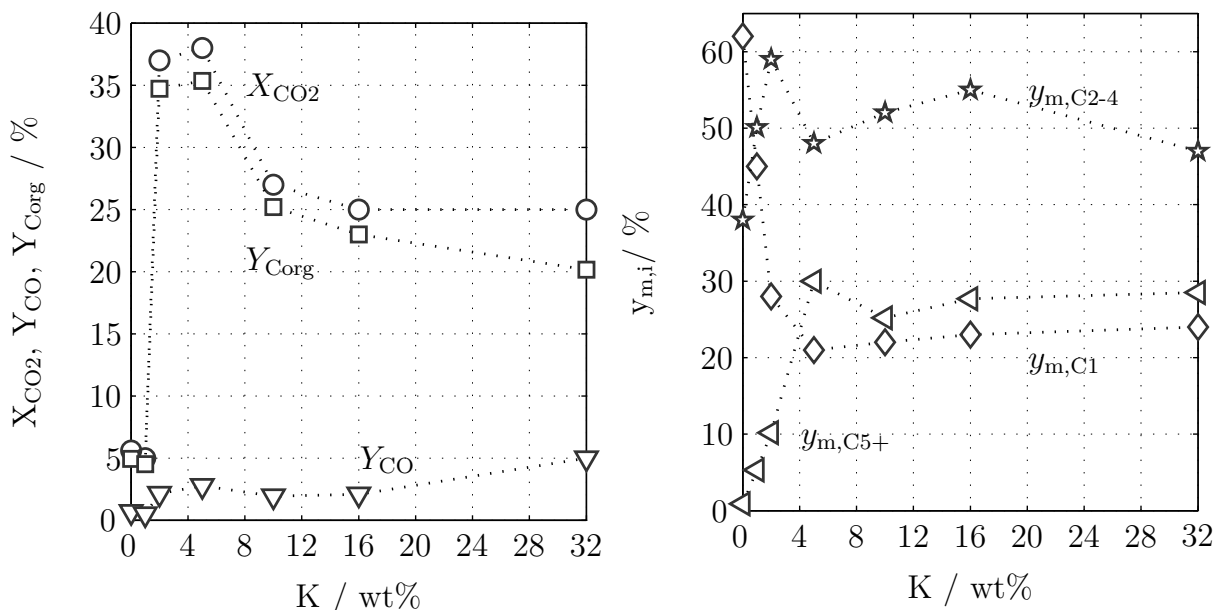


Figure 3.1: Performance of K-modified non supported Fe catalysts with different K contents for  $\text{CO}_2$  hydrogenation reported by You et al. (2013). Conditions:  $T = 340 \text{ }^\circ\text{C}$ ,  $(\text{H}_2/\text{CO}_2)_{\text{in}} = 3$ ,  $p = 2 \text{ MPa}$ ,  $m_{\text{cat}} = 1 \text{ g}$ ,  $\tau_{\text{mod}} = 3000 \text{ kg s/m}^3$ . Results after 10 h of operation.

According to literature, potassium favours C-on-site formation through easier  $\text{CO}/\text{CO}_2$  chemisorption and dissociation (i.e. favours high shift activity, production of high molecular weight hydrocarbons, formation of iron-carbide and inhibition of secondary reactions like hydrogenation). The study of Choi et al. (1996) shows that potassium promotion increases the  $\text{CO}_2$ -shift activity compared with Fe alone at atmospheric pressure and  $300 \text{ }^\circ\text{C}$ . Chemisorption measurements with  $\text{H}_2$  and  $\text{CO}_2$  at different K promotions indicate that  $\text{CO}_2$  chemisorption capacity is enhanced with increasing K whereas that of  $\text{H}_2$  is diminished. According to the results,  $\text{H}_2$  is adsorbed only on Fe and  $\text{CO}_2$  adsorbs favourably on K but also on Fe. With increasing K promotion, K blocks the Fe sites and reduces  $\text{H}_2$  adsorption. At too high potassium promotion, the formation of carbon-on-site is too fast and a solid carbon phase is formed. Carbon accumulates in the catalyst and causes deactivation (Figure 3.2).

The right potassium promotion is essential in Fischer-Tropsch synthesis on iron-catalysts, and affects catalyst activity and selectivity. Typical K values are between 2 - 5 wt % using CO as a reactant. Starting from  $\text{CO}_2$  the concentration of CO is lower (formed via the  $\text{CO}_2$ -shift reaction), therefore at the same K-loading the formation of the active catalyst phases is slower compared with  $\text{H}_2/\text{CO}$  synthesis gas. Higher K amounts are required to hydrogenate  $\text{H}_2/\text{CO}_2$  mixtures compared to  $\text{H}_2/\text{CO}$  (Schulz 2014).

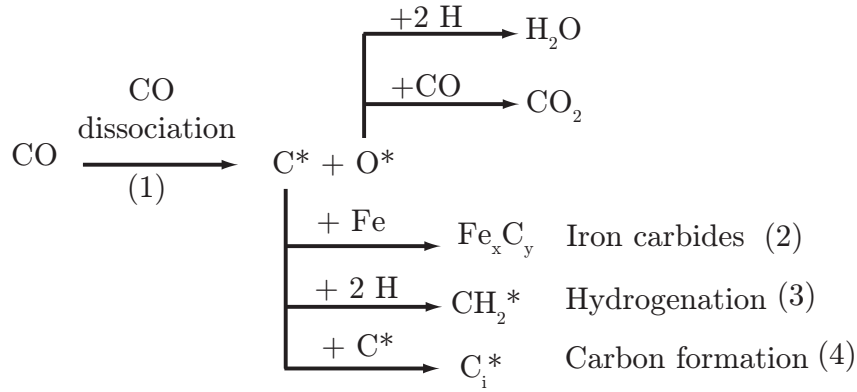
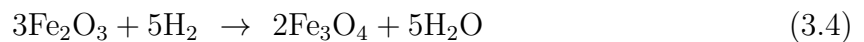


Figure 3.2: Proposed mechanism for CO dissociation in iron catalyst. Elementary reaction steps. Based on Schulz (2014). Active surface sites are represented by \* and  $\text{C}_i$  stands for inactive surface carbon species.

### Proposed active phases

The catalyst precursor (iron oxide  $\text{Fe}_2\text{O}_3$ ) is not active for the FT synthesis, therefore needs to be converted into its active form. During catalyst activation a complex mixture of iron phases is formed. In general, it is recognized that metallic iron, carbidic iron and iron oxides coexist after activation and during FT synthesis. Surface carbidic iron species are consistently agreed upon to be the active phase since the earliest studies in the open literature on this topic. However, even after many recent detailed characterization studies, the exact identity of the active phase(s) remains controversial (Smit et al. 2008).

Catalyst activation starts with the reduction of the iron oxide to metallic iron usually in the presence of  $\text{H}_2$ . In general the reduction takes place in two steps, first, hematite  $\text{Fe}_2\text{O}_3$  is reduced to magnetite  $\text{Fe}_3\text{O}_4$ , and afterwards  $\text{Fe}_3\text{O}_4$  is reduced to metallic iron  $\alpha\text{-Fe}$  (Jin et al. 2000; Jozwiak et al. 2007). The final composition of the catalyst after the reduction depends on the combination of catalyst promoters and reaction conditions (temperature, reduction gas and holding time).



Most of the studies report catalyst activation (transient initial regimes) for the FT synthesis under  $\text{H}_2$  and CO (Niemantsverdriet et al. 1980; Riedel et al. 2003; Schulz et al. 1999). However, some studies have already examined the use of  $\text{CO}_2$  instead of CO during the activation (Gnanamani et al. 2013; Lee et al. 1990; Riedel et al. 2003). Up to six episodes related with catalyst transformations/reconstructions have been identified by Schulz et al. (1999b). According to the authors, a hydrocarbon product with nearly the same composition is obtained at steady state conditions, independent of the gas mixture



(H<sub>2</sub>/CO or a H<sub>2</sub>/CO<sub>2</sub>). Episodes are longer when starting with CO<sub>2</sub>, due to the low partial pressure of CO that slow down the carbiding process (Figure 3.2).

With the H<sub>2</sub>/CO<sub>2</sub> synthesis gas, only traces of CO are present in the product during the first hours. The CO being formed by the CO<sub>2</sub>-shift reaction is adsorbed on the active surface sites of metallic iron (represented by \*) and dissociates to C and O (reaction 1 in Figure 3.2). The dissociation is the rate limiting step. Schulz (2014) proposed, that it is controlled by the amount of potassium. The adsorbed carbon species can further react with the iron species to form iron bulk carbides (reaction 2 in Figure 3.2). This reaction has a low activation energy and takes place readily at typical FT reaction temperatures (Smit et al. 2008). Dissociated CO can react with H<sub>2</sub> to form  $\{-\text{CH}_2\}$ -monomer for chain growth (reaction 3 in Figure 3.2). As long as metallic iron is present, the fastest reaction of dissociated C will be the formation of iron carbide. When more and more carbon species are available (usually due to high potassium promoting), the direct coupling of carbon species is possible and inactive carbon phase is formed on the catalyst surface (reaction 4, in Figure 3.2). Carbon is accumulated on the surface and causes deactivation due to blocking of surface active sites. There are three models (competition model, carbide model and slow activation model) used to explain the catalytically active phase of iron-based FT catalyst and their time-dependent behaviour, all based on the four elementary reactions mentioned and shown in Figure 3.2 (Schulz 2014; Smit et al. 2008).

### 3.1.2 Reaction mechanism and organic product

As previously indicated, the hydrogenation of CO<sub>2</sub> is a two-step reaction. It is well known that magnetite catalyses the CO-shift reaction. It is therefore thought to be the phase responsible for the CO-shift activity of iron-based FT catalyst. It is assumed that the CO<sub>2</sub>-shift reaction follows a mechanism very similar to those proposed for the CO-shift in iron oxides, because no information was found focusing on the mechanism of the CO<sub>2</sub>-shift. Two different mechanisms were proposed to explain the formation of H<sub>2</sub> and CO<sub>2</sub> from H<sub>2</sub>O and CO. Some studies suggest that the appearance of a formate species is intermediate (formate or associative mechanism). The formate species can be formed by the reaction of H<sub>2</sub>O (OH group) and CO in the gas phase or in the adsorbed state, a CO<sub>2</sub> is liberated from the formate species (Newsome 1980; Oki et al. 1973; Spencer 1995). According to Laan et al. (1999), the oxidation or regenerative mechanism is more plausible in connection with the FT synthesis. The reactants separately oxidise or reduce the catalyst surface. The oxygen intermediate can be formed from the dissociation of H<sub>2</sub>O or CO (Lund et al. 1981). Rethwisch et al. (1986) concluded that supported iron oxides operate via a formate mechanism (due to limited change of oxidation state of the iron cations) while unsupported catalysts do so via a direct oxidation. According to Spencer

(1995) the regenerative mechanism is faster than any associative mechanism if catalyst and conditions allow them to operate.

It is generally accepted in the literature that the CO-shift and the FT reaction take place on different types of active sites on the catalyst. Since magnetite is known to co-exist with other iron phases during FT, it plays an important role in determining the overall activity and selectivity of the catalyst (Smit et al. 2008). Magnetite has also been reported as an active phase in FT (Gnanamani et al. 2013).

The exact mechanism for the production of hydrocarbons and oxygenates over iron carbide phases is largely unknown and is a topic of discussion since the first mechanism was proposed in the original paper by Fischer and Tropsch (Fischer et al. 1923; Fischer et al. 1926). Even though it is observed that iron carbide is an active catalyst, it is still disputed in the literature whether or not bulk carbides phases themselves play an active role in the synthesis (Smit et al. 2008). The different mechanisms have been reviewed by several authors. A short overview of the three main mechanisms that have been proposed is given. In general all mechanisms assumed six elementary reaction steps: (i) reactant adsorption; (ii) chain initiation; (iii) chain growth; (iv) chain termination; (v) product desorption; (vi) readsorption and further reaction. They are based on different assumptions of CO activation, formation of the monomer species, and the addition of monomers to growing chains (Bartholomew et al. 2006; Laan et al. 1999). It is likely that all mechanisms contribute to the formation of organic product, however, to what extent this is true is presently unknown.

- The carbene mechanism is the oldest and perhaps most accepted mechanism for FT synthesis on iron. It proposed chain growth by insertion of  $\text{CH}_x$  monomers into metal-carbon bonds. Chain termination can take place either by abstraction or addition of a hydrogen atom from or to the growing chain. This mechanism cannot explain the formation of oxygenates (Figure 3.3).
- The enol mechanism proposes chain growth through undissociative adsorption of CO. Surface hydrogen atoms react with the chemisorbed CO groups to form enol species  $-\text{CH}(\text{OH})$ . The condensation of two enol species yields and adsorbs  $-\text{C}(\text{OH})\text{CH}_3$  species, which is hydrogenated to form an alkene and  $\text{H}_2\text{O}$ . Another possibility is the combination of enol species through a surface polymerization condensation reaction with loss of  $\text{H}_2\text{O}$ .
- The CO insertion mechanism suggests the insertion of CO molecules in the metal-carbon bonds.

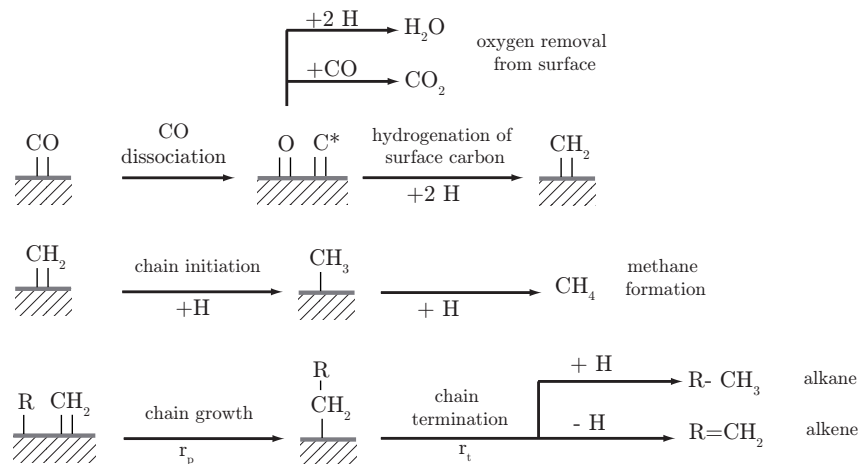


Figure 3.3: Schematic of the carbene mechanism, adopted from Bartholomew et al. (2006).  $r_p$ : rate of chain propagation,  $r_t$ : rate of chain termination. Formation of methane based on Schulz (2007)

During FT synthesis a huge variety of products of different chain length and functionality are formed. The product distribution depends on many reaction variables such as reaction conditions (e.g. temperature, partial pressure of the reactants and product  $H_2O$ ), reaction system, as well as catalyst composition. The main products of the FT synthesis are alkanes and alkenes, mainly  $\alpha$ -alkenes. Typical side products are oxygenates (alcohols, aldehydes, ketones, carboxylic acids) and branched compounds (mainly mono-methyl branched) (Steynberg et al. 2004).

Many mathematical models have been developed to describe FT product distributions. The general product distribution is determined by the ratio of the chain propagation  $r_p$  and chain termination  $r_t$ . A high chain propagation rate will lead to a high molecular weight product distribution, while high termination rate will yield predominantly light products. The most basic model (Anderson-Schulz-Flory) assumes that the FT synthesis is an ideal polymerisation reaction (molar amount of the sum of products for each carbon number decreases exponentially with carbon number), and the product distribution can be predicted by a simple statistical model with the chain growth probability factor,  $\alpha$ , as single parameter (Equation 3.6).

$$\alpha = \frac{r_p}{r_p + r_t} \quad (3.6)$$

According to the Anderson-Schulz-Flory (ASF) model, the molar fraction for each carbon number  $N_C$  is calculated using Equation 3.7

$$y_{n,N_C} = (1 - \alpha) \cdot \alpha^{N_C - 1} \quad (3.7)$$

and the mass fraction is calculated as follows:

$$y_{m,N_C} = N_C \cdot (1 - \alpha)^2 \cdot \alpha^{N_C - 1} \quad (3.8)$$

Figure 3.4 shows the weight fractions of FT hydrocarbon products as a function of the chain growth probability  $\alpha$ . It shows the broad spectrum of products and the complexity to produce one compound or a group of compounds with a high selectivity; only methane can be obtained with 100 % selectivity i.e. at a chain growth probability of zero (methanation). The  $\alpha$  value depends strongly on the catalyst and process conditions. The chain growth probability increases with (i) decreasing temperature, (ii) decreasing  $\text{H}_2/\text{CO}$  partial pressure ratio, and (iii) increasing pressure (Claeys 1997). Typical  $\alpha$  values for iron-based catalysts using  $\text{H}_2$  and  $\text{CO}$  are 0.70 - 0.95 (Bartholomew et al. 2006). Riedel et al. (1999) show that a nearly identical hydrocarbon product composition is obtained using a  $(\text{H}_2/\text{CO})_{\text{in}} = 2.3$  and a  $(\text{H}_2/\text{CO}_2)_{\text{in}} = 2.3$ . This shows that neither methane formation nor chain growth are controlled by the partial pressure of  $\text{CO}$ , in the range investigated.

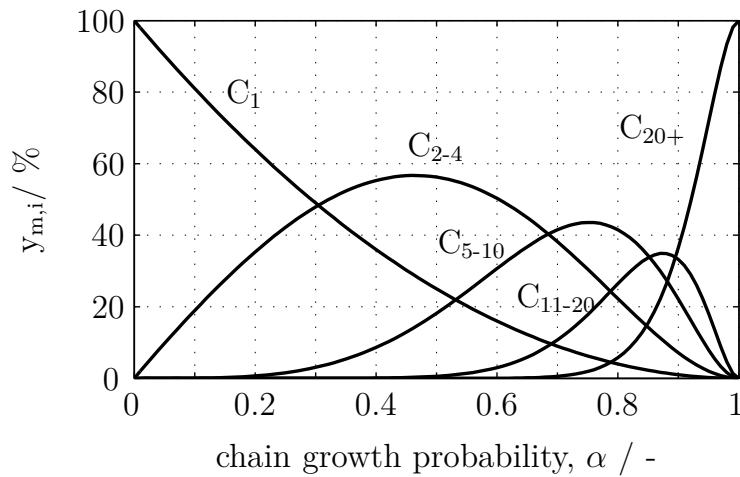


Figure 3.4: Hydrocarbon product distribution in weight C % according to Anderson-Schulz-Flory model as a function of the chain growth probability factor  $\alpha$ , Equation 3.8. Fraction  $\text{C}_{5-10}$ : gasoline,  $\text{C}_{11-20}$ : diesel,  $\text{C}_{20+}$ : wax

The ASF model assumes that only one sort of product is formed and that  $\alpha$  is independent of carbon number. However, significant deviations from the ASF model are reported in the literature, therefore more sophisticated models have been developed considering readsorption of  $\alpha$ -alkene followed by secondary hydrogenation, isomerisation, formation of oxygenates, branching and methanation (Schulz et al. 1995; Schulz et al. 1999).

### 3.1.3 Thermodynamics

The  $\text{CO}_2$ -shift reaction is endothermic, reversible and equimolar (Equation 3.1). The conversion of  $\text{CO}_2$  is determined by the thermodynamic equilibrium and varies between 16 and 43 % (Figure 3.5,  $(\text{H}_2/\text{CO}_2)_{\text{in}} = 3$ ).  $\text{CO}_2$  conversion is favoured at high temperatures, because the reaction is endothermic, but also if an excess of  $\text{CO}_2$  or  $\text{H}_2$  is present (e.g.

( $H_2/CO_2$ )<sub>in</sub> = 5 or ( $H_2/CO_2$ )<sub>in</sub> = 8 in Figure 3.5). If the formation of hydrocarbons is considered ( $C_3H_8$  or  $CH_4$ ),  $CO_2$  conversion increases, however the exothermic formation of hydrocarbons is responsible for a decrease of  $CO_2$  conversion with temperature. The limitation due to the chemical equilibrium is present at ( $H_2/CO_2$ )<sub>in</sub> = 3 in the whole range of temperatures studied and complete conversion is possible from a thermodynamic point of view at higher ( $H_2/CO_2$ )<sub>in</sub> ratios and temperatures lower than 350 °C. From a thermodynamic perspective, the formation of methane and carbon is highly favoured, but under typical FT reaction conditions the chain growing mechanism is kinetically controlled. The FT regime can be remarkably stable against excessive methane formation even at higher temperatures (ca. 350 °C or low  $CO$  partial pressure)(Schulz 2007).

Considering the stoichiometry of the  $CO_2$ -shift in Equation 3.1, the equilibrium constant of the reaction  $K_p$  is defined in terms of the partial pressures and can be calculated with equation 3.9 in the range from 315 to 480 °C, considering the temperature in Kelvin (Graaf et al. 1986).

$$K_p = \frac{p_{CO} \cdot p_{H_2O}}{p_{CO_2} \cdot p_{H_2}} = \frac{1}{10^{(\frac{2073}{T} - 2.029)}} \quad (3.9)$$

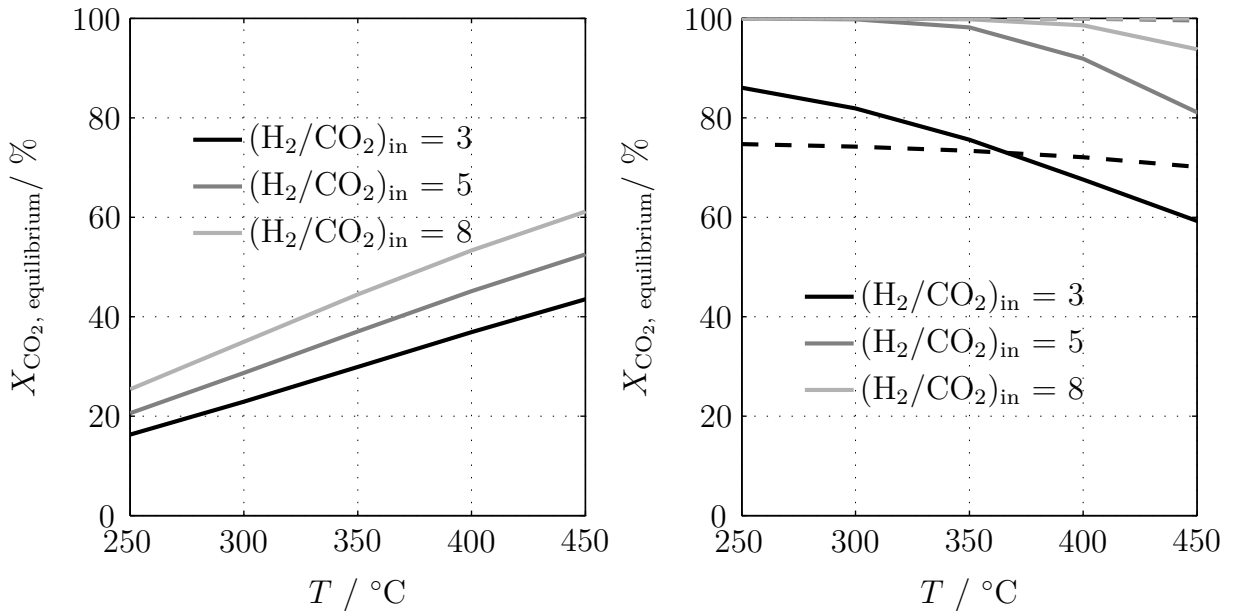


Figure 3.5: Calculated  $CO_2$  equilibrium conversion for different ( $H_2/CO_2$ )<sub>in</sub> ratios as function of temperature for  $p = 1$  MPa considering the following components: (left)  $CO_2$ ,  $CO$ ,  $H_2$  and  $H_2O$ ; (right) full curves:  $CO_2$ ,  $CO$ ,  $H_2$ ,  $H_2O$  and  $C_3H_8$  representing hydrocarbons, dashed curves:  $CO_2$ ,  $CO$ ,  $H_2$ ,  $H_2O$  and  $CH_4$  representing hydrocarbons. Calculated with an RGibbs reactor in ASPEN.

### 3.1.4 Kinetics

Limited information is available concerning the kinetics of the CO<sub>2</sub> shift reaction. Published experimental data indicate that the reaction is very fast over several metallic and oxidic catalysts, having a rather low activation energy and high reaction rates, in comparison with the CO shift reaction (Spencer 1995). A review of the kinetics has been made by Smith et al. (2010) and Zimmerman et al. (1990). A kinetic rate equation similar to equation 3.10 is typically used for the CO shift reaction. Riedel et al. (2001) added a term in the denominator accounting for a possible inhibition of CO<sub>2</sub> and used this expression for the CO<sub>2</sub>-shift reaction (Equation 3.10). The effect of chemical equilibrium limitation is considered by introducing the equilibrium constant  $K_p$  (Equation 3.9).

$$r_{\text{CO}_2\text{-sh}} = k_{\text{CO}_2\text{-sh}} \cdot \frac{p_{\text{CO}_2} \cdot p_{\text{H}_2} - (p_{\text{CO}} \cdot p_{\text{H}_2\text{O}})/K_p}{p_{\text{CO}} + a_{\text{CO}_2\text{-sh}} \cdot p_{\text{H}_2\text{O}} + b_{\text{CO}_2} \cdot p_{\text{CO}_2}} \quad (3.10)$$

Numerous reaction rate equations for the formation of hydrocarbons via Fischer-Tropsch synthesis have been proposed in literature, among them: Atwood et al. (1979), Botes et al. (2006), Deckwer et al. (1986), Huff et al. (1984) and Zimmerman et al. (1990) and more recently Sarkari et al. (2014). Most of these equations consider (H<sub>2</sub>/CO)<sub>in</sub> ratios between 0.5 and 2 and the equations are functions of temperature and partial pressure of H<sub>2</sub>, CO and H<sub>2</sub>O. CO<sub>2</sub> is not present in most cases. At high H<sub>2</sub>O/CO<sub>2</sub> ratios, the inhibiting effect of CO<sub>2</sub> is minor compared with the effect of H<sub>2</sub>O. The presence of CO<sub>2</sub> is related to the CO shift reaction. Small conversions can be described with a first order kinetic in H<sub>2</sub> (Dry et al. 1972). However, with increasing H<sub>2</sub>O partial pressure, reaction rate becomes slower and an inhibition term is required. At increasing conversion, reaction rate decreases not only due to the lower partial pressure of reactants but also due to the inhibited effect of products (Espinoza et al. 1999).

The kinetic rate equations proposed by Zimmerman et al. (1990) gave a good description of the experimental results with a potassium promoted iron catalyst and H<sub>2</sub>-CO mixtures, considering inhibition from H<sub>2</sub>O and CO<sub>2</sub>. This reaction rate equation was selected by Riedel et al. (2001) to describe the formation of hydrocarbons using a (H<sub>2</sub>/CO<sub>2</sub>)<sub>in</sub> ratio of 3 and using a potassium-promoted iron catalyst (Equation 3.11). Kinetic experiments with the same (H<sub>2</sub>/CO<sub>2</sub>)<sub>in</sub> are reported by Rohde (2011) and Unruh (2006) assuming the same reaction rate equations as Riedel et al. (2001). For the three iron catalysts investigated, the inhibition of H<sub>2</sub>O is much higher than of CO<sub>2</sub>.

$$r_{FT} = k_{FT} \frac{p_{\text{CO}} \cdot p_{\text{H}_2}}{p_{\text{CO}} + a_{FT} \cdot p_{\text{H}_2\text{O}} + b_{FT} \cdot p_{\text{CO}_2}} \quad (3.11)$$

According to Riedel et al. (2001) the reaction rate for the FT reaction is more than a hundred times higher than that for the direct hydrocarbon formation. Consequently for the selected catalyst the direct formation of hydrocarbons from CO<sub>2</sub> plays only a

very minor role compared to the indirect formation via CO. Given the variety of rate expressions proposed in the literature for  $(\text{H}_2/\text{CO})_{\text{in}}$ , it seems that, for design purposes, kinetic studies should be performed on the specific catalyst under consideration, using the proposed activation procedure and covering the proposed range of commercial operating conditions (Espinoza et al. 1999).

### 3.1.5 Iron catalyst deactivation

There is much debate on the main causes of the eventual loss of catalytic activity for iron-based FT catalysts. Four main mechanisms of deactivation have been described in the literature and summarised by Smit et al. (2008) (based on  $\text{H}_2$  and CO): (i) transformation of active iron phases into catalytically less active phases or inactive phases. Most groups report the gradual oxidation of active phase to magnetite ( $\text{Fe}_3\text{O}_4$ ), inactive in FT synthesis; (ii) deposition of solid carbonaceous compounds on the surface of the catalyst; (iii) sintering, loss of catalytic surface area due to migration and coalescence; (iv) deactivation by sulphur compounds present in synthesis gas.

Figure 3.6 shows the change in composition of iron catalyst during FT operation. Metallic iron is rapidly converted into a mixture of magnetite, pseudo-cementite and Häag carbide. The pseudo-cementite is soon transformed to Häag carbide and other active carbides for the FT synthesis. Fe metal and carbides are readily oxidized by the product  $\text{H}_2\text{O}$ . Since oxide phases are apparently inactive, the slow conversion of the Häag carbide to  $\text{Fe}_3\text{O}_4$  leads to a slow decline in the FT activity.

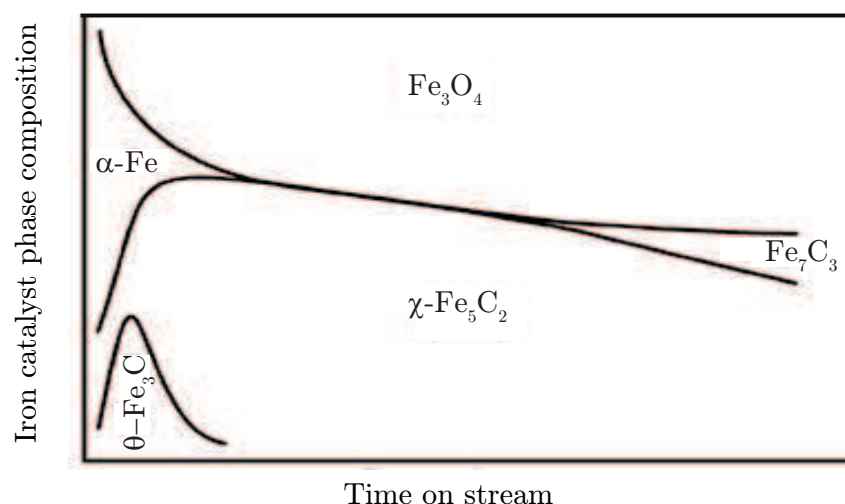
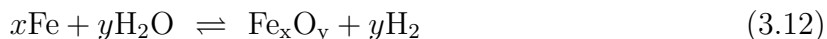
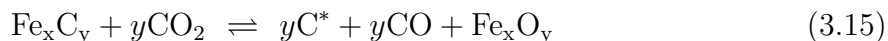
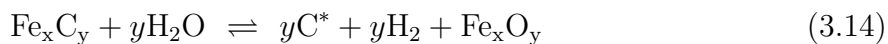


Figure 3.6: Illustrative change in composition of iron catalyst during FT reaction with  $\text{H}_2$  and CO. At time zero, the catalyst is 100 % metallic iron. Operation: fluidized bed reactor,  $T = 330\text{ }^\circ\text{C}$ ,  $p = 2.2\text{ MPa}$ . Phase identified according to X-ray diffraction analysis (reproduced from Steynberg et al. (2004)).

Deactivation by oxidation of the active phase (iron carbides) take place in the presence of H<sub>2</sub>O and/or CO<sub>2</sub> (Equation 3.12 and 3.13).



When these reactions are combined with the reactions of carbide formation (Reaction 3 in Figure 3.2), Equations 3.15 and 3.14 are obtained, representing one of the main proposed mechanisms of deactivation. The oxidation of iron carbides to oxides is clearly shown by Gnanamani et al. (2013) when changing from a synthesis gas based on H<sub>2</sub> and CO to H<sub>2</sub> and CO<sub>2</sub>.



Water vapor is one of the main reaction products in the FT synthesis and has negative effects on the catalyst activity. Iron carbides are considerably more resistant to oxidation by H<sub>2</sub>O than metallic iron. Oxidation of the catalyst becomes more significant when moving further along the catalyst bed in a fixed-bed reactor, or in bigger particles moving into the catalyst pores. The result is a core of iron oxide material and a shell of iron carbide.

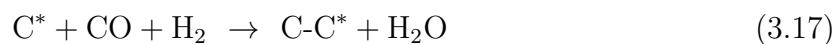
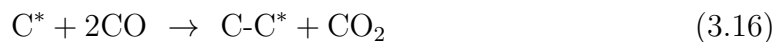
In the case of a H<sub>2</sub> and CO synthesis gas, H<sub>2</sub>O works as an intermediate product. It is produced by the FT synthesis and may be consumed by the CO-shift to form CO<sub>2</sub> and H<sub>2</sub>. At high syngas conversion, oxidation plays an important role in catalyst deactivation due to the increasing H<sub>2</sub>O formation and decrease in H<sub>2</sub> and CO. The increased sintering (increase of average crystal size) and degree of oxidation explain the progressive loss in FT activity in the lower sections of the catalyst bed in a fixed-bed reactor (Steynberg et al. 2004).

If the synthesis gas used is H<sub>2</sub> and CO<sub>2</sub>, H<sub>2</sub>O is produced in the FT synthesis and in the CO<sub>2</sub>-shift. The common product H<sub>2</sub>O plays a major role in suppression of overall CO<sub>2</sub> conversion. This is a key point that differentiates CO<sub>2</sub> hydrogenation from CO hydrogenation (Lee et al. 1990).

Some studies consider catalyst deactivation during CO<sub>2</sub> hydrogenation (Højlund-Nielsen et al. 1982; Hong et al. 2001; Hwang et al. 2001; Riedel et al. 2003). Hwang et al. (2001) report catalyst deactivation due to deposition of carbonaceous materials. They observed a decrease in CO<sub>2</sub> conversion, hydrocarbon yield and chain growth probability, while CO yield increases. Active surface sites of FT catalyst can be “fouled” and become blocked by different kinds of surface poisons. Under typical FT operation conditions, both high molecular weight hydrocarbons and carbonaceous compounds are formed and are able



to drastically lower catalyst activity over time. The first ones slow down the rate of diffusion because they fill the catalyst pores, while carbonaceous compounds permanently block active sites. A common way to describe the deposition of insoluble carbonaceous compounds during reaction is through the Equations 3.16 and 3.17.



At low temperature amorphous carbon is deposited. At higher temperatures ( $T > 280$  °C), graphitic carbon becomes more and more favorable, leading to coke deposition (Smit et al. 2008). Hydrogen treatments at elevated temperatures are commonly used to reactivate catalysts (Bartholomew et al. 2006).

The main challenge in the design of novel iron-based FT catalysts is overcoming the high deactivation rates. The exact structural composition of the active site in these catalysts is still not clearly identified, and despite research efforts into understanding the mechanism of deactivation, stabilization of the active catalyst still remains a challenge.

## 3.2 Flexible operation of catalytic reactors

In general, large-scale catalytic reactors in chemical industry are operated under steady state conditions. The most important operating variables such as temperature, partial pressures, and residence time of reactants are usually kept as constant as possible to get optimum feed conversion or yield for the desired products. An exception to date is the catalytic reduction of  $\text{NO}_x$  (DeNox). This gas cleaning technology is used for exhaust gases emitted in thermal power and waste incineration plants.

In the context of a potential storage technology in which electrical energy is converted to chemical energy in form of chemical energy carriers (Figure 1.2), flexible operation of the chemical reactor may be motivated by the possibility of reducing the size of the  $\text{H}_2$  storage and, consequently, its investment cost (see chapter 4). The present section summarises the activities on the field of flexible operation of catalytic reactors, focusing first on catalyst behaviour under variable conditions, and afterwards on flexible operation of technical reactors with the catalytic reduction of  $\text{NO}_x$  with  $\text{NH}_3$  as example.

### 3.2.1 Catalyst behaviour

The chemical transformation in heterogeneous catalytic reactions relies on a number of physical transport processes, which in turn depend on the operating conditions, influencing the rate of the entire process. Within an industrial situation where the catalyst would be a porous solid and the reactants gaseous seven steps can be observed (Kapteijn et al. 2008). At steady-state conditions, the rates are constant and the overall rate is controlled by the slowest step. Under variable operating conditions, the efficiency of the chemical transformation (i.e. activity and selectivity) may differ from the results under steady-state conditions.

As a result of variable operating conditions in the gas phase (e.g. concentration, temperature), variations in the concentrations of intermediate products participating in the transport processes may occur (e.g. diffusion and/or adsorption). This could lead to storage effects on the catalyst surface, and consequently to a different reaction mechanism than observed under steady-state conditions (including other stages of transition). Moreover, the catalyst itself can undergo significant changes due to its interaction with reactants, e.g. variations in the surface structure and near-surface composition, affecting its catalytic properties. According to Boreskov et al. (1983), the catalyst state is a function of catalyst chemical composition, surface structure and catalytic properties; each reaction medium corresponds with a catalyst state. Under steady-state conditions it is assumed that the catalyst state is constant with time. However, under variable operating

conditions, the catalyst state may vary with time. The amount of time during which a catalyst approaches its new steady state, after a change in reaction conditions, could play an important role in heterogeneous catalytic reactions (Figure 3.7) (Boreskov et al. 1983).

Catalyst deactivation (e.g. during catalytic cracking of vacuum gasoil or dehydrogenation of alkanes) is a well known example of variation of catalyst state during longer periods of operation. Deactivation may cause transient operation of catalytic reactors due to the loss of catalyst activity (Froment et al. 1990).

To date, catalyst developers have focused on the optimum catalyst performance at constant operation conditions. Limited fluctuations in the temperature or concentrations may be incorporated into specific demands regarding “robustness” of the catalyst. For this reason most of today’s catalysts are just not optimally designed to operate under systematic transient conditions (Stankiewicz et al. 1995).

### Forced periodic operation

Since 1967, with the pioneering work of Douglas (1967), lots of research efforts have been focused on the possibility of improving chemical processes by replacing steady-state operation by a periodic forced operation, taking advantage of the dynamic properties of the catalyst and the non-linear properties inherent in a catalytic reactor system.

Certain variable conditions in the fluid phase can cause changes to the catalyst state, which may result in improved selectivity and/or activity compared to the steady-state. The preferable variation to generate the unsteady state conditions is a periodic simple step change (Figure 3.7). This change is more straightforward to implement and more strongly affects the system than other types of inlet parameter forcing (e.g. sinusoidal variation). Manipulated variables for modulation are amplitude, time of cycle, and split of inlet signal and phase angle (when more than one input is forced).

Silveston et al. (1995) distinguished three modes of periodic operation regarding the period of the oscillations  $\tau_p$  and the characteristic time of a certain process  $\tau$ . The process response to an oscillation needs always to be seen in relationship with the time period (and amplitude) of the oscillation.

- $\tau_p \gg \tau$ : The time period of the oscillations is long compared to the response time of the system. Consequently the process operates mainly in the steady-state. The transient portion of the cycle is negligible compared with the cycle period.
- $\tau_p \approx \tau$ : The time period of the oscillation is in the same order of magnitude as the response time of the system. Consequently, the process is always unsteady.
- $\tau_p \ll \tau$ : The time period of the oscillations is very short compared to the response time of the process. The process is not able to follow the variations, and behaves as

if operation were steady-state, defined by the average of the manipulated variable.

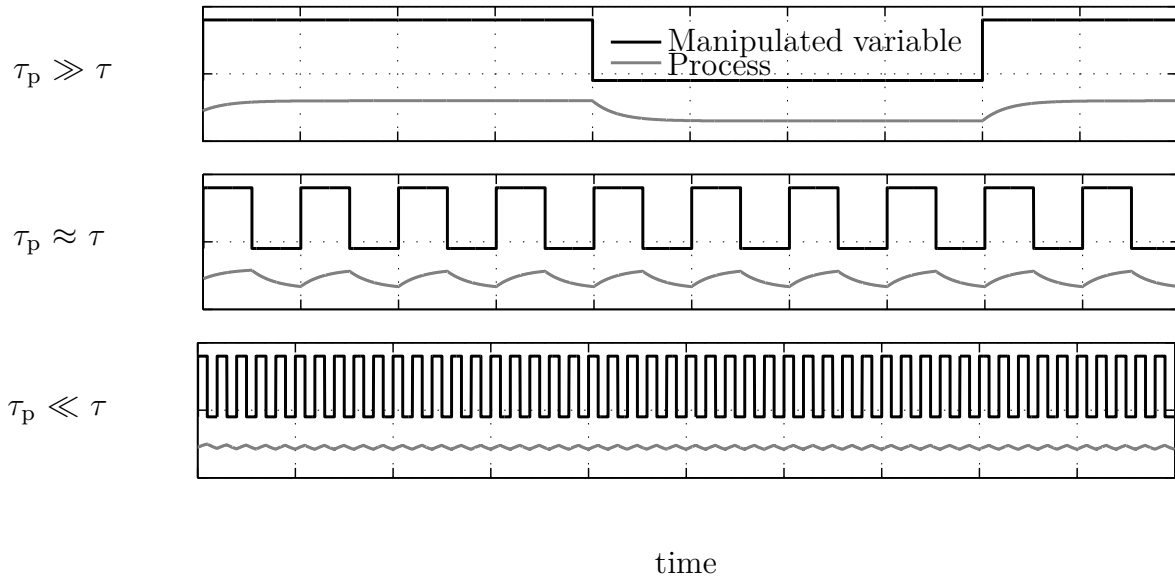


Figure 3.7: Periodic changes in manipulated variables at three different time periods  $\tau_p$  compared with the process response to the variation over the same time scale. Top: time period long compared to process time. Middle: time period similar to the process time. Bottom: time period short compared to process time.

Several chemical reactions have been studied under periodic operation. In most cases, rate and selectivity are the investigated effects, and concentration is the forced parameter. Detailed information about some reactions can be found in Boreskov et al. (1983) and in a review publication from Silveston et al. (1995).

The Fischer-Tropsch synthesis is considered as an attractive reaction for periodic operation, because the steady-state mode goes along with either low activity or poor selectivity to desirable products, or, in the case of certain catalyst, with both of them. Experiments under forced periodic conditions with cobalt, ruthenium and iron are summarized by Adesina et al. (1995). Feimer et al. (1984) carried out step changes in inlet concentration from  $(\text{H}_2/\text{CO})_{\text{in}} = 1.85$  and  $(\text{H}_2/\text{CO})_{\text{in}} = 27.6$ , in both cases to pure  $\text{H}_2$ , with an iron catalyst at 246 °C and 3.8 bar. The aim of Feimer et al. (1984) was to increase the selectivity of the gasoline fraction. The results obtained from these experiments show a large change in product distribution during the first ten minutes after the step change. As a consequence, the authors proposed the use of a periodic operation in that range, with the aim to obtain this enhanced selectivity for continuous operation. A second publication from the same group (Feimer et al. 1985) describes the corresponding periodic operation using the same iron catalyst at duration periods between 1 and 15 minutes; first between  $(\text{H}_2/\text{CO})_{\text{in}} = 0.9$  and pure  $\text{H}_2$ , afterwards in a second experiment, between

$(\text{H}_2/\text{CO})_{\text{in}} = 0.9$  and  $(\text{H}_2/\text{CO})_{\text{in}} = 4.7$ . It was concluded that pulsing  $\text{H}_2$ , in the range of operating conditions examined and with the selected catalyst, is not attractive to increase the yield of hydrocarbons for gasoline production. Cyclic operation affects the product distribution and increases the rate of formation of short chain alkanes (mainly methane) but not the gasoline fraction. According to Silveston et al. (1995), periodic operation is more complicated and probably more expensive than steady-state operation in a chemical process combining reactor(s) and product separation steps. Consequently, if increased conversion is the goal, it could be achieved more cheaply by increasing reactor size or the amount of catalyst employed. Under these circumstances, changing from steady-state to periodic operation could only be justified by a very significant increase in catalyst activity by perhaps 100 % or more.

Transient experiments with periodic input conditions can also be found in literature with different aims (Renken 1993): (i) to determine reaction mechanisms, (ii) to discriminate between various kinetic models, (iii) to evaluate rate constants, and (iv) in the context of steady-state isotopic transient kinetic analysis (SSITKA) (Govender 2010; Shannon et al. 1995).

### 3.2.2 Industrial reactors

Industrial processes are unavoidably subject to (small) variations of the reaction conditions such as reactant composition, reactor pressure and temperature. Scarce literary sources can be found addressing how industries might deal with these variations.

In the future, processes that use  $\text{H}_2$  as reactant will be potential candidates for operation under transient conditions, if the size of the  $\text{H}_2$  storage is to be reduced (e.g. ammonia, methanol, methane, Fischer-Tropsch synthesis) (Schaub et al. 2013). Some research has already been published in this direction in the last two years: Güttel (2013), Rönsch et al. (2014), Schlereth et al. (2014) and Lefebvre et al. (2015), have contributed in the field of methane synthesis, Beerbühl et al. (2014) for  $\text{NH}_3$  production and Eilers et al. (2015) focus on the Fischer-Tropsch synthesis as part of the Biomass-to-Liquid (BtL) process chain. Most of the literature about non-steady state operation of chemical reactors considers forced periodic operation (e.g. reverse flow reactors, pressure swing adsorption) and exhaust gas cleaning technologies in coal power plants and vehicles (e.g.  $\text{NO}_x$  reduction).

Forced periodic operation of chemical reactors has been studied and tested in lab- and pilot- scale with the aim to reach an optimum temperature profile and composition distribution in the reactor. One potential application is periodical flow reversal in fixed bed reactors (Matros et al. 1996). This technique is governed by a combination of reaction and

heat accumulation/exchange in the fixed catalyst bed, making possible an approach to an optimal temperature distribution, and the possibility of exploiting the dynamic properties of the catalyst. The catalyst not only accelerates the chemical reaction but serves as heat exchange and heat accumulation medium. Due to regenerative heat transfer the reactor can maintain autothermal operation (external heat even for weakly exothermic processes is not required) and be operated at low inlet temperatures. Large-scale reverse flow systems were successfully implemented in various plants for catalytic incineration of volatile organic compounds (VOCs) (Novosibirsk Chemical Plant, Russia, 1984) and the treatment of exhaust gases with  $\text{SO}_2$  (Krasnouralsk non-ferrous smelter, Russia, 1982). According to Grozev et al. (1994), the general stage of development of reverse flow reactors may be characterised as commercial level. Examples of industrial-scale applications for the reverse-flow reactors are summarised by Zagoruiko (2012).

Another reported application of forced periodic operation is pressure swing adsorption with reaction. The reactor is loaded with a mixture of catalyst and sorbent in order to selectively remove a by-product during the reaction. The sorbent is periodically regenerated by a purge gas which is introduced at a pressure lower than reaction pressure. The  $\text{CO}_2$ -shift reaction for CO production is perfectly suited for this type of periodic operation, and the conversion of  $\text{CO}_2$  to CO can be significantly increased at a lower temperature if a very selective adsorbent is available to remove  $\text{H}_2\text{O}$  from the reaction zone (e.g. commercial NaX zeolith) (Carvill et al. 1996).

According to Stankiewicz et al. (1995) there has been no true incentive to intentionally disturb the stationary state operation, as no predictable improvement in the reactor performance was expected. The savings in raw materials and energy demand must outweigh the drawbacks associated with the replacement of a stationary production line by a forced periodic production line. The knowledge about periodic operation is insufficient to allow successful industrial implementation. Some practical concerns arise such as: (i) the control of the process and its understanding by the operators, which seems easier in terms of a stationary process, (ii) the good predictability of the stationary mode with respect to stability and safety, (iii) the need for additional investments necessary to synchronize the forced periodic parts of a continuous process with the stationary ones, (iv) the heat integration, which will be more complicated for forced periodic systems, and (v) catalyst degradation, that may be enhanced under periodic forced conditions.

Different examples can be found in literature about flexible operation of catalytic gas cleaning technologies (e.g.  $\text{NO}_x$  reduction, CO removal by methanation). These technologies have in common a high volumetric flow with a low concentration of pollutants to be converted. Due to the strong dilution, high pollutant conversion values and low heat reaction effects are characteristic for these reactions, in spite of the high reaction enthal-

pies. Doesburg et al. (1976a) and Doesburg et al. (1976b) studied the transient behaviour of an adiabatic fixed-bed reactor under almost full-scale conditions for the combined hydrogenation of CO and CO<sub>2</sub> on Ni-based catalysts, used in the purification step of H<sub>2</sub> for NH<sub>3</sub> production. The concentrations of CO and CO<sub>2</sub> used are around 0.1 - 0.5 vol%. Mathematical models of the adiabatic fixed-bed reactor simulate the start-up together with step changes in inlet concentration and temperature. These results were validated with experimental data. It can be observed that the accumulation of heat in the catalyst bed determines the response speed. A change in concentration travels through the reactor with the same velocity as the gas flow, because no net accumulation of CO takes place in the solid phase. Temperature profile changes much more slowly.

### **Catalytic reduction of NO<sub>x</sub> by ammonia**

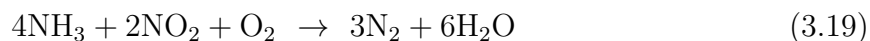
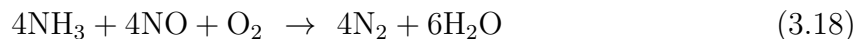
The reduction of nitrogen oxides, from power industry and automotive exhaust gases, is a catalytic reaction that today is successfully operated under non-steady state conditions at industrial scale. Forced periodic operation (i.e. reverse flow reactors and NO<sub>x</sub> storage/reduction catalyst) has also been studied for NO<sub>x</sub> reduction, yet it will not be discussed in this section, as the focus here is on non-forced variable operation.

Composition of exhaust gases, including their concentration of toxic components, varies widely (e.g. for NO<sub>x</sub> 1000 - 1500 ppmv for diesel engines; 150 - 700 ppmv coal combustion). The formation of NO<sub>x</sub> depends on the combustion temperature, concentration of reactants (O<sub>2</sub> and N<sub>2</sub>) during the combustion, contact time of the reactants, type of furnace or engine, and fuel type. Nevertheless, the reduction of nitrogen oxides content in exhaust gases using a catalyst is very effective, with conversion values of 70 - 98 % (Gabrielsson et al. 2008).

In general, two types of reducing agents are used for NO<sub>x</sub> as a function of the oxygen present in the reacting gases: selective reducing agents (NH<sub>3</sub> or hydrocarbons) and non-selective reducing agents (H<sub>2</sub> and CO). If O<sub>2</sub> is present in excess, a selective reducing agent needs to be added because O<sub>2</sub> reacts faster with H<sub>2</sub> or CO than with NO<sub>x</sub>. If the reaction mixture has a low presence of O<sub>2</sub> (air/fuel < 14.6), the reduction of NO<sub>x</sub> with CO or H<sub>2</sub> is favourable. The most recent case of interest is that involving gasoline engines. Three-way catalysts are able to simultaneously remove NO<sub>x</sub>, HC, and CO using a closed loop air-fuel ratio controller that maintains the air/fuel ratio close to stoichiometric by adjusting the flow of fuel. Numerous publications have already studied the transient behaviour of three-way catalysts (Lox 2008; Lox et al. 1993; Tischer et al. 2001; Tischer et al. 2007).

Selective catalytic reduction (SCR) with ammonia as reducing agent is a mature technology, and extensive research has been conducted in the last 10 years leading to improve NO<sub>x</sub> conversion efficiency and NH<sub>3</sub> slip prevention. NH<sub>3</sub> or urea is injected into the ex-

haust gas by the dosing valve in response to the controller's command. Sensors upstream and downstream measure the temperature and the concentration of  $\text{NO}_x$  and  $\text{NH}_3$  (Yuan et al. 2015). Ammonia has greater affinity to nitrogen oxides than to oxygen (that is why it is called selective reduction). Equations 3.18 and Equation 3.19 show the two main reactions. NO normally accounts for 90 - 95 % of  $\text{NO}_x$  in the exhaust gas, therefore the first reaction dominates.



#### Catalyst, reaction mechanism and kinetics

The most commonly used catalyst for SCR is vanadium (active material) on titanium oxide monolithic catalyst (ceramic matrix or carrier). This catalyst normally contains tungsten or molybdenum oxide to increase the surface acidity. The optimum loading of vanadium depends on the type of application, typical values are between 1 - 3 wt%. Catalyst life is guaranteed by the manufacture company from 16000 to 24000 operating hours (2 - 3 years). Catalyst deactivation occurs due to a reduction of the surface area at higher temperatures (approx. 600 - 650 °C, sintering), and due to chemical poisoning and surface fouling (e.g. by ashes) causing non-optimal operation (Gabrielsson et al. 2008).

The SCR mechanism with vanadium catalyst is seen by most workers as an Eley-Rideal (ER) mechanism where ammonia adsorbs onto the surface and reacts with NO, either from the gas phase or weakly adsorbed on the surface. At low temperatures ( $T < 200$  °C) the reaction mechanism is better described as a Langmuir-Hinshelwood mechanism, which suggests adsorption of ammonia and NO species on the surface. Whatever the mechanism, the key step is the formation of a reaction intermediate that decomposes to  $\text{N}_2$  and  $\text{H}_2\text{O}$ . The reoxidation of the surface by  $\text{O}_2$  plays an important role in the overall reaction kinetics.

The rate of reaction is dependent of the  $\text{NO}_x$ ,  $\text{NH}_3$ ,  $\text{O}_2$  and  $\text{H}_2\text{O}$  concentration. Many kinetic estimations are based on a first order reaction, proportional to the concentration of the limiting reagent. Under normal situations in commercial application the  $\text{NH}_3/\text{NO}$  ratio is lower than one and the kinetics become more complicated.  $\text{H}_2\text{O}$  in small percentages has a negative effect on the conversion rate but a positive influence on the selectivity. The effect of  $\text{H}_2\text{O}$  is a competitive adsorption with  $\text{NH}_3$  on the surface, reducing the number of sites available for the SCR reaction. In case of typical stationary applications, the effect of  $\text{H}_2\text{O}$  can be lumped into the normal rate constants (Equation 3.20).

$$-r_{\text{NO}} = k \cdot p_{\text{NO}} \cdot \theta_{\text{NH}_3} \cdot \theta_{\text{O}_2} \quad (3.20)$$

Equation 3.20 shows the rate of reaction according to the Eley-Rideal mechanism, that operates in the typical temperature window for the SCR ( $\theta_{\text{O}_2}$  and  $\theta_{\text{NH}_3}$  represent surface



coverage of  $O_2$  and  $NH_3$  respectively). According to Tronconi et al. (2005), based on model experiments, Eley-Rideal kinetics are always satisfactory to describe steady-state operation (Figure 3.8, left, solid thin lines). However, a modified kinetic rate expression was derived by Tronconi et al. (2005) to describe the  $NH_3$  inhibition effects observed during transient experiments at lower temperatures after a shut off in  $NH_3$  (Figure 3.8, left, solid thick lines). The resulting minimum in the NO concentration corresponds to a maximum in the concentration of  $N_2$ , which indicates that SCR takes place still after the shut off in  $NH_3$ . This, however, cannot be described by the ER kinetics. The inhibiting effect of  $NH_3$ , possibly caused by adsorption competition with NO, and the presence of  $NH_3$  adsorbed onto sites other than the catalyst sites ( $NH_3$  reservoir), explain the transient effect. Such transient effects are of limited interest for steady-state operation, that can be successfully described by the ER kinetics. The observed transient effect is a consequence of variable operation and confirms the existence of adsorption/desorption effects on the catalyst surface. Figure 3.8 left shows the importance of transient experiments to determine kinetic parameters and reaction mechanisms, as already indicated by Renken (1993).

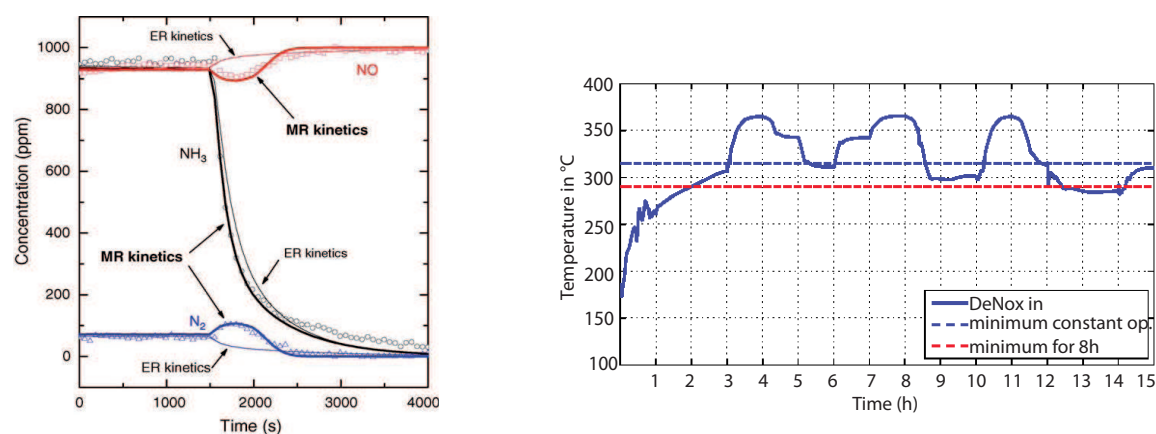


Figure 3.8: Two examples of transient operation of SCR. Left: outlet concentration-time profile of exhaust gases from a diesel engine, shut-off of  $NH_3$  in step form at  $t = 1500$  s over a commercial catalyst in a microreactor (inlet concentrations:  $NO = 1000$  ppm,  $NH_3 = 1000$  ppm,  $H_2O = 1$  % and  $O_2 = 2$  %,  $GHSV = 210000$   $h^{-1}$ ,  $T = 175$  °C). Solid thin lines: kinetic fit by Eley-Rideal (ER) rate expression. Solid thick lines: kinetic fit by modified redox (MR) rate expression. Symbols: experimental data, from Tronconi et al. (2005) Right: temperature-time inlet profile to SCR unit during variable load operation in the hard-coal power plant in Rostock (Meinke 2012)

### Reactor and operation conditions

The selected reactor to carry out the SCR is either a honeycomb ceramic monolith, with longitudinal ducts with square or round cross-section, or a plate catalyst where the catalyst is impregnated. The fixed-bed reactor with monoliths operates fully adiabatically.

The reaction is highly exothermic (Equation 3.18,  $\Delta_{H,R} = -1224$  kJ/mol), but due to the low concentration, the adiabatic temperature increase is low. The DeNO<sub>x</sub> adiabatic reactor unit for gas purification in a power station has a volume around 1000 m<sup>3</sup>, while in the case of the automotive exhaust catalyst, the volume is lower than 0.001 m<sup>3</sup>. These reactors are the biggest and smallest fixed-bed reactors, respectively.

The main advantages of the V-/Ti-oxide honeycomb system are: (i) low pressure drop at high gas velocities, (ii) small catalyst volume, (iii) storage of ammonia in the catalyst, which ensures high flexibility of operation under variable load conditions, (iv) small losses of ammonia, and (v) resistance to poisoning. A disadvantage of this packing is that the flow along the channels is not uniform and therefore double of the catalyst mass is required than with a uniform flow. Installations are, therefore, generally expensive.

In the normal temperature range for the SCR 300 - 450 °C, the reaction is mass transfer controlled, and the activity is optimized by increasing the geometric surface area of the monolith by a higher number of cells and a smaller hydraulic diameter, which allows higher gas velocities (0.4 - 5 m/s). There are some limitations in the optimization of the hydraulic diameter that must be adopted in order to avoid plugging by the fly-ash and to ensure mechanical stability (Gabrielsson et al. 2008).

Control strategies are used to keep the NH<sub>3</sub> slip low, which is challenging due to the difficulties estimating the stored NH<sub>3</sub> on the catalyst. The storage varies spatially from reactor inlet to the outlet and with temperature. The NH<sub>3</sub> storage capacity decreases rapidly as the temperature rises, therefore unacceptably high NH<sub>3</sub> slips may occur during sudden temperature increases.

Figure 3.8 right, shows the inlet temperature to a SCR unit during load changes of a hard-coal thermal power plant installed in Rostock, Germany. A low operation load of the hard-coal power plant is responsible for a lower inlet temperature in the catalyst unit (100 % load  $T_{in} = 375$  °C, 50 % load  $T_{in} = 315$  °C, 30 % load  $T_{in} = 280$  °C). For this power plant, the desired catalyst temperature for a guaranteed high efficiency is 315 °C. At temperatures lower than 300 °C, undesired secondary reactions forming ammonium sulphate deposits take place, blocking the catalyst pores and reducing catalyst activity. The formation of these compounds is thermally reversible at temperatures higher than 300 °C, preferentially at 350 °C for a certain time. This regeneration allows flexible operation of the SCR unit over a range of approx. 8 h between 280 and 300 °C. According to this restriction, a minimum load of 37 % is allowed for this power-plant. There are, however, some strategies that could be followed to further reduce the minimum load (e.g. additional firing)(Meinke 2012).

## 4 Preliminary studies

*This chapter presents two preliminary studies, the first one evaluates the potential of using gaseous hydrocarbon synfuels, produced via hydrogenation of CO<sub>2</sub>, to adjust the heating value of methane (raw SNG). The second preliminary study focuses on the effect that part-load operation of synthesis reactors have on the size of the reactor and the H<sub>2</sub> storage. Conclusions drawn will clearly show these studies to be important to this work as a whole.*

### 4.1 Substitute Natural Gas (SNG) heating value adjustment using Fischer-Tropsch Synthesis

Two different qualities of natural gas are commonly produced and used: low calorific gas (L-gas) and high calorific gas (H-gas), H-gas can be converted into L-gas by adding nitrogen. H-gas in Germany is usually sourced from Eastern Europe, North Sea and from natural gas deposits in the Netherlands, Denmark and Norway. Example compositions of H-Gas can be found in Table 4.1.

Table 4.1: Example composition of H-Gases (DVGW 3.2013)

	C <sub>1</sub>	C <sub>2</sub>	C <sub>3</sub>	C <sub>4</sub>	CO <sub>2</sub>	N <sub>2</sub>	HHV <sub>n</sub>	W <sub>s,n</sub>	d <sub>n</sub>
	vol %	vol %	vol %	vol %	vol %	vol %	MJ/m <sup>3</sup>	MJ/m <sup>3</sup>	-
Russia-H	97.0	1.4	0.5	0.2	0.2	0.9	40.3	53.1	0.57
North Sea-H	88.7	6.9	1.3	0.3	1.9	0.8	41.9	55.4	0.63
Denmark-H	90.1	5.7	2.2	0.9	0.6	0.3	43.7	55.0	0.63

The substitution of natural gas by any other kind of gaseous fuel has to meet several criteria. The requirements for interchangeability of gases differ from country to country. During this study, the contemporary technical standards for natural gas in Germany, based on the technical rules for gas DVGW G 260 (DVGW 3.2013) and DVGW G262 (DVGW 9.2011) are considered.

The aim of this chapter is to show the potential of producing gas mixtures of hydrocarbons (i.e. C<sub>2</sub>H<sub>6</sub>, C<sub>3</sub>H<sub>8</sub>, C<sub>4</sub>H<sub>10</sub>), using H<sub>2</sub> and CO<sub>2</sub> from renewable sources, to adjust the heating

value of methane (raw substitute natural gas). The formation of hydrocarbons takes place according to the Fischer-Tropsch (FT) reaction. Calculations are made for two process options: (i) stand-alone FT plant for the production of ethane, propane and butane as blending material for methane, and (ii) combined production of ethane, propane and butane via FT synthesis and methane via methanation, both using H<sub>2</sub> and CO<sub>2</sub> from renewable resources.

### 4.1.1 Specifications for calculations

#### A. Definitions

The higher calorific value or higher heating value (HHV in J/m<sup>3</sup>) of any compound is computed from the energy release by the complete combustion of the dry hydrocarbon gas in air at constant pressure ( $p = 1013.25$  hPa), and assuming that reactants and products have the same temperature before and after the combustion. Reaction products are CO<sub>2</sub> (gas) and H<sub>2</sub>O (liquid). The difference between higher heating value and lower heating value is the vaporization enthalpy of H<sub>2</sub>O. Higher heating values are usually given based on volume (MJ/m<sup>3</sup>) under standard conditions ( $T = 293$  K and  $p = 1013.25$  hPa), indicated with the subindex n. A constant heating value of a gas mixture does not ensure a constant energy release from a burner after combustion. The flow of natural gas depends on their relative density, viscosity, and pressure difference. If the last two are maintained constant: the rate of flow becomes inversely proportional to the square root of the relative density  $d_n$ . This function is defined as Wobbe index  $W_{s,n}$  (Equation 4.1).

$$W_{s,n} = \frac{\text{HHV}_n}{\sqrt{d_n}} \quad (4.1)$$

Table 4.2: Higher heating value (HHV) and relative density ( $d_n$ ) of relevant components at  $T = 273.15$  K,  $p = 1013.25$  hPa and  $\rho_{n,\text{air}} = 1.293$  kg/m<sup>3</sup>.

		H <sub>2</sub>	CO <sub>2</sub>	CH <sub>4</sub>	C <sub>2</sub> H <sub>6</sub>	C <sub>3</sub> H <sub>8</sub>	C <sub>4</sub> H <sub>10</sub>
HHV <sub>n</sub>	MJ/m <sup>3</sup>	12.75	0	39.75	69.63	98.75	127.87
$d_n$	$(\frac{\rho_{n,i}}{\rho_{n,\text{air}}})$	0.07	1.53	0.55	1.05	1.56	2.07

#### B. Natural gas grid specifications in Germany

According to DVGW (3.2013) and DVGW (9.2011), substitute natural gas needs to comply with the following specifications before being fed to the natural gas grid:

- Higher heating value: 30.2 - 47.2 MJ/m<sup>3</sup>

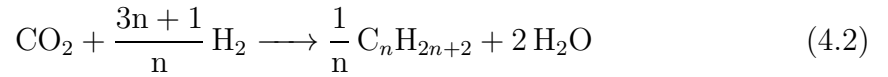
- Wobbe index: 46.1 - 56.5 MJ/m<sup>3</sup>
- Relative density: 0.55 - 0.75
- Maximum H<sub>2</sub> content in H-gas: 2 % (according to DIN EN 51624) and 5 % as potential future value

No specification about CO concentration in the substitute natural gas mixture is given (intermediate product in the CO<sub>2</sub> hydrogenation reaction). Alkenes, FT primary products, are not allowed in the gas grid to avoid polymerization issues. Hydrocarbons with more than four carbon atoms are only allowed in trace concentrations, to avoid condensation problems in the natural gas grid.

### C. Assumptions for calculations

The following assumptions are made in carrying out the calculations:

- The chemical reaction stoichiometry for each hydrocarbon is used



- $T = 273.15 \text{ K}$  and  $p = 100 \text{ kPa}$  (1 bar)
- CO is not considered as intermediate product: one step reaction
- The hydrocarbon product distribution is calculated based on the Anderson-Schulz-Flory (ASF) model (in weight, Equation 3.8). All hydrocarbons are considered to be alkanes. The molar flow of hydrocarbon  $i$  in product gas with a carbon number  $N_C$  is calculated according to Equation 4.3:

$$F_{n,i} = \frac{F_{n,\text{CO}_2,\text{in}} \cdot X_{\text{CO}_2} \cdot y_{m,N_C,i}}{N_{C,i}} \quad (4.3)$$

- Overall H<sub>2</sub> consumption is calculated considering all hydrocarbons ( $N_C = 1 - 200$ ) according to the stoichiometry. The overall CO<sub>2</sub> consumption is defined by the CO<sub>2</sub> conversion. An overall (H<sub>2</sub>/CO<sub>2</sub>)<sub>in</sub> stoichiometric ratio is obtained for each  $\alpha$ .

$$F_{n,\text{H}_2,\text{in}} - F_{n,\text{H}_2,\text{out}} = \sum_{i=1}^{200} \left( F_{n,\text{CO}_2,\text{in}} \cdot X_{\text{CO}_2} \cdot y_{m,i} \cdot \frac{(3 \cdot N_{C,i}) + 1}{N_{C,i}} \right) \quad (4.4)$$

#### 4.1.2 Stand-alone plant

The following calculations assume that a stand-alone plant is operated to produce C<sub>2</sub>-C<sub>4</sub> components via Fischer-Tropsch reaction. These components are afterwards used as blending material for methane to adjust the heating value. This process requires an overall conversion of CO<sub>2</sub> and H<sub>2</sub> close to 100 %, and a high selectivity of C<sub>2</sub>-C<sub>4</sub> components.

The degrees of freedom are the selection of the catalyst and the operating conditions ( $T$ ,  $p$ , residence time and  $(\text{H}_2/\text{CO}_2)_{\text{in}}$  in the case of operation with recycle).

Figure 4.1 left shows the heating value as a function of the parameter  $\alpha$  (chain growth probability, Equation 3.8) for three different  $\text{CO}_2$  conversion values. The HHV of the gas mixture is calculated considering  $\text{CH}_4$ ,  $\text{C}_2\text{H}_6$ ,  $\text{C}_3\text{H}_8$ ,  $\text{C}_4\text{H}_{10}$  and the non converted  $\text{H}_2$  and  $\text{CO}_2$ .  $\text{H}_2\text{O}$  and  $\text{C}_{5+}$  are not present in the mixture, as they are assumed to have been previously separated from the product gas.

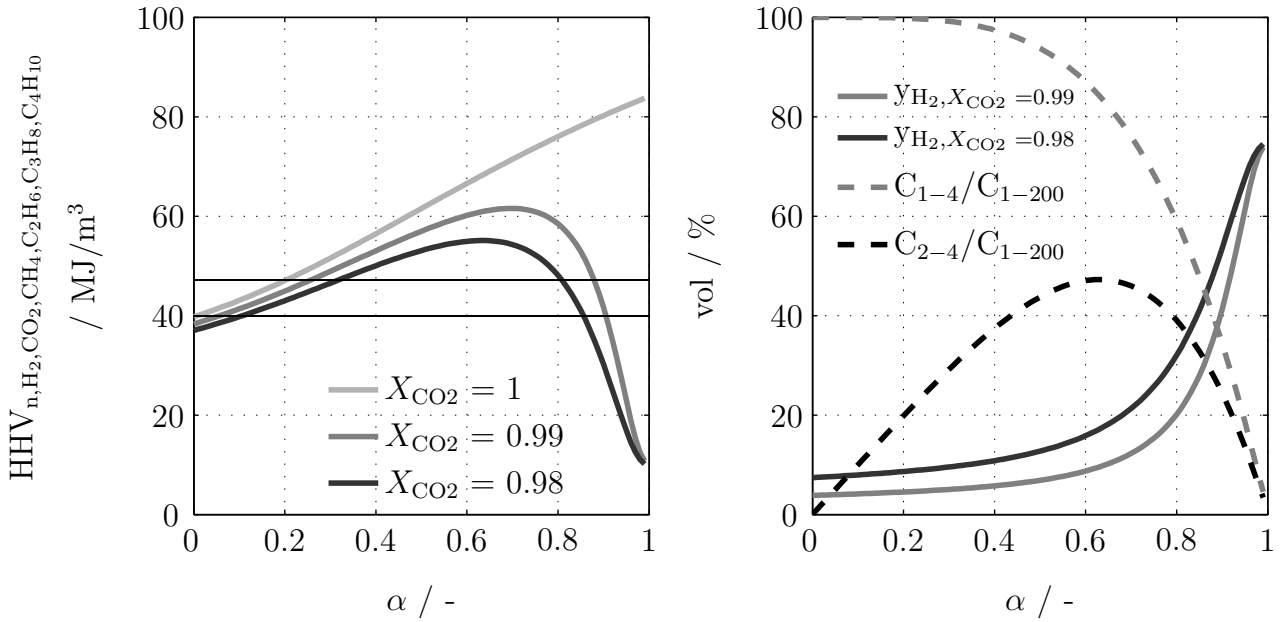


Figure 4.1: Stand-alone Fischer-Tropsch plant for the production of gaseous hydrocarbons. Left: Higher heating value (HHV) of a gas mixture ( $\text{H}_2$ ,  $\text{CO}_2$ ,  $\text{CH}_4$ ,  $\text{C}_2\text{H}_6$ ,  $\text{C}_3\text{H}_8$ ,  $\text{C}_4\text{H}_{10}$ ) from a stand-alone plant after separation of  $\text{C}_{5+}$  and  $\text{H}_2\text{O}$ , as a function of chain growth probability ( $\alpha$ ) and  $\text{CO}_2$  conversion. Horizontal reference lines:  $\text{HHV}_{\text{CH}_4} = 40 \text{ MJ/m}^3$  and  $\text{HHV}_{\text{max}} = 47.2 \text{ MJ/m}^3$  for H-gas. Right: Volume %  $\text{H}_2$  in the product gas as a function of  $\alpha$  and  $\text{CO}_2$  conversion (grey lines), selectivity of  $\text{C}_{1-4}$  and  $\text{C}_{2-4}$  components related to the total amount of hydrocarbons produced.  $(\text{H}_2/\text{CO}_2)_{\text{in}}$  stoichiometric according to  $\alpha$ -value (ASF model) and values in Table 4.2

At full conversion, no  $\text{H}_2$  and  $\text{CO}_2$  are present in the gas mixture, the HHV increases with  $\alpha$  because the vol% of  $\text{C}_3\text{H}_8$  and  $\text{C}_4\text{H}_{10}$  after  $\text{H}_2\text{O}$  separation increases. However, at high values of  $\alpha$  the vol % of  $\text{C}_1$  and  $\text{C}_{2-4}$  hydrocarbons is low (Figure 4.1 right). At conversion values lower than 100 %, the unconverted  $\text{H}_2$  and  $\text{CO}_2$  are present in the gas mixture. The HHV reaches a maximum at a certain  $\alpha$  value, and afterwards, due to the separation of  $\text{C}_{5+}$ , the vol % of  $\text{H}_2$  and  $\text{CO}_2$  in the gas mixture increases, in turn lowering the heating value of the gas mixture (Figure 4.1 right). At a conversion of 98 % the maximum HHV

is found at a lower  $\alpha$  than at 99 %, because the vol % of H<sub>2</sub> and CO<sub>2</sub> in the mixture is higher. H<sub>2</sub> concentrations are clearly above 5 % at conversion of CO<sub>2</sub> lower than 99 % and high values of  $\alpha$ . The high vol% of H<sub>2</sub> decreases when methane is added to the mixture, for example, operating at  $\alpha = 0.6$  and  $X_{\text{CO}_2} = 0.99$  would mean the blending gas has a HHV = 60 MJ/m<sup>3</sup> and 8.75 vol % H<sub>2</sub> in gas. With the addition of 5 m<sup>3</sup> of CH<sub>4</sub>, the mixture is ready to be fed into the natural gas grid (HHV = 41.2 MJ/m<sup>3</sup> and 0.6 vol% H<sub>2</sub>). According to Figure 4.1, two different strategies are possible:

- **Operate at  $\alpha < 0.3$ :** In this range only gaseous hydrocarbons between C<sub>1</sub>-C<sub>4</sub> are produced. The fraction C<sub>5+</sub> is minimised, therefore no separation of long chain hydrocarbons is needed. The maximum HHV of the gas mixture is relatively low, between 51.5 - 46.5 MJ/m<sup>3</sup> as a function of conversion. If values of  $\alpha$  are around 0.15 - 0.20 and the overall conversion is higher than 0.99, the produced gas could be directly fed into the natural gas grid.
- **Operate at  $0.3 < \alpha < 0.8$ :** The production of C<sub>2</sub>-C<sub>4</sub> components can be maximized and consequently the HHV of the gas mixture is also higher, however separation of C<sub>5+</sub> is required (gas mixture = CH<sub>4</sub>, C<sub>2</sub>H<sub>6</sub>, C<sub>3</sub>H<sub>8</sub>, C<sub>4</sub>H<sub>10</sub> and the non converted H<sub>2</sub> and CO<sub>2</sub>). Due to the higher production of C<sub>4</sub>H<sub>10</sub> as  $\alpha$  increases, the HHV increases and reaches a maximum ( $\alpha$  ca. 0.75). Afterwards ( $\alpha > 0.75$ ), the vol % of H<sub>2</sub> increases and lowers the calorific value of the mixture. The reason for this is that the high amount of long chain hydrocarbons produced need to be removed from the mixture. The proportion of C<sub>1</sub>-C<sub>4</sub> components is low, and therefore after separation of C<sub>5+</sub>, the vol% of H<sub>2</sub> in the mixture increases. With this strategy, a maximum of 40 % of C ends in the fraction C<sub>5+</sub> ( $\alpha = 0.8$ ), generally more valuable than methane but nonetheless a mixture which needs to be upgraded to be used as transportation fuel.

Operating a FT reactor using H<sub>2</sub> and CO<sub>2</sub> at  $\alpha$  values higher than 0.8 would not make sense for the targeted production of C<sub>2</sub>-C<sub>4</sub> hydrocarbons. In addition, Riedel et al. (2001) report difficulties in reaching high values of  $\alpha$  starting with CO<sub>2</sub>, independent of the selected catalyst (cobalt, iron).

The selection of the desired strategy depends on the context (i.e. location, local markets) and on the possibility to use the byproduct, either C<sub>1</sub> or C<sub>5+</sub>. Experimental work is required to check whether catalysts are able to produce the desired products starting from H<sub>2</sub> and CO<sub>2</sub> more selectively (see Chapter 5).

### 4.1.3 Combination with methane synthesis

An alternative to the FT stand-alone plant is to have the production of FT components and methane on the same site. This can be carried out in such a way that both syntheses are integrated. Depending on the selected methane synthesis technology, different combinations are possible. The Fischer-Tropsch unit could precede the methanation reactor, however the stability of the C<sub>2</sub>-C<sub>4</sub> hydrocarbons under methanation conditions (i.e. higher temperatures) needs to be evaluated experimentally. The three-phase methanation, typically operated at lower temperatures, could be of interest (Lefebvre et al. 2015). Another possibility is to place the FT unit in-between two methanation beds after H<sub>2</sub>O separation when using a multi-stage methanation reactor (Schaaf et al. 2014).

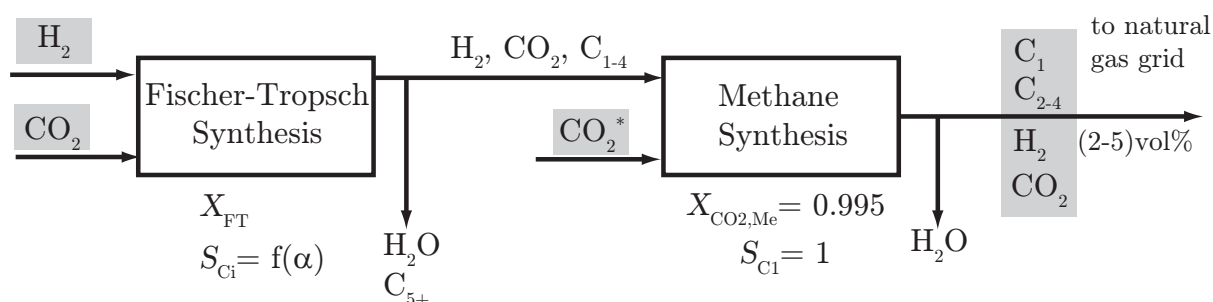


Figure 4.2: Example combination of Fischer-Tropsch synthesis and methane synthesis for the production of H-gas from H<sub>2</sub> and CO<sub>2</sub>. CO<sub>2</sub>\* is calculated by iteration.

The following example calculation is motivated by the possibility to combine both syntheses and produce a final H-gas according to the specifications with 2 and 5 vol% H<sub>2</sub> (Figure 4.2). The requirements for the FT unit in this example are to produce the desired amount of C<sub>2</sub>-C<sub>4</sub> components to reach the specifications of H-gas in the final product. The degrees of freedom are the selection of the catalyst and the operating conditions ( $T$ ,  $p$ , residence time and  $(H_2/CO_2)_{in}$ ).

CO<sub>2</sub> conversion and hydrocarbon selectivity ( $\alpha$  value) are varied in the FT reactor for different  $(H_2/CO_2)_{in}$  to show the potential that operating conditions could have in the final gas specifications (HHV, Wobbe index and relative density). For the methane synthesis reactor, a CO<sub>2</sub> conversion of 0.995 is assumed together with a selectivity to methane of 1 (same requirements as if the methane synthesis is operated in a stand-alone plant).

Calculations are made according to Figure 4.2. This configuration allows the use of over-stoichiometric ratio  $(H_2/CO_2)_{in}$  for the FT synthesis. The complete H<sub>2</sub> flow is fed into the FT unit and the CO<sub>2</sub> flow is split in two (FT and methane synthesis). After the separation of H<sub>2</sub>O and C<sub>5+</sub>, the outlet flow of the FT unit is used as inlet flow for the methanation unit. Once the composition of the incoming flow to the methanation plant is known, an



iterative procedure is needed to calculate the  $\text{CO}_2$  inlet flow in the methanation unit to obtain the desired concentration of  $\text{H}_2$  in the final mixture, 2 or 5 %. The unconverted  $\text{H}_2$  and  $\text{CO}_2$  in the FT unit, added together with the extra  $\text{CO}_2$ , are converted to  $\text{CH}_4$  in the methanation unit.

The  $(\text{H}_2/\text{CO}_2)_{\text{in}}$  value in the FT unit can be selected to optimise the catalyst activity and selectivity. High values of the  $(\text{H}_2/\text{CO}_2)_{\text{in}}$  favour higher  $\text{CO}_2$  conversion in the FT reactor due to the high amount of  $\text{H}_2$  available, however, according to literature,  $\alpha$  would be lower (favour short chain hydrocarbons). If the FT unit is operated at high  $(\text{H}_2/\text{CO}_2)_{\text{in}}$  ratio, a big amount of  $\text{H}_2$  remains unconverted and is converted to  $\text{CH}_4$  in the methanation plant together with extra  $\text{CO}_2$ , being the amount of  $\text{CH}_4$  high, related to the previously produced  $\text{C}_2\text{-C}_4$  components. As a consequence, the HHV of the gas mixture would be low. Example calculations for  $(\text{H}_2/\text{CO}_2)_{\text{in}} = 5$  (Figures 4.3, A.1) and  $(\text{H}_2/\text{CO}_2)_{\text{in}} = 8$  (Figures A.3, A.4) are carried out as examples.

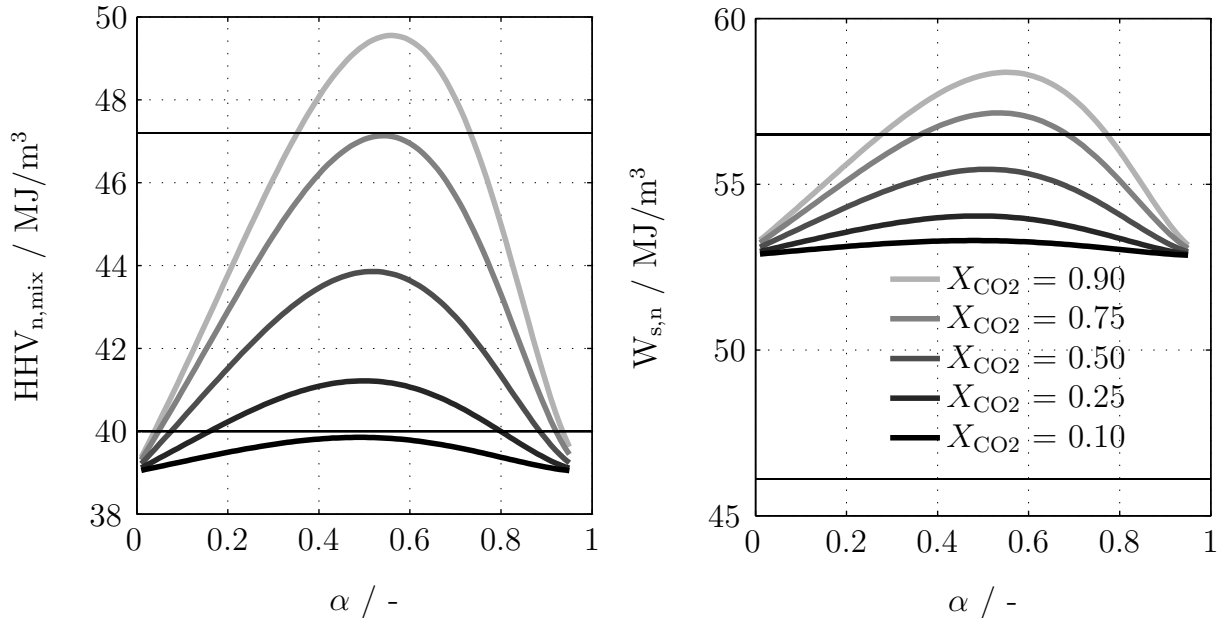


Figure 4.3: HHV and Wobbe index of different gas mixtures with 2 vol% of  $\text{H}_2$  after FT and methanation reactors as a function hydrocarbon selectivity ( $\alpha$ ) and  $\text{CO}_2$  conversions on the FT reactor, operated at  $(\text{H}_2/\text{CO}_2)_{\text{in}} = 5$ . Details about relative density in Figure A.2. Horizontal black lines show the specification values defined in section 4.1.1

Figure 4.3 shows the HHV and Wobbe index for different gas mixtures with 2 vol%  $\text{H}_2$  calculated with a  $(\text{H}_2/\text{CO}_2)_{\text{in}} = 5$  in the FT unit. Low conversion of  $\text{CO}_2$  in the FT unit (ca. 0.10) are not enough (independent of  $\alpha$  value) to reach a HHV of 40 (pure methane) due to the presence of 2 vol %  $\text{H}_2$ . High conversions (ca. 0.90) at  $\alpha$ -values of 0.35 - 0.75 produce a gas with a very high HHV that needs to be mixed with extra methane. If the final gas contains 5 vol %  $\text{H}_2$  instead of 2 vol %, for a constant  $\alpha$  value, a higher  $\text{CO}_2$

conversion is required in the FT unit to reach the same final HHV due to the presence of more  $\text{H}_2$  (Figure A.1). At  $(\text{H}_2/\text{CO}_2)_{\text{in}} = 5$  a wide range of H-gas mixtures can be obtained under specifications at different combinations of  $\text{CO}_2$  conversion and  $\alpha$  values.

At  $(\text{H}_2/\text{CO}_2)_{\text{in}} = 8$  the maximum HHV that can be reached is lower than at  $(\text{H}_2/\text{CO}_2)_{\text{in}} = 5$ , and with a  $\text{CO}_2$  conversion of 0.9 in the FT unit, the maximum HHV is around  $45 \text{ MJ/m}^3$  due to the high amount of methane produce in the methanation plant, using the unconverted  $\text{H}_2$  (Figure A.3 and Figure A.4). If the final gas contains 5 vol% instead of 2 vol% of  $\text{H}_2$ , the maximum HHV is lower than  $44 \text{ MJ/m}^3$ .

### 4.1.4 Conclusion: heating value adjustment using Fischer-Tropsch synthesis

Based on preliminary calculations, the Fischer-Tropsch synthesis has the potential to produce gaseous hydrocarbons from  $(\text{H}_2/\text{CO}_2)_{\text{in}}$  mixtures for heating value adjustment. A stand-alone plant or a combination with the methane synthesis are both viable options according to the preliminary calculations. Experimental work is required to determine which  $\text{CO}_2$  conversion and  $\alpha$  value can be obtained with suited iron-based catalysts.

The combination of FT and methane synthesis may be, according to the stoichiometric calculations, an attractive alternative for producing H-gas mixtures under specifications. This combination offers a wider range of possible operating conditions for the FT unit than the stand-alone plant (making operation at low  $\text{CO}_2$  conversion values possible). However, within the scope of the present work, the combination of FT and methane synthesis is not further discussed.

Experiments in chapter 5 evaluate the effect of catalyst properties and operating conditions on activity and selectivity for the Fischer-Tropsch synthesis alone. Chapter 8 considers a stand-alone FT plant for the production of gaseous hydrocarbons and focuses on the part-load operation of a reactor with recycle.

## 4.2 Effects of part-load operation of synthesis reactor on size of H<sub>2</sub> storage and reactor

The attractiveness to operate a chemical reactor under part-load conditions depends on the H<sub>2</sub> generation pattern and the complexity of the synthesis process. For a given H<sub>2</sub> generation pattern, flexible operation of a catalytic process (i.e. within a range of load and rates of load change) makes possible a reduction of the size of the H<sub>2</sub> storage, and consequently of its investment cost. However, the size of the catalytic reactor per hydrocarbon flow produced increases (due to the higher mass of catalyst needed to convert the maximum feed flow), therefore investment cost for the catalytic process becomes higher. Under certain circumstances, the overall investment required for a constant load operation could be reduced if the synthesis reactor is operated under flexible conditions.

The motivation for reducing the size of the H<sub>2</sub> storage not only lies in the reduction of costs, but also in the consideration of worker's safety: the overall effect of any accident can be much worse when a large inventory of flammable or hazardous material is involved; leakages due to higher pressures are difficult to detect (H<sub>2</sub> is odorless, colorless and tasteless). H<sub>2</sub> leaks can support combustion at very low flow rates (Fthenakis 1993).

The aim of this section is to show under which circumstances it could be attractive to operate a catalytic reactor under variable load conditions. A strong simplified approach is followed, based on correlations from literature and own assumptions.

### 4.2.1 Estimation procedure and assumptions

Table 4.3 gives an overview of the assumptions and boundary conditions used for the calculations.

#### H<sub>2</sub> production from renewable electricity

H<sub>2</sub> is produced via H<sub>2</sub>O electrolysis using renewable electricity. Within this study two different electricity patterns are considered, both representing boundaries for possible future electricity patterns. A real case might be in-between:

- Windfarm: a one-month wind profile from a wind farm in north Germany. This profile represents an intermittent electricity generation with periods of very low or even zero input and high rates of load change (see section 4.2.2)
- Sinus wave function: the sinus wave represents a fluctuating electricity generation profile with smooth changes and no periods of zero input. The sinus wave offers the possibility to study the characteristics of the electricity generation profile with a systematic approach (see section B in the appendix).

The average power considered for both profiles is assumed to be constant of 6.64 MW. This corresponds to an average H<sub>2</sub> production of 1500 m<sup>3</sup>/h (STP). The production of H<sub>2</sub> is proportional to the power generation (Equation 4.5, HHV<sub>H<sub>2</sub></sub> = 3.54 kWh/m<sup>3</sup>, η<sub>Ely</sub> = 0.8, and power generation in MW).

$$F_{v,H_2,Ely} = F_{v,H_2,in,storage} = \frac{P_{el} \cdot 1000 \cdot \eta_{Ely}}{HHV_{H_2}} \quad (4.5)$$

The electrolysis is the most expensive element of the electricity-to-fuel process chain, therefore it is important that the number of full load hours is as high as possible. (Smolinka et al. 2011). The installed capacity of the electrolyser can be adjusted to the maximum power generation point (e.g. Figure 4.6 top,  $P_{el,max} = 36$  MW) if the whole electricity profile should be used. The overload factor of the electrolyser is a design variable, it is a compromise between efficiency and investment; with a high overload factor, the duration of the cell is reduced. According to Siemens (2015) the design of the electrolyser can be set according to one third of the maximum power produced, i.e.  $P_{el,max} = 12$  MW, due to the possibility of operating under a overload of 300 % during 15 minutes (overload factor of 3). Afterwards, the electrolyser needs to be operated below its design load during 15 min. This dynamic behaviour of the electrolyser takes advantage of electricity production peaks, and reduces considerably the investment cost needed.

Table 4.3: Assumptions and boundary conditions used for calculations.

H <sub>2</sub> production from renewable electricity	
H <sub>2</sub> -generation pattern (≈ electricity generation pattern)	- example wind farm - sinus wave function (variable τ <sub>p</sub> , A) (Appendix B)
H <sub>2</sub> -storage	
Storage control strategy	- based on pressure in the storage
Size H <sub>2</sub> -storage	correlates with: - H <sub>2</sub> -generation pattern - storage control strategy - min/max feed flow synthesis (L <sub>min</sub> /L <sub>max</sub> )
Synthesis reactor	
General assumptions	F <sub>v,CO<sub>2</sub>,in,NTP,reactor, average</sub> = 500 m <sup>3</sup> /h (H <sub>2</sub> /CO <sub>2</sub> ) <sub>in</sub> = 3
Low complexity process	GHSV = 20000 1/h
High complexity process	GHSV = 500 1/h
Size reactor	correlates with: - process complexity (GHSV) - min/max feed flow synthesis (L <sub>min</sub> /L <sub>max</sub> )

## H<sub>2</sub> storage

The volume of the H<sub>2</sub> storage  $V_{H_2 \text{ storage}}$  is a function of the H<sub>2</sub> production pattern, the flexibility of the reactor  $L_{\min}$  (Equation 4.6), and the control strategy selected for the H<sub>2</sub> storage. The procedure shown in Figure 4.4 considers two iteration loops. The internal loop makes sure that the maximum and minimum pressures are within the selected limits. The external loop determines the minimal pressure ( $p_{\min}^*$ ) which ensures that the filling degree of the storage at the beginning  $t = 0$  and at the end of the calculation is equal.

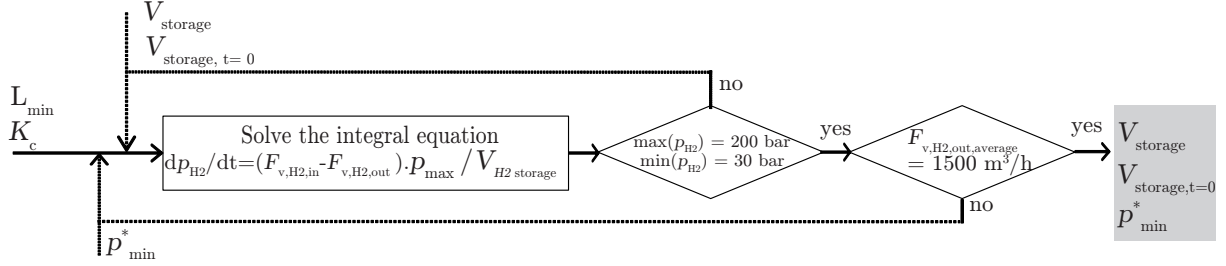


Figure 4.4: Iteration procedure used to calculate the H<sub>2</sub> storage volume  $V_{H_2 \text{ storage}}$ , the initial volume of H<sub>2</sub> in the storage  $V_{H_2 \text{ storage},t=0}$ , and the pressure in the storage above which the reactor load can be higher than  $L_{\min}$ ,  $p_{\min}^*$ . Constant: H<sub>2</sub> generation pattern,  $K_c$ , and minimum load for the reactor,  $L_{\min}$ .

$$L_{\min} = \frac{F_{v,H_2,in,reactor,min}}{F_{v,H_2,in,reactor,max}} \quad (4.6)$$

$$\frac{dp_{H_2}}{dt} = [F_{v,H_2,storage,in} - F_{v,H_2,storage,out}] \cdot \frac{p_{\max}}{V_{H_2 \text{ storage}}} \quad (4.7)$$

### *H<sub>2</sub> storage control strategy: pressure as controlled variable*

According to Equation 4.7, inlet and outlet H<sub>2</sub> flows affect the H<sub>2</sub> pressure in the storage, however neither flow is affected by the pressure in the storage. The inlet H<sub>2</sub> flow is stochastic and predictable to some extent (e.g. based on weather forecast), and the outlet H<sub>2</sub> flow can vary within a range that is defined by the minimum load allowed by the synthesis ( $L_{\min}$ ). The behaviour of the storage without a control strategy is non-self regulating (integrator). Variations in the inlet flow could produce an increase/decrease in the storage pressure outside the designed ranges, and the outlet H<sub>2</sub> flow would remain unaffected. A control strategy is required to maintain the pressure within the desired range. According to a typical control strategy, the storage pressure is selected as a controlled variable, the H<sub>2</sub> outlet flow works as a manipulated variable, and the H<sub>2</sub> inlet flow works as a disturbance.

The outlet H<sub>2</sub> flow is calculated as a function of the pressure in the storage, using a closed control loop with a proportional-only feedback control. Many control algorithms can be

used to correlate the pressure and the H<sub>2</sub> outlet flow. In this chapter just one possibility is presented with the aim of showing the importance of storage control. Different alternatives are possible like the use of a proportional-integral controller (instead of proportional-only), or a different definition of  $K_c$  (proportional constant). It could also be interesting to include information about weather forecast in the calculation of the outlet H<sub>2</sub> flow. In this way, not only the immediate H<sub>2</sub> pressures would be calculated, but there would be an added function of predictability; electricity production in the next few hours/days could be calculated, allowing the storage to operate in a more intelligent way.

The proportional constant  $K_c$  for the controller is defined in Equation 4.8. This definition is based on the importance to regulate the H<sub>2</sub> outlet flow.

$$K_c = \frac{(L_{\max} - L_{\min}) \cdot F_{v,H_2,in,reactor,max}}{p_{max}^* - p_{min}^*} \quad (4.8)$$

It can be assured, for the wind patterns used, that the pressure in the storage varies between 30 - 200 bar, no overpressure occurs (internal loop, Figure 4.4). However, the obtained storage volume can not be extrapolated to other wind patterns even if  $P_{el,max}$  and  $P_{el,average}$  are the same. The pattern itself influences the obtained storage volume.

$$\begin{aligned} F_{v,H_2,out,storage} &= L_{\min} \cdot F_{v,H_2,in,reactor,max} & p_{H_2} &< p_{\min}^* \\ F_{v,H_2,out,storage} &= K_c \cdot (p_{H_2} - p_{\min}^*) + F_{v,H_2,in,reactor,min} & p_{\min}^* &\leq p_{H_2} \leq p_{\max}^* \\ F_{v,H_2,out,storage} &= L_{\max} \cdot F_{v,H_2,in,reactor,max} & p_{H_2} &> p_{\max}^* \end{aligned} \quad (4.9)$$

If Equation 4.9 is included in Equation 4.7, the system becomes self-regulating because the derivative of the pressure is influenced by the pressure in the storage. The selected  $K_c$  value influences the rate of load change in the reactor inlet (for a constant  $L_{\min}$ ). If the size of the storage is big compared to the inlet flow, the time constant of the storage is high, and variations in the outlet flow have a low rate of change. High  $K_c$  values for the storage controller follow to a narrow range of pressures where the H<sub>2</sub> outlet flow is proportional to the pressure in the storage (Figure 4.5). The reactor operates most of the time at maximum or minimum load. Low values of  $K_c$  use a wider range of pressures where the H<sub>2</sub> outlet flow is proportional to the pressure in the storage. The reactor is, most consistently, operated between maximum and minimum load.

A good control strategy enables the use of the storage volume in an optimal way considering also the limitations imposed by the synthesis (e.g. maximum rate of load change allowed). The size of the storage is adequate when the storage pressure is most consistently between  $p_{\min}$  and  $p_{\max}$ . If a storage is most consistently at  $p_{\max}$ , it indicates the storage is small. On the contrary, if the storage operates most of the time at  $p_{\min}$ , the storage is oversized.

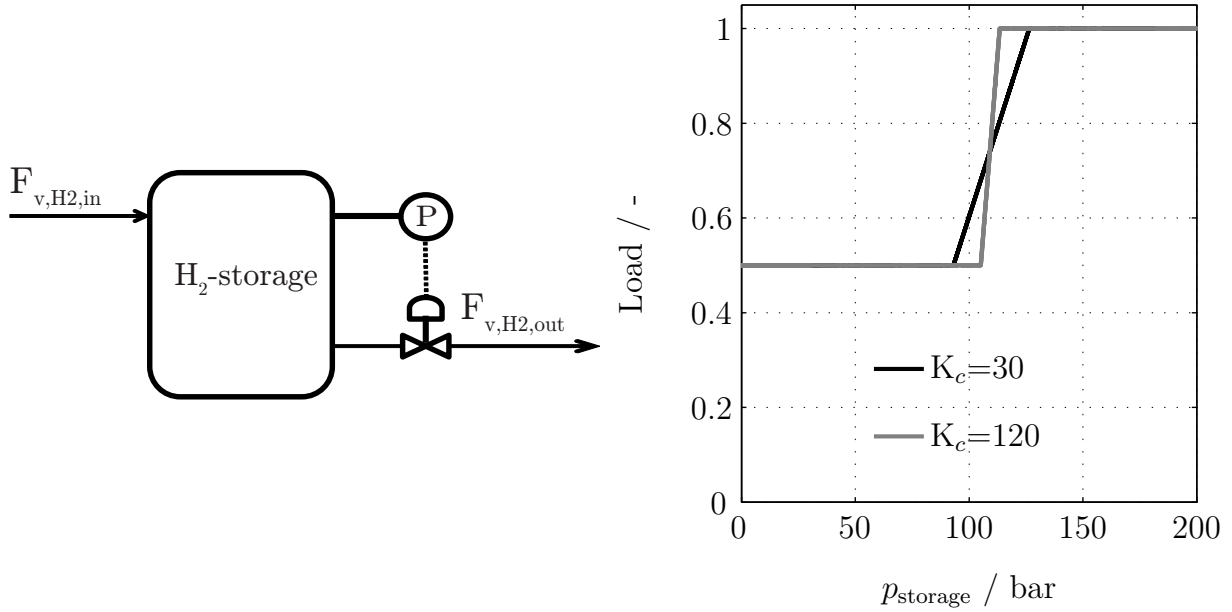
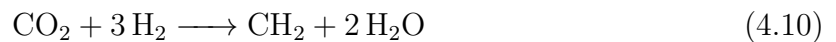


Figure 4.5: Manipulated variable  $F_{v,H_2,out,storage} = F_{v,H_2,in,reactor}$  (normalized as load:  $L = \frac{F_{v,H_2,in,reactor}}{F_{v,H_2,in,reactor,max}}$ , Equation 4.9) as a function of control variable (pressure in the storage) for two different proportional constant values  $K_c$ . Example calculation for a catalytic reactor able to operate in a range of load 50 - 100 % ( $L_{min} = 0.5$ ).

### Synthesis reactor

The chemical reaction considered as example is the  $\text{CO}_2$  hydrogenation to hydrocarbons. It is assumed that the reactor always reaches a  $\text{CO}_2$  conversion of 100 % independent of the inlet flow. Both reactants are fed to the reactor according to the stoichiometric ratio,  $(\text{H}_2/\text{CO}_2)_{in} = 3$ .



The catalyst mass is calculated based on the GHSV (gas hourly space velocity). Two different GHSV are selected as a representative variable to distinguish between a low complexity and a high complexity process (Equation 4.12). Typical GHSV under operation conditions ranges between 3000 and 36000  $\text{h}^{-1}$  for commercial methanol synthesis or between 2000 and 5000  $\text{h}^{-1}$  for commercial fixed-bed methanation. In the present example a factor of 40 between both GHSV is selected to make the difference between both processes significant:

- Low complexity process: corresponds to a catalyst with high activity, therefore the required reactor is small. The selectivity of the desired product is high, therefore either almost no separation units are required or separations of products are easy. For the calculations in this section, it is represented by  $\text{GHSV} = 20000 \text{ h}^{-1}$ .

- High complexity process: corresponds to a catalyst with low activity, therefore the required reactor is big. The selectivity of the desired product is low, therefore a complex separation train of units is required. For the calculations in this section, it is represented by  $GHSV = 500 \text{ h}^{-1}$ .

An average  $\text{CO}_2$  flow of  $500 \text{ m}^3/\text{h}$ , corresponding to a biogas plant, is assumed for calculations. The maximum  $\text{CO}_2$  flow is calculated with Equation 4.11 as a function of reactor flexibility  $L_{\min}$ . The mass of catalyst is a function of the maximum flow of  $\text{H}_2$  and  $\text{CO}_2$  to guarantee a near 100 % conversion at maximum flow and at any other lower flow (Equation 4.13). A  $\rho_{\text{bed}} = 800 \text{ kg/ m}^3$  and a bed porosity of  $\varepsilon = 0.4$ , are assumed as typical values for fixed-bed reactors (Jess et al. 2009).

$$F_{v,\text{CO}_2,\text{in,max}} = \frac{2 \cdot \overline{F_{v,\text{CO}_2,\text{in}}}}{(1 + L_{\min})} \quad (4.11)$$

$$GHSV = \frac{F_{v,\text{in}}}{V_r} = \frac{F_{v,\text{CO}_2,\text{in,max}} \cdot \left( \left( \frac{\text{H}_2}{\text{CO}_2} \right)_{\text{in}} + 1 \right) \cdot \rho_{\text{bed}}}{m_{\text{cat}} \cdot \varepsilon} \quad (4.12)$$

$$m_{\text{cat}} = \frac{F_{v,\text{CO}_2,\text{in,max}} \cdot \left( \left( \frac{\text{H}_2}{\text{CO}_2} \right)_{\text{in}} + 1 \right) \cdot \rho_{\text{bed}}}{GHSV \cdot \varepsilon} \quad (4.13)$$

#### 4.2.2 Case study: electricity production from an example wind farm

Figure 4.6 shows the relevant flows of the electricity-to-fuel process chain, for a case where electricity produced in a wind farm during four weeks is converted into hydrocarbon fuels.

The inlet  $\text{H}_2$  flow is calculated according to Equation 4.5. It is assumed that the electrolyser follows the electricity pattern without any delay one-to-one. The grey horizontal lines in the top-middle figure indicate the range of  $\text{H}_2$  flow that can be fed to the reactor (maximum and minimum load). When the  $\text{H}_2$  flow is above the upper line there is a need for storage, and when it is below the lower line,  $\text{H}_2$  of the storage is used to reach the minimum load. The pressure in the storage varies between 30 and 200 bar. Due to the low electricity production during the first part of the first week, the storage is almost empty and reaches the minimum pressure. During the first week, the reactor is operated at the minimum load. The production of  $\text{H}_2$  increases during the second week, and the pressure in the storage reaches the maximum value. At the beginning of the second week the reactor changes from minimum load operation to maximum load. Operation at maximum load takes place until the end of the third week. The pressure in the storage starts to decrease due to the lower production of electricity. At the end of the fourth week the



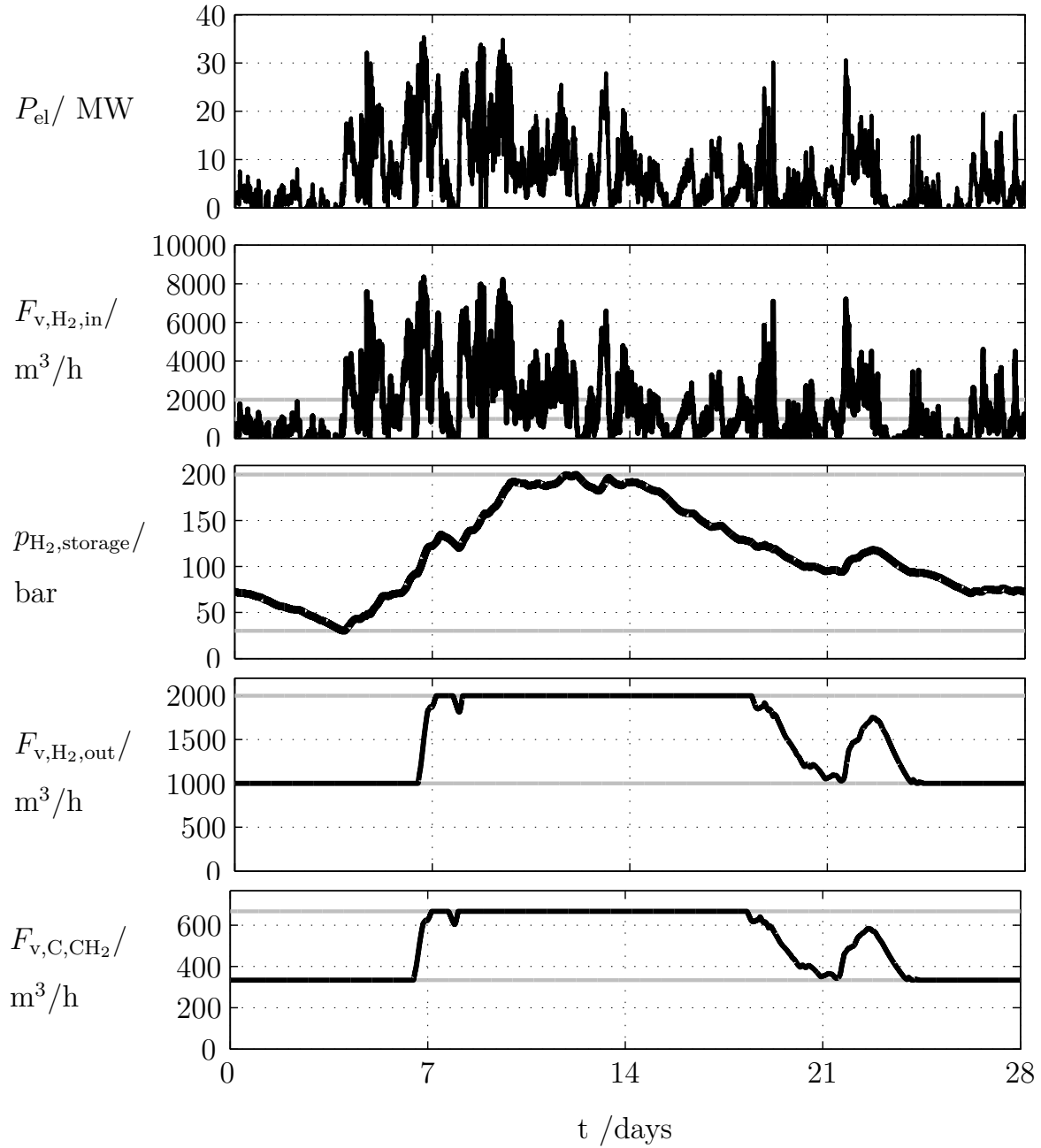


Figure 4.6: Electricity-to-fuel process chain. Top: Power output during one example month from a wind farm in the north of Germany (Aicher et al. 2014). Data collected each minute. Top-middle: Volumetric flow of  $H_2$  produced via electrolysis. Middle: Pressure profile in the  $H_2$  storage ( $p_{max} = 200$  bar,  $p_{min} = 30$  bar,  $V_{H_2 storage} = 1451.5$   $m^3$ ),  $K_c = 30$  (see Figure 4.5). Bottom-middle: Volumetric flow of  $H_2$  leaving the storage with a maximum rate of load change of 0.12 %/min and a range of load of 50 - 100 %,  $(H_2/CO_2)_{in} = 3$ . Bottom: Volumetric flow of C in  $CH_2$  out of the reactor. Average production of hydrocarbons is 500  $m^3/h$ . The overall  $CO_2$  conversion is 100 % independent of operation load  $X_{CO_2} = 100$  %. Horizontal grey lines indicate maximum and minimum allowable values for the respective variable.

filling level of the storage is the same as at  $t = 0$ , and the reactor is again operated at minimum load. The average production of hydrocarbons is  $500 \text{ m}^3/\text{h}$ .

The production of electricity in the present example is intermittent, and consequently, the  $\text{H}_2$  flow produced ranges between  $F_{v,\text{H}_2,\text{Ely}} = 8340 \text{ m}^3/\text{h}$  and  $F_{v,\text{H}_2,\text{Ely}} = 0$ . The selected synthesis can be operated between 50 and 100 % load ( $L_{\min} = 0.5$ ), the maximum  $\text{H}_2$  flow that can be fed to the reactor is  $2000 \text{ m}^3/\text{h}$  and  $666.7 \text{ m}^3/\text{h}$  of  $\text{CO}_2$ .

Figure 4.7 shows the volume of  $\text{H}_2$  storage required as a function of the synthesis flexibility  $L_{\min}$ , and the proportional constant  $K_c$  for the storage controller using the wind farm pattern. The  $\text{H}_2$  storage size can be significantly reduced with increasing reactor flexibility (decreasing  $L_{\min}$ ). The value of the proportional constant of the controller also influences the storage volume. For each  $L_{\min}$ , a minimum value of  $K_c$  exists that corresponds to a  $p_{\min}^* = 30$  and a  $p_{\max}^* = 200$ . This  $K_c$  value is the most conservative one and produces a  $\text{H}_2$  outlet flow with very low rates of change (max.  $0.05 \text{ \%/min}$ ). The value of  $K_c$  shows higher influence at low values of  $L_{\min}$ , however, at values of  $K_c$  higher than 90, no effect in the storage size can be observed, and only a slight difference in the maximum rate of load change appears (for  $L_{\min} = 0.1$ :  $K_c = 120$ ,  $r_L = 0.71 \text{ \%/min}$  and for  $K_c = 90$ ,  $r_L = 0.54 \text{ \%/min}$ ). At high values of  $K_c$ ,  $p_{\min}^*$  is very similar to  $p_{\max}^*$  and the reactor is

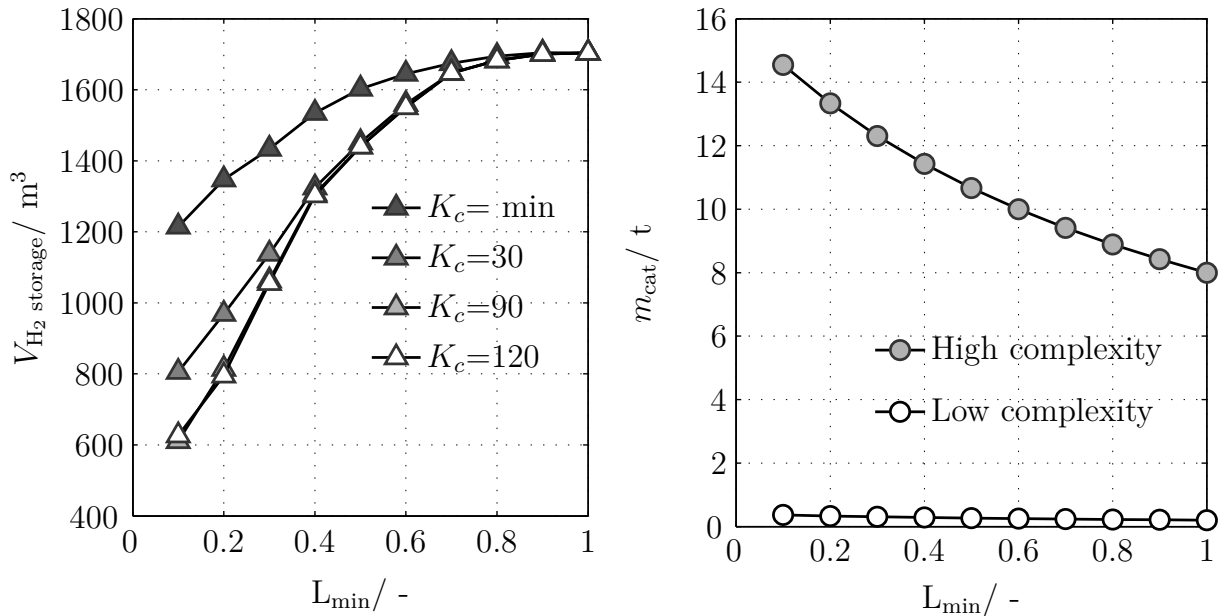


Figure 4.7: Left: effect of reactor flexibility ( $L_{\min}$ ) and proportional constant for the pressure-controller  $K_c$  on  $\text{H}_2$  storage volume. The value of  $K_c$  minimum corresponds to  $p_{\min}^* = 30$  and a  $p_{\max}^* = 200$ , and varies for each  $L_{\min}$  (see Equation 4.8). Right: effect of reactor flexibility ( $L_{\min}$ ) on mass of catalyst for the high and low complexity processes calculated with Equation 4.13. Curves: trends.

operated at minimum and maximum load. Only for a very narrow range of pressures in the storage does the reactor need to operate in-between maximum and minimum load. The mass of catalyst required as a function of reactor flexibility increases when decreasing  $L_{\min}$  (Equation 4.13), as a consequence of the higher maximum volumetric flow that needs to be converted (Equation 4.11). The high complexity synthesis requires a higher mass of catalyst due to the lower GHSV.

Figure 4.8 shows the size of both  $H_2$  storage and reactor relative to  $L_{\min} = 1$ , as affected by reactor flexibility ( $L_{\min}$ ). The increase in the relative size of the reactor is independent of the process complexity. To evaluate if part-load operation of the catalytic process provides an advantage for the overall electricity-to-fuel process compared with a constant single load operation ( $L_{\min} = 1$ ), calculations of the absolute investment cost for  $H_2$  storage and catalytic process are needed. In general, if the size of the required  $H_2$  storage is large, its investment would also be high and it would be attractive to operate the chemical process under part-load, to reduce the size of the  $H_2$  storage. However if the chemical process is complex, the required increase in size would significantly increment the investment cost and the reduction in the size of the  $H_2$ -storage would be irrelevant. Investment cost calculations for the  $H_2$  storage and the catalytic process are outside the scope of this work.

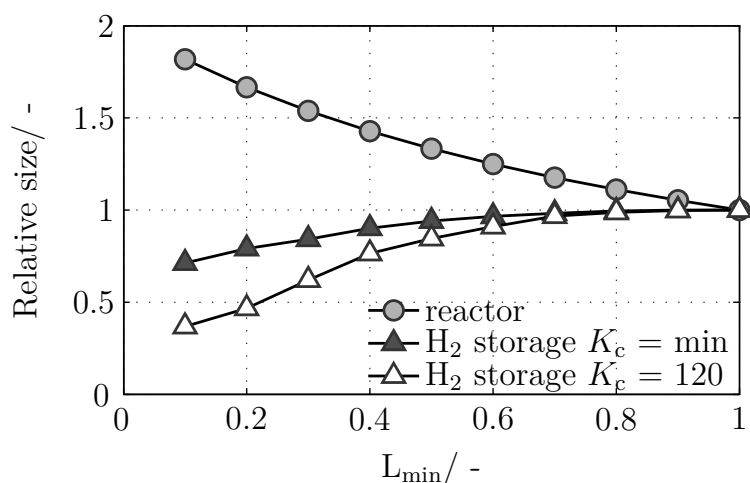


Figure 4.8: Effect of reactor flexibility ( $L_{\min}$ ) on reactor and  $H_2$  storage size relative to  $L_{\min} = 1$  (constant single load reactor operation). Symbols for reactor represent high and low complexity process. Curves: trends.

### 4.2.3 Conclusion and motivation for flexible operation of a synthesis reactor

In this section it is shown that variable operation has the potential to reduce the size of the  $H_2$  storage in the electricity-to-fuel process chain, however an economical evaluation is required to further evaluate the potential of part-load operation of catalytic processes.

A simplified approach based on two case studies is shown. The first case study considers an electricity generation pattern from an example wind farm, and shows that in this particular case a decrease in the size of the H<sub>2</sub> storage is possible if the catalytic reactor is operated under part-load. The sinus wave function (see Appendix B) is used in addition to understand in a systematic way the influence of time period, amplitude, and reactor flexibility on the size of the H<sub>2</sub> storage. With the defined sinus wave function it is possible for amplitudes lower than 6.64 MW ( $f = 1$ ) to avoid the use of a H<sub>2</sub> storage if reactor flexibility is sufficiently high.

Figure 4.9 shows schematically the context where flexible operation of the synthesis may be interesting, the combination of a low complex catalytic process with a complex renewable electricity pattern:

- Complex renewable electricity pattern: sharp and stochastic (long periods of low input combined with long periods of high input) or long time periods combined with high amplitudes. In all these cases, a large H<sub>2</sub> storage size is required if the catalytic process needs to be operated under a constant load.
- Less complex catalytic process: low investment is required for the catalytic process (i.e. high values of GHSV; very active catalyst (small reactor), high product selectivity, (almost no peripheral equipment needed)). An increase in the size of the synthesis due to flexible operation is not significant for the investment cost overall because the savings on the H<sub>2</sub> storage are much higher.

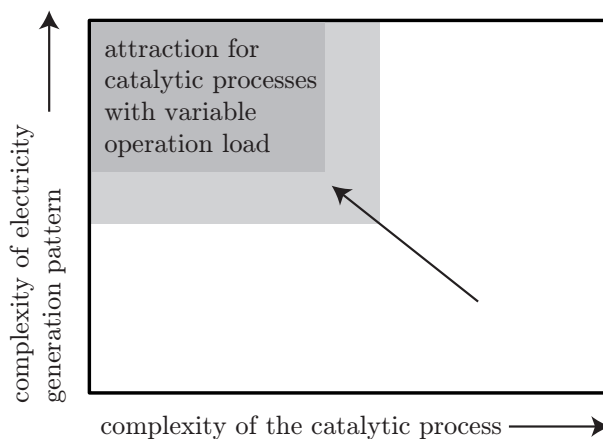


Figure 4.9: Region of interest for variable load operation of catalytic processes.

The storage and reactor investment, calculated for a constant load reactor design ( $L_{\min} = 1$ ), could be useful to decide if there is potential to reduce the overall investment figures, by means of variable load operation of the catalytic process. In general, if the overall investment is dominated by the H<sub>2</sub> storage investment, variable operation becomes attractive from an economic point of view.

**Important details identified in this section for future work**

- Control strategy for the H<sub>2</sub> storage is important to reduce the storage size when operating the reactor under variable load.
- Range of load and rate of load change of the reactor are connected to the size and the control strategy of the H<sub>2</sub> storage. They will be studied in the next chapters in more detail (Chapter 7 and 8).
- The complexity of the catalytic process may play a decisive role in part-load operation (see section 8.4).
- Evaluation of investment cost for H<sub>2</sub> storage and catalytic processes able to operate under part-load conditions is required to further evaluate the potential of part-load operation. It is conceivable that part load operation of a catalytic process becomes more expensive than under steady-state operation: catalytic reactor and reactor attached equipment should be larger and control and automation strategies more complex than for steady-state operation.



# 5 CO<sub>2</sub> hydrogenation with iron catalyst, effect of catalyst composition and reaction conditions: experimental study

*This chapter describes the experimental approach in studying CO<sub>2</sub> hydrogenation to produce gaseous hydrocarbons (C<sub>2</sub>H<sub>6</sub>, C<sub>3</sub>H<sub>8</sub>, C<sub>4</sub>H<sub>10</sub>) with two iron catalysts promoted with different amounts of potassium (K), under a wide range of operating conditions. The aim is to clarify the effects of reaction variables and potassium content on CO<sub>2</sub> conversion, hydrocarbon yield, and hydrocarbon product distribution. A catalyst composition and proper operating conditions are proposed at the end of the chapter with regard to its applicability for heating value adjustment of raw substitute natural gas (methane). The central part of the results shown in this chapter were generated at Engler-Bunte-Institut (KIT). Supporting experiments including in-situ and ex-situ catalyst characterisation were carried out at the Centre for Catalysis Research in the University of Cape Town (group of Prof. M. Claeys) in the context of a diploma thesis co-supervised at KIT.*

## 5.1 Iron-based catalyst promoted with potassium: selection and preparation

The catalysts selected in the present work are based on iron, promoted with potassium (K). Fe/K ratios are 100/2 (g/g) and 100/10 (g/g). K has probably the most significant influence on the overall catalyst performance for CO<sub>2</sub> hydrogenation in comparison with other common promoters (e.g. Mn, Cu). According to literature, low amounts of K are attractive for the production of short chain hydrocarbon alkanes, while higher K promoting favour long chain hydrocarbons (see section 3). The optimal degree of potassium promoting depends on the conditions of the reaction, and therefore needs to be determined experimentally. The two amounts of K are selected with the aim to reach a compromise

between a high CO<sub>2</sub> conversion and a high selectivity to produce C<sub>2-4</sub>.

Catalyst preparation was carried out in the university of Cape Town in the research group of Prof. M. Claeys. The iron catalysts were prepared through quick precipitation from hot (95 °C) aqueous iron nitrate solution (1 M Fe(NO<sub>3</sub>)<sub>3</sub> · 9H<sub>2</sub>O), with an aqueous NH<sub>3</sub> solution (5 %wt.) at pH7 and under vigorous stirring (24000 rpm). After washing with deionized H<sub>2</sub>O, the catalyst precursor was dried for 12 hours at 120 °C in air and crushed to a fraction below 125 μm. This was followed by calcination under airflow (900 ml(STP)/gFe/min) in a fluidized bed reactor at 400 °C for 3 hours (heating rate: 10 °C/min). To achieve the desired potassium loading, the catalyst was impregnated with an aqueous 1 molar K<sub>2</sub>CO<sub>3</sub> solution, and again dried and calcined under the same conditions as above. The catalyst composition was 100 g Fe / 2 g K and 100 g Fe / 10 g K as confirmed by means of Atomic Absorption Spectroscopy analysis (AAS) .

## 5.2 Experimental plan and reaction conditions

Table 5.1 summarises the experimental conditions used in the lab-scale fixed-bed reactor. Detailed information can be found in Table C.1 and C.2.

Table 5.1: Overview of the range of experimental conditions used to carry out experiments in lab-scale fixed-bed reactor.

	$T$ °C	$p$ MPa	$\tau_{\text{mod}}$ kg s/m <sup>3</sup>	$(\text{H}_2/\text{CO}_2)_{\text{in}}$ -	$m_{\text{cat}}$ g
100 g Fe / 2 g K	250 - 330	1, 2	175 - 5000	4, 5, 8, 23, ∞	1, 1.5, 2
100 g Fe / 10 g K	270 - 330	1	400 - 5000	4, 5, 8	2

Table 5.2 summarises the additional experiments carried out in-situ with the magnetometer and the X-ray diffractometer. The aim of these experiments is to gain a complementary understanding of the effect of the reaction conditions on the catalytic system during catalyst reduction, formation, and change in operating conditions (see chapter 7). Additionally, ex-situ X-ray diffraction experiments were carried out from fresh and spent catalyst samples.



Table 5.2: Overview of the range of experimental conditions used to carry out experiments in the magnetometer and X-ray diffractometer

	$T$ °C	$p$ MPa	$\tau_{\text{mod}}$ kg s/m <sup>3</sup>	Magnetometer		X-ray diffractometer	
				(H <sub>2</sub> /CO <sub>2</sub> ) <sub>in</sub> -	$m_{\text{cat}}$ g	(H <sub>2</sub> /CO <sub>2</sub> ) <sub>in</sub> -	$m_{\text{cat}}$ g
100 g Fe / 2 g K	300, 330	1.13	353	5, 8	0.1	5	0.0304
100 g Fe / 10 g K	300	1.13	353, 414	5, $\infty$	0.1	5, $\infty$	0.0304

## 5.3 Experimental setups, procedures and methods

Three different lab-scale setups were used in the present work. The lab-scale setup with the fixed-bed glass reactor is a reactor concept that has been used at the EBI for several years for FT experiments (Claeys 1997; Mena Subiranas 2009; Pabst 2013; Riedel 2002; Rohde 2011; Steen 1993; Unruh 2006).

The two applied catalyst characterisation techniques, namely a capillary X-ray diffraction cell and a magnetometer, were developed in the University of Cape Town and recently patented (Claeys et al. 2010).

### 5.3.1 Experimental studies in lab-scale fixed-bed reactor

A new lab-scale setup (Figure 5.1) similar to the proved lab-scale reactors existing at EBI was designed and built within the present work.

#### 5.3.1.1 Experimental setup

The glass reactor tube ( $d_{\text{int}} = 8$  mm;  $L_t = 700$  mm) is filled with catalyst particles ( $d_p = 50 - 100$   $\mu\text{m}$ ) diluted with SiO<sub>2</sub> ( $d_p = 100 - 160$   $\mu\text{m}$ ) in a weight ratio catalyst to SiO<sub>2</sub> = 1/3 (Figure C.9). The size of the catalyst particles was chosen to avoid intraparticle mass transfer limitations (Claeys et al. 2004), and the larger size SiO<sub>2</sub> particles decrease the pressure drop across the catalyst bed (with the catalyst particles covering the larger SiO<sub>2</sub> particles as an adhering layer). In this way it is possible to achieve a uniform gas flow at low pressure drop. Before being fed into the reactor, catalyst and SiO<sub>2</sub> are physically mixed, and afterwards distilled water is added to avoid particle segregation during reactor filling. The dilution of catalyst almost allows isothermal operation due to the reduction of thermal energy production per volume unit ( $\pm 1 - 3$  °C, depending on

the reaction temperature). The temperature profile along the catalyst bed is measured with a moveable thermocouple inserted in a centrally positioned thermo-well ( $d_{\text{ext}} = 4$  mm). The length of the catalyst bed used varied between 100 and 200 mm depending on the catalyst mass used. A bed of inert particles is placed below the catalyst bed, to reach the proper vertical position for the heating system, and on top of the catalyst bed, to serve as gas mixer and preheating zone. At the bottom of the glass reactor a porous glass frit retains the particles. The glass reactor itself is placed vertically in a metal tube in order to allow experimentation at higher pressures. The annular space between the glass and the metal reactor is sealed with an O-ring to prevent gas recirculation and bypass effects. The metal tube is heated via three alumina blocks with four heating cartridges each ( $L = 200$  mm,  $d_{\text{ext}} = 6$  mm), insulated with glass wool.

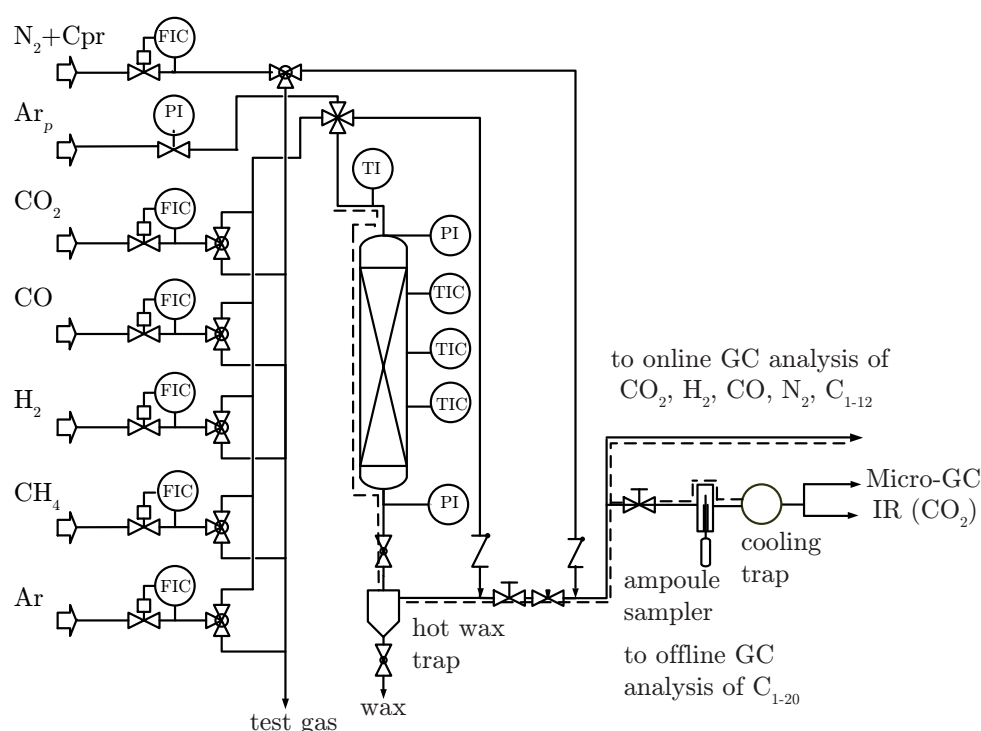


Figure 5.1: Flow scheme of the experimental setup with fixed-bed reactor. Detailed illustration of the fixed-bed in Figure C.9.  $Ar_p$ : pressure regulated Ar flow to maintain the constant pressure in the reactor

The reactant gases, H<sub>2</sub> and CO<sub>2</sub> (purity > 99.995 %), are preheated in the feed line up to 250 °C and enter the reactor at the top. The volumetric gas flows are controlled by mass flow controllers (MFC). To cover a wide range of volumetric flows, two MFCs are used for CO<sub>2</sub> and two for H<sub>2</sub>. The reactor pressure is maintained constant using a pressure-regulated argon flow, which is added after the reactor outlet, and a needle valve. Pressure is measured at the top and bottom of the reactor. The product gases and the added argon are expanded using a manual control valve and a needle valve. After

the reactor, the product flows through a wax trap (at reaction pressure,  $T = 180\text{ °C}$ ) where long chain hydrocarbons condensate. All downstream tubing is electrically heated at  $T = 200\text{ °C}$ . A mixture of nitrogen (N<sub>2</sub>) and cyclopropane (Cpr) (0.5 vol% Cpr) is added to the product flow; these compounds serve as reference gases and allow the calculation of molar flows of various compounds of interest from gas chromatographic analyses. The product gas flow is split into two. The first flow goes to the online gas chromatograph (Agilent 7890A GC), where the product gases are sequentially analysed (each measurement takes 25 min) by means of two flame ionisation detectors (FID) and one thermal conductivity detector (TCD) (Figure D.13). The other part of the product flow is routed to an ampoule sampler (Figure D.10), where pre-evacuated glass ampoules can be filled with the hot gaseous product every minute (Figure D.10). Before the off-gas is vented, the gas flow passes a cooling trap, where water and hydrocarbons condensate at room temperature. Ampoules are afterwards analysed in an offline gas chromatograph (Figure D.11).

### 5.3.1.2 Procedure and methods

Once the reactor is loaded and leakproof, the different H<sub>2</sub> and CO<sub>2</sub> flows required for the experiment are set in the MFC and flow through the cold reactor under reaction pressure. The aim is to check the inlet ratio  $(\text{H}_2/\text{CO}_2)_{\text{in}}$  and the inlet volumetric flow for each setting that is going to be used later during the experiment with the reaction (deviations need to be lower than 2 % from the target value, measurements are done with the online GC). These measurements are repeated at the end of the experiments and average values are used in the data analysis. The composition of the product mixture needs to be within the calibrated ranges in the TCD. The total volumetric flow in the outlet of the test rig is measured after adjusting the position of the throttling valve. Experiments with an inert bed at reaction temperature and a catalyst bed at room temperature show that the lab-scale setup has no catalytic activity.

The catalyst bed is dried (starting at  $T_{\text{room}}$  with a ramp of  $2\text{ °C/min}$ ,  $T_{\text{max}} = 200\text{ °C}$ ) at atmospheric pressure with Argon to evaporate the H<sub>2</sub>O used to mix the catalyst with the SiO<sub>2</sub>. Once dry, the catalyst is reduced in a H<sub>2</sub>/Ar atmosphere (see Table 5.3 for conditions). The reactor is then cooled with Argon to the first reaction temperature,  $300\text{ °C}$ . The pressure of 1 MPa is adjusted and the reactant gas flow set to  $(\text{H}_2/\text{CO}_2)_{\text{in}} = 5$ ,  $\tau_{\text{mod}} = 400\text{ kg s/m}^3$  (Table 5.4). Initial operating conditions are maintained for several days (Figure 5.2). After steady state conditions are reached (CO<sub>2</sub> conversion standard deviation within 10 h lower than 1 %), new reaction conditions are adjusted (Table 5.1). The wax trap and the cooling trap are emptied daily.

Table 5.3: Conditions used for catalyst reduction with the two catalysts in the different setups

	gas	(H <sub>2</sub> /Ar) <sub>in</sub>	$\tau_{\text{mod}}$ kg s/m <sup>3</sup>	$p$ MPa	$T_{\text{start}}$ °C	Ramp K/min	$T_{\text{end}}$ °C	hold h
Fixed-bed lab-scale	(H <sub>2</sub> /Ar) <sub>in</sub>	1/3	3000	0.1	$T_{\text{room}}$	2	400	16
Magnetometer	(H <sub>2</sub> /Ar) <sub>in</sub>	1/3	300	0.1	40	2	400	16
XRD	(H <sub>2</sub> /N <sub>2</sub> ) <sub>in</sub>	1/3	329	0.1	40	2	400	16

Table 5.4: Conditions used for catalyst formation with the two catalysts in the different setups

	gas	(H <sub>2</sub> /CO <sub>2</sub> ) <sub>in</sub>	$\tau_{\text{mod}}$ kg s/m <sup>3</sup>	$p$ MPa	$T$ °C
Fixed-bed lab-scale	H <sub>2</sub> , CO <sub>2</sub>	5	400	1.00	295
Magnetometer	H <sub>2</sub> , CO <sub>2</sub> , N <sub>2</sub>	5	353	1.13	300
XRD	H <sub>2</sub> , CO <sub>2</sub> , N <sub>2</sub>	5	353	1.13	300

### 5.3.1.3 Analysis of products

The analysis of the product gases is done by means of gas chromatography. Detailed information can be found in section D of the appendix. The online GC (Agilent 7890A, JAS) is equipped with five columns (Molecular sieve 5A, Hayesep Q, Hayesep T, GS-Gaspro, HP-5) that make the separation of permanent gases and short chain hydrocarbons possible. However, the integration of the chromatogram corresponding to the long chain hydrocarbons can not be done properly due to the high variability of the basis line. See example chromatograms in Figures D.14, D.15 and D.16.

Analysis of the hydrocarbon products was completed in a new offline GC setup (Figure D.11), assembled and put into service during the present work according to the old setup and Schulz et al. (1984). The offline GC is equipped with two non-polar capillary columns (HP-1) and two FID that enable the analysis of two ampoules, in parallel. Example gas chromatograms can be found in Figure D.12.

### 5.3.1.4 Data analysis and definitions

The molar flows of the organic and inorganic components are calculated based on the peak areas  $A_i$  obtained with the GC (same method for online and offline GCs) related with

the peak area of the reference gas,  $A_{N_2}$  for inorganic components, and  $A_{Cpr}$  for organic components, (Equation 5.1 and 5.2, respectively). The molar flow of reference gas added to the product gas is such:  $F_{V,N_2+Cpr,NTP} = 15$  ml/min,  $y_{n,Cpr} = 0.5$  vol%. Calibration factors ( $f_i$ ) for the inorganic compounds are determined at regular intervals (Table D.4), yet for organic compounds are considered to be 1, except for oxygenates where values are taken from literature (Pabst 2013).  $N_{C,i}$  represents the carbon number.

$$\frac{F_{n,i}}{F_{n,N_2}} = f_i \cdot \frac{A_i}{A_{N_2}} \quad (5.1)$$

$$\frac{F_{n,i}}{F_{n,Cpr}} = \frac{N_{C,Cpr}}{N_{C,i}} \cdot \frac{f_i \cdot A_i}{f_{Cpr} \cdot A_{Cpr}} \quad (5.2)$$

The molar flow of water vapor  $F_{n,H_2O,out}$  can not be measured by means of gas chromatography and is calculated at reactor outlet based on the molar flows of CO and C in organic product (from ampoule analysis) using the stoichiometric coefficients of H<sub>2</sub>O in the CO<sub>2</sub>-shift ( $\nu_{H_2O,CO_2-sh}$ ) and FT reaction ( $\nu_{H_2O,FT}$ ).

$$F_{n,H_2O,out} = \sum_{i=1}^{i=20} F_{n,i,out} \cdot N_{C,i} \cdot (\nu_{H_2O,CO_2-sh} + \nu_{H_2O,FT}) + F_{n,CO,out} \cdot \nu_{H_2O,CO_2-sh} \quad (5.3)$$

The CO<sub>2</sub> conversion  $X_{CO_2}$  is calculated based on the molar flows of CO<sub>2</sub> at the outlet and inlet of the reactor:

$$X_{CO_2} = \frac{F_{n,CO_2,in} - F_{n,CO_2,out}}{F_{n,CO_2,in}} \quad (5.4)$$

The CO yield  $Y_{CO}$  is the molar flow of CO at the outlet divided by the inlet CO<sub>2</sub> molar flow:

$$Y_{CO} = \frac{F_{n,CO,out}}{F_{n,CO_2,in}} \quad (5.5)$$

The yield of organic product  $Y_{Corg}$  is based on the molar flow of C in organic products divided by the molar flow of CO<sub>2</sub>. This molar flow of C comprises all gaseous products at wax trap conditions (at reaction pressure and  $T = 180$  °C).

$$Y_{Corg} = \frac{F_{nC,Corg,out}}{F_{n,CO_2,in}} \quad (5.6)$$

The yield of carbon  $Y_C$  (i.e. carbon not accounted for: heavy hydrocarbons, solid carbon deposited on catalyst) is determined from the carbon balance as the difference between carbon molar flow in the inlet and outlet, divided by the molar flow of CO<sub>2</sub>.

$$Y_C = X_{CO_2} - Y_{CO} - Y_{Corg} \quad (5.7)$$

The selectivity of a component  $i$  can be calculated as a function of yield of  $i$  and CO<sub>2</sub> conversion.

$$S_i = \frac{Y_i}{X_{CO_2}} \quad (5.8)$$

The hydrocarbon product composition is described by the mass fraction on carbon basis:

$$y_{m,i} = \frac{F_{n,i} \cdot N_{C,i}}{\sum_i F_{n,i} \cdot N_{C,i}} \quad i = C_1, C_2, C_3, \dots, C_N \quad (5.9)$$

The modified residence time  $\tau_{\text{mod}}$  is the ratio of the catalyst mass  $m_{\text{cat}}$  (before reduction) divided by the inlet volumetric flow to the reactor under standard temperature and pressure (STP:  $p_{\text{STP}} = 101315 \text{ Pa}$ ,  $T_{\text{STP}} = 273.15 \text{ K}$ ).

$$\tau_{\text{mod}} = \frac{m_{\text{cat}}}{F_{V,\text{in,STP}}} \quad (5.10)$$

For comparison with the thermodynamic equilibrium constant  $K_p$ , a ratio of partial pressures at the reactor outlet is used to calculate  $K_{p,\text{exp}}$ . Partial pressures are calculated based on molar fractions according to Raoult's law.

$$p_i = y_{n,i} \cdot p \quad (5.11)$$

$$K_{p,\text{exp}} = \frac{p_{\text{CO}} \cdot p_{\text{H}_2\text{O}}}{p_{\text{CO}_2} \cdot p_{\text{H}_2}} \quad (5.12)$$

The parameter  $\alpha$  (chain growth probability, ASF model) is determined from experimental results by a least square method. The difference of the mass fraction, between the experimental and calculated results from the ASF model (Equation 3.8), is minimized by adjusting  $\alpha$  (Equation 5.13).

$$\Delta y = \sum_i (y_{m,i,\text{cal}}(\alpha) - y_{m,i,\text{exp}})^2 \quad i = C_3 - C_8 \quad (5.13)$$

Experimental data has a systematic and random error. In order to minimize the random error, the arithmetic mean of a number of data points  $N$  ( $x_i$ ) is used, Equation 5.14.

$$\bar{x} = \frac{1}{N} \sum_{i=1}^N x_i \quad (5.14)$$

The standard deviation  $\sigma$  of the data points shows the variation of the experimental values from the mean. The standard deviation is defined in Equation 5.15.

$$\sigma = \sqrt{\frac{1}{N} \sum_{i=1}^N (x_i - \bar{x})^2} \quad (5.15)$$

Since the standard deviation is only an estimation of the error it is preferable to use a confidence interval ( $\bar{x} \pm \Delta x$ ). The formula to calculate the upper and lower confidence limit is:

$$\Delta x = \frac{\sigma s}{\sqrt{N}} \quad (5.16)$$

where the factor  $s$  is a value from the student's t-distribution. The factor  $s$  is dependent of the number of data points  $N$  and the confidence (e.g.  $s = 2.485$  for  $N = 25$  and confidence 98 %).

### 5.3.2 Supporting in-situ magnetic measurements

In-situ magnetic measurements are carried out in a magnetometer (Figure E.17). Detailed information about the setup, fixed-bed reactor, and procedure can be found in Fischer (2011). It mainly consists of two magnetic poles, two coils, and a moveable sample that, in this case, is replaced by a reactor loaded with catalyst and connected to gas supply tubes in a way that operation of the reactor is possible, and also the magnetization of the catalyst can be followed under reaction conditions. The magnetic poles generate a high uniform magnetic field (-20 to 20 kOe) that, in combination with the vertical movement of the sample, generates a change in the magnetic flux density. This induces a proportional voltage in the pick-up coils, which is used as magnetisation with arbitrary units. Magnetisation is a measurement that can give insight into the catalyst composition, and it can also provide information on the crystallite size and phase changes of the magnetic phases.

The behaviour of a material under an external magnetic field is caused by the ordering of the magnetic moments (ferromagnetic (including ferrimagnetism), antiferromagnetic, diamagnetic and paramagnetic). Ferromagnetic materials are attracted by the external magnetic field via the alignment of the electron spins, and retain a level of magnetism after removal of the external field (remanent magnetisation). Antiferromagnetic materials are very similar to ferromagnetic with the difference that the interaction with the external field is caused by an anti-alignment of neighbouring spins and no remanent magnetism occurs. Paramagnetic and diamagnetic materials offer only a weak magnetism by putting them in an external field. Paramagnetic materials are slightly attracted by the magnetic field, whereas diamagnetic materials are slightly repelled by the magnetic field. Neither of them present remanent magnetism.

The different phases present on an iron catalyst can display ferromagnetic and antiferromagnetic behaviour, but only retain their magnetic properties below their Curie or Néel temperature (see Table 5.5). The final magnetic state depends on the magnetic moments of the material and on the temperature. Above the Curie/Néel temperature no magnetism can be measured. The reason for this is that permanent magnetism changes to induced magnetism and the spins are randomly ordered due to the high thermal energy which does not allow an alignment of the spins. Due to the temperatures applied during the experiments (Table 5.2), only materials with a high Curie temperature can be detected. The expected carbides to be formed during the reaction (e.g. Häag carbide) would not show any magnetisation, while metallic iron and oxides can be magnetised at reduction and formation conditions. However, due to its very low saturation magnetisation (i.e. point at which an increase in external field strength does not result in any further increase in magnetisation), the contribution of hematite to a magnetic reading is negligible in this

study. Consequently, only metallic iron and magnetite contribute to the magnetisation signal produced by the catalyst.

Additional information about this in-situ catalyst characterisation technique can be obtained in previous publications of the research group where these measurements were done (Claeys et al. 2014; Fischer 2011; Fischer et al. 2014; Fischer et al. 2015) or in other literature sources (Chernavskii et al. 2009).

Table 5.5: Magnetic properties of different iron phases

Compound	Name	Magnetism	Curie/Neél temperature
$\alpha$ -Fe	metallic iron	ferromagnetic	770 °C
$\alpha$ -Fe <sub>2</sub> O <sub>3</sub>	hematite	antiferromagnetic	690 °C
Fe <sub>3</sub> O <sub>4</sub>	magnetite	ferrimagnetic	580 °C
Fe <sub>5</sub> C <sub>2</sub>	Häag carbide	ferromagnetic	257 °C
$\theta$ -Fe <sub>3</sub> C	cementite	ferromagnetic	212 °C

In the magnetometer, 0.1 g of catalyst were used to follow magnetisation changes during catalyst reduction and formation (Table 5.3 and 5.4). The magnetisation value was collected every 5 minutes during the reduction and each 10 - 15 minutes during formation. Each recording takes about 2 minutes. The signal of the empty reactor collected in former runs is subtracted from the data obtained with the filled reactor.

### 5.3.3 Supporting in-situ and ex-situ measurements with X-ray diffractometer

X-ray diffraction is one of the oldest and most frequently applied techniques in catalyst characterisation. It is a very useful tool for determining the atomic and molecular structure of crystalline phases by means of lattice structural parameters and to obtain an indication of particle size.

In general, a X-ray diffractometer has three parts: (i) the X-ray source (tube), where the X-rays are generated, (ii) a sample stage, and (iii) a detector, where the intensity of the diffracted radiation is collected. A great advantage of this technique is the considerable penetrating power of X-rays, that can be used to study catalysts under in-situ conditions. X-rays have wavelengths in the Ångstrom range ( $\lambda = 1 - 10 \text{ \AA} = 0.1 - 1 \text{ nm}$ ), sufficiently energetic to penetrate solids, and well suited to probe their internal structure. When X-rays emit from the source and strike the surface of a crystal, some of the rays are scattered on the first layer, others pass the first layer and are later scattered at one of the



next layers. The atomic planes of a crystal cause an incident beam of X-rays to interfere with another one as they leave the crystal. This phenomenon is called X-ray diffraction. If diffracted beams are in phase, constructive interference occurs and a peak occurs in the diffraction pattern. If the beams are not in phase, destructive interference appears and the pattern shows no peak. The tube and the detector are movable, which allows a scanning of the desired  $2\theta$  range by changing the angle with time (the angle is defined between the x-ray source/detector and the sample). The result of the measurement is a diffractogram, a pattern which shows the intensity of the diffracted radiation over the selected  $2\theta$  range. Since most materials have unique diffraction patterns, compounds can be identified by comparing the obtained pattern with existing diffraction patterns of single materials saved in databases (see section E.3). The diffraction pattern can be used to determine the crystal size (Debye-Scherrer equation) and the quantitative phase composition by using the Rietveld refinement (least square approach to refine a theoretical curve profile until it fits, as good as possible, the measured curve). The Rietveld method assumes that all phases are crystalline, thus amorphous phases can not be determined with the Rietveld method.

The diffractometer used for the ex-situ and in-situ measurements is a Bruker D8 Advance laboratory X-ray diffractometer available at the University of Cape Town. It works with a cobalt source ( $\lambda = 0.178897$  nm) and is equipped with a VÅNTEC-2000, Bruker AXS detector. During the in-situ experiments the sample stage is replaced by a capillary cell reactor developed at the University of Cape Town (Figure E.18). This cell can be operated up to 500 °C and 2 MPa. The capillary has a diameter of 2 mm and a catalyst mass between 0.03 - 0.04 g can be used. A reference material (Y<sub>2</sub>O<sub>3</sub>) that does not undergo phase changes under the selected conditions is added to the sample to correlate the signal strengths and allow cell alignment. The gases required for the investigation are fed via MFC to the capillary cell and the gaseous products can be analysed by a GC-TCD (Figure E.19). It is possible to follow the phase composition changes on the catalyst sample during reduction and formation (Table 5.2). XRD spectra are taken in intervals, each scan takes 20 minutes (it needs to cover the selected  $2\theta$  range). The duration of the scan for in-situ experiments is a compromise between a higher resolution of the diffraction pattern and the rate of the changes on the catalyst sample. The  $2\theta$  range is selected at the beginning of the experiment, 5 - 130° for ex-situ and 30 - 80° for in-situ (smaller than for ex-situ because the measurements need to be taken faster). The scan time used for ex-situ analysis is between 1 - 2 h. Long scan times lead to a higher resolution of the diffraction pattern due to a higher number of steps and a longer scan time per step. Analysis of fresh and spent catalyst samples are carried out ex-situ. The qualitative analysis of the diffraction pattern and the Rietveld refinement is completed by a software that includes a database with the structure of the single structures. A good fit between the calculated and the

experimental pattern is indicated by a small  $R_{WP}$  factor.

## 5.4 Experimental results and discussion

This section discusses and compares the results obtained with the 100 g Fe / 2 g K and 100 g Fe / 10 g K catalysts in the lab-scale fixed-bed reactor and complementary information from the investigations carried out with in-situ and ex-situ techniques. The aim is to gain a better understanding of the CO<sub>2</sub> hydrogenation on iron-catalysts, clarify effects of operating conditions and find out attractive operating conditions for the CO<sub>2</sub> hydrogenation to gaseous hydrocarbons.

### 5.4.1 Catalyst activity and selectivity in lab-scale fixed-bed reactor

Experiments in lab-scale involve at first catalyst calcination and reduction (Table 5.3). After reduction the catalyst is not active, therefore time is required to form the active catalyst. This time was described by Fischer et al. (1923) as “Formierung” (formation) in the original publication in German. Once the catalyst has reached its steady-state, variations in the operating conditions (i.e. temperature,  $(H_2/CO_2)_{in}$ ,  $\tau_{mod}$  and pressure) are carried out to evaluate catalyst activity and selectivity.

#### 5.4.1.1 Catalyst formation

Figure 5.2 shows the time dependent patterns of overall CO<sub>2</sub> conversion  $X_{CO_2}$ , yield of CO  $Y_{CO}$ , and organic product  $Y_{Org}$ , together with hydrocarbon selectivity for 100 g Fe / 2 g K, and 100 g Fe / 10 g K during the first hours of operation, under the reaction conditions shown in Table 5.4. At the early stage CO<sub>2</sub> conversion increases rapidly (between minute 0 and 100). The maximum is attained for both catalysts after around 100 minutes. For the 100 g Fe / 10 g K the decrease in the conversion is very light, which may indicate a very fast formation of iron carbides due to the high K content. For the 100 g Fe / 2 g K the decrease in  $X_{CO_2}$  and  $Y_{Org}$  is more significant and slower (approx. 33 h), probably due to the slower formation of iron carbides due to the lower K content in the catalyst (Figure 3.2). The CO<sub>2</sub> conversion values are similar for both catalysts, which indicates that K has almost no effect on the CO<sub>2</sub>-shift activity under the selected conditions.

The yield of CO with the 100 g Fe / 2 g K catalyst is very low (approx. 4 %), which indicates that low partial pressures of CO prevail in the reactor due to the high Fischer-Tropsch activity of the catalyst. These low CO concentrations are sufficient to produce

hydrocarbons via Fischer-Tropsch synthesis. The molar fraction of the intermediate compound CO is low ( $y_{\text{CO}} < 1 \text{ vol}\%$ ), i.e. far away from typical FT conditions (approx.  $y_{\text{CO}} = 33.3 \text{ vol}\%$ , using  $(\text{H}_2/\text{CO})_{\text{in}} = 2$ ). It can be expected that the formation of iron carbides at these conditions is relatively slow due to the low partial pressure of CO and low amount of K. For the 100 g Fe / 10 g K catalyst the yield of CO is much higher under the same conditions (approx. 12 %), this indicates that the Fischer-Tropsch activity is lower compared with the 100 g Fe / 2 g K catalyst. An increase in the K amount decreases the FT activity and therefore the yield of organic product (Figure 3.1).

Potassium shows a strong effect on hydrocarbon selectivity. For the 100 g Fe / 2 g K catalyst the hydrocarbon selectivity was investigated during the first minutes of synthesis using the ampoule technique. The product distribution, calculated in C %, is rich in methane and short chain hydrocarbons, with a small content of C<sub>5+</sub>. Alkanes are the main compounds in the C<sub>2-4</sub> fraction (93 C %). Very low amounts of oxygenates (alcohols), mainly C<sub>1</sub> (approx. 2 ppm) or C<sub>2</sub> (approx. 0.3 ppm), were also detected in the product. The methane selectivity is even higher in the first 100 min of testing, possibly due to the initial presence of metallic iron, which promotes hydrogen availability and hydrogenation reactions. Hydrocarbons can be detected in the product after 25 min (first GC measurement), which indicates that FT activity is already present.

The high H<sub>2</sub>/CO ratio and the low amount of K allows a low C/H ratio on the catalyst surface, responsible for the desorption of short chain hydrocarbons and the hydrogenation of the primary product alkene to alkane. With the 100 g Fe / 10 g K the hydrocarbon product selectivity is shifted to longer chain hydrocarbons, mainly alkanes (approx. 78 % of the C<sub>2-4</sub> fraction). Due to the high amount of K, adsorption of H<sub>2</sub> on the catalyst is difficult and the C/H ratio on the catalyst is high. Surprisingly the C<sub>2-4</sub> fraction is very similar with both catalysts, slightly higher for 100 g Fe / 2 g K. According to the mechanism of formation of hydrocarbons (Anderson-Schulz-Flory model, similar to a polymerisation), a maximum is observed for C<sub>2-4</sub> when the value of  $\alpha$  is near 0.5. In the present case, one product distribution is on the left side of the maximum and the other on the right side, therefore it is a coincidence that they are so similar (Figure 5.7).

The selection of the operating conditions to form the catalyst is of high importance and is responsible for the final catalyst activity and selectivity. The formation of the 100 g Fe / 2 g K catalyst was also studied under different operating conditions,  $T = 330 \text{ }^\circ\text{C}$  with H<sub>2</sub> and CO<sub>2</sub> in a molar ratio 3:1. A slightly higher CO<sub>2</sub> conversion was reached (29 %), however the CO yield increased (8 %) and the yield of organic products was lower (19 %). A higher partial pressure of CO combined with 2 g of K seems to decrease the FT activity. The hydrocarbon product distribution is shifted to a lighter product with methane (63 %), C<sub>2-4</sub> (31 %), and almost no C<sub>5+</sub> (6 %). These formation conditions

produce a catalyst with a lower FT activity that presents no advantages compared with the previous conditions.

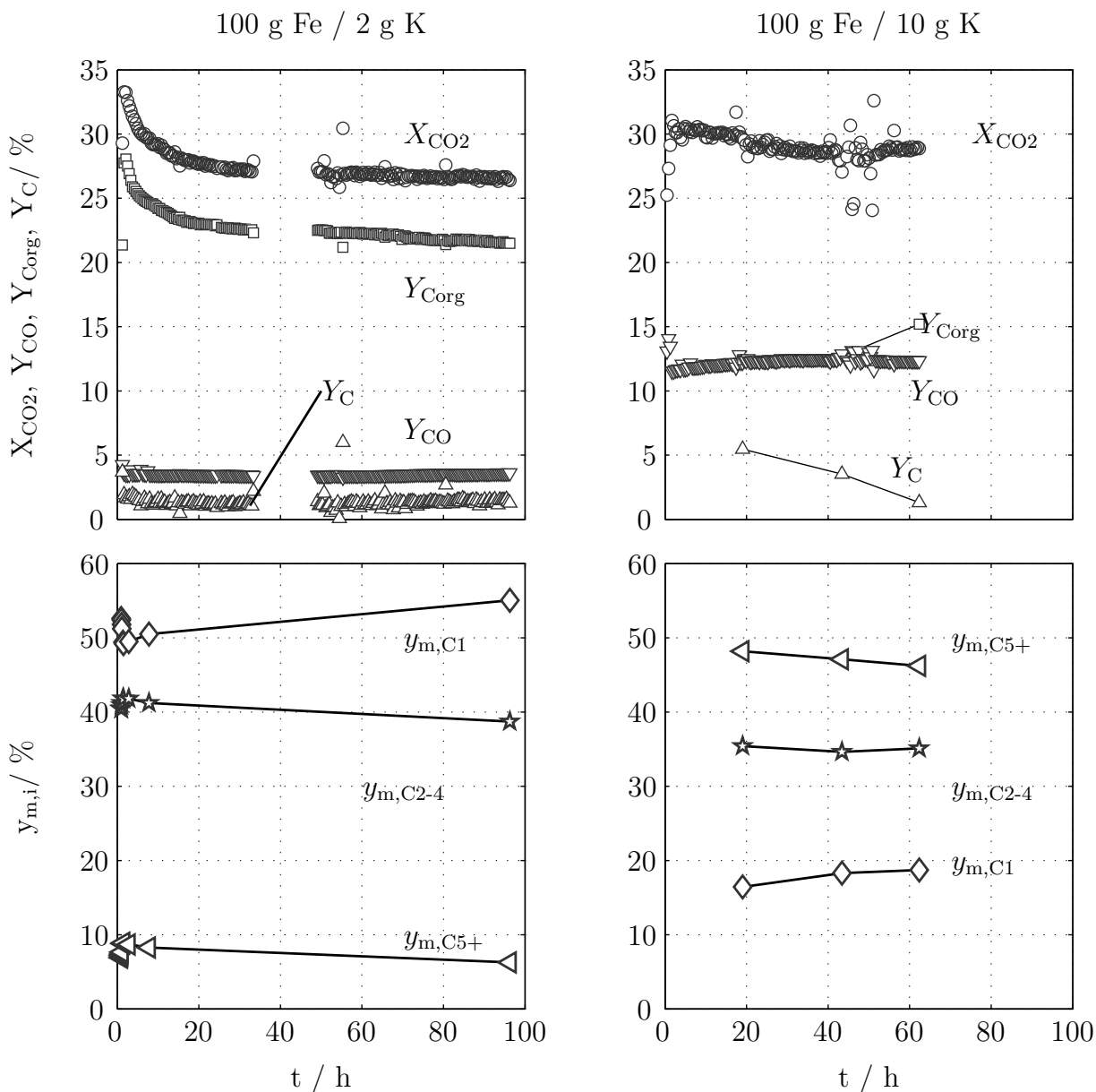


Figure 5.2: CO<sub>2</sub> conversion  $X_{\text{CO}_2}$ , CO yield  $Y_{\text{CO}}$ , organic components yield  $Y_{\text{Corg}}$  and carbon yield  $Y_{\text{C}}$  (top) and hydrocarbon selectivity  $y_{m,i}$  in mass % during catalyst formation. Left: 100 g Fe/ 2g K, Right: 100 g Fe / 10 g K. Conditions see Table 5.4

#### 5.4.1.2 Catalyst stability at reference conditions

The stability of the catalysts is studied using reference operating conditions that are repeated during an experiment. The activity and selectivity under reference operating conditions are compared with values measured at lower time-on-stream. If deviations

from starting activity are higher than 20 %, the experiment does not continue. The selected reference conditions are different for both catalysts, therefore absolute results can not be compared ( $p = 1$  MPa,  $\tau_{\text{mod}} = 400$  kg s/m<sup>3</sup>,  $(\text{H}_2/\text{CO}_2)_{\text{in}} = 4$ ,  $T = 266$  °C for 100 g Fe / 2 g K and  $T = 286$  °C for 100 g Fe / 10 g K).

Figure F.34 left, shows that the 100 g Fe / 2 g K catalyst is stable during almost 50 days of operation. A slight and slow deactivation can be observed in the FT activity. The CO yield tends to increase and the yield of organic carbon decreases, which corresponds to a decrease in the CO<sub>2</sub> conversion. The hydrocarbon selectivity shows a slight increase in methane with time-on-stream and also in the C % of alkene in the fraction C<sub>2-4</sub>.

Figure F.34 right, shows that the run with the 100 g Fe / 10 g K was shorter and the decrease in the CO<sub>2</sub> conversion and yield of organic products is faster over time. Hydrocarbon selectivity remains stable over time with a slight decrease on C<sub>5+</sub> in favour of methane and C<sub>2-4</sub>. Reproducibility with an iron catalyst with a higher content on K is complicated, and values tend to be influenced by the previous operating conditions (Pabst 2013). This could explain the ups and downs for the 100 g Fe / 10 g K.

Figure F.35 right, shows the pressure drop measured at reference conditions for 100 g Fe / 10 g K. An increase with time-on-stream between 400 - 600 h is observed. During these 200 h, higher temperatures (300 - 330 °C) and longer modified residence times were operated and, possibly deactivated the catalyst (e.g. via sintering or deposits of inactive carbonaceous materials). Due to the high amount of K, the concentration of carbon on site is high, favouring the formation of inactive carbon that blocks the catalyst bed and decreases the catalyst activity (Figure 3.2). The deactivation is confirmed at reference conditions, where a lower  $X_{\text{CO}_2}$  and  $Y_{\text{Corg}}$  are calculated. No significant pressure drop was detected with the 100 g Fe / 2 g K catalyst (Figure F.35, left).

In general, it is always better to regenerate the catalyst than to load a new one, even though iron is a cheap catalyst. In-situ regeneration with H<sub>2</sub> under the same conditions as during reduction (Table 5.3) was successfully applied with the 100 g Fe / 2 g K. The same activity and selectivity during the formation period was measured as when the experiment was starting with the fresh catalyst. In-situ reduction makes a high number of experiments possible with the same catalyst bed, avoiding a pressure test and preparation of a new catalyst bed (less amount of fresh catalyst is also required). Regeneration of FT catalyst is common in industrial practice (Bartholomew et al. 2006).

#### 5.4.1.3 Variation of modified residence time

The CO<sub>2</sub> conversion and the hydrocarbon yield increase with modified residence time (Figure 5.3). CO is an intermediate product, being formed by the CO<sub>2</sub>-shift and consumed

by the FT reaction. At short residence times the CO<sub>2</sub>-shift rate is higher than the FT rate due to the high partial pressures of CO<sub>2</sub> and H<sub>2</sub> and the low partial pressure of CO.

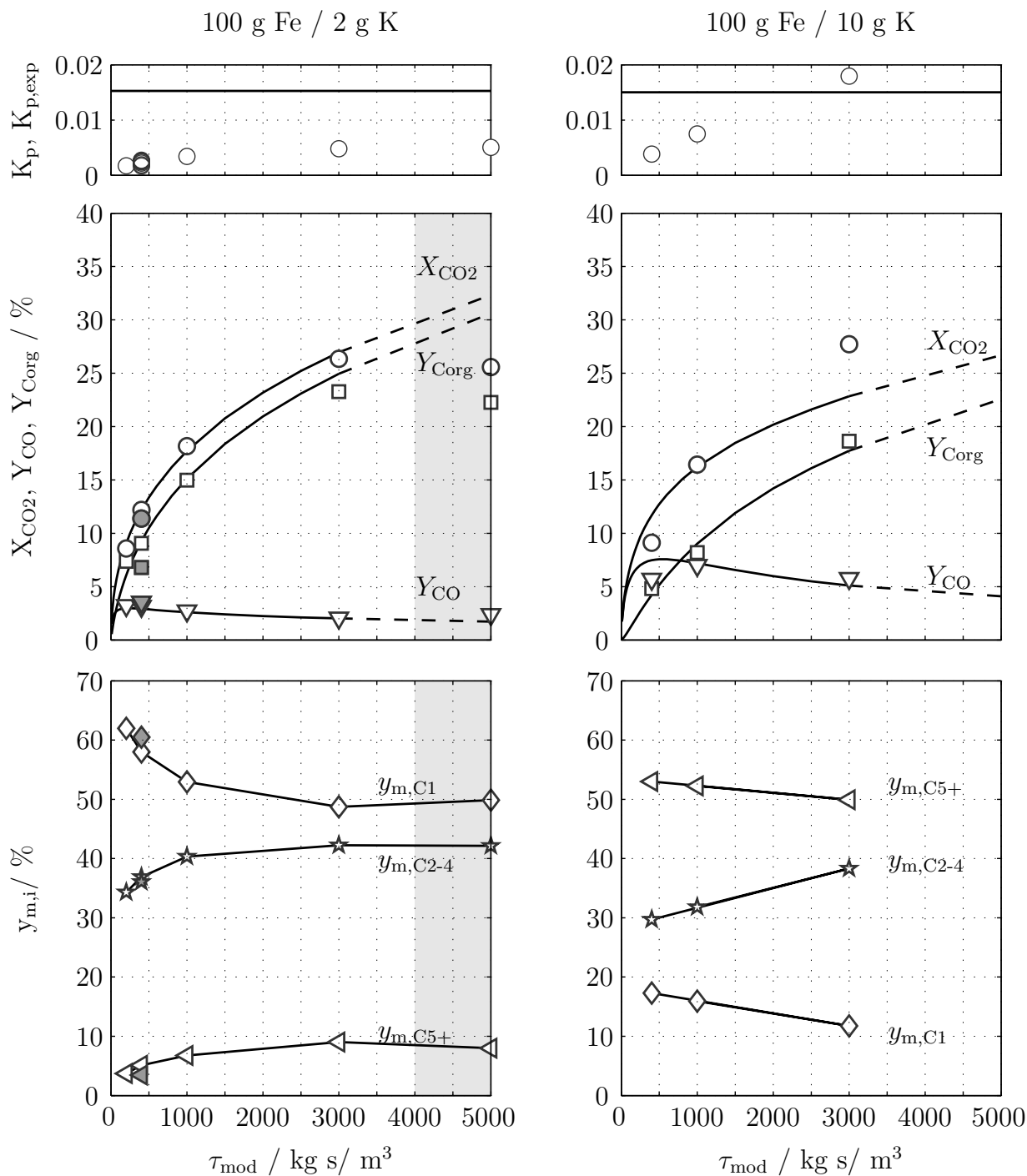


Figure 5.3: Effect of modified residence time on  $K_{p,exp}$ , CO<sub>2</sub> conversion  $X_{CO_2}$ , CO yield  $Y_{CO}$ , yield of organic components  $Y_{Corg}$  (top), and hydrocarbon selectivity in mass  $y_{m,i}$  % (bottom). Curves top: calculated with kinetic model, dashed = extrapolation of kinetic model; Curves bottom: trends. Conditions:  $(H_2/CO_2)_{in} = 4$  and  $p = 1$  MPa. Left: 100 g Fe / 2 g K,  $T = 266$  °C, grey symbols: repeated experiment after 500 h (21 days) of testing. Shaded area: deactivation observed. Right: 100 g Fe / 10 g K,  $T = 265$  °C.

CO yield reaches a maximum and afterwards decreases due to the higher FT rate compared to CO<sub>2</sub>-shift rate ( $r_{\text{FT}}/r_{\text{CO}_2\text{-sh}}$  high).

The CO<sub>2</sub> conversion with both catalysts under the same reaction conditions is similar, which indicates a comparable CO<sub>2</sub>-shift activity. However, in the case of 100 g Fe / 2 g K a higher organic yield and a lower CO yield are present, as a result of high FT activity compared with the 100 g Fe / 10 g K catalyst. The higher amount of K may decrease the FT activity due to the stronger CO<sub>2</sub> adsorption on the catalyst surface.

$K_{p,\text{exp}}$  is calculated according to the partial pressures at the reactor outlet and compared with  $K_p$  for the selected temperature (Figure 5.3, top). In the case of 100 g Fe / 2 g K, due to the higher FT reaction rate (fast removal of CO), the CO<sub>2</sub>-shift reaction is far away from the thermodynamic equilibrium. In contrast, in the 100 g Fe / 10 g K experiment, the CO<sub>2</sub>-shift reaction reaches the equilibrium due to the lower FT reaction rate. In the case of  $\tau_{\text{mod}} = 3000 \text{ kg s/m}^3$ , the experimental value is slightly higher than the thermodynamic equilibrium, which should be connected with the calculation of the H<sub>2</sub>O partial pressure via a C-balance that is not properly closed.

Increasing modified residence time with the 100 g Fe / 10 g K catalyst leads to an increasing error in the carbon balance. This is probably due to deposits of inactive carbon on the catalyst bed connected with the high amount of K present on the catalyst ( $\tau_{\text{mod}} = 3000 \text{ kg s/m}^3$ ,  $Y_C = 3.3 \%$ ). The Boudouard reaction (Equation 5.17, based on Equation 3.16) can be seen as responsible of the formation of C from CO, causing a decrease in the CO yield at higher modified residence times. With the 100 g Fe / 2 g K, the carbon balance could be successfully closed under the selected conditions. This is likely due to the lower amount of K and lower CO partial pressure, that the Boudouard reaction does not take place.

At high modified residence times (i.e.  $\tau_{\text{mod}} = 5000 \text{ kg s/m}^3$ ) with 100 g Fe / 2 g K, the CO<sub>2</sub> conversion and yield of organic carbon do not show an increase, even though the reaction is far away from thermodynamic equilibrium. It seems like the high partial pressure of H<sub>2</sub>O could cause catalyst oxidation, and consequently a change in activity and selectivity (Claeys et al. 2013; Højlund-Nielsen et al. 1982; Lee et al. 1990; Riedel et al. 1999; Steynberg et al. 1999). In contrast, for the 100 g Fe / 10 g K, due to the low FT activity the partial pressure of H<sub>2</sub>O is significantly lower because less hydrocarbons are formed, and therefore no oxidation is observed.



Grey symbols in Figure 5.3 left, show the effect of time-on-stream. After 21 days, CO<sub>2</sub> conversion and organic yield slightly decreases in favour of CO yield. The hydrocarbon

selectivity remains almost constant with a slight decrease in C<sub>5+</sub> in favour of methane.

The hydrocarbon product distribution obtained with both catalysts is significantly different, dominated by short chain hydrocarbons in the case of 100 g Fe / 2 g K and by longer chain hydrocarbons in the case of 100 g Fe / 10 g K (Figure 5.3, bottom). A surprisingly similar proportion of C<sub>2-4</sub> is obtained with both catalysts (approx. 30 - 40 %).

With 100 g Fe / 2 g K the hydrocarbon product distribution is shifted to longer chain hydrocarbons with increased modified residence time (200 - 3000 kg s/m<sup>3</sup>). The chain growth probability increases from 0.20 to 0.32. At a modified residence time of 5000 kg s/m<sup>3</sup> the methane selectivity slightly increases, probably due to catalyst deactivation. The change of the hydrocarbon product distribution with the modified residence time can be explained with the change of reactant and product partial pressures. Low residence times correspond to low CO<sub>2</sub> conversion and thus low H<sub>2</sub>O partial pressure, which is known to result in high methane selectivity and a low chain growth probability (Schulz et al. 1997). At these conditions the H<sub>2</sub>/CO ratios are also large, which further contributes to a lower chain growth probability (Dry 1990). With increasing CO<sub>2</sub> conversion and partial pressure of H<sub>2</sub>O, the formation of longer chain hydrocarbons is favoured (Figure 5.6, right).

In the case of the 100 g Fe / 10 g K, the formation of C<sub>5+</sub> is relatively constant and methane decreases in favour of C<sub>2-4</sub> with increasing modified residence time. A higher partial pressure of H<sub>2</sub>O, due to the higher CO<sub>2</sub> conversion values, is probably responsible for the increasing chain probability ( $\alpha$ ) with modified residence time  $\alpha_{10K} = 0.64 - 0.66$ .

In general, high modified residence times favour the formation of C<sub>2-4</sub>. However in the case of 100 g Fe / 2 g K the proportion of alkenes is low (approx. 7.5 % in the C<sub>2-4</sub> fraction), while for 100 g Fe / 10 g K alkenes dominate the hydrocarbon product (approx. 75 % in the C<sub>2-4</sub>). Secondary reactions of alkene to alkane are complicated in the 100 g Fe / 10 g K system, due to the high amount of K and the difficult access of H<sub>2</sub> to the catalyst surface, nevertheless they are possible more easily in the 100 g Fe / 2 g K system, due to a lower K amount and consequently a different catalyst composition.

#### 5.4.1.4 Variation of ratio (H<sub>2</sub>/CO<sub>2</sub>)<sub>in</sub> and pressure

The molar (H<sub>2</sub>/CO<sub>2</sub>)<sub>in</sub> inlet ratio is varied at constant feed volumetric flow (constant  $\tau_{mod}$ ). Therefore at ratio 8, the molar flow of CO<sub>2</sub> is lower than in case of ratio 4. It can be seen in Table 5.6 that higher inlet ratios favour higher CO<sub>2</sub> conversion and hydrocarbon yield values. The reasons are the higher residence time of CO<sub>2</sub> and the higher partial pressure of H<sub>2</sub> and lower partial pressure of H<sub>2</sub>O.



As to be expected at high  $(\text{H}_2/\text{CO}_2)_{\text{in}}$  ratio and consequently high hydrogen partial pressures, the formation of methane increases and the proportion of  $\text{C}_{5+}$  decreases. However, a clear trend has not been observed for the  $\text{C}_{2-4}$  fraction, that decreases in the case of 100 g Fe / 2 g K and increases for 100 g Fe / 10 g K. The proportion of alkene in the  $\text{C}_{2-4}$  fraction for the 100 g Fe / 10 g K remains constant independent of the  $(\text{H}_2/\text{CO}_2)_{\text{in}}$  ratio (approx. 76 %). This indicates that the concentration of  $\text{H}_2$  in the gas phase is not the limiting parameter in the formation of alkanes, which instead may be determined by the catalyst composition.

Experiments with a  $(\text{H}_2/\text{CO}_2)_{\text{in}}$  ratio of 22 shows that  $\text{CO}_2$  conversion and hydrocarbon yield can reach high levels (approx. 70 %) together with a yield of CO close to zero. Most of the hydrocarbons are methane (approx. 82 %) and the remaining amount belongs to the  $\text{C}_{2-4}$  fraction.

In general, an increase of  $(\text{H}_2/\text{CO}_2)_{\text{in}}$  favours the production of short chain hydrocarbons ( $\text{C}_1$  and  $\text{C}_{2-4}$ ) and allows for higher  $\text{CO}_2$  conversion and hydrocarbon yield values.

Table 5.6: Variation of  $(\text{H}_2/\text{CO}_2)_{\text{in}}$  and pressure at  $\tau_{\text{mod}} = 1000 \text{ kg s/m}^3$

Catalyst	$(\text{H}_2/\text{CO}_2)_{\text{in}}$	$p$ MPa	$T$ °C	$X_{\text{CO}_2}$ %	$Y_{\text{CO}}$ %	$Y_{\text{Corg}}$ %	$Y_{\text{C}}$ %	$y_{\text{m,C1}}$ %	$y_{\text{m,C2-4}}$ %	$y_{\text{m,C5+}}$ %
	4	2	266	20.9	2.0	19.1	-0.3	55.5	38.8	5.7
100 g Fe / 2 g K	8	2	266	32.2	1.9	28.7	1.6	65.8	31.1	3.1
	4	1	266	18.1	2.7	14.9	-0.5	52.9	40.3	6.8
	5	1	266	21.6	3.5	15.5	3.0	58.5	36.8	4.7
100 g Fe / 10 g K	4	1	286	25.5	8.8	14.8	1.8	15.1	34.9	50.0
	8	1	286	40.0	9.4	26.6	4.0	20.3	40.3	39.4

According to Lee et al. (1990) an increase in pressure beyond 1 MPa seems to have no pronounced effect on catalyst activity. The  $\text{CO}_2$ -shift reaction is reversible with an equal number of molecules on each side. Therefore, pressure should have no effect on  $\text{CO}_2$  conversion from a thermodynamic point of view unless the CO produced is consumed by the FT reaction, that becomes faster with pressure. A higher FT activity leads to a higher  $\text{H}_2\text{O}$  partial pressure that decreases the reaction rates, therefore the increase in  $\text{CO}_2$  conversion would not be significant due to the opposed effects. The effect of pressure is investigated with the 100 g Fe / 2 g K at 1 and 2 MPa and constant  $\tau_{\text{mod}}$  for  $(\text{H}_2/\text{CO}_2)_{\text{in}} = 4$  (Table 5.6). Even though  $\tau_{\text{mod}}$  is constant, the real contact time of the gas and the catalyst is double due to the two-fold increase in the total pressure. A small increase of  $\text{CO}_2$  conversion and yield of organic products is measured at higher pressure together

with a slight shift to short chain hydrocarbons. This effect of pressure on hydrocarbon selectivity is not very significant and cannot be fully explained.

#### 5.4.1.5 Variation of temperature

Temperature affects the reaction system from a thermodynamic and a kinetic perspective: higher  $K_p$  values (reaction is endothermic), as well as higher kinetic constants for the CO<sub>2</sub>-shift and FT, favour reaction rates. However, a higher CO<sub>2</sub>-shift and FT activity leads to a higher H<sub>2</sub>O partial pressure that decreases the reaction rates. Temperatures which exceed a certain value favour catalyst deactivation. Temperature also affects the hydrocarbon product distribution and, according to literature, favours desorption of hydrocarbon chains (lower  $\alpha$  values). The temperature effect is studied in the range 245 - 330 °C at different (H<sub>2</sub>/CO<sub>2</sub>)<sub>in</sub> ratios.

Figure 5.4 middle, shows that CO<sub>2</sub> conversion and organic yield increases fast with temperature. This behaviour corresponds to results obtained with the 100 g Fe / 2 g K at (H<sub>2</sub>/CO<sub>2</sub>)<sub>in</sub> = 5 at temperatures below 300 °C. Trends are similar with the 100 g Fe / 10 g K catalyst at (H<sub>2</sub>/CO<sub>2</sub>)<sub>in</sub> = 4 for temperatures below 310 °C.

Figure 5.4 bottom, shows the effect of temperature on the hydrocarbon product distribution. Surprisingly, the methane selectivity is nearly constant with increasing temperature for both catalysts, in spite of the absolute different levels (approx. 60 % for 100 g Fe / 2 g K and 15 % for 100 g Fe / 10 g K). The C<sub>2-4</sub> fraction increases slightly for the 100 g Fe / 2 g K and markedly with the 100 g Fe / 10 g K in detriment of C<sub>5+</sub>.

The behaviour observed on the 100 g Fe / 10 g K catalyst is according to literature, and products shift to shorter chain hydrocarbons with increasing temperature due to a favour desorption. The product distribution obtained with 100 g Fe / 2 g K is almost constant with temperature, and this might be explained by a combined effect of H<sub>2</sub>O and temperature: with increasing temperature, the presence of H<sub>2</sub>O contributes to enhance chain growth probability (also observed in Figure 5.3), but at the same time the increasing temperature favours lower chain growth values, resulting finally in a product distribution almost constant with temperature. The proportion of alkane in the C<sub>2-4</sub> fraction with the 100 g Fe / 2 g K decreases with temperature from 92 to 89 %, being far away from the approx. 22 % of alkane obtained with 100 g Fe / 10 g K.

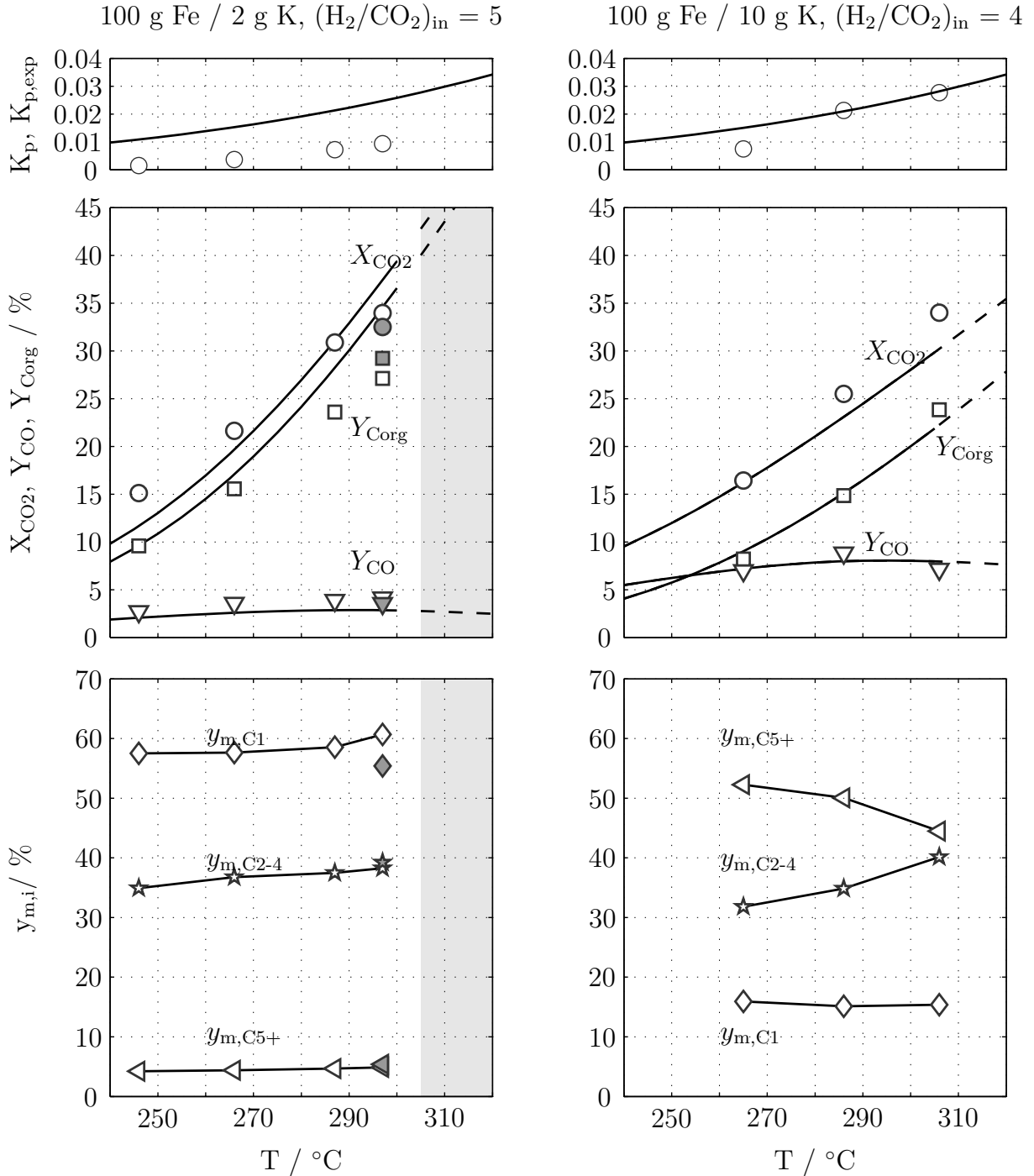


Figure 5.4: Effect of temperature on  $K_{p,exp}$  (top), CO<sub>2</sub> conversion  $X_{CO_2}$ , CO yield  $Y_{CO}$ , yield of organic components  $Y_{Corg}$  (middle), and hydrocarbon selectivity in mass % (bottom). Curves middle: calculated with kinetic model, dashed: extrapolation of kinetic model; Curves bottom: trends. Left: 100g Fe/ 2g K,  $\tau_{mod} = 1000$  kg s/m<sup>3</sup>,  $(H_2/CO_2)_{in} = 5$  and  $p = 1$ MPa; grey symbols time-on-stream (TOS) = 6500 min (4.5 days); white symbols: TOS = 46000-55000 min (32 to 38 days). Shaded area: deactivation observed, (see Figure 5.5),  $Y_C$  approx 4 %. Right: 100g Fe / 10 g K,  $\tau_{mod} = 1000$  kg s/m<sup>3</sup>,  $(H_2/CO_2)_{in} = 4$  and  $p = 1$ MPa.  $Y_C < 3\%$ .

### Catalyst stability at higher temperature

Both catalytic systems deactivate at higher temperatures, however this is due to different reasons:

- 100 g Fe / 2 g K:** at temperatures higher than 297 °C at  $(\text{H}_2/\text{CO}_2)_{\text{in}} = 5$ , it is not possible to achieve stable conditions (Figure 5.5 left). An increase in temperature leads to a loss of FT activity. If a higher temperature (e.g. 320 °C) is applied for a long period of time, the CO<sub>2</sub> conversion and the organic yield end up at values lower than those reached at lower temperatures. The effect of catalyst deactivation is stronger than the increase in activity. The loss of FT activity could be related to the presence of a high H<sub>2</sub>O partial pressure due to the high CO<sub>2</sub> conversion levels achieved, similar results when starting with H<sub>2</sub>/CO as feed gas were presented by Claeys et al. (2013) and Steynberg et al. (1999). Due to the presence of H<sub>2</sub>O, iron carbides oxidise to iron oxides, with no activity for the FT synthesis (see section 3.1.5).

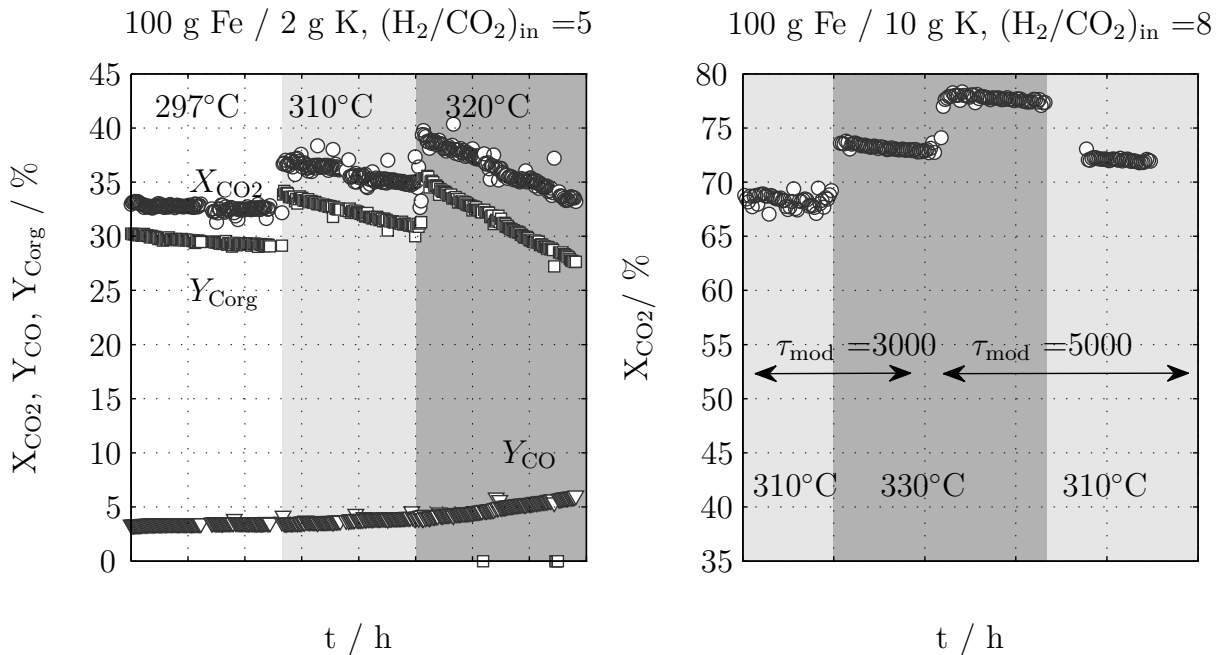


Figure 5.5: Effect of temperature over time. Left: CO<sub>2</sub> conversion  $X_{\text{CO}_2}$ , CO yield  $Y_{\text{CO}}$ , yield of organic components  $Y_{\text{Corg}}$ , at  $\tau_{\text{mod}} = 1000 \text{ kg s/m}^3$  for 100 g Fe / 2 g K. Right: CO<sub>2</sub> conversion at different operating conditions, C balance not closed, CO yield for 100 g Fe / 10 g K in Figure F.36.  $\Delta t = 20 \text{ h}$ .

- 100 g Fe / 10 g K:** stable CO<sub>2</sub> conversion and organic yield is possible at higher temperatures (experiments done until 330 °C,  $(\text{H}_2/\text{CO}_2)_{\text{in}} = 8$ ) and higher modified residence time, with higher absolute values (Figure 5.5 right and Figure F.36). However, during this time, the C-balance cannot be properly closed probably due to the formation of inactive carbon ( $Y_{\text{C}}$  approx. 10 %). Higher CO<sub>2</sub> conversion values than

those expected when considering CO<sub>2</sub>-shift and FT rates (calculated with kinetic parameters) are measured, this indicates that a third reaction could take place at higher temperatures (e.g. Boudouard reaction, Equation 5.17) and this might also explain the slight decrease on the CO yield (without the Boudouard reaction, the conversion of CO<sub>2</sub> would be even higher). After these operating conditions were tried, reference conditions were set (corresponding to a higher volumetric flow). A higher pressure drop was measured (Figure F.35) together with a lower CO<sub>2</sub> conversion, compared with previous reference points, indicating catalyst deactivation due to carbon deposition. Consequently, these operating conditions cannot be applied for long periods of time. 100 g Fe / 10 g K represents the deactivation mechanism commonly described in literature for an iron-based catalyst (Dry 1990; Hwang et al. 2001).

#### 5.4.1.6 Effect of ratio $(p_{\text{H}_2\text{O}}/p_{\text{H}_2})_{\text{out}}$ on 100 g Fe / 2 g K

One of the main differences between CO<sub>2</sub> and CO hydrogenation to hydrocarbons is the resulting partial pressure of H<sub>2</sub>O, or the ratio of  $(p_{\text{H}_2\text{O}}/p_{\text{H}_2})_{\text{out}}$  respectively. Under typical FT conditions with iron catalysts and H<sub>2</sub>/CO as feed gas, H<sub>2</sub>O is produced in the FT reaction and, to a large extent, consumed in-situ in the CO-shift reaction to form H<sub>2</sub> and CO<sub>2</sub>. Consequently, the ratio  $(p_{\text{H}_2\text{O}}/p_{\text{H}_2})_{\text{out}}$  is relatively low. In the case of using H<sub>2</sub>/CO<sub>2</sub> as feed gas, H<sub>2</sub>O is produced in the FT synthesis and also in the CO<sub>2</sub>-shift reaction, consuming H<sub>2</sub>. The resulting value  $(p_{\text{H}_2\text{O}}/p_{\text{H}_2})_{\text{out}}$  will be higher according to Equation 5.18, causing an increased oxidising atmosphere. It is known that H<sub>2</sub>O can cause oxidation of iron catalysts during Fischer-Tropsch synthesis (Bartholomew et al. 2006; Claeys et al. 2013; Mogorosi et al. 2012; Steynberg et al. 1999)(see section 3.1.5). Häag carbide (Fe<sub>5</sub>C<sub>2</sub>) can oxidise to magnetite (Fe<sub>3</sub>O<sub>4</sub>), which is not active for the FT synthesis, in the presence of H<sub>2</sub>O whereas CO<sub>2</sub>, even at very high levels, does not cause oxidation (Claeys et al. 2013). This oxidation is typically reversible (Claeys et al. 2013; Mogorosi et al. 2012). The oxidation of Fe to FeO at  $(p_{\text{H}_2\text{O}}/p_{\text{H}_2})_{\text{out}} > 0.16$  has also been reported by Bartholomew et al. (2006) for the ammonia synthesis with an Fe/K/Al<sub>2</sub>O<sub>3</sub> catalyst.

$$(p_{\text{H}_2\text{O}}/p_{\text{H}_2})_{\text{out}} = \frac{Y_{\text{CO}} + 2 \cdot Y_{\text{Corg}}}{(p_{\text{H}_2}/p_{\text{CO}_2})_{\text{in}} - Y_{\text{CO}} - 3.65 \cdot Y_{\text{Corg}}} \quad (5.18)$$

If all experimental results below 300 °C with the 100 g Fe / 2 g K catalyst, are considered independent of the reaction conditions, the ratio  $(p_{\text{H}_2\text{O}}/p_{\text{H}_2})_{\text{out}}$  correlates directly with the CO<sub>2</sub> conversion and the yield of organic products (Figure 5.6 and Equation 5.18). Due to the characteristics of the 100 g Fe / 2 g K catalyst, and its high FT activity, the yield of organic products is very close to the value of CO<sub>2</sub> conversion due to the lower CO yield, with the partial pressure of H<sub>2</sub>O increasing proportionally to CO<sub>2</sub> conversion.

In the case of the 100 g Fe / 10 g K, the  $(p_{\text{H}_2\text{O}}/p_{\text{H}_2})_{\text{out}}$  ratio seems to be non-critical for the catalyst, within the range where experiments were carried out, even though CO<sub>2</sub> conversion values are similar. Due to the lower FT activity, the CO yield is higher and consequently less H<sub>2</sub> is consumed to produce hydrocarbons and H<sub>2</sub>O. This indicates that for the same CO<sub>2</sub> conversion, the  $(p_{\text{H}_2\text{O}}/p_{\text{H}_2})_{\text{out}}$  ratio would be lower (Equation 5.18). The different catalyst compositions may also be relevant in avoiding catalyst deactivation in the presence of H<sub>2</sub>O.

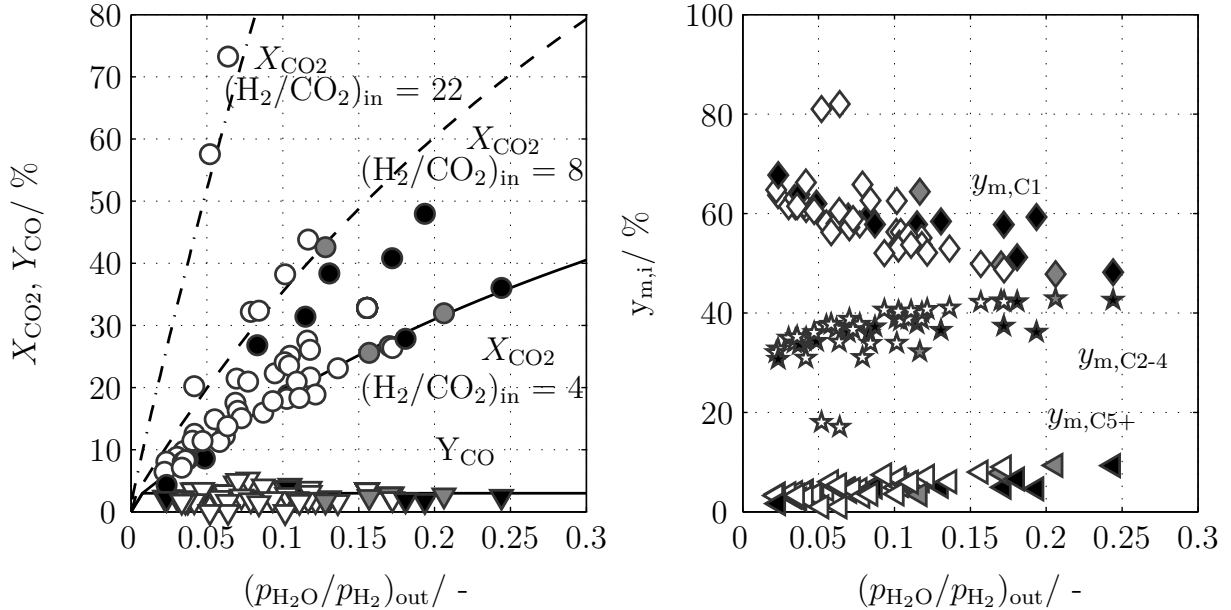


Figure 5.6: Influence of  $(p_{\text{H}_2\text{O}}/p_{\text{H}_2})_{\text{out}}$  on activity and selectivity (in C %) for the 100 g Fe / 2 g K catalyst. Left: CO<sub>2</sub> conversion and CO yield as a function of  $(p_{\text{H}_2\text{O}}/p_{\text{H}_2})_{\text{out}}$ . Curves calculated with Equation 5.18 with  $Y_{\text{CO}} = 3\%$  if  $X_{\text{CO}_2} > 3\%$  and  $Y_{\text{CO}} = X_{\text{CO}_2}$  for  $X_{\text{CO}_2} < 3\%$ . Solid curve for  $(\text{H}_2/\text{CO}_2)_{\text{in}} = 4$ ; dashed curve  $(\text{H}_2/\text{CO}_2)_{\text{in}} = 8$ , dashed-dot curve  $(\text{H}_2/\text{CO}_2)_{\text{in}} = 22$ . Right: Hydrocarbon product distribution  $y_{m,i}$  in weight % as a function of  $(p_{\text{H}_2\text{O}}/p_{\text{H}_2})_{\text{out}}$ . Full symbols black: C balance closed with an error > 5 %. Full symbols grey: deactivation observed. White symbols: stable operation. Conditions:  $p = 1 - 2$  MPa,  $(\text{H}_2/\text{CO}_2)_{\text{in}} = 4, 5, 8, 22$ ,  $T = 245 - 297$  °C and  $\tau_{\text{mod}} = 175 - 5000$  kg s/m<sup>3</sup>

Equation 5.18 is based on the stoichiometry of the CO<sub>2</sub>-shift and FT reaction, it assumes that 2.65 mol of H<sub>2</sub> are consumed in the FT reaction to form the organic product (H/C = 3.3). With this equation it is possible to predict the  $(p_{\text{H}_2\text{O}}/p_{\text{H}_2})_{\text{out}}$  ratio for a certain  $X_{\text{CO}_2}$  and  $Y_{\text{Corg}}$ .

The  $(p_{\text{H}_2\text{O}}/p_{\text{H}_2})_{\text{out}}$  ratio may be responsible for the apparent limitation to reach high CO<sub>2</sub> conversion values with the 100 g Fe / 2 g K catalyst. Based on this finding it is sugges-

ted that there is possibly a limiting value of  $(p_{\text{H}_2\text{O}}/p_{\text{H}_2})_{\text{out}}$ , depending on temperature, catalyst composition, and reaction conditions, at which the catalyst could start changing its composition and consequently its activity and selectivity. An analogous qualitative suggestion regarding the interaction between the gas phase and catalyst composition was presented earlier by Højlund-Nielsen et al. (1982).

Based on Equation 5.18, the molar feed ratio  $(\text{H}_2/\text{CO}_2)_{\text{in}}$  is the most promising variable for decreasing the oxidation potential of the gas mixture and thus reaching high CO<sub>2</sub> conversion and hydrocarbon yield values without catalyst deactivation. Indeed, the results of the present study indicate that for a feed ratio  $(\text{H}_2/\text{CO}_2)_{\text{in}}$  of 8, a maximum CO<sub>2</sub> conversion (44 %) is achieved ( $T = 290$  °C,  $\tau_{\text{mod}} = 1000$  kg s/m<sup>3</sup>,  $p = 2$  MPa), however at  $(\text{H}_2/\text{CO}_2)_{\text{in}} = 22$ , CO<sub>2</sub> conversion values above 70 % are possible without catalyst deactivation, and a hydrocarbon product mainly based on methane is obtained (approx. 80 %) (at  $T = 290$  °C,  $\tau_{\text{mod}} = 1000$  kg s/m<sup>3</sup>,  $p = 2$  MPa). The curves in Figure 5.6, calculated with Equation 5.18, localise the range of the experimental data points for three inlet ratios  $(\text{H}_2/\text{CO}_2)_{\text{in}}$  and variable values of CO<sub>2</sub> conversion and CO yield.

Also the hydrocarbon selectivity is affected by the  $(p_{\text{H}_2\text{O}}/p_{\text{H}_2})_{\text{out}}$  ratio (Figure 5.6, right). At high  $(p_{\text{H}_2\text{O}}/p_{\text{H}_2})_{\text{out}}$  ratios the mass fraction of methane decreases and C<sub>2-4</sub> and C<sub>5+</sub> fractions increase, probably due to the lower H<sub>2</sub> availability and the higher concentration of H<sub>2</sub>O. This ratio seems to have a stronger effect than temperature, modified residence time, or pressure on hydrocarbon product distribution for the 100 g Fe / 2 g K catalyst.

#### 5.4.1.7 Modeling of hydrocarbon product distribution

The Anderson-Schulz-Flory (ASF) model (Equation 3.8) is able to represent, in a rather accurate way, the experimental results obtained in the present study (Figure 5.7). A large number of data points representing a variety of reactions conditions (Table C.1 for 100 g Fe / 2 g K and Table C.2 for 100 g Fe / 10 g K) are represented over  $\alpha$ .

The catalyst composition (amount of K) has a more important effect on the hydrocarbon distribution than the operating conditions. Low amounts of K help to obtain a light hydrocarbon product, while high K promotion shifts the product distribution to longer chain hydrocarbons. The lowest value of  $\alpha$  is for  $(\text{H}_2/\text{CO}_2)_{\text{in}} = 22$ . Small deviations from ideal ASF can be found in the fractions C<sub>2-4</sub> and C<sub>5+</sub>, which are often observed experimentally, and which can be explained with effects of methane formation on non-FT sites and effects of incorporation of primarily formed alkenes (Schulz et al. 1999).

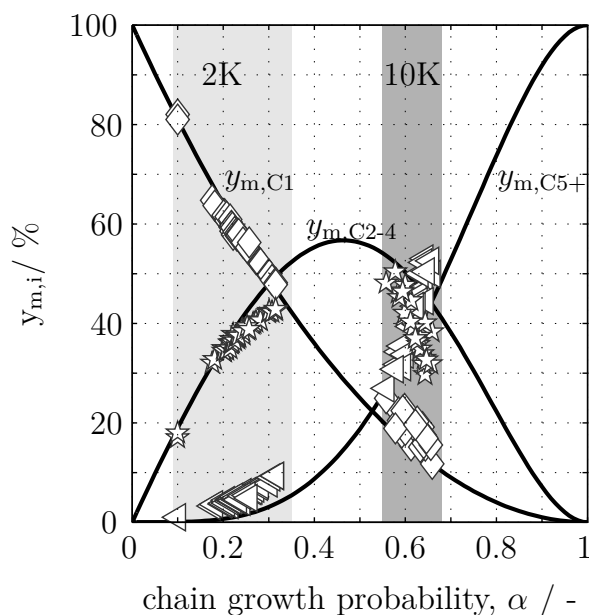


Figure 5.7: Hydrocarbon product distribution in mass % for 100 g Fe / 2 g K and 100 g Fe / 10 g K. Curves calculated with the Anderson-Schulz-Flory (ASF) model. Conditions:  $p = 1 - 2$  MPa,  $(\text{H}_2/\text{CO}_2)_{\text{in}} = 4, 5, 8, 22$ ,  $T = 245 - 297$  °C and  $\tau_{\text{mod}} = 175 - 5000$  kg s/m<sup>3</sup>.

## 5.4.2 Supporting in-situ and ex-situ measurements (X-ray diffractometer and magnetometer)

The complexity of the product composition is a rich source of information about elementary reactions, active sites, and catalyst phases. Based on the characteristics of the hydrocarbon product selectivity measured during catalyst formation and at various operating conditions, it is possible to make some assumptions about catalyst phase compositions. In-situ and ex-situ measurements carried out with both catalysts offer the possibility to validate these assumptions and get a better understanding of the catalytic effects.

### 5.4.2.1 Catalyst reduction

Figure 5.8 shows that at the beginning of the run, carried out in the equipment described in section 5.3.2 and 5.3.3, no magnetisation could be measured under the influence of an external magnetic field of 20 kOe in either catalyst. According to XRD results, the catalyst consists 100 % of Fe<sub>2</sub>O<sub>3</sub> (Figure 5.9) and no crystalline potassium phase could be detected. This is confirmed by ex-situ XRD experiments of the fresh sample (Figure E.30 and Figure E.31). By increasing time, and consequently temperature, an increase in the magnetization is observed.



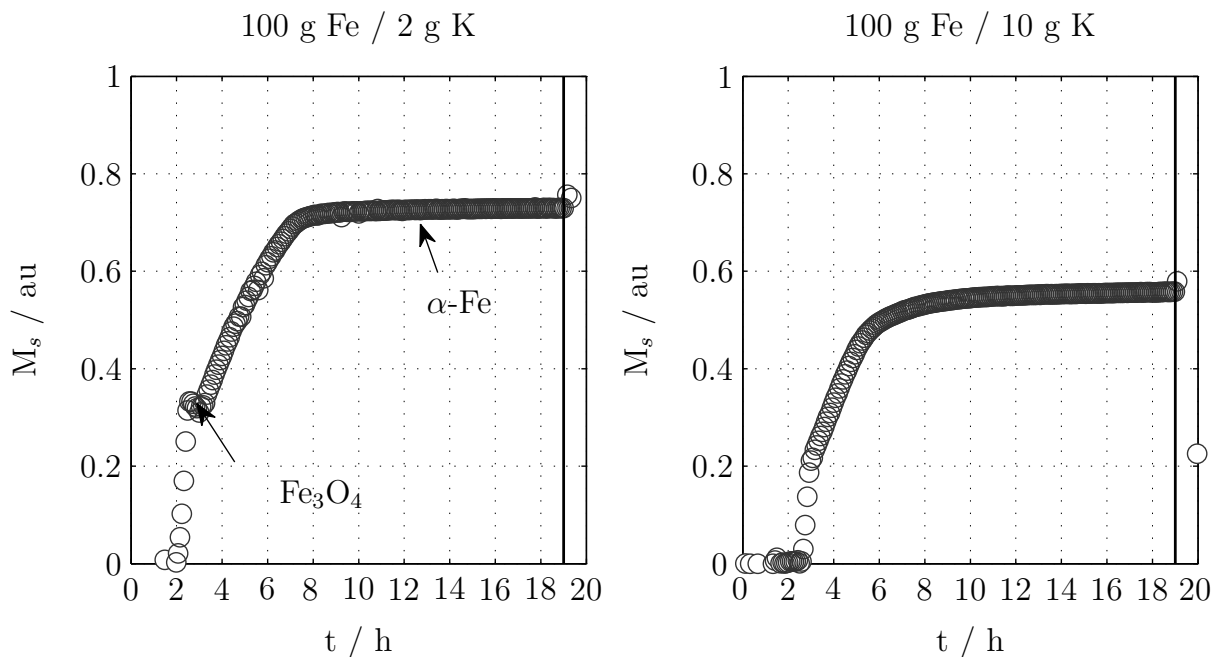


Figure 5.8: Saturation magnetisation  $M_s$  during catalyst reduction (Magnetometer measurement). Left: 100g Fe/ 2g K ; Right: 100g Fe/ 10g K. Experimental results over temperature can be found in Figure E.26.

A two-step reduction, as reported in literature (Equation 3.4 and 3.5), is confirmed by both in-situ methods. The first reduction step, from hematite to magnetite, is detected at 190 °C (after 3 h) for 100 g Fe / 2 g K, and at 280 °C (after 5 h) for 100 g Fe / 10 g K in the XRD measurements (Figure E.27 and Figure 5.9). The reason for this delay (higher temperatures) with the 100 g Fe / 10 g K is the higher K loading. Potassium covers the catalyst surface and blocks some Fe-active sites, reducing the number of Fe active sites available for H<sub>2</sub> adsorption (Choi et al. 1996; Lee et al. 2007). This delay in the first reduction step for the 100 g Fe / 10 g K compared to 100 g Fe / 2 g K is also confirmed by magnetic measurements, however, at different absolute temperatures and times. For the 100 g Fe / 2 g K, the first reduction step starts at 280 °C (after 2 h) and for 100 g Fe / 10 g K at 340 °C (after 3 h) (Figure 5.8 and Figure E.26). The reason for this difference between both methods can be explained by the different heating procedures. In both cases heating rates of 2 K/min are used but during XRD investigations, temperature is held during 20 minutes to do the scan. The long holding time at certain temperatures led to the start of the reduction at a lower temperature than recorded with the magnetometer, where magnetic measurements can be taken in real time without holding steps.

The second reduction step, from magnetite to  $\alpha$ -Fe starts almost at the same temperature for both catalysts (approx. 310 °C, according to XRD). In the magnetic measurements a shoulder is observed. The decrease in the magnetisation is due to the effect of temperature on magnetite (the magnetisation of magnetite decreases with increasing temperature).

From XRD measurements it can be seen that magnetite is present over a large temperature interval (Figure E.27). The higher magnetisation level for the 100 g Fe / 2 g K, in comparison with 100 g Fe / 10 g K, can be in part explained by the presence of more K-containing compounds (the catalyst contains 7 % less iron). The remaining difference can not be fully explained.

The reduction cannot be followed in the lab-scale fixed-bed reactor because H<sub>2</sub> consumption can not be properly analysed. It can also be assumed after the in-situ experiments that the complete reduction of the catalyst sample is possible in the lab-scale fixed-bed reactor because the same procedure was followed.

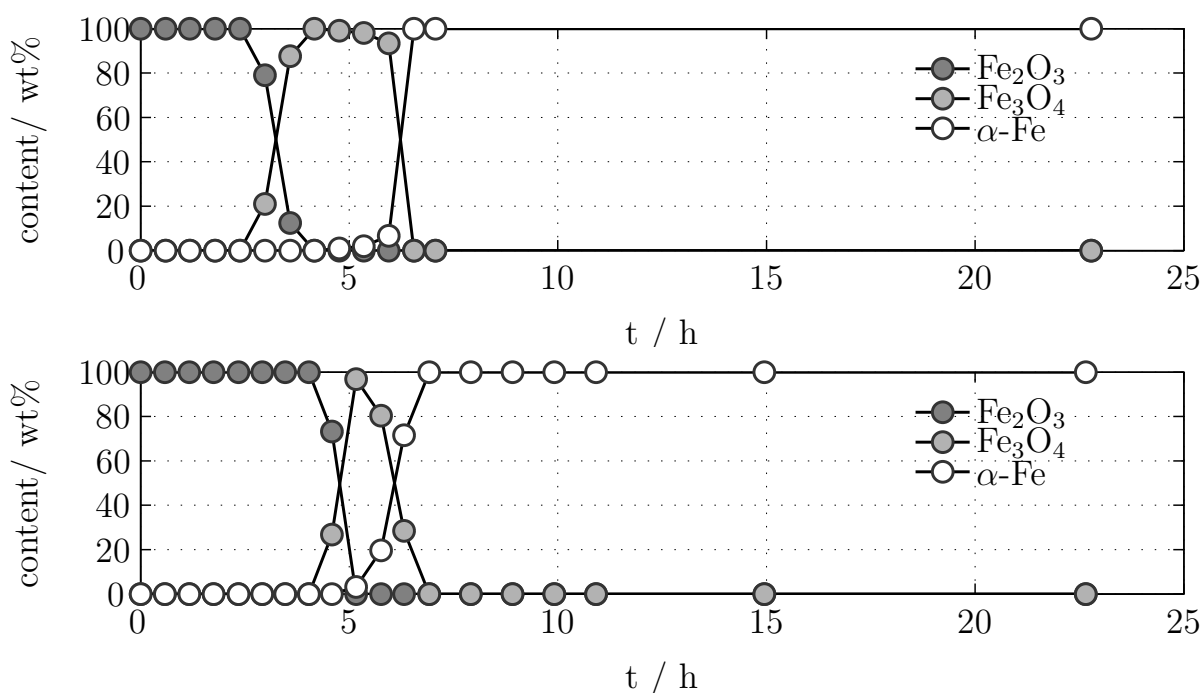


Figure 5.9: The catalyses' phase composition over time under reduction conditions(XRD measurement). Top: 100 g Fe / 2 g K; Bottom: 100 g Fe / 10 g K. Detailed information can be found in Table E.6 (100 g Fe / 2 g K) and E.7 (100 g Fe / 10 g K) and complete diffraction patterns in Figure E.28 (100 g Fe / 2 g K) and E.29 (100 g Fe / 10 g K).

#### 5.4.2.2 Catalyst formation

When H<sub>2</sub> and CO<sub>2</sub> are in contact with the catalyst (Table 5.4), the magnetisation value starts to decrease (Figure 5.10). This indicates the formation of oxides and carbides, both non-magnetic materials under the operating conditions. The decrease in the magnetisation is faster for 100 g Fe / 10 g K than for 100 g Fe / 2 g K. The formation of carbides is favoured by the presence of potassium. 100 g Fe / 2 g K requires around 20 h to reach a steady-state condition, while 100 g Fe / 10 g K reaches its steady-state after 7 h. This

result correlates with the observations done in lab-scale (Section 5.4.1.1) and also with literature (Cubeiro et al. 2000; Schulz 2014).

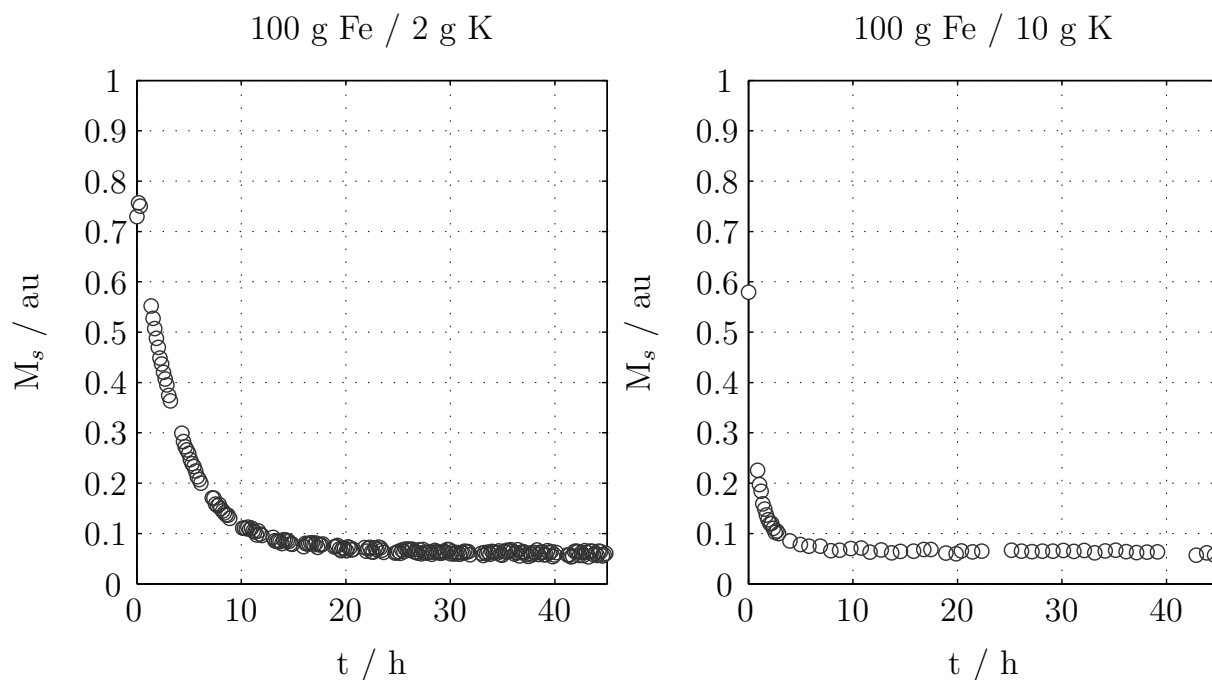


Figure 5.10: Saturation magnetisation  $M_s$  during catalyst formation. Left: 100 g Fe / 2 g K; Right: 100 g Fe / 10 g K. For conditions see Table 5.4

X-ray diffraction patterns at the same conditions support the results obtained with the magnetometer and confirm that phase changes are enhanced in the presence of K. Figure 5.12 shows a fast formation of Häag carbide in the first hour, while for 100 g Fe / 2 g K the formation of Häag carbide is much slower, and increases during the 45 h time-on-stream (Figure 5.11).

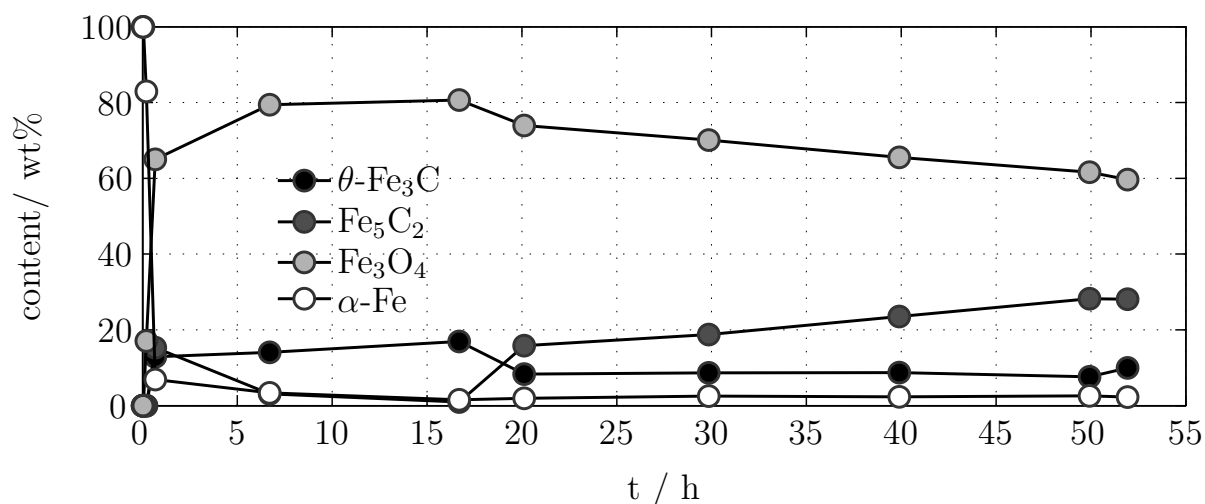


Figure 5.11: Phase composition of the 100 g Fe / 2 g K catalyst during formation (XRD-measurement). Detailed information in Table E.8.

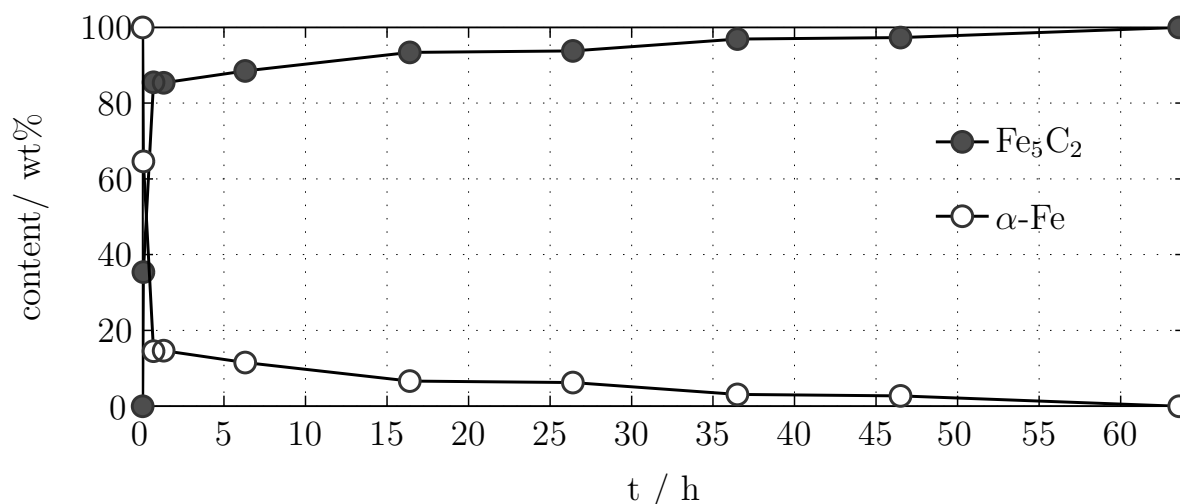


Figure 5.12: Phase composition of the 100 g Fe / 10 g K catalyst during formation (XRD-measurement). Detailed information in Table E.9. For conditions see Table 5.4.

After 45 h time-on-stream under the same operating conditions, the composition of both catalysts is significantly different. 100 g Fe / 2 g K presents 60 % of Fe<sub>3</sub>O<sub>4</sub>, 28 % of Fe<sub>5</sub>C<sub>2</sub>, 10 % of  $\theta$ -Fe<sub>3</sub>C, and approximately 2 % of  $\alpha$ -Fe, while 100 g Fe / 10 g K consists 100 % of Fe<sub>5</sub>C<sub>2</sub>. These different phases present in the catalyst are responsible for the different hydrocarbon selectivities and alkane/alkene content. The results obtained with 100 g Fe / 2 g K are similar to those reported by Riedel et al. (2003) and Gnanamani et al. (2013) with a high contribution of Fe<sub>3</sub>O<sub>4</sub> and a lower presence of Fe<sub>5</sub>C<sub>2</sub>.

It is surprising that a similar magnetisation value is recorded for both catalysts after 45 h, while, according to XRD the content of Fe<sub>3</sub>O<sub>4</sub> (magnetic under operating conditions) is higher in the case of 100 g Fe / 2 g K. A possible explanation could be that X-ray diffraction patterns recorded the phases present near the surface of the capillary cell and not in the middle of the cell. There may be more Fe<sub>3</sub>O<sub>4</sub> in the external layer than in the center of the capillary cell, where iron carbides might be present. Conditions are more homogeneous on the magnetometer, where the magnetisation of the whole sample is measured. It can be understood that Fe<sub>3</sub>O<sub>4</sub> contributes to a higher magnetisation  $M_s$  value in comparison with 100 g Fe / 10 g K during the first 10 h.

#### 5.4.2.3 Analysis of fresh and spent catalyst samples: ex-situ XRD

According to the diffraction patterns of the fresh samples, both catalysts consist of iron oxide Fe<sub>2</sub>O<sub>3</sub> (Figure E.31 and Figure E.30). Two small peaks in the 100 g Fe / 10 g K diffraction pattern ( $2\theta = 30$  and  $36$ ) could not be identified and might belong to a potassium compound.

A significant difference between both compositions of spent catalyst samples is observed by ex-situ XRD (Table 5.7). A different catalyst phase composition between top and bottom is identified for the 100 g Fe / 2 g K catalyst. The top of the catalyst bed consists of a mixture of Fe<sub>5</sub>C<sub>2</sub> and Fe<sub>3</sub>O<sub>4</sub>, while the bottom is strongly dominated by Fe<sub>3</sub>O<sub>4</sub>. The reason for this is the contrast between the reductive environment at the reactor inlet (high partial pressure of H<sub>2</sub>) compared to the more oxidising atmosphere at reactor outlet due to the presence of H<sub>2</sub>O. These results confirmed observations made in lab-scale of the negative effect of H<sub>2</sub>O on the catalyst composition oxidising the iron-carbides to iron-oxides. These results correlate well with those obtained by in-situ XRD at the end of the formation (Figure 5.11 and Figure 5.12). Mossbauer experiments from Soled et al. (1990) show that oxide and carbide are present at the top of the fixed-bed reactor, and only oxides are present at the bottom.

In the case of the 100 g Fe / 10 g K catalyst, the catalyst bed consists 100 % top and bottom of Fe<sub>5</sub>C<sub>2</sub> (Figure E.33), and no catalyst oxidation is present, as indicated from lab-scale results. The peaks that do not belong to Fe<sub>5</sub>C<sub>2</sub> correspond to SiO<sub>2</sub>, also present on the catalyst bed as inert material. By removing the catalyst from the glass reactor, it was observed that it was stuck to the wall, and the particles formed clusters, which could indicate the formation of inactive carbon or liquid products that, at high temperatures led to the carbon deposits.

Table 5.7: Phase composition and particle sizes determined by ex-situ investigations.

Calculations done in "TOPAS 4.1". Diffraction patterns in Figure E.32 and Figure E.33.

		Fe <sub>2</sub> O <sub>3</sub>	Fe <sub>3</sub> O <sub>4</sub>	Fe <sub>5</sub> C <sub>2</sub>	$d_p$ Fe <sub>2</sub> O <sub>3</sub>	$d_p$ Fe <sub>3</sub> O <sub>4</sub>	$d_p$ Fe <sub>5</sub> C <sub>2</sub>	R <sub>WP</sub>
		w%	w %	w %	nm	nm	nm	-
100 g Fe / 2 g K	top	-	37	63	-	51	33	12.571
	bottom	-	96	4	-	51	41	11.522
100 g Fe / 10 g K	top	-	-	100	-	-	41	8.725
	bottom	-	-	100	-	-	42	12.397

## 5.5 Conclusion: selection of catalyst and operating conditions for heating value adjustment

The aim of these experiments was to gain a better understanding of the CO<sub>2</sub> hydrogenation on iron-catalysts and find out attractive operating conditions for the CO<sub>2</sub> hydrogenation to gaseous hydrocarbons in the form of alkanes that can be used for heating value adjustment.

The selectivity of both catalysts for the production of the desired C<sub>2-4</sub> components is similar, however with different byproducts (Figure 5.7 and Figure 5.13):

- Methane is the most abundant component when using 100 g Fe / 2 g K, with the advantage that it can be stored in the natural gas grid together with other gaseous hydrocarbons.
- Long chain hydrocarbons C<sub>5+</sub> are the predominant byproduct with 100 g Fe / 10 g K, together with low amounts of methane. The C<sub>5+</sub> fraction requires upgrading before it can be used as blending material for transportation fuel, this introduces an extra cost, yet the final product is more valuable.

Figure 5.13 shows the selectivity to the fraction C<sub>1</sub> and C<sub>2-4</sub> (left) and only C<sub>2-4</sub> (right) over CO<sub>2</sub> conversion for the two catalysts investigated.

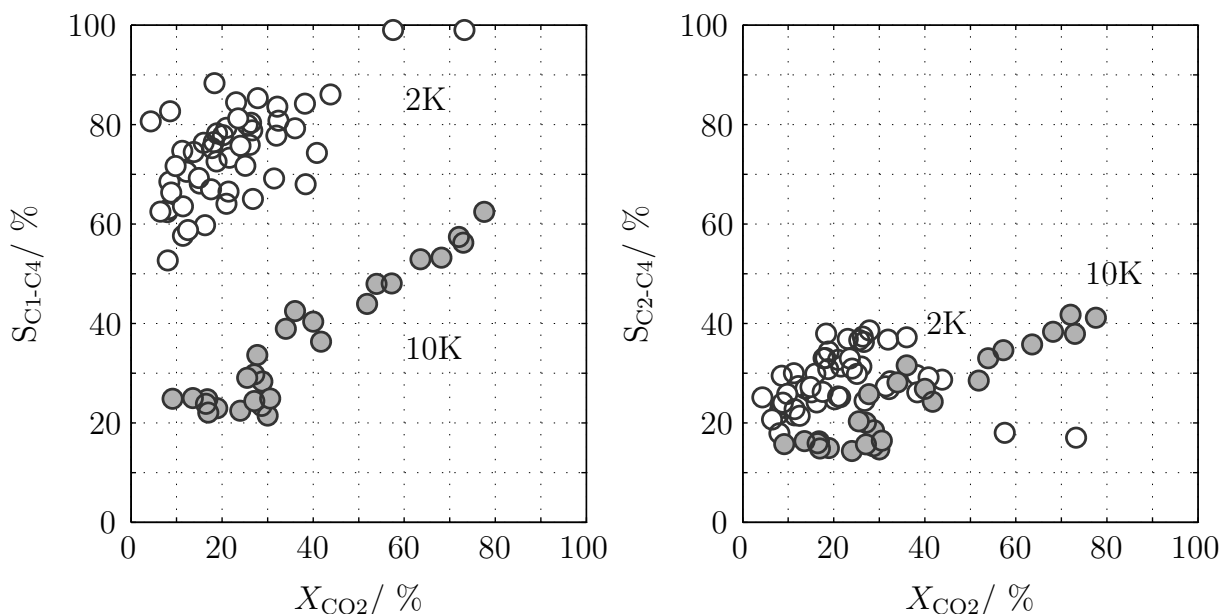


Figure 5.13: Selectivity of gaseous hydrocarbons as a function of  $X_{\text{CO}_2}$ . White symbols: 100g Fe / 2g K; grey symbols: 100g Fe/ 10g K. Left: Fraction C<sub>1-4</sub>. Right: Fraction C<sub>2-4</sub>. Conditions:  $p = 1 - 2$  MPa,  $(\text{H}_2/\text{CO}_2)_{\text{in}} = 4, 5, 8, 22$ ,  $T = 245 - 297$  °C and  $\tau_{\text{mod}} = 175\text{-}5000$  kg s/m<sup>3</sup>

The selectivity to C<sub>2-4</sub> is maximum 40 % for both catalysts. In the case of 100 g Fe / 2 g K, the selectivity to C<sub>2-4</sub> is similar to the hydrocarbon selectivity because organic yield is very close to CO<sub>2</sub> conversion. In the case of 100 g Fe / 10 g K, the hydrocarbon selectivity to C<sub>2-4</sub> is slightly higher than for 100 g Fe / 2 g K but the yield of organic product is lower than the CO<sub>2</sub> conversion due to higher CO yield, therefore selectivity values to C<sub>2-4</sub> are very similar to those obtained with 100 g Fe / 2 g K. The selectivity to C<sub>2-4</sub> in the case of 100 g Fe / 10 g K increases with the CO<sub>2</sub> conversion, however, at the higher CO<sub>2</sub>

conversion values, the catalyst deactivates. When considering C<sub>1</sub> and C<sub>2-4</sub> selectivities the values are higher for 100 g Fe / 2 g K due to the higher amount of methane in the product.

The most challenging issue in CO<sub>2</sub> hydrogenation is to reach a high yield of organic compounds, other than methane. This requires a catalyst with a high shift and FT activity in the proper ratio. According to the two iron catalysts investigated in the present study, the following can be concluded (Table 5.8):

- 100 g Fe / 10 g K is an example of a catalyst that allows high CO<sub>2</sub> conversion values, but due to its low FT activity, organic yield remains low. FT activity becomes higher with temperature and modified residence time, but under these conditions C-containing compounds deposit on the catalyst bed and cause blockage and high pressure drop.
- 100 g Fe / 2 g K is an example of a catalyst with a high FT activity, consequently almost no CO is present in the final product and CO<sub>2</sub> conversion correlates directly with hydrocarbon yield. In this case the limitation is the oxidation of the catalyst due to H<sub>2</sub>O formation. Above a certain level of H<sub>2</sub>O concentration, the iron catalyst starts to modify its composition (iron carbides are transformed to iron oxides), making high CO<sub>2</sub> conversion values almost impossible. The use of membranes to remove H<sub>2</sub>O in-situ and enhance the CO<sub>2</sub> hydrogenation has already been considered by Rohde et al. (2008) and Rohde (2011), although currently available membranes exhibit low stability, permselectivities, and permeances regarding H<sub>2</sub>O under FT conditions.

Table 5.8: Comparison of the two iron catalysts

	100 g Fe / 2 g K	100 g Fe/ 10 g K
Catalyst stability with TOS	high	medium
Catalyst stability at high CO <sub>2</sub> conversion	lower	higher
Activity, $r_{FT}/r_{CO_2-sh}$	high ( $Y_{CO}$ low)	low ( $Y_{CO}$ high)
Hydrocarbon selectivity	C <sub>1</sub> , C <sub>2-4</sub> , alkanes	C <sub>2-4</sub> , C <sub>5+</sub> , alkenes

In agreement with the results obtained in this study, the selection of 100 g Fe / 2 g K seems to be more attractive for the production of short chain alkanes. Operating conditions at higher  $(H_2/CO_2)_{in}$  ratio favour CO<sub>2</sub> conversion and organic product yields without catalyst deactivation, because partial pressure of H<sub>2</sub>O remains low due to the excess of H<sub>2</sub>. The hydrocarbon selectivity shifts to short chain hydrocarbons (with low C<sub>5+</sub>) and hydrogenation of the primary product alkene takes place in-situ, with alkanes being the

majority of the hydrocarbon products. High temperatures and modified residence times also favour the formation of short chain hydrocarbons. CO<sub>2</sub> conversion is however limited caused by the formation of H<sub>2</sub>O (Figure 5.13).

In the following sections only the 100 g Fe / 2 g K catalyst is considered. Chapter 6 considers the kinetic parameters required for the scale-up to a technical size. The behaviour of the 100 g Fe / 2 g K catalyst under transient operation is investigated in chapter 7. Chapter 8 focuses on reactor design for flexible operation, dealing with the limitation in H<sub>2</sub>O partial pressure, to avoid catalyst deactivation.



# 6 Determination of CO<sub>2</sub> hydrogenation kinetics under steady-state conditions: mathematical modelling studies

*This chapter describes the method used to determine the set of kinetic parameter values for the CO<sub>2</sub>-shift and Fischer-Tropsch reaction based the experimental data reported in chapter 5, and reaction rate equations proposed by Riedel et al. (2001). A mathematical model of the fixed-bed reactor is required to determine the kinetic parameters, due to the change of component molar flows along the catalyst bed (integral reactor). Obtained kinetic parameters are compared with those published by Riedel et al. (2001), one of the few studies found in literature focused on determining rate parameters for the combination of CO<sub>2</sub>-shift and FT. Kinetic rate equations help to gain a fair understanding of the complex interplay between both chemical reactions, and additionally make possible a reactor scale-up (chapter 8). Most of the curves shown in chapter 5 are calculated with the parameters determined in this section.*

## 6.1 Fixed-bed reactor mathematical model

The general form of the material balance for a component  $i$  in a fixed-bed reactor is expressed in Equation 6.1 in mol/m<sup>3</sup> s (Baerns et al. 1992). The material balance considers the terms of accumulation, convection, dispersion, and reaction.

$$\underbrace{\varepsilon \cdot \frac{\partial C_i}{\partial t}}_{\text{Accumulation}} = \underbrace{- \operatorname{div}(u \cdot C_i)}_{\text{Convection}} + \underbrace{\operatorname{div}(D_i \cdot \operatorname{grad} C_i)}_{\text{Dispersion}} + \underbrace{\sum_j \nu_{ij} \cdot r_j \cdot \rho_{\text{bed}}}_{\text{Reaction}} \quad (6.1)$$

The general material balance can be simplified according to the characteristics of the lab-scale fixed-bed reactor used:

- Steady state operation: no accumulation term is required.

- No radial profiles:  $d_t/d_p \geq 10$ , perfect mixture can be assumed in radial direction, and wall effects considered negligible.
- No axial dispersion or back-mixing: plug-flow behaviour can be assumed,  $Pe_{ax} = 0.5$ ,  $L_t/d_p > 1000$ ;  $Bo > 100$ , Equation I.30.
- Internal and external mass and heat transfer limitations do not occur. For small particles ( $d_p = 50 - 100 \mu\text{m}$ ) the catalyst is fully utilised (Claeys 1997). Pseudo-homogeneous model, gas and solid, can be treated as a single phase.
- All components are assumed to be gases under reaction conditions.

Equation 6.2 shows the simplified material balance, considering axial convection and reaction under steady-state conditions.  $F_{n,i}$  is the axial molar flow in mol/s of component  $i$ ,  $z$  is the axial direction,  $\nu_{ij}$  is the stoichiometric coefficient of component  $i$  in reaction  $j$  and  $r_j$  is the reaction rate per initial mass of catalyst in mol/(s.kg).

$$\frac{dF_{n,i}}{dz} = \frac{m_{cat}}{L_{bed}} \cdot \sum_j \nu_{ij} \cdot r_j \quad (6.2)$$

Verification of the assumptions of plug-flow behaviour and negligible mass and heat transfer limitations are shown in Table J.14. No energy balance needs to be formulated because temperature variations along the catalyst bed are lower than 1 % of the absolute temperature,  $\Delta T_{max} = 2.5 \text{ K}$ . The fixed-bed reactor is considered to be isothermal. Additionally, no pressure drop along the catalyst bed is considered because the average pressure drop measured along the catalyst bed of all set points is below 3 % of the absolute pressure, i.e. 0.03 MPa in experiments at 1 MPa.

The description of the lab-scale reactor according to the presented assumptions, and using Equation 6.2, has been already described by Mena Subiranas (2009), Pabst (2013), Rohde (2011) and Unruh (2006) for other chemical reactions.

### **Selection of reaction rate equations:**

The chemical reactions considered are the CO<sub>2</sub>-shift and the FT reaction (Equation 3.1 and Equation 3.2). The kind of rate equations used (Equation 3.10 and 3.11 in Table 6.1) is based on earlier work by Riedel et al. (2001), which in turn adopted the equations from Zimmerman et al. (1990), slightly modifying them to add a term for CO<sub>2</sub> inhibition. The effect of the chemical equilibrium limitation is considered by introducing the chemical equilibrium constant  $K_p$  (Equation 3.9).

Table 6.1: Kinetic rate equations selected for CO<sub>2</sub>-shift and Fischer-Tropsch reactions based on Riedel et al. (2001)

CO <sub>2</sub> -shift	$r_{\text{CO}_2\text{-sh}} = k_{\text{CO}_2\text{-sh}} \cdot \frac{p_{\text{CO}_2} \cdot p_{\text{H}_2} - (p_{\text{CO}} \cdot p_{\text{H}_2\text{O}})/K_p}{p_{\text{CO}} + a_{\text{CO}_2\text{-sh}} \cdot p_{\text{H}_2\text{O}} + b_{\text{CO}_2\text{-sh}} \cdot p_{\text{CO}_2}}$
Fischer-Tropsch	$r_{\text{FT}} = k_{\text{FT}} \cdot \frac{p_{\text{CO}} \cdot p_{\text{H}_2}}{p_{\text{CO}} + a_{\text{FT}} \cdot p_{\text{H}_2\text{O}} + b_{\text{FT}} \cdot p_{\text{CO}_2}}$

According to the experiments of Riedel et al. (2001), the formation of hydrocarbons directly from CO<sub>2</sub> (Equation 3.3) is a hundred times slower than the two-step reaction, and consequently has a minor influence on the CO<sub>2</sub> conversion, therefore it is neglected in the present work.

The resulting system of ordinary differential balance equations (Equation 6.2, for each chemical component) is solved using numerical methods (Runge-Kutta solver, ode 45) implemented in MATLAB®. The differential material balance equations are integrated along the catalyst bed and led to calculated molar flows for each component along the reactor length.

## 6.2 Procedure to determine set of kinetic parameters

The mathematical model of the lab-scale reactor is used to determine the set of kinetic parameters of both reactions simultaneously ( $k_{\text{CO}_2\text{-shift}}$ ,  $k_{\text{FT}}$ ,  $a_{\text{CO}_2\text{-shift}}$ ,  $b_{\text{CO}_2\text{-shift}}$ ,  $a_{\text{FT}}$ ,  $b_{\text{FT}}$ ), based on experimental data at varying temperature, pressure, modified residence time, and inlet ratio  $(\text{H}_2/\text{CO}_2)_{\text{in}}$  (Table K.15). The procedure followed is iterative using a non-linear least square analysis (lsqnonline, MATLAB®). The kinetic parameters are varied to adjust the calculated values to the experimental results. The sum of square errors of the differences between the experimental and calculated values (integral yields of CO  $Y_{\text{CO}}$  and hydrocarbons  $Y_{\text{CH}_2}$ ) is minimised.

The lsqnonline solver requires starting values for the parameters that are to be optimised. Due to the strong effect of starting values, an iterative procedure is used, until no differences are found among the parameters obtained by two consecutive calculations. The inhibition parameters,  $a_j$  and  $b_j$ , are considered to be independent of temperature. In a first step,  $a_{\text{FT}}$  and  $b_{\text{FT}}$  are calculated using all experimental data available and constant values for  $k_{\text{CO}_2\text{-shift}}$ ,  $k_{\text{FT}}$  and  $a_{\text{CO}_2\text{-shift}}$ ,  $b_{\text{CO}_2\text{-shift}}$ . The second step calculates  $a_{\text{CO}_2\text{-shift}}$ ,  $b_{\text{CO}_2\text{-shift}}$  using the new calculated values for  $a_{\text{FT}}$ ,  $b_{\text{FT}}$  and constant values for  $k_{\text{CO}_2\text{-shift}}$ ,  $k_{\text{FT}}$ , using again all experimental data available. The third step then calculates  $k_{\text{CO}_2\text{-shift}}$ ,  $k_{\text{FT}}$  for each temperature, using the previously calculated parameters  $a_{\text{FT}}$ ,  $b_{\text{FT}}$

and  $a_{\text{CO}_2\text{-shift}}$ ,  $b_{\text{CO}_2\text{-shift}}$  (steps 1 and 2). With the new calculated  $k_{\text{CO}_2\text{-shift}}$ ,  $k_{\text{FT}}$  values, the algorithm returns to step 1. In this way  $a_{\text{CO}_2\text{-shift}}$ ,  $b_{\text{CO}_2\text{-shift}}$ ,  $a_{\text{FT}}$  and  $b_{\text{FT}}$  are independent of temperature.

Once the kinetic parameters that fit the experimental data the best are calculated, activation energy  $E_A$  and pre-exponential factor  $k_0$  are obtained using the Arrhenius equation for each reaction.

### 6.3 Set of kinetic parameter values for CO<sub>2</sub> hydrogenation: 100 g Fe / 2 g K

Table 6.2 shows the set of kinetic parameters for the 100 g Fe / 2 g K, obtained when following the previous procedure. This set of parameters can describe the experimental results with a maximum error of  $\pm 20\%$  (Figure 6.1 and K.37). The determination of the kinetic parameters involved 32 different combinations of operating conditions (64 points for the mathematical fitting), in the range shown in Table K.15. Experimental data at two different pressure levels, three different  $(\text{H}_2/\text{CO}_2)_{\text{in}}$  ratios, and various modified residence times were used.

Each of the experimental points is measured for about 24 h under constant conditions and the average value of the last 10 h (approx. 25 online-GC measurements) is used. Experimental results which indicate deactivation (Figure 5.6, grey points) or closing of the C-balance with an error higher than 5% (Figure 5.6, black points), are not considered for kinetic determination.

A preliminary set of kinetic parameters is calculated for the 100 g Fe / 10 g K catalyst following the same procedures as for the 100 g Fe / 2 g K (Table K.16). The kinetic parameters are based on 20 different combinations of experimental conditions (Table K.17) resulting on 40 points for the mathematical fitting,  $Y_{\text{CO}}$  and  $Y_{\text{CH}_2}$  are used.

Table 6.2: Kinetic parameter values of the CO<sub>2</sub>-shift and FT reaction over 100 g Fe / 2 g K for Equation 3.10 and Equation 3.11. Range of operating conditions used shown in Table K.15. Parity plots given in Figure 6.1 and Figure K.37.

	$k_j$ (245 °C)	$k_j$ (266 °C)	$k_j$ (286 °C)	$a_j$	$b_j$
	mol/s kg Pa	mol/s kg Pa	mol/s kg Pa	—	—
CO <sub>2</sub> -shift	$1.69 \cdot 10^{-8}$	$5.38 \cdot 10^{-8}$	$1.78 \cdot 10^{-7}$	128	0.8
FT	$7.92 \cdot 10^{-7}$	$1.73 \cdot 10^{-6}$	$3.95 \cdot 10^{-6}$	152	0.5

Figure 6.1 shows that the difference between the experimental and calculated results is always lower than 20 %.  $Y_{\text{CO}}$  and  $Y_{\text{CH}_2}$  are fitted using the mathematical model, while the calculated  $X_{\text{CO}_2}$  is the result, assuming a perfectly closed C-balance, therefore it may differ from the experimental  $X_{\text{CO}_2}$  value. At 245 °C the mean deviation for the fitting is 13.7 %, 9.3 % in the case of 266 °C and 7.3 % in the case of 290 °C. Some examples of the goodness of the fit between calculated and experimental points can also be seen in Figure 5.3 (top) at  $T = 266$  °C or in Figure 5.4 (top) at  $\tau_{\text{mod}} = 1000$  kg s/m<sup>3</sup>.

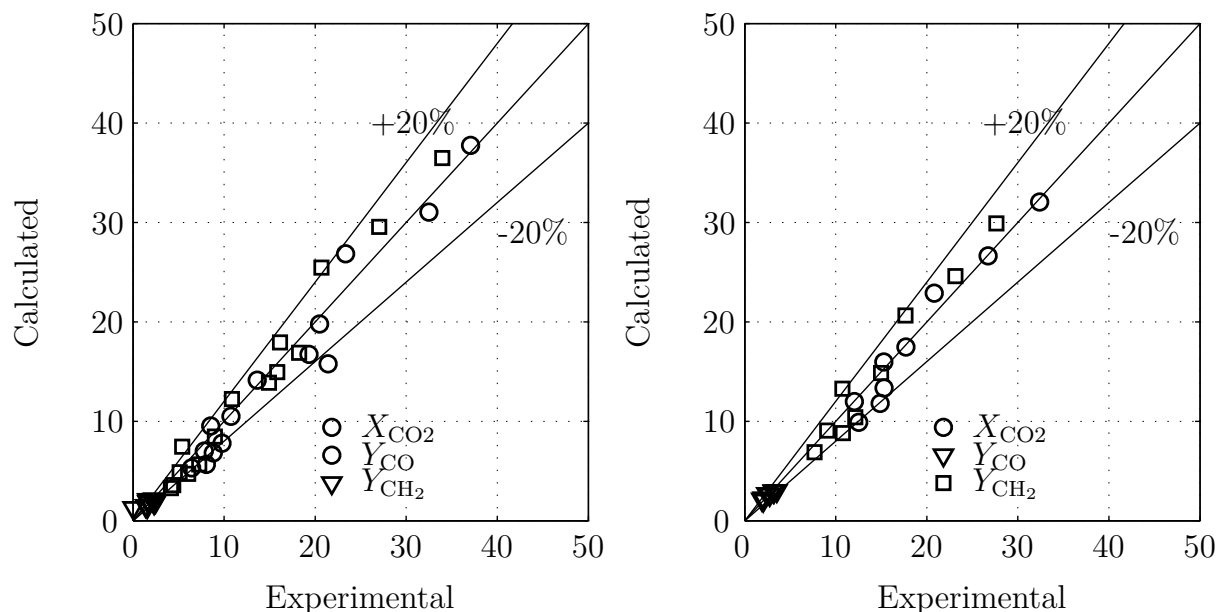


Figure 6.1: Parity plot for  $X_{\text{CO}_2}$ ,  $Y_{\text{CO}}$  and  $Y_{\text{CH}_2}$ . Calculated values using set of kinetic parameters and experimental values at  $T = 250$  °C (left) and  $T = 270$  °C (right). Figure K.37 shows the parity plot at  $T = 290$  °C

Table 6.2 shows that the inhibition term for CO<sub>2</sub> ( $b_j$ ) is low for both reactions. In contrast, inhibition by H<sub>2</sub>O ( $a_j$ ) is strong for both reactions and slightly higher in the case of FT. For the 100 g Fe / 10 g K the inhibition of CO<sub>2</sub> is a little higher than for 100 g Fe / 2 g K especially in the case of FT (Table K.16). This could be related to a strong adsorption of CO<sub>2</sub> on the catalyst surface due to the higher amount of K. The inhibition by H<sub>2</sub>O is lower for the 100 g Fe / 10 g K catalyst, compared with the 100 g Fe / 2 g K, but is still very significant.

For comparison with present results, inhibition parameters for the CO<sub>2</sub>-shift and FT reaction rate determined by Riedel et al. (2001) are studied. There, comparable results were achieved with a 100 g Fe / 10.7 g Cu / 8.9 g K / 13.3 g Al<sub>2</sub>O<sub>3</sub> catalyst (Table K.18). A stronger inhibition from H<sub>2</sub>O than from CO<sub>2</sub> is shown. However, the inhibition of H<sub>2</sub>O is significantly lower than in the present study using 100 g Fe / 10 g K (similar amount of K). This difference could be related with the different range of operating conditions (ratio  $(\text{H}_2/\text{CO}_2)_{\text{in}} = 3$  in contrast with ratio  $(\text{H}_2/\text{CO}_2)_{\text{in}} \geq 4$ ) and/or the different phases

present on the catalyst (100 % iron carbide for 100 g Fe / 10 g K and a mixture of iron carbides and oxides for the catalyst used by Riedel (Riedel et al. 2003)).

The dependency of the reaction rate on temperature is a function exclusively of the kinetic constant, because inhibition coefficients are assumed to be temperature independent. For CO<sub>2</sub>-shift, there is also a limited temperature effect in the equilibrium constant  $K_p$ . Table 6.2 shows that kinetic constants  $k_{\text{CO}_2\text{-shift}}$  and  $k_{\text{FT}}$  are highly dependent on temperature and increase by a factor of 3.3 and 2.3 respectively, for an increase of 20 K. Based on the kinetic constants, activation energies and pre-exponential factors can be calculated according to a linearised form of the Arrhenius equation (Equation K.46, Figure K.38).

Table 6.3 shows that CO<sub>2</sub>-shift is more sensitive to temperature than the FT reaction, indicating a higher temperature dependency. The 100 g Fe / 2 g K catalyst also shows a higher sensitivity than the 100 g Fe / 10 g K. The activation energies reported by Riedel et al. (2001) are lower than in the present case,  $E_{A,FT} = 72$  kJ/mol and  $E_{A,\text{CO}_2\text{-shift}} = 55$  kJ/mol, and the FT reaction is more sensitive than the CO<sub>2</sub>-shift to temperature. The different sensitivity to temperature may be related to the catalyst phase composition, as they differ in all three cases, and also the operating conditions. It is not possible to compare the reaction rates of the three catalyst based on the activation energies, because inhibition terms are different.

Table 6.3: Activation energies and pre-exponential factors determined by linear regression from kinetic constants shown in Table 6.2. See Figure K.38 for linear regression representation.

	100 g Fe / 2 g K		100 g Fe / 10 g K	
	$k_{0,j}$ mol/s kg Pa	$E_{A,j}$ kJ/mol	$k_{0,j}$ mol/s kg Pa	$E_{A,j}$ kJ/mol
CO <sub>2</sub> -shift	$1.612 \cdot 10^6$	139.0	$1.625 \cdot 10^4$	119.4
FT	$2.627 \cdot 10^3$	91.5	$3.53 \cdot 10^0$	71.2

Figure 6.2 shows that for the selected partial pressures, representative for the CO<sub>2</sub> hydrogenation and the investigated temperature range (grey area), the 100 g Fe / 2 g K catalyst is the most active of the three catalysts. The CO<sub>2</sub>-shift rate for 100 g Fe / 2 g K and 100 g Fe / 10 g K is very similar, however the Fischer-Tropsch reaction rate is significantly higher with 100 g Fe / 2 g K than with 100 g Fe / 10 g K, due to the higher content of K. The reaction rates calculated with the parameters from Riedel et al. (2001) indicate a fast CO<sub>2</sub>-shift at lower temperatures but a slow CO<sub>2</sub>-shift at higher temperatures. The Fischer-Tropsch rate observed on the catalyst used by Riedel is similar

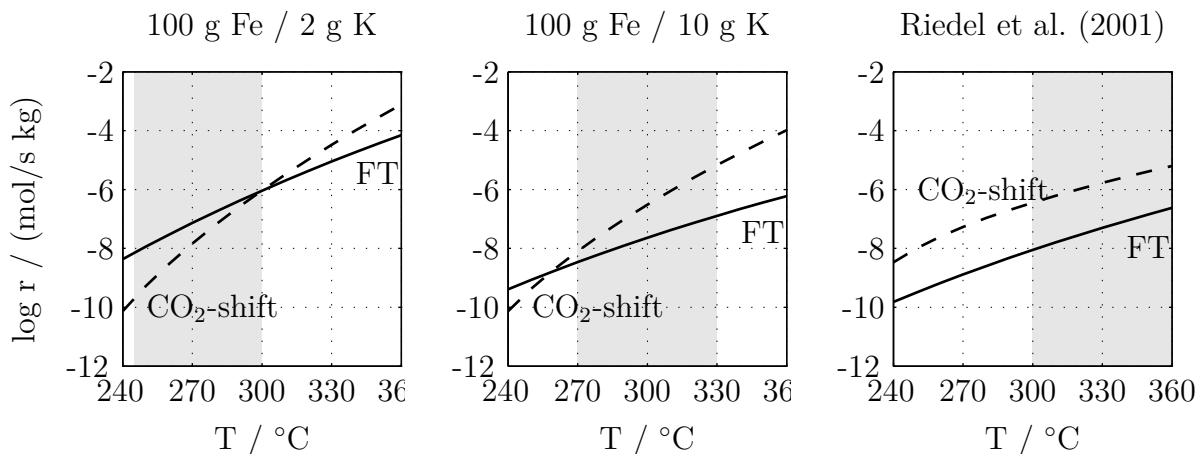


Figure 6.2: Calculated CO<sub>2</sub>-shift and FT reaction rates for the investigated catalysts with the kinetic parameters from Table 6.2 for 100 g Fe / 2 g K, Table K.16 for 100 g Fe / 10 g K, and Table K.18 for the 100 g Fe / 10.7 g Cu / 8.9 g K / 13.3 g Al<sub>2</sub>O<sub>3</sub> investigated by Riedel et al. (2001). Partial pressures are typical for the CO<sub>2</sub> hydrogenation in the present study:  $p_{\text{H}_2} = 0.73$  MPa,  $p_{\text{CO}_2} = 0.14$  MPa,  $p_{\text{H}_2\text{O}} = 0.086$  MPa,  $p_{\text{CO}} = 0.007$  MPa,  $p_{\text{CH}_2} = 0.04$  MPa. Grey area: temperature range where set of kinetic parameters are determined.

to that observed with 100 g Fe / 10 g K, which may be directly related to the comparable amount of potassium present on both catalysts. Potassium promoting has a small effect on the CO<sub>2</sub>-shift reaction and a significant effect on FT reaction rate, reducing the latter rate at high K content.

Figure 6.2 shows that for the catalysts with a higher amounts of K, above 250 °C, the CO<sub>2</sub>-shift reaction is always faster than the FT reaction, meaning that FT is the limiting reaction and the CO<sub>2</sub>-shift is always close to equilibrium. In contrast, in the case of the 100 g Fe / 2 g K, at temperatures below 300 °C the FT reaction is faster than the CO<sub>2</sub>-shift, the latter being the limiting reaction. Therefore partial pressure of CO is always low using this catalyst. At temperatures higher than 300 °C, catalyst stability is very low and no kinetic parameters are available.

## 6.4 Range of validity of the kinetic parameters

The set of kinetic parameters for 100 g Fe / 2 g K can be used to describe catalyst activity in the range of conditions utilised to determine the kinetic parameters (Table K.15). Additionally, the kinetic parameter values can be used to describe the catalyst activity under operating conditions where  $(p_{\text{H}_2\text{O}}/p_{\text{H}_2})_{\text{out}}$  is below 0.10 (Figure 5.6). The kinetic parameters can successfully describe experimental data at  $T = 300$  °C, high  $(\text{H}_2/\text{CO}_2)_{\text{in}}$  and low residence times (e.g.  $\tau_{\text{mod}} = 400$  kg s/m<sup>3</sup>,  $(\text{H}_2/\text{CO}_2)_{\text{in}} = 5 - 8$ , Figure 7.4) or at

$$(\text{H}_2/\text{CO}_2)_{\text{in}} = 22.$$

Above a  $(p_{\text{H}_2\text{O}}/p_{\text{H}_2})_{\text{out}}$  ratio of 0.1 catalyst deactivation is observed, therefore the set of kinetic parameters cannot be used. This behaviour is observed at long modified residence times and intermediate temperatures (e.g.  $\tau_{\text{mod}} = 5000 \text{ kg s/m}^3$ ,  $T = 266 \text{ }^\circ\text{C}$ , Figure 5.3), or high temperatures and intermediate modified residence times (e.g.  $\tau_{\text{mod}} = 1000 \text{ kg s/m}^3$ ,  $(\text{H}_2/\text{CO}_2)_{\text{in}} = 5$ , Figure 5.5).

The range of experimental conditions used to determine the kinetic parameters is wide and therefore a  $\pm 20 \%$  range is considered acceptable. Catalyst composition is assumed to be constant with time during the experiment and validated by repeating experiments under reference conditions (Figure F.34). As shown in Table 5.7, the composition of the catalyst is different at the top and bottom of the catalyst bed. It is assumed that this difference occurs during catalyst formation, and afterwards catalyst composition does not change with time. This assumption is supported on the similar catalyst phase composition obtained from in-situ XRD at the end of the catalyst formation (Figure 5.11), and from ex-situ XRD using spent catalyst samples removed from the fixed-bed (Table 5.7, top and bottom). All in all, the kinetic parameters are identified as a result of a good fit between the experimental and calculated data, according to the selected reaction rate equations.



# 7 Iron catalyst behaviour under variable operating conditions: experimental and mathematical modelling studies

*Solid catalysts are delicate components of the reaction system and as such may be sensitive to variations in reaction mixture composition or temperature. The catalyst itself can undergo significant changes due to its interaction with reagents, e.g. variations in the surface structure and near-surface composition affecting its catalytic properties. The time during which a catalyst approaches its new steady state, after a change in reaction conditions, may play an important role in heterogeneous catalysis (Boreskov et al. 1983).*

*This chapter describes the approach followed to determine whether the activity and selectivity of the 100 g Fe / 2 g K vary due to variations in the reaction mixture composition and/or temperature. Variations are carried out under relevant industrial conditions (in the range where kinetic parameters were determined under steady state conditions, see section 6) and under “extreme” conditions, where no steady-state kinetics are available. Three different methods are presented along with representative example results. The results show the potential of the followed approach and the complementary information obtained from the different methods used. A plausibility check of the results is also possible by comparison of the results.*

## 7.1 General approach

The aim of this chapter is to study the activity and selectivity of 100 g Fe / 2 g K under variable operating conditions for CO<sub>2</sub> hydrogenation to gaseous hydrocarbons. The possibility to describe transient operation using kinetic rate equations, determined under steady-state condition needs to be assessed and discussed. In section 6 a set of kinetic rate parameters are determined for the 100 g Fe / 2 g K catalyst under steady-state conditions, under the assumption that the catalyst composition is constant, and that coverage of catalyst surface by active species is in equilibrium with the gas phase. These assumptions might not be justified under transient operation (see section 3). Differences

between steady-state and transient reaction rates will depend on the catalyst system and on the mechanism of the chemical reaction.

Experiments in the lab-scale setup are carried out within the same range of operating conditions used to determine the kinetic parameters (section 6), and also under extreme operating conditions (where the set of kinetic parameters is not valid), to force the appearance of change on the catalyst (Table 7.1). Three different methods are applied to study the behaviour of 100 g Fe / 2 g K catalyst under variable operating conditions: (i) step change experiments combined with mathematical modelling, (ii) in-situ catalyst

Table 7.1: Overview of methods used to describe catalyst behaviour under variable operating conditions. The modified parameter, and to which range the variations belong, are indicated. Figure numbers indicate examples of the changes. M = magnetometer. Catalyst: 100 g Fe / 2 g K.

Method	Variations within valid range of kinetic parameters <sup>1</sup>		Variations to extreme conditions	
	parameter	example	parameter	example
Step change experiments combined with mathematical modelling	concentration	Fig. 7.4	concentration	Fig. 7.6
		Fig. M.42		Fig. 7.5
		Fig. M.50		Fig. M.45
	temperature <sup>2</sup>	Fig. M.48	temperature <sup>2</sup>	Fig. 7.8
		Fig. 7.7		
		Fig. M.46		
	inlet flow	Fig. M.47		
Magnetometer and XRD in-situ techniques	concentration (M)	Fig. 7.9	concentration (M,XRD)	Fig. 7.10 <sup>3</sup>
			temperature (M)	Fig. 7.9
	Periodic changes	concentration	Fig. 7.11	

<sup>1</sup> industrial relevant conditions

<sup>2</sup> set point changed with a ramp of 2 K/min

<sup>3</sup> experiments carried out with 100 g Fe / 10 g K

characterisation techniques: XRD and magnetometer, and (iii) by periodic change.

## 7.2 Step change experiments combined with mathematical modelling

The approach followed with this methodology (Figure 7.1) relies on the powerful combination of experimental work and mathematical modelling. Experimental work carried out in the lab-scale setup cannot directly show the effect of catalyst behaviour under transient conditions. Therefore a validated mathematical model of the lab-scale setup is required to separate catalytic effects from those related to backmixing and dead time, which is, in fact, associated with the reactor's attached equipment. In the first approach, catalyst activity during transient operation is described using a set of kinetic parameters determined under steady-state conditions.

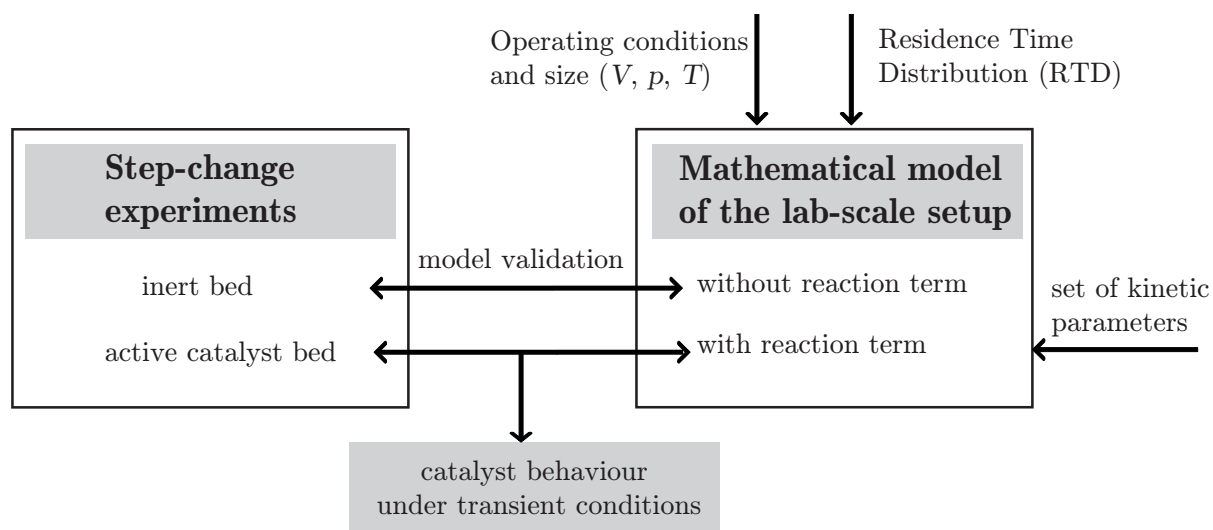


Figure 7.1: Approach followed using step change experiments combined with mathematical modelling to find out if the set of kinetic parameters selected are able to describe the catalyst behaviour under transient conditions.

### 7.2.1 Experimental setup and procedure

The setup described in Figure 5.1 is used for the step change experiments. A micro-GC and a non dispersive infrared gas analyser (BINOS) are additionally installed due to their higher measure frequency. Detailed information about both analytic methods can be found in section D. This setup, originally designed and optimised for steady-state experiments is adjusted for transient experiments, however, due to the characteristics of

the Fischer-Tropsch product a relatively complex sequence of attached equipments for product separation are needed (approx. 80 % of the total setup volume, see Table 7.2). As indicated in section 5, pressure is maintained constant in the reactor using a pressure-regulated Argon flow and a needle valve. The Argon flow varies due to changes in the operating conditions of the reactor (e.g. in volumetric flow,  $(\text{H}_2/\text{CO}_2)_{\text{in}}$  or temperature), and influences the dynamic response of the setup. The flow of  $\text{N}_2+\text{Cpr}$  is constant, however due to changes in the total volumetric flow, the concentration of  $\text{N}_2+\text{Cpr}$  changes due to variations in reactor operation.

### 7.2.2 Development of a mathematical model for the lab-scale setup

The transient behaviour of the reactor's attached units (e.g. hot trap, cooling trap) makes separation of the catalytic effects from the experimental results challenging. The combination of experiments with an appropriate mathematical model is helpful to understand the effects in the lab-scale setup, and to analyse the experimental results.

#### 7.2.2.1 Model equations

The first step in developing a formulation of the mathematical model is the characterisation of the lab-scale setup. Two methods are used to determine the size of the lab-scale setup: (i) measured dimensions of each unit, volumetric flow, temperature, and pressure levels and (ii) residence time distribution experiments (RTD).

#### Characterisation of the lab-scale setup

Table 7.2 shows the volume of the most relevant parts of the lab-scale setup together with the typical ranges of pressure and temperature. The volume of the units is calculated based on length and diameter of the different parts, with the exception of pore volume based on measurements carried out using the BET surface area technique.

Residence time distribution experiments are carried out to determine the distribution of residence times of flowing fluid in the setup (i.e. how long the molecules remain in the setup) (Levenspiel 1999). Real equipment is always a combination of plug flow and perfectly mixed flow behaviour. The residence time distribution can be determined easily using a tracer, in this case  $\text{CO}_2$ , at room temperature and pressure, and with an inert bed. Step changes from pure Ar to  $\text{CO}_2$  are carried out at different volumetric flows, and concentration changes using the IR analysis (Figure M.39).

Table 7.2: Most relevant dimensions of the lab-scale setup and range of operating conditions. Detailed information in Table M.19

	$p$	$T$	$V_{\text{gas}}$
	MPa	°C	cm <sup>3</sup>
Before reactor	1-2	20-250	24
Reactor	1-2	250-330	26
Catalyst bed <sup>1</sup>			1-1.5
Catalyst pore <sup>2</sup>			0.3-0.4
After Reactor			
Hot-trap	1-2	180	20
Sampling line	0.1	0-200	143

$$^1 m_{\text{cat}} = 1.5 - 2 \text{ g}, \varepsilon = 0.4$$

$$^2 V_{\text{pores, SiO}_2} = 1.8 \cdot 10^{-4} \text{ cm}^3/\text{g},$$

$$V_{\text{pores, 100 g Fe} / 2 \text{ g K}} = 1.9 \cdot 10^{-1} \text{ cm}^3/\text{g}$$

The dimensionless form of the concentration measurements, carried out with the BINOS, is represented by the F-curve. From these experiments, and by means of Equation 7.1, it is possible to find out by iteration the number of ideal perfectly mixed flow tanks  $N$  that fit the experimental results best (Figure M.39).  $\Phi$  represents the dimensionless time based on the mean residence time in all  $N$  tanks ( $\Phi = t/(V_{\text{PMF}}/F_v)$ ). Consequently, the volume corresponding to perfectly mixed flow  $V_{\text{PMF}}$  for a certain  $N$  is calculated by an iterative process that minimises the difference between experimental and calculated  $F$ . The plug flow volume is determined from the dead time measured experimentally and with the known inlet volumetric flow. The best fit is obtained for  $N = 3$ , corresponding to a perfectly mixed volume of approx. 80 cm<sup>3</sup>.

$$F = 1 - e^{-N \cdot \Phi} \cdot \left[ 1 + N \cdot \Phi + \frac{(N \cdot \Phi)^2}{2!} + \dots + \frac{(N \cdot \Phi)^{N-1}}{(N-1)!} + \dots \right] \quad (7.1)$$

The total setup volume obtained by both methods is very similar, and around 215 cm<sup>3</sup>. Most of the setup can be represented with a plug flow behaviour (63 %). The three perfectly mixed tanks ( $N = 3$ ) needed to represent the backmixing in the setup, according to the RTD experiment, are identified as hot trap, ampoule sampler, and cooling trap. Each of these three units is represented as a mixed flow unit, a combination of plug flow and perfectly mixed flow (Figure 7.2). The percentage of the total volume, that in a mixed flow unit works as plug flow, is adjusted based on experimental measurements with an inert catalyst bed (the plug flow proportion is 10 % for the hot wax trap, 15 % for

the ampoule sampler, and 10 % for the cooling trap; additionally the micro-GC can be represented with a 50 % PF and 50 % PMF).

### Reaction engineering mathematical model

The mathematical model of the lab-scale setup consists of a combination of plug and perfectly mixed flow units based on RTD experiments and the characteristic of the setup (Figure 7.2).

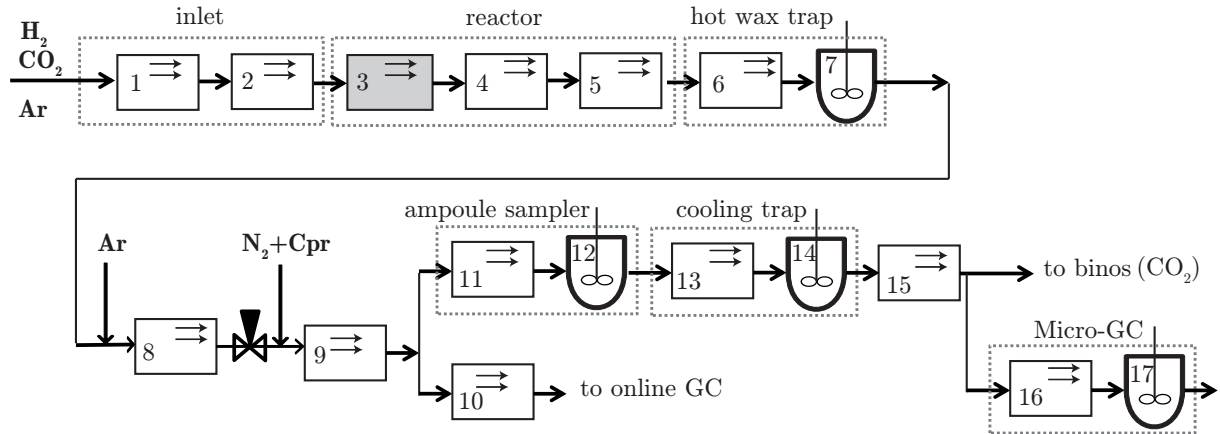


Figure 7.2: Lab-scale setup representation as a combination of ideal flow patterns: plug flow represented with arrows and perfectly mixed flow with a stirrer. Fixed-bed reactor considered as plug flow reactor (grey unit). Detailed information regarding each unit in Table M.19. Flow scheme of the lab-scale setup in Figure 5.1

The mathematical model of the lab-scale setup is based on mass balance equations in the form of partial differential equations: plug-flow, Equation 7.2, and perfectly mixed flow, Equation 7.4. The catalytic reactor is described as plug-flow reactor (PFR), Equation 7.3. Component molar flows change in axial direction and with time, assuming temperature and pressure are constant along the catalyst bed. CO<sub>2</sub>-shift and FT reaction rates determined in section 6 under steady-state operating conditions are implemented. A differential equation is written for each component present in the lab-scale setup, (7 in total: CO, H<sub>2</sub>, CO<sub>2</sub>, H<sub>2</sub>O, C in CH<sub>2</sub>, Ar, N<sub>2</sub>+Cpr) and each unit (17 units) .

$$\frac{\partial c_i}{\partial t} = \frac{-\partial(u \cdot c_i)}{\partial z} \quad (7.2)$$

$$\varepsilon \cdot \frac{\partial c_i}{\partial t} = \frac{-\partial(u \cdot c_i)}{\partial z} + \sum_{j=1}^N (v_{ij} \cdot r_j) \quad (7.3)$$

$$\frac{\partial c_i}{\partial t} = \frac{F_{v,in} \cdot c_{i,in} - F_{v,out} \cdot c_{i,out}}{V} \quad (7.4)$$

The micro-GC requires an extra mathematical model due to the different residence time distribution of the two channels ( $\text{CO}_2$  and  $\text{C}_2\text{H}_6$  are separated in a Plot Q column and  $\text{CO}$  and  $\text{CH}_4$  in a Molsieve column). The difference can be explained due to a lower volumetric flow of gas sample in the Plot Q channel compared with the Molsieve, which operates as expected. This behaviour was validated by step changes from Helium to calibration gas.

The mathematical model assumes that the pressure in the reactor is always constant, therefore Argon flow changes in step form, in the same way as the inlet volumetric flow. In reality, light variations in the reactor pressure are observed due to the slower adjustment of the Argon flow.

The flow of  $\text{N}_2+\text{Cpr}$  is always constant and is used as reference to calculate the molar flows of the other components (Equation 5.1). After a change in volumetric flow, a variation in the concentration of  $\text{N}_2+\text{Cpr}$  occurs in unit 9. It takes some time until the concentration of  $\text{N}_2+\text{Cpr}$  is constant in the GC measurements.

### 7.2.2.2 Solution procedure

The partial differential equations for each component and each unit are solved using the method of lines (section L.1 in the appendix). Concentration, volumetric flow, and molar flow are calculated after each unit over time. The curves at the end of the lab-scale setup (unit 10, 15 or 17) represent the dynamic behaviour of the setup and can be compared with the experimental results obtained at that position.

Initial concentrations for all components at all units are required for  $t = 0$ . The ordinary differential equations (with time) are solved using the ode23s standard solver in MATLAB®. Time discretisation is automatically adjusted by the solver and results are obtained each second. Length discretisation is  $\Delta z = 0.04$  m for the plug flow units and  $\Delta z = 0.004$  m for the plug flow reactor (unit 3).

All experimental results shown in this section are dimensionless to facilitate comparison (Equation 7.5 and Equation 7.6).

$$Z_i = \frac{F_{n,i,t=t} - F_{n,i,t=0}}{F_{n,i,t=\infty} - F_{n,i,t=0}} \quad (7.5)$$

$$Z_i^* = \frac{F_{n,i,t=t} - F_{n,i,t=\infty}}{F_{n,i,t=0} - F_{n,i,t=\infty}} \quad (7.6)$$

### 7.2.2.3 Validation

Validation experiments are carried out under reaction conditions using an inert bed instead of the active catalyst. The dynamic behaviour of the lab-scale without chemical reactions can be measured and compared with the results of the mathematical model (without reaction term for the reactor). Validation until unit 15 is completed using the BINOS

(example Figure 7.3 left and Figure M.40). The validation until unit 17 is completed using the Micro-GC under conditions already validated with the BINOS. This shows that the mathematical model for the Micro-GC can also be validated under various operating conditions (Figure 7.3, right).

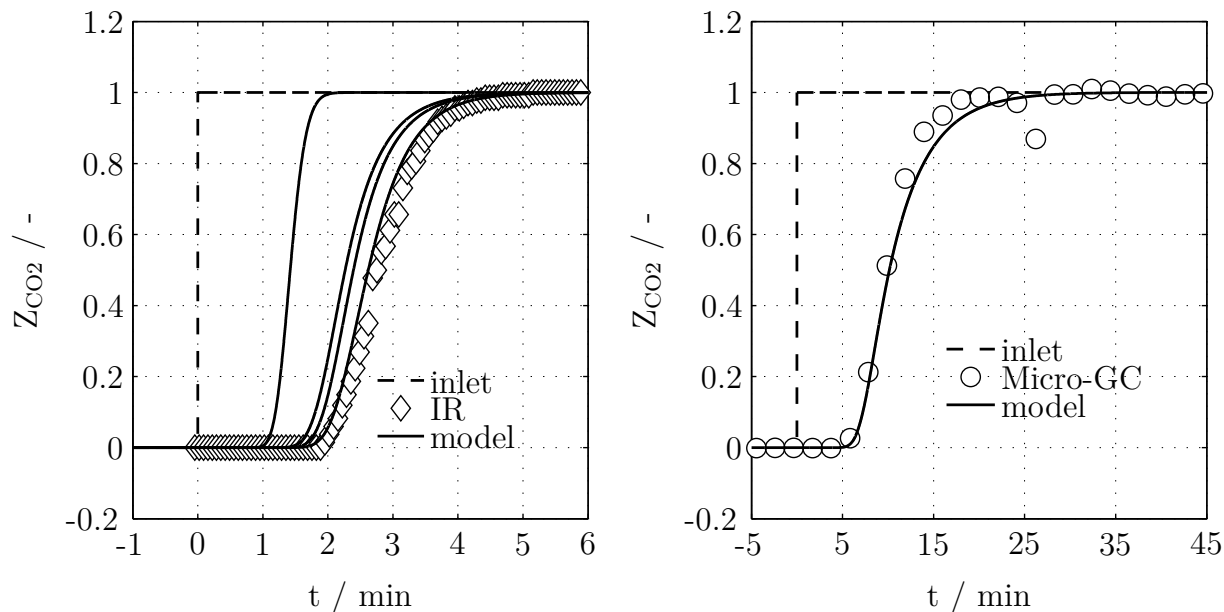


Figure 7.3: Validation of the mathematical model under reaction conditions with a bed of inert material, dimensionless change of  $CO_2$  flows  $Z_{CO_2}$ . Experimental results measured with BINOS (diamond) and with Micro-GC (circle). Conditions:  $p = 1 \text{ MPa}$ ,  $T = 266 \text{ }^\circ\text{C}$ ,  $F_{v,\text{in,STP}} = 300 \text{ cm}^3/\text{min}$ . Change at  $t = 0$  from  $(H_2/CO_2)_{\text{in}} = \infty$  to  $(H_2/CO_2)_{\text{in}} = 5$ . Left: curves calculated with mathematical model after unit 4, 7, 12 and 15. Right: curve calculated after unit 17.

## 7.2.3 Example results

This section shows example results from step changes in inlet concentration, inlet volumetric flow and reactor temperature, within and beyond the range of conditions where kinetic parameters are determined. Figure M.41 shows an example using molar flows.

### 7.2.3.1 Step change in inlet concentration

$(H_2/CO_2)_{\text{in}} = 5$  to  $(H_2/CO_2)_{\text{in}} = 8$

Figure 7.4 shows a change in inlet concentration from  $(H_2/CO_2)_{\text{in}} = 5$  to  $(H_2/CO_2)_{\text{in}} = 8$ . Experimental results show that the dynamic behaviour of the complete setup is



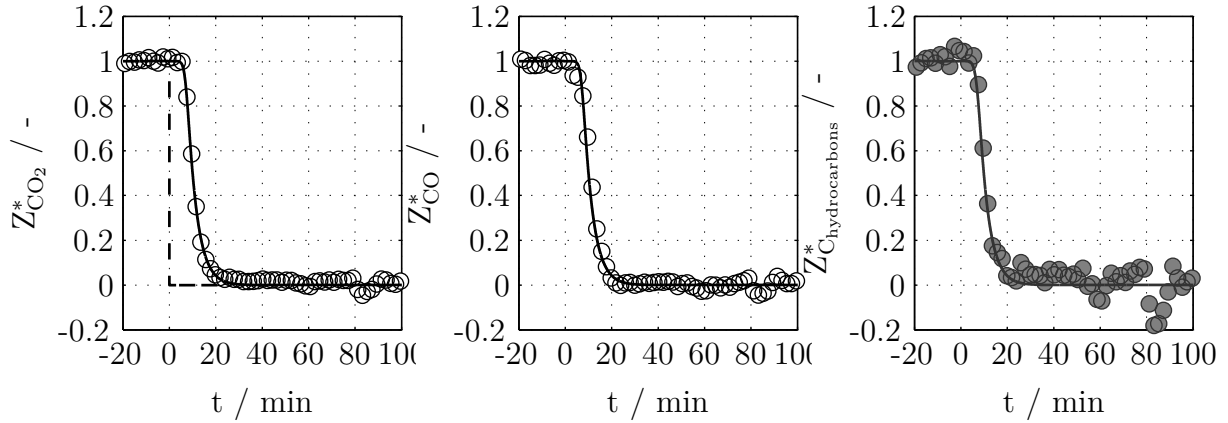


Figure 7.4: Dimensionless change of  $\text{CO}_2$ ,  $\text{CO}$ , and  $\text{C}$  in hydrocarbon outlet flows after a change in inlet concentration from  $(\text{H}_2/\text{CO}_2)_{\text{in}} = 5$  to  $(\text{H}_2/\text{CO}_2)_{\text{in}} = 8$ . Curves: calculated with mathematical model, broken line: change in inlet flow. Symbols: experimental results measured with the Micro-GC. Conditions:  $p = 1 \text{ MPa}$ ,  $T = 295 \text{ }^\circ\text{C}$ ,  $F_{\text{v,in,STP},(\text{H}_2/\text{CO}_2)_{\text{in}} = 5} = 238 \text{ cm}^3/\text{min}$ ,  $F_{\text{v,in,STP},(\text{H}_2/\text{CO}_2)_{\text{in}} = 8} = 233 \text{ cm}^3/\text{min}$ ,  $\tau_{\text{mod,target}} = 400 \text{ kg s}/\text{m}^3$ .

characterised by dead time and backmixing. The kinetic parameter values determined under steady-state conditions are able to describe the outlet flow of  $\text{CO}_2$ ,  $\text{CO}$ , and  $\text{C}$  in hydrocarbons. Figure M.42 shows the change from  $(\text{H}_2/\text{CO}_2)_{\text{in}} = 8$  to  $(\text{H}_2/\text{CO}_2)_{\text{in}} = 5$ . The same experiment is carried out in the magnetometer, (Figure 7.9). There, no changes on the catalyst phase composition (magnetisation value) are observed. It can be concluded that under these operating conditions, the catalyst activity can be described with the kinetic parameters determined under steady-state conditions.

The following examples and supplementary figures in the appendix consider changes in inlet concentration which are not obvious for practical use but may cause changes in the catalyst composition:

#### Ar to $(\text{H}_2/\text{CO}_2)_{\text{in}} = 4$ : “Hot-Stand-By”

Figure 7.5, shows the step change in inlet concentration from pure Argon to a  $(\text{H}_2/\text{CO}_2)_{\text{in}} = 4$  and the response of the lab-scale setup measured at the setup outlet. This example could be relevant if  $\text{H}_2$  and  $\text{CO}_2$  are temporarily unavailable, yet it is necessary to maintain the reactor heat until  $\text{H}_2$  and  $\text{CO}_2$  are again available (“hot-stand-by”). This situation could be challenging for the catalytic reaction due to the strong change of partial pressures in the gas phase.

After several hours of steady state operation,  $\text{H}_2$  and  $\text{CO}_2$  are replaced by Ar for 2 h. Figure 7.5 shows the step-change from Ar back to  $\text{H}_2$  and  $\text{CO}_2$ . The mathematical model, using the kinetic parameter values determined under steady-state conditions, can

describe the transient behaviour of  $\text{CO}_2$ ,  $\text{CO}$  and  $\text{C}$  in hydrocarbons in an accurate way. This indicates that the change in the catalytic reaction due to a change in gas phase to Ar is not significant. Consequently, the activity and selectivity can be described by the rate equations and the kinetic parameter values determined under steady-state conditions. The new steady-state is reached within a few minutes, the delay being caused by dead time and backmixing effects. The difference in the behaviour of  $\text{CO}_2$  and  $\text{C}_2\text{H}_6$  (compared to  $\text{CO}$  and  $\text{CH}_4$ ) is due to the characteristic dynamic response of the Micro GC used.

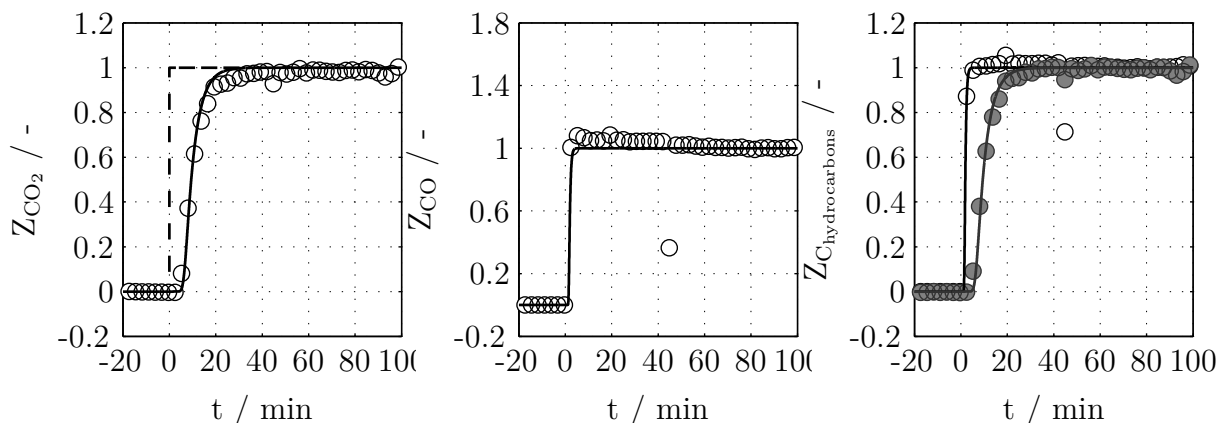


Figure 7.5: Dimensionless change of  $\text{CO}_2$ ,  $\text{CO}$ , and  $\text{C}$  in hydrocarbon outlet flows after a concentration change from Argon to  $(\text{H}_2/\text{CO}_2)_{\text{in}} = 4$  “Hot-stand-by”. Curves: calculated with mathematical model, broken line: change in inlet flow. Symbols: experimental results measured with the Micro-GC. Grey symbols,  $\text{C}$  in  $\text{C}_2\text{H}_6$ ; white symbols,  $\text{C}$  in  $\text{CH}_4$  (right). Conditions:  $F_{\text{v,in,STP,Ar}} = 100 \text{ cm}^3/\text{min}$ ,  $F_{\text{v,in,STP},(\text{H}_2/\text{CO}_2)_{\text{in}} = 4} = 308.7 \text{ cm}^3/\text{min}$ ,  $\tau_{\text{mod,target}} = 400 \text{ kg s}/\text{m}^3$ ,  $p = 1 \text{ MPa}$ ,  $T = 264 \text{ }^\circ\text{C}$ . Catalyst:  $100 \text{ g Fe} / 2 \text{ g K}$ .

### $\text{H}_2$ to $(\text{H}_2/\text{CO}_2)_{\text{in}} = 5$ : “Hot-Stand-By”

Figure 7.6 shows the step change in inlet concentration from pure  $\text{H}_2$  to a  $(\text{H}_2/\text{CO}_2)_{\text{in}}$  mixture and the response measured at the setup outlet together with the results from the mathematical model. This example could be relevant if  $\text{H}_2$  is available without  $\text{CO}_2$ . This situation is challenging for the catalyst because  $\text{H}_2$  is not an inert gas like Argon. Experiments are carried out in the same way as with Argon.

The mathematical model (again with kinetic parameter values determined under steady-state conditions) can describe the transient behaviour of  $\text{CO}_2$ , which indicates that the  $\text{CO}_2$ -shift activity ( $\text{CO}_2$ -shift active sites:  $\text{Fe}_3\text{O}_4$ ) seems to be unaffected by the sole presence of  $\text{H}_2$ . However, the mathematical model is not able to describe the transient behaviour of the  $\text{CO}$ ,  $\text{CH}_4$ , or  $\text{C}_2\text{H}_6$  flows. It seems that after two hours under  $\text{H}_2$  atmosphere, the iron-based catalyst has lost part of the Fischer-Tropsch activity, probably

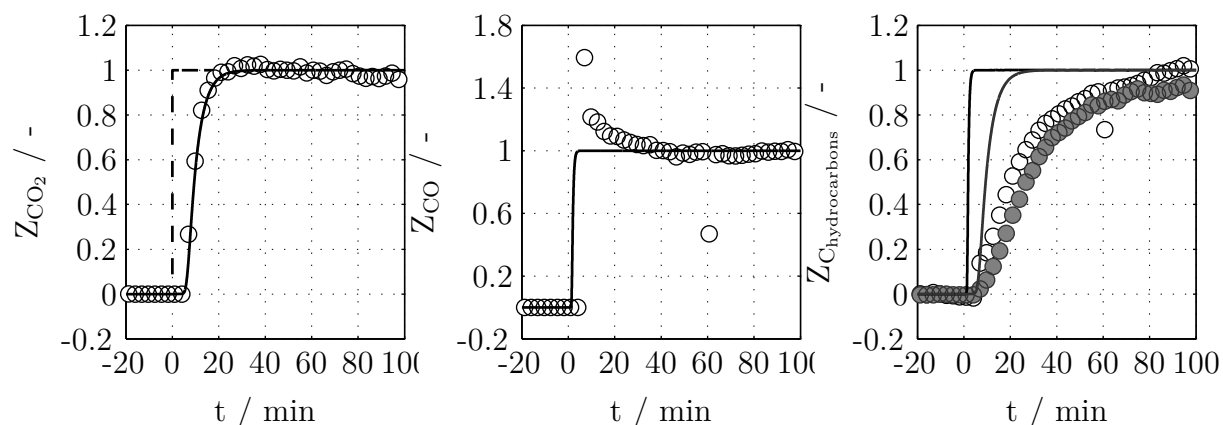


Figure 7.6: Dimensionless change of  $\text{CO}_2$ ,  $\text{CO}$ , and  $\text{C}$  in hydrocarbon outlet flows after a concentration change from  $\text{H}_2$  to  $(\text{H}_2/\text{CO}_2)_{\text{in}} = 5$  “Hot-stand-by”. Curves: calculated with mathematical model, broken line: change in inlet flow. Symbols: experimental results measured with Micro-GC. Grey symbols:  $\text{C}$  in  $\text{C}_2\text{H}_6$  and white symbols:  $\text{C}$  in  $\text{CH}_4$  (right). Conditions:  $F_{\text{v,in,STP,H}_2} = 300 \text{ cm}^3/\text{min}$ ,  $F_{\text{v,in,STP,(H}_2/\text{CO}_2)_{\text{in}}=5} = 309.3 \text{ cm}^3/\text{min}$ ,  $\tau_{\text{mod,target}} = 400 \text{ kg s}/\text{m}^3$ ,  $p = 1 \text{ MPa}$ ,  $T = 264 \text{ }^\circ\text{C}$ . Catalyst:  $100 \text{ g Fe} / 2 \text{ g K}$

due to the hydrogenation of the iron carbides (FT active sites:  $\text{F}_x\text{C}_y$  (Riedel et al. 2003)) to iron metal (see magnetisation measurement in Figure 7.10).

Once  $\text{C}$ -containing compounds ( $\text{CO}_2$ ,  $\text{CO}$ ) are again available in the gas atmosphere, surface reactions need to take place to form iron carbides first. It is only after this that hydrocarbons can then be produced on the newly formed FT sites, resulting in a transient slow hydrocarbon formation (Figure 7.6 right and Figure 3.2). It is interesting to see that methane formation is slightly faster than ethane formation, in agreement with the typical mechanisms of a polymerisation reaction (Feimer et al. 1984). The hydrocarbon product distribution cannot be described with the mathematical model because no reaction kinetics accounting for the formation of each hydrocarbon have been implemented.

The maximum in the transient  $\text{CO}$  behaviour can be explained by the fast formation of  $\text{CO}$  via  $\text{CO}_2$ -shift and the slower consumption via FT-Synthesis. The steady-state kinetics implemented in the mathematical model assumed a constant catalyst composition independent of the reaction mixture (no reactions of the solid are considered), therefore the model is not able to describe the experimental measurements. A modification of the FT reaction, considering a  $\text{C}$ -storage, will be needed to describe the formation of the iron carbides. The same experiment carried out in-situ, with XRD and magnetometer, verified the change in the catalyst composition after some hours under  $\text{H}_2$  atmosphere (Figure 7.10).

The comparison of this results with the experimental results collected directly after the

reduction (Figure M.43) indicates that after 2 h under  $H_2$  atmosphere the catalyst is not again fully reduced. The maximum in CO is higher immediately after catalyst reduction than after 2 h under  $H_2$  atmosphere, therefore the formation of iron carbides takes more time after reduction.

The change from  $(H_2/CO_2)_{in} = 5$  to pure  $H_2$  is shown in Figure M.44. After 30 minutes under  $H_2$  atmosphere, a maximum in the  $CH_4$  flow is observed. This result confirms the hydrogenation of carbon containing compounds present on the catalyst surface to methane.

Step changes are carried out several times and it is observed that high reproducibility can be achieved. Figure M.45 shows the change from pure  $H_2$  to  $(H_2/CO_2)_{in} = 4$ , with very similar results to those shown in Figure 7.6. A slower formation of hydrocarbons can be observed, consistent with the lower partial pressure of  $H_2$  (high  $H_2$  concentrations favour FT activity).

These results are, in general, in agreement with Feimer et al. (1984), who carried out similar changes from pure  $H_2$  to a  $(H_2/CO)_{in}$  mixture. They reported a maximum in the rate of hydrocarbon formation during the first minutes, however in the present case a slow formation of hydrocarbons is observed, which can be related to the use of  $CO_2$  instead of CO as carbon source.

Short treatments with  $H_2$  in-situ are reported in literature to be used to reactivate catalysts (mild rejuvenation) (Bartholomew et al. 2006).

In conclusion, feed gas consisting of pure  $H_2$  (or pure  $CO_2$ , seen in different experiments not shown here) causes compositional changes on the catalyst surface. In the case of a  $H_2$  atmosphere, these changes are reversible and iron carbides can be formed again in presence of a C-source. In the case of a pure  $CO_2$  atmosphere, the changes in the catalyst composition are irreversible and a loss in catalyst activity can be observed when changing to  $H_2/CO_2$  mixtures. If  $H_2$  and  $CO_2$  are both present in the feed gas ( $(H_2/CO_2)_{in}$  varied from 4 to 8) or if Argon is selected as inert gas, the activity and selectivity can be accurately described with the mathematical model, using the steady-state rate equations.

### 7.2.3.2 Step change in inlet volumetric flow

Changes in volumetric feed flow are probably most typical when operating a reactor under transient conditions. However, due to the design of the lab-scale plant, the dynamic effects of the Ar and  $N_2+Cpr$  flows also influence the transient behaviour of the setup.

Figure 7.7 shows a step change in inlet volumetric flow from  $24\text{ cm}^3/\text{min}$  to  $300\text{ cm}^3/\text{min}$ , where the mathematical model (with steady state kinetics) is able to describe the ex-

perimental results, except during the first minutes. In the first moment, an increase in feed volumetric flow causes an increase in reactor pressure. The volumetric flow of Argon needed to maintain constant pressure in the reactor decreases, however, the desired pressure can still not be reached and the position of the needle valve (responsible for the expansion from reaction pressure to ambient conditions, see Figure 5.1) needs to be manually adjusted to reach the desired pressure in the reactor and, simultaneously the desired outlet volumetric flow. This adjustment takes some minutes and it is responsible for the two or three points measured after the change that cannot be described with the mathematical model. The mathematical model assumes that the volumetric flow of each unit in the lab-scale setup changes at the same time as the feed flow, and that the pressure always remains constant.

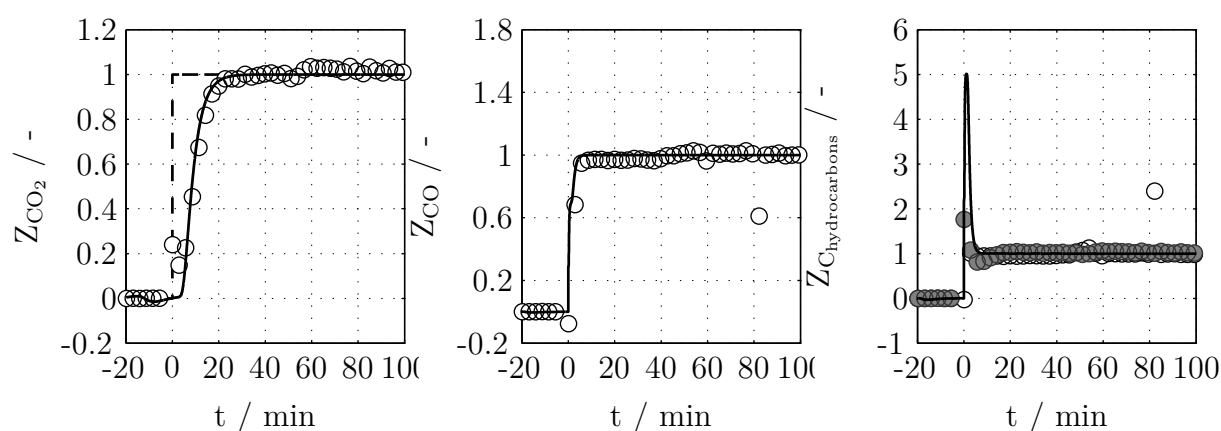


Figure 7.7: Dimensionless change of CO<sub>2</sub>, CO, and C in hydrocarbon outlet flows after a change in inlet volumetric flow from  $F_{v,in,STP} = 24 \text{ cm}^3/\text{min}$  to  $F_{v,in,STP} = 300 \text{ cm}^3/\text{min}$  (STP). Curves: calculated with mathematical model, broken line: change in inlet flow. Symbols: experimental results measured with Micro-GC. Grey symbols: C in C<sub>2</sub>H<sub>6</sub> and white symbols: C in CH<sub>4</sub> (right). Conditions:  $(\text{H}_2/\text{CO}_2)_{in} = 4$ ,  $p = 2 \text{ MPa}$ ,  $T = 245 \text{ }^\circ\text{C}$ . Catalyst: 100 g Fe / 2 g K

The dimensionless C flow in hydrocarbons (Figure 7.7 right) exhibit a maximum, which can be explained firstly by the increase of the total volumetric flow at  $t = 0$  (considering constant concentration in the setup outlet, molar flow increases). Secondly, the decrease in Argon flow causes an increase in the concentration of the other components, and consequently on its molar flows, that after a certain dead time reaches the setup outlet. The change in feed volumetric flow has produced a concentration change at the reactor outlet. Due to backmixing and dead time, this concentration change reaches the outlet of the setup after the residence time effects of the Ar and N<sub>2</sub>+Cpr flows. These combined dynamic effects can only be separated and analysed with the help of the mathematical model. More examples at different operating conditions can be found in Figure M.46 and

Figure M.47.

Experimental changes were carried out in the range where kinetic parameters are valid and no transient effect due to the chemical reaction is observed. According to the examples shown, activity and selectivity can be accurately described with the mathematical model, using the steady-state rate equations.

### 7.2.3.3 Step change in reactor temperature

Figure 7.8 shows a change in reactor temperature from 270 °C to 330 °C and back to 270 °C. The set of kinetic parameters determined under steady-state conditions is not valid for temperatures higher than 300 °C due to catalyst deactivation (high  $(p_{\text{H}_2\text{O}}/p_{\text{H}_2})_{\text{out}}$  ratio, Figure 5.5). The loss of FT activity at 330 °C can be observed due to the increase in the CO flow and the decrease in the flow of  $\text{CH}_4$  and  $\text{C}_2\text{H}_6$ . When temperature is again decreased to 270 °C, CO flow is higher, as  $\text{CH}_4$  and  $\text{C}_2\text{H}_6$  flows are lower than before the temperature increase, which indicates a catalyst deactivation (a change in catalyst state). These experimental results cannot be described with the mathematical model as no kinetic parameters are available.

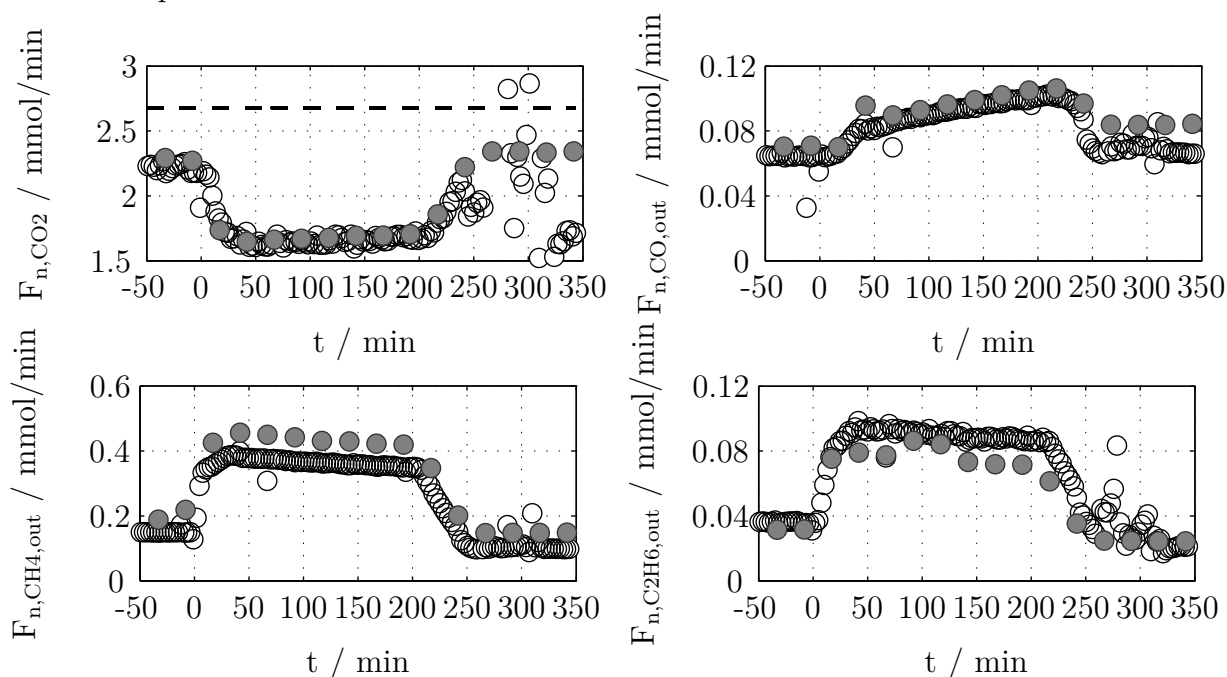


Figure 7.8: Measured outlet flows during temperature change from 270 °C, at  $t = 0$  to 330 °C, with a ramp of 2 K/min. At  $t = 201$  min back to 270 °C.

White symbols: Micro-GC (each 3 min), grey symbols: Online-GC (each 25 min). Broken line: inlet flow of  $\text{CO}_2$   $F_{n,\text{CO}_2,\text{in}}$ . Conditions:  $F_{v,\text{in,STP}} = 300$   $\text{cm}^3/\text{min}$ ,  $(\text{H}_2/\text{CO}_2)_{\text{in}} = 4$ ,  $p = 1$  MPa. Catalyst: 100 g Fe / 2 g K.

Similar experiments are carried out from 270 °C to 300 °C and back to 270 °C, (Figure

M.48). In this case, no deactivation is observed. Using the set of kinetic parameters determined under steady-state conditions, the mathematical model is not able to describe adequately temperature changes in the fixed-bed (Figure M.49). The change of temperature is implemented in the mathematical model assuming a linear change over time, with the same ramp (K/min) for the complete catalyst bed (i.e. isothermal bed conditions assumed). It was experimentally measured that after a change in the set point of the three temperature controllers, the top part of the reactor bed reaches the new set point much faster than the bottom part. Also, heating and cooling rates of the fixed-bed are different, observable in Figure 7.8 and Figure M.48. The simplification of a constant ramp might be the reason for the difference between experimental and calculated values. To improve the mathematical model, temperature needs to be measured at different positions of the catalyst bed continuously over time. With a moveable thermo-well, as used during the steady-state experiments, it is not possible to reach such accuracy.

## 7.3 Magnetometer and XRD: in-situ techniques

After the catalyst formation reported in Figure 5.10 for the magnetometer and in Figure 5.11 and Figure 5.12 for the X-ray diffractometer, changes in operating conditions are made to evaluate possible changes in the catalyst state due to variations of the reactant composition or temperature.

### 7.3.1 Results and discussion

Changes in inlet composition are carried out using the same operating conditions than in the step changes carried out in the lab-scale setup. Change in concentrations from  $(\text{H}_2/\text{CO}_2)_{\text{in}} = 5$  to  $(\text{H}_2/\text{CO}_2)_{\text{in}} = 8$  and back to  $(\text{H}_2/\text{CO}_2)_{\text{in}} = 5$  are carried out in the magnetometer equivalent to the step change carried out in lab-scale (Figure 7.4 and Figure M.42). Variations from  $(\text{H}_2/\text{CO}_2)_{\text{in}} = 5$  to pure  $\text{H}_2$  and back to  $(\text{H}_2/\text{CO}_2)_{\text{in}} = 5$  are carried out with 100 g Fe / 10 g K in the XRD and the magnetometer. The same variation carried out in lab-scale for 100 g Fe / 2 g K can be seen in Figure 7.6. Additionally, a change in reactor temperature from 300 to 330 °C is carried out with the magnetometer at  $(\text{H}_2/\text{CO}_2)_{\text{in}} = 5$ , and can be compared with the result obtained in lab-scale, Figure 5.5.

### 7.3.1.1 Step change in inlet concentration

$(\text{H}_2/\text{CO}_2)_{\text{in}} = 5$  to  $(\text{H}_2/\text{CO}_2)_{\text{in}} = 8$  and back to  $(\text{H}_2/\text{CO}_2)_{\text{in}} = 5$

Figure 7.9 shows a change in gas inlet composition from  $(\text{H}_2/\text{CO}_2)_{\text{in}} = 5$  to  $(\text{H}_2/\text{CO}_2)_{\text{in}} = 8$  carried out with the magnetometer and the 100 g Fe / 2 g K catalyst (from 2 to 3 in Figure 7.9). A step change under similar experimental conditions is carried out in the lab-scale setup (Figure 7.4 and Figure M.42). No change in the magnetisation is observed during 20 h, which indicates that the catalyst composition does not vary with the variation in the operating conditions. This result fits well with the observations in lab-scale, where no catalytic effect is noted, and kinetic parameters determined under steady state conditions are able to describe the transient behaviour.

A recent study from Mutz et al. (2015) follows a similar approach for the  $\text{CO}_2$  methanation. Structural changes on the Nickel catalyst are observed due to variations of inlet concentration (from  $\text{H}_2/\text{CO}_2$  to  $\text{CO}_2$ ) using operando X-ray absorption spectroscopy (XAS). Gnanamani et al. (2013) report a change in the catalyst composition when  $\text{H}_2/\text{CO}$  is switched to  $\text{H}_2/\text{CO}_2$  using an iron catalyst and Mössbauer investigations. The content of iron oxide increases in favour of iron carbide and an unknown iron oxide phase is formed.

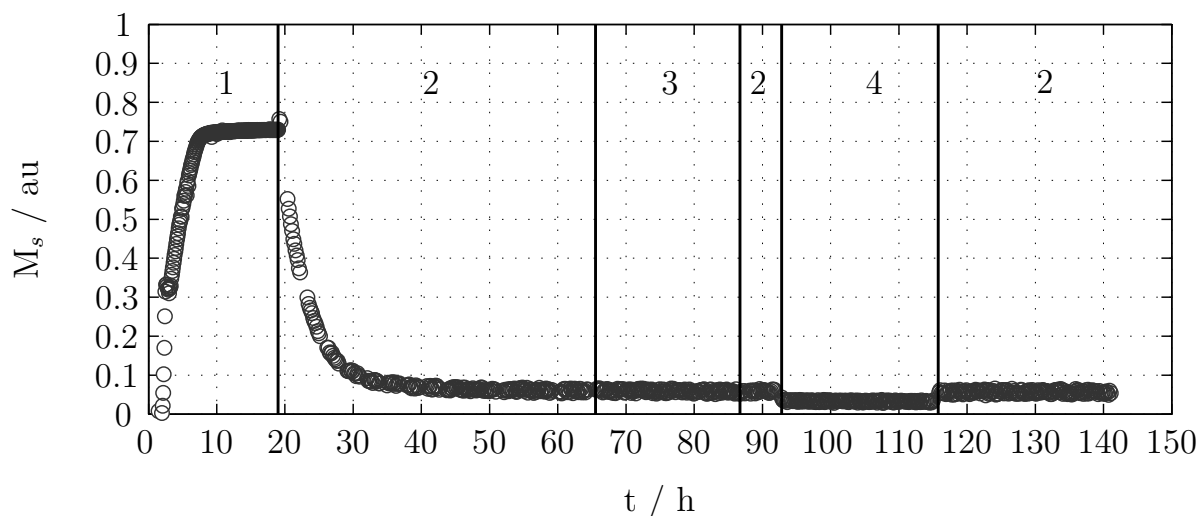


Figure 7.9: Saturation magnetisation  $M_s$  during the reduction (1) and catalyst formation (2) and variations in various operating conditions. Reduction conditions: Table 5.3, formation conditions: Table 5.4, conditions (3):  $T = 300$  °C,  $(\text{H}_2/\text{CO}_2)_{\text{in}} = 8$ ; conditions (4):  $T = 330$  °C,  $(\text{H}_2/\text{CO}_2)_{\text{in}} = 5$ . Catalyst: 100 g Fe / 2 g K.

$(\text{H}_2/\text{CO}_2)_{\text{in}} = 5$  to  $\text{H}_2$  and back to  $(\text{H}_2/\text{CO}_2)_{\text{in}} = 5$ : “Hot-Stand-By”

Figure 7.10 shows an increase in the magnetisation value under pure  $\text{H}_2$  atmosphere what is related with the hydrogenation of iron carbides and the formation of  $\alpha$ -Fe (ferromag-



netic under these operating conditions). This change in the catalyst phase composition is confirmed by the XRD method (Table 7.3). The decomposition of Häag carbide to  $\alpha$ -Fe (from 2 to 3) is slower than the formation of iron carbides from  $\alpha$ -Fe after the re-introduction of  $\text{CO}_2$  (from 3 to 2). These results fit well together with the observations reported in lab-scale, where a delay in the formation of hydrocarbons is observed after the reintroduction of  $\text{CO}_2$  (Figure 7.6 and Figure M.44).

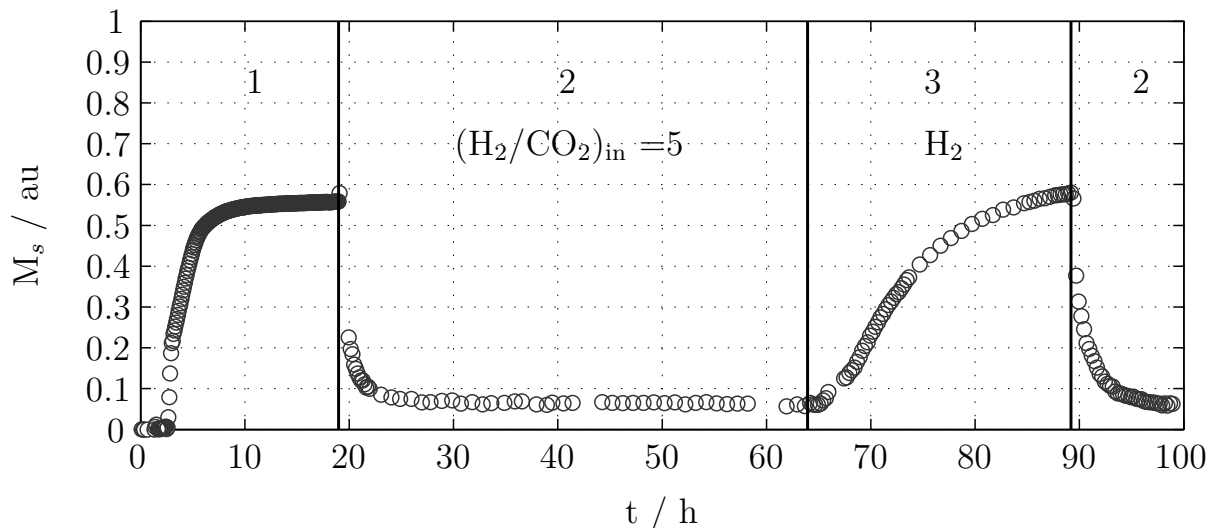


Figure 7.10: Saturation magnetisation  $M_s$  measured with the magnetometer during catalyst reduction (1), catalyst formation (2), and variations in operating conditions. Reduction conditions: Table 5.3; formation conditions: Table 5.4. Operating conditions at (3):  $T = 300\text{ }^\circ\text{C}$ ,  $p = 1.13\text{ MPa}$ ,  $(\text{H}_2/\text{CO}_2)_{\text{in}} = \infty$ . Catalyst: 100 g Fe / 10 g K

The main difference between the results obtained from XRD and magnetometer is the time required for the catalyst composition change. Results from XRD experiments (Table 7.3) show that it takes around 10 h to see a significant change in the catalyst composition (increase in  $\alpha$ -Fe and decrease in  $\text{Fe}_5\text{C}_2$ ), and this change becomes significant after 20 h. According to the magnetometer results (Figure 7.10) after 1.5 h under  $\text{H}_2$  atmosphere, an increase of the saturation magnetisation could be observed. After 25 h, the measured value of  $M_s$  is similar to the one measured right after the reduction. This indicates a total hydrogenation of  $\text{Fe}_5\text{C}_2$  and only  $\alpha$ -Fe present. However, after the reintroduction of  $(\text{H}_2/\text{CO}_2)_{\text{in}}$  the formation of the catalyst is faster than after the reduction, which might indicate that the structure/surface of the catalyst is different allowing the fast formation of active sites (iron carbides). No information from XRD is available to confirm this hypothesis.

The differences in the time measured by XRD and magnetometer might be related to the position where the measurement is taken. While the magnetometer considers the whole reactor, XRD measurements are taken on the external surface of the capillary, not being

able to reach the center. It is plausible, that the formation of  $\alpha$ -Fe starts earlier on the middle of the capillary cell and it takes time until  $\alpha$ -Fe is formed close to the capillary wall (see section 5). According to lab-scale experiments, catalyst changes take place within 2 h under  $H_2$  atmosphere (reflected by a change in selectivity after reintroduction of  $CO_2$ ), indicating that the time recorded with the magnetometer might be more realistic.

Table 7.3: Phase composition and particle sizes of the catalyst 100 g Fe / 10 g K during inlet concentration change from  $(H_2/CO_2)_{in} = 5$  to  $(H_2/CO_2)_{in} = \infty$  determined by XRD. At  $t = 64.2$  h  $CO_2$  is switched off. Conditions  $T = 300$  °C,  $p = 1.13$  MPa,  $(H_2/N_2)_{in} = 6.23$ ,  $\tau_{mod} = 414$  kg s/m<sup>3</sup>, values calculated in “TOPAS 4.1” via Rietveld refinement.

time	$\alpha$ -Fe	$Fe_5C_2$	$d_p$ $\alpha$ -Fe	$d_p$ $Fe_5C_2$	$R_{WP}$
h	w %	w %	nm	nm	-
63.6	0	100	-	43	11.903
69.1	2	98	40	43	11.924
79.1	9	91	34	46	12.612
90.1	23	77	37	41	12.517

### 7.3.1.2 Step change in temperature

Figure 7.9 shows a change in temperature from 300 °C (2) to 330°C (4) at  $(H_2/CO_2)_{in} = 5$ . A small drop in the magnetisation is observed. However, this change is probably caused by the temperature influencing the saturation of Häag carbide, and not by a change in the catalyst composition. The change in the magnetisation occurs directly after temperature is changed, without a transition period. The saturation magnetisation remains constant over the time. When the conditions are switched back to the initial ones (2), the magnetisation switches back immediately to the same value which was recorded previously. In lab-scale, catalyst deactivation is observed at 330 °C, which is inconsistent with the results from the magnetometer. A possible reason is that a higher modified residence time is used on lab-scale compared with the magnetometer ( $\tau_{mod} = 1000$  kg s/m<sup>3</sup> instead of  $\tau_{mod} = 400$  kg s/m<sup>3</sup>).

## 7.4 Periodic changes

The aim of the periodic change experiments is to find out if the catalyst activity and selectivity vary due to the variation of the reaction medium (at different duration periods:

$\tau_p = 200, 20, 2, 0.33$  min ). In addition, the effect that repeated variations of the gas phase composition have on the catalyst stability within the operation window is also evaluated.

Figure 7.11 shows the inlet and outlet molar flow of  $\text{CO}_2$ , with variations in the inlet concentration according to each duration period. Under the selected reaction conditions, the residence time of the gas in the total setup is approximately 6 minutes, and in the reactor approximately 1 minute. The resulting changes in outlet are determined by the combined effects of chemical reaction rate, backmixing, and setup residence time. Figure 7.11, top shows the dynamic response of the lab-scale setup at long time periods ( $\tau_p = 200$  min). Dead time is approx. 10 min and backmixing effects can be observed until minute 30. Due to the long duration period, the lab-scale setup reaches steady-state operation before a new change occurs, as shown schematically in Figure 3.7 top.

At  $\tau_p = 20$  min, the  $\text{CO}_2$  outlet molar flow never reaches the steady-state values (Table 7.4). The lab-scale setup is always operated under transient conditions (Figure 3.7, middle). At lower duration periods, variations in the inlet are much faster than the characteristic time of the setup, therefore a constant value is measured at the setup outlet (Figure 3.7, bottom).

Table 7.4: Steady-state  $\text{CO}_2$  and  $\text{C}_2\text{H}_6$  outlet molar flows at  $(\text{H}_2/\text{CO}_2)_{\text{in}} = 4$  and  $(\text{H}_2/\text{CO}_2)_{\text{in}} = 8$  and average values. Experimental conditions:  $T = 266$  °C,  $p = 1$  MPa,  $\tau_{\text{mod,target}} = 1000$  kg s/m<sup>3</sup>.

		$(\text{H}_2/\text{CO}_2)_{\text{in}} = 4$	$(\text{H}_2/\text{CO}_2)_{\text{in}} = 8$	Average
$F_{\text{n,CO}_2,\text{out}}$	$10^{-3}$ mmol/min	662.4	286.2	474.3
$F_{\text{n,C}_2\text{H}_6,\text{out}}$	$10^{-3}$ mmol/min	13.3	11.2	12.3

To evaluate the catalyst activity and selectivity, the time-average values of  $\text{CO}_2$  and  $\text{C}_2\text{H}_6$  outlet molar flows are calculated for each duration period (Table 7.5). The first 30 minutes of the signal are not considered for the time-average value due to the backmixing effects and dead time in the lab-scale setup. The time-average values of the  $\text{CO}_2$  outlet flow for the four duration periods investigated are nearly identical and no trend can be identified. The same pattern occurs in the case of the product  $\text{C}_2\text{H}_6$ , however a small increase in the molar flow of  $\text{C}_2\text{H}_6$  is observed at short period times. This trend in  $\text{C}_2\text{H}_6$  is also reported by Feimer et al. (1985) in similar experiments, however in the present case, due to the low number of data, no conclusions can be drawn.

Time-average values are almost equal to the average outlet molar flows corresponding to  $(\text{H}_2/\text{CO}_2)_{\text{in}} = 4$  and  $(\text{H}_2/\text{CO}_2)_{\text{in}} = 8$  (Table 7.4), and also to the  $\text{CO}_2$  outlet molar flow corresponding to  $(\text{H}_2/\text{CO}_2)_{\text{in}} = 5.43$  (average ratio between  $(\text{H}_2/\text{CO}_2)_{\text{in}} = 4$ , and

$(\text{H}_2/\text{CO}_2)_{\text{in}} = 8$ ). This indicates that catalyst activity is the same as under steady-state conditions, and that the characteristic time of the catalytic reaction is irrelevant for the dynamic response of the lab-scale setup under the selected conditions, dominated by backmixing effects in the lab-scale setup.

Table 7.5: Time-average  $\text{CO}_2$  and  $\text{C}_2\text{H}_6$  outlet molar flows during periodic changes in inlet concentration between  $(\text{H}_2/\text{CO}_2)_{\text{in}} = 4$  and  $(\text{H}_2/\text{CO}_2)_{\text{in}} = 8$  for different duration periods  $\tau_p$ . Experimental conditions:  $T = 266$  °C,  $p = 1$  MPa,  $\tau_{\text{mod,target}} = 1000$  kg s/m<sup>3</sup>.

		$\tau_p$ /min			
		200	20	2	1/3
$\overline{F_{\text{n,CO}_2,\text{out}}}$	$10^{-3}$ mmol/min	473.4	477.7	471.1	476.0
$\overline{F_{\text{n,C}_2\text{H}_6,\text{out}}}$	$10^{-3}$ mmol/min	12.3	12.5	12.7	13.0

It can be concluded from these experiments that under the selected operating conditions the activity and selectivity of the catalyst remain constant and also independent of the duration of the period. No deactivation of the catalyst is observed after the periodic changes in comparison with the catalyst activity measured before these changes started.

These results are in agreement with those obtained during step changes, indicating that variations in the catalyst state are negligible here, and therefore kinetic parameters determined under steady-state conditions can be used to describe the catalyst activity.

This method offers an approach evaluating catalyst activity and selectivity under transient conditions, without the necessity of supporting mathematical models. In cases where a change in catalyst state (including catalyst chemical composition, surface structure and catalytic properties) is observed, under step change conditions (e.g. change to pure  $\text{H}_2$ , Figure 7.6), experiments with periodic variations and consistent operating conditions offer the possibility to compare the characteristic time of the catalyst change with the duration of the period, and consequently obtain an order of magnitude of how fast catalyst changes take place.

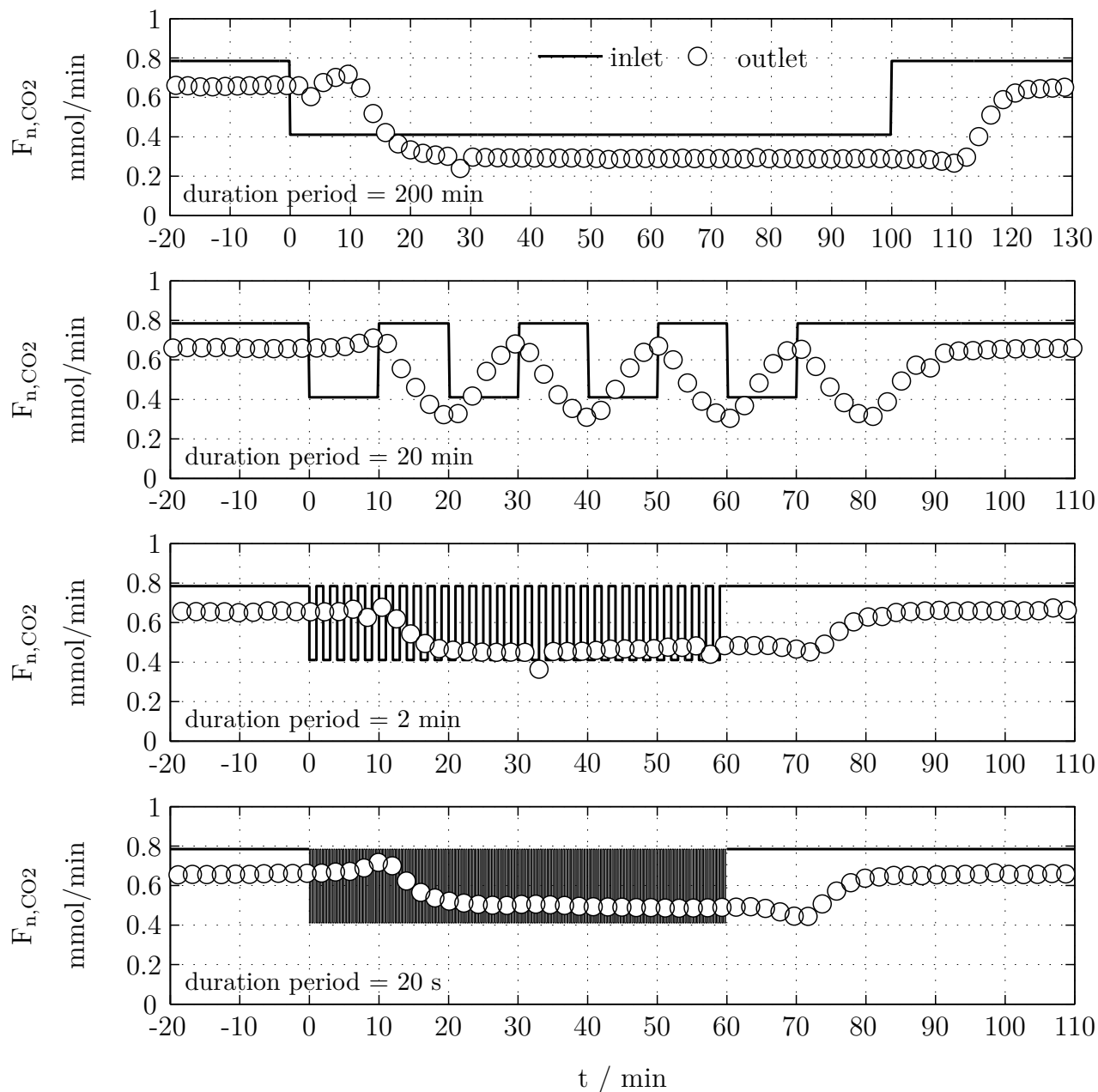


Figure 7.11: Inlet and outlet CO<sub>2</sub> flows during periodic changes in inlet concentration from  $(H_2/CO_2)_{in} = 4$  to  $(H_2/CO_2)_{in} = 8$  at four different duration periods. Symbols: data measured with micro-GC. Lines: inlet flows. Conditions:  $T = 266$  °C,  $p = 1$  MPa,  $\tau_{mod} = 1000$  kg s/m<sup>3</sup>. Figure M.51 zoom for  $\tau_p = 20$  s.

## 7.5 Conclusion: catalyst behaviour under variable operating conditions

Selected example results show the potential of the proposed approach to study catalyst behaviour under transient reaction conditions in a lab-scale setup, in the context of an industrial process. This combination of methods can be used with other reactions. A similar strategy is presently being applied for the Fischer-Tropsch synthesis at low temperature with cobalt (Eilers et al. 2015)).

Each of the three methods presented provide different kinds of information (e.g. reactor's attached equipment behaviour, catalyst phase composition, and characteristic time) and is based on a different procedure (experimental work with or without support by a mathematical model of the setup). The three methods are complementary and, due to the different approach followed, it is possible to confirm the plausibility of the results obtained when using similar reaction conditions.

The three methods indicate that under industrial relevant conditions (range where kinetic parameters are known) the selected iron catalyst is not a limiting factor for transient operation as long as the range of stable steady-state conditions is not exceeded. No changes of the catalyst state (i.e. chemical composition, surface structure and catalytic properties) or in adsorption/desorption processes have been observed. Catalyst activity and selectivity is the same as under steady-state conditions.

Under "extreme" conditions (e.g. a pure  $H_2$  atmosphere) step changes and in-situ methods indicate a change of the catalyst state (transformation of iron carbide to iron metal). Formation and reaction of iron carbides seem to be very dynamic under the selected operating conditions. These conditions are in general not relevant for industrial operation but confirm that solid catalysts are sensible materials, and that operating conditions influence the catalyst state. A characteristic time for the catalyst changes can be calculated based on measurements carried out with the magnetometer.

According to the present results, it is justified to use the set of kinetic parameters determined under steady-state conditions to describe transient operation within the range of validity of the kinetic parameters. These parameters are suitable to be used in the scale-up of the lab-scale fixed-bed reactor to a large-scale multi-tubular reactor to be operated under variable load conditions. In a similar way as shown in the lab-scale experiments, most significant limitations for transient operation in the large-scale process could be related to the reactor attached equipment (e.g. separators, piping).

# 8 Industrial fixed-bed reactor design for part-load and transient operation: conceptual studies

*Chapter 4 introduced the potential to operate chemical reactors in a flexible way in the context of the electricity-to-fuel process chain. The present chapter preliminarily evaluates the conceptual design of an industrial-scale fixed-bed reactor able to operate under flexible load conditions (i.e. within a load and rate of load change ranges, always satisfying that conversion and selectivity are according to specifications). The CO<sub>2</sub> hydrogenation to gaseous hydrocarbons studied in chapter 5 is selected as example fuel synthesis reaction. The set of kinetic parameters determined in chapter 6, together with the understanding gained during the transient experiments in lab-scale set-up (chapter 7), are implemented in the scale-up of the fixed-bed reactor. The results shown in this chapter and additional calculations presented in the Appendix N are based on steady-state and non-steady state mathematical models for fixed-bed reactors. The concept of characteristic times (time scales) is introduced at the end of the chapter to give an overview of the main processes involved in a chemical plant and highlight the importance of considering the whole chemical process when evaluating flexibility. The knowledge acquired with the CO<sub>2</sub> hydrogenation reaction is extrapolated to other fuel related syntheses that have the potential to be operated in a flexible way.*

## 8.1 Multitubular fixed-bed reactor with recycle for CO<sub>2</sub> hydrogenation to gaseous hydrocarbons

Table 8.1 summarises the main characteristics of the CO<sub>2</sub> hydrogenation to gaseous hydrocarbons, considered in this chapter as an example fuel synthesis reaction, to evaluate flexible operation of chemical reactors. The complex hydrocarbon product distribution typical of the FT synthesis is not taken into account in the calculations and all hydrocarbons formed are assumed to be propane C<sub>3</sub>H<sub>8</sub>. Most relevant parameters for reactor

design are the heat of reaction and the deactivation of the catalyst in the presence of products (requirement  $(p_{\text{H}_2\text{O}}/p_{\text{H}_2})_{\text{out}} \leq 0.1$ ). Three main differences appear in comparison with the low temperature Fischer-Tropsch (LTFT): (i) the liquid product is absent, (ii) the heat of reaction is lower due to the endothermic  $\text{CO}_2$ -shift reaction, and (iii) the production of  $\text{H}_2\text{O}$  is higher, being by-product of the  $\text{CO}_2$ -shift and FT reaction.

Table 8.1: Main characteristics of the  $\text{CO}_2$  hydrogenation reaction with the selected catalyst. Kinetic constants in Table 6.2

$\text{CO}_2$ -shift ( $R_1$ )	$\text{CO}_2 + \text{H}_2 \rightleftharpoons \text{CO} + \text{H}_2\text{O}$
Fischer-Tropsch ( $R_2$ )	$\text{CO} + \frac{7}{3} \text{H}_2 \longrightarrow \frac{1}{3} \text{C}_3\text{H}_8 + \text{H}_2\text{O}$
Heat of reaction	$\Delta_R H_{300^\circ\text{C}, R1}^0 = 39.7 \text{ kJ/mol}$ $\Delta_R H_{300^\circ\text{C}, R2}^0 = -174.2 \text{ kJ/mol}$
Catalyst	100 g Fe/ 2g K
Catalyst restrictions	limited range of conditions $(p_{\text{H}_2\text{O}}/p_{\text{H}_2})_{\text{out}} \leq 0.1$ $T_{\text{max}} = 300 \text{ }^\circ\text{C}$
Reaction kinetics	$r_1 = k_1 \cdot \frac{p_{\text{CO}_2} \cdot p_{\text{H}_2} - \frac{p_{\text{CO}} \cdot p_{\text{H}_2\text{O}}}{K_p}}{p_{\text{CO}} + a_{1,\text{H}_2\text{O}} \cdot p_{\text{H}_2\text{O}} + b_{1,\text{CO}_2} \cdot p_{\text{CO}_2}}$ $r_2 = k_2 \cdot \frac{p_{\text{CO}} \cdot p_{\text{H}_2}}{p_{\text{CO}} + a_{2,\text{H}_2\text{O}} \cdot p_{\text{H}_2\text{O}} + b_{2,\text{CO}_2} \cdot p_{\text{CO}_2}}$
$E_A$	$E_{A,1} = 138.9 \text{ kJ/mol}; E_{A,2} = 94.6 \text{ kJ/mol}$
$k_0$	$k_{0,1} = 1.6 \cdot 10^6 \text{ mol/s kg Pa}; k_{0,2} = 2.6 \cdot 10^3 \text{ mol/s kg Pa}$
$a$	$a_1 = 128; a_2 = 152$
$b$	$b_1 = 0.8; b_2 = 0.5$

A catalytic fixed-bed reactor is proposed to carry out the  $\text{CO}_2$  hydrogenation to gaseous hydrocarbons in large-scale under flexible load conditions. Catalytic fixed-bed reactors are the most important type of reactors in the basic chemical industry, petrochemical industry, and petroleum refining (Froment 1974). Their main advantages include their simplicity, low cost and minimal maintenance, high pressure operation, and easier scaling-up. Long catalyst life (e.g.  $\geq 3$  months) is required because catalyst replacement is an expensive and tedious affair. One of the most critical points of fixed-bed reactors is temperature control for high exothermic reactions.

The adiabatic temperature increase is a decisive parameter to select between adiabatic or



non-adiabatic operation. In the case of the  $\text{CO}_2$  hydrogenation for a stoichiometric feed  $(\text{H}_2/\text{CO}_2)_{\text{in}} = 10/3$  at  $p = 2$  MPa and  $T = 280$  °C, the  $\Delta T_{\text{ad}}$  is around 1000 K. Reactions with a  $\Delta T_{\text{ad}} \geq 1000$  K are considered to be strongly exothermic. At temperatures lower than 250 °C the  $\text{CO}_2$ -shift rate is very slow and at temperatures above 300 °C, catalyst deactivation takes place. Therefore, the preferred temperature range here is 250 to 300 °C, the maximum  $\Delta T$  allowed is 50 K. With a such a small temperature difference, 20 stages will be needed to carry this reaction adiabatically assuming interstage cooling. This seems to be uneconomical (typical adiabatic reactors have between 3 and 5 stages).

A non-adiabatic reactor with cooling medium is selected to guarantee a good temperature control and heat management (Figure 8.1). The selected cooling medium is a heat transfer oil (Sasol 2009). Boiling water cannot be used due to the higher pressures required to reach temperatures of around 280 - 300 °C. The temperature of the heat transfer medium needs to be close to the desired catalyst temperature. Large heat transfer areas per catalyst volume and sufficiently large mass flow velocity of the reaction gases are important to ensure good heat transport from the packing to the heat exchange surface.

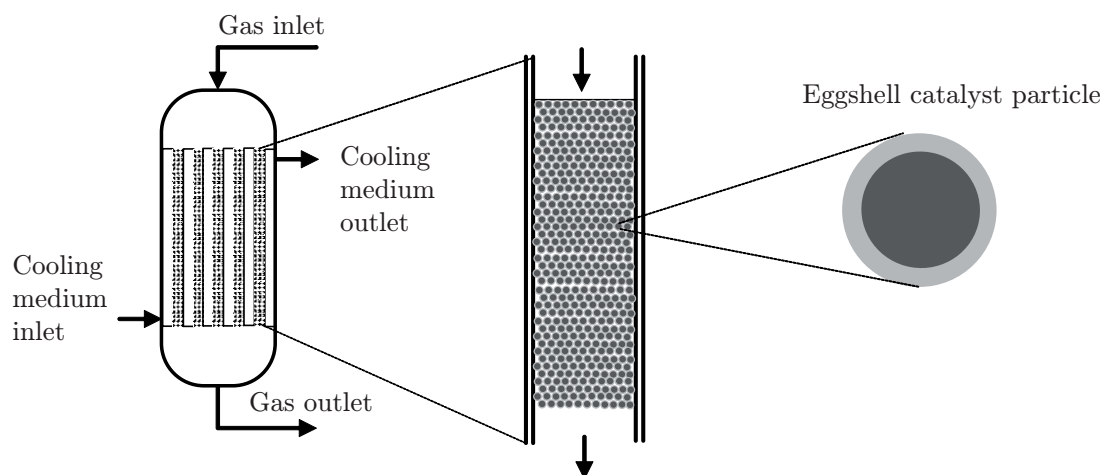


Figure 8.1: Simplified representation of a multitubular reactor for an exothermic synthesis reaction, a reactor tube, and an eggshell catalyst particle

Commercial LTFT multitubular reactor dimensions are considered as orientation for the design of a large-scale reactor for the  $\text{CO}_2$  hydrogenation, despite the difference in the chemical reaction characteristics (Table 8.2). LTFT reactors are operated under steady-state conditions using synthesis gas (mixture of  $\text{H}_2$  and  $\text{CO}$ ). However, the reactor design is dominated by similar features as in the case of the  $\text{CO}_2$  hydrogenation: heat removal, product selectivity, and catalyst deactivation in particular (Bartholomew et al. 2006). Commercial HTFT reactors, operated at temperatures around 340 °C, are fluidised beds. Fixed-bed reactors are not recommended at higher temperatures due to the high tendency of carbon deposition on the catalyst ( $\text{CO}$  partial pressure is high). In the case of the  $\text{CO}_2$

hydrogenation and for the selected catalyst, 100 g Fe / 2 g K, deactivation is not due to carbon deposition but due to a high  $(p_{\text{H}_2\text{O}}/p_{\text{H}_2})_{\text{out}}$  ratio. Therefore the FB reactor remains as an alternative for the CO<sub>2</sub> hydrogenation with 100 g Fe / 2 g K.

Table 8.2: Commercially applied Fischer-Tropsch processes operated in fixed-bed multi-tubular reactors. Fe-based reactor (ARGE) operated by Sasol and Co-based reactor operated by Shell, (Bartholomew et al. 2006)

	Reactor characteristics				Operating conditions			
	$L_t$	NT	$d_t$	$d_p$	$p$	$T$	$(\text{H}_2/\text{CO})_{\text{in}}$	$R_F$
	m	-	cm	mm	bar	°C	-	-
Fe-based	12	2050	5	2.5	25	220	1.25	1.9
					27	235 (max. 254)	2 (1.85)	
Co-based	20	8000	3	2.0	40	237	2.15	-

### Reactor with product separation and recycle of H<sub>2</sub>, CO<sub>2</sub> and CO

Activity loss is observed with the 100 g Fe / 2 g K catalyst at  $(p_{\text{H}_2\text{O}}/p_{\text{H}_2})_{\text{out}} \geq 0.1$  (see chapter 5). Low catalyst stability at high H<sub>2</sub>O pressures is a common issue in FT synthesis, therefore for the LTFT synthesis, single pass CO conversions are limited to about 50 - 70 %. To reach higher overall conversions, two or three reactors in series can be used with interstage H<sub>2</sub>O separation. Another option is an internal recycle of the gases leaving the FT synthesis reactor after separation (e.g. ARGE reactor operates with a recycle/fresh volume ratio of 1.9 (Bartholomew et al. 2006; Steynberg et al. 2004)). These two alternative configurations allow the control of the partial pressures in the catalytic reactor and are also appealing options for carrying out the CO<sub>2</sub> hydrogenation under steady-state conditions. The use of membranes to remove H<sub>2</sub>O in-situ under FT conditions have already been considered in detail by Rohde et al. (2008) and Rohde (2011). The authors conclude that currently available membranes exhibit low stability, permselectivities, and permeances regarding H<sub>2</sub>O separation under FT conditions. Hence, they are not an option at the moment.

The configuration with recycle appears to be most attractive to carry out the CO<sub>2</sub> hydrogenation to gaseous hydrocarbons under flexible load (Figure 8.2). It considers a reactor with product separation and recycle of H<sub>2</sub> and CO<sub>2</sub> together with the intermediate product CO. This configuration has an extra design variable available, the conversion per pass or recycle ratio, and this is advantageous for variable load operation.

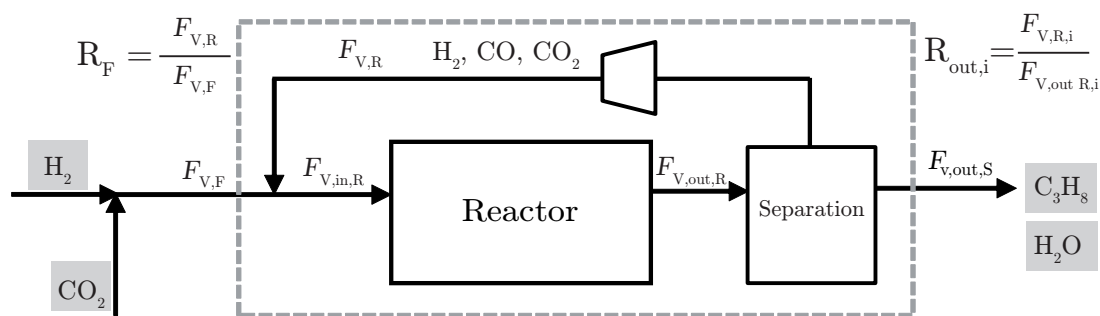


Figure 8.2: Recycle reactor used for the CO<sub>2</sub> hydrogenation. Separation units assumed as an ideal system. Detailed information about the separation units can be found in figure N.58

Moreover, the use of a recycle allows for the operation of the reactor under more favourable conditions compared with a one-pass reactor: (i) high average reaction rates along the catalyst bed can be achieved due to the presence of CO (intermediate product) at reactor inlet and a lower partial pressure of H<sub>2</sub>O, (ii) heat removal is more effective due to the higher gas velocities, (iii) overall high conversions are possible, and (iv) the  $(H_2/CO_2)_{in}$  ratio can be adjusted in the reactor which may be above the stoichiometric ratio. The  $(H_2/CO_2)_{in}$  ratio is the only operational variable which has the potential to enable high CO<sub>2</sub> conversion and hydrocarbon yield at low  $(p_{H_2O}/p_{H_2})_{out}$  ratios (Figure 5.6). The disadvantages of recycle reactors are, however, related to high operational costs (i.e. high energy demand), large separation units, need of a recycle gas compressor (Equation N.59), repeated heating and cooling and loss of material due to the purge.

A crucial point of this configuration might be the behaviour of the separation units under variable load conditions. The separation of H<sub>2</sub>, CO<sub>2</sub>, and CO from H<sub>2</sub>O and hydrocarbons is not an easy task (Figure N.58): the reactor outlet flow needs to be cooled to condense reaction water and higher hydrocarbon products (in case they are produced). Afterwards, CO<sub>2</sub> is separated in a CO<sub>2</sub>-scrubber unit to avoid freezing up the subsequent cryogenic unit with solid CO<sub>2</sub>. The gas is decompressed and the water vapour content of the gas is decreased to -70 °C dew point (dehydration). Cryogenic cooling and separation are needed to separate H<sub>2</sub> from light hydrocarbons (Steynberg et al. 2004).

Having chosen the conversion per pass, the recycle ratio is an immediate consequence to reach the required overall conversion (Equation 8.1). When designing reactors for one load operation an economical optimum exists for the conversion per pass that balances reactor size against the combination of product separation load and recycle ratio. However, if the reactor is operated under variable load conditions and the overall conversion needs to be maintained constant, the recycle ratio will be a consequence of the operation load, due to the constant size of the reactor. Flexibility is obtained for the reactor via the recycle

ratio. This approach is discussed in detail in chapter 8.3.

$$X_{\text{overall}} = (1 + R_F) \cdot X_{\text{pp}} \quad (8.1)$$

A potential alternative or complementary strategy to obtain flexibility for variations in load could be to modify the reactor temperature (as manipulated variable), with higher temperatures at high volumetric flows and lower temperatures at low volumetric flows. The aim is to modify the reaction rate according to the residence time of the gas in the reactor (load), trying to maintain the conversion per pass almost constant, and in this way decrease variations on the recycle ratio between full and part load operation. The rate of temperature change of the cooling medium needs to be adjusted to the rate of load change. Temperature adjustment to maintain conversion constant is a strategy used in industrial practice, when a catalyst deactivates (e.g. in catalytic reforming of naphtha, where the catalyst slowly deactivates by coke deposition, (Froment et al. 1990)).

The use of reactors in series with interstage  $\text{H}_2\text{O}$  separation is attractive for one load operation (steady-state) but the evaluation of its potential for variable load operation is out of the scope of the present work. A high number of reactors is required to reach a high flexibility. However, the possibility to separate only  $\text{H}_2\text{O}$  and feed the gaseous products together with the unconverted  $\text{H}_2$ ,  $\text{CO}$ , and  $\text{CO}_2$  into the next reactor could decrease separation costs. An attractive balance between number of reactors and separation units might be possible. When the reactors in series are operated under minimum load, only gaseous hydrocarbon products are present on the last reactors. These gases need to behave as inert in contact with the catalyst. Experimental work is required to prove this specification.

## 8.2 Single tube reactor model and catalyst particle

### 8.2.1 Tube model equations

The phenomena taking place in a reactor tube filled with catalyst particles can be described by the combination of material balance, energy balance, and kinetic rate expressions. The material and energy balances can be written as follows (Equation 8.2 and Equation 8.3) (Froment 1974).

$$\varepsilon \cdot \frac{\partial c_i}{\partial t} = - (u_{\text{sf}} \cdot \frac{\partial c_i}{\partial z} + c_i \cdot \frac{\partial u_{\text{sf}}}{\partial z}) + \sum_{j=1}^N (v_{ij} \cdot r_j) \quad (8.2)$$

$$\begin{aligned}
(\varepsilon \cdot \rho_g \cdot c_{p,g} + (1 - \varepsilon) \cdot \rho_s \cdot c_{p,s}) \cdot \frac{\partial T}{\partial t} = & -\rho_g \cdot c_{p,g} \cdot (u_{sf} \cdot \frac{\partial T}{\partial z} + T \cdot \frac{\partial u_{sf}}{\partial z}) + \sum_{j=1}^N (-\Delta_R H_j^0 \cdot r_j) - \\
& - \frac{4U_{\text{eff}}}{d_t} (T - T_{\text{cooling}})
\end{aligned}
\tag{8.3}$$

These mathematical expressions do not distinguish between conditions in the fluid and the catalyst ( $T_g = T_s = T$  and  $c_g = c_s = c$ ). Calculations justifying the use of a pseudohomogeneous model are done based on correlations found in literature (Table J.13). According to Froment (1974) the differences between fluid and solid surface conditions in industrial practice are small due to the high velocities. In addition, in this early stage of design, lower levels of information are available (e.g. less is known about the characteristics of a catalyst particle with representative dimensions, i.e. pore distribution, pore diameter, porosity, tortuosity, etc), therefore it is justified to use a mathematical model with a low degree of sophistication.

Temperature and concentration gradients occur in axial direction. The only transport mechanism operating in this direction is the overall flow (convection) and this is considered to be of the ideal plug flow type. Axial dispersion can be neglected if Bodenstein number is higher than 100 (Equation I.30). This criteria is generally satisfied for technical fixed-bed reactors (Baerns et al. 1992). Axial heat conductivity is negligible in comparison with heat transfer by convection. However due to the use of a cooling medium, heat is transported to the wall (heat exchange surface) perpendicular to the flow by radial conductivity.

Even though the model is considered to be pseudohomogeneous, the solid contributes significantly to heat transfer in radial direction, and the heat transfer coefficient considers the catalyst bed, the wall, and the cooling medium (Equation 8.6). Radial profiles in flow velocity exist in fixed-bed reactors due to the different packing density near the wall. However, if  $d_t/d_p \geq 10$  radial variations in flow velocity can be neglected (no wall effects)(Froment 1974).

Variations in concentration and temperature occur with position and time (accumulation term). The accumulation term considers gas as a mass storage, and catalyst and gas as heat storage materials. These terms are responsible for the rates of heat up and cool down of the catalyst bed. The mass of reactor wall is not considered as heat storage material because its temperature is very similar to the one of the cooling medium ( $\alpha_{\text{wall}} \ll \lambda_{\text{wall}}/s$  and  $\alpha_{\text{wall}} \ll \alpha_{\text{out}}$ ), see section 8.2.2 and Figure N.52).

Pressure drop along the fixed-bed can be calculated with the equation proposed by Ergun (Equation 8.4 for spheres, (Eigenberger 2000)). The pressure drop depends strongly on the bed porosity  $\varepsilon$ , that can be influenced by the form of the catalyst particle (see section 8.2.3). High values of  $\varepsilon$ , large particles, and low gas velocities favour a low pressure drop

(Figure N.55). Mass and heat transfer are strongly correlated with the pressure loss. Pressure is only considered to change in axial direction, and variations in radial direction are negligible due to the assumption of plug-flow.

$$\frac{\partial p}{\partial z} = -\frac{u_{\text{sf}}}{d_p} \cdot \frac{1 - \varepsilon}{\varepsilon^3} \cdot (1.75 \cdot \rho_g \cdot u_{\text{sf}} + 150 \cdot \frac{\eta_g}{d_p} \cdot (1 - \varepsilon)) \quad (8.4)$$

The momentum balance equation is not considered because variation of pressure with time is much faster than changes in composition or temperature. After a change in inlet flow, it is assumed that the pressure profile along the catalyst bed changes instantaneously. The inlet and outlet flows are assumed to change at the same time.

The gas velocity changes along the catalyst bed due to the volume reduction produced by the chemical reaction (according to the stoichiometry of the reaction 54 % volume reduction occurs by complete conversion). For calculation, a global material balance of the gas phase considering all components is carried out (Equation 8.5).

$$\frac{\partial u_{\text{sf}}}{\partial z} = \frac{\sum_{j=1}^N (v_{ij} \cdot r_j)}{\frac{p}{R \cdot T}} \quad (8.5)$$

### Solution of the mathematical model

The mathematical model consists of a mixture of ordinary and partial differential equations. In total, eight equations need to be solved simultaneously: five material balances (Equation 8.2), formulated for each component (these equations are related by the stoichiometric coefficients of the reaction), one energy balance, (Equation 8.3), one pressure drop equation (Equation 8.4), and one global material balance of the gas phase (Equation 8.5). Temperature, concentrations, pressure, and gas velocity are the dependent variables. They are functions of the two independent variables:  $z$  the axial coordinate and  $t$ , time. The solution will be in the form  $c_i = f(z, t)$ ,  $T = f(z, t)$ ,  $p = f(z)$  and  $u_{\text{sf}} = f(z)$ .

The method of lines (MOL), explained in detail by Schiesser et al. (2009), is used to replace the derivatives with algebraic approximations, for example finite differences, so that only one variable (typically time) is left. The partial differential equations are transformed into a system of ordinary differential equations (ODEs) which are solved by finite differences. More information about the MOL can be found in the section L.1 of the appendix.

The set of differential equations is solved at each grid-point. The reactor length is divided in axial direction. The size of the grid (discretisation) is a compromise between the degree of accuracy and the computational work. This compromise is especially important for transient calculations, where the reactor profiles are calculated for each time step. Values for  $\Delta z = 0.001$  m and for  $\Delta t = 1$  s are typically used.

For steady-state calculations, the accumulation term is set to zero and the ordinary differential equations are integrated along the catalyst bed. Boundary conditions are defined at the inlet of the reactor (at  $z = 0$ ): concentrations  $c_{i,z=0}$ , temperature  $T_{z=0}$ , pressure  $p_{z=0}$ , and gas velocity  $u_{sf,z=0}$ .

For transient calculation, the set of differential equations is integrated along the catalyst bed for each time step. The same boundary values as for steady-state calculation are required, together with extra initial values. Concentration, temperature, pressure, and gas velocity profiles along the catalyst bed need to be previously calculated. It is important to calculate the initial values with the same axial discretisation which will be used for the transient calculation. Differences between the given initial values and those that MATLAB® calculates at the beginning of the simulation for  $t = 0$  need to be avoided. Density, heat capacity, viscosity, heat transfer coefficient, and reaction rate are calculated for each grid-point as a function of temperature, concentrations, pressure, and gas velocity.

## 8.2.2 Radial heat transport

The main difficulty of fixed-bed reactors is the removal of reaction heat. Heat needs to be transported perpendicular to the flow to the heat exchange surface. The radial gradient depends strongly on tube diameter, fluid properties, and fluid velocity. A major concern when choosing between a one or a two-dimensional model is the accuracy in representing the temperature profiles (Figure N.52). In the present study, the maximum axial hot spot is about 20 °C, which means a temperature increase of 7 % for 280 °C. For the CO<sub>2</sub> hydrogenation, a one dimensional model with modified heat transport coefficient is selected (Equation 8.6), as computation demand is lower compared with the 2D model due to a reduction in the number of grid-points (only axial discretisation needed).

The use of a modified heat transport coefficient avoids calculations in two dimensions (Equation 8.6). The heat transfer coefficient in the bed side ( $\alpha_{in}$ ) is expressed as a function of the effective thermal conductivity of the bed  $\lambda_{eff,r}$  and the wall heat transfer coefficient  $\alpha_{wall}$ . The latter of which describes the complex interplay between convective flow at the tube wall and conduction transport by contact between the particles and the wall. Both parameters are decisive in temperature control, the radial thermal conductivity being the most important one (Figure N.53). Values for the overall heat transport coefficient as a function of gas velocity and particle diameter can be seen in Figure N.55 and Table N.20 for a tube diameter of 3 cm, and in Figure N.54 for a 6 cm tube diameter. The thin reactor wall is assumed to be made of steel. The external heat transfer coefficient to the cooling medium  $\alpha_{out}$  is assumed to be very high. No energy balance is calculated for the heating medium, assumed to be isothermal due to its high heat capacity and mass of

cooling medium.

$$\frac{1}{U_{\text{eff}}} = \frac{1}{\alpha_{\text{wall}}} + \frac{r_t}{4 \cdot \lambda_{\text{eff,r}}} + \frac{s}{\lambda_{\text{wall}}} + \frac{1}{\alpha_{\text{out}}} \quad (8.6)$$

Radial transfer conductivity and wall heat transfer coefficients are strongly dependent on the catalyst form used, its size, the thermal characteristics of the catalyst ( $\lambda_p$ ) and of the gas ( $\lambda_g$ ), and the gas velocity. The thermal conductivity of the gas is considerably lower than the thermal conductivity of the catalyst, therefore beds with a low porosity favour an effective radial heat transfer (the porosity of the bed is defined by the selection of the catalyst particle, see section 8.2.3). Large particles are attractive for a good conductivity but have a lower wall heat transfer coefficient. The selection of a high conductivity catalyst support material will increase the conductivity of the bed and favour radial heat transfer. High gas velocity also favours as well an efficient heat transfer. Heat transport under transient conditions is strongly influenced by the catalyst density and heat capacity. High catalyst density and heat capacity make changes in reactor temperature slow (heat-up or cool-down), (see section 8.3.4), characteristic times)

### 8.2.3 Catalyst particle: eggshell

The selected catalytic function for the CO<sub>2</sub> hydrogenation to gaseous hydrocarbons is iron promoted with potassium (100 g Fe / 2 g K), however the catalyst particles used in lab-scale cannot be used for a technical reactor. The selection of the catalyst particle shape and size for the industrial fixed-bed reactor requires a compromise between a low pressure drop and an acceptable heat and mass transport.

The shape of the catalyst particle strongly influences the bed porosity. Hollow cylinders of thin wall thickness ( $\varepsilon \approx 0.6 - 0.8$ ) are preferred to spheres ( $\varepsilon \approx 0.37 - 0.4$ ) or solid cylinders ( $\varepsilon \approx 0.35$ ). High bed porosities favour a lower pressure drop, but particle manufacturing becomes costly and catalyst particle stability low. In the present study, spheres are selected due to its easier mathematical description compared with other catalyst shapes, even though their use in industrial reactors is very occasional.

The size of the catalyst particle is also a compromise between a good internal mass transfer (low pore diffusion resistance) favoured by small particles, and a low pressure drop favoured by large particles. Heat transfer conductivity is better when using large particles, although wider tube diameters are required to avoid wall effects, which in turn has a negative effect on radial heat removal (Figure N.55). The use of eggshell catalyst pellets introduces design flexibility by decoupling the characteristic diffusion distance in catalyst pellets from pressure drop (responsible of internal mass transfer limitations).



In the present work, eggshell spheres of alumina (DURANIT<sup>®</sup>, VFF (2015)) are assumed to be coated with the active material, iron. The thickness of active material  $\chi_{\text{shell}}$  appears as a new design variable (degree of freedom) for the catalyst particle (instead of using an effectiveness factor). The heat conductivity of the particle and the active mass density  $\rho_{\text{active,R}}$  change as a function of the thickness of active material (Figure N.56). The advantages of eggshell catalysts are a complete use of the catalyst active mass (no internal mass transfer), the lower pressure drop due to the use of large particles, and the lower heat production per reactor volume compared with a full contact (100 % active material) due to the presence of inert material. The disadvantages are the requirement of larger reactors and increased manufacturing cost for the catalyst pellets.

In the LTFT synthesis, catalyst particle diameters are around 1 - 3 mm due to pressure drop constraints. With this particle size, diffusion is limited due to the presence of liquid inside the pores, and consequently the effectiveness factor is lower than one. The ARGE reactor uses cylindrical particles with a  $L_p = 5$  mm and  $d_p = 2.5$  mm (Jess et al. 2009). Present catalyst research focuses on the use of structured catalysts (e.g. core-shell) and reactors (e.g. monolithic honeycombs) to increase the number of degrees of freedom and, in the end, the reactor productivity (Güttel 2015).

## 8.3 Recycle system for part-load operation

A fixed-bed reactor with recycle is the configuration selected to carry out the CO<sub>2</sub> hydrogenation under part-load conditions (Figure 8.2). This chapter shows the procedure developed to design a recycle system accompanied by a reference example calculation. The recycle system needs to guarantee a minimum specified overall conversion within the whole range of load for which it is designed.

### 8.3.1 Design procedure for the given design restrictions of the catalytic CO<sub>2</sub> hydrogenation

Figure 8.3 shows the procedure developed to design recycle systems for reactions limited by the partial pressure of products, as is the case for the CO<sub>2</sub> hydrogenation investigated here. This procedure has two degrees of freedom for design, the diameter of the tube  $d_t$  and the desired flexibility of the reactor  $L_{\text{min}}$ . An average fresh feed flow needs to be defined, and consequently a maximum and minimum flow can be calculated according to Equation 8.7 and 8.8. Prior selection of operating conditions ( $p$ ,  $(\text{H}_2/\text{CO}_2)_{\text{in}}$ ,  $T_{\text{in}}$  and  $T_{\text{cooling}}$ ) is required. Design variables for the catalyst particle ( $d_p$ ,  $\chi_{\text{shell}}$ ) are set at the beginning of the calculation.

$$F_{v,\text{CO}_2,\text{min}} = L_{\text{min}} \cdot F_{v,\text{CO}_2,\text{max}} \quad (8.7)$$

$$F_{v,\text{CO}_2,\text{average}} = \frac{F_{v,\text{CO}_2,\text{min}} + F_{v,\text{CO}_2,\text{max}}}{2} \quad (8.8)$$

In a recycle system,  $X_{i,\text{overall}}$ ,  $X_{i,\text{pp}}$ ,  $R_{\text{F}}$  and  $R_{\text{out}}$  are connected by two balance equations (Equation N.58 and N.57). Consequently, when two of them are selected the other two can be calculated by the corresponding equations. In the case of a reaction limited by the partial pressure of products, the maximum conversion per pass is fixed due to the partial pressure constraint  $(p_{\text{H}_2\text{O}}/p_{\text{H}_2})_{\text{out}}$ , and this limitation is reached with the minimum volumetric flow. For the maximum volumetric flow, the overall conversion is specified by design.  $R_{\text{out}}$  is maintained constant for the minimum and maximum operation load. An iterative process using maximum and minimum flow is required to find out the value of  $R_{\text{out}}$  (Figure 8.3).

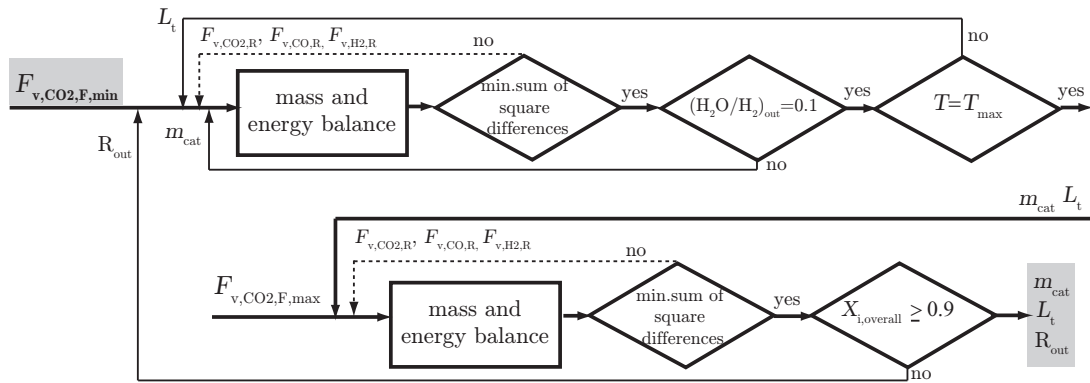


Figure 8.3: Procedure followed to calculate  $m_{\text{cat}}$ ,  $L_t$  and  $R_{\text{out}}$  for fixed values of  $d_t$  and  $L_{\text{min}}$ , assuming catalyst deactivation at  $(p_{\text{H}_2\text{O}}/p_{\text{H}_2})_{\text{out}} \geq 0.1$  and a desired overall conversion of 0.9. Constant values for the design variables shown in Table 8.3 and an average flow  $F_{v,\text{CO}_2,\text{average}}$  need to be selected.

Following Figure 8.3, calculation starts using the minimum flow. Three nested fittings are programmed to determine  $m_{\text{cat}}$  and  $L_t$  according to the reaction restrictions in partial pressure and temperature respectively.

1. Supposed a value of  $R_{\text{out}}$  for  $\text{CO}_2$ ,  $\text{CO}$  and  $\text{H}_2$ . A starting value for  $R_{\text{out}}$  can be calculated based on the expected conversion per pass for the maximum flow and with the specified overall conversion.
2. Supposed values for the recycle flow,  $\text{CO}_2$ ,  $\text{CO}$  and  $\text{H}_2$ .
3. Supposed a catalyst mass value.
4. Supposed a tube length value.

5. Integrate the material balance, energy balance, pressure drop, and change of gas velocity along the catalyst bed (Equations 8.2, 8.3, 8.4 and 8.5). Calculations are done under steady-state conditions; concentration, temperature, pressure, and velocity profiles along the catalyst bed are obtained.
6. Reactor outlet flows are compared with those supposed in step 2. An iterative procedure is used (`lsqnonlin` in MATLAB®) to minimise the square difference between the supposed and the calculated flows until convergence (internal loop).
7. The ratio of outlet partial pressures  $(p_{\text{H}_2\text{O}}/p_{\text{H}_2})_{\text{out}}$  is compared with the known restriction. An iterative procedure is used (`lsqnonlin`) to find out the  $m_{\text{cat}}$  that corresponds to a  $(p_{\text{H}_2\text{O}}/p_{\text{H}_2})_{\text{out}} = 0.1$  (intermediate loop).
8. Maximum temperature in the catalyst bed is compared with the maximum temperature allowed. An iterative procedure is used (`lsqnonline`) to find out the  $L_t$  that corresponds to the maximum temperature allowed.
9. Calculations are next carried out with the maximum flow, and the  $m_{\text{cat}}$  and  $L_t$  previously calculated, to check that overall conversion is according to the specifications.
10. Supposed values for the CO<sub>2</sub>, CO, and H<sub>2</sub> recycle flow (same as in step 2)
11. Integrate the material balance, energy balance, pressure drop, and change of gas velocity along the catalyst bed (same as in step 5).
12. Reactor outlet flows are compared with those supposed in step 11. The same iterative procedure presented in step 6 is used.
13. Overall conversion is calculated and compared with that desired. If the values are not equal, return to step 1, adjust the value of  $R_{\text{out}}$  and repeat the procedure.
14. Calculate reactor volume (Equation 8.9), number of tubes (Equation 8.10) and electric power required by the compressor (Equation N.59).

The reactor volume is calculated based on the density of active mass referred to reactor volume, according to Equation 8.9.

$$V_r = \frac{m_{\text{cat}}}{\rho_{\text{active,R}}} \quad (8.9)$$

The number of tubes can be calculated using  $L_t$  in Equation 8.10

$$NT = \frac{V_r}{L_t \cdot \pi \left(\frac{d_t}{2}\right)^2} \quad (8.10)$$

The number of tubes is an indicator of the size of the vessel. Usually, the distance between two catalyst tubes is equal to a diameter tube that corresponds to the cooling medium. Due to the square relationship, the volume of the vessel becomes factor 4 larger than the calculated volume for the reactor (Luyben 2007), see Equation 8.11.

$$V_{\text{vessel}} = \frac{\pi \cdot (2 \cdot d_t)^2 \cdot L_t \cdot NT}{4} \quad (8.11)$$

A detailed economic evaluation (investment and operation cost) is required to select the optimum  $d_t$  for a certain flexibility (represented as  $L_{\text{min}}$ ). Within the present work, the size of the reactor vessel is selected as indicator for the investment cost, while the electric power required by the recycle compressor is the indicator for operation cost. Calculation of investment and operating cost figures is outside the scope of this thesis. The design procedure developed for the recycle system is specifically suited for CO<sub>2</sub> hydrogenation as an example reaction with constraints regarding temperature and partial pressures. Section N.4 in the appendix outlines a procedure developed for a chemical reaction only restricted with respect to temperature. In the case of any other chemical reaction and type of reactor, the design procedure has to be adapted to their specific characteristics.

### 8.3.2 Example results

The procedure shown in Figure 8.3 is applied to design an example catalyst tube of a multitubular fixed-bed reactor with recycle to be operated in the load range 70 - 100 % (reference case), for a fixed tube diameter of 3 cm and selected values for the required design variables. The desired minimal overall conversion of CO<sub>2</sub> in the reactor is 90 %, providing that temperature is lower than 300 °C and the maximum value of the  $(p_{\text{H}_2\text{O}}/p_{\text{H}_2})_{\text{out}}$  ratio is 0.1.

#### 8.3.2.1 Selection of values for operation and design variables

Design variables for the catalyst particle are shown in Table 8.3. Catalyst shape is considered to be a sphere, therefore bed porosity is  $\varepsilon = 0.4$ . Sphere diameter is a compromise between pressure drop and tube diameter (based on Jess et al. (2009)). The thickness of active material is calculated to avoid internal mass transfer limitations (Equation J.44). The active density (Equation N.56) and particle conductivity (Equation I.37) are a consequence of the selected  $\chi_{\text{shell}}$  and  $d_p$ .

The selected operating conditions to carry out the reaction are shown in Table 8.3 (right):

- The main reason for carrying out the reaction at 2 MPa is to avoid intermediate compression before the product gas is fed to the natural gas grid.
- Selected inlet temperature belongs to the range of temperatures used in the experimental work. High inlet temperatures increase  $K_p$  and favour reaction rates, however the difference to the maximum allowed temperature becomes small.

- Cooling temperature is assumed to be the same as inlet temperature.
- The inlet concentrations in the reactor are according to stoichiometry (assuming formation of  $C_3H_8$ ). Even though it has been shown in chapter 5 that high  $(H_2/CO_2)_{in}$  ratios favour the formation of short chain alkanes, stoichiometric values are selected to simplify load changes under transient conditions.
- The selected basis for calculation is  $F_{v,CO_2,average} = 500 \text{ m}^3/\text{h}$  (STP), according to the  $CO_2$  typically produced in a biogas plant.

Table 8.3: Catalyst particle design variables: sphere,  $d_p$  and  $\chi_{shell}$  and selected operating conditions.

catalyst particle design variables					operating conditions			
$d_p$	$\chi_{shell}$	$\rho_{active,R}$	$\lambda_p$	$\varepsilon$	$T_{in}$	$p$	$(\frac{H_2+CO}{CO+CO_2})_{in}$	$T_{cooling}$
m	$\mu\text{m}$	kg/ $\text{m}^3$	W/mK	-	$^\circ\text{C}$	MPa	-	$^\circ\text{C}$
0.003	150	214.1	5.6	0.4	280	2	10/3	280

Table 8.4 shows gas properties at reference operating conditions calculated with correlations shown in the appendix (Equations: H.6, H.12, H.8, H.10, H.14, H.7). Catalyst properties are directly related to the catalyst composition, mainly to the properties of the inert material. Values from literature are used for the calculations (Table 8.5).

Table 8.4: Gas properties at reference operating conditions  $T = 280 \text{ }^\circ\text{C}$ ,  $p = 2 \text{ MPa}$  and  $(H_2/CO_2)_{in} = 10/3$ 

$\rho_g$	$c_{p,g}$	$\eta_g$	$\nu_g$	$\lambda_g$	$M_g$
kg/ $\text{m}^3$	J/kg K	Pa s	$\text{m}^2/\text{s}$	J/s m K	g/mol
5.08	$2.81 \cdot 10^3$	$2.36 \cdot 10^{-5}$	$4.64 \cdot 10^{-6}$	$1.92 \cdot 10^{-1}$	11.69

Table 8.5: Catalyst particle properties

Property	Units	Value	Comments	References
$\rho_{p,s}$	kg/ $\text{m}^3$	1316	$\rho_{bed} = 790 \text{ kg}/\text{m}^3$ , $\varepsilon = 0.4$	Jess et al. (2009)
$C_{p,s}$	J/s m K	1100	DURANIT <sup>®</sup>	VFF (2015)
$\lambda_{Fe}$	W/m K	20	typical of iron catalyst	Bub et al. (1980)
$\lambda_s$	W/m K	4	DURANIT <sup>®</sup>	VFF (2015)

### 8.3.2.2 Reference case: tube diameter 3 cm and load range 70 - 100 %

According to the procedure shown in section 8.3.1 and the selected values for the design variables shown in section 8.3.2.1, a multitubular fixed-bed reactor with recycle is designed to be operated with a flexibility of  $L_{\min} = 0.7$  ( $F_{v,\text{CO}_2,\text{max}} = 588.2 \text{ m}^3/\text{h}$  (STP) and  $F_{v,\text{CO}_2,\text{min}} = 411.8 \text{ m}^3/\text{h}$  (STP)). The selected tube diameter is 0.03 m.

Table N.24 shows calculated results for the designed recycle system. It needs a total active catalyst mass of 0.45 t, which corresponds to a reactor volume of  $2.12 \text{ m}^3$ , in order to convert at least 90 % of an average  $\text{CO}_2$  volumetric flow of  $500 \text{ m}^3/\text{h}$ . The multitubular reactor consists of 956 tubes, each of them with a length of 3.14 m and a tube diameter of 0.03 m.

Figure 8.4 shows the calculated total molar flows of the chemical components along the catalyst bed at minimum and maximum operation load. Molar flow of CO is almost constant along the catalyst bed, meaning that the rate of CO formation via  $\text{CO}_2$ -shift equals the rate of consumption via FT. Operation at minimum load leads to a conversion

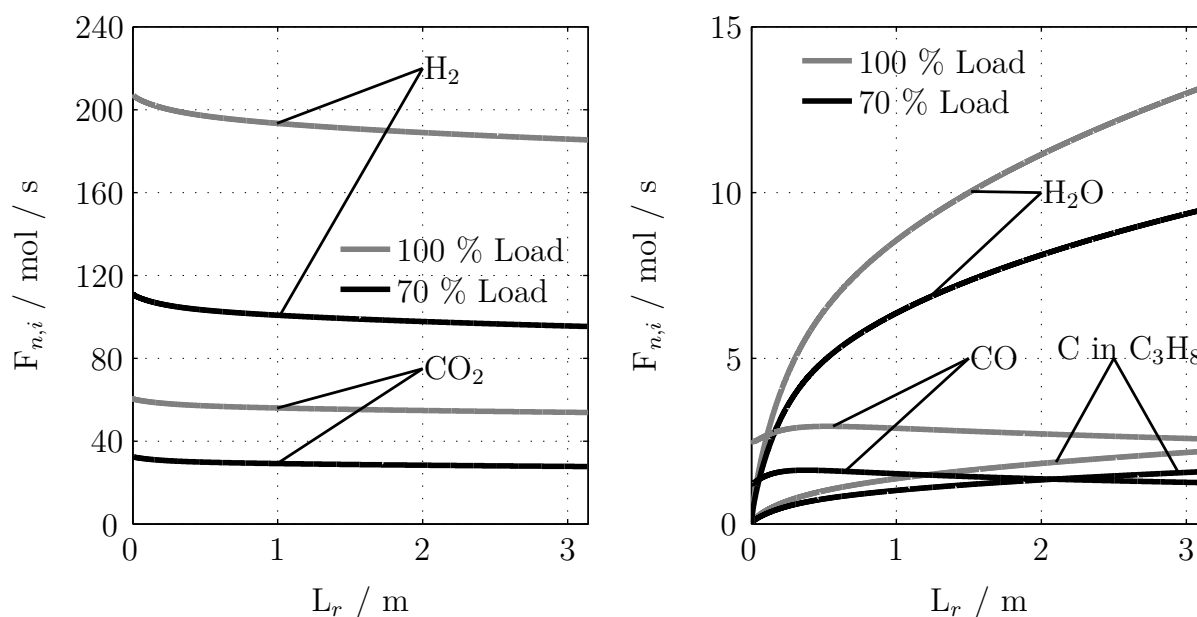


Figure 8.4: Total molar flows of reactants and products along the catalyst bed for maximum and minimum operation load (100 - 70 %,  $L_{\min} = 0.7$ ). Details recycle reactor:  $d_t = 0.03 \text{ m}$ ,  $L_t = 3.14 \text{ m}$ ,  $m_{\text{cat}} = 0.45 \text{ t}$ , and  $\text{NT} = 956$ . Information of other design variables used for calculation can be found in section 8.3.2.1. Profiles of partial pressures along catalyst bed in Figure N.60.

per pass of 15 % and consequently a recycle ratio  $R_F = 5.55$ . The overall conversion is 93 % and  $R_{\text{out}} = 0.988$ . The partial pressure restriction,  $(p_{\text{H}_2\text{O}}/p_{\text{H}_2})_{\text{out}} = 0.1$ , is not passed at the reactor outlet ( $L_t = 3.14 \text{ m}$ ). In order to reach an overall conversion of 90

% when this reactor is operated at maximum load, the average reaction rate along the catalyst bed increases (at minimum operation load the reaction rate is about 30 % lower than at maximum operation load,  $\overline{r_{FT,L_{max}}} = \overline{r_{CO_2-sh,L_{max}}} = 3.1 \text{ mol/ m}^3\text{s}$  versus  $\overline{r_{FT,L_{min}}} = \overline{r_{CO_2-sh,L_{min}}} = 2.2 \text{ mol/ m}^3\text{s}$ ). However the residence time of the gas in the catalyst bed decreases, leading to a decrease in the conversion per pass (from 15 % to 11 %) and an increase in the recycle ratio ( $R_F = 7.56$ ). The pressure drop increases by approx. a factor 3, compared with operation at minimum load, due to the higher gas velocity along the catalyst bed. The electric power required for the recycle compressor increases by approx. a factor 6 ( $P_{el,R-compressor} = 23.8 \text{ kW}$  at  $L_{max}$  and  $P_{el,R-compressor} = 3.7 \text{ kW}$  at  $L_{min}$ ) due to the recycle flow being twice as high, and the pressure drop thrice as high (Figure N.61).

Figure 8.5 left shows the temperature profiles along the catalyst bed for 100 % and 70 % load situations. The hot spot at minimum load reaches 300 °C, however when the reactor is operated at maximum load, the maximum temperature of the hot spot decreases to 297 °C. The reason for a lower hot spot at maximum load is the higher overall heat transfer coefficient, due to a higher gas velocity. Figure 8.5 right shows that CO<sub>2</sub>-shift and FT reaction rate decrease significantly along the catalyst bed, and especially in the first centimeters. The formation of H<sub>2</sub>O is responsible for the decrease of the reaction rate. H<sub>2</sub>O strongly inhibits both reaction rates. Even though temperature increases in the first centimeters, increasing the value of the kinetic constant, the effect of H<sub>2</sub>O is much higher and therefore the reaction rate decreases. Detailed information of the contribution of the different terms of the reaction rate can be found in Figure N.62.

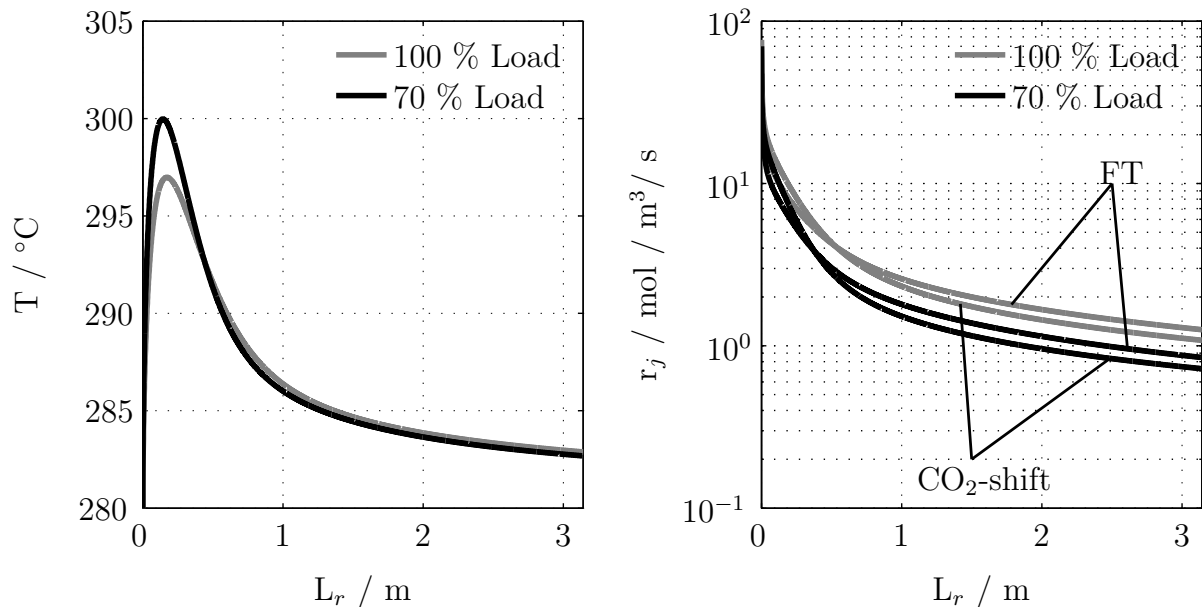


Figure 8.5: Temperature profile and reaction rates along the catalyst bed for maximum and minimum operation load of the recycle reactor. Detailed information of the terms involved in the reaction rate can be found in Figure N.62.

The flexibility of the reactor is directly connected with the characteristics of the chemical reaction. The maximum CO<sub>2</sub> molar flow in the fresh feed that can be converted is a function of the maximum reaction rate and the mass of active catalyst available (kinetic limitation). In the case of CO<sub>2</sub> hydrogenation, the maximum reaction rate is at  $z = 0$  (where no H<sub>2</sub>O is present). For a certain  $L_{\min}$  value, the mass of active catalyst is determined for the minimum fresh flow. The maximum CO<sub>2</sub> flow that can be converted per pass is calculated by multiplying the maximum reaction rate by the available mass of active catalyst ( $F_{n,\text{CO}_2,\text{max,rr}}$ ). In case the molar flow of CO<sub>2</sub> in fresh feed is higher than  $F_{n,\text{CO}_2,\text{max,rr}}$ , the reactor would not be able to reach the desired overall conversion (maximum reaction rate corresponds to  $X_{i,\text{pp}} = 0$  and  $R_F = \infty$ ), and consequently this  $L_{\min}$  value cannot be operated. For the reaction kinetics used in the present study and an average CO<sub>2</sub> flow of 500 m<sup>3</sup>/h, values lower than  $L_{\min} = 0.05$  can not be operated.

Even though the reaction rates for CO<sub>2</sub> hydrogenation are attractive for flexible operation, the low value of the allowed maximum conversion per pass leads to high energy requirements for recycle compression ( $X_{i,\text{pp}} = 14.7\%$  under the selected operating conditions). With a reactor designed for  $L_{\min} = 0.5$ , the conversion per pass at the maximum load is around 3% and the required recycle ratio value is approximately 22.

Design variables and reactor flexibility ( $L_{\min}$ ) have a strong effect on the reactor design and on the resulting energy demand. Preliminary calculations in section N.5.1 of the appendix evaluate the effect of tube diameter and load range on reactor design.

### 8.3.3 Simulation of example load change in a recycle reactor 100 to 70 % with a rate of 5 %/ min

The reactor conceptually designed to operate in a range of load 70 - 100% (section 8.3.2.2) is used in the present section to describe the transient operation from maximum to minimum load (100 - 70%) with a selected rate of load change of 5%/min (for comparison, see step change calculation in Appendix N.7, Figures N.67, N.68, and N.69).

The rate of load change for the chemical reactor is related to the rate of load change of the H<sub>2</sub> production and the size of the H<sub>2</sub> storage. High rates of load change might be risky for the equipment attached to the reactor (i.e. heat exchangers, compressors, etc.). Values of 10 - 15%/min are indicated by some companies working on process design and construction (Graf et al. 2014). The value assumed for the present calculation is, in comparison, conservative.

Figure 8.6 left shows the change in the CO<sub>2</sub> fresh feed flow of the reactor over time, starting at  $t = 5$  s. The fresh feed flow is decreased with a rate of 5%/min until an



operation load of 70 % is reached. The  $\text{CO}_2$  flow and the C flow in  $\text{C}_3\text{H}_8$  at the system outlet over time also decrease with a similar dynamic. By comparison of the  $\text{CO}_2$  flows it is possible to calculate the overall conversion in the system. Figure 8.6, right shows the  $\text{CO}_2$  inlet and outlet flows. The difference between both flows is related with the conversion per pass. The molar flows of the other components over time can be seen in Figure N.65.

The dynamic behaviour of the fresh feed flow can be observed in the recycle flow but with some delay. At the very beginning of the change, fresh feed decreases and is mixed with the steady state recycle flow. The change in the reactor inlet flow is small, but enough to slightly change the conversion per pass, and consequently the recycle flow and the new inlet flow to the reactor. For this calculation it is assumed for simplicity that no dead time exists in the recirculation due to the separation units. The gas coming out of the reactor at  $t = t_1$ , in the case of being recycled, will be fed into the reactor at  $t = t_1 + \Delta t$ . In reality, the time required for separation and recirculation is expected to be significant, however without a design of the separation units it is not possible to make a good guess. The recycle flow reaches its steady-state after 420 s, while the fresh feed flow is constant after 366 s.

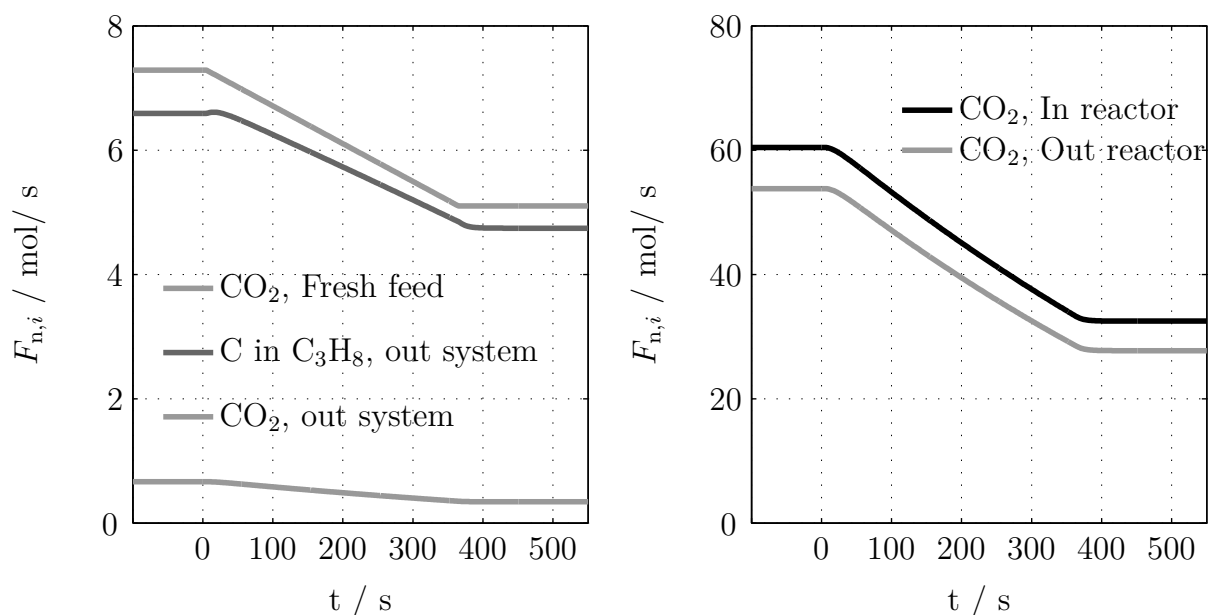


Figure 8.6: Molar flows during change from maximum operation load to 70 % with a rate of 5 %/ min. Left:  $\text{CO}_2$  and C in  $\text{C}_3\text{H}_8$  at system inlet and outlet. Right:  $\text{CO}_2$  at reactor inlet and reactor outlet. Molar flows of all other components in Figure N.65.

Fresh feed flow decreases by 30 % as desired, in contrast the recycle flow decreases by almost 50 %. This can be explained due to the 50 % lower inlet flow to the reactor and consequent higher conversion per pass. The minimum overall conversion of 90 % is

always satisfied (Figure 8.7). An increase in the conversion per pass due to the lower feed flow requires a lower  $R_F$ . Considering  $R_{\text{out}}$  as constant, the overall conversion per pass increases almost linear. The molar flow of unconverted  $\text{CO}_2$  decreases when the reactor is operated at minimum load.

The weak maximum in the value of the recycle ratio is due to the faster change in outlet concentration compared with the volumetric flow (Figure N.66). Right after the decrease in volumetric flow, the molar flows of the recycle components decrease at reactor outlet. Once the change is finished ( $t = 366$  s), the fresh flow is constant, but it takes some more seconds until the concentrations at the reactor outlet reach the new steady state. Due to these changes in reactor outlet concentration, the recycle ratio varies slightly (Figure N.66).

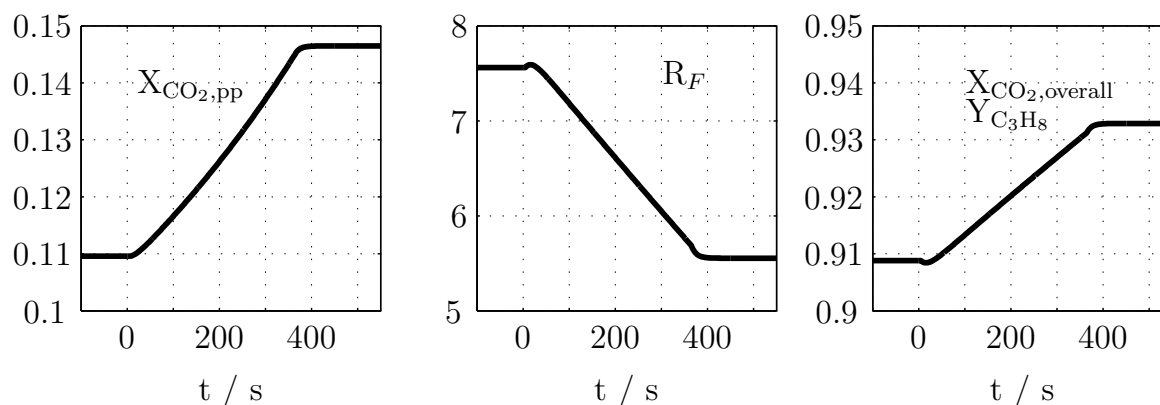


Figure 8.7: Conversion per pass, recycle ratio, and overall conversion during the change in fresh feed flow (Figure N.65, top left).  $R_{\text{out}} = 0.988$  for  $\text{CO}_2$ ,  $\text{CO}$  and  $\text{H}_2$

Transient behaviour can be observed in temperature and molar flow profiles along the catalyst bed (Figure 8.8). The transient temperature profile is strongly influenced by the catalyst density and heat capacity, both responsible for the dynamic thermal behaviour of the bed. Due to the use of a relatively low rate of change (5 %/min), changes are smooth along the catalyst bed. It is interesting to see the contrast with the step change especially in temperature, as the catalyst bed is heated by the reaction heat (Figure N.69). Temperature approaches the new steady state slower than concentrations, due to the different accumulation terms, however concentration and temperature reach the new steady-state at the same time because they are linked by the reaction term.

In this example, calculations are done for a stoichiometric inlet concentration. However advantages can be seen in operating this reaction under overstoichiometric conditions (section 5). This is also possible with a recycle reactor. However, when operating the reactor under transient conditions, a change in inlet flow needs to be combined with a change in inlet concentration. If the reactor is operated at  $(\text{H}_2/\text{CO}_2)_{\text{in}} = 5$  and a change

to a lower feed flow occurs, excess  $\text{H}_2$  remains in the recycle without being consumed and  $(\text{H}_2/\text{CO}_2)_{\text{in}}$  becomes higher than 5. Therefore the change in inlet flow needs to be combined with a lower  $(\text{H}_2/\text{CO}_2)_{\text{in}}$  in the feed during the first minutes, to use the  $\text{H}_2$  stored in the recycle.

It can be concluded from the example calculations, that transition from one operation point to the other does not seem to be a problem for a fixed-bed reactor, if the reactor is properly designed according to maximum and minimum flow, and catalyst limitations are considered (here  $T_{\text{max}} = 300\text{ }^\circ\text{C}$ ,  $(p_{\text{H}_2\text{O}}/p_{\text{H}_2})_{\text{out}} \leq 0.1$ ). Temperature and  $(p_{\text{H}_2\text{O}}/p_{\text{H}_2})_{\text{out}}$  limitations are never exceeded (Figure 8.8). Information about reactor-attached equipment should be included in the mathematical model to further analyse the dynamic behaviour of the overall chemical process. It is expected that attached equipment plays an important role in the flexibility of industrial-scale processes in a similar way as observed during transient experiments on lab-scale.

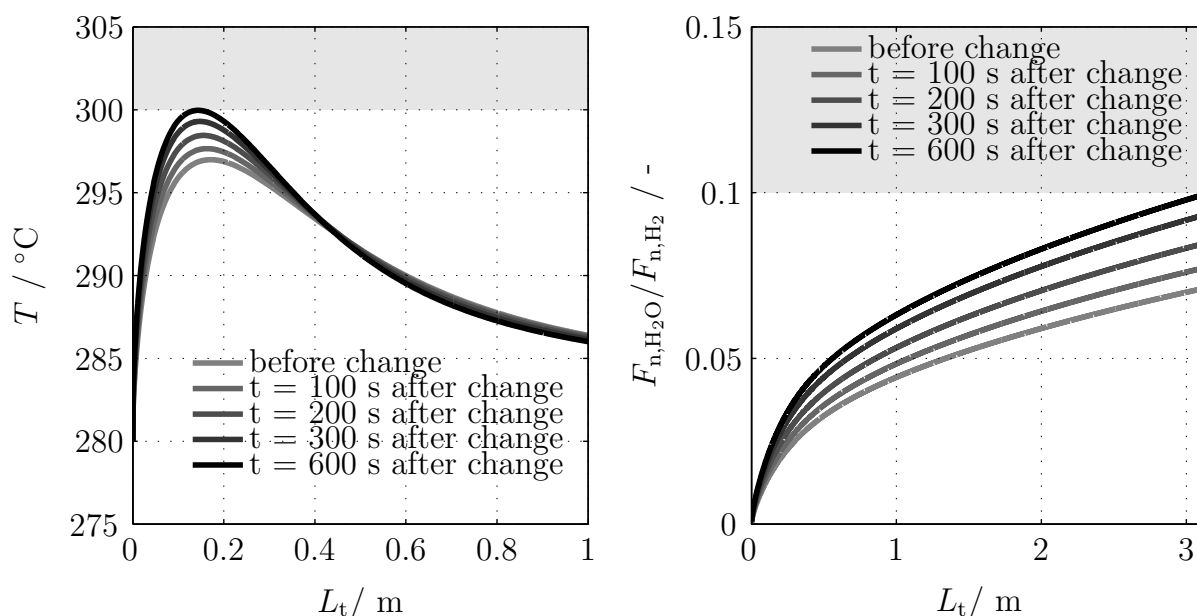


Figure 8.8: Calculated axial profiles of temperature and ratio of molar flow  $(p_{\text{H}_2\text{O}}/p_{\text{H}_2})_{\text{out}}$  along the catalyst bed at different times after a change in reactor load i.e. fresh feed flow with a rate of 5 %/ min from 100 % load to 70 % load. Grey: not acceptable for catalyst stability reasons, see Figure 5.5 and Figure 5.6.

### 8.3.4 Characteristic times of the processes involved in a fixed-bed catalytic reactor

A chemical plant is an example of a complex, high order, non-linear process that can be often described by a group of time constants. Processes involving chemical reaction, mass

transfer, and heat transfer take place at different time and length scales (i.e. catalyst particle, reactor and attached equipment). A characteristic time  $\tau$  is a measure of the time it takes to observe a significant change in a given process resulting from an input disturbance.

$$\text{characteristic time} = \tau = \frac{\text{capacity}}{\text{rate}} \quad (8.12)$$

The comparison of the characteristic times of the different processes with the characteristic time of the inlet disturbance might help to significantly simplify the number of processes that need to be considered in the mathematical model describing the overall process. Processes that are much faster (small value of the time constant) than the characteristic time of the inlet disturbance are put in equilibrium or into a steady state (i.e. transient portion of the change is negligible, Figure 3.7, top). On the other hand, processes that are slower than the characteristic time of the change (large value of the time constant) are considered as time-invariant (Figure 3.7, bottom).

In a future renewable energy system, characteristic times for variations in inlet conditions in a flexible chemical plant might vary between minutes ( $10^2$  s) and days ( $10^5$  -  $10^6$  s). Those processes with a similar characteristic time as the inlet variation will operate under transient conditions. Figure 8.9 shows the characteristic times of the processes taking place on the catalyst particle and in the chemical reactor designed in section 8.3.3. Characteristic times are evaluated for the maximum (grey) and minimum (white) operation load, in both cases along the catalyst bed (for  $z = 0$  and for  $z = L$ , Figure 8.9). A definition of the characteristic times and average characteristic time values can be seen in Table 8.6.

### Characteristic times for processes in the catalyst particle

The characteristic times for the process taking place in the catalyst particle are formulated based on a heterogeneous balance of the catalyst particle positioned in a flowing stream. Temperature and concentration are considered in three different regions: the bulk fluid phase, the boundary layer surrounding the particle, and the particle itself. Variations at the inlet of the reactor propagate through the fluid and may change the conditions at the outer edge of the boundary layer, and consequently in the boundary layer and the particle itself. Most of the characteristic times referring to the catalyst particle have already been defined in the literature (Boreskov et al. 1983; Finlayson et al. 2000), or are used as dimensionless groups to evaluate the necessity to use a pseudohomogeneous or heterogeneous model (e.g. Table J.13). To calculate the transfer coefficients, a representative position, temperature, pressure, gas velocity, and reaction rate need to be selected to write the material and energy balance as dimensionless (in this case equations are shown for  $z = 0$  but values are also calculated for  $z = L$ ).

The catalyst particle involves processes taking place in series (i.e. external mass transfer,

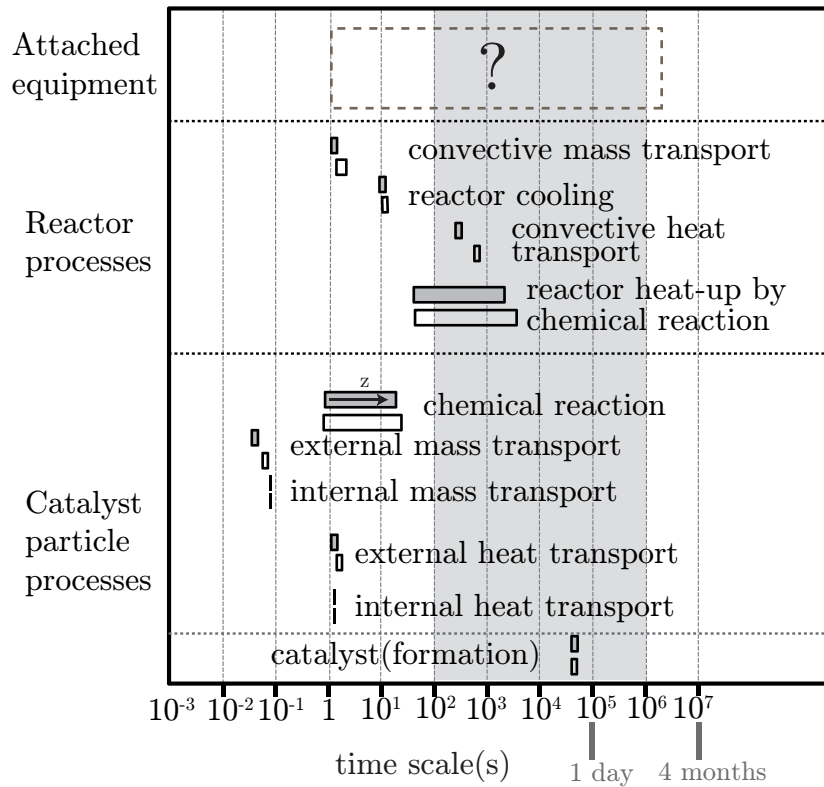


Figure 8.9: Characteristic times values in fixed-bed hydrogenation of  $\text{CO}_2$  for maximum (grey) and minimum load (white) 100 - 70 % respectively along the catalyst bed, for  $z = 0$  and  $z = L$ . Example reactor designed in section 8.3.3,  $L_t = 3.13$  m,  $d_t = 0.03$  m. Grey area: expected characteristic changes for inlet conditions. Values for attached equipment based on Lerou et al. (1996). Definitions in Table 8.6.

internal mass transfer, and chemical reaction), the slower process would dominate the long-term behavior, making the faster processes insignificant by comparison. According to the calculated values, the mass and heat transfer processes taking place on the catalyst particle are faster than the chemical reaction rate (with the exception of the first 10 cm in the fixed bed where external heat transfer rate is slower than chemical reaction). This means that mass and heat transport on the catalyst particle do not need to be considered because they are fast in comparison to the chemical reaction rate. The characteristic time for external and internal heat transport in a catalyst particle connects the accumulation term of the catalyst particle with the heat transfer coefficient gas-particle and the effective heat conductivity inside the catalyst particle respectively (Eigenberger et al. 2008).

Internal mass and heat transport processes are independent of the operation load and depend mostly on the characteristics of the catalyst particle (e.g. size of the pores, type of pores, particle composition). Internal mass transport limitations can be, to a large extent, decreased with the use of eggshell catalysts. External mass and heat transfer

depend directly on the gas velocity; it may occur that due to a change in load, the process becomes controlled by mass/heat transfer rather than by the chemical reaction.

Due to variations in the operating conditions (i.e. partial pressures, temperature, or other parameters), changes might occur on the catalytic reaction (i.e. modification of the reaction mechanism, accumulation of species on the catalyst surface, or a change on the catalyst composition), resulting in a different catalyst activity and/or selectivity (Boreskov et al. 1983). In chapter 7 experiments, within the range of conditions where the steady state kinetics are determined, are presented together with experiments under extreme conditions. A characteristic time for changes of catalyst properties can be determined from experiments carried out in the magnetometer, e.g. with a change of the gas atmosphere from pure  $H_2$  to synthesis gas ( $H_2+CO_2$ )(Figure 7.10). A characteristic time for the resulting catalyst formation can be calculated assuming a first order process and a step change based on experimental results. The characteristic time is calculated as 63.2 % of the total time required for the change ( $\tau_{cat} = 15.6 \text{ h} = 5.6 \cdot 10^4 \text{ s}$ ). Even though this process is not very relevant for the chemical plant (it would only occur at the very beginning or in case of a shut-off or regeneration) it is included as reference in Figure 8.9. Within the range where the kinetic parameters were determined, no change of the catalyst is observed. Therefore it is not possible to determine a characteristic time (see chapter 7).

### Characteristic times for processes in the catalytic fixed-bed reactor

Characteristic times for the one-dimensional fixed-bed reactor are derived from the non-steady state mass and energy balance, Equation N.64 and Equation N.65, with dimensionless variables defined in Equations N.60, N.62, N.63 and N.61. The definition of the dimensionless variables for concentration and temperature can be done using the inlet, the average, or the outlet concentration/ temperature. The same is applicable for the gas velocity. The dynamics of the momentum balance in the reactor are neglected because they are much faster than the composition and temperature dynamics (range  $10^{-3} - 10^{-2}$ , calculated with speed of sound).

- The characteristic time of the mass transfer by convection in the reactor with recycle is relatively short, due to the short catalyst tubes ( $L_t = 3.14 \text{ m}$ ) and the high gas velocities used in the recycle reactor.
- The characteristic time of the reaction varies strongly along the catalyst bed due to the production of  $H_2O$  and resulting decrease in the reaction rate. The ratio between the characteristic times of convective mass transport and chemical reaction equals the conversion per pass. Due to the short characteristic time of the convective transport, the conversion per pass is low (11 - 15 %). Higher conversion is not allowed in order to avoid catalyst deactivation.

- The characteristic time of convective heat transport is directly related to the gas velocity. In this case the difference between the characteristic time at maximum and minimum load can be clearly observed.
- The characteristic time of the reactor heat-up by chemical reaction is the longest. Heat processes in the fixed-bed reactor are much slower than mass transfer processes due to the difference in the storage terms.
- The characteristic time of reactor cooling remains almost constant along the reactor tube. The heat transfer coefficient is affected by gas velocity, however due to the low conversion per pass, the volume contraction by chemical reaction is relatively low, and variations in gas velocity are not significant. By comparing the characteristic times of cooling and reaction it is possible to understand the presence of hot spots. If the time constant of the reaction is lower than that of the reactor cooling, the cooling system is not able to remove the heat, produced faster, and hot spots appear (e.g. close to the reactor inlet). On the contrary, if the time constant of the cooling is equal to or lower than the time constant of the reaction, the reactor remains isothermal (e.g. close to the reactor outlet) (Figure N.70).

### **Characteristic times for processes taking place in the equipment attached to the chemical reactor**

The characteristic times for the catalyst particle and the chemical reactor need to be compared with the characteristic times of the other equipment units taking part in the chemical process (i.e. separation units, compression, pipes, heat exchangers, etc). Separation units, in the case of a reactor with recycle, might be accompanied by long characteristic times due to its significant size. An alternative could be to use a higher number of smaller units or advanced control strategies, however both alternatives may be accompanied with higher investment costs.

It is important to keep in mind that the increment in costs due to flexible operation of the chemical plant needs to be less than the reduction on the investment for the H<sub>2</sub> storage. If expected characteristic times for variations in inlet conditions are between minutes (10<sup>2</sup> s) and days (10<sup>5</sup> - 10<sup>6</sup> s), the dynamic behaviour of the overall chemical plant might depend on the characteristic time of the attached equipment, as long as the catalytic reactor is operated within the range of conditions where the catalyst is stable. The detailed evaluation of the attached equipment is outside the scope of this work and therefore a box without values and a question mark is used in Figure 8.9.

Table 8.6: Definitions of characteristic times for the different processes taking place in the catalyst pellet and in the catalytic reactor. Example values calculated for maximum and minimum operation load of the recycle reactor considering the CO<sub>2</sub>-shift as reaction. The characteristic times are calculated using average values along the catalyst bed for maximum and minimum operation load:

Table N.25

Process	Definition	Characteristic time (s)	
		L <sub>max</sub> = 1	L <sub>min</sub> = 0.7
Reactor processes			
Convective mass transport	$\frac{\varepsilon \cdot V_r}{F_{v,op,in}}$	1.4	2.7
Reactor cooling	$\frac{\varepsilon \cdot \rho_g \cdot c_{p,g} + (1 - \varepsilon) \cdot \rho_s \cdot c_{p,s}}{4 \cdot U_{eff}/d_t}$	10.3	14.4
Convective heat transport	$\frac{\varepsilon \cdot \rho_g \cdot c_{p,g} + (1 - \varepsilon) \cdot \rho_s \cdot c_{p,s}}{\rho_g \cdot c_{p,g} \cdot (\bar{u}_{sf}/L_t)}$	469.3	888.9
Reactor heat-up by chemical reaction	$\frac{\varepsilon \cdot \rho_g \cdot c_{p,g} + (1 - \varepsilon) \cdot \rho_s \cdot c_{p,s}}{(-\Delta H_R) \cdot \bar{r}_i/T_0}$	1118.2	1555.9
Catalyst particle processes			
Chemical reaction	$\frac{\varepsilon \cdot \bar{c}_i}{\bar{r}_i}$	11.9	16.2
External mass transport	$\frac{1}{\beta/d_p}$	0.1	0.1
Internal mass transport	$\frac{1}{D_{eff}/\chi_{shell}^2}$	0.1	0.1
External heat transport	$\frac{\rho_s \cdot c_{p,s}}{\alpha_{gas}/d_p}$	2.2	3.1
Internal heat transport	$\frac{\rho_s \cdot c_{p,s}}{\lambda_p/d_p^2}$	2.3	2.3

## 8.4 Effects of chemical reaction/catalyst characteristics on reactor design for part-load operation

In general, all reactions using hydrogen as reactant have the potential to be operated under flexible conditions due to the fluctuating nature of hydrogen when produced from



renewable sources. The previous chapters discussed the flexibility of fixed-bed reactors using the CO<sub>2</sub> hydrogenation to gaseous hydrocarbons as example reaction. Now general aspects regarding flexible operation of fixed-bed reactors for other fuel-related synthesis that demand H<sub>2</sub> will be outlined and qualitatively discussed, based on the information given in Table 8.7.

Table 8.7 summarises general information of different fuel related routes using H<sub>2</sub> as reactant and potentially fixed-bed synthesis reactors: methane synthesis, CO<sub>2</sub> hydrogenation to gaseous hydrocarbons, LT-Fischer Tropsch reaction and methanol-to-hydrocarbons. A first indication of the feasibility to operate these reactions under flexible conditions is outlined based on the information in Table 8.8.

The hydrogenation of CO and CO<sub>2</sub> to methane is a highly exothermic reaction favoured at low temperatures and high pressures from a thermodynamic point of view. Nickel is the catalyst of choice due to its high activity and selectivity towards methane, and its relatively low cost. The main disadvantage of Nickel is its reaction with CO to form carbonyls at lower temperatures (Mills et al. 1974). Reactor choice is based on the way exothermic heat of reaction is controlled in order to prevent thermodynamic conversion limitation, catalyst deactivation by carbon deposition and catalyst sintering (Götz et al. 2015). Due to the high activation energy, the reaction is very sensitive to changes in temperature, and the system highly non linear (risk of runaways) (Luyben 2007).

Flexible operation of methane synthesis reactors seems promising in the near future. Heat management needs to be efficient enough to avoid strong temperature variations that could lead to a decrease of catalyst life time due to catalyst cracking or sintering (Götz et al. 2015). New concepts are being developed to produce methane under isothermic conditions (Götz et al. 2015; Lefebvre et al. 2015), as an alternative to multitubular (e.g. Linde isothermal reactor) or adiabatic reactors with interstage cooling (Schaaf et al. 2014). Nickel catalysts are stable in the presence of products, and the selectivity to methane is high as long as side reactions like the CO-shift are controlled.

The low temperature FT aims to produce diesel fuel after hydrocracking of the FT-wax. Details about this reaction have been introduced at the beginning of this chapter (Table 8.2). An important issue for flexible operation is the high exothermicity in combination with temperature-sensitivity of product selectivities, what makes the use of slurry bubble column reactors attractive in comparison to trickle-bed reactors (Sie et al. 1999). Fixed-bed reactors are usually operated with a recycle of gas and liquid to avoid strong radial temperature profiles. The main disadvantage for flexible operation is the change of product selectivity at higher conversion (more methane is produced), and the negative effect of H<sub>2</sub>O on the reaction rate, which could result in catalyst deactivation. Therefore, maximum conversion before H<sub>2</sub>O removal is limited to about 50 % (Steynberg et al. 2004).

Table 8.7: Fuel related synthesis reactions using H<sub>2</sub> as reactant in fixed-bed reactor

Reaction	$\Delta_R H_{298K}^0$ <sup>1</sup> kJ/mol	Equilibrium constraints with T	Reaction rate equation	$E_A$ kJ/mol	Product selectivity	Catalyst deactivation
Methanation	-206.2 (CO) -165.1 (CO <sub>2</sub> )	at high T	$r = \frac{p_{CO} \cdot p_{H_2}}{f(p_{CO}, p_{H_2O})}$	240 - 244 <sup>2</sup>	CH <sub>4</sub> and CO <sub>2</sub> (CO) high CH <sub>4</sub> >99 (CO <sub>2</sub> )	coke formation (CO) Ni-carbonyl (CO)
CO <sub>2</sub> hydroge- nation to C <sub>2-4</sub>	-125.0 (CO <sub>2</sub> ) <sup>3</sup>	none	$r = \frac{p_{CO_2} \cdot p_{H_2} - (p_{CO} \cdot p_{H_2O})/K_p}{f(p_{CO_2}, p_{CO}, p_{H_2O})}$ $r = \frac{p_{CO} \cdot p_{H_2}}{f(p_{CO_2}, p_{CO}, p_{H_2O})}$	139 95	complex, <sup>4</sup> T-sensitive	at high CO <sub>2</sub> conversion (high (p <sub>H<sub>2</sub>O</sub> /p <sub>H<sub>2</sub>)<sub>out</sub> ratios)</sub>
LT-Fischer- Tropsch (Co)	-115.1 (CO) <sup>5</sup>	none	$r = \frac{p_{CO} \cdot p_{H_2}}{f(p_{CO})}$	93 - 103 <sup>6</sup>	complex, <sup>4</sup> T-sensitive	at high CO conversions
Methanol <sup>7</sup>	-128.1 (CO) -86.9 (CO <sub>2</sub> )	at high T	$r = \frac{p_{CO} \cdot p_{H_2} - (p_{MeOH}/K_p)}{f(p_{H_2O})}$	75 - 100	high MeOH > 99.9 %	sintering at T > 250 °C at high concentrations of CO and/or CO <sub>2</sub>
Dimethylether (DME)	51.3 (MeOH)	at high T	$r = \frac{p_{MeOH} - (p_{H_2O} \cdot p_{DME})/K_p}{f(p_{H_2O})}$ <sup>8</sup>	144 <sup>8</sup>	high	at high H <sub>2</sub> O partial pressures
MTG <sup>9</sup>	-55.7 (MeOH)	none		35 - 90	complex, <sup>4</sup> T-sensitive	“coking”

<sup>1</sup> Wired Chemist (2015) (values for reaction enthalpy)<sup>2</sup> Xu et al. (1989)<sup>3</sup> assuming C<sub>3</sub>H<sub>8</sub> as final product<sup>4</sup> mixture of hydrocarbons<sup>5</sup> assuming C<sub>10</sub>H<sub>22</sub> as final product<sup>6</sup> Yates et al. (1991), Laan et al. (1999)<sup>7</sup> Hansen et al. (2008)<sup>8</sup> Bercic et al. (1992)<sup>9</sup> Exxon Mobil (2015), Kvisle et al. (2008), Schulz (2010)

Methanol synthesis is an exothermic reaction limited at high temperatures by the thermodynamic equilibrium. It is usually operated at higher pressures (4 - 15 MPa). Modern catalysts offer a selectivity above 99.9 %. The rate of formation of methanol is improved by the presence of small amounts of CO<sub>2</sub>. The CO-shift reaction needs to be considered to calculate the variations in the gas composition. The reaction rate is inhibited by H<sub>2</sub>O. The key challenge in reactor design lies in the way exothermic heat of reaction is removed, to be efficient and economical in a similar way as the methanation reaction. Two main variants are (i) multitubular fixed-bed with cooling medium, (ii) adiabatic multistage fixed-bed reactor with intermediate cooling. The use of recycle is common in the methanol synthesis to reach a high methanol yield, to avoid the presence of H<sub>2</sub>O, and to maintain a low temperature (ca. 250 °C) due to dilution of the feed (Hansen et al. 2008). Typical recycle values are between 3 - 7 with a conversion per pass of 8 - 15 % (two cooled tubular reactors operating in series with recycle)(Bartholomew et al. 2006).

The methanol synthesis appears as an attractive synthesis to be operated in a flexible way as long as the removal of reaction heat is carried out in an efficient way. Methanol is, nowadays, one of the top ten petrochemicals and its increased use in the future has been proposed by different authors (Bertau et al. 2014; Connolly et al. 2014).

Methanol can be dehydrated to dimethylether (DME) over an acid zeolith catalyst. The use of DME as fuel additive for diesel engines is being investigated due to its high cetane number and high volatility. At operating temperature (approx. 300 °C) the reaction is slightly exothermic ( $\Delta_R H_{300^\circ C}^0 = -23$  kJ/mol) and is carried out in an adiabatic reactor. In the typical temperature range, no significant side-reactions take place and the equilibrium conversion for pure methanol exceeds 90 %. The formation of DME is inhibited by the presence of H<sub>2</sub>O (Bercic et al. 1992), and the acidic catalyst can also deactivate under high H<sub>2</sub>O partial pressures (Kim et al. 2006). The DME synthesis, due to its low heat of reaction and high selectivity to the final product, is considered to be an “easy” reaction and has a higher potential to be operated under flexible conditions.

DME is a key intermediate in the production of synthetic gasoline via Methanol-to-Gasoline (MTG). An equilibrium mixture of methanol, DME and H<sub>2</sub>O is converted to light alkenes (the formation of DME from methanol is faster than the formation of hydrocarbons, therefore methanol, DME, and H<sub>2</sub>O are essentially in equilibrium). A final reaction step leads to the synthesis of higher alkenes, n/iso alkanes, aromatics, and cycloalkanes. The shape selective zeolith used for the MTG process (e.g. H-ZSM-5) limits the hydrocarbon synthesis to carbon numbers up to ten. The reaction is exothermic, whilst the conversion of methanol to hydrocarbons and water is virtually complete and essentially stoichiometric. Most of the hydrocarbon products are in the gasoline range, but by-products like a fraction C<sub>2-4</sub> (LPG) are also found in the product. The main dif-

ferences with the LT-Fischer Tropsch process are the final fuel product (gasoline versus diesel) and the heat of the reaction. The MTG reactor system operates with a recycle of the gas phase (mostly light hydrocarbons) after H<sub>2</sub>O separation. The main disadvantage of this reaction is catalyst deactivation due to carbon deposits (i.e. coke formation) in the zeolith (Exxon Mobil 2015). In recent times, other reactions similar to MTG have become increasingly important like Methanol-to-Olefins (MTO) or Methanol-to-Propene (MTP). Due to the broad spectrum of products and catalyst deactivation, flexible operation of MTG reactors seems challenging, as a shift in the product distribution might occur due to changes in the operating conditions, especially in flow (Kvisle et al. 2008).

Methane, methanol and DME syntheses can be seen as relatively feasible routes to be operated under flexible conditions, due to the high and robust selectivity of the desired product with limited sensitivity towards temperature variations and catalyst stability. The CO<sub>2</sub> hydrogenation to gaseous hydrocarbons, LT-Fischer-Tropsch synthesis, and Methanol-to-Gasoline, can be seen as more complex in this respect (Table 8.8).

Table 8.8: Qualitative evaluation of the feasibility of synthesis reactors to be operated under flexible conditions (with respect to reactor engineering aspects)

Reaction/Synthesis	Feasibility	Main Features
Methanation	higher	Efficient heat transfer is required, high selectivity to the desired product
CO <sub>2</sub> hydrogenation to C <sub>2-4</sub>	moderate	Complex product selectivity and CO <sub>2</sub> conversion limited. Efficient heat transfer required
LT-Fischer-Tropsch (Co)	moderate	Complex product selectivity and CO <sub>2</sub> conversion limited. Efficient heat transfer required
Methanol	higher	Efficient heat transfer required, high selectivity to the desired product
Dimethylether	higher	Low heat of reaction and high selectivity to the desired product
MTG	moderate	Complex product selectivity and catalyst deactivation due to “coking”

The methodology applied in the present study can be used to investigate the operating flexibility of catalytic synthesis reactors in any of the fuel-related processes presented here. Mathematical models offer the possibility to get an understanding of flexible operation with a given reaction and type of reactor. However, representative parameters need to be implemented. Some of them can only be obtained by experimental work (e.g. kinetic parameters, catalyst behaviour under representative transient operating conditions).

## 9 Conclusion and outlook

The results of this thesis have contributed to the field of the Fischer-Tropsch synthesis, with systematic catalytic experiments using CO<sub>2</sub> as carbon source. Information about the effect of potassium as a catalyst promotor and operating conditions have helped to gain a better understanding about the combined reactions involved. In addition, methods to evaluate potential limiting factors of reactor flexibility (i.e. temperature, catalyst behaviour) have been developed and applied to a catalytic fixed-bed reactor, using the CO<sub>2</sub> hydrogenation with Fe/K catalysts as example reaction.

The main results of this thesis, together with recommendations for the future, are summarised in two sections as follows:

### Assessment of the production of gaseous hydrocarbon syngases from H<sub>2</sub> and CO<sub>2</sub>

- The evaluation of a series of literature publications indicated that studies using H<sub>2</sub> and CO<sub>2</sub> mixtures have been already made. However, most of them focus on the effect of promoters at constant operating conditions and few studies focus on the effect of operating conditions on the reaction network. Iron-based catalysts are considered the most promising due to their bifunctionality, in spite of the limited CO<sub>2</sub> conversion attainable. Scarce information about CO<sub>2</sub>-shift and Fischer-Tropsch reaction rates, in combination, has been found in literature. The Fischer-Tropsch reaction has the potential to remove CO from the system and thus increase the CO<sub>2</sub> conversion.
- Experimental results with 100 g Fe / 2 g K show an attractive hydrocarbon selectivity for the production of gaseous hydrocarbon syngases (hydrocarbons are already alkanes). However, hydrocarbon yield and CO<sub>2</sub> conversion are limited. Partial pressure ratios of  $(p_{\text{H}_2\text{O}}/p_{\text{H}_2})_{\text{out}} \geq 0.10$  oxidise the catalyst and decrease the Fischer-Tropsch activity. Experiments with a high (H<sub>2</sub>/CO<sub>2</sub>)<sub>in</sub> inlet ratio, (H<sub>2</sub>/CO<sub>2</sub>)<sub>in</sub> = 22, enable high CO<sub>2</sub> conversion and hydrocarbon yield values without catalyst deactivation. The hydrocarbon product distribution under these conditions is as follows (in weight): CH<sub>4</sub> 82 %, C<sub>2-4</sub> 16 %, and C<sub>5+</sub> 2 %. Yield of CO is close to zero.
- Experimental results with 100 g Fe / 10 g K show a hydrocarbon product distribu-

tion shift to longer chain hydrocarbons, which is less interesting for heating value adjustment of SNG. Fischer-Tropsch activity is lower in comparison with 100 g Fe / 2 g K, therefore a low hydrocarbon yield is obtained under same operating conditions. The catalyst deactivates due to the formation of inactive carbon, favoured by the high amount of potassium on the catalyst surface.

According to these conclusions, if CO<sub>2</sub> is the selected C-source, it seems challenging to find a catalyst able to reach a high hydrocarbon yield, based on CO<sub>2</sub>, without deactivation. Further investigation is recommended to find intelligent ways of operating this reaction according to these constraints. An option could be a combination with methane synthesis, that would enable the operation at high (H<sub>2</sub>/CO<sub>2</sub>)<sub>in</sub> ratios.

### **Flexibility of fixed-bed catalytic reactors as a future component of a renewable energy system.**

Flexible operation of chemical reactors is a field of research where numerous aspects play an important role, with limited knowledge available at the present (e.g. reaction engineering, materials, control strategies, heat integration, etc.). Within this work, general aspects and limitations of flexible reactor operation using an example fuel synthesis reaction and a suited fixed-bed reactor have been identified and different methods have been developed to evaluate the restrictions that catalyst and large-scale reactor design could impose on the attainable reactor flexibility (i.e. temperature control, pressure drop). These methods combine experimental work in the lab-scale setup with mathematical modelling of the setup and a larger-scale reactor.

#### Catalyst behaviour under variable operating conditions

- Periodic operation was intensively studied during the 80's and 90's with the aim of improving catalyst activity and selectivity compared to steady-state operation. Numerous studies can be found in literature for different reactions. These experiments are helpful to get a better understanding of the catalytic system and its interactions with the fluid phase. However, the reported variations on the gas phase are strong (often using a pure reactant during some time) and not relevant for the dynamic operation expected in the context of the electricity-to-fuel process (Figure 1.2). In this context, due to the use of a H<sub>2</sub> storage, the expected variations on the gas phase composition are milder than those reported in periodic experiments.
- No changes to the catalyst state (i.e. chemical composition, surface structure, and catalytic properties) have been observed at variable operating conditions, in the range of conditions where kinetic parameters were determined. Three different methods were used, and all indicate that catalyst activity remains constant under variable operating conditions (the set of kinetic parameters determined under steady-state conditions can be used to describe transient operation).

- Changes to the catalyst's chemical composition and properties were observed when operating conditions were changed to "extreme" conditions (e.g. pure H<sub>2</sub> atmosphere, high temperatures), using step changes and in-situ methods (here, no periodic changes were carried out). Under these conditions, the catalyst activity could not be described by the set of kinetic parameters determined under steady-state conditions. The reactor should not be operated under these extreme conditions, to avoid catalyst deactivation/reduction. In the special case of the FT synthesis with iron, it has been shown that the formation and hydrogenation of iron carbides is reversible and highly dynamic.

It could be attractive to find out the time that the catalyst can be operated under deactivating/reducing conditions, before a change on the catalyst occurs. In this work, variations were made every 2 h and catalyst changes could be observed. Future work could focus on the determination of the time that a catalyst can operate under certain operating conditions, under which it would deactivate over a long time. Similar effects have already been studied for electrolysis (able to operate during 15 minutes at 300 % load).

#### Pre-feasibility study on flexible operation of industrial fixed-bed reactor

- The selective catalytic reduction of NO<sub>x</sub> is a successful example of flexible operation of a catalytic reaction. Lots of research efforts have optimised the complex reaction system before and during commercialisation. However, significant differences exist in comparison with a catalytic reaction that uses fluctuating H<sub>2</sub>, mainly due to the strong dilution with air, in the case of DeNox, which reduces the heat effects and the concentration of reactants to be converted.
- A procedure has been developed to design a recycle system able to operate a catalytic fixed-bed reactor for an exothermic temperature-sensitive synthesis reaction under variable load. The characteristics of the recycle system are determined by specific limitations of the catalyst system and the example reaction (CO<sub>2</sub> hydrogenation on Fe), e.g. with catalyst sensitivity towards partial pressure of products and temperature. Simulation results of transient reactor operation, after a change in load, do not show complications if the reactor design is consistent with the constraints of the chemical reaction. However, information about reactor-attached equipment on the dynamic response of the system has not been considered. Sensitivity analysis is required to evaluate the effects of operating conditions and design variables: e.g.  $T_{\text{in}} = T_{\text{cooling}}$ , loading of active catalyst,  $\chi_{\text{shell}}$ , (H<sub>2</sub>/CO<sub>2</sub>)<sub>in</sub> ratio, particle diameter  $d_{\text{p}}$  and selection of the catalyst shape.
- The importance of the reactor's attached equipment for the dynamic response of the system has been identified during the transient experiments on lab-scale. It is expected that the attached equipment plays an important role in the flexibility of

industrial-scale processes. Further investigation in this topic is recommended also in connection with investment costs.

- According to the present calculations, flexible operation would lead to an increase in size of the reactor vessel (higher investment cost) and/or in the power demand for the recycle compressor (higher operating cost) compared with reactors designed for steady-state operation. The cost increase, due to flexible operation of the chemical process, needs to be lower than the decrease in the investment cost for the H<sub>2</sub> storage to make flexible operation attractive. Economic evaluations are required to assess the overall cost reduction potential of flexible operation of chemical reactors.
- The concept of characteristic times can be used to show, in a simplified way, the effect that the individual processes involved in a chemical plant have in the dynamic response of the system.
- The methods developed in the present study can be used to investigate the dynamic behaviour of catalytic synthesis reactors other fuel-related processes.

Further exploration on the following topics related to flexibility of chemical reactors and plants is recommended:

- Experimental work to further develop and validate the mathematical model: for example, one tube with representative diameter, filled with catalyst particles and surrounded by cooling medium would help to gain insight in transient effects (e.g. reaction effects combined with heat transport). At the moment, no information about flexible operation of industrial-scale fixed-bed reactors is available .
- Catalyst research: development of a catalyst for flexible operation, less sensitive to variations and optimised for a range of operating conditions rather than for one fixed operating condition.
- Process system analysis: the chemical plant needs to be considered as a whole under variable operating conditions. The decisions made in the reactor design are often the most important of the whole process because they determine the separation chains, compression requirements, heat requirement, etc. The complete flowsheet needs to be considered to determine the optimal configuration, defined as a good balance between investment and operation costs, and flexibility.
- Control and automation strategies: control would play a major role in the process, for example, the proportional controller that was implemented for the H<sub>2</sub> storage. Important reductions to the size of the required storage were obtained with an adequate setting.
- New reactor designs and reactor concepts: this work presents a first approach to



evaluating flexible operation based on conventional designs, that are presently used for steady-state operation. Transient operation may require new designs and innovative concepts (e.g. micro structured reactors, combining high heat transfer and low pressure drop (Güttel 2015))



# 10 Summary

## Introduction and objectives

The transition of the energy production system, from fossil to renewable resources, enables economic growth and low energy-related emissions with an expected population of 9 billion by 2050 (IEA 2015; Jess et al. 2011). However, it constitutes a major challenge for today's society. This transition requires the development and implementation of effective and economically attractive new technologies to successfully integrate renewable energies in the energy production system.

Future primary energy supply will be based to a large extent on renewable sources like wind and solar, leading to electricity with fluctuating generation characteristics. As chemical energy carriers will still be needed in mobile and other applications, conversion of electricity into chemical energy may then become important. For example, fluctuating electricity can be converted into hydrocarbon fuels via hydrogen as intermediate, replacing fossil fuels and being attractive as a long-term storage in excess electricity generation situations. A general flow diagram of an electricity-to-hydrocarbon process is shown in Figure 10.1, indicating electrolysis for fluctuating  $H_2$  generation, some  $H_2$  storage and the catalytic synthesis reactor.

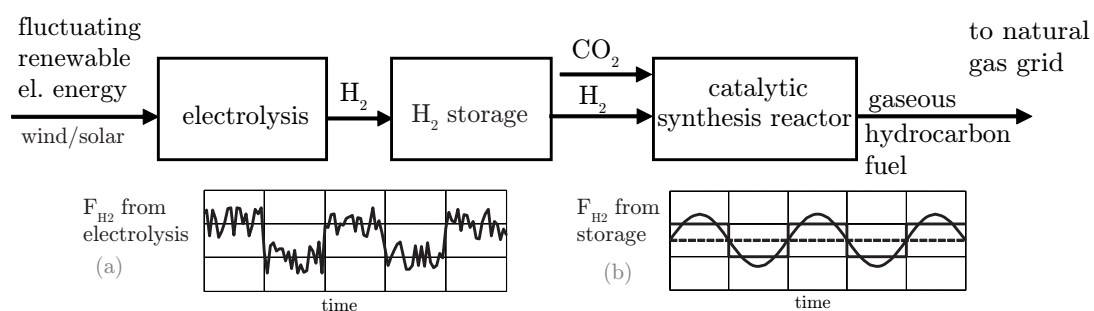


Figure 10.1: Flow diagram of an electricity-to-fuel process chain with  $H_2$  as intermediate and gaseous hydrocarbons as product. (a) Example  $H_2$  flow pattern produced via  $H_2O$  electrolysis from fluctuating electricity, (b) example  $H_2$  flow pattern at storage outlet for the production of hydrocarbon fuels using  $CO_2$ ; dashed line: large  $H_2$  storage size, catalytic reactor operating at steady-state conditions; full lines:  $H_2$  storage smaller with two different control strategies, catalytic reactor operating under transient conditions.

Potential sources of concentrated CO<sub>2</sub> are biomass fermentation either to ethanol or to methane, biomass combustion or gasification (leading to CO/ CO<sub>2</sub> mixtures) and industrial processes like iron and steel production or calcination in the cement industry. CO<sub>2</sub> captured from air is also seen as an alternative in the literature in spite of the high energy demand (Jess et al. 2011; Weimer et al. 1996; Zeman 2007).

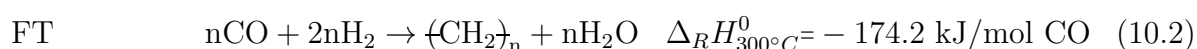
This thesis focuses on two different aspects related with the catalytic reactor synthesis in Figure 10.1:

- Production of gaseous hydrocarbon synfuels (C<sub>2</sub>H<sub>6</sub>, C<sub>3</sub>H<sub>8</sub>, C<sub>4</sub>H<sub>10</sub>) from H<sub>2</sub> and CO<sub>2</sub> to adjust the heating value of methane (raw SNG): the aim is to gain a better understanding of the CO<sub>2</sub> hydrogenation on iron-catalyst and find out attractive operating conditions.
- Fundamentals of fixed-bed reactor design for flexible operation (operation at varying load with frequent changes between different load situations at different rates of load change): the aims are to (i) identify general aspects and limitations of flexible fixed-bed reactor operation using the CO<sub>2</sub> hydrogenation as example reaction and (ii) develop methods to study transient reactor operation based on a combination of experimental work and conceptual studies using mathematical models.

### CO<sub>2</sub> hydrogenation to gaseous hydrocarbons: heating value adjustment

Literature publications indicate that studies using H<sub>2</sub> and CO<sub>2</sub> mixtures to produce hydrocarbons have been already carried out, in most cases with the aim to produce short chain alkenes as bulk chemicals or long chain alkanes as transportation fuels. Most of these studies focus on the effect of catalyst promoters at constant operating conditions and only few studies focus on the effect of operating conditions on the reaction network, as it is the case of the present study.

The CO<sub>2</sub> hydrogenation to hydrocarbons is described in previous studies as a two-step catalytic reaction with CO as intermediate product (Equation 10.1 and 10.2 ) (Lee et al. 1992; Riedel et al. 2001). The Fischer-Tropsch reaction has the potential to remove CO produced via CO<sub>2</sub>-shift and thus increase the CO<sub>2</sub> conversion, however the formation of H<sub>2</sub>O by both reactions could have a negative effect on catalyst activity (Lee et al. 1990).



Iron-based catalysts are considered the most promising catalysts due to their bifunctionality (CO<sub>2</sub>-shift and Fischer-Tropsch). Potassium is the most common promoter in iron-based catalyst and affects catalyst activity and selectivity (favours formation of

carbon-on-site, i.e. CO<sub>2</sub>-shift activity, production of long chain hydrocarbons, inhibition of secondary reactions)(Schulz 2014). Two catalysts promoted with potassium were selected for the present work (100 g Fe / 2 g K and 100 g Fe / 10 g K) with the aim to clarify the effects of reaction variables and potassium content on CO<sub>2</sub> conversion, hydrocarbon yield and hydrocarbon product distribution.

The desired hydrocarbon product (C<sub>2</sub>H<sub>6</sub>, C<sub>3</sub>H<sub>8</sub>, C<sub>4</sub>H<sub>10</sub>) is able to replace liquefied petroleum gases (LPG), for heating value adjustment of substitute natural gas. The hydrocarbon product distribution obtained from Fischer-Tropsch synthesis depends on reaction variables (e.g.  $T$ ,  $p$ ,  $(\text{H}_2/\text{CO}_2)_{\text{in}}$ ) as well as on catalyst composition. Due to the characteristics of the FT reaction, similar to a polymerisation, a variety of products of different chain length and functionality are formed. The primary product of the FT synthesis are  $\alpha$ -alkenes, therefore an hydrogenation step is required to produce the desired alkanes. Fischer-Tropsch hydrocarbon product distribution can be mathematically described using the Anderson-Schulz-Flory model. This model assumes that FT is an ideal polymerisation reaction and the hydrocarbon product distribution can be predicted using a single parameter, the chain growth probability  $\alpha$  (relating chain propagation and chain termination). Figure 10.2 shows hydrocarbon weight fractions as a function of chain growth probability  $\alpha$ , curves calculated with ASF model and symbols from own experimental work.

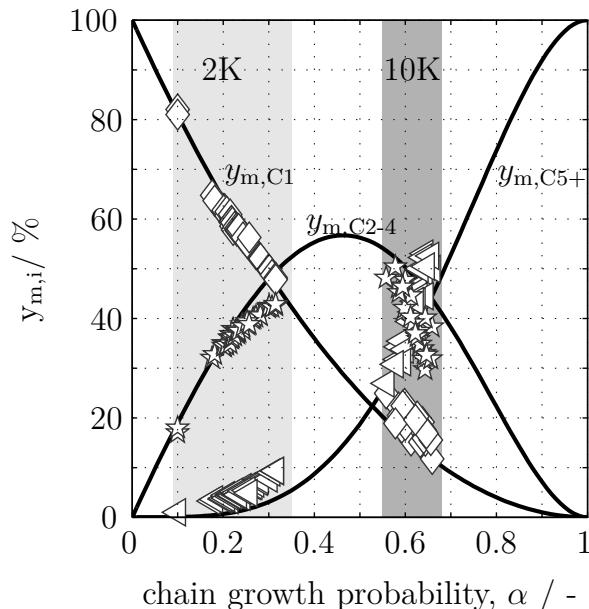


Figure 10.2: Measured hydrocarbon product distribution in mass % for 100 g Fe / 2 g K and 100 g Fe / 10 g K. Curves calculated with the Anderson-Schulz-Flory (ASF) model. Conditions:  $p = 1 - 2$  MPa,  $(\text{H}_2/\text{CO}_2)_{\text{in}} = 4, 5, 8, 22$ ,  $T = 245 - 297$  °C and  $\tau_{\text{mod}} = 175 - 5000$  kg s/m<sup>3</sup>.

The central part of the experimental work was carried out in a new designed and built

lab-scale setup with a fixed-bed reactor. Supporting experiments including in-situ and ex-situ catalyst characterization techniques were carried out at the Centre of Catalysis Research in the University of Cape Town (group of Prof. M. Claeys), with the aim to clarify the effect of K on catalyst reduction and formation processes (e.g. Figure 10.5). Figure 10.2 shows that both catalysts show a similar selectivity for the fraction  $C_{2-4}$ , according to the results obtained in a similar range of operating conditions. Methane and  $C_{5+}$  are always present in the hydrocarbon mixture, however in different extent: 100 g Fe / 10 g K catalyst leads to a larger fraction of  $C_{5+}$  that can not be used for heating value adjustment and needs to be separated and can be further upgraded to be used as transportation fuel (hydrocarbons are mostly in form of alkenes). In contrast, the production of  $C_{5+}$  with 100 g Fe / 2 g K is low and methane is the main component of the mixture. This gas mixture can be used as blending gas for heating value adjustment and therefore be stored in the natural gas grid (hydrocarbons are mostly in form of alkanes). The selection of the catalyst composition would depend on the possibilities to use the byproduct (e.g. location of the plant).

The most challenging issue in  $CO_2$  hydrogenation is to reach a high yield of organic compounds, different from methane. Based on the two iron catalysts investigated in the present study, the following can be concluded (Table 10.1):

Table 10.1: Comparison of the two iron catalysts

	100 g Fe / 2 g K	100 g Fe/ 10 g K
Catalyst stability with TOS	high	medium
Catalyst stability at high $CO_2$ conversion	lower	higher
Activity, $r_{FT}/r_{CO_2-sh}$	high ( $Y_{CO}$ low)	low ( $Y_{CO}$ high)
Hydrocarbon selectivity	$C_1$ , $C_{2-4}$ , alkanes	$C_{2-4}$ , $C_{5+}$ , alkenes

- 100 g Fe / 10 g K is an example of a catalyst that allows high  $CO_2$  conversion values, but due to its low FT activity, organic yield remains low. FT activity becomes higher with temperature and modified residence time, but under these conditions C-containing compounds deposit on the catalyst bed and cause blockage and high pressure drop.
- 100 g Fe / 2 g K is an example of a catalyst with a high FT activity, consequently almost no CO is present in the final product and  $CO_2$  conversion correlates directly with organic yield. In this case the limitation to reach high organic yield values is the oxidation of the catalyst due to  $H_2O$  formation. Above a certain level of the ratio  $(p_{H_2O}/p_{H_2})_{out}$ , the iron catalyst starts to modify its composition (iron carbides are

transformed to iron oxides), making high  $\text{CO}_2$  conversion values almost impossible (Figure 10.3).

Based on the results obtained in this study, the 100 g Fe / 2 g K catalyst seems to be more attractive for the production of gaseous alkanes. High temperatures and modified residence times favour the formation of short chain hydrocarbons and  $\text{CO}_2$  conversion. However, above certain values, limitations on catalyst stability exist due to an increase in the  $(p_{\text{H}_2\text{O}}/p_{\text{H}_2})_{\text{out}}$  ratio (Figure 10.3). Reactor operation at high values of  $(\text{H}_2/\text{CO}_2)_{\text{in}}$  (e.g.  $(\text{H}_2/\text{CO}_2)_{\text{in}} = 22$ ) favour  $\text{CO}_2$  conversion and organic product yield without catalyst deactivation. Partial pressure of  $\text{H}_2\text{O}$  then remains low due to the excess of  $\text{H}_2$  (Figure 10.3).

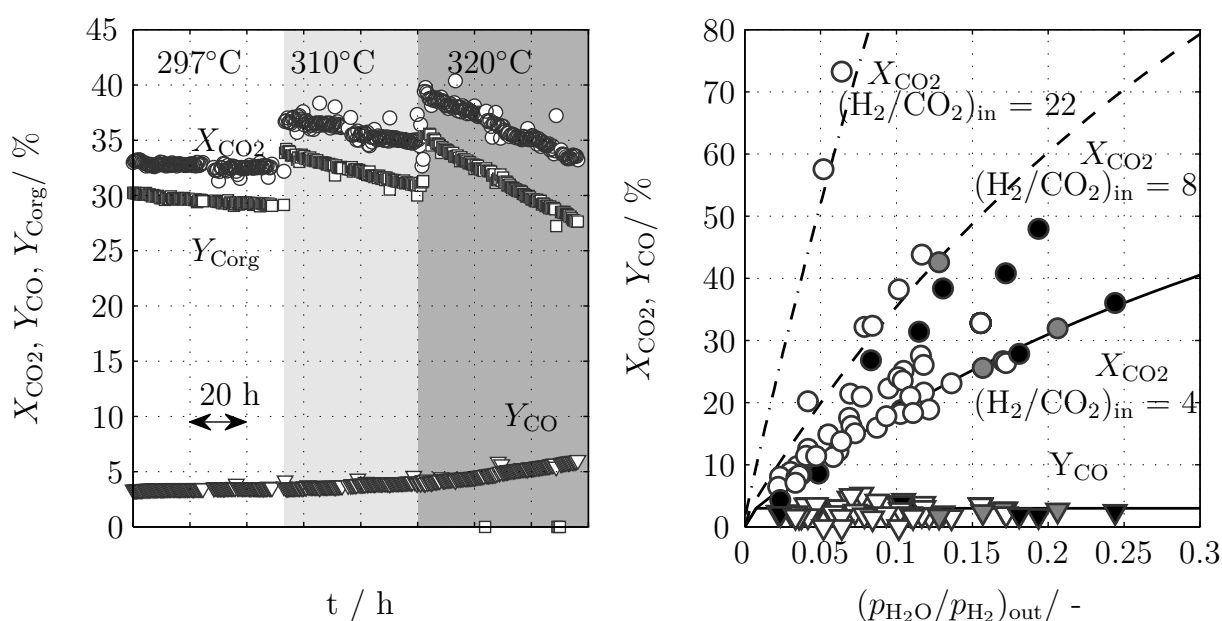


Figure 10.3: Left: effect of temperature over time on  $\text{CO}_2$  conversion  $X_{\text{CO}_2}$ , CO yield  $Y_{\text{CO}}$ , yield of organic components  $Y_{\text{Corg}}$ , at  $\tau_{\text{mod}} = 1000 \text{ kg s/m}^3$ ,  $\Delta t = 20 \text{ h}$ . Right: influence of  $(p_{\text{H}_2\text{O}}/p_{\text{H}_2})_{\text{out}}$  on  $\text{CO}_2$  conversion and CO yield. Curves based on stoichiometry, for orientation: solid  $(\text{H}_2/\text{CO}_2)_{\text{in}} = 4$ ; dashed  $(\text{H}_2/\text{CO}_2)_{\text{in}} = 8$ , dashed-dot  $(\text{H}_2/\text{CO}_2)_{\text{in}} = 22$ . Full symbols black: C-balance closed with an error  $> 5 \%$ . Full symbols grey: deactivation observed. White symbols: stable operation. Conditions:  $p = 1 - 2 \text{ MPa}$ ,  $(\text{H}_2/\text{CO}_2)_{\text{in}} = 4, 5, 8, 22$ ,  $T = 245 - 297 \text{ }^\circ\text{C}$  and  $\tau_{\text{mod}} = 175 - 5000 \text{ kg s/m}^3$ . Catalyst: 100 g Fe / 2 g K.

According to these results, if  $\text{CO}_2$  is selected as C-source, it seems challenging to find a catalyst (potassium content) able to reach high organic yield values without deactivation. An alternative could be the combination of  $\text{C}_{2-4}$  synthesis with a subsequent methane synthesis. That would enable the operation of the Fischer-Tropsch reactor at high

$(\text{H}_2/\text{CO}_2)_{\text{in}}$  ratios, and the production of gas mixtures according to H-gas specifications (DVGW 3.2013; DVGW 9.2011).

A set of kinetic parameter values is determined for the  $\text{CO}_2$ -shift and FT reaction based on experimental results with 100 g Fe / 2 g K under steady-state conditions. These parameters help to gain a fair understanding of the complex interplay between both reactions and additionally make possible a reactor scale-up. A mathematical model of the lab-scale fixed-bed reactor is required to integrate the molar flows along the catalyst bed and compare calculated and experimental values. The procedure is iterative with the aim to minimise the sum of square differences.

The results obtained in this thesis contribute to the field of the Fischer-Tropsch synthesis with systematic catalytic experiments using  $\text{CO}_2$  as C-source. Production of gaseous hydrocarbons for heating value adjustment from  $\text{H}_2$  and  $\text{CO}_2$  mixtures is possible, however constraints exist in the maximum yield of organic product due to catalyst deactivation in the presence of products ( $(p_{\text{H}_2\text{O}}/p_{\text{H}_2})_{\text{out}} \geq 0.1$ ) or at higher temperatures (above 300 °C).

### **Flexible operation of catalytic reactors**

In the context of Figure 10.1, flexible operation of the catalytic reactor may be motivated by the possibility to reduce the size of the  $\text{H}_2$  storage needed and consequently its investment cost. Flexible operation of catalytic chemical reactors is a field of research where a lot of aspects may play a role, with limited knowledge available at present (e.g. reaction engineering, catalyst and material behaviour, control strategies, heat integration, etc.) and with scarce examples in practical process applications today. The selective catalytic reduction (SCR) of  $\text{NO}_x$  is a successful example of flexible operation of a catalytic reaction. However, significant differences exist in comparison with a catalytic reaction that uses fluctuating  $\text{H}_2$ , mainly due to the strong dilution with air in the case of SCR, which reduces the heat effects and the concentration of reactants to be converted.

Within this work, different methods have been developed to evaluate the restrictions that catalyst and large-scale reactor design could impose on the attainable reactor flexibility (i.e. temperature control, pressure drop). These methods combine experimental work in the lab-scale setup with mathematical modelling of the setup and a larger-scale reactor.

#### *i) Catalyst behaviour under variable operating conditions*

Solid catalysts are delicate components of the reaction system and as such may be sensitive to variations in reaction mixture composition or temperature. The catalyst itself can undergo significant changes due to its interaction with reagents, e.g. variations in the surface structure and near-surface composition affecting its catalytic properties (Boreskov et al. 1983).

Forced periodic operation was intensively studied during the 80's and 90's with the aim of



improving catalyst activity and selectivity compared to steady-state operation. Numerous studies can be found in literature for different reactions (Boreskov et al. 1983; Silveston et al. 1995). These experiments are helpful to get a better understanding of the catalytic system and its interactions with the fluid phase. However, the reported variations on the gas phase are strong (often using a pure reactant during some time) and not relevant for the dynamic operation expected in the context of the electricity-to-fuel process (Figure 10.1). In this context, due to the use of a H<sub>2</sub> storage, the expected variations on the gas phase composition are milder than those reported in periodic experiments.

Three different methods are developed to determine whether the activity and selectivity of the 100 g Fe / 2 g K vary due to variations in the reaction mixture composition, flow and/or temperature: (1) step change experiments combined with mathematical modelling, (2) in-situ techniques: magnetometer and X-Ray Diffractometry (XRD) and (3) periodic changes. Variations are carried out under relevant industrial conditions (in the range where kinetic parameters were determined under steady-state conditions) and under “extreme” conditions, where no steady-state kinetics are available (examples in Figures 10.4 and 10.5):

- Variations under relevant industrial conditions: no changes to the catalyst state (i.e. chemical composition, surface structure, and catalytic properties) can be observed at variable operating conditions, in the range of conditions where kinetic parameters were determined. All three methods indicate that catalyst activity remains constant under variable operating conditions and can be described by the set of kinetic parameters determined under steady-state conditions.
- Variations under “extreme” conditions: changes to the catalyst’s chemical composition and properties were observed when the reactor was operated under “extreme” conditions (e.g. pure H<sub>2</sub> atmosphere, high temperatures), using step changes (Figure 10.4) and in-situ methods (Figure 10.5) (here, no periodic changes were carried out). Under these conditions, the catalyst activity could not be described by the set of kinetic parameters determined under steady-state conditions.

Figure 10.4 shows a representative example of a step change experiment in inlet concentration, from pure H<sub>2</sub> to a (H<sub>2</sub>/CO<sub>2</sub>)<sub>in</sub> mixture, combined with mathematical modelling. The mathematical model (with kinetic parameter values determined under steady-state conditions) can describe the transient behaviour of CO<sub>2</sub>, which indicates that the CO<sub>2</sub>-shift activity (CO<sub>2</sub>-shift active sites: Fe<sub>3</sub>O<sub>4</sub>) seems to be unaffected by the presence of pure H<sub>2</sub>. However, the mathematical model is not able to describe the transient behaviour of the CO, CH<sub>4</sub>, or C<sub>2</sub>H<sub>6</sub> flows. It seems that after two hours under H<sub>2</sub> atmosphere, the iron-based catalyst has lost part of the Fischer-Tropsch activity, due to the hydrogenation of the iron carbides (FT active sites: F<sub>x</sub>C<sub>y</sub> (Riedel et al. 2003)) to iron metal. This result

was confirmed using in-situ measurements in a magnetometer, where the high magnetisation values under  $H_2$  atmosphere, due to the presence of iron-metal, contrast with the low magnetisation values under  $H_2/CO_2$  gas mixture, due to the presence of iron carbides (Figure 10.5).

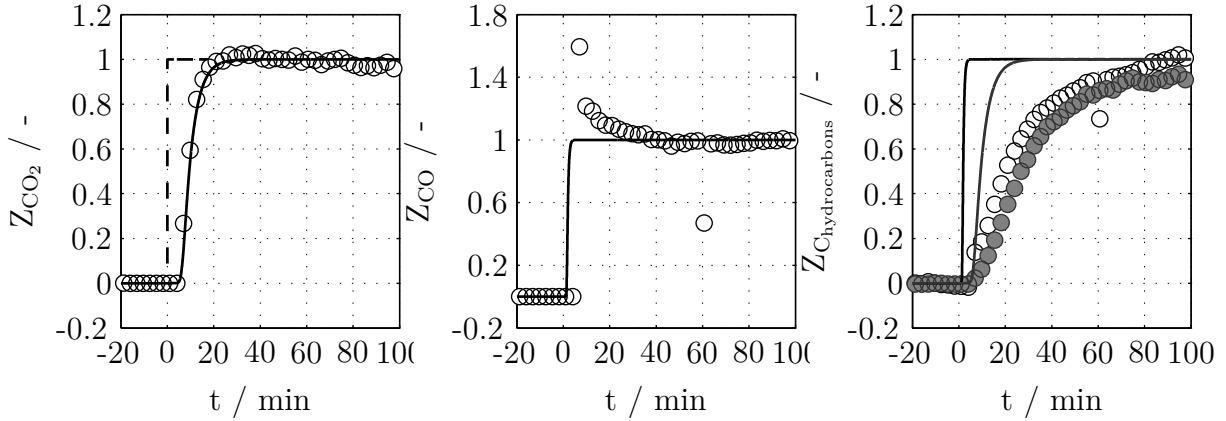


Figure 10.4: Dimensionless change of  $CO_2$ ,  $CO$ , and  $C$  in hydrocarbon outlet flows after a concentration change from  $H_2$  to  $(H_2/CO_2)_{in} = 5$  “Hot-stand-by”. Curves: calculated with mathematical model, broken line: change in inlet flow. Symbols: experimental results measured with Micro-GC at setup outlet. Grey symbols:  $C$  in  $C_2H_6$  and white symbols:  $C$  in  $CH_4$  (right). Conditions:  $F_{v,in,STP,H_2} = 300 \text{ cm}^3/\text{min}$ ,  $F_{v,in,STP,(H_2/CO_2)_{in}=5} = 309.3 \text{ cm}^3/\text{min}$ ,  $\tau_{mod,target} = 400 \text{ kg s}/\text{m}^3$ ,  $p = 1 \text{ MPa}$ ,  $T = 264 \text{ }^\circ\text{C}$ . Catalyst:  $100 \text{ g Fe} / 2 \text{ g K}$

The results show the potential of the approach followed and the complementary information obtained from the different methods used. A plausibility check of the results is also possible by comparison. These results are helpful in the design of a part-load reactor because they indicate under which conditions the reactor should not be operated to avoid catalyst deactivation/reduction. In the special case of the FT synthesis with iron, it has been shown that the formation and hydrogenation of iron carbides is reversible and highly dynamic.

*ii) Pre-feasibility study on flexible operation of industrial-scale fixed-bed reactor*

An industrial-scale multitubular fixed-bed reactor with recycle is proposed to carry out the  $CO_2$  hydrogenation to gaseous hydrocarbons under flexible load conditions (i.e. operation within a load range always satisfying that conversion and selectivity are according to specifications) (Figure 10.6). The configuration with recycle considers a reactor with product separation and recycle of  $H_2$  and  $CO_2$  together with the intermediate product  $CO$ . This configuration has an extra design variable available compared with the one-pass reactor, the conversion per pass or recycle ratio, and this is advantageous for variable load operation. The characteristics of the recycle system are determined by specific lim-

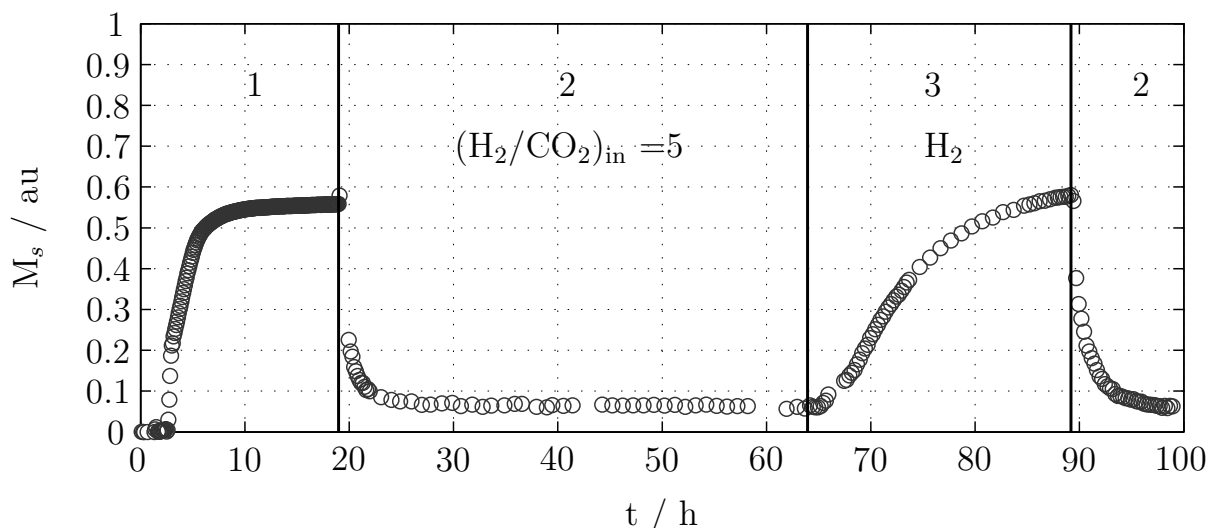


Figure 10.5: Saturation magnetisation  $M_s$  measured with the magnetometer during catalyst reduction (1), catalyst formation (2), and variations in operating conditions. Reduction conditions (1):  $T = 400\text{ }^\circ\text{C}$  during 16 h,  $p = 0.1\text{ MPa}$ ,  $(\text{H}_2/\text{Ar})_{\text{in}} = 1/3$ ,  $\tau_{\text{mod}} = 300\text{ kg s/m}^3$ ; formation conditions (2):  $T = 300\text{ }^\circ\text{C}$ ,  $p = 1.13\text{ MPa}$ ,  $(\text{H}_2/\text{CO}_2)_{\text{in}} = 5$ ,  $\tau_{\text{mod}} = 353\text{ kg s/m}^3$ . Operating conditions at (3):  $T = 300\text{ }^\circ\text{C}$ ,  $p = 1.13\text{ MPa}$ ,  $(\text{H}_2/\text{CO}_2)_{\text{in}} = \infty$ . Catalyst: 100 g Fe / 10 g K

itations of the catalyst system. The most relevant parameters in the case of the  $\text{CO}_2$  hydrogenation are the heat of reaction and the deactivation of the catalyst in the presence of products  $(p_{\text{H}_2\text{O}}/p_{\text{H}_2})_{\text{out}} > 0.1$  (Figure 10.3). A procedure to design a flexible reactor system is proposed based on steady-state and non-steady-state balance equations and experimental data previously collected in the lab-scale setup (i.e. set of kinetic parameters determined based on experiments under steady-state conditions and information gained during transient experiments).

The use of a recycle allows the operation of the reactor under more favourable conditions compared with a one-pass reactor: (i) high average reaction rates along the catalyst bed can be achieved due to the presence of CO (intermediate product) at reactor inlet and a lower partial pressure of  $\text{H}_2\text{O}$ , (ii) heat removal is more effective due to the higher gas velocities, (iii) overall high conversion is possible, and (iv) the  $(\text{H}_2/\text{CO}_2)_{\text{in}}$  ratio can be adjusted in the reactor which may be above the stoichiometric ratio. The  $(\text{H}_2/\text{CO}_2)_{\text{in}}$  ratio is the only operational variable which has the potential to enable high  $\text{CO}_2$  conversion and hydrocarbon yield at low  $(p_{\text{H}_2\text{O}}/p_{\text{H}_2})_{\text{out}}$  ratios (Figure 10.3). The disadvantages of recycle reactors are, however, related to high operational costs (i.e. high energy demand), large separation units, need of a recycle gas compressor, repeated heating and cooling, and loss of material due to the purge.

A crucial point of this configuration might be the behaviour of the separation units under variable load conditions. The separation of  $\text{H}_2$ ,  $\text{CO}_2$ , and  $\text{CO}$  from  $\text{H}_2\text{O}$  and hydrocarbons is not an easy task and requires cryogenic cooling at temperatures around  $-70\text{ }^\circ\text{C}$  to separate  $\text{H}_2$  from light hydrocarbons, after the removal of  $\text{CO}_2$  in a  $\text{CO}_2$ -scrubber.

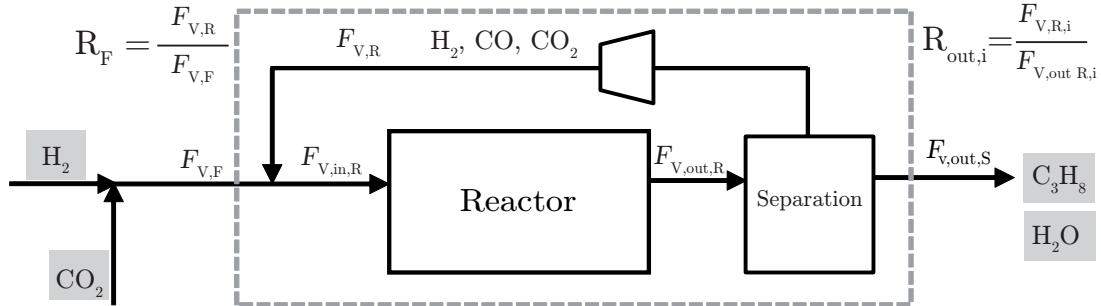


Figure 10.6: Recycle reactor used for the  $\text{CO}_2$  hydrogenation. Separation units assumed as an ideal system.

An example multitubular fixed-bed reactor with recycle is conceptually designed to be operated between 70 - 100 % load according to the procedure developed. The desired minimal overall conversion of  $\text{CO}_2$  is 90 %, provided that temperature is lower than  $300\text{ }^\circ\text{C}$  and the value of the  $(p_{\text{H}_2\text{O}}/p_{\text{H}_2})_{\text{out}}$  ratio is below 0.1 (Figure 10.3). The selected basis for calculation is  $F_{\text{v,CO}_2,\text{average,STP}} = 500\text{ m}^3/\text{h}$ , according to the  $\text{CO}_2$  typically produced in a biogas plant. Transient operation from maximum to minimum load (100 - 70 %) with a selected rate of load change of 5 % / min is described using non-steady-state mathematical models. Calculated results shown that transient operation does not seem to be a problem for the fixed-bed reactor, if the reactor is properly designed according to maximum and minimum flow and catalyst limitations are considered (e.g.  $T_{\text{max}} = 300\text{ }^\circ\text{C}$ ,  $(p_{\text{H}_2\text{O}}/p_{\text{H}_2})_{\text{out,max}} = 0.1$ ). Temperature and  $(p_{\text{H}_2\text{O}}/p_{\text{H}_2})_{\text{out}}$  limitations are never exceeded (Figure 10.7). The transient temperature profile is strongly influenced by the catalyst density and heat capacity, both responsible for the dynamic thermal behaviour of the bed. Due to the use of a relatively low rate of change, changes are smooth along the catalyst bed.

The decisions made in reactor design are often the most important of the whole chemical plant because they determine the separation chains, compression requirements, heat requirements, etc. However information about reactor-attached equipment should be included in the mathematical model to further analyse the dynamic behaviour of the overall chemical process. It is expected that reactor-attached equipment plays an important role in the flexibility of industrial-scale processes, in a similar way as observed during transient experiments on lab-scale.

The concept of characteristic times has been used to show in a simplified way the effect

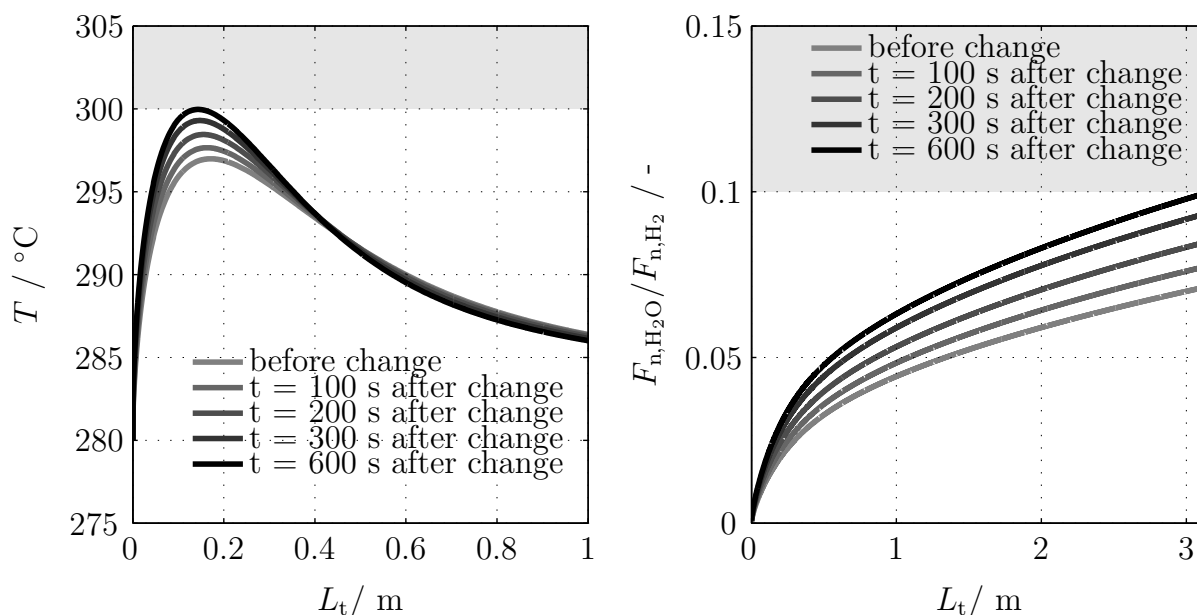


Figure 10.7: Calculated axial profiles of temperature and ratio of molar flow ( $p_{\text{H}_2\text{O}}/p_{\text{H}_2}$ )<sub>out</sub> along the catalyst bed at different times after a change in reactor load i.e. fresh feed flow with a rate of 5 %/ min from 100 % load to 70 % load. Grey: not acceptable for catalyst stability reasons, Figure 10.3.

that the individual processes involved in a chemical plant have in the dynamic response of the system. Processes involving chemical reaction, mass and heat transfer take place at different time and length scales (i.e. catalyst particle, reactor and attached equipment). The comparison of the characteristic times of the different processes with the characteristic time of the inlet disturbance may help to simplify the number of processes that need to be considered in the mathematical model of the process. Characteristic times are defined for different processes based on dimensionless balance equations and calculations for the example fixed-bed reactor with recycle.

In general, all reactions using hydrogen as reactant have the potential to be operated under flexible conditions due to the fluctuating nature of hydrogen when produced from renewable sources. Characteristic aspects regarding flexible operation of fixed-bed reactors for other fuel related synthesis (i.e. methane synthesis, low-temperature (LT)-Fischer-Tropsch reaction, methanol-to-hydrocarbons) are outlined and qualitatively discussed, based on information from literature. Methanol, dimethylether, and methane syntheses can be seen as routes relatively easy to be operated under flexible conditions, due to the high and robust selectivity of the desired product, with limited sensitivity towards temperature variations and catalyst stability. The LT-Fischer-Tropsch synthesis, Methanol-to-Gasoline, and CO<sub>2</sub> hydrogenation to gaseous hydrocarbons can be seen as more complex processes in this respect.

### Conclusions and outlook

This thesis demonstrates that gaseous hydrocarbons for heating value adjustment can be produced from  $\text{H}_2$  and  $\text{CO}_2$  using an iron-based catalyst promoted with potassium (100 g Fe / 2 g K). Catalytic constraints have been identified, limiting the maximum yield of organic product due to catalyst deactivation in the presence of products ( $p_{\text{H}_2\text{O}}/p_{\text{H}_2}$ )<sub>out</sub>  $\geq$  0.1 or at higher temperature (above 300 °C). The molar feed ratio ( $\text{H}_2/\text{CO}_2$ )<sub>in</sub> is the most promising variable in order to reach high  $\text{CO}_2$  conversion and hydrocarbon yield without catalyst deactivation. Hydrocarbon product selectivity depends strongly on the content of potassium on the catalyst.

Flexible operation of chemical reactors is motivated by the possibility to reduce  $\text{H}_2$  storage, however limited knowledge is available at the moment. Methods to evaluate potential limiting factors of reactor flexibility (i.e. catalyst behaviour, reactor design) have been developed and applied to a catalytic fixed-bed reactor, using  $\text{CO}_2$  hydrogenation to gaseous hydrocarbons as example reaction.

This thesis concludes that the flexibility of the chemical process is directly related to the characteristics of the chemical reaction, this would determine the complexity of reactor design and reactor-attached equipment. Economic evaluation of the overall process is required to further evaluate the potential of flexible operation of chemical plants. The methods developed in the present study can be used to investigate the dynamic behaviour of catalytic synthesis reactors in other fuel-related processes.

# 11 Zusammenfassung

## Einleitung und Zielsetzung

Schätzungen gehen davon aus, dass die Weltbevölkerung im Jahre 2050 9 Milliarden Menschen umfasst. In diesem Zusammenhang kann der Übergang des Energiesystems, von fossilen Energieträgern zu erneuerbaren Energien, ökonomisches Wachstum bei niedrigen energiebezogene Emissionen ermöglichen (IEA 2015; Jess et al. 2011). Dieser Übergang stellt jedoch eine große Herausforderung für die heutige Weltgemeinschaft dar, welche nur durch die erfolgreiche Entwicklung und Einbindung effektiver und ökonomisch tragbarer, neuer Technologien in das bestehende Energiesystem bewältigt werden.

Die zukünftige Primärenergiebereitstellung wird zu einem Großteil auf Elektrizität aus erneuerbaren Quellen mit fluktuierender Erzeugungscharakteristik, wie z.B. Wind- und Solarenergie, basieren. Zukünftig werden weiterhin chemische Energieträger für mobile und andere Anwendungen notwendig sein, daher kann die Wandlung von Elektrizität in chemische Energieträger unter diesen Randbedingungen wichtig werden. Beispielsweise kann fluktuierende Elektrizität mittels Wasserstoff als Zwischenprodukt in Kohlenwasserstoffenergieträger umgewandelt werden, wodurch fossile Energieträger ersetzt werden können und eine attraktive Möglichkeit der Langzeitspeicherung in Überschusssituationen bezüglich elektrischer Energie zur Verfügung steht. Abbildung 11.1 zeigt ein vereinfachtes Blockfließbild eines ‘Electricity-to-fuel’ Prozesses mit einer Elektrolyse zur Produktion von Wasserstoff, einem Wasserstoffspeicher und einem katalytischen Synthesereaktor.

Mögliche Quellen konzentrierten Kohlenstoffdioxids sind die Biomassefermentation zur Erzeugung von Ethanol bzw. Biogas, die Biomasseverbrennung oder -vergasung (Erzeugung eines Produktgases aus  $\text{CO}_2$  und  $\text{CO}$ ) und industrielle Prozesse wie die Eisen- bzw. Stahlerzeugung und die Kalzinierung in der Zementherstellung. Die Gewinnung von  $\text{CO}_2$  aus der Luft wird in der Literatur trotz des hohen Energiebedarfs ebenfalls als eine mögliche  $\text{CO}_2$ -Quelle angesehen (Jess et al. 2011; Weimer et al. 1996; Zeman 2007).

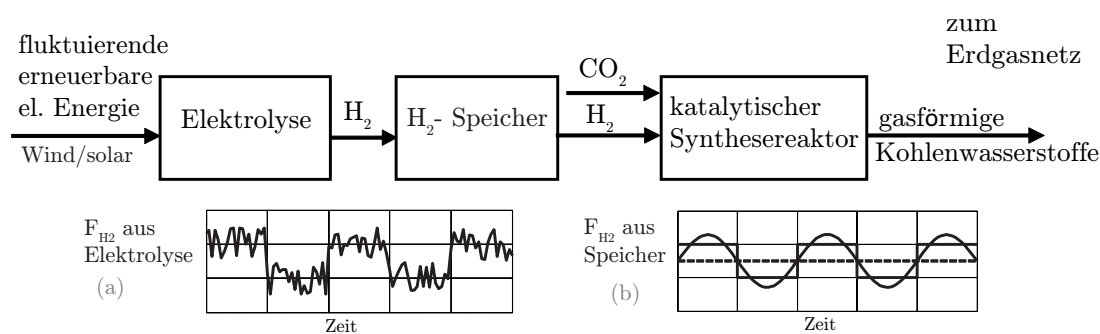


Abbildung 11.1: Prozess zur Erzeugung gasförmiger Kohlenwasserstoffe aus erneuerbarer Elektrizität mit  $H_2$  als Zwischenprodukt. (a) Beispiel  $H_2$ -Strom aus  $H_2O$ -Elektrolyse aus fluktuierender Elektrizität, (b) Beispiel  $H_2$ -Strom aus  $H_2$ -Speicher zur Erzeugung gasförmiger Kohlenwasserstoffe mit  $CO_2$ ; gestrichelte Linie: großer  $H_2$ -Speicher und stationär betriebener katalytischer Synthesereaktor; durchgezogene Linie: kleiner  $H_2$ -Speicher mit zwei verschiedenen Regelungsstrategien und variabel betriebenen katalytischen Synthesereaktor.

Die vorliegende Arbeit behandelt zwei verschiedene Aspekte:

- Erzeugung gasförmiger Kohlenwasserstoffenergieträger ( $C_2H_6$ ,  $C_3H_8$ ,  $C_4H_{10}$ ) aus Wasserstoff und Kohlenstoffdioxid zur Anpassung des Brennwertes von Methan (roh SNG): Das Ziel ist es, ein tieferes Verständnis der  $CO_2$ -Hydrierung an einem Eisenkatalysator zu erlangen und geeignete Betriebsbedingungen zu ermitteln.
- Grundlegende Auslegung eines Festbettreaktors für flexiblen Betrieb (Betrieb bei variabler Last mit häufigen Lastwechseln und verschiedenen Lastwechselraten): Die Zielsetzung umfasst (i) die Identifikation der allgemeinen Aspekte variabler Betriebsweise und deren Limitierungen in einem Festbettreaktor mit der  $CO_2$ -Hydrierung als Beispielreaktion und (ii) die Entwicklung von Methoden, um den variablen Reaktorbetrieb mit Hilfe einer Kombination von Experimenten und auf mathematischen Modellen basierenden Konzeptstudien zu untersuchen.

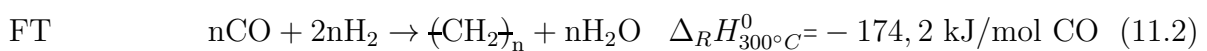
### **$CO_2$ -Hydrierung zur Erzeugung gasförmiger Kohlenwasserstoffe: Brennwertanpassung**

In der Literatur finden sich Studien in denen die Erzeugung von Kohlenwasserstoffen ausgehend von  $H_2$  und  $CO_2$  behandelt wird. In den meisten Fällen sollen entweder kurzkettige Alkene als Grundchemikalien oder langkettige Alkane zur Nutzung als chemischer Energieträger erzeugt werden. Die Mehrheit dieser Untersuchungen befasst sich mit dem Einfluss des Katalysatorpromotors bei konstanten Betriebsbedingungen. Nur wenige Untersuchungen behandeln, wie in der vorliegenden Untersuchung, den Einfluss der



Betriebsbedingungen auf das Reaktionsnetzwerks.

Die CO<sub>2</sub>-Hydrierung zur Erzeugung von Kohlenwasserstoffen wird in vorausgegangenen Untersuchungen als katalytische Zwei-Schritt-Reaktion mit CO als Zwischenprodukt beschrieben (Gleichungen 11.1 und 11.2)(Lee et al. 1992; Riedel et al. 2001). Durch die Fischer-Tropsch-Reaktion wird CO entfernt, welches durch die CO<sub>2</sub>-Shift-Reaktion erzeugt wird. Dadurch kann der CO<sub>2</sub>-Umsatz erhöht werden. Allerdings kann das bei beiden Reaktionen gebildete H<sub>2</sub>O einen negativen Einfluss auf die Katalysatoraktivität haben (Lee et al. 1990).



Eisenbasierte Katalysatoren werden aufgrund ihrer Bifunktionalität (CO<sub>2</sub>-Shift und Fischer-Tropsch) als die vielversprechendsten Katalysatoren angesehen. Kalium ist der, auf eisenbasierten Katalysatoren, am häufigsten eingesetzte Promotor und beeinflusst Aktivität und Selektivität (begünstigt: Adsorption von Kohlenstoff am Aktivzentrum, daraus folgt hohe CO<sub>2</sub>-Shift-Aktivität, Erzeugung langkettiger Kohlenwasserstoffe und Inhibierung von Sekundärreaktionen) (Schulz 2014). Zwei mit Kalium promotierte Katalysatoren (100 g Fe / 2 g K und 100 g Fe / 10 g K) wurden für die vorliegende Arbeit ausgewählt, um die Einflüsse der Reaktionsbedingungen und des Kaliumgehalts auf den CO<sub>2</sub>-Umsatz, die Kohlenwasserstoffausbeute und die Kohlenwasserstoffproduktselektivität zu untersuchen.

Das gewünschte Produkt (C<sub>2</sub>H<sub>6</sub>, C<sub>3</sub>H<sub>8</sub>, C<sub>4</sub>H<sub>10</sub>) für die Brennwertanpassung von Erdgassubstitut kann LPG (liquefied petroleum gas) ersetzen. Die Kohlenwasserstoffproduktverteilung, die mit der Fischer-Tropsch-Synthese erreicht wird, hängt sowohl von den Reaktionsbedingungen (z.B.  $T$ ,  $p$ ,  $(\text{H}_2/\text{CO}_2)_{\text{ein}}$ ) als auch von der Katalysatorzusammensetzung ab. Wegen der Ähnlichkeit der Fischer-Tropsch-Reaktion zu einer Polymerisationsreaktion wird eine Vielzahl an Produkten mit unterschiedlicher Kettenlänge erzeugt. Das Primärprodukt der FT-Synthese sind  $\alpha$ -Alkene, daher ist ein Hydrierungsschritt notwendig um die gewünschten Alkane zu erzeugen. Die Fischer-Tropsch-Kohlenwasserstoffproduktverteilung kann mathematisch über das Anderson-Schulz-Flory-Modell beschrieben werden. In diesem Modell wird die FTS als ideale Polymerisationsreaktion angesehen. Die Kohlenwasserstoffproduktverteilung kann demnach mit einem einzelnen Parameter, dem Parameter für die Kettenwachstumswahrscheinlichkeit  $\alpha$  (gebildet aus der Kettenwachstums- und Kettenabbruchsgeschwindigkeit), beschrieben werden. Abbildung 11.2 zeigt die Massenanteile der Kohlenwasserstoffe als Funktion der Kettenwachstumswahrscheinlichkeit  $\alpha$ . Die Kurven sind mit dem ASF-Modell berechnet, die Symbole entstammen eigenen experimentellen Untersuchungen.

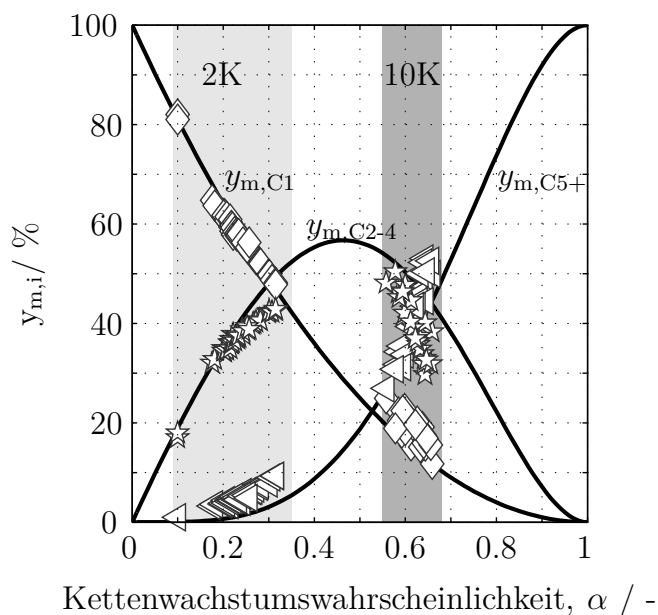


Abbildung 11.2: Experimentell gemessene Kohlenwasserstoffproduktverteilung in Gewichts-% für 100 g Fe / 2 g K und 100 g Fe / 10 g K. Kurven gerechnet mit Anderson-Schulz-Flory-Modell (ASF). Betriebsbedingungen:  $p = 1 - 2$  MPa,  $(\text{H}_2/\text{CO}_2)_{\text{ein}} = 4, 5, 8, 22$ ,  $T = 245 - 297$  °C und  $\tau_{\text{mod}} = 175 - 5000$  kg s/m<sup>3</sup>.

Der Hauptteil der experimentellen Arbeit wurde in einer neu konzipierten und gebauten Laboranlage mit einem Festbettreaktor durchgeführt. Unterstützende Experimente einschließlich in-situ und ex-situ Untersuchungen zur Charakterisierung des Katalysators wurden am ‘Centre of Catalysis Research’ an der Universität von Kapstadt (Arbeitsgruppe Prof. M. Claeys), mit dem Ziel, den Effekt von Kalium auf die Reduktions- und die Formierungsprozesse zu zeigen, durchgeführt (z.B. Abbildung 11.5). Die Abbildung 11.2 zeigt, dass beide Katalysatoren im gleichen Bereich der Reaktionsbedingungen eine ähnliche Selektivität für die Fraktion C<sub>2-4</sub> aufweisen. Methan und C<sub>5+</sub> sind immer im Kohlenwasserstoffproduktgemisch vorhanden, allerdings nicht im gleichen Ausmaß: Für den 100 g Fe / 10 g K Katalysator wird eine größere Fraktion C<sub>5+</sub> gebildet, welche nicht für die Brennwertanpassung zur Verfügung steht und abgetrennt werden muss, um zur Nutzung als chemischer Energieträger für mobile Anwendungen weiter aufbereitet zu werden (die Kohlenwasserstoffe bestehen zum Großteil aus Alkenen). Im Gegensatz dazu ist Methan das Hauptprodukt des 100 g Fe / 2 g K-Katalysators bei gleichzeitig niedriger Bildungsrate von C<sub>5+</sub>. Das Produktgas eignet sich daher als Zumischgas für die Brennwertanpassung und kann im Erdgasnetz gespeichert werden (die erzeugten Kohlenwasserstoffe liegen größtenteils als Alkane vor). Die Katalysatorwahl hängt maßgeblich davon ab wie das Nebenprodukt genutzt werden kann (z.B. vom Standort der Anlage).

Die größte Herausforderung der CO<sub>2</sub>-Hydrierung stellt das Erreichen hoher Ausbeute

an organischen Komponenten bei gleichzeitiger Unterdrückung der Methanbildung dar. Basierend auf den in dieser Arbeit angestellten Untersuchungen zweier eisenbasierter Katalysatoren kann folgendes geschlussfolgert werden (Tabelle 11.1):

- Der 100 g Fe / 10 g K Katalysator ist ein Beispiel für einen Katalysator der hohe CO<sub>2</sub>-Umsätze erlaubt aber aufgrund seiner geringen FT-Aktivität geringe Ausbeuten an organischen Komponenten aufweist. Die FT-Aktivität nimmt mit der Temperatur und der modifizierten Verweilzeit zu. Allerdings lagern sich unter diesen Bedingungen C-haltige Komponenten im Katalysatorbett ab und führen zur Verstopfung des Bettes und einem hohen Druckverlust über die Schüttung.
- Der 100 g Fe / 2 g K Katalysator ist ein Beispiel für einen Katalysator mit einer hohen FT-Aktivität. Daher ist fast kein CO im Produktgas vorhanden und der CO<sub>2</sub>-Umsatz korreliert direkt mit der Ausbeute an organischen Komponenten. In diesem Fall werden hohe Ausbeuten an organischen Komponenten durch die Oxidation des Katalysators aufgrund der Bildung von H<sub>2</sub>O verhindert. Oberhalb eines gewissen  $(p_{\text{H}_2\text{O}}/p_{\text{H}_2})_{\text{aus}}$ -Verhältnisses verändert der eisenbasierte Katalysator seine Zusammensetzung (Eisenkarbide wandeln sich in Eisenoxide um). Dies macht hohe CO<sub>2</sub>-Umsatz unmöglich (Abbildung 11.3).

Tabelle 11.1: Vergleich eisenbasierter Katalysatoren

	100 g Fe / 2 g K	100 g Fe/ 10 g K
Katalysatorstabilität mit TOS	hoch	mittel
Katalysatorstabilität bei hohem CO <sub>2</sub> -Umsatz	niedriger	höher
Aktivität, $r_{\text{FT}}/r_{\text{CO}_2\text{-sh}}$	hoch ( $Y_{\text{CO}}$ niedrig)	niedrig ( $Y_{\text{CO}}$ hoch)
Kohlenwasserstoffselektivität	C <sub>1</sub> , C <sub>2-4</sub> , Alkane	C <sub>2-4</sub> , C <sub>5+</sub> , Alkene

Basierend auf den Ergebnissen dieser Arbeit scheint der 100 g Fe / 2 g K Katalysator geeigneter für die Erzeugung gasförmiger Alkane zu sein. Hohe Temperaturen und modifizierte Verweilzeiten begünstigen die Bildung von kurzkettigen Kohlenwasserstoffen und hohe CO<sub>2</sub>-Umsätze. Allerdings werden oberhalb gewissen Temperaturen und Verweilzeiten zu hohe  $(p_{\text{H}_2\text{O}}/p_{\text{H}_2})_{\text{aus}}$ -Verhältnisse erreicht (Abbildung 11.3). Der Betrieb bei hohen  $(\text{H}_2/\text{CO}_2)_{\text{ein}}$ -Verhältnissen (z.B.  $(\text{H}_2/\text{CO}_2)_{\text{ein}} = 22$ ) begünstigt den CO<sub>2</sub>-Umsatz und die Ausbeute an organischen Komponenten, ohne dass der Katalysator desaktiviert, da der H<sub>2</sub>O-Partialdruck aufgrund des H<sub>2</sub>-Überschusses gering bleibt (Abbildung 11.3).

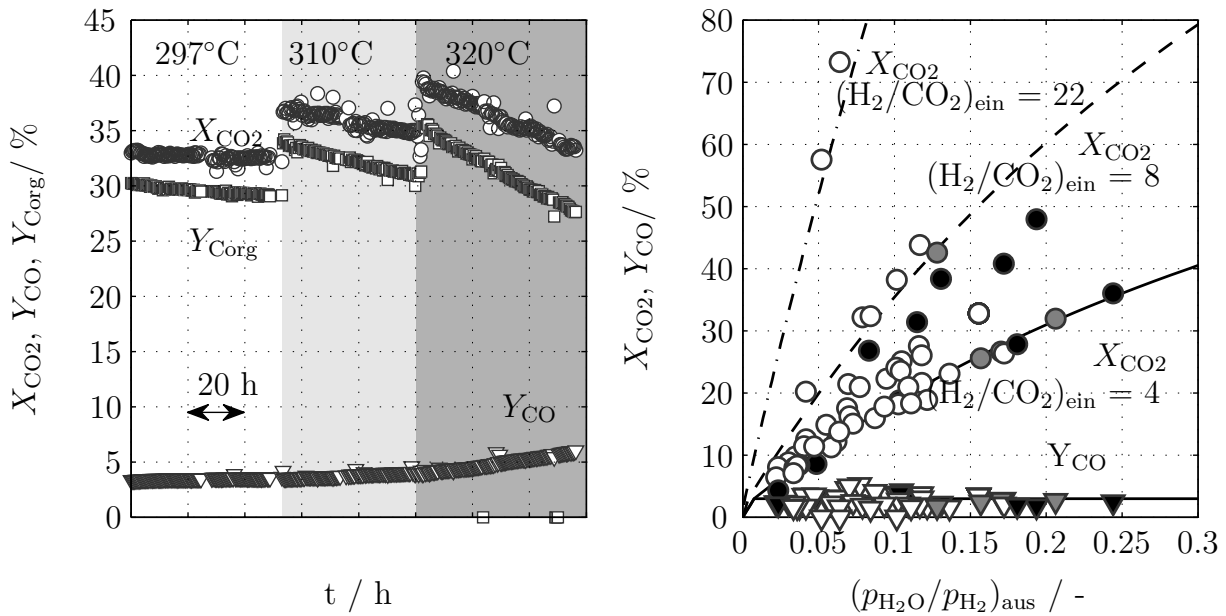


Abbildung 11.3: Links: Temperatureffekt auf CO<sub>2</sub>-Umsatz  $X_{CO_2}$ , CO Ausbeute  $Y_{CO}$ , Ausbeute an organischen Komponenten  $Y_{Corg}$ , über Zeit,  $\tau_{mod} = 1000$  kg s/m<sup>3</sup>,  $\Delta t = 20$  h. Rechts: Einfluss von  $(p_{H_2O}/p_{H_2})_{aus}$  auf CO<sub>2</sub>-Umsatz und CO Ausbeute. Kurven für  $X_{CO_2}$  zur Orientierung, gerechnet anhand der Stöchiometrie: durchgezogen  $(H_2/CO_2)_{ein} = 4$ ; gestrichelt  $(H_2/CO_2)_{ein} = 8$ , strichpunktiert  $(H_2/CO_2)_{ein} = 22$ . Symbole schwarz: C-Bilanz geschlossen mit einem Fehler  $> 5$  %. Symbole grau: Desaktivierung beobachtet. Symbole weiß: stabiler Zustand. Betriebsbedingungen:  $p = 1 - 2$  MPa,  $(H_2/CO_2)_{ein} = 4, 5, 8, 22$ ,  $T = 245 - 297$  °C and  $\tau_{mod} = 175 - 5000$  kg s/m<sup>3</sup>. Katalysator: 100 g Fe / 2 g K.

Entsprechend dieser Ergebnisse ist es eine besondere Herausforderung einen Katalysator (bzgl. des Kaliumgehalts) zu finden, mit dem ohne Katalysatordesaktivierung hohe Ausbeuten an organischen Komponenten aus CO<sub>2</sub> erzielt werden können. Eine Alternative würde die Kombination dieser Synthese mit einer anschließenden Methansynthese darstellen. Dies würde den Betrieb des Fischer-Tropsch-Reaktors bei hohen  $(H_2/CO_2)_{ein}$ -Verhältnissen und die Erzeugung eines Gases mit einer Zusammensetzung gemäß H-Gas Spezifikationen erlauben (DVGW 3.2013; DVGW 9.2011).

Kinetische Parameter wurden für die CO<sub>2</sub>-Shift und die FT-Reaktion auf Basis experimenteller Ergebnisse mit dem 100 g Fe / 2 g K Katalysator unter stationären Bedingungen bestimmt. Diese Parameter helfen, um ein gewisses Verständnis für die komplexe Verknüpfung beider Reaktionen zu erlangen. Außerdem kann mit Hilfe der kinetischen Parameter ein Reaktor-Scale-Up durchgeführt werden. Ein mathematisches Modell des Laborfestbettreaktors wird benötigt um die Stoffströme entlang des Katalysatorbettes zu integrieren und die berechneten Werte mit den experimentell ermittelten Werten zu ver-

gleichen. Dieses Vorgehen wird iterativ, mit dem Ziel die Fehlerquadrate zu minimieren, durchgeführt.

Die in dieser Arbeit erhaltenen Ergebnisse fügen sich in die aus der Literatur bekannten systematischen Untersuchungen der FTS mit  $\text{CO}_2$  als C-Quelle ein. Die Erzeugung gasförmiger Kohlenwasserstoffe für die Brennwertanpassung mittels  $\text{H}_2$  und  $\text{CO}_2$  ist möglich. Allerdings existieren Limitierungen für die maximale Ausbeute organischer Komponenten, da eine Desaktivierung des Katalysators in Gegenwart der Produkte ( $(p_{\text{H}_2\text{O}}/p_{\text{H}_2})_{\text{aus}} > 0,1$ ) oder bei hohen Temperaturen (oberhalb  $300\text{ }^\circ\text{C}$ ) beobachtet wurde.

### Variabler Betrieb katalytischer Reaktoren

Der variable Betrieb des katalytischen Reaktors kann sich aufgrund einer Verkleinerung des  $\text{H}_2$ -Speichervolumens und damit der Investitionskosten lohnen (Abbildung 11.1). Die variable Betriebsweise katalytischer, chemischer Reaktoren ist ein Forschungsbereich in dem viele Aspekte eine Rolle spielen können (bzgl. Reaktionstechnik, Katalysator- und Materialverhalten, Regelungstechnik, Wärmeintegration, etc.) und wenige aktuelle, praktische Anwendungsfälle existieren. Die selektive katalytische Reduktion (SCR) von  $\text{NO}_x$  ist ein Beispiel für eine variable Betriebsweise eines katalytischen Reaktors, welche erfolgreich angewendet wird. Allerdings existieren entscheidende Unterschiede bezüglich der hohen Verdünnung mit Luft im Fall der SCR, welche die spezifische Wärmefreisetzung und die Konzentration an umzusetzenden Edukten reduziert, im Vergleich mit einer katalytischen Reaktion, die einen fluktuierenden  $\text{H}_2$ -Strom nutzt.

Innerhalb dieser Arbeit wurden verschiedene Methoden entwickelt, um zu untersuchen, inwiefern der Katalysator und die Auslegung des großskaligen Reaktors die Reaktorflexibilität limitieren (z.B. Temperaturkontrolle, Druckverlust). Diese Methoden kombinieren experimentelle Arbeiten in der Laboranlage mit mathematischer Modellierung des Versuchsaufbaus und eines großskaligen Reaktors.

#### *i) Katalysatorverhalten bei variabler Betriebsweise*

Feststoffkatalysatoren sind empfindliche Komponenten des Reaktionssystems und können als solche sensibel gegenüber Änderungen der Reaktionsatmosphäre und der Reaktionstemperatur sein. Der Katalysator kann sich aufgrund seiner Interaktion mit den reagierenden Spezies verändern, z.B. können Änderungen der Oberflächenstruktur und der oberflächennahen Zusammensetzung die katalytischen Eigenschaften beeinflussen (Boreskov et al. 1983).

Aufgezwungene periodische Änderungen wurden in den 80er und 90er Jahren intensiv untersucht, um die Katalysatoraktivität und -selektivität im Vergleich zu stationärer Betriebsweise zu verbessern. Eine Vielzahl an Untersuchungen kann in der Literatur für verschiedene Reaktionen gefunden werden (Boreskov et al. 1983; Silveston et al. 1995). Die

se Untersuchungen helfen ein besseres Verständnis des katalytischen Systems und seiner Interaktion mit der fluiden Phase zu erlangen. Allerdings sind die berichteten Variationen der Gasphasenzusammensetzung groß (oftmals wird während einer bestimmten Zeit ein Reaktant pur zugegeben) und daher nicht relevant für die variable Betriebsweise des in dieser Arbeit vorgestellten Electricity-to-Fuel-Prozesses (Abbildung 11.1). In diesem Zusammenhang sind die erwarteten Änderungen der Gasphasenzusammensetzung aufgrund des H<sub>2</sub>-Speichers milder als die in der Literatur berichteten Gasphasenänderungen.

Drei verschiedene Methoden wurden entwickelt, um zu untersuchen, ob sich die Aktivität und die Selektivität des 100 g Fe / 2 g K-Katalysators aufgrund einer Variation der Gasphasenzusammensetzung, des Volumenstromes oder der Temperatur ändert: (1) Sprungversuche kombiniert mit mathematischer Modellierung, (2) in-situ-Techniken: Magnetometer und Röntgen-Diffraktometrie und (3) periodische Änderungen unter relevanten Bedingungen (im Bereich in dem die kinetischen Untersuchungen unter stationären Bedingungen durchgeführt wurden) und unter extremen Bedingungen für die keine stationäre Kinetik verfügbar ist (Beispiele in Abbildung 11.4 und 11.5).

- Variation unter relevanten industriellen Bedingungen: Es können keine Änderung des Katalysatorzustandes (d.h. chemische Zusammensetzung, Oberflächenstrukturen und katalytische Eigenschaften) für variable Betriebsbedingungen, im Bereich der Reaktionsbedingungen für den kinetische Parameter bestimmt wurden, festgestellt werden. Alle drei eingesetzten Methoden zeigen, dass die Katalysatoraktivität für variable Reaktionsbedingungen konstant bleibt und mit den unter stationären Bedingungen ermittelten kinetischen Parametern beschrieben werden kann.
- Variation unter extremen Bedingungen: Es wurden im Rahmen der Sprung- und in-situ-Versuche (Abbildung 11.4, und 11.5) Änderungen der chemischen Zusammensetzung des Katalysators und der Katalysatoreigenschaften während des Betriebs des Reaktors unter extremen Bedingungen festgestellt (z.B. reine H<sub>2</sub>-Atmosphäre, hohe Temperaturen) (Hier wurden keine periodischen Änderungen durchgeführt). Unter diesen Bedingungen konnte die Katalysatoraktivität nicht mit den unter stationären Bedingungen ermittelten kinetischen Parametern beschrieben werden.

Abbildung 11.4 zeigt ein repräsentatives Beispiel eines Versuches mit sprunghafter Änderung der Eingangskonzentration von reinem H<sub>2</sub> zu einer H<sub>2</sub>/CO<sub>2</sub>-Mischung zusammen mit den Ergebnissen der mathematischen Modellierung. Das mathematische Modell (mit unter stationären Bedingungen bestimmten kinetischen Parametern) kann das instationäre Verhalten von CO<sub>2</sub> beschreiben, was darauf hindeutet, dass die CO<sub>2</sub>-Shift-Aktivität (CO<sub>2</sub>-Shift-aktive Zentren: Fe<sub>3</sub>O<sub>4</sub>) unbeeinflusst von der Anwesenheit reinen Wasserstoffs ist. Allerdings, kann das mathematische Modell nicht das instationäre Verhalten der CO-, CH<sub>4</sub>- oder C<sub>2</sub>H<sub>6</sub>-Ströme beschreiben. Es zeigt sich, dass der eisenbasierte Katalysator nach zwei

Stunden unter Wasserstoffatmosphäre ein Teil seiner Fischer-Tropsch-Aktivität wegen der Hydrierung der Eisenkarbide zu metallischem Eisen (FT-aktive Zentren:  $F_xC_y$  (Riedel et al. 2003)) verloren hat. Dieses Ergebnis wurde mittels in-situ Messungen in einem Magnetometer bestätigt. Die Anwesenheit von metallischem Eisen unter  $H_2$ -Atmosphäre führt zu einer hohen Magnetisierung. Die unter  $H_2/CO_2$ - Atmosphäre vorliegende Eisencarbidphase führt hingegen zur einer niedrigeren Magnetisierung des Katalysators (Figure 11.5).

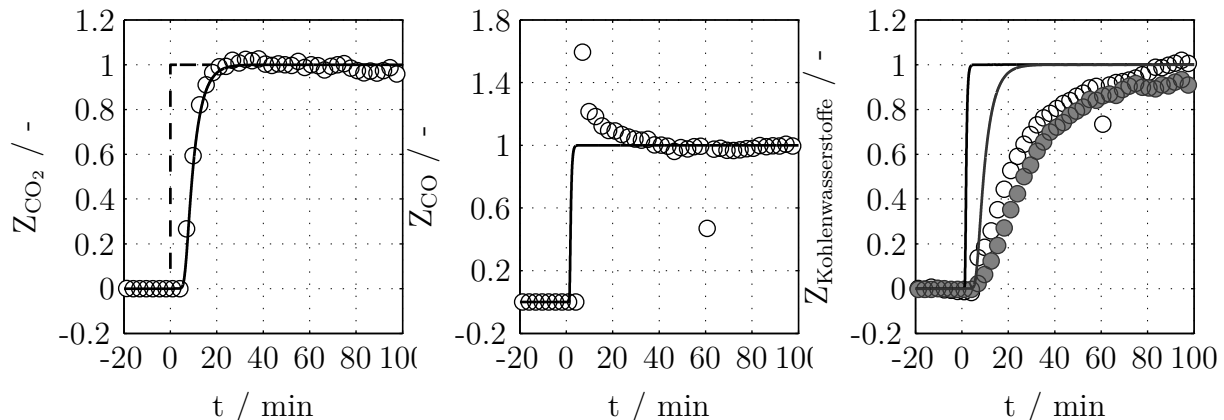


Abbildung 11.4: Normierte  $CO_2$ -,  $CO$ -, und Kohlenwasserstoffe-C-Austrittsströme nach Sprungänderung der Eintrittszusammensetzung von  $H_2$  (Schlumberbetrieb) zu  $(H_2/CO_2)_{\text{ein}} = 5$ . Kurven gerechnet mit mathematischem Modell, gestrichelt: Änderung des Eintrittsstroms. Symbole: gemessen mit Mikro-GC, graue Symbole: C in  $C_2H_6$  und weiße Symbole: C in  $CH_4$  (Rechts). Betriebsbedingungen:  $F_{v,\text{ein},NTP,H_2} = 300 \text{ cm}^3/\text{min}$ ,  $F_{v,\text{ein},NTP,(H_2/CO_2)_{\text{ein}}=5} = 309.3 \text{ cm}^3/\text{min}$ ,  $\tau_{\text{mod,soll}} = 400 \text{ kg s/m}^3$ ,  $p = 1 \text{ MPa}$ ,  $T = 264 \text{ }^\circ\text{C}$ . Katalysator:  $100 \text{ g Fe} / 2 \text{ g K}$

Die Ergebnisse zeigen das Potential des verfolgten Ansatzes und die sich ergänzenden Informationen, die mit den unterschiedlichen Methoden gewonnen werden können. Weiterhin kann die Plausibilität der einzelnen Ergebnisse mittels Vergleich untereinander überprüft werden. Die Ergebnisse sind hilfreich um einen Reaktor für Teillast auszulegen, da sie zeigen unter welchen Bedingungen ein Reaktor nicht betrieben werden sollte, um Katalysatordeaktivierung bzw. -reduktion zu vermeiden. Für den speziellen Fall der FT-Synthese mit Eisen konnte gezeigt werden, dass die Formierung und die Hydrierung der Eisencarbide reversibel und hochdynamisch ist.

#### ii) Voruntersuchung zur Möglichkeit variablen Betriebs eines industriellen Festbettreaktors

Die Nutzung eines industriellen Rohrbündelreaktor mit Eduktrückführung wird vorgeschlagen, um die  $CO_2$ -Hydrierung unter variablen Bedingungen durchzuführen, d.h. Betrieb innerhalb eines Lastbereichs, in dem der geforderte Umsatz und die geforderte Selektivität

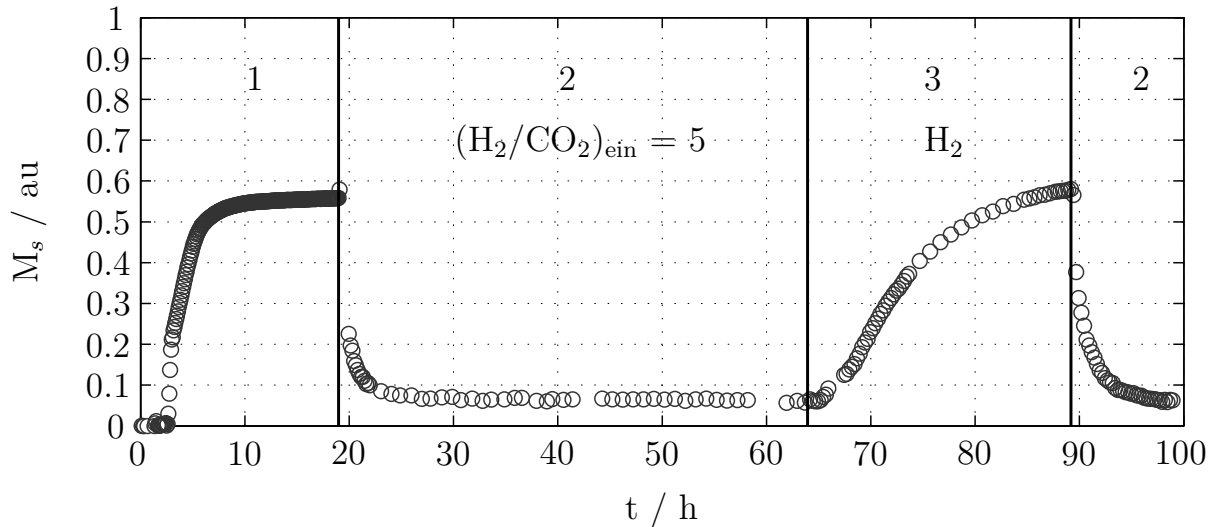


Abbildung 11.5: Sättigungsmagnetisierung  $M_s$  gemessen mittels Magnetometer während Katalysatorreduktion (1), Katalysatorformierung (2), und Änderungen der Betriebsbedingungen. Betriebsbedingungen: Reduktion (1),  $T = 400\text{ °C}$  während 16 h,  $p = 0.1\text{ MPa}$ ,  $(\text{H}_2/\text{Ar})_{\text{ein}} = 1/3$ ,  $\tau_{\text{mod}} = 300\text{ kg s/m}^3$ ; Formierung (2),  $T = 300\text{ °C}$ ,  $p = 1.13\text{ MPa}$ ,  $(\text{H}_2/\text{CO}_2)_{\text{ein}} = 5$ ,  $\tau_{\text{mod}} = 353\text{ kg s/m}^3$ ; (3):  $T = 300\text{ °C}$ ,  $p = 1.13\text{ MPa}$ ,  $(\text{H}_2/\text{CO}_2)_{\text{ein}} = \infty$ . Katalysator: 100 g Fe / 10 g K

immer erreicht werden (Abbildung 11.6). Die Konfiguration mit Rückführung beinhaltet einen Reaktor mit Produktabtrennung und einer Rückführung von  $\text{H}_2$  und  $\text{CO}_2$  zusammen mit dem Zwischenprodukt  $\text{CO}$ . Diese Konfiguration besitzt mit dem per-pass-Umsatz bzw. mit dem Rückführungsverhältnis eine für den variablen Betrieb vorteilhafte, zusätzliche Auslegungsvariable verglichen mit einem one-pass-Reaktor. Die Charakteristiken des Rückführungssystems werden durch die spezifischen Limitierungen des Katalysatorsystem bestimmt. Die relevanten Parameter für den Fall der  $\text{CO}_2$ -Hydrierung sind die Reaktionsenthalpie und die Desaktivierung des Katalysators bei Produktanwesenheit ( $(p_{\text{H}_2\text{O}}/p_{\text{H}_2})_{\text{aus}} > 0,1$ ) (Abbildung 11.3). Eine Vorgehensweise zur Auslegung eines variablen Reaktorsystems wird, basierend auf stationären und instationären Bilanzgleichungen und zuvor in der Laboranlage ermittelten experimentellen Ergebnissen (d.h. unter stationären Bedingungen ermittelte kinetische Parameter und während der Versuche unter instationären Bedingungen ermittelten Informationen), vorgeschlagen.

Die Nutzung einer Eduktrückführung erlaubt den Betrieb des Reaktors unter günstigeren Bedingungen im Vergleich zu einem one-pass-Reaktor: (1) eine hohe mittlere Reaktionsrate entlang der Katalysatorschüttung kann durch die Anwesenheit von  $\text{CO}$  (Zwischenprodukt) im Reaktoreintritt und niedrigere  $\text{H}_2\text{O}$ -Partialdrücke erreicht werden, (2) durch die höheren Gaseschwindigkeiten ist die Wärmeabfuhr effektiver, (3) ein hoher Gesamtumsatz ist möglich und (4) das  $(\text{H}_2/\text{CO}_2)_{\text{ein}}$ -Verhältnis kann höher als das stöchio-



metrische Verhältnis eingestellt werden. Das  $(\text{H}_2/\text{CO}_2)_{\text{ein}}$ -Verhältnis ist der einzige Betriebsparameter, welcher hohe  $\text{CO}_2$  Umsätze und Kohlenwasserstoffausbeuten bei kleinen  $(p_{\text{H}_2\text{O}}/p_{\text{H}_2})_{\text{aus}}$ -Verhältnissen erlaubt (Abbildung 11.3). Die Nachteile des Reaktor mit Eduktrückführung sind die hohen Betriebskosten (d.h. hoher Energiebedarf), große Trennapparate, ein zusätzlicher Kompressor für die Rückführung, mehrmaliges Heizen und Kühlen und der Stoffverlust im Purge-Strom.

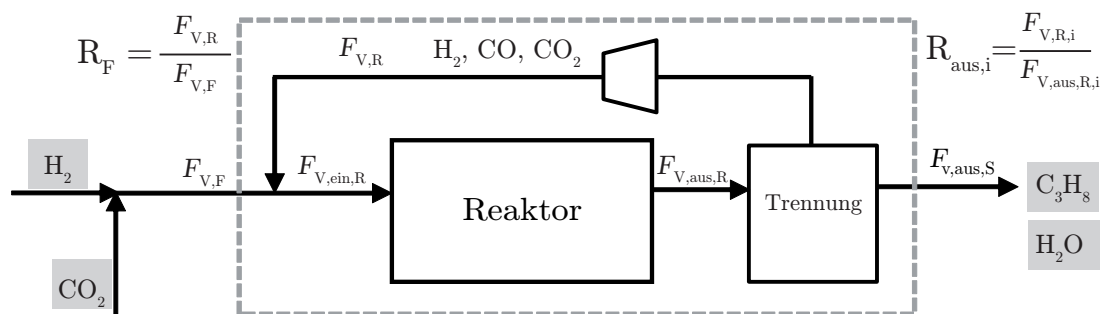


Abbildung 11.6: Reaktor mit Eduktrückführung für die  $\text{CO}_2$ -Hydrierung. Ideale Trennung angenommen.

Ein entscheidender Punkt dieser Konfiguration könnte das Verhalten der Trennapparate unter variablen Lastbedingungen sein. Die Trennung von  $\text{H}_2$ ,  $\text{CO}_2$  und  $\text{CO}$  von  $\text{H}_2\text{O}$  und den Kohlenwasserstoffen ist nicht einfach zu bewerkstelligen und erfordert kryogene Kühlung bei Temperaturen von ca.  $-70\text{ }^\circ\text{C}$ , um  $\text{H}_2$  von den leichten Kohlenwasserstoffen zu trennen, nachdem  $\text{CO}_2$  in einer  $\text{CO}_2$ -Wäsche abgetrennt wurde.

Ein Rohrbündelreaktor mit Eduktrückführung wird beispielhaft für einen Betrieb im Lastbereich von 70 bis 100 % gemäß der oben erläuterten Vorgehensweise ausgelegt. Der angestrebte minimale  $\text{CO}_2$ -Gesamtumsatz ist 90 % bei gleichzeitiger Einhaltung einer Maximaltemperatur von  $300\text{ }^\circ\text{C}$  und einem  $(p_{\text{H}_2\text{O}}/p_{\text{H}_2})_{\text{aus}}$ -Verhältnis kleiner als 0,1 (Abbildung 11.3). Die Berechnung basiert auf einem gewählten mittleren  $\text{CO}_2$ -Volumenstrom  $F_{\text{v,CO}_2,\text{mittel,NTP}} = 500\text{ m}^3/\text{h}$ , der typischerweise von einer Biogasanlage produziert wird. Der variable Betrieb mit einer Last von 70 - 100 % und einer Lastwechselrate von 5 % / min wird mit Hilfe von instationären mathematischen Modellen beschrieben. Die berechneten Ergebnisse zeigen, dass der variable Betrieb kein Problem für den Festbettreaktor darstellt, wenn der Reaktor entsprechend dem maximalen und minimalen Volumenstrom und der Katalysatorbeschränkungen ausgelegt wird (z.B.  $T_{\text{max}} = 300\text{ }^\circ\text{C}$ ,  $(p_{\text{H}_2\text{O}}/p_{\text{H}_2})_{\text{aus,max}} = 0,1$ ). Die Beschränkungen bezüglich Temperatur- und  $(p_{\text{H}_2\text{O}}/p_{\text{H}_2})_{\text{aus}}$ -Verhältnis werden nicht überschritten (Abbildung 11.7). Das Temperaturprofil bei variablem Reaktorbetrieb wird stark durch die Dichte und die Wärmekapazität des Katalysators beeinflusst. Beides ist für den Wärmehaushalt des Katalysatorbettes verantwortlich. Die Änderungen entlang des Katalysatorbettes sind aufgrund der relativ geringen Lastwechselrate gleichmäßig.

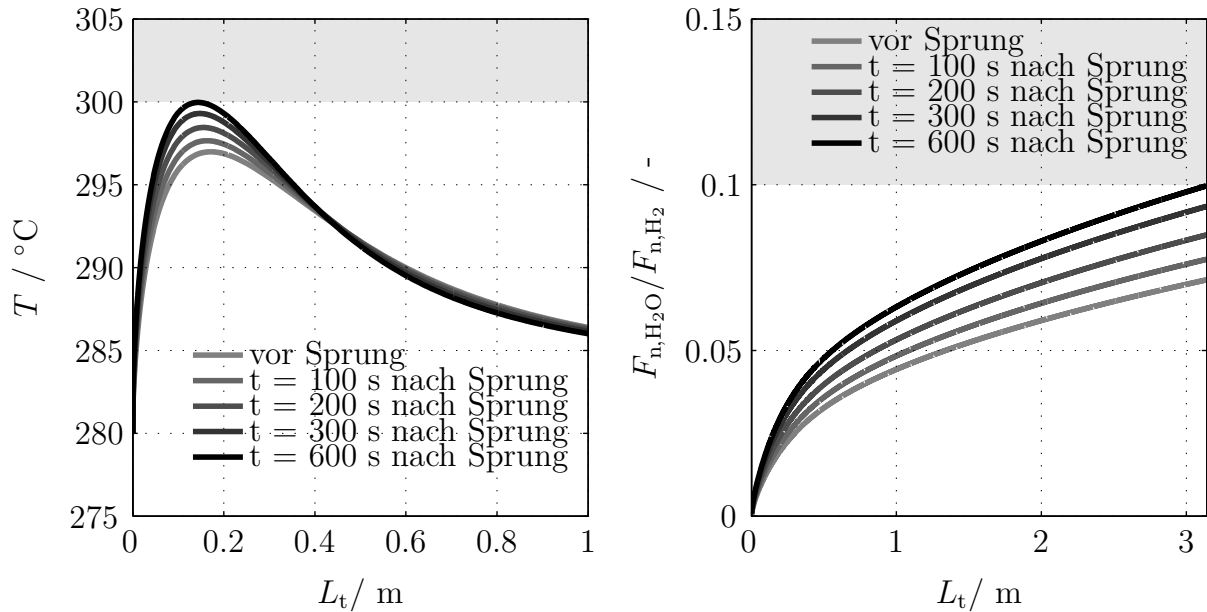


Abbildung 11.7: Berechnete axiale Temperaturen und  $(p_{\text{H}_2\text{O}}/p_{\text{H}_2})_{\text{aus}}$ -Verhältnisse über Reaktorlänge für verschiedene Zeiten nach Änderung der Last von 100 % zu 70 %, mit einer Lastwechselrate von 5 %/min. Graue Fläche: nicht erlaubter Betriebsbereich wegen geringer Katalysatorstabilität, Abbildung 11.3.

Die Reaktorauslegung ist oft entscheidend für die Auslegung der gesamten chemischen Anlage, da sie sich auf die benötigten Trennapparate, Kompressoren und den Wärmebedarf, etc. auswirkt. Allerdings sollten Informationen über die Reaktorperipherie in das mathematische Modell einfließen, um weitere Untersuchungen des dynamischen Verhaltens der gesamten chemischen Anlage durchführen zu können. Es wird davon ausgegangen, dass die Reaktorperipherie eine wichtige Rolle für die Flexibilität eines industriellen Prozesses spielt. Entsprechender wurde während der instationären Versuche im Labormaßstab festgestellt.

Mit Hilfe des Konzepts der charakteristischen Zeiten konnte in einer vereinfachten Form gezeigt werden, dass die einzelnen Prozesse innerhalb einer chemischen Anlage einen Einfluss auf die dynamische Systemantwort haben. Die angesprochenen Prozesse können chemische Reaktionen, Stoff- und Wärmetransport beinhalten, die mit unterschiedlichen Zeitskalen bzw. innerhalb unterschiedlicher Längenskalen ablaufen (z.B. Katalysatorpartikel, Reaktor, Reaktorperipherie). Der Vergleich der charakteristischen Zeiten der verschiedenen Prozesse mit der charakteristischen Zeit der Eintrittsstörung kann helfen, die Anzahl der Prozesse, die bei der mathematischen Modellierung berücksichtigt werden müssen, zu reduzieren. Die charakteristischen Zeiten sind für die verschiedenen Prozesse auf Basis von entdimensionierten Stoffbilanzen und Berechnungen für den beispielhaft ausgelegten Festbettreaktor mit Rückführung bestimmt worden.

Allgemein können alle Reaktionen die Wasserstoff als Edukt nutzen unter variablen Bedingungen betrieben werden, da der erzeugte Wasserstoffstrom aufgrund der fluktuierenden Natur erneuerbarer Quellen ebenfalls eine fluktuierende Charakteristik aufweist. Daher wird die variable Betriebsweise von Festbettreaktoren für andere Reaktion zur Erzeugung von Brennstoffen (z.B. Methansynthese, Niedertemperatur-Fischer-Tropsch-Synthese, Methanol-to-Hydrocarbon Synthese) basierend auf Literaturinformationen besprochen. Die Methanol-, die Dimethylether, und die Methansynthese können als Verfahren angesehen werden, die, aufgrund der hohen und wenig temperatursensitiven Selektivität zum Wunschprodukt und einer gewissen Katalysatorstabilität, relativ einfach unter variablen Bedingungen betrieben werden können. Die Niedertemperatur-Fischer-Tropsch-Synthese, der Methanol-to-Gasoline-Prozess und die CO<sub>2</sub>-Hydrierung zu gasförmigen Kohlenwasserstoffen können in dieser Hinsicht hingegen als relativ komplexe Reaktion angesehen werden.

### Schlussfolgerung und Ausblick

Diese Arbeit zeigt, dass gasförmige Kohlenwasserstoffe, mit Hilfe eines eisenbasierten und mit Kalium promotierten Katalysators (100 g Fe / 2 g K) aus H<sub>2</sub> und CO<sub>2</sub>, zur Brennwertanpassung erzeugt werden können. Reaktionsstechnische Limitierungen bezüglich des Katalysators wurden beobachtet ( $(p_{\text{H}_2\text{O}}/p_{\text{H}_2})_{\text{aus}} > 0,1$ ). Das Stoffmengenverhältnis  $(\text{H}_2/\text{CO}_2)_{\text{ein}}$  ist der erfolgversprechendste Parameter im Hinblick auf die Realisierung hoher CO<sub>2</sub>-Umsätze und Kohlenwasserstoffausbeuten, ohne dass der Katalysator deaktiviert. Die Kohlenwasserstoffproduktselektivität hängt stark vom Kaliumgehalt des Katalysators ab.

Die variable Betriebsweise chemischer Reaktoren ermöglicht es, die Größe des Wasserstoffspeichers zu reduzieren. Allerdings sind dazu heutzutage noch keine weiterführenden Studien verfügbar. In dieser Arbeit wurden Methoden entwickelt und für den Fall eines katalytischen Festbettreaktors mit der Beispielreaktion der CO<sub>2</sub>-Hydrierung zu gasförmigen Kohlenwasserstoffen angewendet, um potentiell limitierende Faktoren für die Reaktorflexibilität (bzgl. Katalysatorverhalten und Reaktorauslegung) zu untersuchen.

Zusammenfassend kann gesagt werden, dass die Flexibilität eines chemischen Prozesses direkt von der Charakteristik der chemischen Reaktion, die Komplexität des Reaktor- und Peripheriedesigns bestimmt, abhängt. Eine Wirtschaftlichkeitsbetrachtung des Gesamtprozesses ist notwendig und das Potential der variablen Betriebsweise einer chemischen Anlage bewerten zu können. Die in dieser Arbeit entwickelten Methoden können genutzt werden, um das dynamische Verhalten von katalytischen Synthesereaktoren für andere Prozesse, mit denen Chemische Energieträger erzeugt werden können, zu untersuchen.



# References

- Adesina, A.A.; Hudgins, R.R.; Silveston, P.L.: Fischer-Tropsch synthesis under periodic operation. In: *Catalysis Today* 25.2 (1995), pp. 127–144. ISSN: 0920-5861. DOI: 10.1016/0920-5861(95)00103-M.
- AG Energiebilanzen: *Auswertungstabellen zur Energiebilanz Deutschland 1990-2013*. 2014. URL: [www.ag-energiebilanzen.de](http://www.ag-energiebilanzen.de), visited on 10/11/2014.
- AG Energiebilanzen: *Energieverbrauch in Deutschland im Jahr 2014*. 2015. URL: [www.ag-energiebilanzen.de/20-0-Berichte.html](http://www.ag-energiebilanzen.de/20-0-Berichte.html), visited on 23/04/2015.
- Aicher, T.; Iglesias Gonzalez, M.; Schaub, G.; Götz, M.: Betrachtungen des Gesamtsystems im Hinblick auf Dynamik und Prozessintegration (Teilprojekt 5): Research Project : Speicherung elektrischer Energie aus regenerativen Quellen im Erdgasnetz – H<sub>2</sub>O-Elektrolyse und Synthese von Gaskomponenten. In: *DVGW-Zeitschrift: energie – wasser-praxis* 65 (2014), pp. 51–55.
- Ali, M.B.; Saidur, R.; Hossain, M.S.: A review on emission analysis in cement industries. In: *Renewable and Sustainable Energy Reviews* 15.5 (2011), pp. 2252–2261. ISSN: 13640321. DOI: 10.1016/j.rser.2011.02.014.
- Atwood, H. E.; Bennett, C. O.: Kinetics of the Fischer-Tropsch Reaction over Iron. In: *Ind. Eng. Chem. Process Des Dev* 18.1 (1979), p. 163.
- Baerns, M.; Renken, A.; Hofmann, H.: *Chemische Reaktionstechnik: Lehrbuch der Technischen Chemie-Band 1. 2.*, durchges. Aufl. Vol. 1. Lehrbuch der technischen Chemie. Stuttgart [u.a.]: Thieme, 1992. ISBN: 9783136875025.
- Bartholomew, C. H.; Farrauto, R. J.: *Fundamentals of industrial catalytic processes*. 2nd ed. Hoboken and N.J: Wiley, 2006. ISBN: 9780471457138.
- Beerbühl, S. S.; Kolbe, B.; Roosen, C.; Schultmann, F.: Ammoniaksynthese als Beispiel einer stofflichen Nutzung von intermittierend erzeugtem Wasserstoff. In: *Chemie Ingenieur Technik* 86.5 (2014), pp. 649–657. ISSN: 0009286X. DOI: 10.1002/cite.201300167.
- Bercic, G.; Levec, J.: Intrinsic and global reaction rate of methanol dehydration over  $\gamma$ -alumina pellets. In: *Industrial & engineering chemistry research* 31.4 (1992), pp. 1035–1040. ISSN: 0888-5885. DOI: 10.1021/ie00004a010.

- Bertau, M.; Offermanns, H.; Plass, L.; Schmidt, F.; Wernicke, H. J., eds.: *Methanol: The Basic Chemical and Energy Feedstock of the Future: Asinger's Vision Today*. Springer-Verlag Berlin and Heidelberg GmbH & Co. K, 2014. ISBN: 3642397085.
- BMU: *Langfristszenarien und Strategien- Leitstudie 2010: Langfristszenarien und Strategien für den Ausbau der erneuerbaren Energien in Deutschland bei Berücksichtigung der Entwicklung in Europa und global*. Ed. by DLR, Fraunhofer IWES, IfmE. 2010. URL: [www.dlr.de/tt/desktopdefault.aspx/tabid-2885/4422\\_read-15254](http://www.dlr.de/tt/desktopdefault.aspx/tabid-2885/4422_read-15254), visited on 11/10/2014.
- BMU: *Energy Sources in Figures: National and International Development*. Ed. by Federal Ministry for the Environment, Nature Conservation and Nuclear Safety: Renewable. 2012. URL: [www.fes-japan.org/wp-content/uploads/2013/04/broschuere\\_ee\\_zahlen\\_en\\_bf.pdf](http://www.fes-japan.org/wp-content/uploads/2013/04/broschuere_ee_zahlen_en_bf.pdf), visited on 11/10/2014.
- Boreskov, G. K.; Matros, Y. S.: Unsteady-State Performance of Heterogeneous Catalytic Reactions. In: *Catalysis Reviews* 25.4 (1983), pp. 551–590. ISSN: 0161-4940. DOI: 10.1080/01614948308078056.
- Botes, F. G.; Breman, B. B.: Development and Testing of a New Macro Kinetic Expression for the Iron-Based Low-Temperature Fischer–Tropsch Reaction. In: *Industrial & Engineering Chemistry Research* 45.22 (2006), pp. 7415–7426. ISSN: 0888-5885. DOI: 10.1021/ie060491h.
- Brunner, C.; Teufel, F.: The Competition of Different Measures to Increase Flexibility in Energy Systems with a High Share of Fluctuating Renewable Energy Sources. In: *Green* 3.1 (2013), pp. 59–67. ISSN: 1869-8778. DOI: 10.1515/green-2013-0002.
- Bub, G.; Baerns, M.: Prediction of the Performance of Catalytic Fixed bed reactors for Fischer-Tropsch Synthesis. In: *Chemical Engineering Science* 35 (1980), pp. 348–355. ISSN: 0009-2509.
- Bukur, D. B.; Mukesh, D.; Patel, S. A.: Promoter effects on precipitated iron catalysts for Fischer-Tropsch synthesis. In: *Industrial & engineering chemistry research* 29.2 (1990), pp. 194–204. ISSN: 0888-5885. DOI: 10.1021/ie00098a008.
- Carvill, B. T.; Hufton, J. R.; Anand, M.; Sircar, S.: Sorption-enhanced reaction process. In: *AIChE Journal* 42.10 (1996), pp. 2765–2772. ISSN: 0001-1541. DOI: 10.1002/aic.690421008.
- Centi, G.; Perathoner, S.: Opportunities and prospects in the chemical recycling of carbon dioxide to fuels. In: *Catalysis Today* 148.3–4 (2009), pp. 191–205. ISSN: 0920-5861. DOI: 10.1016/j.cattod.2009.07.075.
- Centi, G.; Quadrelli, E. A.; Perathoner, S.: Catalysis for CO<sub>2</sub> conversion: a key technology for rapid introduction of renewable energy in the value chain of chemical industries. In: *Energy & Environmental Science* 6.6 (2013), p. 1711. ISSN: 1754-5692. DOI: 10.1039/c3ee00056g.

- Chernavskii, P. A.; Dalmon, J.-A.; Perov, N. S.; Khodakov, A. Y.: Magnetic Characterization of Fischer-Tropsch Catalysts. In: *Oil & Gas Science and Technology - Revue de l'IFP* 64.1 (2009), pp. 25–48. ISSN: 1294-4475. DOI: 10.2516/ogst/2008050.
- Choi, P. H.; Jun, K. W.; Lee, S. J.; Choi, M. J.; Lee, K. W.: Hydrogenation of carbon dioxide over alumina supported Fe-K catalysts. In: *Catalysis Letters* 40.1-2 (1996), pp. 115–118. ISSN: 1011-372X. DOI: 10.1007/BF00807467.
- Claeys, M.: *Selektivität, Elementarschritte und kinetische Modellierung bei der Fischer-Tropsch-Synthese: Doctoral Dissertation Universität Karlsruhe*. 1997.
- Claeys, M.; Schulz, H.: Effects of internal mass transfer on activity and selectivity in iron based Fischer-Tropsch synthesis. In: *Preprints of Symposia - Division of Petroleum Chemistry, American Chemical Society*. 49, Part 2 (2004), pp. 195–199.
- Claeys, M.; Steen, E. van; Visagie, J.; Loosdrecht, J. van de: 'A Magnetometer'. Pat. WO 2010/004419 A2. 2010.
- Claeys, M.; Moodley, P.; Harilal, A.; Ferreira, A.: Oxidation of Hägg Carbide at High Temperature Fischer-Tropsch Synthesis captured in-situ. In: *10th Natural Gas Conversion Symposium, Doha, Qatar* (2013).
- Claeys, M.; Dry, M. E.; Steen, E. van; Plessis, E. du; Berge, P.J. van; Saib, A.M.; Moodley, D.J.: In situ magnetometer study on the formation and stability of cobalt carbide in Fischer-Tropsch synthesis. In: *Journal of Catalysis* 318.0 (2014), pp. 193–202. ISSN: 0021-9517. DOI: 10.1016/j.jcat.2014.08.002.
- Connolly, D.; Mathiesen, B.V.; Ridjan, I.: A comparison between renewable transport fuels that can supplement or replace biofuels in a 100% renewable energy system. In: *Energy* 73 (2014), pp. 110–125. ISSN: 0360-5442. DOI: 10.1016/j.energy.2014.05.104.
- Cubeiro, M.; Morales, H.; Goldwasser, M.; Pérez-Zurita, M.; González-Jiménez, F.: Promoter Effect of Potassium on an Iron Catalyst in the Carbon Dioxide Hydrogenation Reaction. In: *Reaction Kinetics and Catalysis Letters* 69.2 (2000), pp. 259–264. ISSN: 0133-1736. DOI: 10.1023/A:1005639630809.
- Deckwer, W. D.; Kokuun, R.; Sanders, E.; Ledakowicz, S.: Kinetic studies of Fischer-Tropsch synthesis on suspended iron/potassium catalyst - rate inhibition by carbon dioxide and water. In: *Industrial & Engineering Chemistry Process Design and Development* 25.3 (1986), pp. 643–649. DOI: 10.1021/i200034a008.
- DENA Power to gas: *Integration erneuerbaren Stroms in das Erdgasnetz: Power to Gas – eine innovative Systemlösung für die Energieversorgung von morgen entwickeln*. 2012. URL: [www.powertogas.info/power-to-gas/energiesystem-der-zukunft.html](http://www.powertogas.info/power-to-gas/energiesystem-der-zukunft.html), visited on 23/04/2015.
- Doesburg, H. van; Jong, W. A. de: Transient behaviour of an adiabatic fixed-bed methanator—I: Experiments with binary feeds of CO or CO<sub>2</sub> in hydrogen. In: *Chemical Engineering Science* 31.1 (1976), pp. 45–51. ISSN: 0009-2509. DOI: 10.1016/0009-2509(76)85007-5.

- Doesburg, H. van; Jong, W. A. de: Transient behaviour of an adiabatic fixed-bed methanator—II: Methanation of mixtures of carbon monoxide and carbon dioxide. In: *Chemical Engineering Science* 31.1 (1976), pp. 53–58. ISSN: 0009-2509. DOI: 10.1016/0009-2509(76)85008-7.
- Douglas, J. M.: Periodic Reactor Operation. In: *Industrial & Engineering Chemistry Process Design and Development* 6.1 (1967), pp. 43–48. ISSN: 0196-4305. DOI: 10.1021/i260021a008.
- Droste-Franke, B.; Klüser, R.; Noll, T.: *Balancing renewable electricity: Energy storage, demand side management, and network extension from an interdisciplinary perspective*. Vol. 40. Ethics of science and technology assessment. Heidelberg and New York: Springer, 2012. ISBN: 3642251579.
- Dry, M. E.: Fischer-Tropsch synthesis over iron catalysts. In: *Catalysis Letters* 7.1-4 (1990), pp. 241–251. ISSN: 1011-372X. DOI: 10.1007/BF00764506.
- Dry, M. E.; Shingles, T.; Boshoff, L.J.: Rate of the Fischer-Tropsch reaction over iron catalysts. In: *Journal of Catalysis* 25.1 (1972), pp. 99–104. ISSN: 0021-9517. DOI: 10.1016/0021-9517(72)90205-9.
- DVGW: *Technische Regel. Arbeitsblatt G 260. Gasbeschaffenheit. Deutsche Vereinigung des Gas- und Wasserfaches e.V. - Technisch-wissenschaftlicher Verein*. Bonn, 3.2013.
- DVGW: *Technische Regel - Arbeitsblatt DVGW G 262 (A). Entwurf. Deutsche Vereinigung des Gas- und Wasserfaches e.V. - Technisch-wissenschaftlicher Verein*. Bonn, 9.2011.
- EEX: *Transparency in Energy Markets - Homepage*. 2014. URL: [www.eex-transparency.com](http://www.eex-transparency.com), visited on 23/04/2015.
- Eigenberger, G.: ‘Fixed-Bed Reactors, Vol. B.4’. In: *Ullmann’s Encyclopedia of Industrial Chemistry*. Wiley-VCH Verlag GmbH & Co. KGaA, 2000, pp. 199–238. ISBN: 9783527306732.
- Eigenberger, G.; Werther, J.; Schoenfelder, H.; Beenackers, A. A. C. M.; St. Matros, Y.; Bunimovich, G. A.; Donati, G.; Habashi, N.; Miracca, I.; Sanfilippo, D.: ‘Reaction Engineering (Chap.10)’. In: *Handbook of Heterogeneous Catalysis*. Weinheim and Germany: Wiley-VCH Verlag GmbH, 2008, pp. 1399–1487. ISBN: 9783527619474. DOI: 10.1002/9783527619474.ch10.
- Eilers, H.; Schaub, G.: Fischer-Tropsch-Synthese unter instationären Bedingungen im Suspensionsreaktor: experimentelle und rechnerische Studien. In: *Chemie Ingenieur Technik* 87.6 (2015), pp. 837–842. ISSN: 0009286X. DOI: 10.1002/cite.201400138.
- ENTSO-E: *European Network of Transmission System Operators for Electricity*. 2014. URL: [www.entsoe.eu/data/data-portal/consumption/Pages/default.aspx](http://www.entsoe.eu/data/data-portal/consumption/Pages/default.aspx), visited on 23/04/2015.



- Espinoza, R.L.; Steynberg, A.P.; Jager, B.; Vosloo, A.C.: Low temperature Fischer–Tropsch synthesis from a Sasol perspective. In: *Applied Catalysis A: General* 186.1–2 (1999), pp. 13–26. ISSN: 0926-860X. DOI: 10.1016/S0926-860X(99)00161-1.
- European Commission: *Heating and Cooling in the European Energy Transition: Challenges and Facts*. 2015. URL: [heating-and-cooling-in-europe.eu/HEATING%20AND%20COOLING\\_brochure.pdf](http://heating-and-cooling-in-europe.eu/HEATING%20AND%20COOLING_brochure.pdf), visited on 27/04/2015.
- Exxon Mobil: *Methanol to Gasoline (MTG) Production of Clean Gasoline from Coal*. 2015. URL: [www.exxonmobil.com/Apps/RefiningTechnologies/files/sellsheet\\_09\\_mtg\\_brochure.pdf](http://www.exxonmobil.com/Apps/RefiningTechnologies/files/sellsheet_09_mtg_brochure.pdf), visited on 11/02/2015.
- Feimer, J. L.; Silveston, P. L.; Hudgins, R. R.: Influence of Forced Cycling on the Fischer–Tropsch Synthesis. Part I. Response to Feed Concentration Step-Changes. In: *The Canadian Journal of Chemical Engineering* 62.2 (1984), pp. 241–248. ISSN: 1939-019X. DOI: 10.1002/cjce.5450620212.
- Feimer, J. L.; Silveston, P. L.; Hudgins, R. R.: Influence of Forced Cycling on the Fischer–Tropsch Synthesis. Part II. Response to Feed Concentration square-waves. In: *The Canadian Journal of Chemical Engineering* 63.1 (1985), pp. 86–92. ISSN: 1939-019X. DOI: 10.1002/cjce.5450630114.
- Fiato, R. A.; Iglesia, E.; Rice, G. W.; Soled, S. L.: ‘Iron catalyzed CO<sub>2</sub> hydrogenation to liquid hydrocarbons’. In: *Studies in Surface Science and Catalysis : Advances in Chemical Conversions for Mitigating Carbon Dioxide Proceedings of the Fourth International Conference on Carbon Dioxide Utilization*. Ed. by T. Inui, M.; Anpo, M.; Izui, K.; Yanagida, S.; Yamaguchi, T. Vol. 114. Elsevier, 1998, pp. 339–344. ISBN: 0167-2991. DOI: 10.1016/S0167-2991(98)80767-2.
- Finlayson, B. A.; Biegler, L. T.; Grossmann, I. E.: ‘Mathematics in Chemical Engineering’. In: *Ullmann’s Encyclopedia of Industrial Chemistry*. Wiley-VCH Verlag GmbH & Co. KGaA, 2000. ISBN: 9783527306732. DOI: 10.1002/14356007.b01\_01.pub2.
- Fischer, F.; Tropsch, H.: Über die Herstellung synthetischer Ölgemische (Synthol) durch Aufbau aus Kohlenoxyd und Wasserstoff. In: *Brennstoff-Chemie* 18 (1923), pp. 276–285.
- Fischer, F.; Tropsch, H.: Die Erdölsynthese bei gewöhnlichem Druck aus den Vergasungsprodukten der Kohlen. In: *Brennstoff-Chemie* 7 (1926), pp. 97–116.
- Fischer, N.: *Preparation of Nano and Ångström sized Cobalt Ensembles and their Performance in the Fischer-Tropsch Synthesis: Doctoral Dissertation University of Cape Town*. 2011.
- Fischer, N.; Clapham, B.; Feltes, T.; Steen, E. van; Claeys, M.: Size-Dependent Phase Transformation of Catalytically Active Nanoparticles Captured In-Situ. In: *Angewandte Chemie International Edition* 53.5 (2014), pp. 1342–1345. DOI: 10.1002/anie.201306899.

- Fischer, N.; Clapham, B.; Feltes, T.; Claeys, M.: Cobalt-Based Fischer–Tropsch Activity and Selectivity as a Function of Crystallite Size and Water Partial Pressure. In: *ACS Catalysis* 5.1 (2015), pp. 113–121. ISSN: 2155-5435. DOI: 10.1021/cs500936t.
- Froment, G. F.: Fixed Bed Catalytic Reactors. Technological and Fundamental Design Aspects. In: *Chemie Ingenieur Technik* 46.9 (1974), pp. 374–386. ISSN: 0009286X. DOI: 10.1002/cite.330460903.
- Froment, G. F.; Bischoff, K. B.: *Chemical reactor analysis and design*. 2nd ed. Wiley series in chemical engineering. New York: Wiley, 1990. ISBN: 9780471521907.
- Fthenakis, V. M.: *Prevention and Control of Accidental Releases of Hazardous Gases*. Wiley, 1993. ISBN: 9780471284086.
- Fujimoto, K.; Shikada, T.: Selective synthesis of C<sub>2</sub>-C<sub>5</sub> hydrocarbons from carbon dioxide utilizing a hybrid catalyst composed of a methanol synthesis catalyst and zeolite. In: *Applied Catalysis* 31.1 (1987), pp. 13–23. ISSN: 0166-9834. DOI: 10.1016/S0166-9834(00)80663-6.
- Fujimoto, K.; Yokota, K.: Effective hydrogenation of carbon dioxide with two-stage reaction system. In: *Chemistry Letters* 4 (1991), pp. 559–562. DOI: 10.1246/cl.1991.559.
- Gabrielsson, P.; Pedersen, H.G.: ‘Flue Gases from Stationary Sources (Chap. 11.3)’. In: *Handbook of Heterogeneous Catalysis*. Weinheim and Germany: Wiley-VCH Verlag GmbH, 2008, pp. 2345–2385. ISBN: 9783527619474.
- Gahleitner, G.: Hydrogen from renewable electricity: An international review of power-to-gas pilot plants for stationary applications. In: *International Journal of Hydrogen Energy* 38.5 (2013), pp. 2039–2061. ISSN: 0360-3199. DOI: 10.1016/j.ijhydene.2012.12.010.
- German Federal Government: *Gesetz für den Ausbau erneuerbare Energien (Erneuerbare-Energien-Gesetz): EEG*. 2014. URL: [www.gesetze-im-internet.de/eeg\\_2014/](http://www.gesetze-im-internet.de/eeg_2014/), visited on 23/04/2015.
- Gnanamani, M.K.; Jacobs, G.; Hamdeh, H.H.; Shafer, W.D.; Davis, B.H.: Fischer–Tropsch synthesis: Mössbauer investigation of iron containing catalysts for hydrogenation of carbon dioxide. In: *Catalysis Today* 207.0 (2013), pp. 50–56. ISSN: 0920-5861. DOI: 10.1016/j.cattod.2012.02.059.
- Götz, M.; Lefebvre, J.; Mörs, F.; McDaniel Koch, A.; Graf, F.; Bajohr, S.; Reimert, R.; Kolb, T.: Renewable Power-to-Gas: A technological and economic review. In: *Renewable Energy* (2015), pp. –. ISSN: 0960-1481. DOI: 10.1016/j.renene.2015.07.066.
- Govender, N. S.: *Mechanistic study of the high-temperature Fischer-Tropsch synthesis using transient kinetics: PhD Eindhoven University of Technology*. 2010. ISBN: 9038623402.
- Graaf, G. H.; Sijtsema, P. J.J.M.; Stamhuis, E. J.; Joosten, G. E.H.: Chemical equilibria in methanol synthesis. In: *Chemical Engineering Science* 41.11 (1986), pp. 2883–2890. ISSN: 0009-2509. DOI: 10.1016/0009-2509(86)80019-7.

- Graf, F.; Götz, M.; Henel, M.; Schaaf, T.; Tichler, R.: *Technoökonomische Studie von Power-to-Gas-Konzepten: Teilprojekte B-D, Abschlussbericht, DVGW-Förderkennzeichen G 3/01/12 TP B-D*. Ed. by DVGW- Forschung. 2014. URL: [www.dvgw - innovation.de/fileadmin/dvgw/angebote/forschung/innovation/pdf/g3\\_01\\_12\\_tp\\_b\\_d.pdf](http://www.dvgw-innovation.de/fileadmin/dvgw/angebote/forschung/innovation/pdf/g3_01_12_tp_b_d.pdf), visited on 05/05/2015.
- Grozev, G. G.; Sapundzhiev, C. G.; Elenkov, D. G.: Unsteady-State SO<sub>2</sub> Oxidation: Practical Results. In: *Industrial & Engineering Chemistry Research* 33.9 (1994), pp. 2248–2250. ISSN: 0888-5885. DOI: 10.1021/ie00033a031.
- Güttel, R.: Study of Unsteady-State Operation of Methanation by Modeling and Simulation. In: *Chemical Engineering & Technology* 36.10 (2013), pp. 1675–1682. ISSN: 1521-4125. DOI: 10.1002/ceat.201300223.
- Güttel, R.: Structuring of Reactors and Catalysts on Multiple Scales: Potential and Limitations for Fischer-Tropsch Synthesis. In: *Chemie Ingenieur Technik* (2015). ISSN: 0009286X. DOI: 10.1002/cite.201400107.
- Hansen, J. B.; Højlund Nielsen, P. E.: ‘Methanol Synthesis’. In: *Handbook of Heterogeneous Catalysis*. Weinheim and Germany: Wiley-VCH Verlag GmbH, 2008. ISBN: 9783527619474. DOI: 10.1002/9783527610044.hetcat0148.
- Hettel, B.: ‘CO<sub>2</sub> Hydrogenation to Substitute Natural Gas (SNG) components- catalyst characterization: Master Thesis, University of Cape Town and KIT’. 2014.
- Højlund-Nielsen, P. E.; Bøgild-Hansen, J.: Conversion limitations in hydrocarbon synthesis. In: *Journal of Molecular Catalysis* 17.2–3 (1982), pp. 183–193. ISSN: 0304-5102. DOI: 10.1016/0304-5102(82)85029-3.
- Hong, J. S.; Hwang, J. S.; Jun, K. W.; Sur, J. C.; Lee, K. W.: Deactivation study on a coprecipitated Fe-Cu-K-Al catalyst in CO<sub>2</sub> hydrogenation. In: *Applied Catalysis A: General* 218.1–2 (2001), pp. 53–59. ISSN: 0926-860X. DOI: 10.1016/S0926-860X(01)00617-2.
- Huff, G. A.; Satterfield, C. N.: Intrinsic kinetics of the Fischer-Tropsch synthesis on a reduced fused-magnetite catalyst. In: *Industrial & Engineering Chemistry Process Design and Development* 23.4 (1984), pp. 696–705. ISSN: 0196-4305. DOI: 10.1021/i200027a012.
- Hwang, J. S.; Jun, K. W.; Lee, K. W.: Deactivation and regeneration of Fe-K/alumina catalyst in CO<sub>2</sub> hydrogenation. In: *Applied Catalysis A: General* 208.1–2 (2001), pp. 217–222. ISSN: 0926-860X. DOI: 10.1016/S0926-860X(00)00701-8.
- IEA: *Global energy-related emissions of carbon dioxide stalled in 2014*. 3.2015. URL: [www.iea.org/newsroomandevents/news/2015/march/global-energy-related-emissions-of-carbon-dioxide-stalled-in-2014.html](http://www.iea.org/newsroomandevents/news/2015/march/global-energy-related-emissions-of-carbon-dioxide-stalled-in-2014.html), visited on 27/04/2015.

- IEA: *Energy and Climate Change, World Energy Outlook Special Report*. 2015. URL: [www.iea.org/publications/freepublications/publication/WE02015SpecialReportonEnergyandClimateChange.pdf](http://www.iea.org/publications/freepublications/publication/WE02015SpecialReportonEnergyandClimateChange.pdf), visited on 02/07/2015.
- Jarass, L.; Obermair, G. M.; Voigt, W.: *Windenergie: Zuverlässige Integration in die Energieversorgung*. 2., vollständig neu bearbeitete Aufl. Berlin and Heidelberg: Springer Berlin Heidelberg, 2009. ISBN: 3540852530.
- Jess, A.; Kern, C.: Modeling of Multi-Tubular Reactors for Fischer-Tropsch Synthesis. In: *Chemical Engineering & Technology* 32.8 (2009), pp. 1164–1175. ISSN: 1521-4125. DOI: 10.1002/ceat.200900131.
- Jess, A.; Kaiser, P.; Kern, C.; Unde, R. B.; Olshausen, C. von: Considerations concerning the Energy Demand and Energy Mix for Global Welfare and Stable Ecosystems. In: *Chemie Ingenieur Technik* 83.11 (2011), pp. 1777–1791. ISSN: 0009286X. DOI: 10.1002/cite.201100066.
- Jin, Y.; Datye, A. K.: Phase Transformations in Iron Fischer–Tropsch Catalysts during Temperature-Programmed Reduction. In: *Journal of Catalysis* 196.1 (2000), pp. 8–17. ISSN: 0021-9517. DOI: 10.1006/jcat.2000.3024.
- Jozwiak, W.K.; Kaczmarek, E.; Maniecki, T.P.; Ignaczak, W.; Maniukiewicz, W.: Reduction behavior of iron oxides in hydrogen and carbon monoxide atmospheres. In: *Applied Catalysis A: General* 326.1 (2007), pp. 17–27. ISSN: 0926-860X. DOI: 10.1016/j.apcata.2007.03.021.
- Kapteijn, F.; Moulijn, J. A.; Emig, G.; Dittmeyer, R.; Kärger, J.: ‘Kinetics and Transport Processes (Chap.6)’. In: *Handbook of Heterogeneous Catalysis*. Weinheim and Germany: Wiley-VCH Verlag GmbH, 2008, pp. 1189–1261. ISBN: 9783527619474. DOI: 10.1002/9783527619474.ch6.
- Kim, H.; Choi, D. H.; Nam, S. S.; Choi, M. J.; Lee, K. W.: ‘The selective synthesis of lower olefins(C<sub>2</sub> - C<sub>4</sub>) by the CO<sub>2</sub> hydrogenation over Iron catalysts promoted with Potassium and supported on ion exchanged(H, K) Zeolite-Y’. In: *Studies in Surface Science and Catalysis : Advances in Chemical Conversions for Mitigating Carbon Dioxide Proceedings of the Fourth International Conference on Carbon Dioxide Utilization*. Ed. by T. Inui, M.; Anpo, M.; Izui, K.; Yanagida, S.; Yamaguchi, T. Vol. 114. Elsevier, 1998, pp. 407–410. ISBN: 0167-2991. DOI: 10.1016/S0167-2991(98)80782-9.
- Kim, S.D.; Baek, S.C.; Lee, Y.J.; Jun, K.W.; Kim, M.J.; Yoo, I.S.: Effect of alumina content on catalytic performance of modified ZSM-5 for dehydration of crude methanol to dimethyl ether. In: *Applied Catalysis A: General* 309.1 (2006), pp. 139–143. ISSN: 0926-860X. DOI: 10.1016/j.apcata.2006.05.008.
- Kopyscinski, J.; Schildhauer, T. J.; Biollaz, S. M.A.: Production of synthetic natural gas (SNG) from coal and dry biomass – A technology review from 1950 to 2009. In: *Fuel* 89.8 (2010), pp. 1763–1783. ISSN: 0016-2361. DOI: 10.1016/j.fuel.2010.01.027.

- Kvisle, S.; Fuglerud, T.; Kolboe, S.; Olsbye, U.; Lillerud, K. P.; Vora, B. V.: ‘Methanol-to-Hydrocarbons (Ch. 13.14)’. In: *Handbook of Heterogeneous Catalysis*. Weinheim and Germany: Wiley-VCH Verlag GmbH, 2008, pp. 2950–2965. ISBN: 9783527619474. DOI: 10.1002/9783527610044.hetcat0149.
- Laan, G. P. van der; Beenackers, A. A. C. M.: Kinetics and Selectivity of the Fischer–Tropsch Synthesis: A Literature Review. In: *Catalysis Reviews* 41.3-4 (1999), pp. 255–318. ISSN: 0161-4940. DOI: 10.1081/CR-100101170.
- Lasserre, P.: *The global cement industry: Global Strategic Management Mini Cases Series*. 2007. URL: [philippelasserre.net/contenu/Download/Global\\_Cement\\_industry.pdf](http://philippelasserre.net/contenu/Download/Global_Cement_industry.pdf), visited on 28/04/2015.
- Lee, J. F.; Chern, W. S.; Lee, M. D.; Dong, T. y.: Hydrogenation of carbon dioxide on iron catalysts doubly promoted with manganese and potassium. In: *The Canadian Journal of Chemical Engineering* 70.3 (1992), pp. 511–515. ISSN: 1939-019X. DOI: 10.1002/cjce.5450700314.
- Lee, M. D.; Lee, J. F.; Chang, C. S.: Catalytic behavior and phase composition change of iron catalyst in hydrogenation of carbon dioxide. In: *Journal of Chemical Engineering of Japan* 23.2 (1990), pp. 130–136. DOI: 10.1252/jcej.23.130.
- Lee, T.; Lu, Y.: Influence of the Feed Gas Composition on the Fischer-Tropsch Synthesis in Commercial Operations. In: *Journal of Natural Gas Chemistry* 16.4 (2007), pp. 329–341. ISSN: 1003-9953. DOI: 10.1016/S1003-9953(08)60001-8.
- Lefebvre, J.; Götz, M.; Bajohr, S.; Reimert, R.; Kolb, T.: Improvement of three-phase methanation reactor performance for steady-state and transient operation. In: *Fuel Processing Technology* 132.0 (2015), pp. 83–90. ISSN: 0378-3820. DOI: 10.1016/j.fuproc.2014.10.040.
- Lerou, J. J.; Ng, K. M.: Chemical reaction engineering: A multiscale approach to a multiobjective task. In: *Chemical Engineering Science* 51.10 (1996), pp. 1595–1614. ISSN: 0009-2509. DOI: 10.1016/0009-2509(96)00022-X.
- Levenspiel, O.: *Chemical reaction engineering*. 3rd ed. New York: Wiley, 1999. ISBN: 9780471254249.
- Lox, E. S.: ‘Automotive Exhaust Treatment (Chap. 11.2)’. In: *Handbook of Heterogeneous Catalysis*. Weinheim and Germany: Wiley-VCH Verlag GmbH, 2008. ISBN: 9783527619474. DOI: 10.1002/9783527610044.hetcat0120.
- Lox, E. S.; Lindner, D.; Engler, B. H.: ‘Transient Phenomena in Three-Way Catalysis’. In: *Precision Process Technologies*. Ed. by Weijnen, M. P.C.; Drinkenburg, A. A.H. Kluwer Academic Publishers, 1993, pp. 463–472.
- Lund, C. R.F.; Dumesic, J. A.: Strong oxide-oxide interactions in silica-supported magnetite catalysts. 1. X-ray diffraction and Moessbauer spectroscopy evidence for interaction. In: *The Journal of Physical Chemistry* 85.21 (1981), pp. 3175–3180. DOI: 10.1021/j150621a034.

- Luyben, W. L.: *Chemical reactor design and control*. [New York], Hoboken and N.J.: AIChE and Wiley-Interscience, 2007. ISBN: 0470134917.
- Martin, H.; Nilles, M.: Radiale Wärmeleitung in durchströmten Schüttungsrohren. In: *Chemie Ingenieur Technik* 65.12 (1993), pp. 1468–1477. ISSN: 0009286X. DOI: 10.1002/cite.330651206.
- Martinelli, M.; Visconti, C. G.; Lietti, L.; Forzatti, P.; Bassano, C.; Deiana, P.: CO<sub>2</sub> reactivity on Fe–Zn–Cu–K Fischer–Tropsch synthesis catalysts with different K-loadings. In: *Catalysis Today* 228 (2014), pp. 77–88. ISSN: 0920-5861. DOI: 10.1016/j.cattod.2013.11.018.
- Matros, Y. SH.; Bunimovich, G. A.: Reverse-Flow Operation in Fixed Bed Catalytic Reactors. In: *Catalysis Reviews* 38.1 (1996), pp. 1–68. ISSN: 0161-4940. DOI: 10.1080/01614949608006453.
- Meinke, S.: *Modellierung thermischer Kraftwerke vor dem Hintergrund steigender Dynamikanforderungen aufgrund zunehmender Windenergie- und Photovoltaikeinspeisung: Doctoral Dissertation Universität Rostock*. 2012.
- Mena Subiranas, A.: *Combining Fischer-Tropsch synthesis (FTS) and hydrocarbon reactions in one reactor: Doctoral Dissertation Universität Karlsruhe*. 2009. ISBN: 3866443307.
- Metz, B.: *Carbon Dioxide Capture and Storage: Special Report of the Intergovernmental Panel on Climate Change*. Cambridge University Press, 2005. ISBN: 9780521866439.
- Mills, G. A.; Steffgen, F. W.: Catalytic Methanation. In: *Catalysis Reviews* 8.1 (1974), pp. 159–210. ISSN: 0161-4940. DOI: 10.1080/01614947408071860.
- Mogorosi, R. P.; Fischer, N.; Claeys, M.; Steen, E. van: Strong-metal–support interaction by molecular design: Fe–silicate interactions in Fischer–Tropsch catalysts. In: *Journal of Catalysis* 289.0 (2012), pp. 140–150. ISSN: 0021-9517. DOI: 10.1016/j.jcat.2012.02.002.
- Müller, K.; Mokrushina, L.; Arlt, W.: Thermodynamic Constraints for the Utilization of CO<sub>2</sub>. In: *Chemie Ingenieur Technik* 86.4 (2014), pp. 497–503. ISSN: 0009286X. DOI: 10.1002/cite.201300152.
- Muradov, N.Z.; Veziroğlu, T.N.: ‘Energy Options in a Carbon-Constrained World: An Advent of Carbon-Neutral Technologies: Chapter 1’. In: *Carbon Neutral Fuels and Energy Carriers: Synthetic Hydrocarbon Fuels from Lignocellulosic Biomass*. Ed. by Muradov, N. Z.; Veziroğlu, T.N. Taylor and Francis, CRC press, 2010.
- Mutz, B.; Carvalho, H. W.P.; Mangold, S.; Kleist, W.; Grunwaldt, J. D.: Methanation of CO<sub>2</sub>: Structural response of a Ni-based catalyst under fluctuating reaction conditions unraveled by operando spectroscopy. In: *Journal of Catalysis* 327.0 (2015), pp. 48–53. ISSN: 0021-9517. DOI: 10.1016/j.jcat.2015.04.006.
- Netzentwicklungsplan Strom: *Netzentwicklungsplan 2014, zweiter Entwurf* — *netzentwicklungsplan.de: Grid development plan*. 2015. URL: [www.netzentwicklungsplan.de](http://www.netzentwicklungsplan.de).

- netzentwicklungsplan.de/netzentwicklungsplan - 2014 - zweiter - entwurf, visited on 23/04/2015.
- Newsome, D. S.: Water-gas Shift Reaction. In: *Catalysis reviews Softcover ed* 21.2 (1980), pp. 275–281.
- Niemantsverdriet, J. W.; Kraan, A. M. Van der; Dijk, W. L. van; Baan, H. S. van der: Behavior of metallic iron catalysts during Fischer-Tropsch synthesis studied with Moessbauer spectroscopy, x-ray diffraction, carbon content determination, and reaction kinetic measurements. In: *The Journal of Physical Chemistry* 84.25 (1980), pp. 3363–3370. DOI: 10.1021/j100462a011.
- Oki, S.; Mezaki, R.: Identification of rate-controlling steps for the water-gas shift reaction over an iron oxide catalyst. In: *The Journal of Physical Chemistry* 77.4 (1973), pp. 447–452. DOI: 10.1021/j100623a006.
- Owen, R. E.; O’Byrne, J. P.; Mattia, D.; Plucinski, P.; Pascu, S. I.; Jones, M. D.: Cobalt catalysts for the conversion of CO<sub>2</sub> to light hydrocarbons at atmospheric pressure. In: *Chemical communications* 49.99 (2013), pp. 11683–11685. DOI: 10.1039/c3cc46791k.
- Pabst, K.: *Katalysatorkonfigurationen für die Kombination von Fischer-Tropsch-Synthese und Hydroprocessing in einem Reaktor - Experimentelle Untersuchungen und mathematische Modellierung: Doctoral Dissertation KIT*. Verfahrenstechnik. München: Verlag Dr. Hut, 2013. ISBN: 3843912319.
- Raje, A.P.; O’Brien, R.J.; Davis, B.H.: Effect of Potassium Promotion on Iron-Based Catalysts for Fischer–Tropsch Synthesis. In: *Journal of Catalysis* 180.1 (1998), pp. 36–43. ISSN: 0021-9517. DOI: 10.1006/jcat.1998.2259.
- Rebbsdat, S.; Mayer, D.: ‘Ethylene Oxide, Vol. 13’. In: *Ullmann’s Encyclopedia of Industrial Chemistry*. 2001, pp. 547–572. DOI: 10.1002/14356007.a10\_117.
- Renken, A.: Transient operation for the purpose of modeling heterogeneous catalytic reactions. In: *International Chemical Engineering (A Quarterly Journal of Translations from Russia, Eastern Europe and Asia);(United States)* 33.1 (1993).
- Rethwisch, D. G.; Dumesic, J. A.: Adsorptive and catalytic properties of supported metal oxides: III. Water-gas shift over supported iron and zinc oxides. In: *Journal of Catalysis* 101.1 (1986), pp. 35–42. ISSN: 0021-9517. DOI: 10.1016/0021-9517(86)90226-5.
- Riedel, T.: *Reaktionen von CO<sub>2</sub> bei der Fischer-Tropsch Synthese- Kinetik und Selektivität: Doctoral Dissertation Universität Karlsruhe*. Shaker Verlag, 2002. ISBN: 3-8322-1217-5.
- Riedel, T.; Walter, S.; Claeys, M.; Schulz, H.; Schaub, G.: ‘Fuels and petrochemicals from CO<sub>2</sub> via Fischer-Tropsch synthesis — steady state catalyst activity and selectivity’. In: *Studies in Surface Science and Catalysis : Advances in Chemical Conversions for Mitigating Carbon Dioxide Proceedings of the Fourth International Conference on Carbon Dioxide Utilization*. Ed. by T. Inui, M.; Anpo, M.; Izui, K.; Yanagida,

- S.; Yamaguchi, T. Vol. 114. Elsevier, 1998, pp. 443–446. ISBN: 0167-2991. DOI: 10.1016/S0167-2991(98)80791-X.
- Riedel, T.; Claeys, M.; Schulz, H.; Schaub, G.; Nam, S. S.; Jun, K. W.; Choi, M. J.; Kishan, G.; Lee, K. W.: Comparative study of Fischer–Tropsch synthesis with  $H_2/CO$  and  $H_2/CO_2$  syngas using Fe- and Co-based catalysts. In: *Applied Catalysis A: General* 186.1–2 (1999), pp. 201–213. ISSN: 0926-860X. DOI: 10.1016/S0926-860X(99)00173-8.
- Riedel, T.; Schaub, G.; Jun, K. W.; Lee, K. W.: Kinetics of  $CO_2$  hydrogenation on a K-promoted Fe catalyst. In: *Industrial & engineering chemistry research* 40.5 (2001), pp. 1355–1363. ISSN: 0888-5885.
- Riedel, T.; Schulz, H.; Schaub, G.; Jun, K. W.; Hwang, J. S.; Lee, K. W.: Fischer–Tropsch on Iron with  $H_2/CO$  and  $H_2/CO_2$  as Synthesis Gases: The Episodes of Formation of the Fischer–Tropsch Regime and Construction of the Catalyst. In: *Topics in Catalysis* 26.1-4 (2003), pp. 41–54. ISSN: 1022-5528. DOI: 10.1023/B:T0CA.0000012986.46680.28.
- Rohde, M. P.: *In-situ  $H_2O$  removal via hydrophilic membranes during Fischer-Tropsch and other fuel-related synthesis reactions: Doctoral Dissertation KIT*. KIT Scientific Publishing, 2011. ISBN: 978-86644-640-3.
- Rohde, M. P.; Schaub, G.; Khajavi, S.; Jansen, J. C.; Kapteijn, F.: Fischer–Tropsch synthesis with in situ  $H_2O$  removal – Directions of membrane development. In: *Microporous and Mesoporous Materials* 115.1–2 (2008), pp. 123–136. ISSN: 1387-1811. DOI: 10.1016/j.micromeso.2007.10.052.
- Rongxian, B.; Yisheng, T.; Yizhuo, H.: Study on the carbon dioxide hydrogenation to iso-alkanes over Fe–Zn–M/zeolite composite catalysts. In: *Fuel Processing Technology* 86.3 (2004), pp. 293–301. ISSN: 0378-3820. DOI: 10.1016/j.fuproc.2004.05.001.
- Rönsch, S.; Matthischke, S.; Müller, M.; Eichler, P.: Dynamische Simulation von Reaktoren zur Festbettmethanisierung: Dynamic Simulation of Fixed-Bed Methanation Reactors. In: *Chemie Ingenieur Technik* 86.8 (2014), pp. 1198–1204. ISSN: 0009286X. DOI: 10.1002/cite.201300046.
- Sabatier, P.; Senderens, J.B.: Nouvelles synthèses du méthane. In: *Académie des Sciences* 134 (1902), p. 514.
- Sarkari, M.; Fazlollahi, F.; Ajamein, H.; Atashi, H.; Hecker, W.C.; Baxter, L.L: Catalytic performance of an iron-based catalyst in Fischer–Tropsch synthesis. In: *Fuel Processing Technology* 127.0 (2014), pp. 163–170. ISSN: 0378-3820. DOI: 10.1016/j.fuproc.2014.05.003.
- Sasol: *Marlotherm, Heat-transfer fluids*. 2009. URL: [www.sasoltechdata.com/MarketingBrochures/Marlotherm.pdf](http://www.sasoltechdata.com/MarketingBrochures/Marlotherm.pdf), visited on 17/06/2015.



- Schaaf, T.; Grünig, J.; Schuster, M.; Rothenfluh, T.; Orth, A.: Methanation of CO<sub>2</sub> - storage of renewable energy in a gas distribution system. In: *Energy, Sustainability and Society* 4.1 (2014). DOI: 10.1186/s13705-014-0029-1.
- Schaaf, T.; Grünig, J.; Schuster, M.; Orth, A.: Speicherung von elektrischer Energie im Erdgasnetz – Methanisierung von CO<sub>2</sub>-haltigen Gasen: Storage of Electrical Energy in a Gas Distribution System – Methanation of CO<sub>2</sub>-Containing Gases. In: *Chemie Ingenieur Technik* 86.4 (2014), pp. 476–485. ISSN: 0009286X. DOI: 10.1002/cite.201300144.
- Schaub, G.; Pabst, K.: ‘Synthetic Hydrocarbon Fuels from Lignocellulosic Biomass’. In: *Carbon-Neutral Fuels and Energy Carriers*. Ed. by Muradov, N.Z.; Veziroğlu, T.N. Taylor and Francis, CRC press, 2011, pp. 465–491. ISBN: 978-1-4398-1857-2.
- Schaub, G.; Eilers, H.; Iglesias González, M.: ‘Chemical Storage of Renewable Electricity via Hydrogen – Principles and Hydrocarbon Fuels as an Example’. In: *Transition to Renewable Energy Systems*. Wiley-VCH Verlag GmbH & Co. KGaA, 2013, pp. 619–628. ISBN: 9783527673872. DOI: 10.1002/9783527673872.ch30.
- Schaub, G.; Turek, T.: ‘Zukunftsfähige Techniken zur Energiewandlung und Energienutzung – Orientierung und Beispiele’. In: *Vom Praktisch-Werden der Ethik in interdisziplinärer Sicht*. Ed. by Maring, Matthias. Vol. 7. Schriftenreihe des Zentrums für Technik- und Wirtschaftsethik am Karlsruher Institut für Technologie. Karlsruhe: KIT Scientific Publishing, 2014, pp. 331–340. ISBN: 3731503255.
- Schiesser, W. E.; Griffiths, G. W.: *A compendium of partial differential equation models: Method of lines analysis with Matlab*. Cambridge and New York: Cambridge University Press, 2009. ISBN: 0521519861.
- Schlereth, D.; Hinrichsen, O.: A fixed-bed reactor modeling study on the methanation of CO<sub>2</sub>. In: *Chemical Engineering Research and Design* 92.4 (2014), pp. 702–712. ISSN: 0263-8762. DOI: 10.1016/j.cherd.2013.11.014.
- Schulz, H.: ‘Comparing Fischer-Tropsch synthesis on iron- and cobalt catalysts: The dynamics of structure and function’. In: *Studies in Surface Science and Catalysis 163 : Fischer-Tropsch Synthesis, Catalyst and Catalysis*. Ed. by Davis, B. H.; Ocelli, M. L. Vol. 163. Elsevier, 2007, pp. 177–199. ISBN: 0167-2991. DOI: 10.1016/S0167-2991(07)80479-4.
- Schulz, H.: “Coking” of zeolites during methanol conversion: Basic reactions of the MTO-, MTP- and MTG processes. In: *Catalysis Today* 154.3–4 (2010), pp. 183–194. ISSN: 0920-5861. DOI: 10.1016/j.cattod.2010.05.012.
- Schulz, H.: Selforganization in Fischer–Tropsch synthesis with iron- and cobalt catalysts. In: *Catalysis Today* 228 (2014), pp. 113–122. ISSN: 0920-5861.
- Schulz, H.; Böhringer, W.; Kohl, C. P.; Rahman, N. M.; Will, A.: *Entwicklung und Anwendung der Kapillar-GC-Gesamtprobetechnik für Gas/Dampf- Vielstoffgemische: Projekt 320*. Ed. by DGMK. 1984.

- Schulz, H.; Steen, E. van; Claeys, M.: Specific inhibition as the kinetic principle of the Fischer-Tropsch synthesis. In: *Topics in Catalysis* 2.1-4 (1995), pp. 223–234. ISSN: 1022-5528. DOI: 10.1007/BF01491969.
- Schulz, H.; Claeys, M.; Harms, S.: ‘Effect of water partial pressure on steady state Fischer-Tropsch activity and selectivity of a promoted cobalt catalyst’. In: *Natural Gas Conversion IV*. Ed. by M. de Pontes, R.L. Espinoza, C.P. Nicolaides, J.H. Scholtz; M.S. Scurrill. Vol. 107. Studies in Surface Science and Catalysis. Elsevier, 1997, pp. 193–200. DOI: 10.1016/S0167-2991(97)80334-5.
- Schulz, H.; Claeys, M.: Kinetic modelling of Fischer-Tropsch product distributions. In: *Applied Catalysis A: General* 186.1–2 (1999), pp. 91–107. ISSN: 0926-860X. DOI: 10.1016/S0926-860X(99)00166-0.
- Schulz, H.; Schaub, G.; Claeys, M.; Riedel, T.: Transient initial kinetic regimes of Fischer-Tropsch synthesis. In: *Applied Catalysis A: General* 186.1-2 (1999), pp. 215–227. ISSN: 0926-860X.
- Schüth, F.: Chemical Compounds for Energy Storage. In: *Chemie Ingenieur Technik* 83.11 (2011), pp. 1984–1993. ISSN: 0009286X. DOI: 10.1002/cite.201100147.
- Schweitzer, C.: Synthesizing strengths of 1st and 3rd generation biorefineries. Biomethanol as a biorefinery product. In: *International Sugar Journal* (2014), pp. 64–70.
- Shannon, S. L.; Goodwin Jr., J. G.: Characterization of Catalytic Surfaces by Isotopic-Tranient Kinetics during Steady-State Reaction. In: *Chemical Reviews* 95 (1995), pp. 677–695.
- Sie, S. T.; Krishna, R.: Fundamentals and selection of advanced Fischer-Tropsch reactors. In: *Applied Catalysis A: General* 186.1–2 (1999), pp. 55–70. ISSN: 0926-860X. DOI: 10.1016/S0926-860X(99)00164-7.
- Siemens: *SILYZER - Hydrogen Solutions*. 2015. URL: [www.industry.siemens.com/topics/global/en/pem-electrolyzer/silyzer/Pages/silyzer.aspx](http://www.industry.siemens.com/topics/global/en/pem-electrolyzer/silyzer/Pages/silyzer.aspx), visited on 27/04/2015.
- Silveston, P.; Hudgins, R. R.; Renken, A.: Periodic operation of catalytic reactors—introduction and overview. In: *Catalysis Today* 25.2 (1995), pp. 91–112. ISSN: 0920-5861. DOI: 10.1016/0920-5861(95)00101-K.
- Smit, E. de; Weckhuysen, B. M.: The renaissance of iron-based Fischer-Tropsch synthesis: on the multifaceted catalyst deactivation behaviour. In: *Chemical Society reviews* 37.12 (2008), pp. 2758–2781. ISSN: 0306-0012. DOI: 10.1039/b805427d.
- Smith, B.; Loganathan, M.; Shantha, M. S.: A Review of the Water Gas Shift Reaction Kinetics. In: *International Journal of Chemical Reactor Engineering* 8.1 (2010). ISSN: 1542-6580. DOI: 10.2202/1542-6580.2238.
- Smolinka, T.; Günther, M.; Garcke, J.: *Stand und Entwicklungspotenzial der Wasserelektrolyse zur Herstellung von Wasserstoff aus regenerativen Energien: NOW-Studie*. 2011. URL: [www.now-gmbh.de/fileadmin/user\\_upload/RE\\_Publikationen\\_NEU\\_](http://www.now-gmbh.de/fileadmin/user_upload/RE_Publikationen_NEU_)

- 2013/Publikationen\_NIP/NOW-Studie-Wasserelektrolyse-2011.pdf, visited on 11/12/2012.
- Soled, S.; Iglesia, E.; Fiato, R.A.: Activity and selectivity control in iron catalyzed Fischer-Tropsch synthesis. In: *Catalysis Letters* 7.1-4 (1990), pp. 271–280. ISSN: 1011-372X. DOI: 10.1007/BF00764508.
- Spencer, M.S.: On the activation energies of the forward and reverse water-gas shift reaction. In: *Catalysis Letters* 32.1-2 (1995), pp. 9–13. ISSN: 1011-372X. DOI: 10.1007/BF00806097.
- Stankiewicz, A.; Kuczynski, M.: An industrial view on the dynamic operation of chemical converters. In: *Chemical Engineering and Processing: Process Intensification* 34.4 (1995), pp. 367–377. ISSN: 0255-2701. DOI: 10.1016/0255-2701(95)00537-4.
- Steen, E. van: *Elementarschritte der Fischer-Tropsch CO-Hydrierung mit Eisen- und Kobaltkatalysatoren: Doctoral Dissertation Universität Karlsruhe*. 1993.
- Steynberg, A. P.; Espinoza, R. L.; Jager, B.; Vosloo, A. C.: High temperature Fischer-Tropsch synthesis in commercial practice. In: *Applied Catalysis A: General* 186.1–2 (1999), pp. 41–54. ISSN: 0926-860X. DOI: 10.1016/S0926-860X(99)00163-5.
- Steynberg, A. P.; Dry, M. E.: *Fischer-Tropsch technology*. Vol. 152. Studies in Surface Science and Catalysis. Amsterdam and Boston: Elsevier, 2004. ISBN: 0080472796.
- TENNET: *Actual and forecast photovoltaic energy feed-in*. 2014. URL: [www.tennettso.de/site/en/Transparency/publications/network-figures/actual-and-forecast-photovoltaic-energy-feed-in-land?tag=7&monat=04&jahr=2013&country\\_token=COUNTRY\\_TOKEN&lang=en\\_EN](http://www.tennettso.de/site/en/Transparency/publications/network-figures/actual-and-forecast-photovoltaic-energy-feed-in-land?tag=7&monat=04&jahr=2013&country_token=COUNTRY_TOKEN&lang=en_EN), visited on 23/04/2015.
- Tischer, S.; Correa, C.; Deutschmann, O.: Transient three-dimensional simulations of a catalytic combustion monolith using detailed models for heterogeneous and homogeneous reactions and transport phenomena: Structured Catalysts and Reactors. In: *Catalysis Today* 69.1–4 (2001), pp. 57–62. ISSN: 0920-5861. DOI: 10.1016/S0920-5861(01)00355-8.
- Tischer, S.; Jiang, Y.; Hughes, K.; Patil, M.; Murtagh, M.: Three-Way-Catalyst Modeling- A Comparison of 1D and 2D Simulations. In: *Society of Automotive Engineers Technical Paper* (2007), pp. 01–1071.
- Tronconi, E.; Nova, I.; Ciardelli, C.; Chatterjee, D.; Bandl-Konrad, B.; Burkhardt, T.: Modelling of an SCR catalytic converter for diesel exhaust after treatment: Dynamic effects at low temperature. In: *Catalysis Today* 105.3–4 (2005), pp. 529–536. ISSN: 0920-5861. DOI: 10.1016/j.cattod.2005.06.043.
- UBA: *Energy target 2050: 100 % renewable electricity supply*. Ed. by Umweltbundesamt. 2014. URL: [www.umweltbundesamt.de/sites/default/files/medien/publikation/add/3997-0.pdf](http://www.umweltbundesamt.de/sites/default/files/medien/publikation/add/3997-0.pdf), visited on 10/11/2014.

- UBA: *Treibhausgasneutrales Deutschland im Jahr 2050. Hintergrundpapier*. Ed. by Umweltbundesamt. 2014. URL: [www.umweltbundesamt.de/en/publikationen/treibhausgasneutrales-deutschland-im-jahr-2050](http://www.umweltbundesamt.de/en/publikationen/treibhausgasneutrales-deutschland-im-jahr-2050), visited on 11/11/2014.
- UBA: *UBA's 2014 emissions data indicates trend reversal in climate protection*. 2015. URL: [www.umweltbundesamt.de/en/press/pressinformation/ubas-2014-emissions-data-indicates-trend-reversal](http://www.umweltbundesamt.de/en/press/pressinformation/ubas-2014-emissions-data-indicates-trend-reversal), visited on 23/04/2015.
- Unruh, D.: *Fischer-Tropsch-Synthese mit Synthesegasen aus Biomasse- Verbesserung der Kohlenstoffnutzung durch Anwendung eines Membranreaktors: Doctoral Dissertation Universität Karlsruhe*. Berichte aus der Verfahrenstechnik. Aachen: Shaker, 2006. ISBN: 383225529X.
- VDI: *VDI-Wärmeatlas: Berechnungsunterlagen für Druckverlust, Wärme- und Stoffübertragung*. 10., bearb. und erw. Aufl. Berlin and Heidelberg [u.a.]: Springer, 2006. ISBN: 9783540297161.
- VFF: *Duranit, Vereinigte Füllkörper-Fabriken*. 2015. URL: [www.vff-duranit.de](http://www.vff-duranit.de), visited on 12/05/2015.
- Wang, W.; Wang, S.; Ma, X.; Gong, J.: Recent advances in catalytic hydrogenation of carbon dioxide. In: *Chemical Society Reviews* 40.7 (2011), pp. 3703–3727. DOI: 10.1039/C1CS15008A.
- Weimer, T.; Schaber, K.; Specht, M.; Bandi, A.: Methanol from atmospheric carbon dioxide: A liquid zero emission fuel for the future. In: *Proceedings of the International Energy Agency Greenhouse Gases: Mitigation Options Conference* 37.6–8 (1996), pp. 1351–1356. ISSN: 0196-8904. DOI: 10.1016/0196-8904(95)00345-2.
- Wired Chemist: *Standard Heats and Free Energies of Formation and Absolute Entropies of Organic Compounds*. 2015. URL: [www.wiredchemist.com/chemistry/data/entropies-organic](http://www.wiredchemist.com/chemistry/data/entropies-organic), visited on 17/06/2015.
- Xiaoding, X.; Moulijn, J. A.: Mitigation of CO<sub>2</sub> by Chemical Conversion: Plausible Chemical Reactions and Promising Products. In: *Energy & Fuels* 10.2 (1996), pp. 305–325. ISSN: 0887-0624. DOI: 10.1021/ef9501511.
- Xu, J.; Froment, G. F.: Methane steam reforming, methanation and water-gas shift: I. Intrinsic kinetics. In: *AIChE Journal* 35.1 (1989), pp. 88–96. ISSN: 1547-5905. DOI: 10.1002/aic.690350109.
- Yates, I. C.; Satterfield, C. N.: Intrinsic kinetics of the Fischer-Tropsch synthesis on a cobalt catalyst. In: *Energy & Fuels* 5.1 (1991), pp. 168–173. ISSN: 0887-0624. DOI: 10.1021/ef00025a029.
- You, Z.; Deng, W.; Zhang, Q.; Wang, Y.: Hydrogenation of carbon dioxide to light olefins over non-supported iron catalyst. In: *Chinese Journal of Catalysis* 34.5 (2013), pp. 956–963. ISSN: 1872-2067. DOI: 10.1016/S1872-2067(12)60559-2.

- Yuan, X.; Liu, H.; Gao, Y.: Diesel Engine SCR Control: Current Development and Future Challenges. In: *Emission Control Science and Technology* 1.2 (2015), pp. 121–133. ISSN: 2199-3629. DOI: 10.1007/s40825-015-0013-z.
- Zagoruiko, A. N.: The reverse-flow operation of catalytic reactors: history and prospects. In: *Current topics in Catalysis* 10 (2012), pp. 113–129.
- Zakkour, P.; Cook, G.: *CCS Industry Roadmap: High purity CO<sub>2</sub> sources: Sectoral Assessment – Final Draft Report*. 2010. URL: [www.unido.org/fileadmin/user\\_media/Services/Energy\\_and\\_Climate\\_Change/Energy\\_Efficiency/CCS/High\%20Purity\\_FINAL\%20DRAFT.pdf](http://www.unido.org/fileadmin/user_media/Services/Energy_and_Climate_Change/Energy_Efficiency/CCS/High\%20Purity_FINAL\%20DRAFT.pdf), visited on 28/04/2015.
- Zeman, F.: Energy and Material Balance of CO<sub>2</sub> Capture from Ambient Air. In: *Environmental Science & Technology* 41.21 (2007), pp. 7558–7563. DOI: 10.1021/es070874m.
- Zimmerman, W. H.; Bukur, D. B.: Reaction kinetics over iron catalysts used for the fischer-tropsch synthesis. In: *The Canadian Journal of Chemical Engineering* 68.2 (1990), pp. 292–301. ISSN: 1939-019X. DOI: 10.1002/cjce.5450680215.



# Notation

## Symbols (Latin)

Symbol	Description	Definition	Dimension
$A$	amplitude sinus wave function	-	-
$A_i$	peak area (GC)	-	-
$A_R$	reactor cross sectional area	$\frac{\pi}{4}d_t^2$	m <sup>2</sup>
$a_j$	inhibition coefficient for H <sub>2</sub> O in reaction $j$		-
$b_j$	inhibition coefficient for CO <sub>2</sub> in reaction $j$		-
$C$	catalyst cost		€/kg
$c_i$	concentration	$\frac{\dot{m}}{V}$	mol/m <sup>3</sup>
$c_{p,g}$	heat capacity of gas mixture	-	J/kg K
$c_{p,i}$	heat capacity of component $i$	-	J/kg K
$c_{p,s}$	heat capacity of solid	-	J/kg K
$d$	diameter	basic dimension	mm, m
$d_p$	diameter of particle, pellet		mm, m
$D_{12}$	molecular diffusion coefficient	Eq. H.11	m <sup>2</sup> /s
$D_{Kn}$	Knudsen Diffusion	Eq. I.25	m <sup>2</sup> /s
$D_{pore}$	pore diffusion	-	m <sup>2</sup> /s
$D_{eff,ax}$	effective axial dispersion	Eq. I.26	m <sup>2</sup> /s
$D_{eff}$	effective diffusion	Eq. I.26	m <sup>2</sup> /s
$E_{A,j}$	activation energy	$-RT \ln \left( \frac{k_j}{k_{0,j}} \right)$	J/mol
$F$	F-curve	Eq.7.1	
$f_i$	GC calibration factor		-
$f$	frequency sinus curve		-
$F_{i,j}$	factor for calculation thermal conductivity and viscosity	-	kg/s
$F$	flow rate	-	
GHSV	gas hourly space velocity	Eq.4.12	1/h

## Notation

$I$	investment	-	€
$k_j$	reaction rate constant		mol/s kg Pa
$k_{0,j}$	pre-exponential factor	-	mol/s kg Pa
$K_p$	equilibrium constant	$\prod_i p_i^{\nu_i}$	-
$K_c$	proportional constant controller	Eq. 4.8	m <sup>3</sup> /(h bar)
$L$	length	basic dimension	
$L_{\text{bed}}$	catalyst bed length		m, mm
$L_t$	reactor tube length	-	m
$L_p$	length of pellet		m, mm
$L$	load	-	-
$M_s$	saturation magnetisation	-	
$m_{\text{cat}}$	catalyst mass	-	kg
$\tilde{m}$	amount of substance	basic dimension	mol
$\tilde{M}_g$	molecular mass of the gas mixture	g/mol	
$\tilde{M}_i$	molecular mass of component $i$	g/mol	
$N$	number of data points, units	-	-
$N_C$	carbon number	-	-
$NT$	number of tubes	-	-
$P_{\text{el}}$	Electric power	-	W
$p$	reaction pressure		Pa/bar
$p_i$	partial pressure	Eq. 5.11	Pa
$R$	universal gas constant	8.314	J/mol K
$R_F$	recycle ratio	$\frac{F_{n,R}}{F_{n,F}}$	-
$R_{\text{out}}$	recycle ratio	$\frac{F_{n,R}}{F_{n,\text{out}}}$	-
$R^2$	correlation coefficient	-	-
$R_{\text{WP}}$	Weight-profile R factor, Rietveld refinement	-	
$r_j$	reaction rate		mol/s kg
$r_t$	tube radius	-	m
$r_{\text{pore}}$	pore radius	-	m
$r_L$	rate of load change	-	%/ min
$S_i$	selectivity	Eq. 5.8	
$s$	reactor wall thickness	-	m
$s$	students factor		-
$t$	time	basic dimension	s
$T$	absolute Temperature	basic dimension	K
$U_{\text{eff}}$	heat transport coefficient	-	W/m <sup>2</sup> K
$u_{\text{sf}}$	superficial flow velocity	$\frac{4F_{V,\text{in}}}{\pi d_R^2}$	m/s



---

$V$	volume	basic dimension	$\text{m}^3$
$W_{\text{compressor,R}}$	work recycle compressor	-	W
$X_i$	conversion	Eq. 5.4	-
$y_{\text{m},i}$	hydrocarbon mass fraction	Eq. 5.9	-
$y_{\text{n},i}$	hydrocarbon mole fraction		-
$Y_i$	yield	Eq. 5.5	-
$z$	axial variable	-	m
$Z$	dimensionless molar flow	Eq. 7.5	-
$Z^*$	dimensionless molar flow	Eq. 7.6	-

---

## Symbols (Greek)

Symbol	Description	Definition	Dimension
$\alpha$	chain growth probability	Eq. 3.6	-
$\alpha_g$	heat transport coefficient gas-particle	Eq. I.20	W/ m <sup>2</sup> K
$\alpha_{out}$	heat transport coefficient wall-cooling medium	-	W/ m <sup>2</sup> K
$\alpha_{wall}$	heat transport coefficient bed-wall	-	W/ m <sup>2</sup> K
$\alpha_{in}$	heat transport coefficient catalyst bed	-	W/ m <sup>2</sup> K
$\beta$	mass transfer coefficient gas-particle	Eq. I.17	m/ s
$\eta_i$	dynamic viscosity of component i	Eq. H.8	Pa s
$\eta_g$	dynamic viscosity of the gas mixture	Eq. H.9	Pa s
$\gamma$	ratio of specific heat	-	-
$\lambda_i$	thermal conductivity of component i	Eq. H.16	W/ m K
$\lambda_g$	thermal conductivity of the gas mixture	Eq. H.14	W/ m K
$\lambda_p$	thermal conductivity of the particle	Eq. I.37	W/ m K
$\lambda_{bed}$	thermal conductivity of the catalyst bed	Eq. I.31	W/ m K
$\lambda_{eff,r}$	effective thermal radial conductivity of the catalyst bed	Eq. I.38	W/ m K
$\varepsilon$	porosity	$1 - \frac{\rho_{bed}}{\rho_s}$	-
$\nu_{i,j}$	stoichiometric coefficient	-	-
$\nu_g$	kinematic viscosity of the gas mixture	Eq. H.10	m <sup>2</sup> / s
$\rho$	density		kg/m <sup>3</sup>
$\rho_g$	gas density	Eq.H.6	kg /m <sup>3</sup>
$\rho_{active,R}$	mass-density of active material in the bed	$m_{active}/V_R$	kg/m <sup>3</sup>
$\rho_{active,p}$	mass-density of active material in the particle	$m_{cat}/V_p$	kg/m <sup>3</sup>
$\rho_{catalyst,p}$	mass-density of the catalyst particle	$m_{cat}/V_p$	kg/m <sup>3</sup>
$\rho_{support,p}$	mass-density of support in the particle	$m_{support}/V_p$	kg/m <sup>3</sup>
$\rho_{bed}$	mass-density of the bed	$m_{cat}/V_R$	kg/m <sup>3</sup>

---

$\rho_s$	solid density		kg/m <sup>3</sup>
$\sigma$	standard deviation	Eq. 5.15	-
$\tau$	characteristic time	Eq. 8.12	s
$\tau_{\text{mod}}$	modified residence time	Eq. 5.10	kg s/m <sup>3</sup>
$\tau_L$	tortuosity	-	-
$\tau_p$	time period	-	-
$\theta_i$	degree of coverage	-	-
$\chi_{\text{shell}}$	thickness active material	-	m
$\Phi$	dimensionless time	$\Phi$	= -
		$t/(V_{\text{PMF}}/F_v)$	

---

## Abbreviations

Symbol	Description
Bo	Bodenstein Number
CFCs	Chlorofluorocarbons
CPr	cyclopropane
Da	Damköhler
DH	direct hydrogenation
DME	dimethylether
DeNox	denitrification
Ely	Electrolyser
ER	Eley-Rideal
FB	fixed-bed
FID	flame ionisation detector
FT	Fischer-Tropsch
GC	gas chromatograph
GHG	greenhouse gas
$(\text{H}_2/\text{CO}_2)_{\text{in}}$	$(p_{\text{H}_2}/p_{\text{CO}_2})_{\text{in}}$
HC	hydrocarbon
HHV	higher heating value
LPG	liquefied petroleum gas
LHV	lower heating value
liq	liquid
MFC	mass flow controller
MTG	methanol-to-gasoline
NG	natural gas
NT	number of tubes
Nu	Nusselt
ODE	Ordinary Differential Equation
Pe	Peclet
PEM	Polymer electrolyte membrane
PFR	plug flow reactor
PV	Photovoltaic
Pr	Prandtl
rel	relative
RE	renewable energies
Re	Reynolds
SCR	selective catalytic reduction
SNG	substitute natural gas

---

STP	standard Temperature and Pressure ( $T = 273.15 \text{ K}$ , $p = 101315 \text{ Pa}$ )
Sc	Schmidt
Sh	Sherwood
TCD	thermal conductivity detector
TOS	time-on-stream
UBA	Umwelt Bundesamt
VOC	volatil organic carbon

---

## Indices

---

Symbol	Description
ad	adiabatic
av	average
bed	bed of catalyst
cal	calculated
cat	catalyst
eff	effective
el	electric
eq	equivalent
exp	experimental
ext	external
F	fresh
g	gas
$i$	index for component
in	inlet
in R	inlet reactor
int	internal
$j$	index for reaction
m	mass
max	maximum value
min	minimum value
mean	mean value
mod	modified
n	molar
out	outlet
out R	outlet reactor
out S	outlet system

## Notation

---

ov	overall
p	particle, pellet
pp	per pass
prop	propagation
R	recycle
R-c	recycle compressor
r	reactor
rr	reaction rate
ref	reference
rel	relative
S	system
s	solid
shell	catalyst shell
t	tube
term	termination
v	volumetric
vessel	reactor vessel

---

# Appendix

## **A Heating value adjustment using Fischer-Tropsch Synthesis: combination Fischer-Tropsch and methane synthesis, extra figures**

Figure A.1 shows the HHV and Wobbe index for the combination of FT and methane synthesis using a  $(\text{H}_2/\text{CO}_2)_{\text{in}} = 5$  in the FT reactor and with the aim to produce a gas mixture with 5 vol% of  $\text{H}_2$ . Figure A.2 shows the relative density of the gas for 2 and 5 vol %.

Figure A.3, A.4 and A.5 show the results from calculations done for a FT reactor operated at  $(\text{H}_2/\text{CO}_2)_{\text{in}} = 8$ ,  $X_{\text{CO}_2}$  and hydrocarbon selectivity ( $\alpha$ ) are varied. Gas mixtures with 2 and 5 vol % are considered.

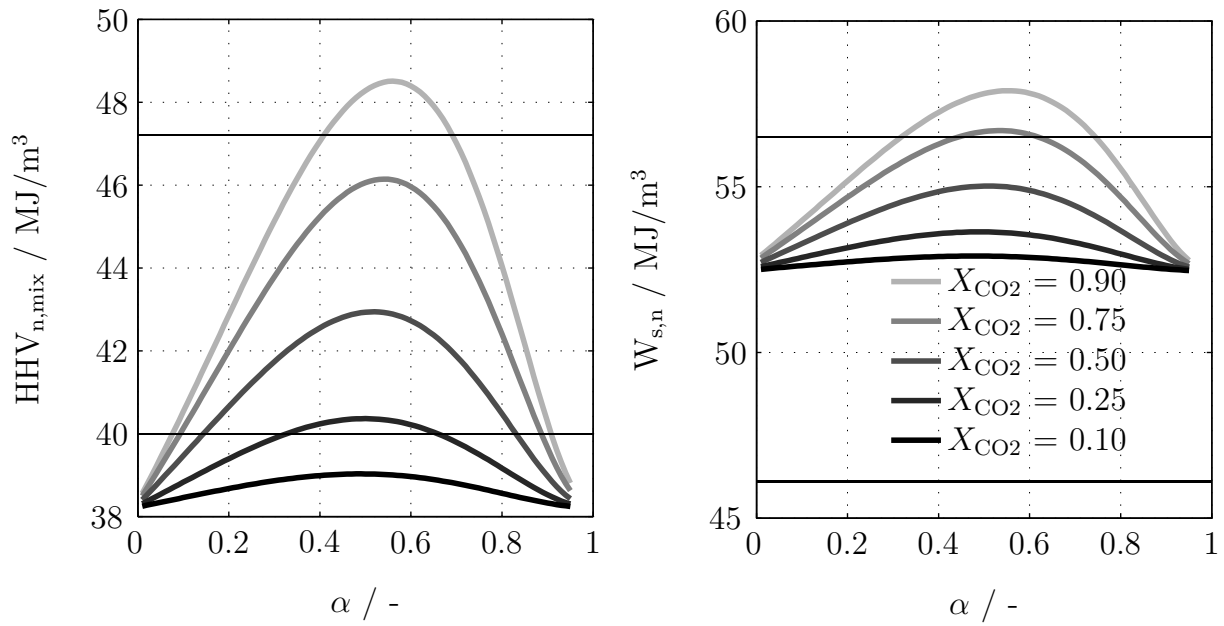


Figure A.1: HHV and Wobbe index of different gas mixtures with 5 vol% of  $\text{H}_2$  after FT and methanation reactors as a function hydrocarbon selectivity ( $\alpha$ ) and  $\text{CO}_2$  conversions on the FT reactor, operated at  $(\text{H}_2/\text{CO}_2)_{\text{in}} = 5$ . Details about relative density in Figure A.2. Horizontal black lines show the specification values defined in section 4.1.1

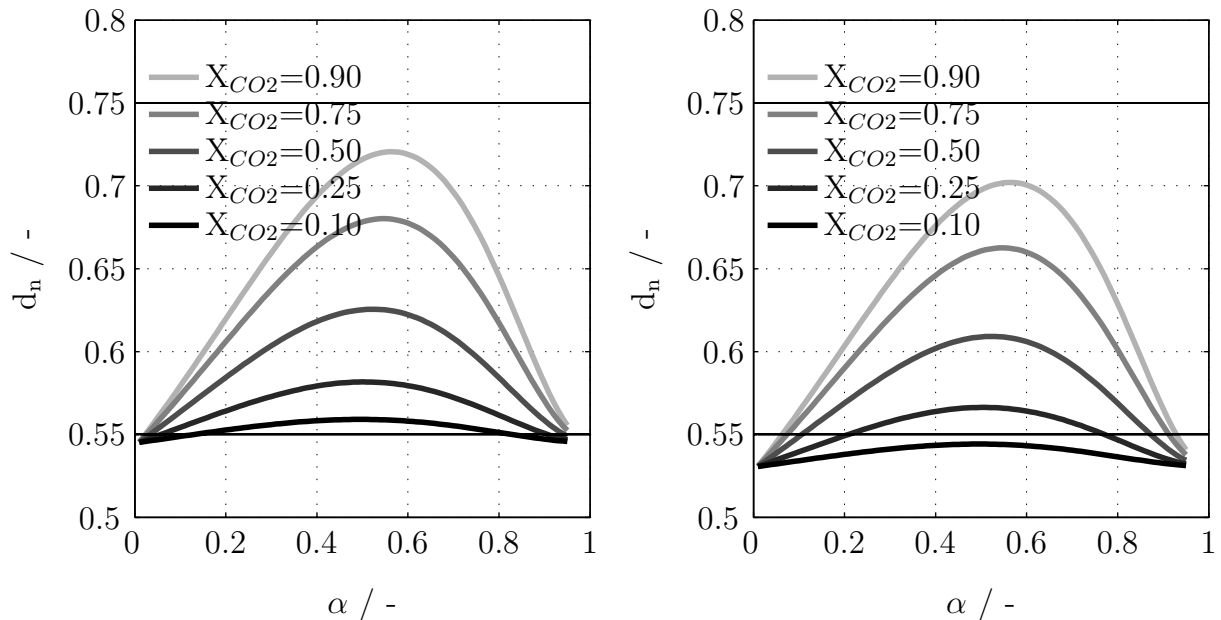


Figure A.2: Relative density for different gas mixtures with 2 vol%  $\text{H}_2$  (left) and 5 vol%  $\text{H}_2$  (right) as a function of  $\text{CO}_2$  conversion in the FT unit and hydrocarbon selectivity ( $\alpha$ ) for a  $(\text{H}_2/\text{CO}_2)_{\text{in}} = 5$  in the FT reactor. Horizontal black lines show the specification values defined in section 4.1.1



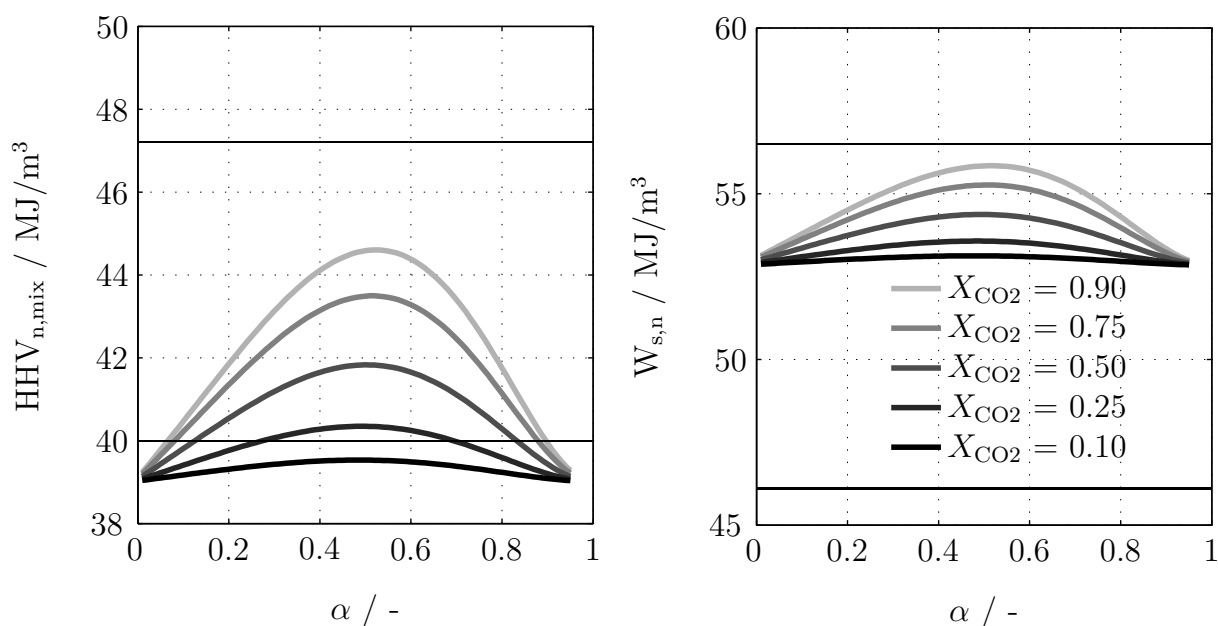


Figure A.3: HHV and Wobbe index for different gas mixtures with 2 vol% H<sub>2</sub> after FT and methanation reactors as a function hydrocarbon selectivity ( $\alpha$ ) and CO<sub>2</sub> conversions on the FT reactor, operated at  $(\text{H}_2/\text{CO}_2)_{\text{in}} = 8$ . Details about relative density in Figure A.5. Horizontal black lines show the specification values defined in section 4.1.1

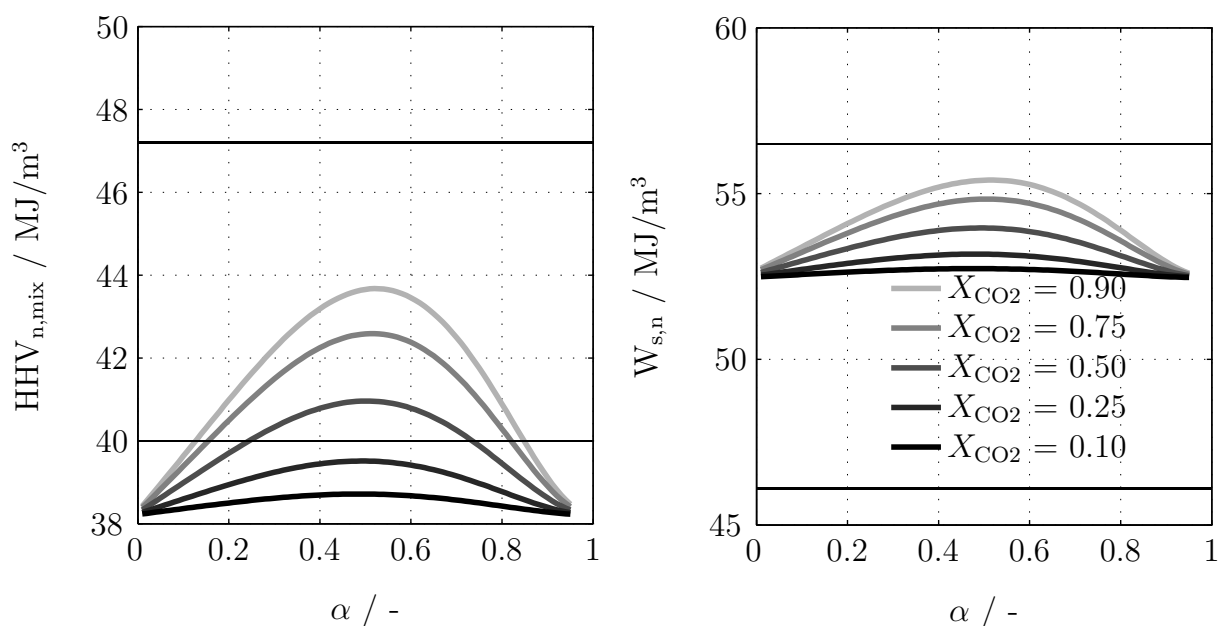


Figure A.4: HHV and Wobbe index for different gas mixtures with 5 vol% H<sub>2</sub> after FT and methanation reactors as a function hydrocarbon selectivity ( $\alpha$ ) and CO<sub>2</sub> conversions on the FT reactor, operated at  $(\text{H}_2/\text{CO}_2)_{\text{in}} = 8$ . Details about relative density in Figure A.5. Horizontal black lines show the specification values defined in section 4.1.1

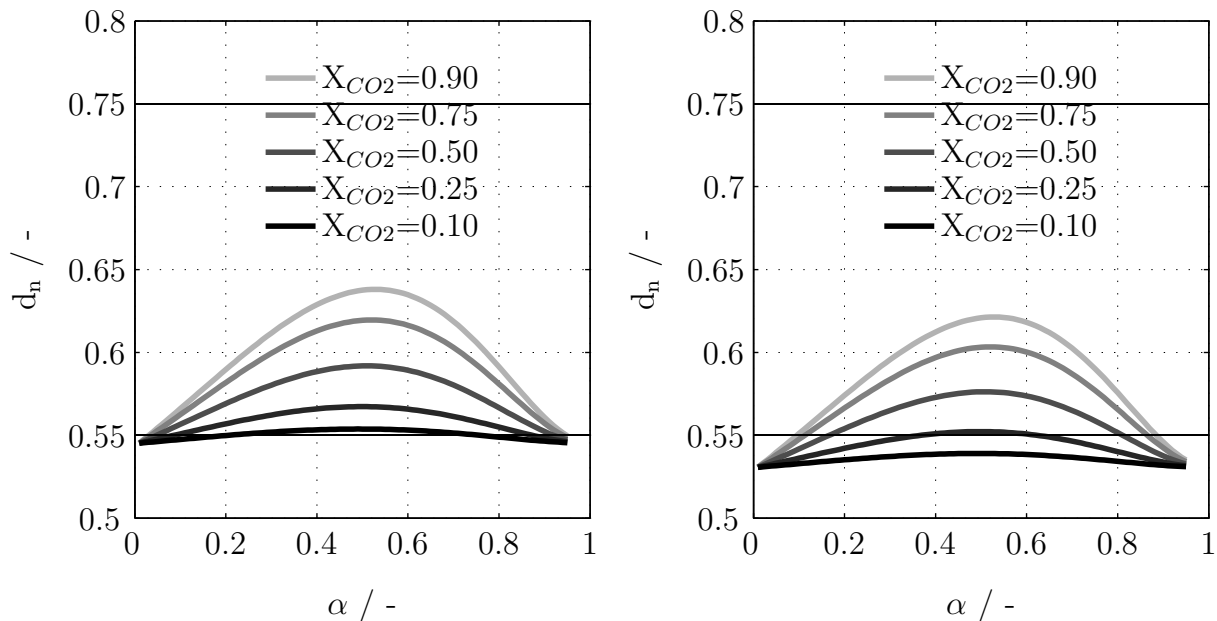


Figure A.5: Relative density for different gas mixtures with 2 vol%  $H_2$  (left) and 5 vol%  $H_2$  (right) as a function of  $CO_2$  conversion in the FT unit and hydrocarbon selectivity (represented by  $\alpha$ ) for a  $(H_2/CO_2)_{in} = 8$ . Horizontal black lines show the boundary values defined in section 4.1.1

## B Effects of part-load operation of synthesis reactor on size of $H_2$ storage and reactor: electricity production according to a sinus wave function

The fluctuating nature of electricity production can be mathematically described by a sinus wave function as a periodic input. Sinus wave functions are preferred for mathematical problems versus simple stepwise periods, which are preferred for experimental work (easier to perform and affecting the system more strongly). Two different parameters can be adjusted in a sinus wave, the amplitude (deviation from the average value) and the time period  $\tau_p$ . The amplitude ( $A$ ) is calculated based on the average electricity production. Figure B.6 shows an example sinus wave with  $\tau_p = 10080$  min (7 days) and  $A = 0.8 \cdot P_{el,average} = 5.3$  MW. The average electricity production is  $P_{el,average} = 6.64$  MW, the same as for the wind farm (Figure 4.6).

The aim of this section is to study, in a systematic way, the influence of  $\tau_p$  and amplitude on the  $H_2$  storage size. Sinus waves are limited considering the rate of load change (at long  $\tau_p$  rate of load change is low and therefore the change is smooth).

The amplitude of the sinus wave function is defined based on the average value (Equation

B.2). The factor  $f$ , varying between 0 and 1, modified the amplitude of the sinus wave function. A value of  $f = 1$  indicates that the function reaches a maximum value that is two times the average value, with a minimum value that is zero. A value of  $f = 0$  indicates that the function becomes a straight line and equals the average (Equation B.1). The maximum value for the sinus wave is 13.3 MW, significantly lower than the 36 MW of the windfarm, nevertheless both have the same average production of electricity.

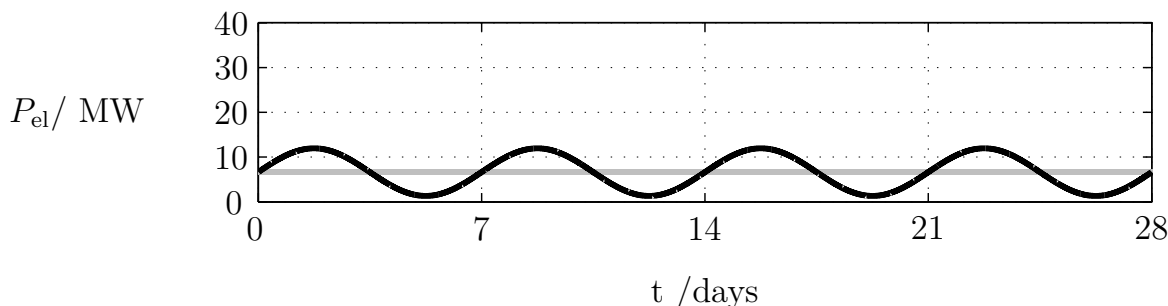


Figure B.6: Example electricity generation represented as a sinus wave  $f = 0.8$  and  $\tau_p = 10080$  minutes (7 days).  $P_{el,max} = 11.95$  MW,  $P_{el,average} = 6.64$  MW

$$P_{el} = A \cdot \sin\left(\frac{2 \cdot \pi}{\tau_p} \cdot t\right) + P_{el,average} \quad (\text{B.1})$$

$$A = f \cdot P_{el,average} \quad (\text{B.2})$$

The necessity of a  $\text{H}_2$  storage using a sinus wave depends on reactor flexibility  $L_{\min}$  and amplitude of the sinus wave function ( $f$ ) (Figure B.7). The curve represented in Figure B.7 is the result of the equality between the inlet  $\text{H}_2$  flow to the storage, Equation 4.5, and the maximum  $\text{H}_2$  flow that can be fed to the reactor for a certain  $L_{\min}$ , Equation 4.11 and  $(\text{H}_2/\text{CO}_2)_{\text{in}} = 3$ . At high amplitudes (high values of  $f$ ), high reactor flexibilities (low values of  $L_{\min}$ ) are needed to avoid the use of a  $\text{H}_2$  storage. The exception is  $f = 1$  (maximum amplitude), where the sinus wave function reaches a value of zero. In this case,  $\text{H}_2$  storage is required.

Figure B.7, right shows the inlet  $\text{H}_2$  flows in the storage for different amplitudes compared with the maximum and minimum  $\text{H}_2$  flow allowed for  $L_{\min} = 0.5$ . At the amplitude corresponding to  $f = 0.33$  the maximum  $\text{H}_2$  flow in the storage is the same as in the reactor, therefore the  $\text{H}_2$  flow could be directly fed into the reactor. Amplitudes higher than 0.33 require the use of a  $\text{H}_2$  storage. Partial-load operation of the reactor combined with a sinus wave function that does not reach  $f = 1$  make possible operation without  $\text{H}_2$  storage.

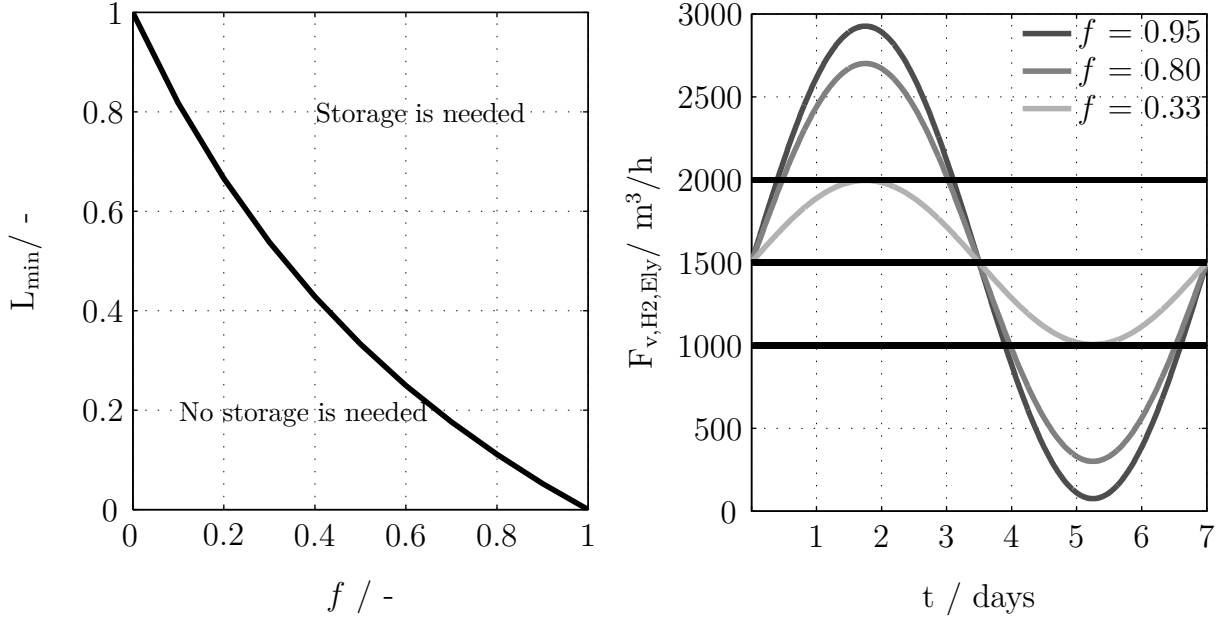


Figure B.7: Left: Necessity of storage as a function of reactor  $L_{\min}$  and amplitude of the sinus wave curve represented as  $f$  (see Equation B.2). Right: H<sub>2</sub> volumetric flow to the storage inlet calculated with a sinus wave at different amplitudes for a constant  $\tau_p = 10080$  min. Horizontal lines represent maximum, average and minimum H<sub>2</sub> flow that can be fed to the reactor for a  $L_{\min} = 0.5$ .

The size of a H<sub>2</sub> storage depends on the amplitude (represented as  $f$ ), the time period  $\tau_p$ , and the reactor flexibility  $L_{\min}$ . Figure B.8, (left) shows that the size of the storage increases with time period and amplitude. The relationship between time period and storage size is linear with a constant amplitude. If time period becomes 7 times longer (e.g.  $\tau_p = 1$  day to  $\tau_p = 7$  days) the  $V_{H_2 \text{ storage}}$  required is also seven times bigger ( $V_{H_2 \text{ storage}, \tau_p = 1} = 25.2 \text{ m}^3$  and  $V_{H_2 \text{ storage}, \tau_p = 7} = 176.4 \text{ m}^3$ ).

Figure B.8, (right) compares the H<sub>2</sub> inlet flow to the storage with the maximum and minimum H<sub>2</sub> flow allowed for the reactor with a  $L_{\min} = 0.5$  for two different time periods. The area above the highest horizontal line corresponds to the amount of H<sub>2</sub> that needs to be stored ( $V_{H_2 \text{ storage}}$ ). At short time periods this area is smaller than at longer ones.

The four week wind farm profile requires a  $V_{H_2 \text{ storage}} = 1703 \text{ m}^3$  for  $L_{\min} = 1$ . The same storage volume is obtained with a sinus wave function,  $\tau_p = 28$  days (4 weeks) and an amplitude between 5.3 MW ( $f = 0.80$ ) and 6.3 MW ( $f = 0.95$ ) ( $V_{H_2 \text{ storage}, f = 0.80} = 1516 \text{ m}^3$ ,  $V_{\text{storage}, f = 0.95} = 1800 \text{ m}^3$ ). The reason is that the sinus wave function has very low rates of load change and also never reaches a period of zero input. In contrast, the example wind farm profile is not regular at all, and the first week, with a very low electricity production, determines the size of the H<sub>2</sub> storage. Therefore the two profiles studied are considered as examples of potential fluctuating conditions in the future, a real case might

be something intermediate.

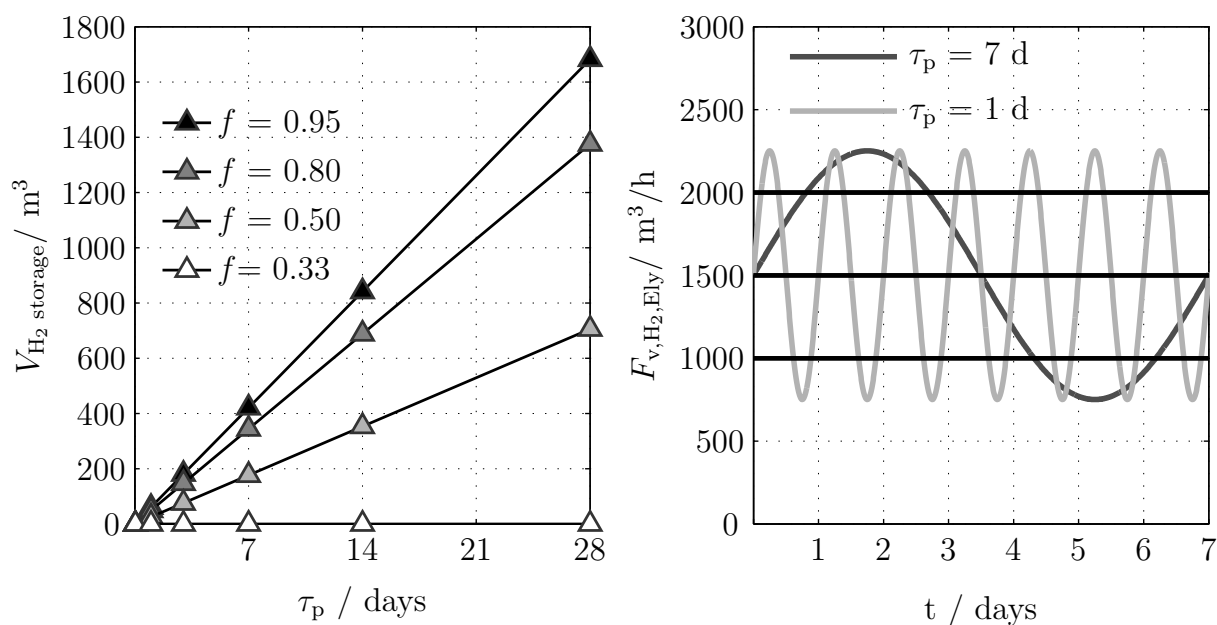


Figure B.8: Left: Size of H<sub>2</sub> storage as a function of amplitude, and time period for a synthesis reactor that is operated between  $L_{\max} = 1$  and  $L_{\min} = 0.5$ . Right: H<sub>2</sub> inlet flow in the storage as a function of the time period when  $f = 0.5$ . Horizontal lines represent maximum, average, and minimum H<sub>2</sub> flow that can be fed to the reactor.

## C Experimental studies in lab-scale fixed-bed reactor: plan and conditions

Table C.1 and C.2 summarised the experiments carried out in lab-scale fixed-bed reactor.

Table C.1: Experimental conditions tested with the 100 g Fe/ 2g K catalyst

$m_{\text{cat}}$ g	$p$ MPa	$(\text{H}_2/\text{CO}_2)_{\text{in}}$ -	$T$ °C	$\tau_{\text{mod}}$ kg s/ m <sup>3</sup>
2	1	4	250	200/400/1000/3000/5000
2	1	4	270	200/400/1000/3000/5000
2	1	4	290	200/400/1000/3000/5000
2	1	4	300	400
2	1	4	330	400
2	1	5	300	400
2	1	8	270	1000
2	2	4	250	400/1000/3000/5000
2	2	4	270	400/1000/3000
2	2	8	250	1000/3000/5000
2	2	8	270	1000/3000
2	2	8	290	1000
2	2	23	290	400/1000
1.5	1	5	250	175/200/300/400/1000/2000/3000
1.5	1	5	270	175/200/300/400/1000/2000/3000
1.5	1	5	290	175/200/300/400/1000/2000/3000
1.5	1	5	300	100/175/200/250/300/400/600/800/1000
1.5	1	5	310	1000
1.5	1	5	320	1000

Table C.2: Experimental conditions tested with the 100 g Fe/ 10g K catalyst

$m_{\text{cat}}$ g	$p$ MPa	$(\text{H}_2/\text{CO}_2)_{\text{in}}$ -	$T$ °C	$\tau_{\text{mod}}$ kg s/ m <sup>3</sup>	
			4	270	400/1000/3000
			4	290	400/1000/3000
			4	310	200/400/1000
	2	10	8	290	400/1000/3000
			8	310	400/1000/3000/5000
			8	330	400/1000/3000/5000

Figure C.9 shows the lab-scale fixed-bed reactor for FT experiments. The glass tube is inserted into a tubular stainless steel reactor shell that is directly heated by three different heating zones.

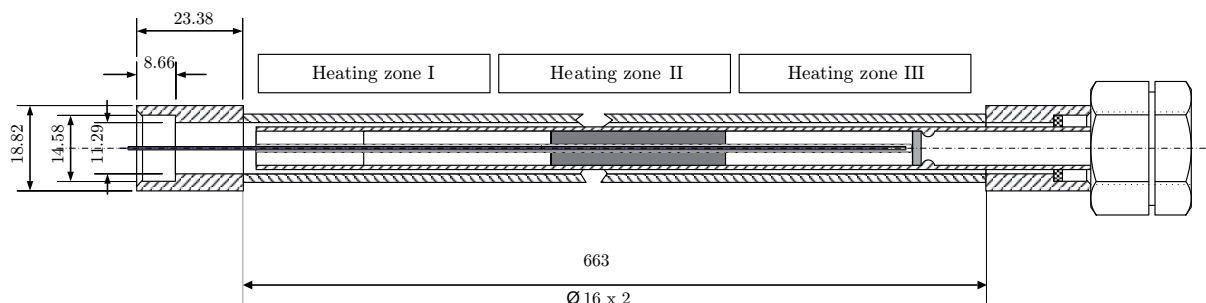


Figure C.9: Schematic illustration of the lab-scale fixed-bed reactor. Values for the dimensions are given in mm

## D Analysis of products: supporting information

This chapter describes the analytical methods applied within this work. Gas composition were measured with an online GC equipped with a TCD and two FID, for the dynamic experiments a Micro-GC and a non dispersive infrared (BINOS) Gas Analyzer. Detailed hydrocarbon analysis were carried out in an offline GC.

### D.1 Offline gas chromatograph

Figure D.10 shows the cross section of an ampoule sampler. The product gas stream mixed with reference gas flows through the sampling chamber. The capillary of a preheated and evacuated glass ampoule is inserted through the septum into the sampling chamber. By breaking the tip of the capillary mechanically by turning the fork, the evacuated fills up rapidly with a representative sample of the product gas. Then, the ampoule is sealed by melting off the capillary with the flame of a propane burner. The sealed ampoule can be stored and the sample can be analyzed later in an off-line gas chromatograph (Figure D.11)(Rohde 2011). This method was developed at the Engler-Bunte-Institut and is described in detailed in Schulz et al. (1984). The advantages of this method are a) rapid sampling, very useful for transient experiments and b) storage of samples which allows a very detailed analysis.

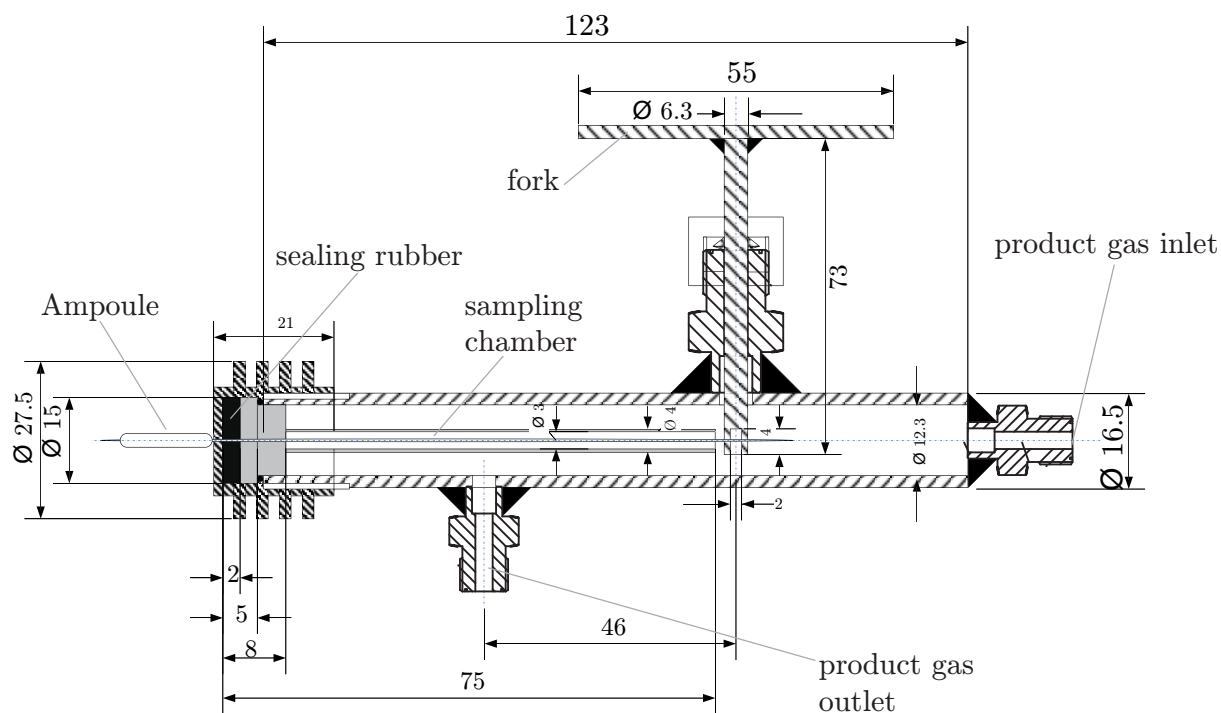


Figure D.10: Cross section of the ampoule sampler. Length in mm. Schulz et al. (1984)

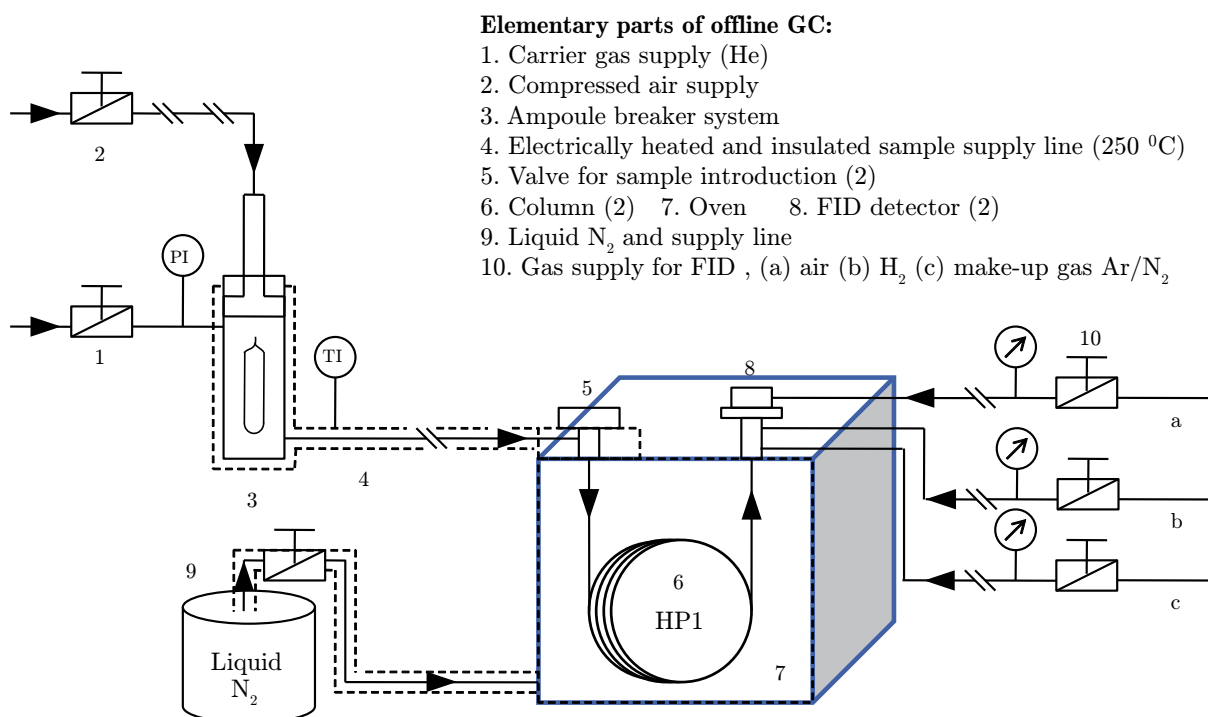


Figure D.11: Offline setup with a Gas Chromatograph Agilent 6890N, valves in OFF position. Column HP-1 50 m 0.20 mm 0.5  $\nu$  m

Ampoule samples are analyzed in GC (Agilent 6890N), equipped with two ampoules breakers, dedicated to detailed hydrocarbon analysis (Figure D.11). The ampoule sample



is broken by pneumatic force in an ampoule breaker. The carrier gas He transports the sample to a HP1 column (50 m, 0.20 mm, 0.5  $\mu$  m). The temperature is ramped up from - 80 °C to 300 °C according to a temperature program (starting slope 15 K/min until 0 °C, slope is changed to 3 K/min until the final temperature is reached). The components are detected in a flame ionization detector.

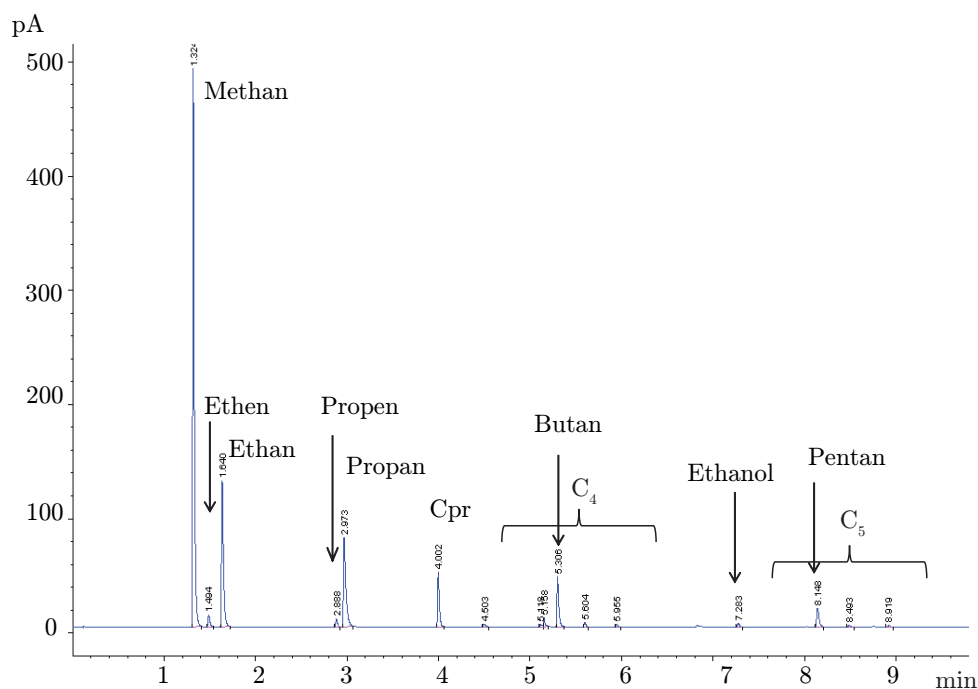


Figure D.12: Example gas chromatogram obtained from analysis in the offline GC HP-5890 with flame ionisation detector. Glass ampoule with gas sample from experiment with 100 g Fe / 2 g K.

## D.2 Online Gas Chromatograph

The online analysis is done with a 7890A GC system (Figure D.13). This system include 5 columns (Table D.3), one TCD (thermal conductivity detector) and two FID (flame ionization detector). The TCD is used to detect the inorganic compounds and the FID's are used for the organic compounds. The strategy to separate the products is realized with 4 valves. In the off position, the product gas stream through V4, V1 and V2. When the measurement begins the valve V4 switches into the ON position after 0.1 min (gas sampling valve). If V4 is in ON position, no product gas from the reactor enter the system and the gas in both sample loops (with V1 and V2) is expanded to atmospheric pressure. This time is important to assure that the sampling loop is always filled with the same volume of gas. After 0.2 min V1 and V2 are switched into ON position. In the case of the TCD channel, the gas is transported to the Plot-T, where H<sub>2</sub>O and long chain hydrocarbons are retained. The gas without H<sub>2</sub>O and long chain hydrocarbons streams

through the Haysep Q. By switching valve 3 it is possible to avoid that  $\text{CO}_2$  and the short chain hydrocarbons reach the MS5A.  $\text{H}_2$  is the fastest component and reaches the WLD first, afterwards  $\text{Ar} + \text{O}_2$  (V3 is in off position). After 5 min the V3 is switched to the ON position and  $\text{CO}_2$ ,  $\text{C}_2\text{H}_6$  and  $\text{C}_2\text{H}_4$  reached the TCD. At 11.6 min V3 is switched to position OFF and  $\text{N}_2$ ,  $\text{CH}_4$  and  $\text{CO}$  already separated in the MS5A reach the TCD. At minute 6.1 valve 1 is switched back to off position and is flush with the carrier gas to remove the  $\text{H}_2\text{O}$  and the hydrocarbons retained. In the case of the channel with the flame ionization detector, the sample gas flows through the HP5 and GasPro. After 2.8 minutes valve 2 is switched back to off position. The light hydrocarbons have already reached the GasPro column, while the long chain hydrocarbons remain in the HP5. The carrier gas (S/S inlet Back) transport the sample through the GasPro to the FID front, where the molecules between  $\text{C}_1$  and  $\text{C}_5$  are detected. The hydrocarbons longer than  $\text{C}_5$  are detected in the FID back, using as carrier gas the helium from AUX 2. The switching time at 2.8 minutes determines that until  $\text{C}_5$ , molecules are seen in the front detector and longer molecules in the back detector.

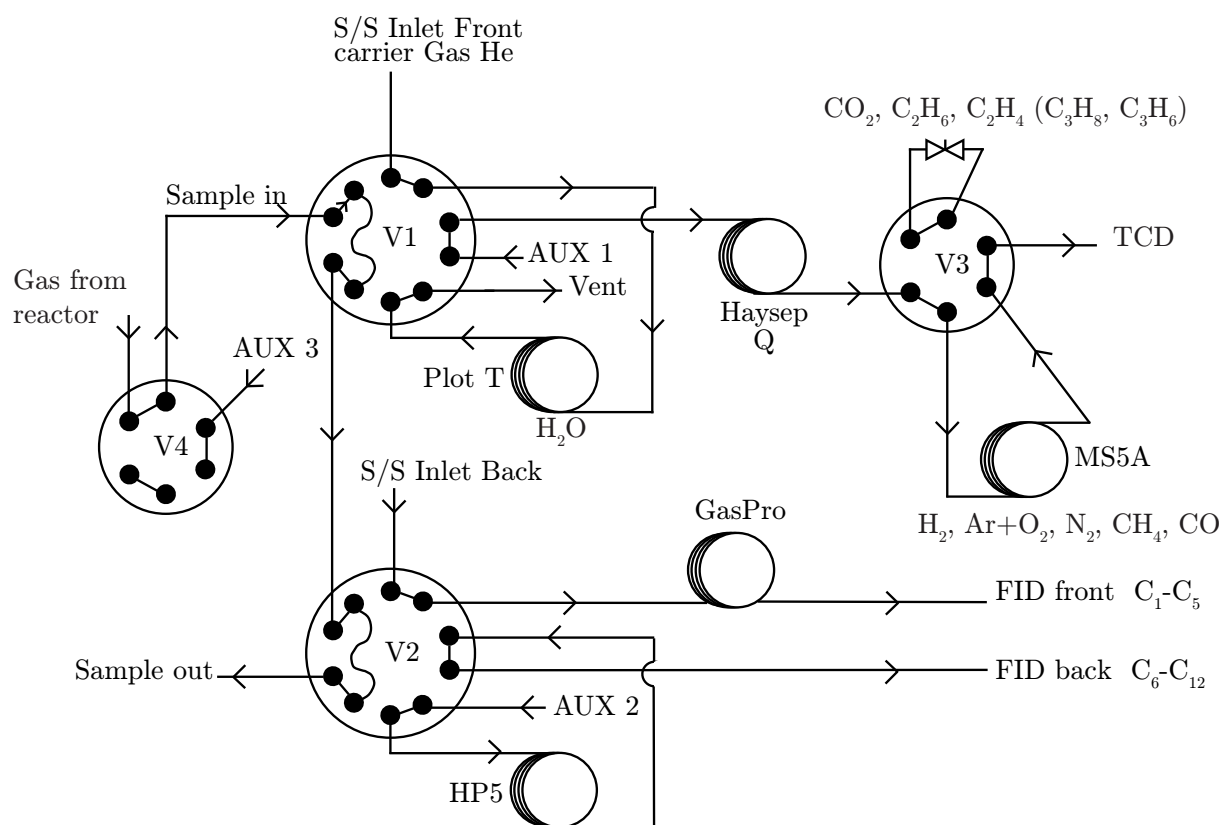


Figure D.13: Columns line-up of the online gas chromatograph Agilent 7890 (Agilent/-JAS). Auxiliary detector, thermal conductivity detector (TCD): product analysis of permanent gases  $\text{CO}_2$ ,  $\text{H}_2$ ,  $\text{CO}$ ,  $\text{N}_2$ ,  $\text{CH}_4$ ,  $\text{C}_2\text{H}_6$ ,  $\text{C}_2\text{H}_4$ . Front and back detectors (flame ionization, FID), product analysis of hydrocarbons until  $\text{C}_{12}$

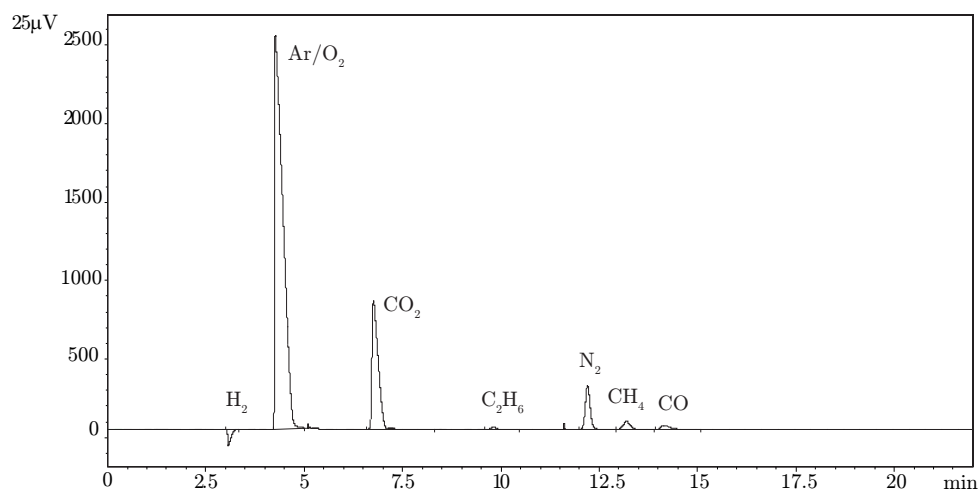


Figure D.14: Example gas chromatogram of the inorganic components and methane with  $N_2$  as reference component obtained with the GC Agilent 7890A and a thermal conductivity detector, Figure D.13. Example 100 g Fe / 2 g K,  $T = 290\text{ }^\circ\text{C}$ ,  $\tau_{\text{mod}} = 400\text{ kg s/m}^3$ ,  $p = 1\text{ MPa}$  and  $(H_2/CO_2)_{\text{in}} = 4$ .

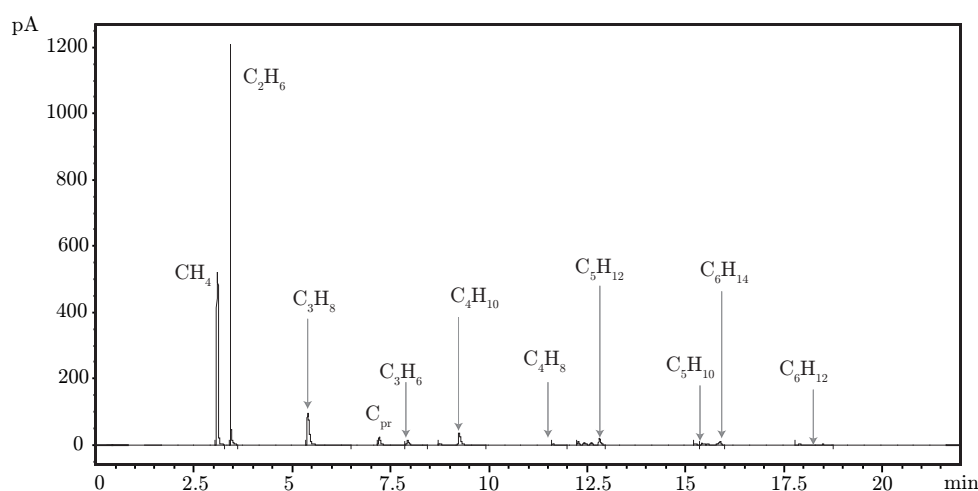


Figure D.15: Example gas chromatogram of the organic components with  $C_{\text{pr}}$  as reference component obtained with the GC Agilent 7890A and a flame ionization detector (front), Figure D.13. Example 100 g Fe / 2 g K,  $T = 290\text{ }^\circ\text{C}$ ,  $\tau_{\text{mod}} = 400\text{ kg s/m}^3$ ,  $p = 1\text{ MPa}$  and  $(H_2/CO_2)_{\text{in}} = 4$ .

To control the separation within the columns the temperature at time zero is  $40\text{ }^\circ\text{C}$ . After 4.5 min the temperature is heated up to  $165\text{ }^\circ\text{C}$  with a slope of  $10\text{ K/min}$ . Afterwards the temperature is hold for 5 min at  $165\text{ }^\circ\text{C}$ . The valve box is heated at  $150\text{ }^\circ\text{C}$  to avoid condensation of long chain hydrocarbons. A run time takes 22 minutes. Front SS Inlet He and Back SS Inlet He are heated at  $250\text{ }^\circ\text{C}$  and  $200\text{ }^\circ\text{C}$  respectively. The pressure in the first one is 3.5 bar and in the second one 1.5 bar.

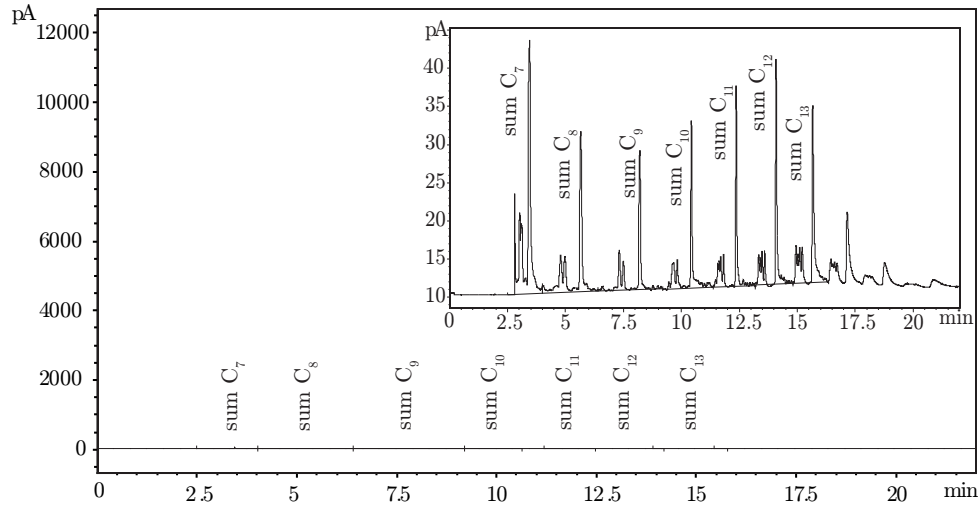


Figure D.16: Example gas chromatogram of the organic components obtained with the GC Agilent 7890A and a flame ionization detector (back), separation process in Figure D.13. Example 100 g Fe / 2 g K,  $T = 290\text{ }^{\circ}\text{C}$ ,  $\tau_{\text{mod}} = 400\text{ kg s/m}^3$ ,  $p = 1\text{ MPa}$  and  $(\text{H}_2/\text{CO}_2)_{\text{in}} = 4$ .

Table D.3: Details of gas chromatogram columns in online GC 7890A

Molecular sieve	2 m x 1/16" 100 - 120 mesh
Hayesep Q	2 m x 1/16"; <sub>d</sub> 100 - 120 mesh
Hayesep T	2 m x 1/16" 100-120 mesh
GS-Gaspro	30 m x Diam = 0.320
HP-5	30 m x 0.32 x 0.25 m

Table D.4: Correlation for the TCD between peak area and amount ( $y_{\text{V},i}$ , vol-%), correlation factor and range of validity.

Species	Area correlation	$R^2$	range of validity (vol-%)
$\text{H}_2$	$12.82 \cdot y_{\text{V},i}/(\text{vol-\%})$	0.9983	3-50
$\text{Ar}/\text{O}_2$	$957.21 \cdot y_{\text{V},i}/(\text{vol-\%})$	0.9999	10-48
$\text{CO}_2$	$986.83 \cdot y_{\text{V},i}/(\text{vol-\%})$	1	1-30
$\text{N}_2$	$857.19 \cdot y_{\text{V},i}/(\text{vol-\%})$	0.9997	7-94
$\text{CH}_4$	$665.51 \cdot y_{\text{V},i}/(\text{vol-\%})$	0.99987	1-20
$\text{CO}$	$902.75 \cdot y_{\text{V},i}/(\text{vol-\%})$	0.99989	0.1-30

### D.3 Micro-GC

The Micro-GC is a two channel measuring instrument with one column in each channel (channel A and B). The product gas is separated in the columns and detected by two TCD's. With this GC H<sub>2</sub>, CO<sub>2</sub>, CO, CPr, N<sub>2</sub>, CH<sub>4</sub> and C<sub>2</sub>H<sub>6</sub> can be detected. In order to determine the molar flows of the detected species, N<sub>2</sub> and CPr are used as reference components ( $F_{V,N_2+CPr,STP} = 15$  ml/min;  $y_{n,CPr} = 0.5$  vol %). Helium is used as carrier gas and the columns are operating at constant temperature. The sample time is set to 0.5 min and the runtime is 2 min. The detailed operating conditions are listed in Table D.5. Two different Micro-GC, with the same channels, were used in the present work.

Table D.5: Details of the column and the operating conditions of the Micro-GC

	channel A	channel B
type of column	PoraPlotQ	molesieve
temperature	80°C	90°C
injection time	255 ms	100 ms

## E Supporting results: in-situ and ex-situ measurements

### E.1 Magnetometer setup

Figure E.17 shows the setup to carry out the magnetic measurements. The magnetometer can be operated under fixed-bed flow conditions with temperatures up to 650 °C and pressure higher than 50 bar. The external field strength can be controlled in the range between -20 and 20 kOe. Gases are fed into the reactor via mass flow controllers. Samples of the gaseous products can be collect in evacuated glass ampoules and afterwards analysed off-line using a Gas Chromatograph (GC). The gas product can also be analysed on-line via GC with a thermal conductivity detector (GC-TCD). The gas flow to both sample points can be regulated with a needle valve. A hot and cold trap are also installed in the magnetometer setup. The cold trap condensates the H<sub>2</sub>O which is form during the process.

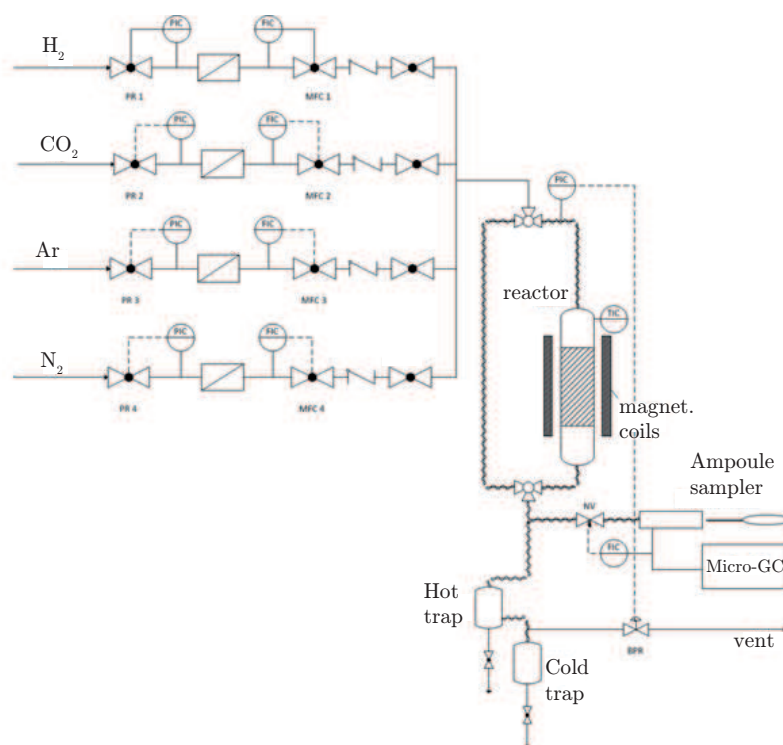


Figure E.17: Setup used for the magnetic measurements in the University of Cape Town (Fischer 2011)

## E.2 X-ray diffractometer setup

Figure E.18 shows the capillary cell used for the experiments and Figure E.19 the setup for in-situ measurements (Fischer et al. 2014). The gases  $N_2$ ,  $CO_2$  and  $H_2$ , which are used in this investigation are fed via mass flow controller. The MFCs regulate the gas flows through the 1/16 inch tubings, which are connected with the capillary cell reactor. The system pressure can be adjusted with a back pressure regulator. The three way valve which is positioned in front of the reactor entrance makes a bypassing of the reactor possible, until the feed stream is stabilized. Samples of the gaseous products can be collected in glass ampoules and afterwards analysed off-line with a GC-FID. The gaseous products can be also analysed on-line via GC-TCD.

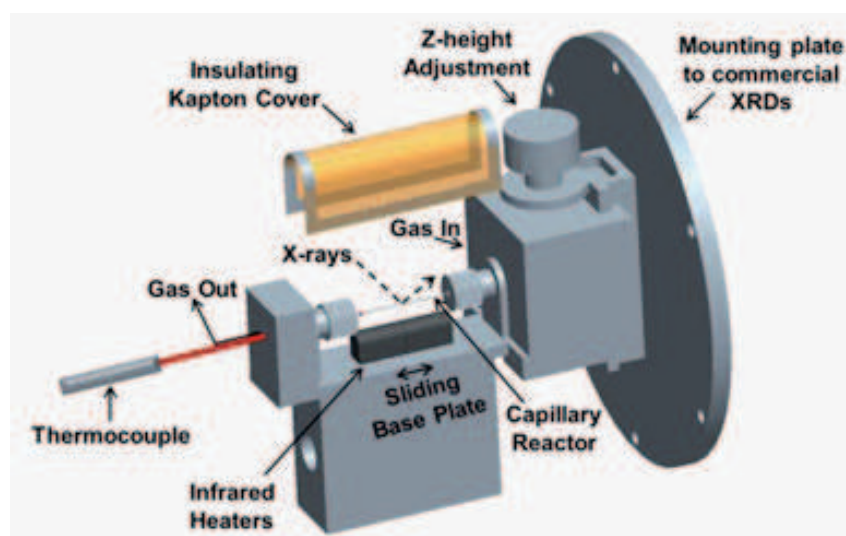


Figure E.18: Capillary cell reactor, (Fischer et al. 2014)

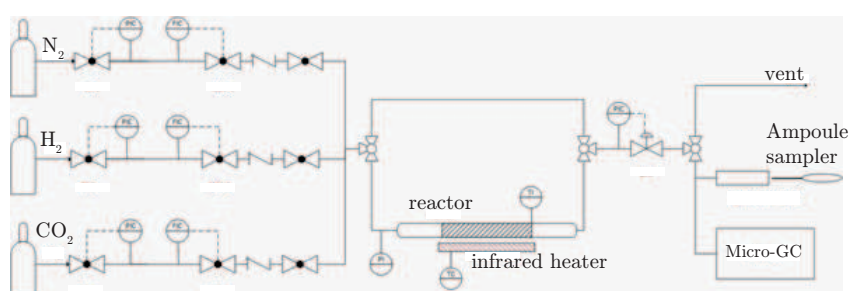


Figure E.19: Setup for in-situ XRD measurements, (Hettel 2014)

### E.3 Diffraction pattern for phase determination

Diffraction pattern for all catalyst phases determined during ex-situ and in-situ investigations from the international Centre for Diffraction Data

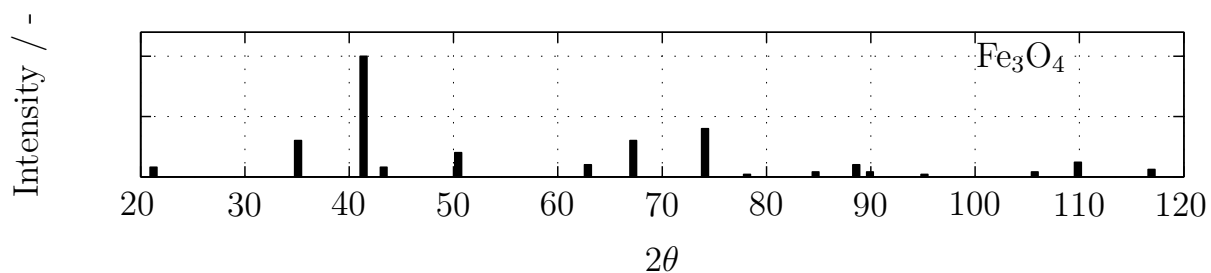
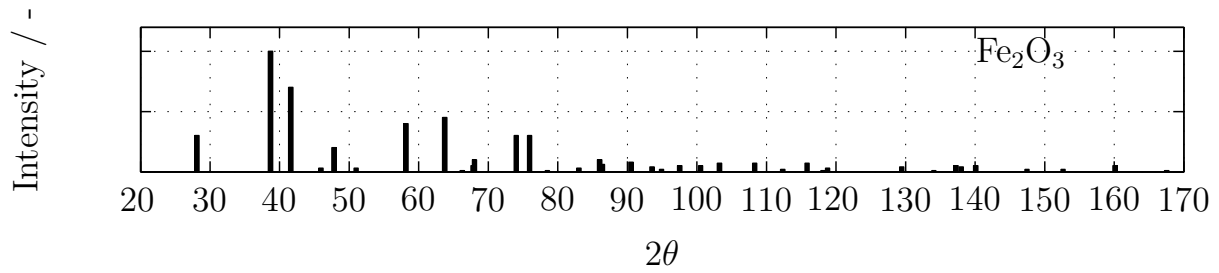
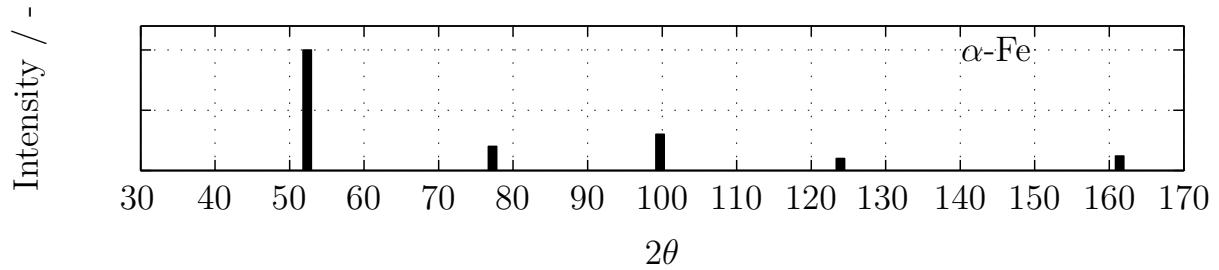
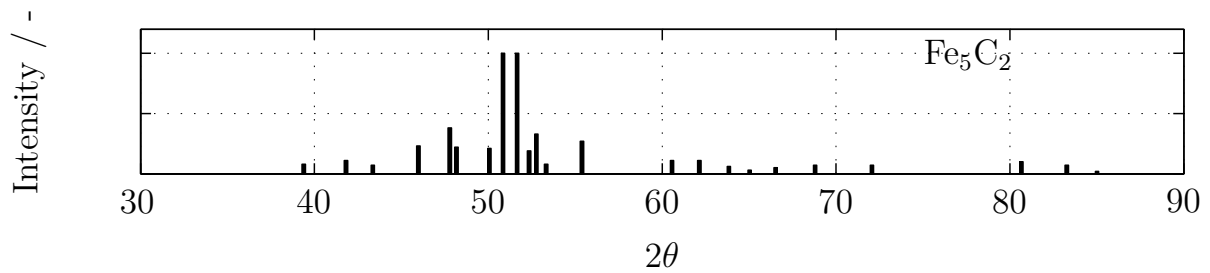
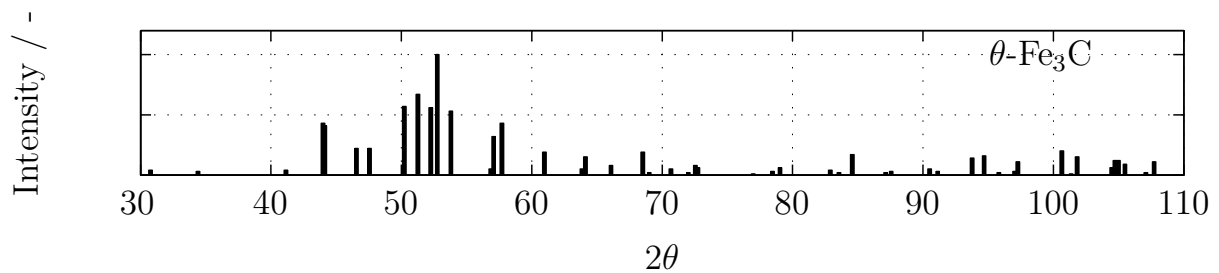
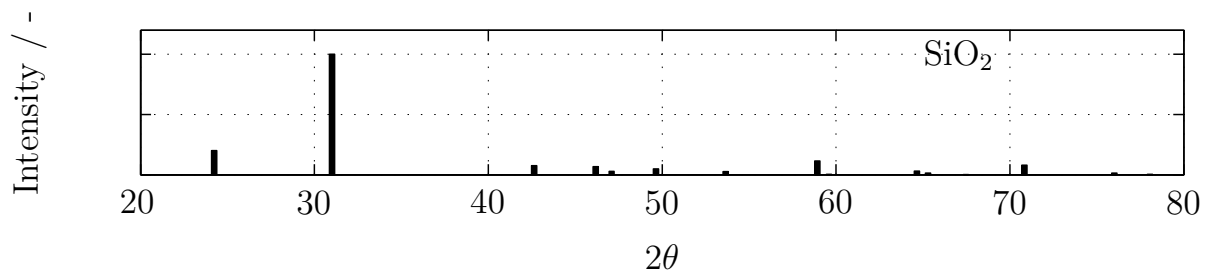


Figure E.20: Magnetite  $\text{Fe}_3\text{O}_4$ , PDF No: 01-087-0246

Figure E.21: Hematite  $\text{Fe}_2\text{O}_3$ , PDF No: 00-033-0664Figure E.22: Metallic iron,  $\alpha\text{-Fe}$ , PDF No: 00-006-0696Figure E.23: Hägg carbide,  $\text{Fe}_5\text{C}_2$ , PDF No: 00-051-0997Figure E.24: Cementite,  $\theta\text{-Fe}_3\text{C}$ , PDF No: 00-035-0772Figure E.25: Quartz,  $\text{SiO}_2$ , PDF No: 00-046-1045



## E.4 Catalyst reduction: Magnetometer

Figure E.26 shows the saturation magnetisation  $M_s$  for 100 g Fe / 2 g K and 100 g Fe / 10 g K under reduction conditions. The holding time for the 400 °C is 16 h and during this time the  $M_s$  value increases (Figure 5.8).

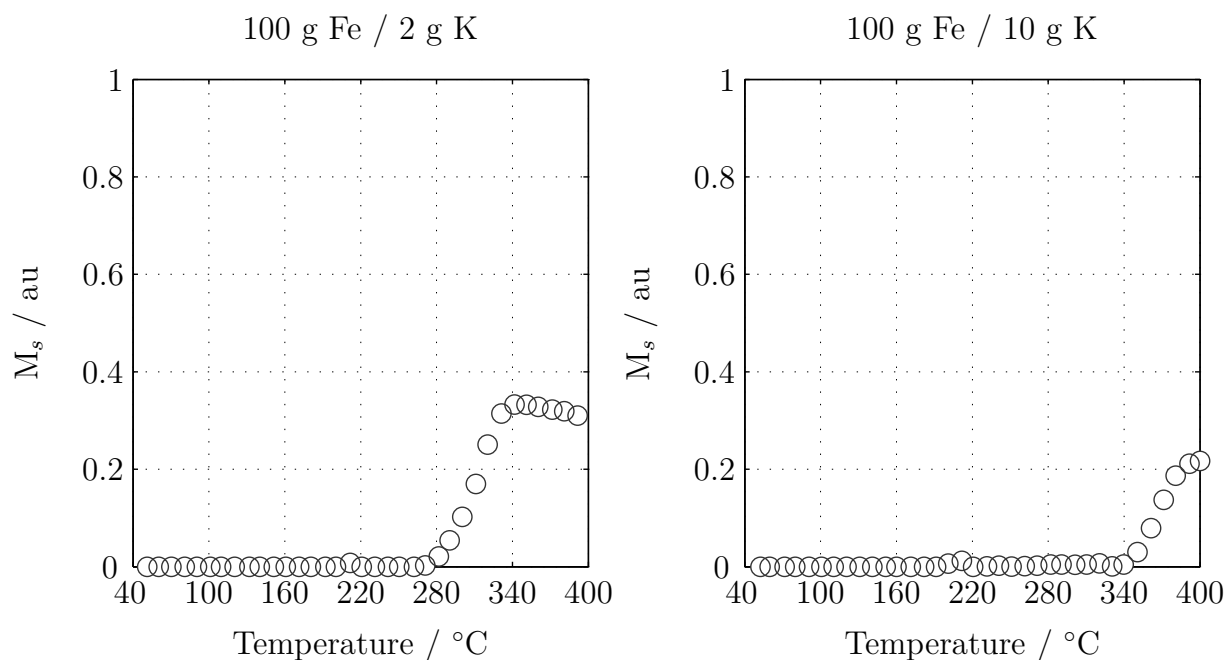


Figure E.26: Saturation magnetisation  $M_s$  during catalyst reduction (Magnetometer-measurement). Left: 100g Fe/ 2g K ; Right: 100g Fe/ 10g K

## E.5 Catalyst reduction: Diffraction patterns, X-ray diffractometer

Figure E.27 shows the content of the different iron-phases over temperature. These figures are based on the diffraction patterns recorded during reduction (Figure E.28 and Figure E.29). The phase composition and particle size for the analysed diffraction patterns (using TOPAS 4.1) are summarised in Table E.6 and Table E.7.

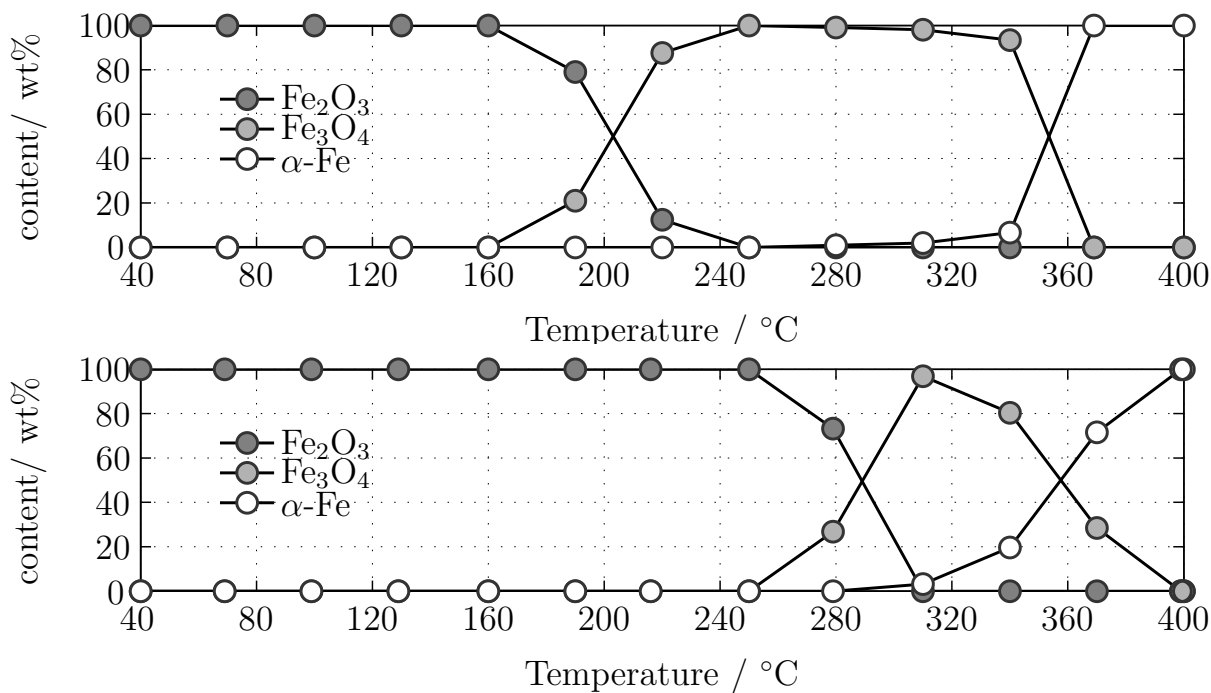


Figure E.27: Change of catalysts phase composition with temperature temperatures (XRD-measurement). Top: 100 g Fe / 2 g K; Bottom: 100 g Fe / 10 g K. Detailed information in Table E.6 (100 g Fe / 2 g K) and E.7 (100 g Fe / 10 g K) and complete diffraction patterns in Figure E.28 (100 g Fe / 2 g K) and E.29 (100 g Fe / 10 g K)

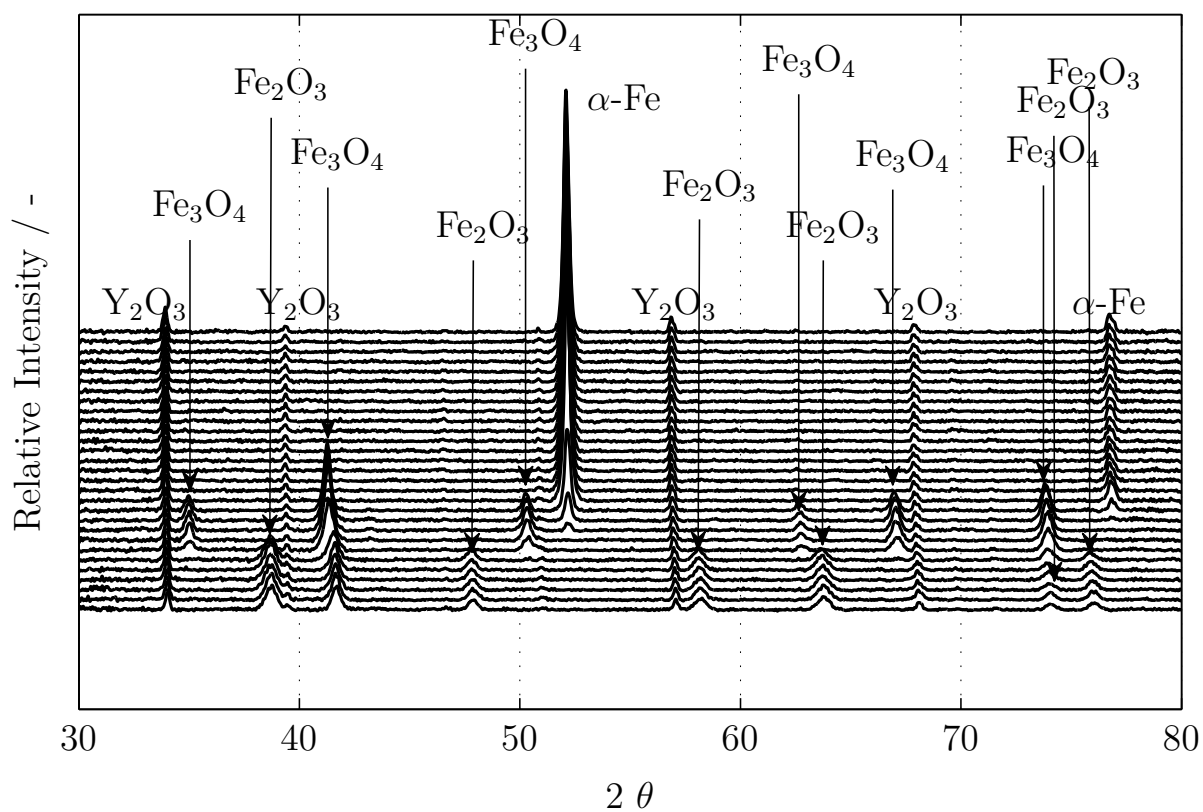


Figure E.28: Complete diffraction pattern recorded during the reduction of 100 g Fe / 2 g K. Conditions: see Table 5.3

Table E.6: Phase composition and particle sizes of the catalyst 100 g Fe / 2 g K during reduction in XRD. Calculations done "TOPAS 4.1". Figure E.28 shows the complete diffraction pattern. Conditions: see Table 5.3

time	$T$	Fe <sub>2</sub> O <sub>3</sub>	Fe <sub>3</sub> O <sub>4</sub>	$\alpha$ -Fe	$d_p$ Fe <sub>2</sub> O <sub>3</sub>	$d_p$ Fe <sub>3</sub> O <sub>4</sub>	$d_p$ $\alpha$ -Fe	R <sub>WP</sub>
h	°C	w %	w %	w %	nm	nm	nm	-
0	39	100	0	0	22	-	-	7.915
0.60	70	100	0	0	23	-	-	7.677
1.18	100	100	0	0	21	-	-	7.726
1.78	130	100	0	0	22	-	-	7.943
2.38	160	100	0	0	22	-	-	7.744
2.98	190	79	21	0	24	2	-	7.897
3.58	220	12	88	0	27	28	-	7.948
4.17	250	0	100	0	-	35	-	7.937
4.77	280	0	99	1	-	38	55.3	7.997
5.35	310	0	98	2	-	40	64.1	8.098
5.95	340	0	93	7	-	43	74.1	7.957
6.55	369	0	0	100	-	-	69.9	7.669
7.07	400	0	0	100	-	-	72.1	7.473

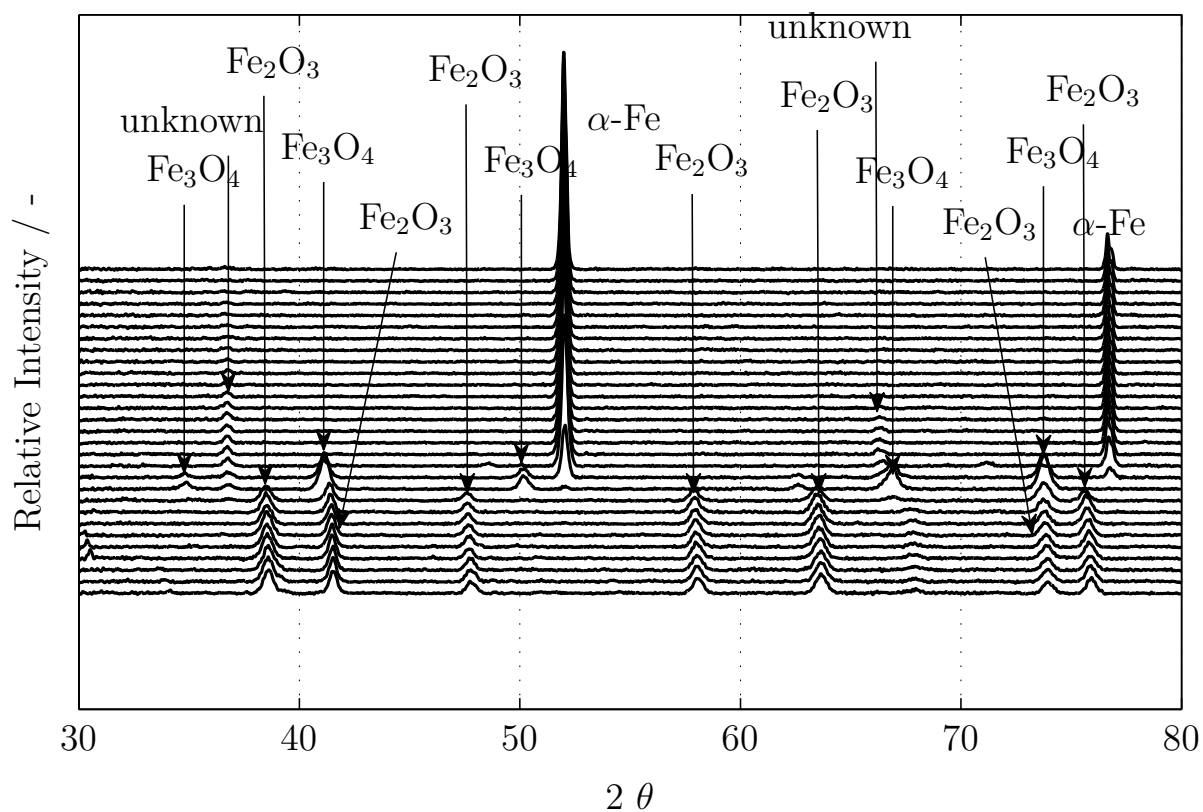


Figure E.29: Complete diffraction pattern recorded during the reduction of 100 g Fe / 10 g K. Conditions: see Table 5.3

Table E.7: Phase composition and particle sizes of the catalyst 100 g Fe / 10 g K during reduction in XRD. Calculations done "TOPAS 4.1". Conditions: see Table 5.3. Values in brackets are to high compared with the visual evaluation of the pattern.

time	$T$	Fe <sub>2</sub> O <sub>3</sub>	Fe <sub>3</sub> O <sub>4</sub>	$\alpha$ -Fe	$d_p$ Fe <sub>2</sub> O <sub>3</sub>	$d_p$ Fe <sub>3</sub> O <sub>4</sub>	$d_p$ $\alpha$ -Fe	R <sub>WP</sub>
h	°C	w %	w %	w %	nm	nm	nm	-
0	39	100	0	0	25	-	-	10.809
0.58	69	100	0	0	25	-	-	10.834
1.17	99	100	0	0	25	-	-	10.838
1.75	129	100	0	0	26	-	-	10.858
2.33	158	100	0	0	26	-	-	10.692
2.91	190	100	0	0	27	-	-	11.092
3.46	216	100	0	0	27	-	-	11.314
4.03	249	100	0	0	28	-	-	11.877
4.58	279	73	(27)	-	28	16	-	12.124
5.18	310	0	97	3	-	25	16	12.594
5.77	340	0	80	20	-	27	66	12.860
6.33	369	0	(28)	72	-	19	77	12.417
6.92	399	0	0	100	-	-	89	12.418
7.93	400	0	0	100	-	-	114	10.858
22.66	400	0	0	100	-	-	150	12.705

## E.6 Catalyst formation

Table E.8 and Table E.9 show the results from the analysis of some diffraction patterns during formation (XRD).

Table E.8: Phase composition and particle sizes of the catalyst 100 g Fe / 2 g K during catalyst formation followed in XRD. Calculations done in "TOPAS 4.1".  
Conditions: see Table 5.4

time	$\alpha$ -Fe	Fe <sub>3</sub> O <sub>4</sub>	Fe <sub>5</sub> C <sub>2</sub>	$\theta$ -Fe <sub>3</sub> C	$d_p$ $\alpha$ -Fe	$d_p$ Fe <sub>3</sub> O <sub>4</sub>	$d_p$ Fe <sub>5</sub> C <sub>2</sub>	$d_p$ $\theta$ -Fe <sub>3</sub> C	R <sub>WP</sub>
h	w %	w %	w %	w %	nm	nm	nm	nm	-
0	100	0	0	0	85	-	-	-	7.501
0.05	100	0	0	0	76	-	-	-	8.793
0.2	83	17	0	0	76	47	-	-	11.531
0.67	7	65	15	13	75	56	23	60	10.354
6.7	3	79	3	14	88	56	35	55	11.843
13.74	2	81	1	17	60	55	20	53	13.355
20.13	2	74	16	8	66	72	57	72	8.145
29.85	3	70	19	9	65	69	45	69	7.898
39.89	2	66	23	9	38	66	44	104	7.733
49.92	3	62	28	8	53	66	27	112	7.909
51.93	2	60	28	10	63	66	45	72	8.105

Table E.9: Phase composition and particle sizes of the catalyst 100 g Fe / 10 g K during formation in XRD. Calculations done "TOPAS 4.1". Conditions: see Table 5.4.

time	$\alpha$ -Fe	$\text{Fe}_5\text{C}_2$	$d_p$ $\alpha$ -Fe	$d_p$ $\text{Fe}_5\text{C}_2$	R <sub>WP</sub>
h	w %	w %	nm	nm	-
0	100	0	193	-	8.025
0.05	65	35	101	24	11.008
0.67	14	86	53	50	10.799
1.3	15	85	49	48	10.850
6.3	11	89	27	47	10.439
16.4	7	93	32	52	7.891
26.4	6	94	36	53	8.470
36.5	3	97	36	47	9.120
46.5	3	97	59	49	9.893
63.6	0	100	-	43	11.903

## E.7 Supporting ex-situ measurements: fresh and spent catalyst samples

Figure E.30 and Figure E.31 show the diffraction pattern of a fresh sample of 100 g Fe / 2 g K and 100 g Fe / 10 g K (respectively) determined by ex-situ XRD.

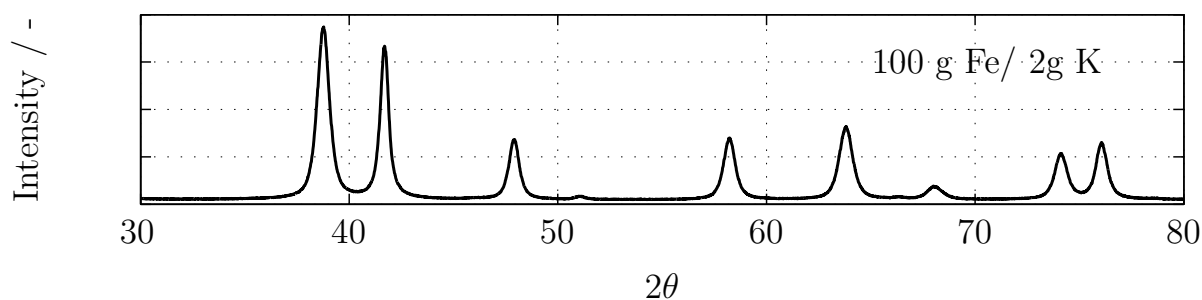


Figure E.30: Diffraction pattern of raw 100 g Fe / 2 g K.



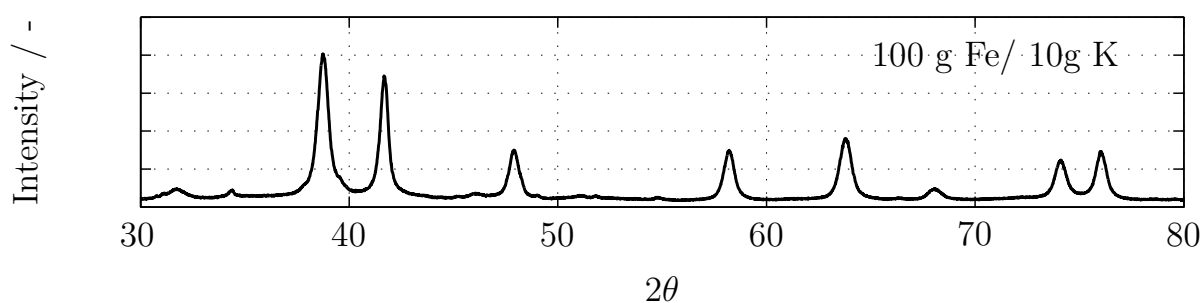


Figure E.31: Diffraction pattern of raw 100 g Fe / 10 g K.

Figure E.32 and Figure E.33 shows the diffraction pattern of a spent catalyst sample of 100 g Fe / 2 g K and 100 g Fe / 10 g K, respectively. A sample from the top of the catalyst bed and other from the bottom were analysed. The sample of 100 g Fe / 2 g K was taken after 50 days in operation and the 100 g Fe / 10 g K sample after 26 days in operation (Figure F.34).

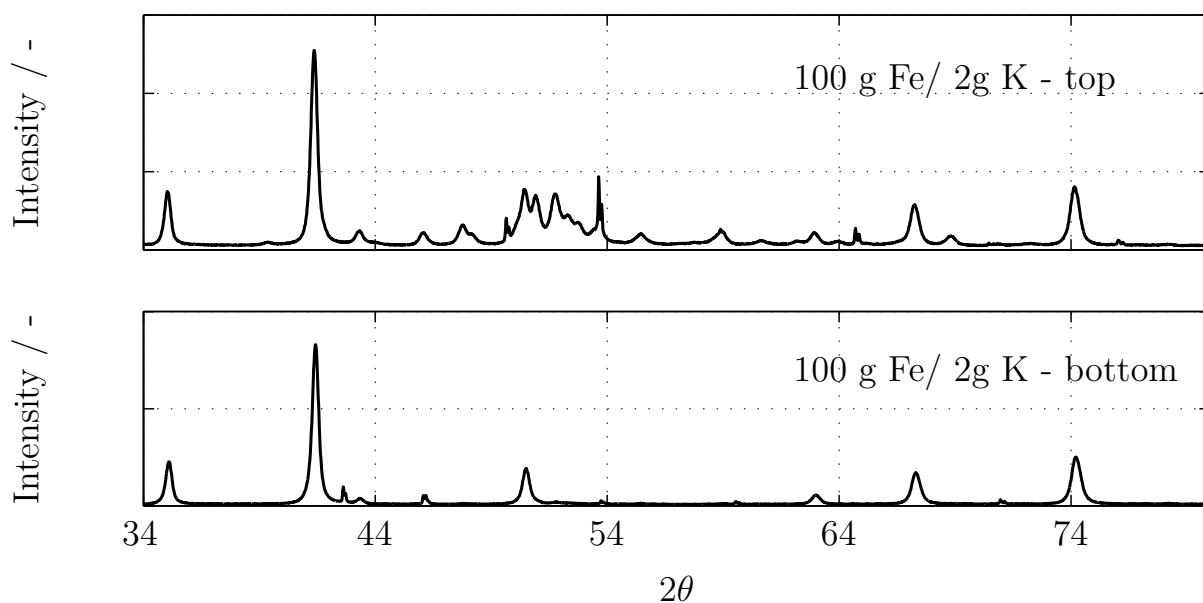


Figure E.32: Diffraction pattern of 100 g Fe / 2 g K spent samples from top and bottom of the fixed-bed lab-scale reactor

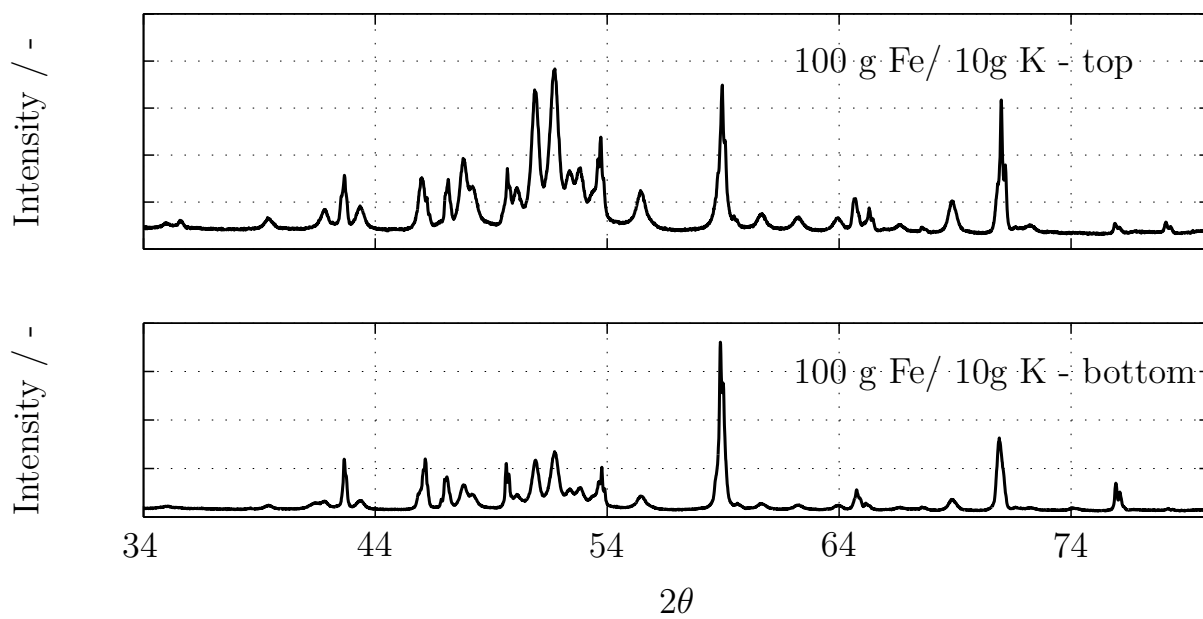


Figure E.33: Diffraction pattern of 100 g Fe / 10 g K spent samples from top and bottom of the fixed-bed lab-scale reactor

## F Experimental studies in lab-scale fixed-bed reactor: extra figures

Figure F.34 shows catalyst activity and selectivity over time-on-stream at reference conditions. Figure F.35 reveal the pressure drop at reference conditions over time-on-stream.

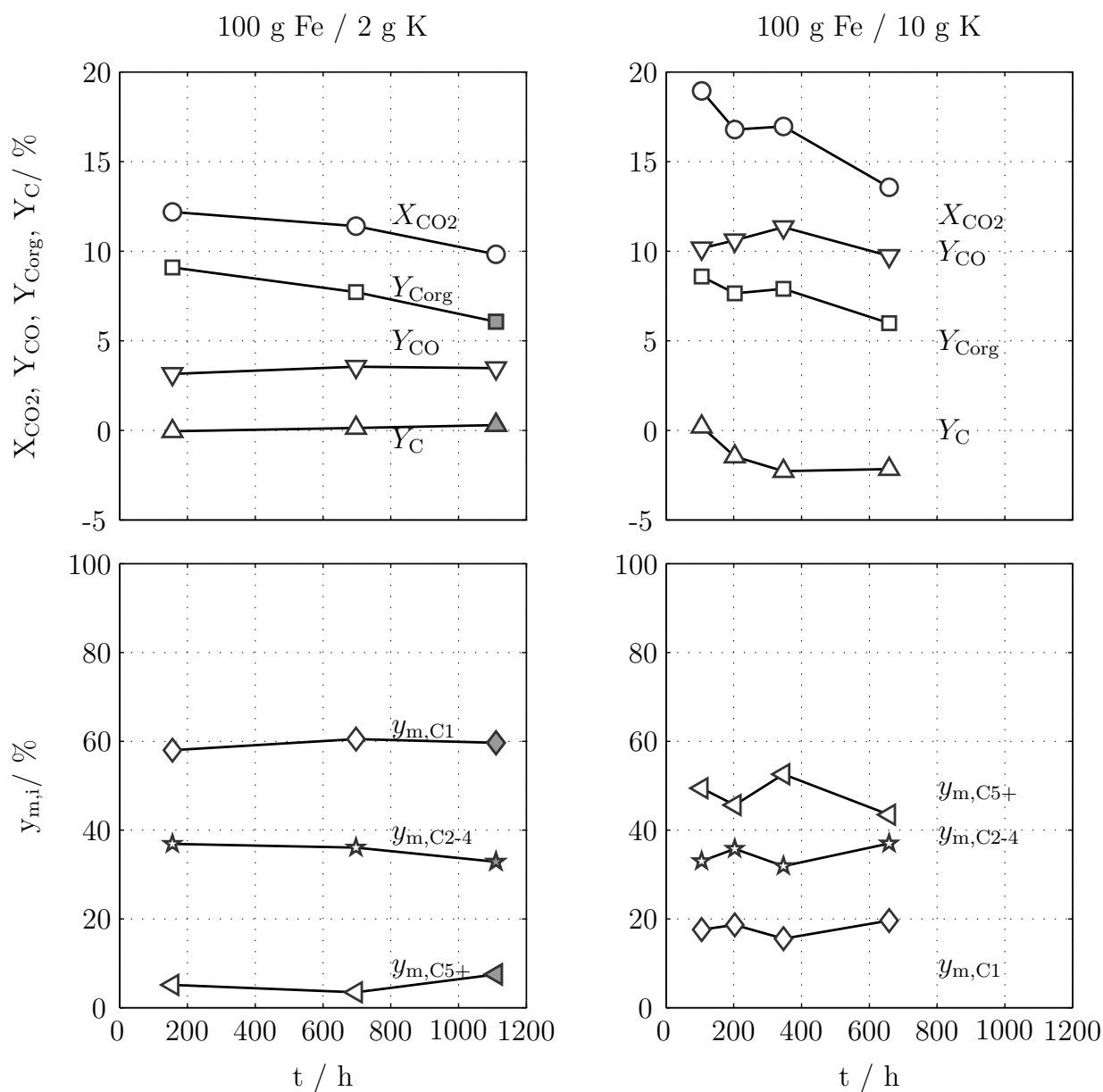


Figure F.34:  $CO_2$  conversion  $X_{CO_2}$ , CO yield  $Y_{CO}$ , yield organic components  $Y_{Corg}$  and carbon yield  $Y_C$  (top) and hydrocarbon selectivity in mass % under reference conditions at different times during the experiments. Left: 100 g Fe / 2 g K,  $T = 266$  °C,  $\tau_{mod} = 400$  kg s/m<sup>3</sup>,  $(H_2/CO_2)_{in} = 4$  and  $p = 1$  MPa. Right: 100 g Fe / 10 g K,  $T = 286$  °C,  $\tau_{mod} = 400$  kg s/m<sup>3</sup>,  $(H_2/CO_2)_{in} = 4$  and  $p = 1$  MPa. Grey symbols: online GC. White symbols: ampoules and offline GC.

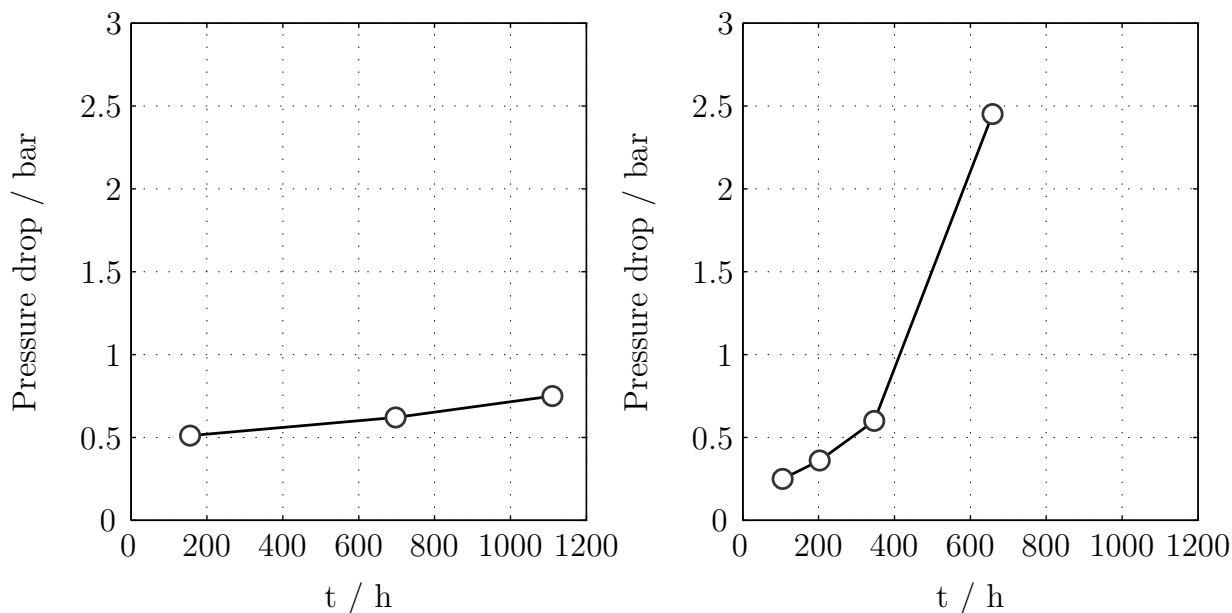


Figure F.35: Pressure drop with 100 g Fe / 2 g K and 100 g Fe / 10 g K measured at reference conditions. 100 g Fe / 10 g K:  $T = 286\text{ }^{\circ}\text{C}$ ,  $\tau_{\text{mod}} = 400\text{ kg s/m}^3$ ,  $(\text{H}_2/\text{CO}_2)_{\text{in}} = 4$  and  $p = 1\text{ MPa}$ ; 100 g Fe / 2 g K:  $T = 266\text{ }^{\circ}\text{C}$ ,  $\tau_{\text{mod}} = 400\text{ kg s/m}^3$ ,  $(\text{H}_2/\text{CO}_2)_{\text{in}} = 4$  and  $p = 1\text{ MPa}$

Figure F.36 shows the effect of temperature on CO yield using 100 g Fe / 10 g K at higher modified residence times.

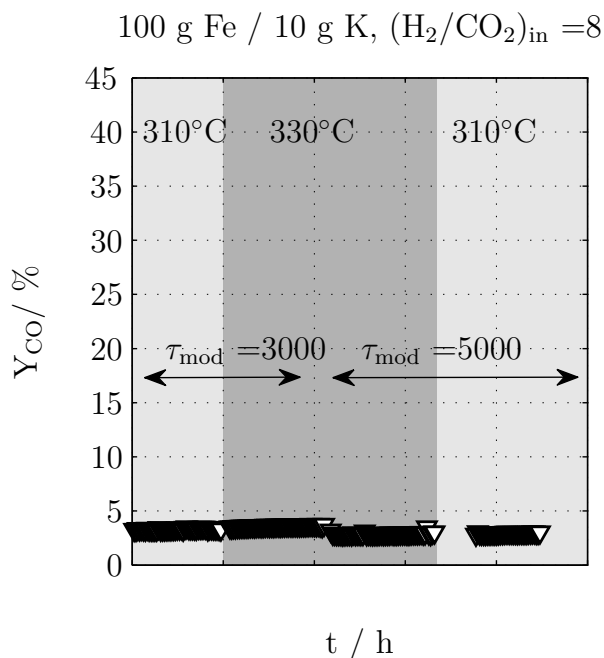


Figure F.36: Effect of temperature over time on CO yield  $Y_{\text{CO}}$  with 100 g Fe/ 10 g K.  $\Delta t = 20\text{ h}$ .

## G Basic dimensionless numbers

Reynolds number:

$$Re_p = \frac{u_{sf} \cdot d_p}{\nu_g} \quad (\text{G.3})$$

Schmidt number:

$$Sc = \frac{\nu}{D_{1,2}} \quad (\text{G.4})$$

Prandtl number: momentum diffusivity to thermal diffusivity. Depends only on the fluid and the fluid state.  $Pr < 1$  thermal diffusivity dominates

$$Pr = \frac{\nu_g \cdot \rho_g \cdot c_{p,g}}{\lambda_g} \quad (\text{G.5})$$

## H Calculation of physical properties for a gas mixture

### H.1 Gas density, $\rho_g$

The density of the gas mixture is calculated with the ideal gas law in  $\text{kg/m}^3$

$$\rho_g = \frac{p \cdot \tilde{M}_g}{R \cdot T} \quad (\text{H.6})$$

with

$$\tilde{M}_g = \sum \tilde{y}_i \cdot \tilde{M}_i \quad (\text{H.7})$$

### H.2 Dynamic viscosity, $\eta_g$

The dynamic viscosity of a gaseous component is calculated with the following equation. The units are Pa s

$$\eta_i = A + B \cdot T + C \cdot T^2 + D \cdot T^3 + E \cdot T^4 \quad (\text{H.8})$$

For the calculation of the viscosity of a gaseous mixture the formula is comparable to H.14.

$$\eta_g = \sum_i \frac{y_{m,i} \cdot \lambda_i}{\sum_j y_{m,j} \cdot F_{ij}} \quad (\text{H.9})$$

The correlation for  $F_{ij}$  is given in equation H.15.

Table H.10: Parameter for calculation of  $\eta_{g,i}$ , VDI (2006)

	A	B	C	D	E
H <sub>2</sub>	$0.18024 \cdot 10^{-5}$	$0.27174 \cdot 10^{-7}$	$-0.13395 \cdot 10^{-10}$	$0.00585 \cdot 10^{-12}$	$-0.00104 \cdot 10^{-15}$
CO <sub>2</sub>	$-0.18024 \cdot 10^{-5}$	$0.65989 \cdot 10^{-7}$	$-0.37108 \cdot 10^{-10}$	$0.015868 \cdot 10^{-12}$	$-0.00300 \cdot 10^{-15}$
H <sub>2</sub> O	$-0.10718 \cdot 10^{-5}$	$0.35248 \cdot 10^{-7}$	$0.03575 \cdot 10^{-10}$	0	0
CO	$0.01384 \cdot 10^{-5}$	$0.74306 \cdot 10^{-7}$	$-0.62996 \cdot 10^{-10}$	$0.03948 \cdot 10^{-12}$	$-0.01032 \cdot 10^{-15}$
C <sub>3</sub> H <sub>8</sub>	$0.07353 \cdot 10^{-5}$	$0.20874 \cdot 10^{-7}$	$0.24208 \cdot 10^{-10}$	$-0.03914 \cdot 10^{-12}$	$0.01784 \cdot 10^{-15}$

### H.3 Kinematic viscosity, $\nu_g$

Kinematic viscosity  $\nu_g$  and dynamic viscosity  $\eta_g$  are linked through the gas density. The units of the kinematic viscosity are m<sup>2</sup>/s.

$$\nu_g = \frac{\eta_g}{\rho_g} \quad (\text{H.10})$$

### H.4 Binary molecular diffusion coefficient, $D_{12}$

The binary diffusion coefficient can be calculated with H.11 in cm<sup>2</sup>/s VDI (2006) Da 27

$$D_{12} = \frac{0.00143 \cdot T^{1.75} ((\widetilde{M}_1)^{-1} + (\widetilde{M}_2)^{-1})^{1/2}}{p\sqrt{2}((\sum \Delta_{v1})^{1/3} + (\sum \Delta_{v2})^{1/3})^2} \quad (\text{H.11})$$

being  $\Delta_{vi}$  the diffusion volume. For H<sub>2</sub> the value is 6.12 and for CO<sub>2</sub> 26.9.

### H.5 Specific heat capacity, $c_{p,g}$

For the calculation of the specific heat capacity of the gas (Equation H.12) is used.  $c_{p,g}$  is calculated in J/kg K.  $y_i$  are gas mass fractions.

$$c_{p,g} = \sum y_i \cdot c_{p,i} \quad (\text{H.12})$$

$c_{p,g}$  for every gas component has to be calculated according to equation H.13. Correlation are taken from VDI (2006) Da.

$$c_{p,i} = A + B \cdot T + C \cdot T^2 + D \cdot T^3 + \frac{E}{T^2} \quad (\text{H.13})$$

The parameter for the different components are given in H.11.

Table H.11: Parameter for calculation of  $c_{p,i}$ , VDI (2006), Dca

	A	B	C	D	E
H <sub>2</sub>	13973.40	1,256	-0.000892	0.000660 · 10 <sup>-3</sup>	-0.000229 · 10 <sup>-3</sup>
CO <sub>2</sub>	617.3	0.950	-0.000388	0.000050 · 10 <sup>-3</sup>	0.000189 · 10 <sup>-3</sup>
H <sub>2</sub> O	1833.1	-0.035	0.000696	-0.000215 · 10 <sup>-3</sup>	-0.000026 · 10 <sup>-3</sup>
CO	1048.4	-0.152	0.000477	-0.00019 · 10 <sup>-3</sup>	-0.000022 · 10 <sup>-3</sup>
C <sub>3</sub> H <sub>8</sub>	203.1	5.628	-0.002004	0.000147 · 10 <sup>-3</sup>	-0.000014 · 10 <sup>-3</sup>

## H.6 Thermal conductivity, $\lambda_g$

The thermal conductivity of a gas mixture is calculated with the rule from Wassiljeva, Mason and Saxena in W/(m K),  $y_{m,i}$  are the molar fractions VDI (2006) Da

$$\lambda_g = \sum_i \frac{y_{m,i} \cdot \lambda_i}{\sum_j y_{m,j} \cdot F_{ij}} \quad (\text{H.14})$$

with

$$F_{ij} = \frac{[1 + (\eta_i/\eta_j)^{1/2}(\widetilde{M}_j/\widetilde{M}_i)^{1/4}]^2}{\sqrt{8(1 + \widetilde{M}_i/\widetilde{M}_j)}} \quad (\text{H.15})$$

The calculation of the dynamic viscosity is necessary H.8.

The thermal conductivity of each gaseous component has to be calculated VDI (2006) Da.

$$\lambda_i = A + B \cdot T + C \cdot T^2 + D \cdot T^3 + E \cdot T^4 \quad (\text{H.16})$$

Table H.12: Parameter for calculation of  $\lambda_{g,i}$ 

	VDI (2006) Dca				
	A	B	C	D	E
H <sub>2</sub>	0.65 · 10 <sup>-3</sup>	0.767 · 10 <sup>-3</sup>	-0.687050 · 10 <sup>-6</sup>	0.506510 · 10 <sup>-9</sup>	-0.138540 · 10 <sup>-12</sup>
CO <sub>2</sub>	-3.882 · 10 <sup>-3</sup>	0.053 · 10 <sup>-3</sup>	0.071460 · 10 <sup>-6</sup>	-0.070310 · 10 <sup>-9</sup>	0.018090 · 10 <sup>-12</sup>
H <sub>2</sub> O	0.46 · 10 <sup>-3</sup>	-0.046 · 10 <sup>-3</sup>	0.051150 · 10 <sup>-6</sup>	0	0
CO	-0.78 · 10 <sup>-3</sup>	0.103 · 10 <sup>-3</sup>	-0.067590 · 10 <sup>-6</sup>	0.039450 · 10 <sup>-9</sup>	-0.009470 · 10 <sup>-12</sup>
C <sub>3</sub> H <sub>8</sub>	-6.66 · 10 <sup>-3</sup>	0.053 · 10 <sup>-3</sup>	0.101810 · 10 <sup>-6</sup>	0	0

## I Transport coefficients: gas - catalyst particle

### I.1 Mass transfer coefficient gas-catalyst particle, $\beta$

Mass transfer coefficient between gas phase (bulk) and the catalyst particle (Baerns et al. 1992)

$$\beta = \frac{Sh \cdot D}{d_p} \quad (\text{I.17})$$

$$Sh = j_m \cdot Re_p \cdot Sc^{1/3} \quad (\text{I.18})$$

$$j_m = \frac{1.15}{\sqrt{\varepsilon_p}} \cdot Re_p^{-0.5} \quad (\text{I.19})$$

for  $Re_p$  between 0.1 and 1000 (Baerns et al. 1992)

### I.2 Heat transfer coefficient gas-catalyst particle, $\alpha_g$

$$\alpha_g = \frac{Nu \cdot \lambda_g}{d_p} \quad (\text{I.20})$$

with

$$Nu = j_h \cdot Re_p \cdot Pr^{1/3} \quad (\text{I.21})$$

The calculation of the j-factor  $j_h$  is taken from Baerns et al. (1992)

$$j_h = \frac{1.15}{\sqrt{\varepsilon_p}} \cdot Re_p^{-0.5} \quad (\text{I.22})$$

### I.3 Mass transfer in the catalyst particle- effective pore diffusion coefficient, $D_{\text{eff}}$

Porous catalyst have different connected porous. This is considered using the tortuosity.

$$D_{\text{eff}} = D_{\text{pore}} \cdot \varepsilon_p \cdot \frac{1}{\tau_L} = D_{\text{pore}} \cdot \varepsilon_p^{1.5} \quad (\text{I.23})$$

The diffusion in porous is affected by the Knudsen diffusion coefficient and by the molecular diffusion, assuming one cylindrical pore. The Knudsen diffusion for mesopores can be calculated with I.25.

$$\frac{1}{D_{\text{pore}}} = \frac{1}{D_{12}} + \frac{1}{D_{Kn}} \quad (\text{I.24})$$



$$D_{Kn} = 9700 \cdot r_{pore} \cdot \sqrt{\frac{T}{\tilde{M}_g}} \quad (I.25)$$

Where T is temperature in K and  $\tilde{M}_g$  is the molar mass in g/mol. For calculations the molar mass of CO<sub>2</sub> is used. The value of  $D_{Kn}$  is calculated in cm<sup>2</sup>/s. The assumed average  $r_{pore}$  is  $4 \cdot 10^{-9}$  m. In the range of mesoporen (2-50 nm)

## I.4 Transport coefficients in fixed-bed reactor

### I.5 Axial dispersion-Peclet Axial- Bodenstein Number

The axial dispersion can be calculated based on the axial Peclet number

$$D_{eff,ax} = \frac{\overline{u_{sf}} \cdot d_p}{Pe_{ax}} \quad (I.26)$$

The calculation of axial Peclet-number is taken from VDI (2006) Mh 5 .

$$\frac{1}{Pe_{ax}} = \frac{\delta_{bed}}{Pe_0} + \frac{1}{K_{ax}} \quad (I.27)$$

with  $K_{ax} = 2$

The molecular Peclet number:

$$Pe_0 = \frac{\overline{u_{sf}} \cdot d_p}{D_{1,2}} \quad (I.28)$$

$$\frac{\delta_{bed}}{\delta} = 1 - \sqrt{1 - \varepsilon} \quad (I.29)$$

The Bodenstein number compares the convective and diffusive terms in a fixed bed reactor. For values of Bodenstein  $> 100$ , the axial dispersion can be neglected and the assumption of plug-flow is justified VDI (2006) Dee 3.

$$Bo = Pe_{ax} \frac{L_t}{d_p} \quad (I.30)$$

### I.6 Thermal conductivity of the catalyst bed $\lambda_{bed}$

The correlations for  $\lambda_{bed}$  are taken from the VDI (2006) Mh and Dee 3 using the model presented by Zehner, Bauer and Schlünder.

$$\lambda_{bed} = k_{bed} \cdot \lambda_g \quad (I.31)$$

with

$$k_{bed} = 1 - \sqrt{1 - \varepsilon} + \sqrt{1 - \varepsilon} \cdot k_c \quad (\text{I.32})$$

with

$$k_c = \frac{2}{N} \cdot \left( \frac{B}{N^2} \frac{k_p - 1}{k_p} \ln \frac{k_p}{B} - \frac{B + 1}{2} - \frac{B - 1}{N} \right) \quad (\text{I.33})$$

with

$$N = 1 - \frac{B}{k_p} \quad (\text{I.34})$$

with B calculated for catalyst particles assuming spheres.

$$B = 1.25 \cdot \left( \frac{1 - \varepsilon}{\varepsilon} \right)^{10/9} \quad (\text{I.35})$$

with

$$k_p = \frac{\lambda_p}{\lambda_g} \quad (\text{I.36})$$

With  $\lambda_p$  being the thermal conductivity of the catalyst particle.

The thermal conductivity of an egg-shell catalyst particle combines the conductivity of the active material and the inert material. Assuming an sphere.

$$\lambda_p = \frac{2 \cdot \chi_{shell}}{d_p} \cdot \lambda_{active} + \frac{(1 - 2 \cdot \chi_{shell})}{d_p} \cdot \lambda_{inert} \quad (\text{I.37})$$

## 1.7 Effective radial thermal conductivity of the catalyst bed, $\lambda_{eff,r}$

The effective radial thermal conductivity of the catalyst bed is calculated according to the model of Winterberg et al. (VDI (2006), Mh 8) for sphere particles.

$$\lambda_{eff,r} = \lambda_{bed} + \frac{Re_p \cdot Pr \cdot \lambda_g}{K_r} \quad (\text{I.38})$$

$$K_r = K_\infty \cdot \left( 2 - \left( 1 - 2 \cdot \left( \frac{d_p}{d_t} \right)^2 \right) \right) \quad (\text{I.39})$$

$$K_\infty = 8$$

## I.8 Heat transfer coefficient at the internal reactor wall, $\alpha_{\text{wall}}$

The calculation of  $\alpha_{\text{wall}}$  is done following the correlations of Martin and Nilles VDI (2006) Mh 8 and Martin et al. (1993)

$$\alpha_{\text{wall}} = \alpha_0 + 0.19 \cdot \frac{\lambda_g}{d_p} \cdot Re_p^{0.75} \cdot Pr^{0.33} \quad (\text{I.40})$$

with

$$\alpha_0 = \left(1.3 + 5 \cdot \frac{d_p}{d_t}\right) \cdot \frac{\lambda_{\text{bed}}}{d_p} \quad (\text{I.41})$$

## J Lab-scale fixed-bed reactor: mathematical model

Table J.13 shows the criteria used to evaluate the use of a pseudohomogeneous mathematical model to describe the lab-scale fixed-bed reactor.

Table J.13: Criteria used to determine mass and heat transfer limitations. Taken from Baerns et al. (1992). In Equation J.44, the characteristic length of the catalyst particle is  $\chi_{\text{shell}}$  in the case of the industrial scale reactor and for the lab-scale reactor  $d_p$ .

---

Interparticle mass gradients	$DaII = \frac{r_{p,\text{eff}} \cdot d_p}{c_i \cdot \beta}$	$<$	$\frac{0.3}{m}$	(J.42)
------------------------------	---	-----	-----------------	--------

Interparticle temperature gradients	$DaIII = \frac{\Delta_R H \cdot r_{p,\text{eff}} \cdot d_p}{\alpha_g \cdot T}$	$<$	$0.15 \cdot \frac{R \cdot T}{E_A}$	(J.43)
-------------------------------------	--	-----	------------------------------------	--------

Intraparticle mass gradients	$w = \frac{r_{p,\text{eff}} \cdot \chi_{\text{shell}}^2}{c_i \cdot D_{\text{eff}}}$	$<$	0.6	(J.44)
------------------------------	---	-----	-----	--------

Intraparticle heat gradients	$DaIV = \frac{\Delta_R H \cdot r_{p,\text{eff}} \cdot d_p^2}{\lambda_p \cdot T}$	$<$	$4 \cdot \frac{R \cdot T}{E_A}$	(J.45)
------------------------------	--	-----	---------------------------------	--------

---

Table J.14 shows that internal and external mass- and heat transfer limitations are negligible in the lab-scale fixed-bed reactor according to the values calculated (Table J.13). Representative values for gas and catalyst properties are given together with values for the characteristic number under the selected conditions.

Table J.14: Estimation of the significance of internal and external mass- and heat transfer limitations in the lab-scale fixed-bed reactor, on basis of correlations shown in H and I and the criteria listed in Table J.13

<b>conditions</b>			<b>gas properties</b>		
$T$	°C	280	$c_{\text{CO}_2}$	mol/m <sup>3</sup>	43.5
$p$	MPa	1	$\rho_{\text{gas}}$	kg/m <sup>3</sup>	2.29
$F_{\text{v,in}}$	cm <sup>3</sup> /min	300	$\eta_{\text{g}}$	Pa.s	$2.31 \cdot 10^{-5}$
<b>reactor</b>			$\nu_{\text{g}}$	m <sup>2</sup> /s	$1.02 \cdot 10^{-5}$
$L$	m	0.21	$D_{12}$	m <sup>2</sup> /s	$1.97 \cdot 10^{-5}$
$A$	m <sup>2</sup>	$3.77 \cdot 10^{-5}$	$\lambda_{\text{g}}$	W/mK	$2.03 \cdot 10^{-1}$
$u_{\text{sf}}$	m/s	0.027	$\alpha_{\text{g}}$	W/m <sup>2</sup> K	$1.35 \cdot 10^3$
$\varepsilon$		0.4	$c_{p,\text{g}}$	J/kgK	$3.10 \cdot 10^3$
<b>reaction</b>			$\beta$	m/s	$7.84 \cdot 10^{-2}$
$r_{\text{CO}_2,\text{max}}$	mol/kg s	0.1	<b>characteristic numbers</b>		
$\rho_{\text{bed}}$	kg/m <sup>3</sup>	255.3	$\text{Re}_{\text{p}}$		$2.67 \cdot 10^{-1}$
$E_{A,\text{average}}$	kJ/mol	116.8	Pr		$3.52 \cdot 10^{-1}$
$\Delta H_{\text{R}}$	kJ/mol	-134.4	Sc		$5.10 \cdot 10^{-1}$
<b>catalyst</b>			Nu		$6.63 \cdot 10^{-1}$
$d_{\text{p}}$	m	$1.00 \cdot 10^{-4}$	Sh		$3.96 \cdot 10^{-1}$
$D_{\text{eff}}$	m <sup>2</sup> /s	$3.25 \cdot 10^{-7}$	$\text{Pe}_{\text{ax}}$		0.45
$\lambda_{\text{p}}$	W/m K	20	Bo		$9.44 \cdot 10^2$
$r_{\text{pore}}$	m	$4.00 \cdot 10^{-9}$	<b>transport resistance</b>		
			Da II < 0.3		$1.93 \cdot 10^{-3}$
			w < 0.6		$4.50 \cdot 10^{-2}$
			Da III < 0.01		$4.60 \cdot 10^{-4}$
			Da IV < 0.16		$3.10 \cdot 10^{-6}$

## K Determination of CO<sub>2</sub> hydrogenation kinetics under steady-state conditions: extra figures

The range of operational conditions used to determine the set of kinetic parameters with the 100 g Fe / 2 g K catalyst is shown in Table K.15. Figure K.37 shows the parity plot at  $T = 290$  °C, between experimental and calculated values using the set of kinetic parameters for 100 g Fe / 2 g K.

Table K.15: Range of experimental conditions tested with the 100 g Fe / 2 g K catalyst to determine kinetic parameters shown in Table 6.2.

		minimum	maximum
$T$	°C	245	286
$p$	MPa	1	2 (245 - 266 °C)
$(\text{H}_2/\text{CO}_2)_{\text{in}}$	-	4	8
$\tau_{\text{mod}}$	kg s/m <sup>3</sup>	175	3000 (266 °C) 1000 (286 °C)

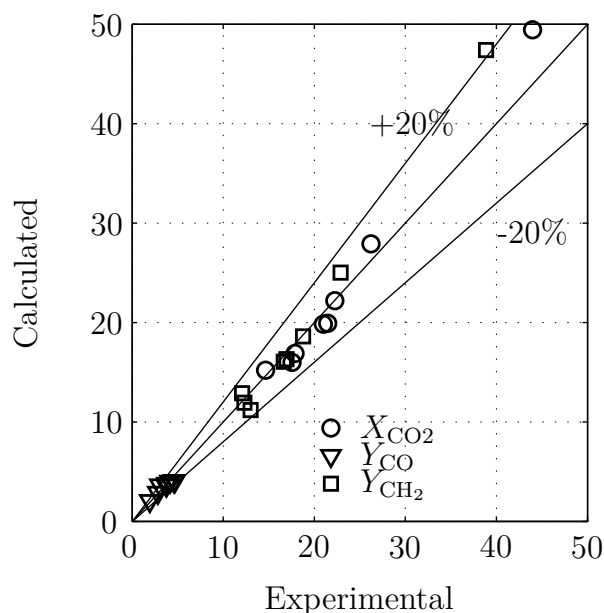


Figure K.37: Parity plot for 100 g Fe / 2 g K at  $T = 290$  °C

A preliminary set of kinetic parameters is determined for 100 g Fe / 10 g K using the procedure described in chapter 6. Table K.16 shows the set of parameter values and Table K.17 the range of validity. The set of kinetic parameters determined by Riedel et al. (2001) are shown in Table K.18 for comparison with own results.

Table K.16: Kinetic parameter values of the CO<sub>2</sub>-shift and FT reaction for 100 g Fe / 10 g K, Equation 3.10 and Equation 3.11. Range of operation conditions used shown in Table K.17.

	$k_j$ (270 °C)	$k_j$ (290 °C)	$k_j$ (310 °C)	$k_j$ (330 °C)	$a_j$	$b_j$
	mol/s kg Pa	mol/s kg Pa	mol/s kg Pa	mol/s kg Pa	–	–
CO <sub>2</sub> -shift	$3.30 \cdot 10^{-8}$	$1.48 \cdot 10^{-7}$	$3.82 \cdot 10^{-7}$	$4.54 \cdot 10^{-7}$	126.8	1.0
FT	$4.19 \cdot 10^{-7}$	$7.96 \cdot 10^{-7}$	$1.53 \cdot 10^{-6}$	$1.96 \cdot 10^{-6}$	124.4	9.3

Table K.17: Range of experimental conditions tested with the 100 g Fe / 10 g K catalyst to determined kinetic parameters shown in Table K.16.

		minimum	maximum
$T$	°C	270	330
$p$	MPa	1	1
$(\text{H}_2/\text{CO}_2)_{\text{in}}$	-	4	8
$\tau_{\text{mod}}$	kg s/m <sup>3</sup>	200	5000

Table K.18: Kinetic parameter values for the Equation 3.10, Equation 3.11 and Equation 3.3 (Riedel 2002).

	$k_j$ (300 °C)	$k_j$ (330 °C)	$k_j$ (360 °C)	$a_j$	$b_j$
	mol/s kg Pa	mol/s kg Pa	mol/s kg Pa	–	–
CO <sub>2</sub> -shift	$1.34 \cdot 10^{-7}$	$2.50 \cdot 10^{-7}$	$3.96 \cdot 10^{-7}$	65	7.5
FT	$2.04 \cdot 10^{-7}$	$4.27 \cdot 10^{-7}$	$8.50 \cdot 10^{-7}$	33	2.7
DH	$1.64 \cdot 10^{-9}$	$19.7 \cdot 10^{-9}$	$2.45 \cdot 10^{-9}$	60	66

Activation energies and pre-exponential factors are calculated using a linearised form of the Arrhenius equation, (Equation K.46) based on the kinetic constants obtained at different temperatures. The activation energy is calculated from the slope of the linear function and the pre-exponential factor from the y-intercept (Figure K.38). Results can be seen in Table 6.3.

$$\ln(k_j) = \frac{-E_A}{R} \cdot \frac{1}{T} + \ln(k_0) \quad (\text{K.46})$$

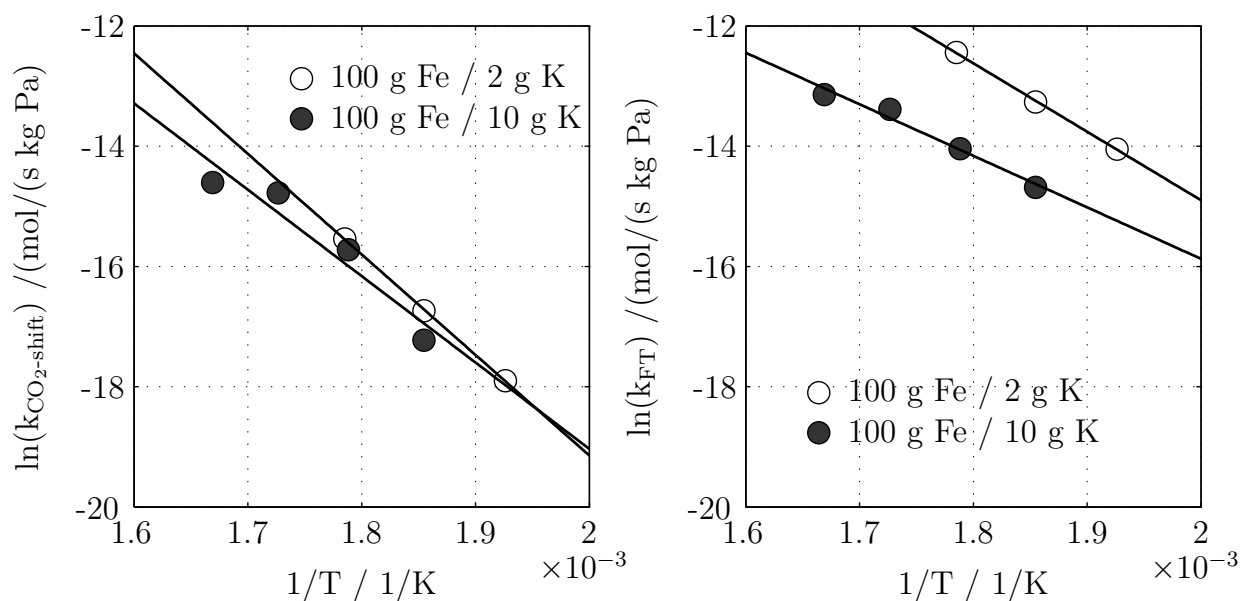


Figure K.38: Logarithm of the reaction rate constant versus the reciprocal absolute temperature for 100 g Fe / 10 g K and 100 g Fe / 2 g K. Curves: linear regression. Left:  $\text{CO}_2$ -shift reaction. Right: Fischer-Tropsch reaction. Values in Table 6.3. Correlation coefficients:  $R_{\text{CO}_2\text{-shift},2\text{K}}^2 = 0.972$ ,  $R_{\text{CO}_2\text{-shift},10\text{K}}^2 = 0.912$ .  $R_{\text{FT},2\text{K}}^2 = 0.974$  and  $R_{\text{FT},10\text{K}}^2 = 0.976$ .

## L Solution of ordinary and partial differential equations

There exist several solving methods for ODEs, an overview of the different methods is given and some examples are further introduced. Solutions of ODEs can either be of an implicit or explicit type. Both approaches are based on finite differences (FD). FD replaces differential quotients by difference quotients, on basis of a cartesian coordinate system. Three different ways are possible, backward, forward and central differences.

$$\begin{aligned}\frac{dy}{dt} &= \frac{y_t - y_{t-1}}{\Delta t} && \text{(backward)} \\ \frac{dy}{dt} &= \frac{y_{t+1} - y_t}{\Delta t} && \text{(forward)} \\ \frac{dy}{dt} &= \frac{y_{t+1} - y_{t-1}}{2 \cdot \Delta t} && \text{(central)}\end{aligned}\tag{L.47}$$

### Explicit methods

Explicit methods calculate a new point based on known points, it is a linear method, easy to follow, however with stability problems, as they are not stable for too big step sizes. Euler forwards is a first order explicit method, with a first order accuracy.

$$\begin{aligned}\frac{y_{t+1} - y_t}{\Delta t} &= f(y_t) \\ \Rightarrow y_{t+1} &= y_t + \Delta t \cdot f(y_t)\end{aligned}\tag{L.48}$$

The Runge-Kutta method is 4<sup>th</sup> order explicit. It is more precise than 1<sup>st</sup> order but it needs four times more calculation time, because 4 intermediate points are evaluated ( $k_1 - k_4$ ).

$$\begin{aligned}\frac{y_{t+1} - y_t}{\Delta t} &= \frac{1}{6} \cdot (k_1 + 2 \cdot k_2 + 2 \cdot k_3 + k_4) \\ \Rightarrow y_{t+1} &= y_t + \frac{1}{6} \cdot \Delta t \cdot (k_1 + 2 \cdot k_2 + 2 \cdot k_3 + k_4) \\ k_1 &= f(t) \\ k_2 &= f\left(t + \frac{\Delta t}{2} \cdot k_1\right) \\ k_3 &= f\left(t + \frac{\Delta t}{2} \cdot k_2\right) \\ k_4 &= f\left(t + \Delta t \cdot k_3\right)\end{aligned}\tag{L.49}$$

### Implicit methods

Implicit methods are stable for every step size, but in order to calculate a new point  $t+1$ , a function of nonlinear equations of  $f(y_{t+1})$  has to be determined and thus, iteration is



necessary. Implicit methods are not as easy comprehensible as explicit methods, but their stability is better.

A first order implicit method is Euler backwards (Finlayson et al. 2000).

$$\begin{aligned}\frac{y_{t+1} - y_t}{\Delta t} &= f(y_{t+1}) \\ \Rightarrow y_{t+1} &= y_t + \Delta t \cdot f(y_{t+1})\end{aligned}\tag{L.50}$$

A combination of the trapezoid rule used with finite differences method is called Crank-Nicholson, it is a second order implicit method (Finlayson et al. 2000).

$$y_{t+1} = y_t + \frac{\Delta t}{2} \cdot [f(y_t) + f(y_{t+1})]\tag{L.51}$$

Partial differential equations are, in contrast to ordinary differential equations, dependent of two or more independent variables. In this work these variables are time and one (1D model) or two (2D model) space dimensions. In general three basic forms of partial differential equations can be distinguished (Finlayson et al. 2000):

1. Hyperbolic equations can be classified according to the derivation in x. First-order means that there exist only first-order derivatives in x (Schiesser et al. 2009). An example for a hyperbolic equations is

$$\frac{\partial y}{\partial t} + \frac{\partial y}{\partial x} = 0\tag{L.52}$$

2. In elliptic equations no derivatives in t occur (Schiesser et al. 2009). The following equation is a model elliptic problem.

$$\left(\frac{\partial^2 y}{\partial x^2} + \frac{\partial^2 y}{\partial z^2}\right) = 0\tag{L.53}$$

3. Parabolic equations are the third type of PDE, where only second-order derivatives in x occur (Schiesser et al. 2009), which can be seen in the next equation.

$$\frac{\partial y}{\partial t} = \left(\frac{\partial^2 y}{\partial x^2} + \frac{\partial^2 y}{\partial z^2}\right)\tag{L.54}$$

Also a mixture of these types is possible. Each type of PDE has to be treated in different manner. Further information about the different types of PDE and about the solving methods are given in (Finlayson et al. 2000).

## L.1 Method of lines (MOL)

The basic idea of the MOL is to replace the spatial derivatives in the PDE with algebraic approximations. Once this is done, the spatial derivatives are no longer explicitly in terms

of the spatial independent variables. Thus, only the initial-value variable, typically time in a physical problem, remains. In other words, with only one remaining independent variable, we have a system of ODEs that approximate the original PDE. The challenge is to formulate the approximating system of ODEs. Once this is done, we can apply any integration algorithm for initial-value ODEs to compute an approximate numerical solution to the PDE. Thus, one of the salient features of the MOL is the use of existing, and generally well-established, numerical methods for ODEs. Detailed information about this method can be found in Schiesser et al. (2009)

$$\begin{aligned}\frac{\partial f}{\partial t} + \frac{\partial f}{\partial x} &= 0 \\ \frac{\partial f}{\partial t} + \frac{f_j - f_{j-1}}{\Delta x} &= 0\end{aligned}\tag{L.55}$$

## M Iron catalyst behaviour under variable operating conditions: experiments in lab-scale setup

### M.1 Characterization of the lab-scale setup

Figure M.39 shows a three representative examples of residence time distribution experiments carried out in the lab-scale setup. Table M.19 shows the temperature, pressure and volume of the different parts of the lab-scale set up. The PF- volume corresponds to the volume with plug flow, while PMF-volume corresponds to volume with perfectly mixed flow. Typical volumetric flows under operation conditions are indicated on the Table.

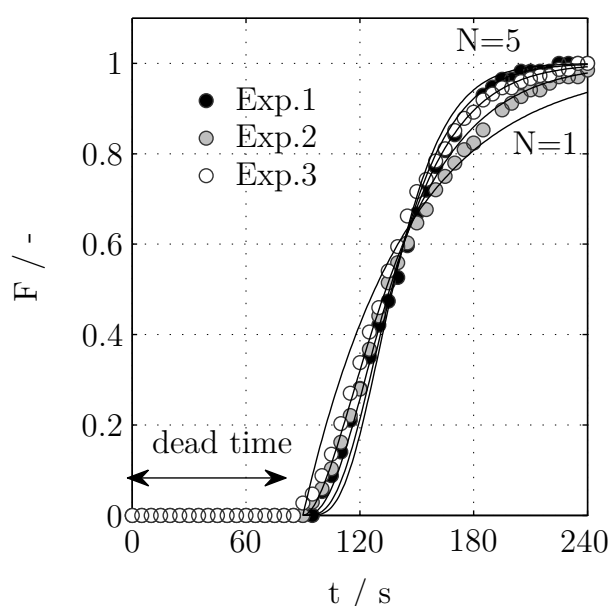


Figure M.39: Residence time distribution (RTD) experiments using  $\text{CO}_2$  as tracer. Dimensionless outlet  $\text{CO}_2$  concentration (F-curve) versus time after a step change in  $\text{CO}_2$  concentration at  $t = 0$  from 0 to 25 vol %  $\text{CO}_2$  (mixture Ar/ $\text{CO}_2$ ). Curves calculated with Equation 7.1 for different N values. Symbols: experimental values measured with Binos-IR. Operating conditions:  $p = 0.1$  MPa,  $T = 24$  °C,  $F_{v,\text{in,STP}} = 90$  cm<sup>3</sup>/min (average of the 3 experiments). Reactor: inert bed.

Table M.19: Characterization of the lab-scale setup with fixed-bed reactor. Volumetric flows according to RTD experiments.  $F_{v,STP} = 90 \text{ cm}^3/\text{min}$

	1	2	3	4	5	6-7	8	9	10	11-12	13-14	15	to IR	Total
$T$ ( $^{\circ}\text{C}$ )	24	24	24	24	24	24	24	24	24	24	24	24	24	
$p$ (MPa)	0.1	0.1	0.1	0.1	0.1	0.1	0.1	0.1	0.1	0.1	0.1	0.1	0.1	
$L_1$ (m)	0.8	1.2	0.2	0.4	0.5	0.18	0.4	0.8	1	0.16	0.4	0.6		
$L_2$ (m)	0.6			0.3							0.1			
$D_1$ (mm)	3.80	3.80	6.93	6.93	3.80	12.0	3.80	3.80	1.73	15.3	3.80	1.73		
$D_2$ (mm)	1.73			6.93							1.73			
$V_{\text{gas}}$ ( $\text{cm}^3$ )	10.48	13.61	3.02	17.34	5.67	20.36	4.54	9.07	2.34	29.42	84.77	1.40	11.46	<b>211.12</b>
$V_{\text{gas, PF}}$ ( $\text{cm}^3$ )	10.48	13.61	3.02	17.34	5.67	10.18	4.54	9.07		14.71	44.77	1.40	11.46	<b>146.24</b>
$V_{\text{gas, PMF}}$ ( $\text{cm}^3$ )						10.18				14.71	40.00			<b>64.89</b>
$F_{v,op}$ $\text{cm}^3/\text{min}$	98.89	98.89	98.89	98.89	98.89	98.89	98.89	98.89	5	93.89	93.89	93.89	93.89	
$u_{sf}$ (m/s)	0.145	0.145	0.109	0.044	0.145	0.015	0.145	0.145	0.036	0.009		0.670		
Dead Time (s)	6.36	8.26	1.83	10.52	3.44	6.18	2.75	5.50	0.00	9.40	28.61	0.90	7.32	<b>91.06</b>
Time (s)	6.36	8.26	1.83	10.52	3.44	12.35	2.75	5.50	28.04	18.80	54.171	0.90	7.32	160.24
Time (min)	0.11	0.14	0.03	0.18	0.06	0.21	0.05	0.09	0.47	0.31	0.90	0.01	0.12	2.67

## M.2 Validation of the lab-scale mathematical model

Figure M.40 shows an experimental example carried out to validate the mathematical model using IR analysis.

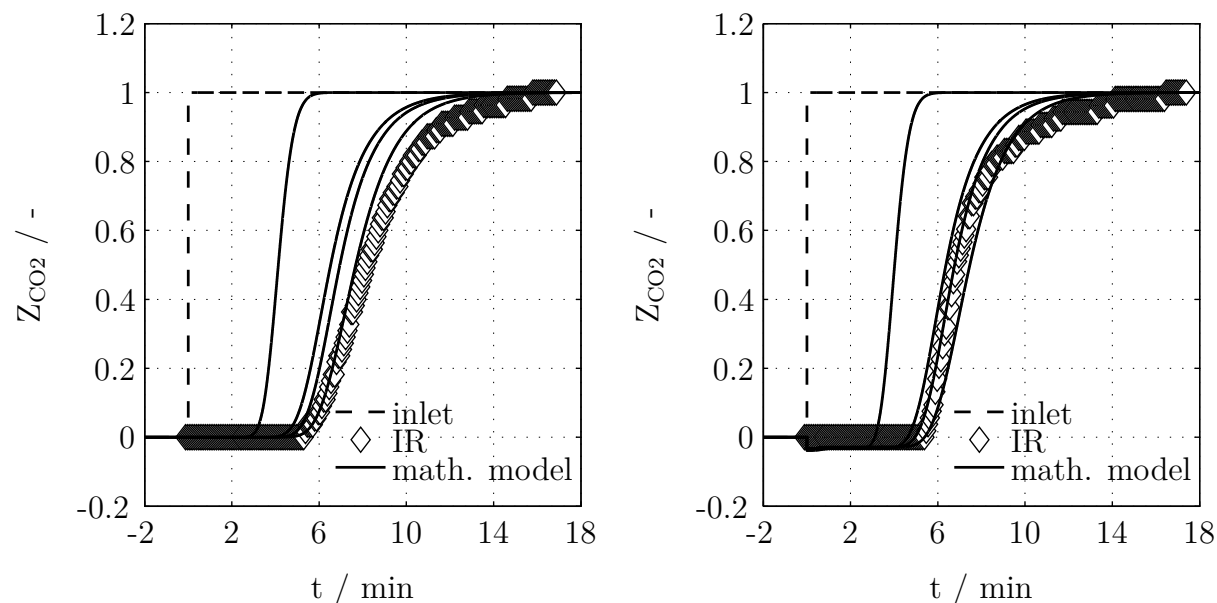


Figure M.40: Step change in inlet concentration for validation of the mathematical model under reaction conditions using a bed of inert material. Dimensionless change of  $\text{CO}_2$  flows  $Z_{\text{CO}_2}$ . Symbols: experimental results measured with IR. Curves: calculated with mathematical model, outlet flows of units 4, 7, 12, 15. Operating conditions:  $p = 1 \text{ MPa}$ ,  $T = 266 \text{ }^\circ\text{C}$ ,  $F_{v,\text{in,STP}} = 90 \text{ cm}^3/\text{min}$ . Change at  $t = 0$ , left: from  $(\text{H}_2/\text{CO}_2)_{\text{in}} = \infty$  to  $(\text{H}_2/\text{CO}_2)_{\text{in}} = 8$ ; right: from  $(\text{H}_2/\text{CO}_2)_{\text{in}} = 8$  to  $(\text{H}_2/\text{CO}_2)_{\text{in}} = \infty$ .

### M.3 Extra experimental results for step changes combined with mathematical model

Figure M.41 shows an example result of a change in inlet concentration using molar flows. Same information dimensionless is shown in Figure M.50.

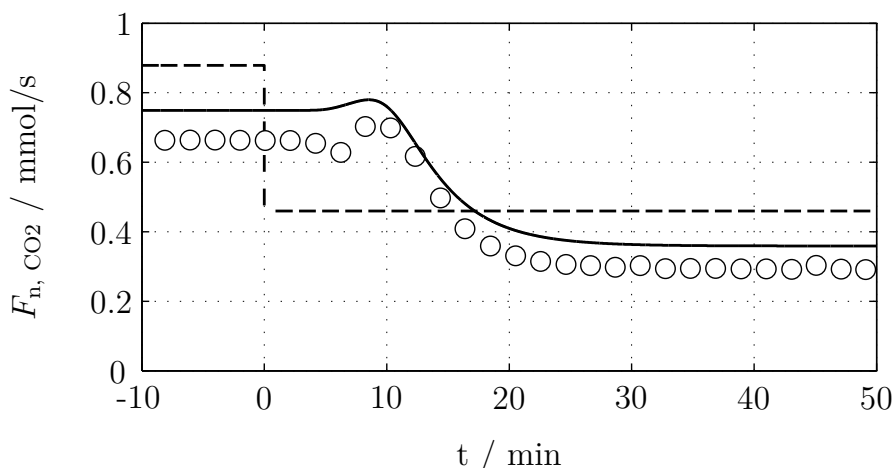


Figure M.41: Example results in molar flow for a step change in inlet concentration from  $(\text{H}_2/\text{CO}_2)_{\text{in}} = 4$  to  $(\text{H}_2/\text{CO}_2)_{\text{in}} = 8$ . Conditions:  $p = 1$  MPa,  $T = 264$  °C,  $\tau_{\text{mod,target}} = 1000$  kgs / m<sup>3</sup>,  $F_{\text{v,in,STP},(\text{H}_2/\text{CO}_2)_{\text{in}}=4} = 94.7$  cm<sup>3</sup>/min,  $F_{\text{v,in,STP},(\text{H}_2/\text{CO}_2)_{\text{in}}=8} = 102.7$  cm<sup>3</sup>/min. Curves: calculated with mathematical model, broken line: change in inlet flow, solid line: setup outlet (unit 17). Symbols: measured with Micro-GC.

#### M.3.1 Step changes in inlet concentration

Figure M.42 shows the change in inlet concentration from  $(\text{H}_2/\text{CO}_2)_{\text{in}} = 8$  to  $(\text{H}_2/\text{CO}_2)_{\text{in}} = 5$ . According to the mathematical kinetic model, the average CO<sub>2</sub>-shift reaction rate along the catalyst bed increases from  $(\text{H}_2/\text{CO}_2)_{\text{in}} = 8$  to  $(\text{H}_2/\text{CO}_2)_{\text{in}} = 5$  and FT remains constant (under steady-state conditions). During the first minutes, the CO molar flow is higher than at steady-state conditions, what indicates that CO<sub>2</sub>-shift reaction rate is higher compared with steady-state conditions or the FT reaction rate lower, however no dynamic effect is observed on the hydrocarbons. This effect is confirmed with measurements with the online GC. However this dynamic effect is based on only one measurement. No dynamic effect is observed when the change occurs from  $(\text{H}_2/\text{CO}_2)_{\text{in}} = 5$  to  $(\text{H}_2/\text{CO}_2)_{\text{in}} = 8$ .

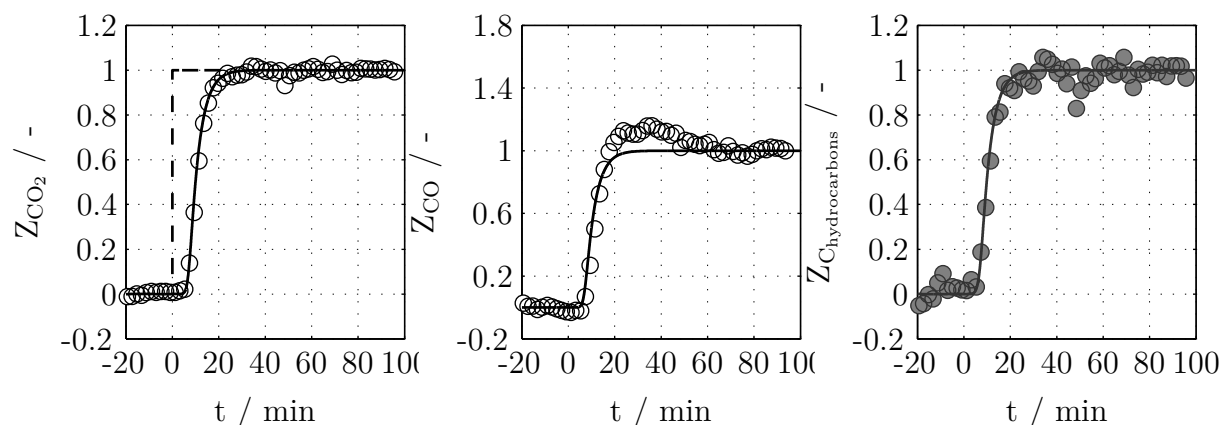


Figure M.42: Dimensionless change of  $\text{CO}_2$ ,  $\text{CO}$ , and  $\text{C}$  in hydrocarbon outlet flows after a concentration change from  $(\text{H}_2/\text{CO}_2)_{\text{in}} = 8$  to  $(\text{H}_2/\text{CO}_2)_{\text{in}} = 5$ . Curves: calculated with mathematical model, broken line: change in inlet flow. Dimensionless using Equation 7.5. Symbols: experimental results measured with Micro-GC. Conditions:  $F_{v,\text{in,STP},(\text{H}_2/\text{CO}_2)_{\text{in}}=8} = 233 \text{ cm}^3/\text{min}$ ,  $F_{v,\text{in,STP},(\text{H}_2/\text{CO}_2)_{\text{in}}=5} = 238 \text{ cm}^3/\text{min}$ ,  $\tau_{\text{mod,target}} = 400 \text{ kg s}/\text{m}^3$ ,  $p = 1 \text{ MPa}$ ,  $T = 295 \text{ }^\circ\text{C}$ . Catalyst:  $100 \text{ g Fe} / 2 \text{ g K}$

Figure M.43 shows the formation of the  $100 \text{ g Fe} / 2 \text{ g K}$  over time, represented in the same way as the transient experiments.

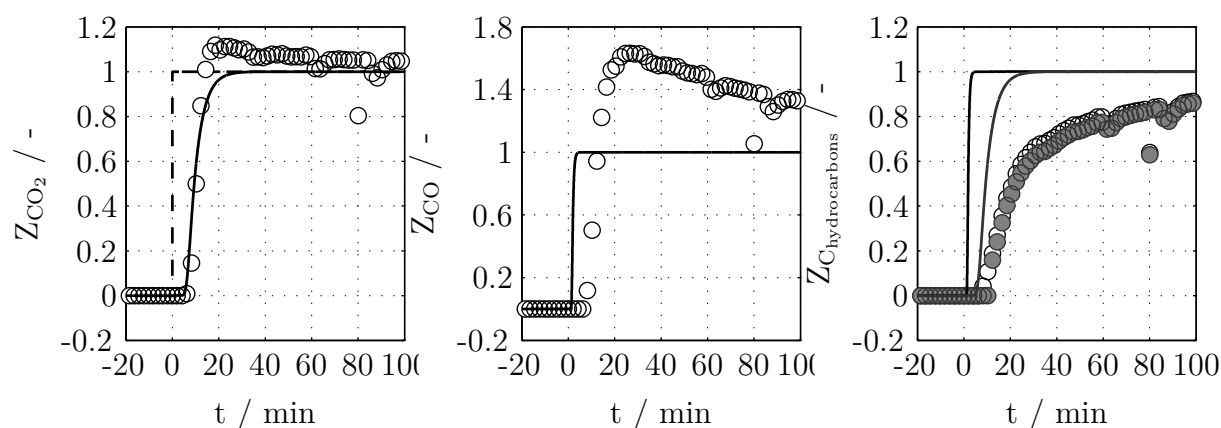


Figure M.43: Dimensionless change of  $\text{CO}_2$ ,  $\text{CO}$ , and  $\text{C}$  in hydrocarbon outlet flows after a concentration change from  $\text{H}_2$  (after catalyst reduction) to  $(\text{H}_2/\text{CO}_2)_{\text{in}} = 5$  “catalyst formation”. Curves: calculated with mathematical model, broken line: change in inlet flow. Dimensionless using Equation 7.5. Symbols: experimental results measured with Micro-GC. Grey symbols:  $\text{C}$  in  $\text{C}_2\text{H}_6$  and white symbols:  $\text{C}$  in  $\text{CH}_4$  (right). Conditions:  $F_{v,\text{in,STP},(\text{H}_2/\text{CO}_2)_{\text{in}}=5} = 309.3 \text{ cm}^3/\text{min}$ ,  $\tau_{\text{mod,target}} = 400 \text{ kg s}/\text{m}^3$ ,  $p = 1 \text{ MPa}$ ,  $T = 300 \text{ }^\circ\text{C}$ . Catalyst:  $100 \text{ g Fe} / 2 \text{ g K}$

Figure M.44 shows the step change from  $(\text{H}_2/\text{CO}_2)_{\text{in}} = 5$  to pure  $\text{H}_2$ .

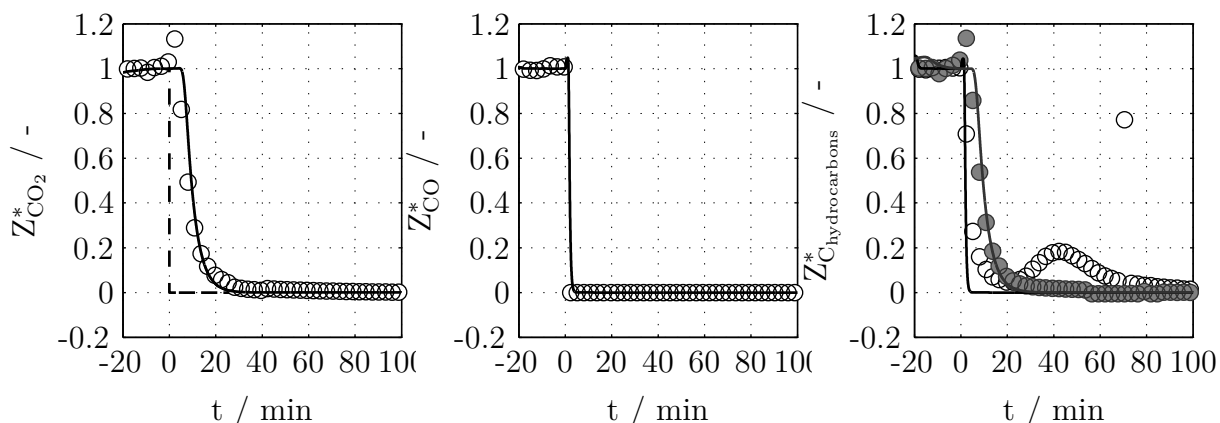


Figure M.44: Dimensionless change of  $\text{CO}_2$ ,  $\text{CO}$ , and  $\text{C}$  in hydrocarbon outlet flows after a concentration change from  $(\text{H}_2/\text{CO}_2)_{\text{in}} = 5$  to  $\text{H}_2$ . Curves: calculated with mathematical model, broken line: change in inlet flow. Dimensionless using Equation 7.6. Symbols: experimental results measured with Micro-GC. Grey symbols:  $\text{C}$  in  $\text{C}_2\text{H}_6$  and white symbols:  $\text{C}$  in  $\text{CH}_4$  (right). Conditions:  $F_{\text{v,in,STP}} = 300 \text{ cm}^3/\text{min}$ ,  $\tau_{\text{mod,target}} = 400 \text{ kg s}/\text{m}^3$ ,  $p = 1 \text{ MPa}$ ,  $T = 264 \text{ }^\circ\text{C}$ . Catalyst:  $100 \text{ g Fe} / 2 \text{ g K}$

Figure M.45 shows the change from pure  $\text{H}_2$  to  $(\text{H}_2/\text{CO}_2)_{\text{in}} = 4$ .

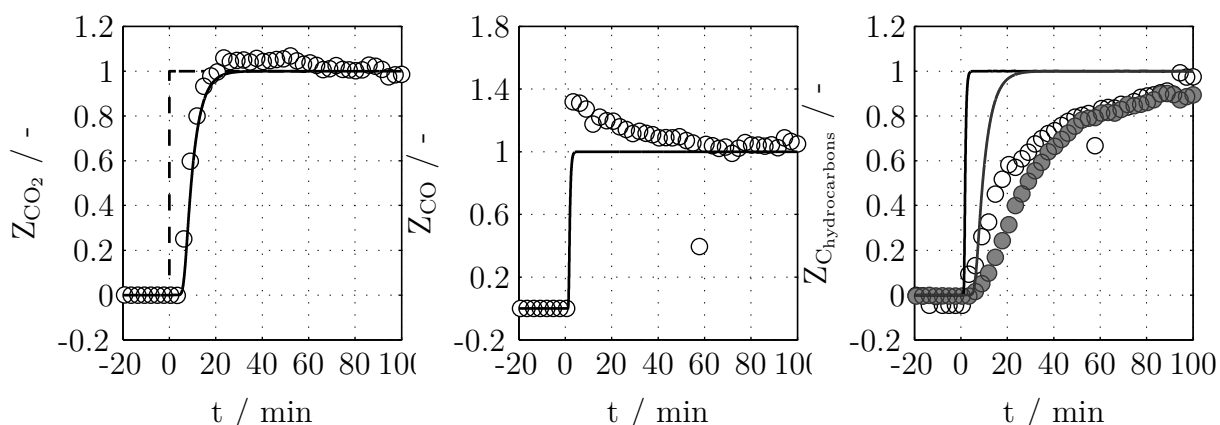


Figure M.45: Dimensionless change of  $\text{CO}_2$ ,  $\text{CO}$ , and  $\text{C}$  in hydrocarbon outlet flows after a concentration change from  $\text{H}_2$  to  $(\text{H}_2/\text{CO}_2)_{\text{in}} = 4$  “Hot-stand-by”. Curves: calculated with mathematical model, broken line: change in inlet flow. Dimensionless using Equation 7.5. Symbols: experimental results measured with Micro-GC. Grey symbols:  $\text{C}$  in  $\text{C}_2\text{H}_6$  and white symbols:  $\text{C}$  in  $\text{CH}_4$  (right). Conditions:  $F_{\text{v,in,STP}} = 300 \text{ cm}^3/\text{min}$ ,  $\tau_{\text{mod,target}} = 400 \text{ kg s}/\text{m}^3$ ,  $p = 1 \text{ MPa}$ ,  $T = 264 \text{ }^\circ\text{C}$ . Catalyst:  $100 \text{ g Fe} / 2 \text{ g K}$ .



### M.3.2 Step change in inlet volumetric flow

Figure M.46 and Figure M.47 show a step change in inlet volumetric flow at  $p = 1$  MPa. The dynamic behaviour of the lab-scale setup is fast (represented by the CO flow).

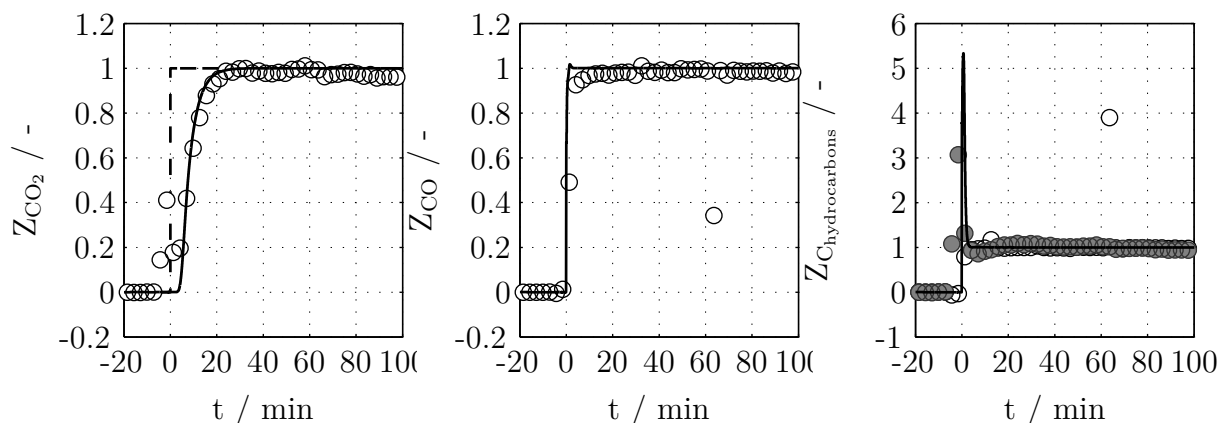


Figure M.46: Dimensionless change of  $\text{CO}_2$ ,  $\text{CO}$ , and  $\text{C}$  in hydrocarbon outlet flows after a change in inlet volumetric flow from  $F_{v,\text{in,STP}} = 40 \text{ cm}^3/\text{min}$  to  $F_{v,\text{in,STP}} = 300 \text{ cm}^3/\text{min}$  (STP). Curves: calculated with mathematical model, broken line: change in inlet flow. Dimensionless using Equation 7.5. Symbols: experimental results measured with Micro-GC. Grey symbols:  $\text{C}$  in  $\text{C}_2\text{H}_6$  and white symbols:  $\text{C}$  in  $\text{CH}_4$  (right). Conditions:  $(\text{H}_2/\text{CO}_2)_{\text{in}} = 4$ ,  $p = 1$  MPa,  $T = 245$  °C. Catalyst: 100 g Fe / 2 g K

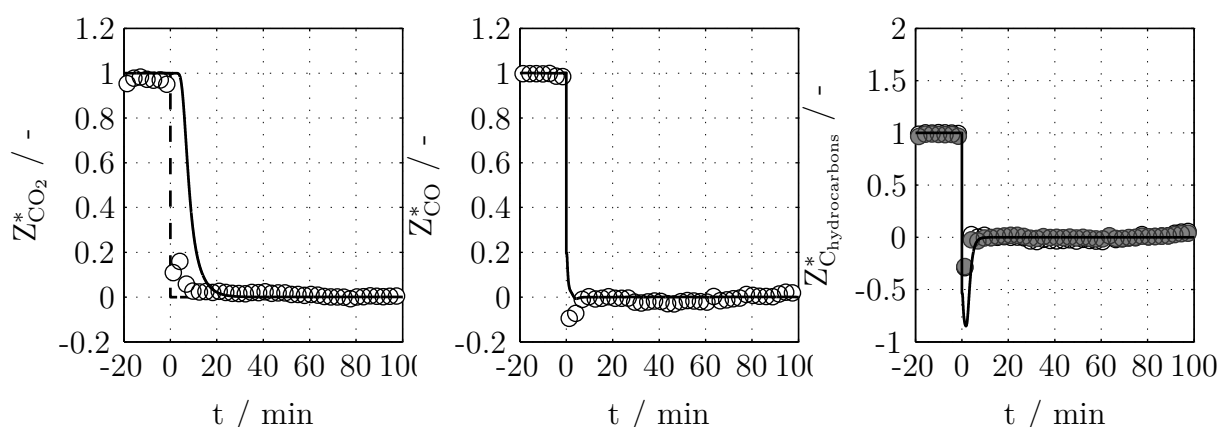


Figure M.47: Dimensionless change of  $\text{CO}_2$ ,  $\text{CO}$ , and  $\text{C}$  in hydrocarbon outlet flows after a change in inlet volumetric flow from  $F_{v,\text{in,STP}} = 300 \text{ cm}^3/\text{min}$  to  $F_{v,\text{in,STP}} = 120 \text{ cm}^3/\text{min}$ . Curves: calculated with mathematical model, broken line: change in inlet flow. Dimensionless using Equation 7.6. Symbols: experimental results measured with Micro-GC. Grey symbols:  $\text{C}$  in  $\text{C}_2\text{H}_6$  and white symbols:  $\text{C}$  in  $\text{CH}_4$  (right). Conditions:  $(\text{H}_2/\text{CO}_2)_{\text{in}} = 4$ ,  $p = 1$  MPa,  $T = 265$  °C. Catalyst: 100 g Fe / 2 g K

### M.3.3 Step change in reactor temperature

Figure M.48 and M.49 show a change in reactor temperature carried out in the lab-scale setup. It can be observed that heating is much faster than cooling. The molar flow of  $\text{CH}_4$  and  $\text{C}_2\text{H}_6$  are calculated assuming an  $\alpha = 0.25$  for the ASF model. The experimental values correspond to the alkane product, while the ASF model calculates the total number of hydrocarbons at a certain C-number.

At 300 °C the formation of alkene increases and this could explain part of the deviation between the flow of  $\text{C}_2\text{H}_6$  experimental measured and calculated. Temperature is a very sensible parameter for catalyst activity and seems that the mathematical model is not able to represent  $\text{CO}$  and  $\text{C}_2\text{H}_6$  flows. The white symbols represent measurement with the Micro-GC (each 3 min) and grey symbols with the online-GC.

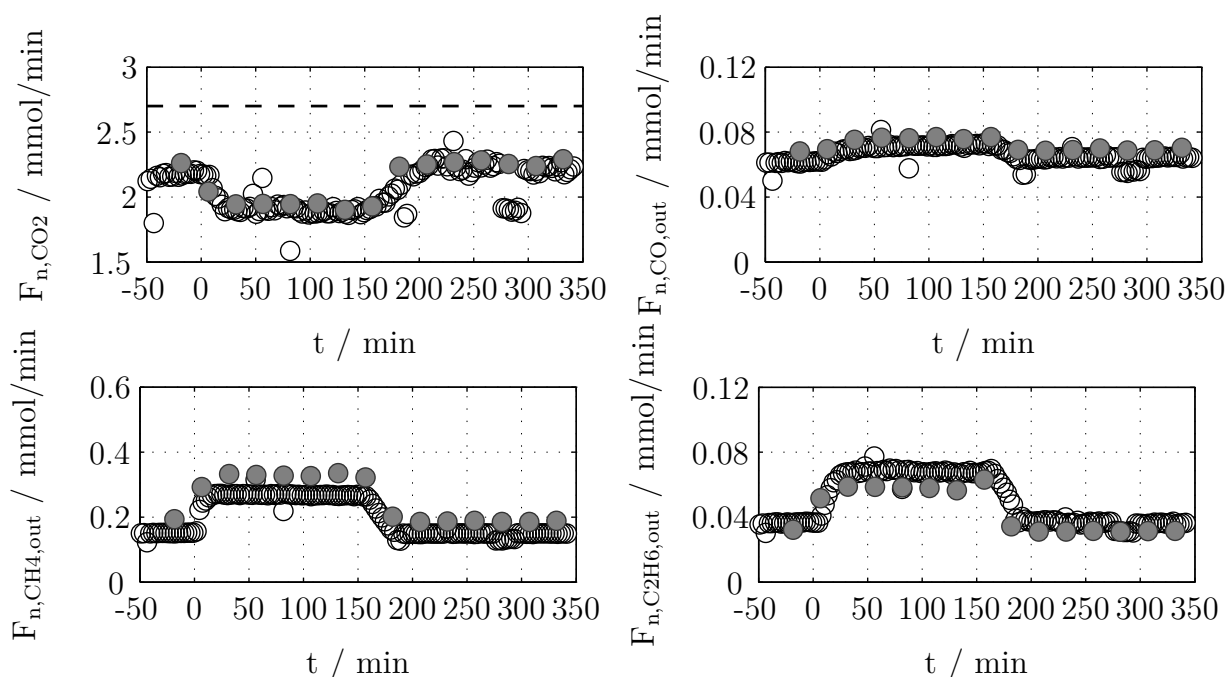


Figure M.48: Measured outlet flows during temperature change from 270 °C, at  $t = 0$  to 300 °C, with a ramp of 2 K/min. At  $t = 155$  min back to 270 °C. White symbols: Micro-GC (each 3 min), grey symbols: Online-GC (each 25 min). Broken line: inlet flow of  $\text{CO}_2$   $F_{n,\text{CO}_2,\text{in}}$ . Conditions:  $F_{v,\text{in,STP}} = 300 \text{ cm}^3/\text{min}$ ,  $(\text{H}_2/\text{CO}_2)_{\text{in}} = 4$ ,  $p = 1 \text{ MPa}$ . Catalyst: 100 g Fe / 2 g K.

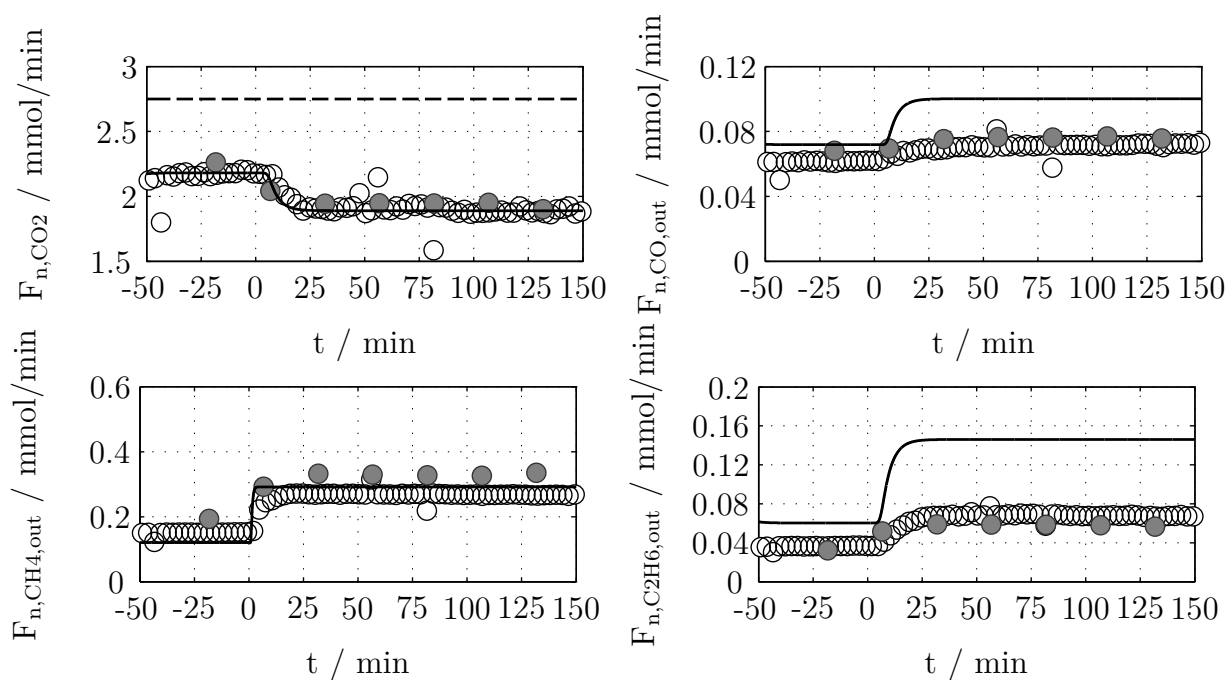


Figure M.49: Measured outlet flows of  $\text{CO}_2$ ,  $\text{CO}$ ,  $\text{CH}_4$ , and  $\text{C}_2\text{H}_6$  during a temperature change from  $270\text{ }^\circ\text{C}$ , at  $t = 0$  to  $300\text{ }^\circ\text{C}$ , with a ramp of  $2\text{ K/min}$ . Curves: calculated with mathematical model, broken line: inlet flow of  $\text{CO}_2$ ,  $F_{n,\text{CO}_2,\text{in}}$ . White symbols: Micro-GC (each 3 min), grey symbols: online-GC (each 25 min). Conditions:  $F_{v,\text{in,STP}} = 300\text{ cm}^3/\text{min}$ ,  $(\text{H}_2/\text{CO}_2)_{\text{in}} = 4$ ,  $p = 1\text{ MPa}$ . Catalyst:  $100\text{ g Fe} / 2\text{ g K}$ .

## M.4 Periodic changes

Figure M.50 shows a step change from  $(\text{H}_2/\text{CO}_2)_{\text{in}} = 4$  to  $(\text{H}_2/\text{CO}_2)_{\text{in}} = 8$ . Even though the change is in concentration, a minimum (overshoot) is observed because the absolute volumetric flows are slightly different. This effect can also be observed during the first minutes of periodic operation (Figure 7.11). The Micro-GC is mainly responsible of the dead time due to the low volumetric flow of sample gas.

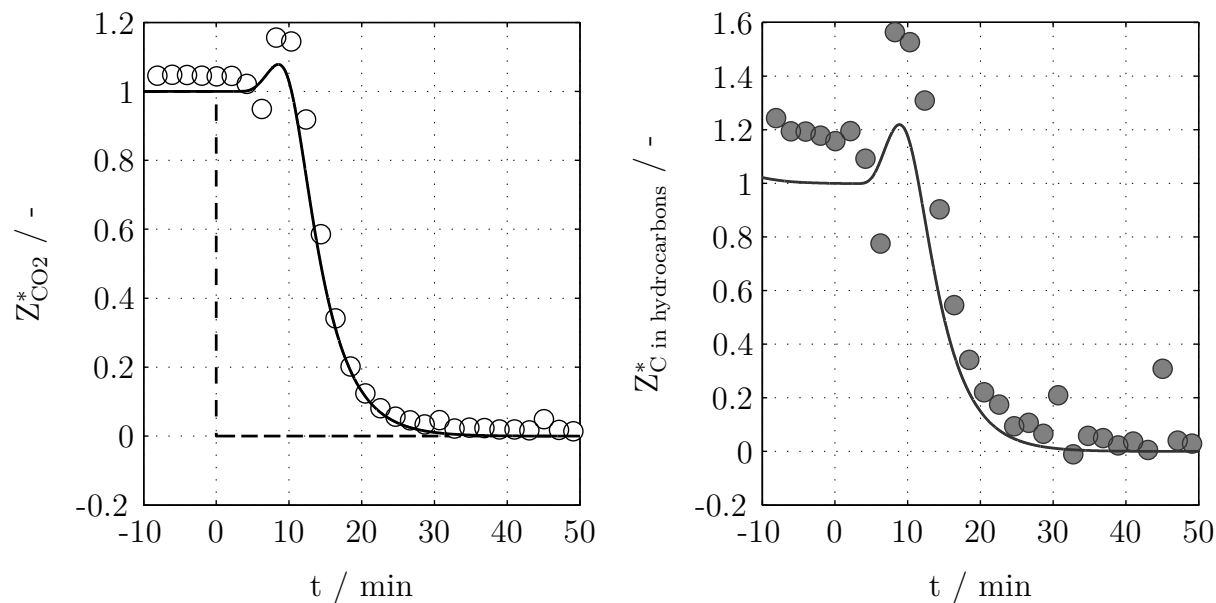


Figure M.50: Dimensionless change of CO<sub>2</sub> inlet and outlet flow (left) and C in hydrocarbon outlet flows (right) after a concentration change from  $(\text{H}_2/\text{CO}_2)_{\text{in}} = 4$  to  $(\text{H}_2/\text{CO}_2)_{\text{in}} = 8$ . Curves: calculated with mathematical model, broken line: change in inlet flow. Symbols: experimental results measured with Micro-GC. Conditions:  $F_{\text{v,in,STP},(\text{H}_2/\text{CO}_2)_{\text{in}}=4} = 94.7 \text{ cm}^3/\text{min}$ ,  $F_{\text{v,in,STP},(\text{H}_2/\text{CO}_2)_{\text{in}}=8} = 102.7 \text{ cm}^3/\text{min}$ ,  $\tau_{\text{mod,target}} = 1000 \text{ kg s}/\text{m}^3$ ,  $p = 1 \text{ MPa}$ ,  $T = 264 \text{ }^\circ\text{C}$ . Methane and CO not properly separated. Catalyst: 100 g Fe / 2 g K

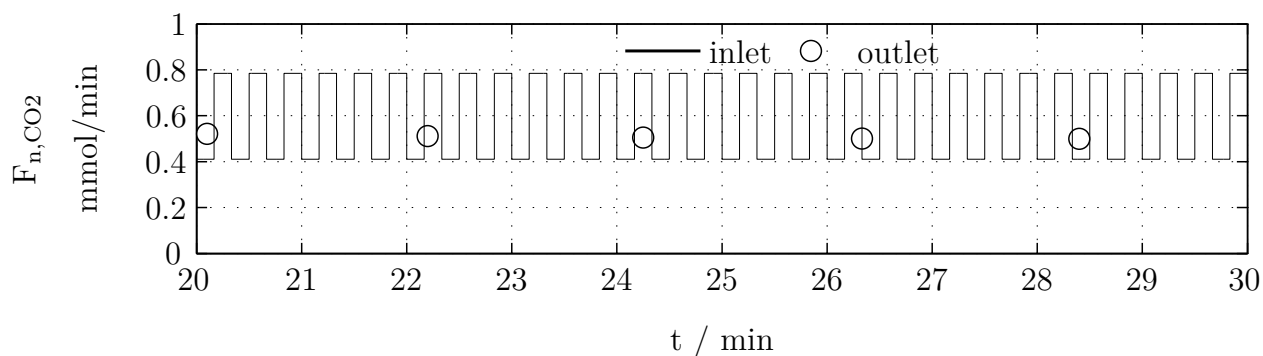


Figure M.51: Inlet and outlet CO<sub>2</sub> flows during periodic changes in inlet concentration from  $(\text{H}_2/\text{CO}_2)_{\text{in}} = 4$  to  $(\text{H}_2/\text{CO}_2)_{\text{in}} = 8$  at  $\tau_p = 20 \text{ s}$ . Symbols: data measured with micro-GC. Curves: inlet flows. Conditions:  $T = 266 \text{ }^\circ\text{C}$ ,  $p = 1 \text{ MPa}$ ,  $\tau_{\text{mod}} = 1000 \text{ kg s}/\text{m}^3$ .

## N Industrial fixed bed reactor design for part-load and transient operation: extra figures

### N.1 Heat transport in fixed-bed reactor

Figure N.52 left shows an example axial temperature profiles calculated along the catalyst bed with the 1D model and the 2D model. The curve shape for both models is very similar. The accuracy of the 2D model is higher and the maximum temperature is reached for  $r = 0$  as expected. Figure N.52 right shows the radial temperature profile at  $z = 0.6$ , where the maximum temperature occurs. The temperature difference between  $r_t = 0$  and  $r_t = r_{t,max}$  is 14 °C (Figure N.52 right).

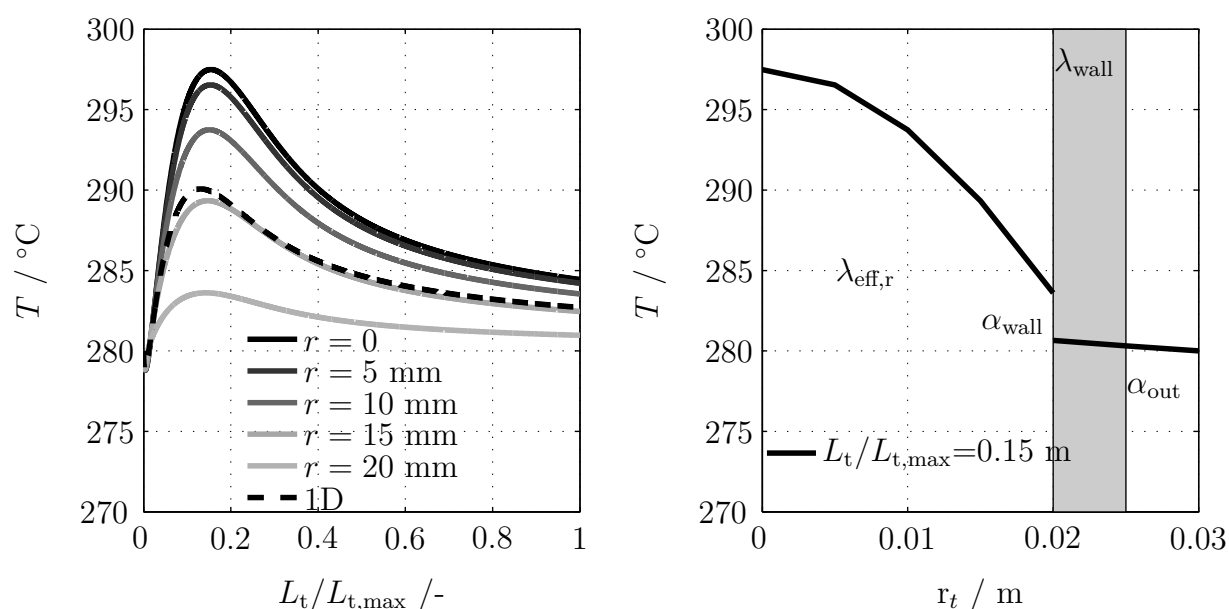


Figure N.52: Axial and radial temperature profiles in fixed-bed reactor. Left: calculated with one and two dimensional model. Right: calculated with two dimensional model for  $z = 0.6$  m. Example reaction characteristics, Table 8.1, operation conditions:  $T_{\text{in}} = T_{\text{cooling}} = 280$  °C,  $p = 2$  MPa,  $\overline{u_{sf}} = 0.37$  m/s,  $X_{\text{CO}_2} = 0.2$ . Catalyst particle:  $d_p = 0.003$  m,  $\chi_{\text{shell}} = 150$   $\mu\text{m}$ . Reactor geometry:  $L_t = 4$  m  $d_t = 4$  cm

Table N.20 shows a range of values for the different heat transfer coefficients in fixed bed reactor. Figure N.53 represents the two most important coefficients,  $\alpha_{\text{wall}}$  and radial conductivity for a  $d_t = 3$  cm versus superficial gas velocity. Figure N.54 shows the heat transfer coefficient for  $d_t = 6$  cm and the radial conductivity, significantly lower than in the case of  $d_t = 3$  cm.

Figure N.55 shows the effect of superficial gas velocity and particle size for the heat transfer coefficient and the pressure drop for a  $d_t = 3$  cm.

Table N.20: Heat transport coefficients in fixed-bed reactor calculated for  $u_{sf} = 0.001-3$  m/s,  $d_p = 3 \cdot 10^{-3}$  m and  $d_t = 3 \cdot 10^{-2}$  m

Symbol	Range of values	Units
$\alpha_{wall}$	670 – 2500	W/m <sup>2</sup> K
$\lambda_{eff,r}$	1.1-9.0	W/ m K
$\frac{4 \cdot \lambda_{eff,r}}{r_t}$	300-2400	W/m <sup>2</sup> K
$\lambda_{wall}$	50	W/ m K
s	$5 \cdot 10^{-3}$	m
$\frac{\lambda_{wall}}{s}$	$1 \cdot 10^4$	W/m <sup>2</sup> K
$\alpha_{out}$	$1 \cdot 10^4$	W/m <sup>2</sup> K
$U_{eff}$	200-990	W/m <sup>2</sup> K

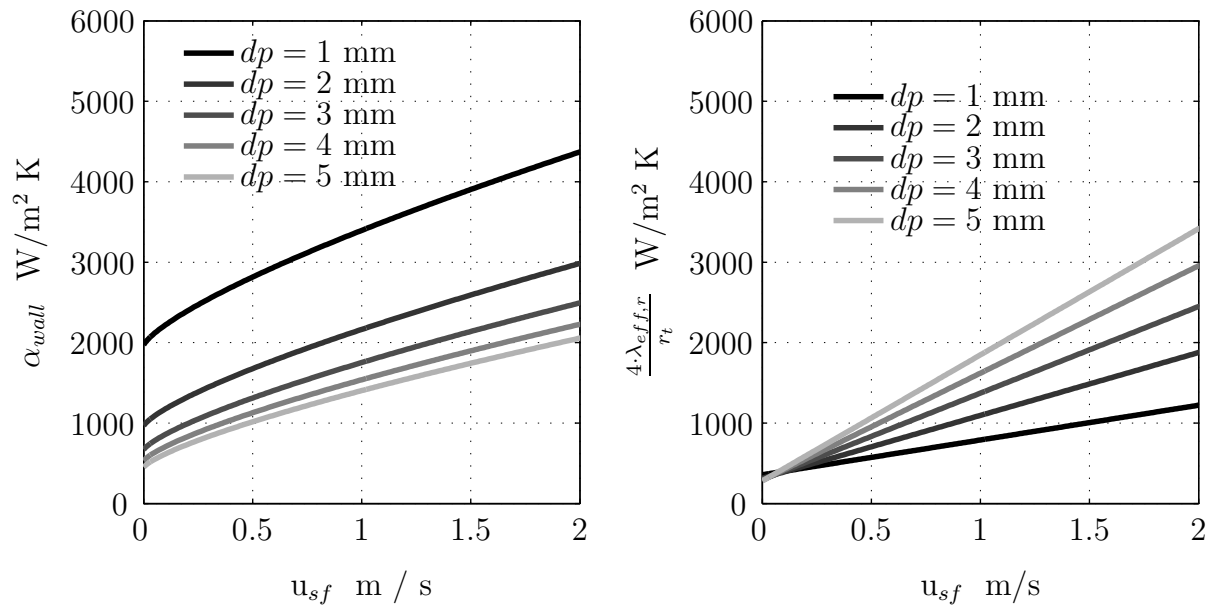


Figure N.53: Terms of the overall heat transport coefficient. Heat transfer coefficient in the reactor wall and effective radial thermal conductivity in the catalyst bed as a function of superficial gas velocity and particle diameter.  $d_t = 0.03$  m  $\chi_{shell} = 200 \mu\text{m}$ . Gas properties calculated at  $T = 280$  °C,  $p = 2$  MPa,  $X_{CO_2} = 0.1$ .

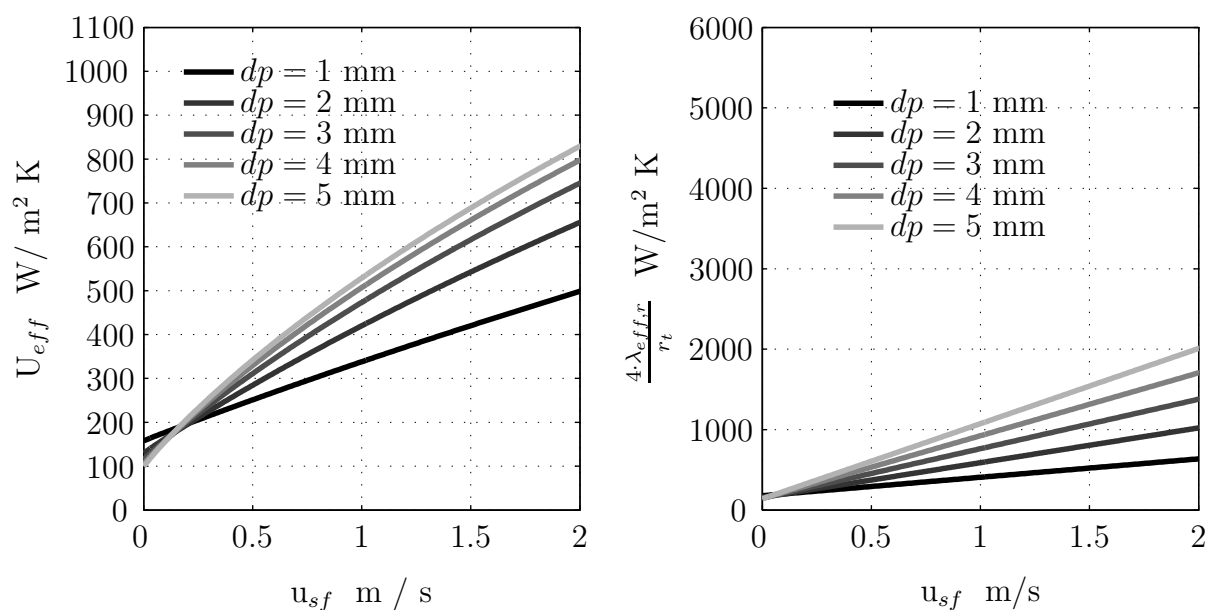


Figure N.54: Overall heat transfer coefficient and effective radial thermal conductivity in the catalyst bed as a function of superficial gas velocity and particle diameter.  $d_t = 0.06$  m,  $\chi_{shell} = 200$   $\mu m$ . Gas properties calculated at  $T = 280$   $^{\circ}C$ ,  $p = 2$  MPa,  $X_{CO_2} = 0.1$ .

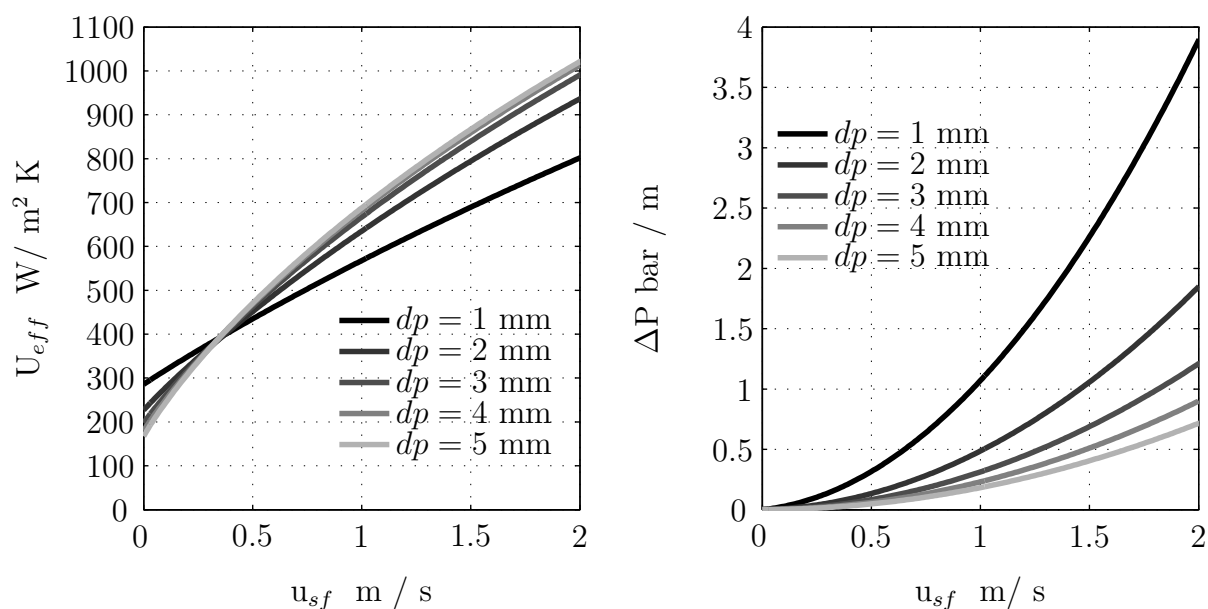


Figure N.55: Heat transfer coefficient and pressure drop (8.4) as a function of superficial gas velocity and particle diameter.  $d_t = 0.03$  m,  $\chi_{shell} = 200$   $\mu m$ . Gas properties calculated at  $T = 280$   $^{\circ}C$ ,  $p = 2$  MPa,  $X_{CO_2} = 0.1$ . Complementary figures with the separated heat transport coefficients and the effect of the  $d_t$  on the heat transfer coefficient can be find in appendix N.1

The calculation of the active density is a function of the  $d_p$  and  $\chi_{shell}$  (Equation N.56)

$$\rho_{active,R} = \frac{m_{active}}{V_p} = \frac{\rho_{p,s} \cdot (V_p - V_s)}{V_p} = \frac{\rho_{p,s} \cdot 4/3 \cdot \pi \left( \left( \frac{d_p}{2} \right)^3 - \left( \frac{d_p}{2} - \chi_{shell} \right)^3 \right)}{4/3 \cdot \pi \cdot \left( \frac{d_p}{2} \right)^3} \quad (N.56)$$

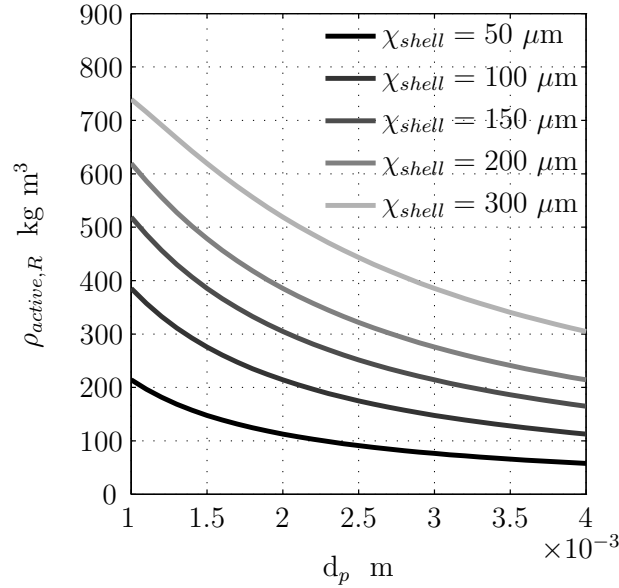


Figure N.56: Active mass density for reactor volume as a function of particle diameter and thickness of active material. Assuming sphere particles and  $\varepsilon = 0.4$  for the reactor bed. Values for active material and support see Table 8.5.



## N.2 Evaluation of criteria to use a pseudo-homogeneous mathematical model to describe the fixed-bed reactor

Table N.21 shows that it is not completely justified to use of a pseudohomogeneous model. At the reactor inlet the reaction rate is relative high and the reaction suffers from external heat transport limitations in the catalyst film (around 14 cm of the catalyst bed). The criteria are fulfilled according to the outlet and average values. The criteria are defined in Table J.13.

Table N.21: Evaluation of the criteria that allowed the use of a pseudohomogeneous model at three positions in the fixed bed recycle reactor: inlet, outlet and average reactor bed for the CO<sub>2</sub> hydrogenation reaction. The value of  $\frac{R \cdot T}{E_A} = 0.039$ .  $L_t = 3.14$  m  $d_t = 0.03$ m

	Da II < 0.3 Eq.J.42	w < 0.6 Eq.J.44	Da III < 0.012 Eq.J.43	Da IV < 0.16 Eq.J.45
$L_{\max} = 1$				
$z = 0$	$6.7 \cdot 10^{-2}$	$9.0 \cdot 10^{-2}$	$3.1 \cdot 10^{-2}$	$3.4 \cdot 10^{-2}$
$z = L$	$1.8 \cdot 10^{-3}$	$2.2 \cdot 10^{-3}$	$4.9 \cdot 10^{-4}$	$5.0 \cdot 10^{-4}$
$z = \bar{z}$	$4.9 \cdot 10^{-3}$	$6.2 \cdot 10^{-3}$	$1.1 \cdot 10^{-3}$	$1.2 \cdot 10^{-3}$
$L_{\min} = 0.70$				
$z = 0$	$9.1 \cdot 10^{-2}$	$9.0 \cdot 10^{-2}$	$3.8 \cdot 10^{-2}$	$3.0 \cdot 10^{-2}$
$z = L$	$1.7 \cdot 10^{-3}$	$1.5 \cdot 10^{-3}$	$4.6 \cdot 10^{-4}$	$3.3 \cdot 10^{-4}$
$z = \bar{z}$	$5.0 \cdot 10^{-3}$	$4.5 \cdot 10^{-3}$	$1.1 \cdot 10^{-3}$	$8.2 \cdot 10^{-4}$

### N.3 Reactor with recycle: recycle compressor and separation units

For a certain overall conversion in a reactor with recycle, once the conversion per pass is fixed, the recycle ratio can be calculated with Equation N.57 and Equation N.58, i.e. two equations and two unknowns. Results in Table N.22.

$$X_{i,pp} = \frac{F_{n,i,F} \cdot (1 + R_F) - F_{n,i,out}}{F_{n,i,F} \cdot (1 + R_F)} = 1 - \frac{F_{n,i,R}}{R_{out} \cdot F_{n,i,F} \cdot (1 + R_F)} = 1 - \frac{R_F}{(1 + R_F) \cdot R_{out}} \quad (\text{N.57})$$

$$X_{i,overall} = 1 - \frac{F_{n,i,out} \cdot (1 - R_{out})}{F_{n,i,F}} = 1 - \frac{F_{n,i,R} \cdot (1 - R_{out})}{R_{out} \cdot F_{n,i,F}} = 1 - \left( \frac{(1 - R_{out}) \cdot R_F}{R_{out}} \right) \quad (\text{N.58})$$

Table N.22: Conversion per pass, recycle ratio based on fresh feed and recycle ratio based on outlet flow for an overall conversion of 90 %. Calculated with equations N.57 and N.58

$X_{i,pp}$	$R_F$	$R_{out}$
0.10	8.00	0.99
0.20	3.50	0.97
0.30	2.00	0.95
0.40	1.25	0.93
0.50	0.80	0.89
0.60	0.50	0.83
0.70	0.29	0.74
0.80	0.13	0.56

#### N.3.1 Recycle compressor

Equation N.59 and values in Table N.23 are used to calculate the electric power required by the recycle compressor (Luyben 2007).

$$W_{\text{compressor,R}} = \frac{R \cdot T_s \cdot \gamma}{(1 - \gamma) \cdot \eta} \cdot \left[ \left( \frac{P_r}{P_s} \right)^{\frac{\gamma-1}{\gamma}} - 1 \right] \cdot F_{n,R} \quad (\text{N.59})$$

Table N.23: Values used to calculate the work of the recycle compressor. R is the universal gas constant

Name	Symbol	Units	Value
Compression temperature	$T_s$	K	313
Ratio of specific heats	$\gamma$	-	1.375 <sup>1</sup>
Compressor efficiency	$\eta$	-	1
Pressure outlet of the compressor	$P_r$	bar	20
Pressure inlet of the compressor	$P_s$	bar	varies

<sup>1</sup>  $\gamma$  is calculated assuming a mixture of H<sub>2</sub> ( $\gamma=1.405$ ), CO<sub>2</sub> ( $\gamma=1.289$ ) and CO ( $\gamma=1.4$ ) in proportion 70 %- 25 %- 5% respectively

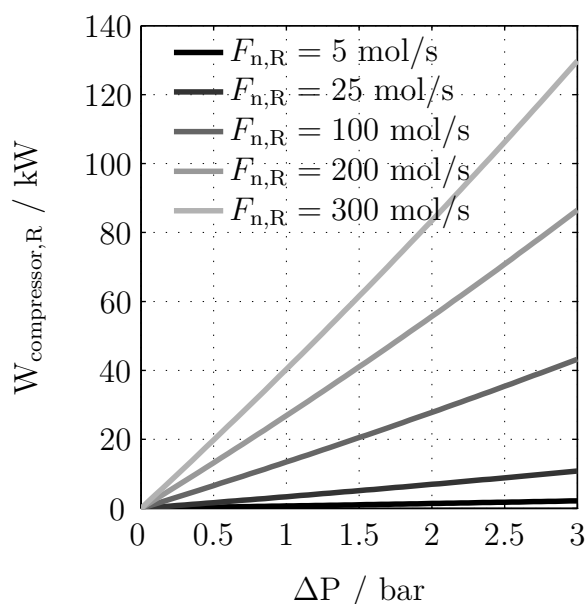


Figure N.57: Work of the recycle compressor as a function of molar flow and pressure drop in the reactor.  $P_s$  is the pressure reactor outlet calculated with equation N.59 and values of Table N.23 (the pressure drop in the separation units is not considered).

### N.3.2 Separation units needed for the CO<sub>2</sub> hydrogenation to gaseous hydrocarbons

Figure N.58 shows the process units required for the separation of the gaseous products to be able to recirculate CO<sub>2</sub>, CO and H<sub>2</sub>. The pressure along the separation units can be

maintained close to the pressure at reactor outlet but temperature needs to be strongly decrease (cryogenic temperatures). In case  $\text{CO}_2$  is coming from a biogas plant,  $\text{CO}_2$  separation could be shared by both processes.

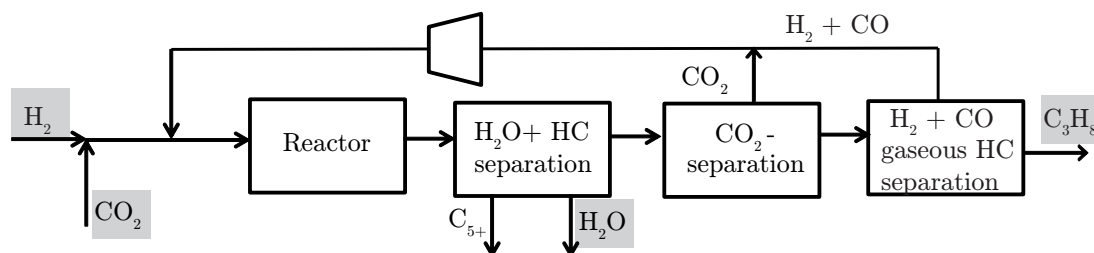


Figure N.58: Separation chain processes proposed for the  $\text{CO}_2$  hydrogenation to short chain hydrocarbons

#### N.4 Design procedure for a recycle system with only temperature limitations

Figure N.59 shows the design procedure proposed for a reaction without constraints in the presence of products but with temperature limitations.

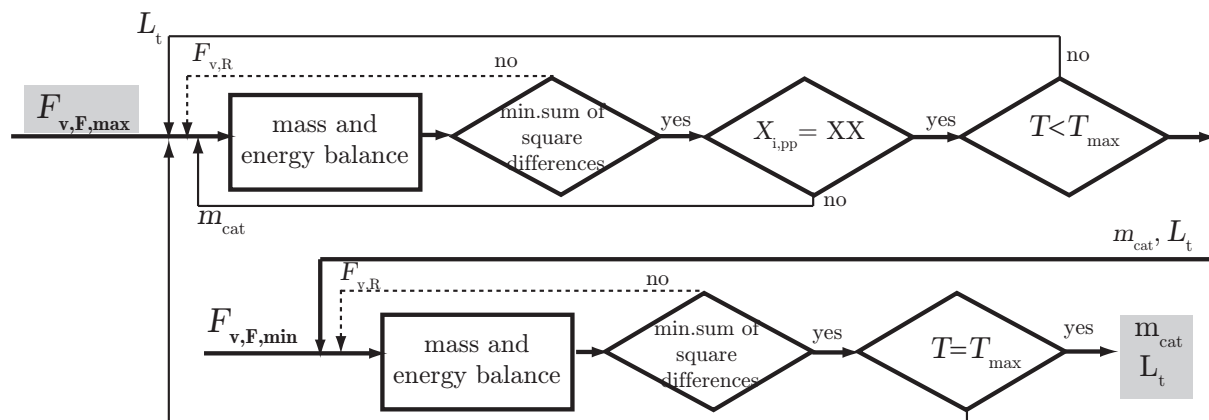


Figure N.59: Procedure followed to determine the catalyst mass  $m_{\text{cat}}$  and the tube length  $L_t$  for fixed values of  $L_{\text{min}}$  and  $d_t$  for a system with recycle with restriction in temperature. The  $X_{i,\text{pp}}$  is a design variable. Constant values for the design variables in Table 8.3 and an average flow  $F_{v,\text{CO}_2,\text{average}}$  need to be selected.

If the reaction is only restricted by temperature, the conversion per pass appears as an extra design variable that can be optimised (Figure N.59). A further advantage compared with a chemical reaction with partial pressure constraints and temperature limitations is that the mass of catalyst could be calculated for the maximum flow using the selected

conversion per pass. Calculations with the minimum flow give as result the tube length, which guarantees that the maximum temperature is not exceeded. The selection of the conversion value per pass for the maximum volumetric flow is a compromise between the mass of catalyst and the size of the recycle compressor. The extreme case would be a one-pass reactor where no recycle compressor is needed and the mass of catalyst is designed to reach the overall conversion. High conversion per pass requires a high mass of the catalyst, but, due to the small recycle ratio, energy demand for the compressor will be low. When operated at lower loads, part of the catalyst might not be used because full conversion can be reached before reactor outlet, and consequently no recycle is required. On the contrary, if the selected conversion per pass is low, a smaller mass of the catalyst is required but more energy is demanded for the compressor due to the higher recycle ratio. Low conversion per pass might be an option for reactions with a high heat effect because, due to the smaller reactors, a recycle might exist at minimum flow, also making the heat transfer more efficient due to the higher gas velocity.

## N.5 Reference case recycle system: extra figures

Figure N.60 shows the partial pressure profiles along the catalyst bed for maximum and minimum load in the recycle reactor. Figure N.61 shows pressure drop and superficial gas velocity along the catalyst bed for maximum and minimum load in the designed recycle reactor.

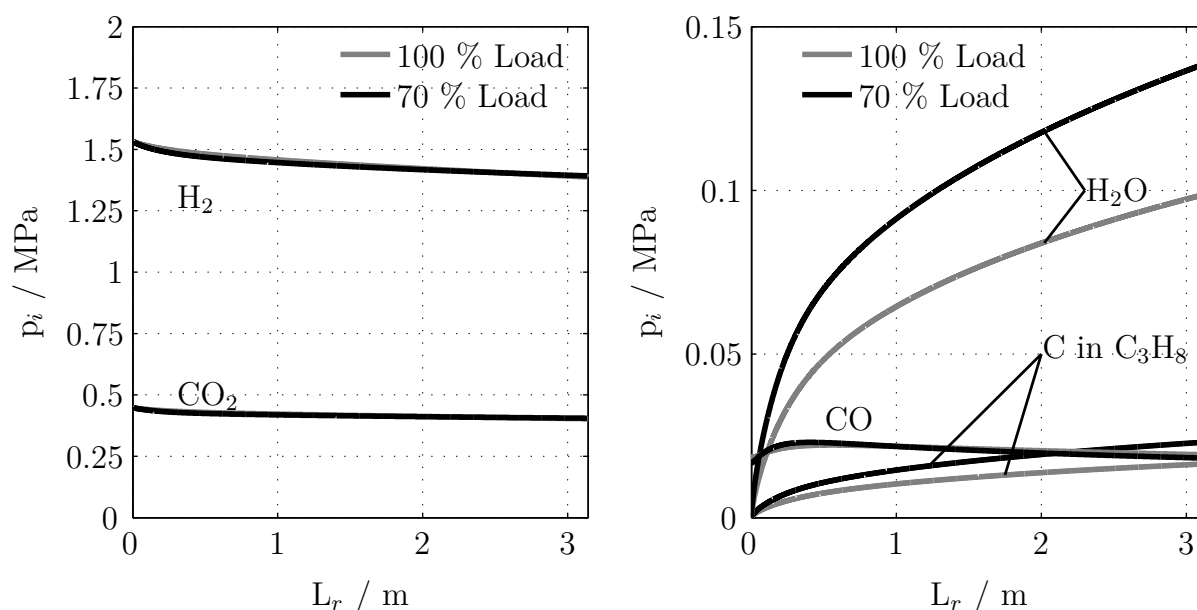


Figure N.60: Partial pressures of reactants and products along the catalyst bed for maximum and minimum operation load

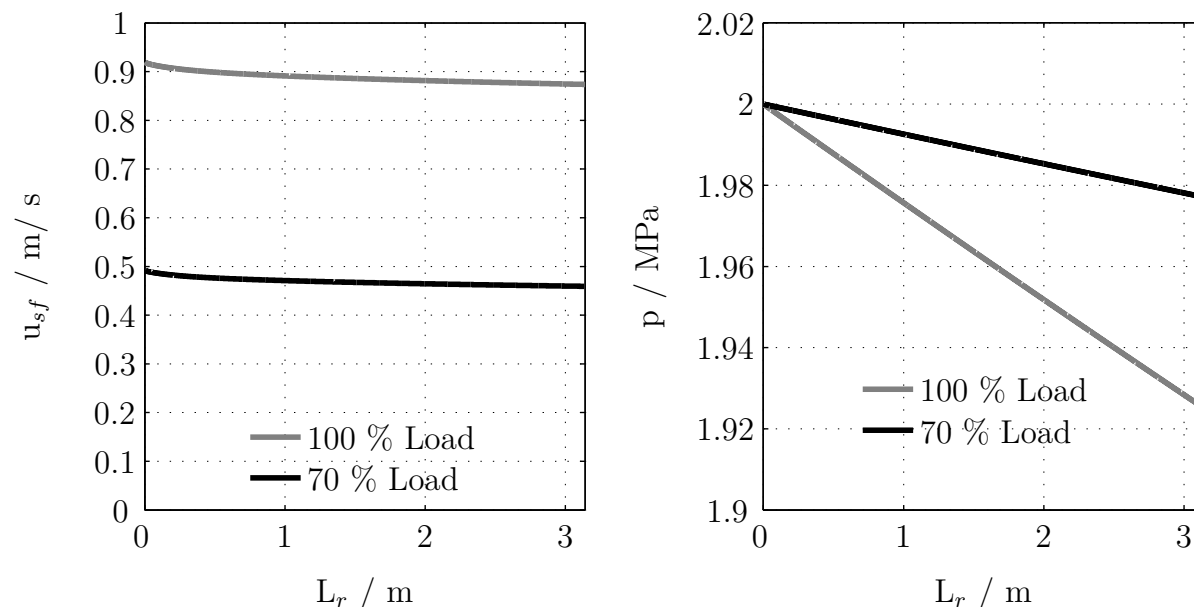


Figure N.61: Superficial gas velocity and pressure drop along the catalyst bed for maximum and minimum operation load for the  $\text{CO}_2$  hydrogenation to gaseous hydrocarbons

Reaction rate is strong influenced by the partial pressure of  $\text{H}_2\text{O}$ . Figure N.62 shows variations of the kinetic constant, numerator and denominator related to the values at  $z = 0$ . An increase of factor 90 is observed for the denominator and can be explained due to the formation of  $\text{H}_2\text{O}$ , that strong inhibits the reaction rate.

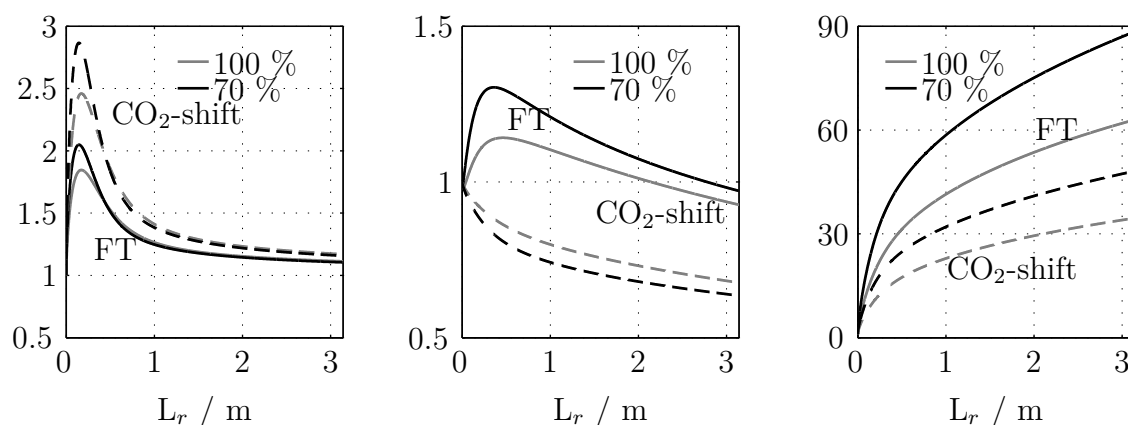


Figure N.62: Terms involved in the reaction rate equations (in Table 6.1 and Table 6.2) along the catalyst bed relative to the value at  $z = 0$  (dimensionless). Left: kinetic constants. Middle: nominator. Right: denominator. Curves: Fischer-Tropsch: continuous;  $\text{CO}_2$ -shift: dashed; maximum load (grey) and minimum load (black).

## N.5.1 Effect of design variables on recycle system design

### Effect of tube diameter on recycle system

For the reference case, a tube diameter of 3 cm is selected, this is the smallest possible tube diameter when using 3 mm particles ( $d_t/d_p \geq 10$ ). The effect of a larger tube diameter on reactor design is shown in Table N.24 for a reactor flexibility of  $L_{\min} = 0.7$ .

An increase in the tube diameter decreases the radial heat transfer efficiency and, for a constant gas velocity, the overall heat transfer coefficient would be lower (Equation 8.6, Figure N.54 and Figure N.55). An increase in the gas velocity per tube is required to improve the overall heat transfer coefficient and not exceed the maximum temperature ( $T_{\max} = 300$  °C). For a certain inlet flow, an increase in gas velocity per tube can be achieved by a reduction in the number of tubes. A lower number of tubes requires longer tubes.

The effect of longer tubes can be seen by the higher pressure drop at minimum and maximum flow. The required  $m_{\text{cat}}$  increases slightly with  $d_t$  as average reaction rates are lower due to the lower pressure level. At maximum load, the effect of pressure drop is more significant and leads to a lower conversion per pass and higher recycle ratio, in comparison with the reference case. The increase in pressure drop and recycle ratio correlates directly with an increase in the electric power required by the recycle compressor.

An increase in  $d_t$  involves a decrease in the number of tubes, and consequently also on the vessel size leading to a lower investment cost. However, due to the longer tubes, the power demand for the recycle compressor increases, which indicates higher operational costs.

Table N.24: Example reactor designs for the CO<sub>2</sub> hydrogenation for a  $T_{\max} = 300$  °C for three tube diameters  $d_t$  and  $L_{\min} = 0.7$ . Catalyst particle:  $d_p = 0.003$  m and  $\rho_{\text{active,R}} = 214.07$  kg/m<sup>3</sup>.  $X_{\text{ov}} \geq 0.9$ .

$d_t$	$L_t$	NT	$m_{\text{cat}}$	$V_r$	$R_{\text{out}}$	L= 0.7			L= 1			
						$X_{\text{ov}}$	$\Delta p$	$R_F$	$X_{i,\text{pp}}$	$\Delta p$	$R_F$	$P_{\text{el,R-c}}$
m	m	-	t	m <sup>3</sup>	-	-	bar	-	-	bar	-	kW
0.030	3.14	956	0.45	2.12	0.988	0.93	0.23	5.55	0.11	0.75	7.56	23.83
0.035	4.99	449	0.46	2.16	0.988	0.93	0.83	5.55	0.10	2.90	7.92	104.27
0.040	7.35	247	0.49	2.28	0.990	0.94	2.32	5.68	0.09	9.08	9.43	510.43

Figure N.63 shows pressure drop along the catalyst bed for the three different tube dia-

meter  $d_t$ . The tube diameter influences the reactor length, and consequently the pressure drop. Density and viscosity are strongly influenced by pressure, therefore curves are calculated at  $p = 1.5$  MPa and  $p = 2$  MPa. In the calculations for the symbols, density and viscosity are calculated for each differential length along the catalyst bed using the complete mathematical model of the fixed-bed reactor.

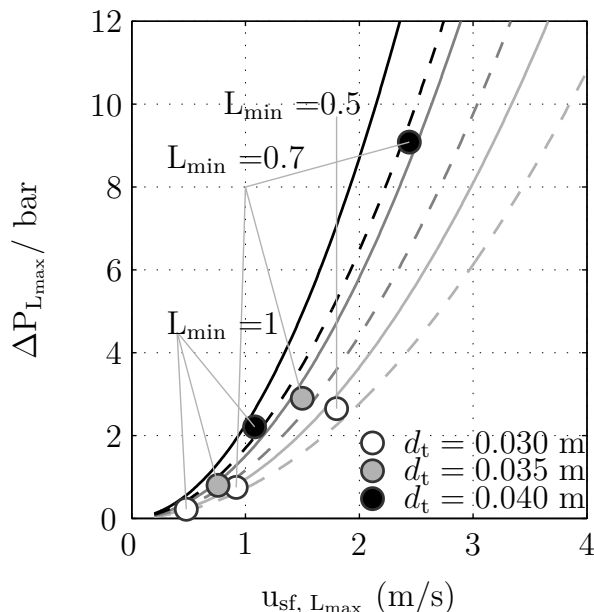


Figure N.63: Pressure drop as a function of superficial gas velocity (average value along catalyst bed) for maximum load. Symbols: results from calculations at different  $L_{\min}$  and tube diameter, white symbols  $d_t = 0.030$  m, grey symbols  $d_t = 0.035$  m and black symbols  $d_t = 0.040$  m. Curves calculated with Ergun equation (Equation 8.4) at  $T = 280$  °C,  $(\text{H}_2/\text{CO}_2)_{\text{in}} = 10/3$ ,  $\varepsilon = 0.4$  and  $d_p = 3$  mm. Dashed curves:  $p = 1.5$  MPa, continuous curves  $p = 2$  MPa. Black curve:  $L_t = 7.20$  m, grey curve  $L_t = 4.91$  m and light grey curve  $L_t = 3.08$  m.

### Effect of load range on reactor design

The effect of  $L_{\min}$  is evaluated for a constant  $F_{v,\text{CO}_2,\text{average}} = 500$  m<sup>3</sup>/h. At lower values of  $L_{\min}$ , the difference between  $F_{v,\text{CO}_2,\text{min}}$  and  $F_{v,\text{CO}_2,\text{max}}$  becomes larger, the minimum fresh flow decreases, and the maximum fresh flow increases with  $L_{\min}$  (Equation 8.7).

Reactor volume is calculated according to the minimum flow, therefore if  $L_{\min}$  decreases for a constant tube diameter, less mass of catalyst is required to reach the restriction  $(p_{\text{H}_2\text{O}}/p_{\text{H}_2})_{\text{out}}$  (desired conversion per pass). The geometry of the tubes remains constant (i.e.  $d_t = 3$  cm,  $L_t = 3.14$  m) as well as the flow per reactor tube, consequently the number of tubes required to reach the desired overall conversion is lower (Figure N.64, left and middle).



The maximum power required by the recycle compressor is calculated at maximum operation load. With decreasing  $L_{\min}$ , and for a constant tube diameter, reactors become smaller and  $F_{v,\text{CO}_2,\text{max}}$  higher. This combination results in low residence times, and even though the average reaction rate is higher than at minimum load, the conversion per pass decreases. Recycle flows get larger and, inevitably, gas velocity increases, resulting in an increase in pressure drop, and also consequently in the electric power required by the recycle compressor (Figure N.64, right).

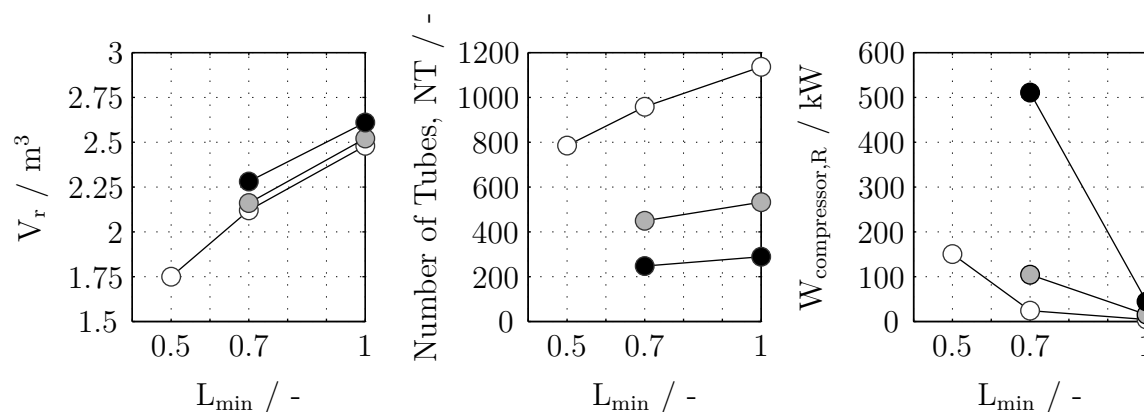


Figure N.64: Effect of specified load range (expressed as minimum load  $L_{\min}$ ) on the reactor design: volume, number of tubes, and electric power required by the recycle compressor at  $F_{v,\text{max}}$  ( $L = 1$ ) for three different tube diameters: white symbols  $d_t = 0.030$  m, grey symbols  $d_t = 0.035$  m, and black symbols  $d_t = 0.040$  m

In contrast with the reactor design for  $L_{\min} = 1$ , a reactor design for part-load operation needs to find a compromise between operation at the maximum and minimum flow. To increase the flexibility of a reactor from  $L_{\min} = 1$  to  $L_{\min} = 0.7$  two alternatives can be followed:

- maintain the same tube diameter as for  $L_{\min} = 1$ : require a less number of tubes, therefore a smaller reactor vessel but a higher power demand for the compressor when the reactor is operated at maximum load, due to the higher pressure drop (Example in Figure N.64,  $d_t = 0.03$  m for  $L_{\min} = 1$  and  $L_{\min} = 0.7$ ). Resulting in a lower investment cost and higher operating costs.
- select a smaller tube diameter than for  $L_{\min} = 1$ : the length of the tubes is decreased and consequently the number of tubes increased. The size of the reactor vessel becomes larger, however  $V_r$  is smaller. At high operation load, lower energy demand for the recycle compressor is required (Example in Figure N.64,  $L_{\min} = 1$  with  $d_t = 0.04$  m and  $L_{\min} = 0.7$  with  $d_t = 0.03$  m). Resulting in a higher investment cost and lower operating costs.

## N.6 Simulation of transient operation: extra figures

Figure N.65 shows the molar flows during a change in fresh feed volumetric flow from 100 to 70 % load with a rate of load change of 5 %/ min.

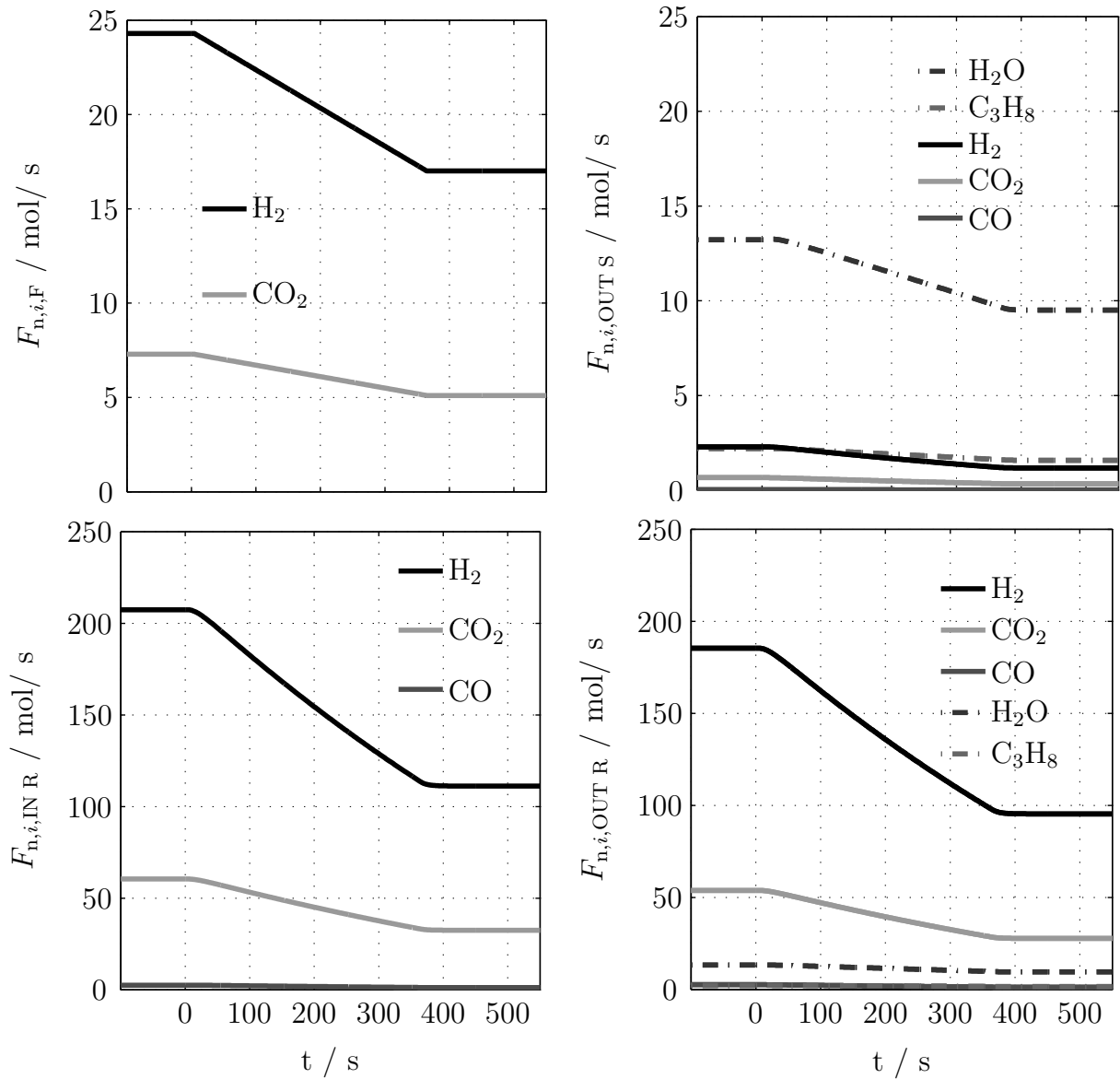


Figure N.65: Change in fresh feed molar flow (top left) from maximum operation load to 70 % with a rate of 5 %/ min. Outlet of the system (top right). Bottom: molar flows of components at reactor inlet (left) and reactor outlet (right)

Figure N.66 shows the dimensionless CO<sub>2</sub> concentration and volumetric flow at reactor outlet.

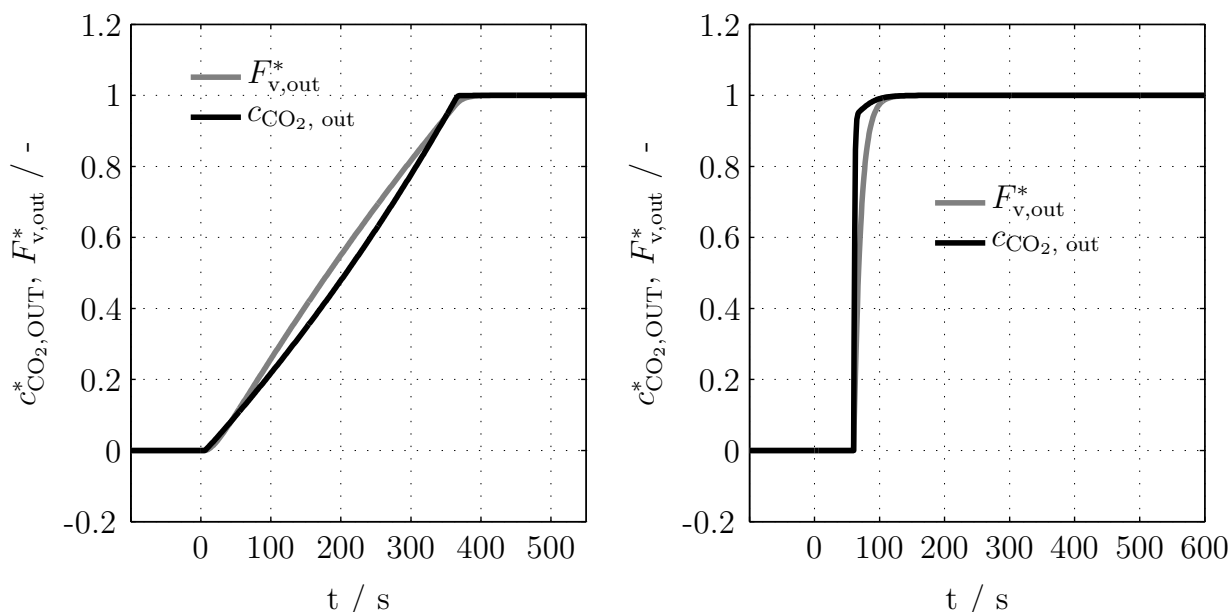


Figure N.66: Dimensionless changes of CO<sub>2</sub> outlet concentration and total volumetric flow after a change in fresh feed volumetric flow from 100 to 70 % load. Left: rate of load change 5% /min. Right: step change.

## N.7 Simulation of example load change in a recycle reactor 100 to 70 % : step change in fresh feed flow

Figure N.68, N.67 and N.69 show the a step change in fresh feed flow at  $t = 60$  s at constant inlet concentration.

Figure N.67 shows how molar flows decrease with time. The fresh feed flows become lower after the change and this influences the molar flows at reactor inlet and outlet, however due to the mixture of fresh feed and recycle, the change of the volumetric flow that affects the reactor is slower than a step change. At the lower operation load, the conversion per pass is higher and the concentration of products (H<sub>2</sub>O and C<sub>3</sub>H<sub>8</sub>) at reactor outlet is higher. Due to the lower volumetric flow the molar flow of H<sub>2</sub>O and C<sub>3</sub>H<sub>8</sub> become also lower with time. A maximum in the molar flow of H<sub>2</sub>O and C<sub>3</sub>H<sub>8</sub> is observed at reactor outlet right after the change. This maximum can be explained due to a faster increase of the H<sub>2</sub>O concentration during the first four seconds in comparison with the decrease in the volumetric flow (Figure N.66). After this four seconds the decrease in the volumetric flow dominates and lower the molar flow of H<sub>2</sub>O or C<sub>3</sub>H<sub>8</sub>.

Once the change in volumetric flow occurs, the recycle ratio is calculated with the recycle

flow still according to the previous operation load and an already low volumetric flow in the fresh feed, therefore a very high  $R_F$  is obtained (Figure N.68). The overall conversion shows a minimum at the moment of the change which indicates that the molar flow of  $\text{CO}_2$  in the fresh feed is already low and the flow at the outlet of the system is still according to the last operation load (still high). The dynamic response of the overall conversion, recycle ratio and conversion per pass is consequence of the slower changes at reactor outlet compared with the step change carried out in the fresh feed (Figure N.68).

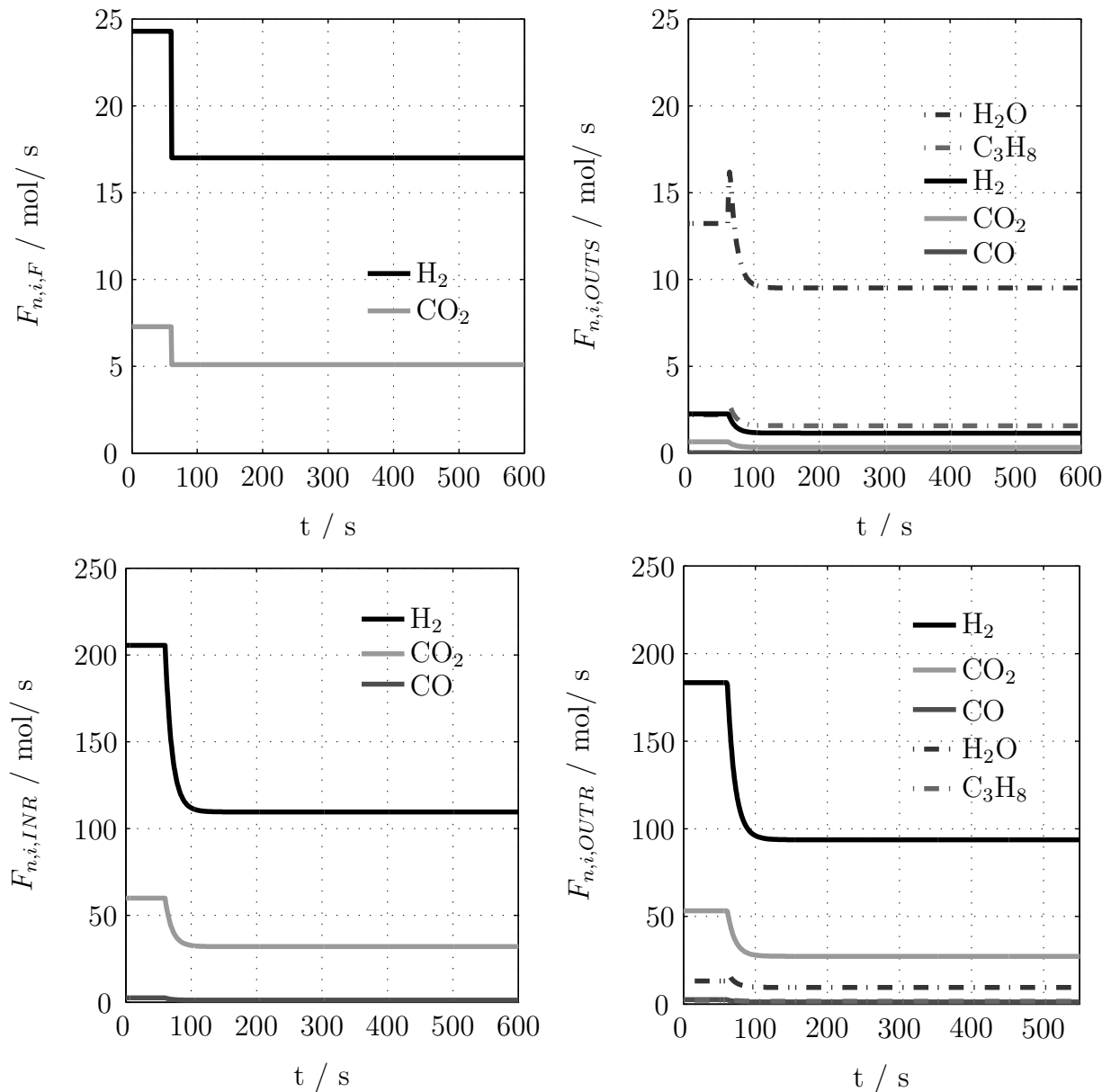


Figure N.67: Step change in the fresh feed from maximum operation load to 70 %.

Components molar flows in fresh feed, recycle flow, inlet and outlet of the reactor

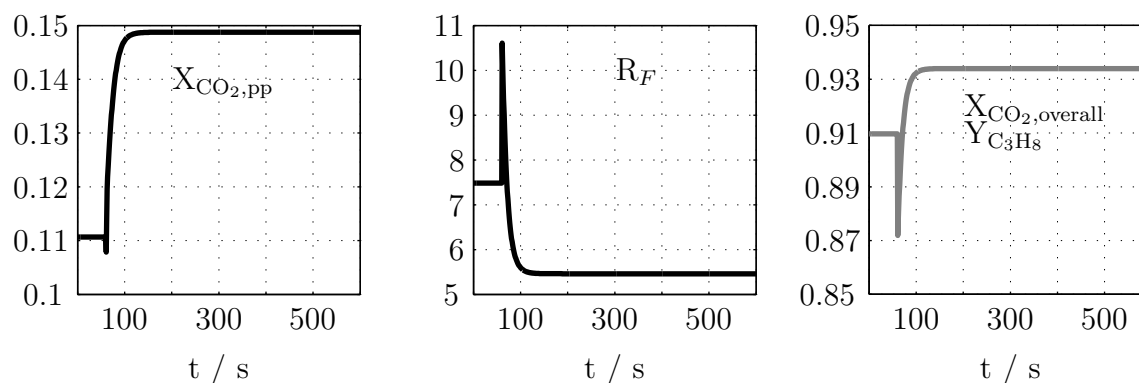


Figure N.68: Conversion per pass, recycle ratio and overall conversion after a step change in fresh feed flow

Figure N.69 shows that after 60 s of the change the temperature profile is close to the new steady state but not fully stationary. In contrast, the ratio  $\text{H}_2\text{O} / \text{H}_2$  is calculated along the catalyst bed for different times. It reaches the new steady state much faster than temperature. The resulting values are slightly higher than  $(p_{\text{H}_2\text{O}}/p_{\text{H}_2})_{\text{out}} = 0.1$  and  $T = 300 \text{ }^\circ\text{C}$  due to the discretization used for the transient calculation,  $\Delta z = 0.01 \text{ m}$  instead of  $\Delta z = 0.001 \text{ m}$ .

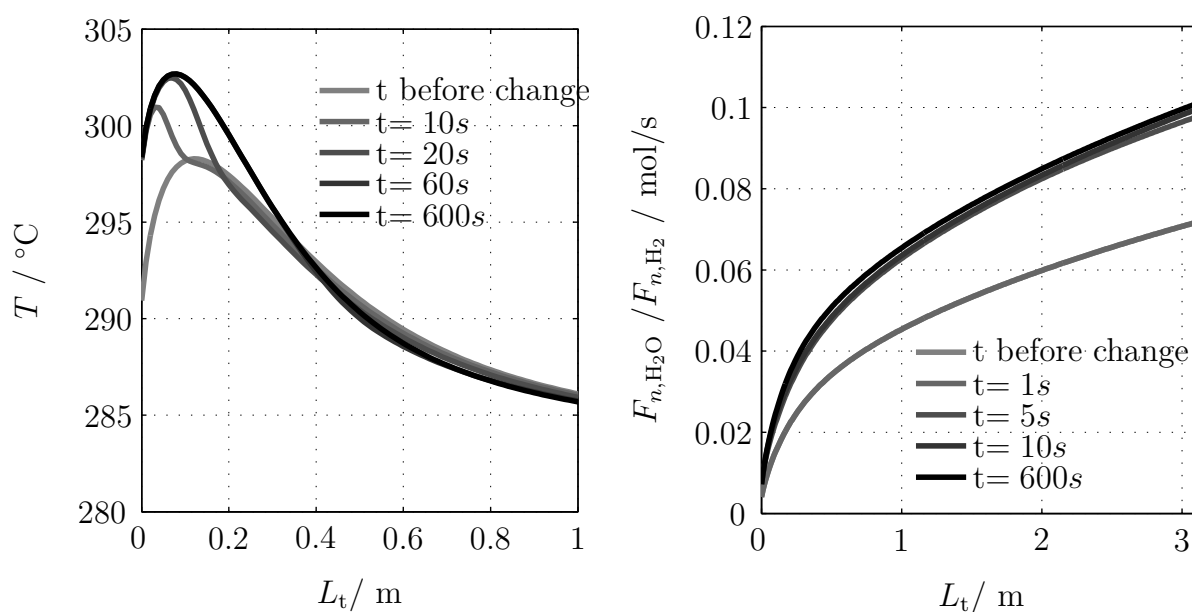


Figure N.69: Temperature and ratio of molar flows of  $\text{H}_2\text{O} / \text{H}_2$  along the catalyst bed at different times after a step change in volumetric flow. Calculations done with  $\Delta z = 0.01 \text{ m}$

## N.8 Characteristic times

Dimensionless mass and energy equations used to derive the characteristic times:

$$T^* = \frac{T}{T_0} \quad (\text{N.60}) \quad Z^* = \frac{z}{L_r} \quad (\text{N.61})$$

$$c^* = \frac{c}{c_i} \quad (\text{N.62}) \quad u^* = \frac{u_{sf}}{\bar{u}_{sf}} \quad (\text{N.63})$$

$$\frac{\partial c_i^*}{\partial t} = \frac{-[u^* \cdot \frac{\partial c_i^*}{\partial z^*} + c_i^* \cdot \frac{\partial u_{sf}^*}{\partial z^*}]}{\frac{\varepsilon \cdot L_r}{u_{sf}}} + \frac{1}{\frac{\varepsilon \cdot c_i}{\sum_{j=1}^N (v_{ij} \cdot r_j)}} \quad (\text{N.64})$$

$$\frac{\partial T^*}{\partial t} = \frac{-[T^* \cdot \frac{\partial u_{sf}^*}{\partial z} + u_{sf}^* \cdot \frac{\partial T^*}{\partial z}]}{\frac{\varepsilon \cdot \rho_g \cdot c_{p,g} + (1-\varepsilon) \cdot \rho_s \cdot c_{p,s}}{\rho_g \cdot c_{p,g}} \frac{u_{sf}}{L_r}} + \frac{(T^* - T_{cooling}/T_0)}{\frac{\varepsilon \cdot \rho_g \cdot c_{p,g} + (1-\varepsilon) \cdot \rho_s \cdot c_{p,s}}{\frac{4 \cdot U_{eff}}{d_t}}}} + \frac{1}{\frac{\varepsilon \cdot \rho_g \cdot c_{p,g} + (1-\varepsilon) \cdot \rho_s \cdot c_{p,s}}{\frac{(-\Delta_R H_j^0 \cdot r_j)}{T_0}}} \quad (\text{N.65})$$

Table N.25 shows the values for the transport coefficients and other quantities used to calculate the characteristic times.

Table N.25: Transport coefficient used to calculate the characteristic times. Conditions:  $T = 280$  °C,  $p = 2$  MPa,  $L_t = 3.14$  m,  $d_t = 0.03$  m  $V_r = 2.12$  m<sup>3</sup> and the corresponding average gas velocity. The gas composition is calculated with the average CO<sub>2</sub> conversion and  $(\text{H}_2/\text{CO}_2)_{in} = 10/3$ . Gas and catalyst properties in Table 8.4 and Table 8.5. Average CO<sub>2</sub>-shift reaction rate  $\bar{r}_i$ , see Figure 8.5, right.

Process	Symbol	Unit	$L_{max} = 1$	$L_{min} = 0.7$
Mass transport gas-particle	$\beta$	m/s	$5.1 \cdot 10^{-2}$	$3.7 \cdot 10^{-2}$
Internal diffusion	$D_{eff}$	m <sup>2</sup> / s	$3.1 \cdot 10^{-7}$	$3.1 \cdot 10^{-7}$
Heat transport gas-particle	$\alpha_{gas}$	W/ m <sup>2</sup> K	$1.9 \cdot 10^3$	$1.4 \cdot 10^3$
Thermal conductivity particle	$\lambda_p$	W/ m K	5.6	5.6
Average reaction rate	$\bar{r}_i$	mol/ m <sup>3</sup> s	3.1	2.2
Overall heat transfer coefficient	$U_{eff}$	W/ m <sup>2</sup> K	619.0	441.9
Average superficial gas velocity	$\bar{u}_{sf}$	m/ s	0.9	0.5
Average CO <sub>2</sub> conversion	$X_{CO_2}$	%	11.0	15.0

Figure N.70 indicates the relationship of characteristic times of chemical reaction and reactor cooling. If the characteristic time of the reaction is shorter than the time of cooling, a hot spot is observed because the generated heat can not be removed fast enough.

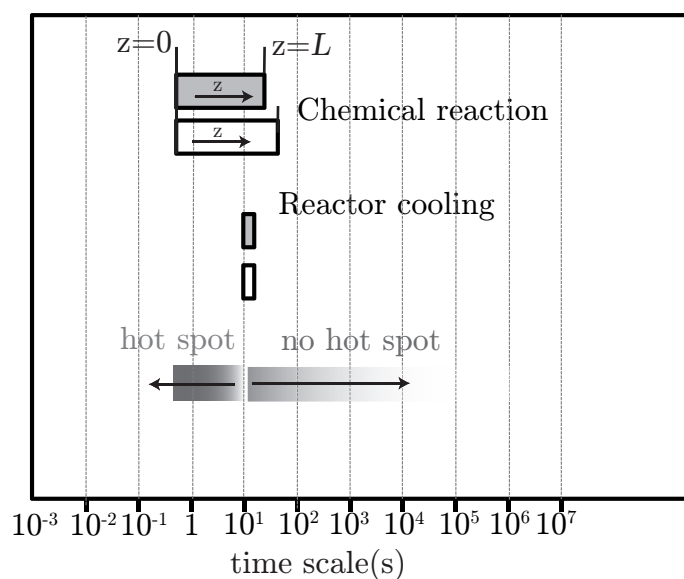


Figure N.70: Variation of the characteristic times along the catalyst bed using the formation of hot spot in fixed-bed reactor as example. Hot spot is the consequence when the chemical reaction is faster than the reactor cooling. Grey 100 % load, white 70 % load. Left end of horizontal bar: reactor inlet, right end of horizontal bar: reactor outlet.





# Curriculum Vitae

## Personal Information

Name: María Iglesias González  
Date of birth: 14/02/1986  
Place of birth: León (Spain)  
Nationality: Spanish

## Education

09/1989 - 06/2004 General grammar school, Colegio Manuel Peleteiro, Santiago de Compostela, Spain  
10/2004 - 05/2010 Study of Chemical Engineering, University of Santiago de Compostela (USC), Santiago de Compostela, Spain.  
07/2009 - 09/2009 Internship at Procter & Gamble, Brussels, Belgium.  
09/2009 - 05/2010 Diploma Thesis, Engler-Bunte-Institut at Karlsruhe Institute of Technology (KIT), Karlsruhe, Germany

## Work Experience

07/2010 - 09/2010 Research assistant, Engler-Bunte-Institut at Karlsruhe Institute of Technology (KIT), Germany.  
10/2010 - 09/2015 Research Fellow, Engler-Bunte-Institut at Karlsruhe Institute of Technology (KIT), Germany.

**Publications (related to doctoral thesis)**

Schaub G., Eilers H., Iglesias González M., *Chemical Storage of Renewable Electricity via Hydrogen - Principles and Hydrocarbon fuels as Example*, Chapter 30 in: D.Stolten, V. Scherer (Ed), *Transition to Renewable Energy Systems*, Wiley-VCH Verlag, Weinheim, 2013, 619-628

Iglesias González M., Edzang R., Schaub G., *Combinations of CO/CO<sub>2</sub> Reactions with Fischer-Tropsch Synthesis*, *Catalysis Today*, 215, 2013, 194-200, DOI: 10.1016/j.cattod.2013.04.019

Aicher Th., Iglesias González M., Schaub G., Götz M., *Power-to-Gas - Betrachtungen des Gesamtsystems im Hinblick auf Dynamik und Prozessintegration*, *Energie-Wasser-Praxis*, 11, 2014, 51-55 (in SEE-Spezial Power-to-Gas pp. 28-59)

Iglesias González M., Schaub G., *Power-to-Gas - Brennwertanpassung von Erdgas-Ersatzgas*, *Energie-Wasser-Praxis*, 11, 2014, 48-50, (in SEE-Spezial Power-to-Gas pp. 28-59)

Iglesias González M., de Vries C., Claeys M., Schaub G., *Chemical Energy Storage in Gaseous Hydrocarbons via Iron Fischer-Tropsch Synthesis from H<sub>2</sub>/CO<sub>2</sub> - Kinetics, Selectivity and Process Considerations*, *Catalysis Today* 242.A, 2015, 184-192, DOI: 10.1016/j.cattod.2014.05.020

Iglesias González M., Schaub G., *Fischer-Tropsch Synthesis with H<sub>2</sub>/CO<sub>2</sub> - Approach to Study Catalyst Behaviour under Transient Conditions*, *Chem.-Ing.-Tech.*, 87 (6), 2015, 848-854, DOI: 10.1002/cite.201400137

Iglesias González M., Schaub G., *Gaseous Hydrocarbon Synfuels from Renewable Electricity via H<sub>2</sub>/CO<sub>2</sub> - Flexibility of Fixed Bed Catalytic Reactors*, *Int. Journal of Chem. Reactor Eng.*, 2015, DOI: 10.1515/ijcre-2014-0135

Iglesias González M., Eilers H., Schaub G., *Flexible Operation of Fixed-Bed reactors for a Catalytic Fuel Synthesis - CO<sub>2</sub> Hydrogenation as Example Reaction*, *Energy Technology*, 2015, DOI: 10.1002/ente.201500259

Fischer N., Henkel R., Hettel B., Iglesias González M., Schaub G., Claeys M., *Hydrocarbons via CO<sub>2</sub> Hydrogenation over Iron Catalyst - the Effect of Potassium on Structure and Performance*, *Catal. Lett.*, 2015, 1-9, DOI: 10.1007/s10562-015-1670-9

**Oral presentations**

Iglesias González M., *Chemical Energy Storage in SNG Components via Fischer-Tropsch Synthesis from  $H_2/CO_2$  - Kinetics, Selectivity and Process Considerations*, XI<sup>th</sup> European Congress on Catalysis (Europacat), Lyon (FR), 2013. Oral Presentation in Discussion Symposia and Poster Presentation

Iglesias González M., *Gaseous Hydrocarbons Synfuels from Renewable Electricity via  $H_2/CO_2$  - Flexibility of Fixed-Bed Catalytic Reactors*, 4<sup>th</sup> International Congress on Green Process Engineering, Sevilla (ES), 2014. Keynote Presentation

Iglesias González M., *Flexible Operation of Catalytic Fuel Synthesis Reactors - Experimental and Modeling Analysis of Fixed-Bed Reactors*, Energy, Science & Technology (EST), Karlsruhe (DE), 2015.